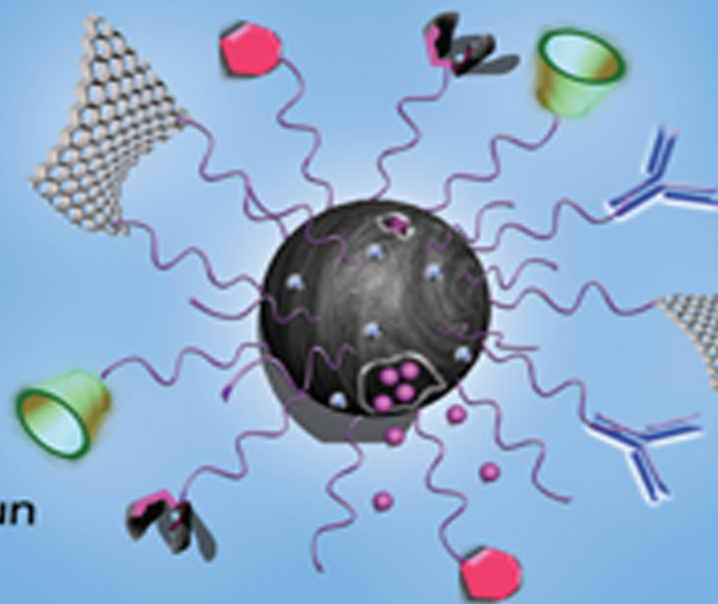


Advanced Materials Series

ADVANCED FUNCTIONAL MATERIALS

Edited by
Ashutosh Tiwari
and Lokman Uzun



 Scrivener
Publishing

WILEY

Advanced Functional Materials

Scrivener Publishing

100 Cummings Center, Suite 541J
Beverly, MA 01915-6106

Advanced Materials Series

The Advanced Materials Series provides recent advancements of the fascinating field of advanced materials science and technology, particularly in the area of structure, synthesis and processing, characterization, advanced-state properties, and applications. The volumes will cover theoretical and experimental approaches of molecular device materials, biomimetic materials, hybrid-type composite materials, functionalized polymers, supramolecular systems, information- and energy-transfer materials, biobased and biodegradable or environmental friendly materials. Each volume will be devoted to one broad subject and the multidisciplinary aspects will be drawn out in full.

Series Editor: Dr. Ashutosh Tiwari

Biosensors and Bioelectronics Centre
Linköping University
SE-581 83 Linköping
Sweden
E-mail: ashutosh.tiwari@liu.se

Publishers at Scrivener

Martin Scrivener(martin@scrivenerpublishing.com)
Phillip Carmical (pcarmical@scrivenerpublishing.com)

Advanced Functional Materials

Edited by

Ashutosh Tiwari and Lokman Uzun



WILEY

Copyright © 2015 by Scrivener Publishing LLC. All rights reserved.

Co-published by John Wiley & Sons, Inc. Hoboken, New Jersey, and Scrivener Publishing LLC, Salem, Massachusetts.

Published simultaneously in Canada.

No part of this publication may be reproduced, stored in a retrieval system, or transmitted in any form or by any means, electronic, mechanical, photocopying, recording, scanning, or otherwise, except as permitted under Section 107 or 108 of the 1976 United States Copyright Act, without either the prior written permission of the Publisher, or authorization through payment of the appropriate per-copy fee to the Copyright Clearance Center, Inc., 222 Rosewood Drive, Danvers, MA 01923, (978) 750-8400, fax (978) 750-4470, or on the web at www.copyright.com. Requests to the Publisher for permission should be addressed to the Permissions Department, John Wiley & Sons, Inc., 111 River Street, Hoboken, NJ 07030, (201) 748-6011, fax (201) 748-6008, or online at <http://www.wiley.com/go/permission>.

Limit of Liability/Disclaimer of Warranty: While the publisher and author have used their best efforts in preparing this book, they make no representations or warranties with respect to the accuracy or completeness of the contents of this book and specifically disclaim any implied warranties of merchantability or fitness for a particular purpose. No warranty may be created or extended by sales representatives or written sales materials. The advice and strategies contained herein may not be suitable for your situation. You should consult with a professional where appropriate. Neither the publisher nor author shall be liable for any loss of profit or any other commercial damages, including but not limited to special, incidental, consequential, or other damages.

For general information on our other products and services or for technical support, please contact our Customer Care Department within the United States at (800) 762-2974, outside the United States at (317) 572-3993 or fax (317) 572-4002.

Wiley also publishes its books in a variety of electronic formats. Some content that appears in print may not be available in electronic formats. For more information about Wiley products, visit our web site at www.wiley.com.

For more information about Scrivener products please visit www.scrivenerpublishing.com.

Cover design by Russell Richardson

Library of Congress Cataloging-in-Publication Data:

ISBN 978-1-118-99827-4

Printed in the United States of America

10 9 8 7 6 5 4 3 2 1

Contents

Preface xv

Part 1: Functional Metal Oxides: Architecture, Design, and Applications

1 Development of Toxic Chemicals Sensitive Chemiresistors Based on Metal Oxides, Conducting Polymers and Nanocomposites Thin Films	3
<i>Sadia Ameen, M. Shaheer Akhtar, Hyung-Kee Seo, and Hyung-Shik Shin</i>	
1.1 Introduction	4
1.2 Semiconducting Metal Oxide Nanostructures for Chemiresistor	6
1.2.1 Prospective Electrode of TiO ₂ Nanotube Arrays for Sensing Phenyl Hydrazine	6
1.2.2 Aligned ZnO Nanorods with Porous Morphology as Potential Electrode for the Detection of p-Nitrophenylamine	10
1.2.3 ZnO Nanotubes as Smart Chemiresistor for the Effective Detection of Ethanolamine Chemical	17
1.3 Conducting Polymers Nanostructures for Chemiresistors	21
1.3.1 Sea-Cucumber-Like Hollow Polyaniline Spheres as Efficient Electrode for the Detection of Aliphatic Alcohols	21
1.3.2 The Sensing Properties of Layered Polyaniline Nanosheets toward Hazardous Phenol Chemical	30
1.3.3 Prospective Electrode of Polypyrrole Nanobelts for the Detection of Aliphatic Alcohols	36

1.4	Semiconducting Nanocomposites for Chemoresistors	44
1.4.1	Hydrazine Chemical Sensing by Modified Electrode of Polyaniline/Graphene Nanocomposite Thin Film	44
1.5	Conclusions and Outlook	48
	Acknowledgments	49
	References	49
2	The Synthetic Strategy for Developing Mesoporous Materials through Nanocasting Route	59
	<i>Rawesh Kumar and Biswajit Chowdhury</i>	
2.1	Introduction to Nanocasting	59
2.2	Steps of Nanocasting	61
2.2.1	Infiltration	61
2.2.2	The Casting Step	67
2.2.3	Template Removal by Dissolution or by Oxidation at High Temperatures	68
2.3	Porous Silica as Template for Inorganic Compounds	68
2.3.1	Nanocast Cobalt Oxides, Cerium Oxide, and Copper Oxide	71
2.3.2	Nanocast Chromium Oxides	73
2.3.3	Nanocast Indium Oxides and Nickel Oxide	74
2.3.4	Nanocast Molybdenum and Manganese Oxide	75
2.3.5	Nanocast Iron Oxide	76
2.3.6	Nanocast Tungsten Oxide	77
2.3.7	Nanocast Tin Oxide	77
2.3.8	Nanocast BiVO_4 and B_4C	78
2.3.9	Nanocast Metal	79
2.3.10	Nanocast Metal Sulfides	80
2.3.11	Nanocasted Ceramics	83
2.3.12	Nanocasted Mesoporous YPO_4	84
2.3.13	Potential Application	84
2.4	Porous Silica as Template for Mesoporous Carbon	86
2.4.1	CMK Family	86
2.4.2	NCC-1, UF-MCN, SNU-1, MCF, and MCCF	89
2.4.3	Hollow Mesoporous Carbon Sphere/Prism	92
2.4.4	Ordered Mesopores Carbon with Surface Grafted Magnetic Particles	94
2.4.5	Surface Modified Mesoporous Nitrogen Rich Carbon by Nanocasting	98
2.4.6	Potential Application	100

2.5	Porous Carbon as Template for Inorganic Compound	104
2.5.1	Nanocasted Silica by Porous Carbon Template	104
2.5.2	Nanocasted Alumina and Nanocasted MgO	106
2.5.3	Nanocasted CeO ₂ and ZnO	107
2.5.4	Nanocasted CuO	109
2.5.5	Nanocasted Other Metal Oxide	109
2.5.6	Mesoporous Sphere of Metal Oxide and Phosphate	110
2.5.7	Nanocast Ceramics	110
2.5.8	Mesoporous Hydroxyapatite and Phosphates	112
2.5.9	Potential Application	113
2.6	Future Prescriptive	113
2.7	Limitation	114
2.8	Conclusion	115
	Acknowledgments	116
	References	116
3	Spray Pyrolysis of Nano-Structured Optical and Electronic Materials	127
	<i>Nurdan Demirci Sankir, Erkan Aydin, Esma Ugur, and Mehmet Sankir</i>	
3.1	Introduction	128
3.2	Spray Pyrolysis Technology	128
3.2.1	Flame Spray Pyrolysis	131
3.2.2	Mist Generation Technologies	132
3.3	Nanoparticles Created via Spray Pyrolysis Method	134
3.3.1	Copper Oxides	136
3.3.2	Indium Oxide	136
3.3.3	Tin Oxide	138
3.3.4	Titanium Dioxide	139
3.3.5	Zinc Oxide	141
3.4	Nanopillars and Nanoporous Structures	142
3.4.1	Hematite (α -Fe ₂ O ₃)	143
3.4.2	Tin Oxide (SnO ₂)	146
3.4.3	Titanium Dioxide	146
3.4.4	Zinc Oxide	147
3.5	Nanocrystalline Thin Film Deposition by Spray Pyrolysis	150
3.5.1	Nanocrystalline Cu-Based Chalcopyrite Thin Films	150
3.5.2	Nanocrystalline Kesterite Thin Films	156

3.5.3	Nanocrystalline Metal Oxide Thin Films	161
3.5.4	Nanocrystalline Chalcogenide Thin Films	165
3.6	Conclusion	167
	Acknowledgments	168
	References	168
4	Multifunctional Spinel Ferrite Nanoparticles for Biomedical Application	183
	<i>Noppakun Sanpo, Cuie Wen, Christopher C. Berndt, and James Wang</i>	
4.1	Introduction	183
4.2	Ferrites	187
4.2.1	Cubic Ferrites	187
4.2.2	Hexagonal Ferrites	189
4.3	The Sol–Gel Method	189
4.3.1	The Sol–Gel Processing Method	189
4.3.2	Applications	194
4.4	Chelating Agents	195
4.4.1	Mineral Processing Examples of Using Chelating Agents	195
4.4.2	Organic Acids	198
4.5	Approach and Methodology	199
4.5.1	Fabrication of Spinel Ferrite Nanoparticles	199
4.5.2	Analytical Techniques Employed	200
4.5.3	Biocompatibility Study	201
4.6	Experimental Results	202
4.6.1	Differential Scanning Calorimetry and Thermo Gravimetric Analyses	202
4.6.2	Raman Analyses	202
4.6.3	Particle Size Analysis	204
4.6.4	Microstructure of Spinel Ferrite Nanoparticles	205
4.6.5	XRD Analysis	206
4.6.6	Contact Angle Measurement and Roughness Parameters	210
4.6.7	Antibacterial Activities of the Spinel Ferrite Nanoparticles	210
4.6.8	Biocompatibility of Spinel Ferrite Nanoparticles	212

4.7	Concluding Remarks	213
	Acknowledgements	214
	References	214
5	Heterostructures Based on TiO₂ and Silicon for Solar Hydrogen Generation	219
	<i>Dilip Kumar Behara, Arun Prakash Upadhyay, Gyan Prakash Sharma, B.V. Sai Krishna Kiran, Sri Sivakumar and Raj Ganesh S. Pala</i>	
5.1	Introduction	220
5.2	Overview of Heterostructures	221
5.2.1	Motivation/Importance of Heterostructured Nanomaterials	221
5.2.2	Classification of Heterostructures	223
5.2.3	Discussion on Other Heterostructure Classifications	232
5.2.4	Challenges/Key Issues in Forming Heterostructures	233
5.3	TiO ₂ Heterostructures	234
5.3.1	Heterojunctions of TiO ₂ Polymorphic Phases	234
5.3.2	TiO ₂ Heterojunctions with Metals (Metal-Semiconductor Junctions)	238
5.3.3	Core-Shell Structures	245
5.3.4	Janus Structures	251
5.4	Silicon Based Heterostructures	253
5.4.1	Silicon Based Heterostructures for PEC Application	253
5.4.2	Heterojunctions vs Multijunction Silicon	258
5.4.3	Pros/Cons in Improvement of Si Heterostructures for Energy Harvesting and Conversion	261
5.5	Some Unaddressed Issues of Heterostructures in Relation to Photocatalysis	261
5.5.1	Measures to be Taken in Perspective of Photocatalysis of Heteronanostructures	262
5.6	Summary/Conclusions and Future Outlook	262
	Acknowledgment	263
	Notes on Contributors	263
	References	264

6 Studies on Electrochemical Properties of MnO₂ and CuO Decorated Multi-Walled Carbon Nanotubes as High-Performance Electrode Materials	283
<i>Mohan Raja</i>	
6.1 Introduction	283
6.2 Experimental	285
6.2.1 Materials	285
6.2.2 Preparation and Fabrication of Supercapacitor Cell	285
6.3 Characterization	286
6.4 Results and Discussion	286
6.5 Conclusion	292
References	293

Part 2: Multifunctional Hybrid Materials: Fundamentals and Frontiers

7 Discotic Liquid Crystalline Dimers: Chemistry and Applications	297
<i>Shilpa Setia, Sandeep Kumar and Santanu Kumar Pal</i>	
7.1 Introduction	298
7.2 Structure-Property Relationship of Discotic Dimers	300
7.2.1 Discotic Dimers Based on Anthraquinone Core	300
7.2.2 Discotic Dimers Based on Benzene Core	304
7.2.3 Discotic Dimers Based on Cyclotetraveratrylene Core	309
7.2.4 Discotic Dimers Based on Dibenzo[a,c]phenazine Core	309
7.2.5 Discotic Dimers Based on Hexa- <i>peri</i> -Hexabenzocoronene (HBC) Core	313
7.2.6 Discotic Dimers Based on Phthalocyanine Core	316
7.2.7 Discotic Dimers Based on Porphyrin Core	325
7.2.8 Discotic Dimers Based on Pyranose Sugars	330
7.2.9 Discotic Dimers Based on Pyrene Core	332
7.2.10 Discotic Dimers Based on Scylloinositol Dimer	334
7.2.11 Discotic Dimers Based on Triphenylene Core	334
7.3 Applications	357
7.3.1 Dopants for Liquid Crystal Display Mixtures	357
7.3.2 Organic Light-Emitting Diodes (OLEDs)	360
7.4 Conclusions and Outlook	361
References	362

8	Supramolecular Nanoassembly and Its Potential	367
	<i>Alok Pandya, Heena Goswami, Anand Lodha and Pinkesh Sutariya</i>	
8.1	Supramolecular Chemistry	368
8.1.1	Supramolecular Interactions	371
8.1.2	Types of Supramolecules	373
8.2	Nanochemistry	376
8.2.1	Why Nano	379
8.2.2	Chemical Approach of Nanomaterials	379
8.2.3	Gold and Silver Nanoparticles	382
8.2.4	Self-Assembled Monolayer	383
8.3	Supramolecular Nanoassembly	384
8.3.1	Cations Receptors	384
8.3.2	Anion Receptors	387
8.3.3	Biomolecule Receptor	388
8.3.4	Pesticide Detection	390
8.3.5	Other Nanomaterials Supported Supramolecules	391
8.4	Conclusion and Future Prospects	394
	References	396
	Suggested Further Reading	397
9	Carbon-Based Hybrid Composites as Advanced Electrodes for Supercapacitors	399
	<i>S.T. Senthilkumar, K. Vijaya Sankar, J. S. Melo, A. Gedanken, and R. Kalai Selvana</i>	
9.1	Introduction	400
9.1.1	Background	400
9.2	Principle of Supercapacitor	402
9.2.1	Basics of Supercapacitor	402
9.2.2	Charge Storage Mechanism of SC	404
9.3	Activated Carbon and their Composites	410
9.4	Carbon Aerogels and Their Composite Materials	411
9.5	Carbon Nanotubes (CNTs) and their Composite Materials	415
9.6	Two-Dimensional Graphene	417
9.6.1	Electrochemical Performance of Graphene	418
9.6.2	Graphene Composites	419
9.6.3	Doping of Graphene with Heteroatom	423
9.7	Conclusion and Outlook	424
	Acknowledgements	425
	References	425

10	Synthesis, Characterization, and Uses of Novel-Architecture Copolymers through Gamma Radiation Technique	433
	<i>H. Iván Meléndez-Ortiz and Emilio Bucio</i>	
10.1	Introduction	434
10.2	Ionizing Radiation	435
	10.2.1 Type of Radiation	435
	10.2.2 X-Ray and Gamma-Rays	436
	10.2.3 Electron Beam	437
	10.2.4 Alpha Particles	437
	10.2.5 Neutrons	438
10.3	Gamma-Ray Measurements	438
	10.3.1 Dosimetry	438
	10.3.2 Fricke Dosimetry Method	440
	10.3.3 Units of Radioactivity and Radiation Absorption	441
10.4	Synthesis of Graft Polymers by Gamma-Rays	441
	10.4.1 Radiation Grafting	441
	10.4.2 Simultaneous or Mutual Method	442
	10.4.3 Pre-irradiation Method	443
	10.4.4 Pre-irradiation Oxidative Method	444
	10.4.5 Parameter Influencing Grafted Copolymers Synthesis	444
10.5	Different Architecture of Polymers	449
	10.5.1 Stimuli-Responsive Networks Grafted onto Polypropylene for the Sustained Delivery of NSAIDs	449
	10.5.2 Radiation Grafting of Glycidyl Methacrylate onto Cotton Gauzes for Functionalization with Cyclodextrins and Elution of Antimicrobial Agents	450
	10.5.3 Binary Graft Modification of Polypropylene for Anti-inflammatory Drug-Device Combo Products	450
	10.5.4 Temperature- and pH-Sensitive IPNs Grafted onto Polyurethane by Gamma Radiation for Antimicrobial Drug-Eluting Insertable Devices	452
	10.5.5 Temperature-Responsiveness and Biocompatibility of DEGMA/OEGMA Radiation Grafted onto PP and LDPE Films	453
	10.5.6 Acrylic Polymer-Grafted Polypropylene Sutures for Covalent Immobilization or Reversible Adsorption of Vancomycin	453

10.6	Polymer Characterization	455
10.6.1	Swelling Measurements	455
10.6.2	Surface Plasmon Resonance Spectroscopy (SPR)	455
10.6.3	Infrared (IR)	456
10.6.4	Nuclear Magnetic Resonance Spectroscopy (NMR)	456
10.6.5	Thermal Transition	456
10.6.6	Contact Angle	457
10.6.7	Atomic Force Microscopy (AFM)	457
	Acknowledgments	458
	References	458
11	Advanced Composite Adsorbents: Chitosan versus Graphene	463
	<i>George Z. Kyzas</i>	
11.1	Introduction	463
11.2	Chitosan-Based Materials	465
11.2.1	Synthesis and Various Modifications	466
11.3	Graphene-Based Materials	478
11.3.1	Adsorption Applications	479
11.4	Graphene/Chitosan Composite Adsorbents	483
11.5	Conclusions	488
	References	489
12	Antimicrobial Biopolymers	493
	<i>S. Sayed and M.A. Jardine</i>	
12.1	Introduction	493
12.2	Biopolymers	496
12.2.1	ϵ -Poly-L-Lysine	496
12.2.2	Chitin and Chitosan	500
12.3	Synthetic Biodegradable Polymers	506
12.3.1	Quaternary Polymers	506
12.3.2	Polyethylenimine	510
12.3.3	Antimicrobial Peptide Mimics	511
12.4	Metal Loading	514
12.4.1	Silver	515
12.4.2	Magnesium	516
12.4.3	Zinc	517
12.4.4	Titanium	517
12.5	Assessment of Antimicrobial/Antifungal Testing Methods	518

12.5.1	Diffusion	519
12.5.2	Dilution	520
12.5.3	Metabolic Based Assays	521
12.5.4	Discrepancies in Testing Methods	522
12.6	Conclusion	525
	References	526
13	Organometal Halide Perovskites for Photovoltaic Applications	535
	<i>Sai Bai, Yizheng Jin, and Feng Gao</i>	
13.1	Introduction	535
13.2	Fundamentals of Organometal Halide Perovskite Solar Cells	537
13.2.1	Brief History of Perovskite Solar Cells	537
13.2.2	Crystal Structure and Optoelectronic Properties of Perovskites	538
13.2.3	Device Architecture Evolution of Solid-State Perovskite Solar Cells	542
13.3	Deposition Methods and Crystal Engineering of Organometal Halide Perovskites	547
13.3.1	One-Step Precursor Deposition	547
13.3.2	Vapor Assisted Solution Process and Interdiffusion Method	551
13.3.3	Vacuum Deposition	553
13.3.4	Solution and Crystal Engineering	555
13.4	Commercialization Challenges and Possible Solutions	558
13.5	Summary and Conclusion	561
	Acknowledgements	562
	References	562
	Index	567

Preface

Functional materials are gaining significant attention in the areas of energy conversion and storage, sensing, electronics, photonics, and biomedicine. The parameters such as size, shape, and surface functions are critical to control the properties for different applications and, because of their unique properties, functional materials are very effective. A range of methods have been developed for preparation and functionalization of organic, inorganic, and hybrid structures, which are the necessary building blocks for the top-down as well as bottom-up architecture of various advanced functional materials. They possess unique physico-chemical properties such as large surface areas, good conductivity and mechanical strength, high thermal stability, and desirable flexibility, which together make a new type of materials phenomenon.

This book compiles the objectives related to functional materials and provides detailed reviews of fundamentals, novel production methods, and frontiers of functional materials, including metallic oxides, conducting polymers, carbon nanotubes, discotic liquid crystalline dimers, calixarenes, crown ethers, chitosan, and graphene. After discussing the production and characterization of these materials, their uses and applications for sensitive chemiresistors, optical and electronic materials, solar hydrogen generation, supercapacitors, display and organic light-emitting diodes (OLED), functional adsorbents, and antimicrobial and biocompatible layer formation are highlighted.

This volume in the Advanced Materials Book Series includes 13 chapters divided into two main areas. In Part 1, Functional Metal Oxides: Architecture, Design and Applications, distinguished researchers present recent efficient strategies such as nanocasting, spray pyrolysis, sol-gel, and wet chemical methods to develop functional metal oxides in respect to architecture, design, and applications; meanwhile, they summarize their uses as chemiresistors for sensitive detection of toxic chemicals, high-performance fuel cell electrodes of mesoporous materials through nanocasting

route, spray-pyrolyzed thin-film solar cells, biomedical agent, solar hydrogen generators, and supercapacitors.

Part 2, Multifunctional Hybrid Materials: Fundamentals and Frontiers, includes several hybrid materials such as discotic liquid crystalline dimers, supramolecular nanoassemblies, carbon-based hybrid materials, organometal halide Perovskites, novel-architecture copolymers by gamma radiation, graphene, chitosan, and antimicrobial biopolymers. In this part, prominent authors present fundamental approaches for production of multifunctional hybrid materials while designating their frontier applications such as OLEDs, flexible displays, artificial receptors for detection platform, supercapacitors for advanced electrodes, photovoltaic applications, stimuli-responsive carriers for the sustained and targeted drug delivery, selective and efficient adsorbent materials, and antimicrobial surface.

The book is written for a wide readership, including university students and researchers from diverse backgrounds such as chemistry and chemical engineering, materials science and nanotechnology engineering, physics, life sciences, agriculture and biotechnology, petroleum and natural gas technology, forensic science, and biomedical engineering. It can be used not only as a textbook for undergraduate and graduate students but also as a review and reference book for researchers in the materials science, bioengineering, medical, physics, forensics, agriculture, biotechnology, and nanotechnology arenas. We hope that the chapters of this book will provide the reader with valuable insight into functional materials in respect to the fundamentals of architecture, design, and applications.

Editors
Ashutosh Tiwari, PhD, DSc
Lokman Uzun, PhD

January 12, 2015

Part 1

FUNCTIONAL METAL OXIDES: ARCHITECTURE, DESIGN, AND APPLICATIONS

Development of Toxic Chemicals Sensitive Chemiresistors Based on Metal Oxides, Conducting Polymers and Nanocomposites Thin Films

Sadia Ameen¹, M. Shaheer Akhtar², Hyung-Kee Seo¹, and Hyung-Shik Shin^{*1}

¹*Energy Materials & Surface Science Laboratory, Solar Energy Research Center, School of Chemical Engineering, Chonbuk National University, Jeonju, Republic of Korea*

²*New & Renewable Energy Material Development Center (NewREC), Chonbuk National University, Jeonbuk, Republic of Korea*

Abstract

Semiconductor materials in nanoscale are gaining a significant attention in the areas of energy conversion and storage, sensing, electronics, photonics, and biomedicine. The parameters such as size, shape, and surface characteristics are significant to control the properties for different applications and thus, semiconducting nanostructured materials of one dimension (1D) are effectively used to fabricate a variety of chemosensors. Particularly, the properties of semiconducting nanostructured materials are altered to achieve high flexibility in various applications. On the other hand, the conducting polymers like polypyrrole, polythiophene, polyaniline, and polyfuran are p-type semiconductors of unique electronic properties, low-energy optical transitions, low ionization potential, and high electron affinity, which are promising for the application of conductometric polymer sensors. The harmful chemicals such as volatile and non-volatile organics are extensively detected by the sensor technology. The sensitivity, selectivity, and stability are the most important aspects of investigation for a variety of sensors. Among several sensors, the electrochemical method provides the advantages of high sensitivity, wide linear range, economical, rapid response, portability, and ease of operating procedure.

*Corresponding author: hsshin@jbnu.ac.kr

In this chapter, we have briefly discussed the semiconducting metal oxides nanostructures like TiO_2 , ZnO , conducting polymers, and nanocomposites for the efficient detection of harmful and toxic chemicals. The chapter includes brief literature surveys, properties, and the latest research advancements for the development of various metal oxide nanostructures, nanocomposites, and conducting polymer-based nanomaterials as efficient electrode for detecting harmful chemical through the effective electrochemical technique. The modified electrodes with different inorganic, organic nanomaterials and nanocomposites are reviewed for the reliable and effective detection of harmful chemicals by electrochemical and current–voltage (I–V) characteristics.

Keywords: Semiconductor materials, nanoscale aspects, conducting polymer, nanocomposites thin films, chemiresistors, chemosensors

1.1 Introduction

In recent years, numerous intensive research efforts in the field of nanotechnology have shown great potential. There has been a significant improvement for the synthesis of desired organic/inorganic nanomaterials for the applications in areas of energy conversion, sensing, electronics, photonics, and biomedicine. With the development of nanoscience and nanotechnology, one-dimensional (1D) semiconducting nanostructured materials like nanotubes, nanorods, nanosheets, nanoballs, and other nanostructured materials have been widely applied for the fabrication of varieties of chemosensors. It is generally accepted that 1D nanostructure are ideal systems for exploring a large number of novel phenomena at nanoscale and investigating the size and dimensionality dependence of structure properties for potential applications [1]. Among the inorganic semiconductor nanomaterials, 1D metal oxide nanostructures are the focus of current research efforts in nanotechnology since they are the most common minerals on earth due to their special shapes, compositions, and chemical, and physical properties [2]. On the other hand, the nanocomposites generally contain more than one single component and achieve the properties which are different from those of single component nanomaterials and thus, could be widely used for the effective fabrication of chemiresistors to detect the harmful toxic chemicals. The conducting polymers like polypyrrole (PPy), polythiophene, polyindol, polyaniline (PANI), and polyfuran are known p-type semiconductors with unique electronic properties, low energy optical transitions, low ionization potential and high electron affinity [3] and thus, widely used

as sensitive materials for conductometric polymer sensors. The conducting polymers could be easily synthesized through simple chemical or electrochemical process and their conductivities could be altered by modifying the electronic structures through doping or de-doping procedures [4] and therefore, conducting polymers could suitably work as an effective working electrode and might offer the fast response toward the detection of various harmful chemicals. The sensor technology is popularly known for the detection of harmful chemicals and the sensitivity, selectivity, and stability are the most important aspect of investigation of a variety of sensors. Up to now, efforts have been made by controlling the sensors structures [5, 6], sensor fabrication techniques [7], and surface modification [8] to detect the toxic chemicals. Among several sensors like fluorescence based chemical sensors [9], chemically modified electrode chemical sensors [10] and chemiluminescence based sensors [11], the electrochemical method provides the advantages of high sensitivity, wide linear range, economical, rapid response, portability and ease of operating procedure [12, 13]. However, the electrochemical method is still a challenge to enhance the electron transfer rate over the surface of working electrode for sensors. Therefore, the modifications of the electrodes with different inorganic and organic nanomaterials could be promising for the reliable and effective detection of harmful chemicals by electrochemical and current–voltage (I–V) characteristics. In this chapter, we have briefly discussed the semiconducting metal oxides nanostructures like TiO_2 , ZnO , conducting polymers, and nanocomposites for the efficient detection of harmful and toxic chemicals. The preparation methods, morphologies, the physical and chemical properties of metal oxides, nanocomposites, and conducting polymers have shown the significant impacts on the optical, electrical, and electronic properties of the nanomaterials and their performances for detecting the harmful chemicals. The chapter briefly surveys several metal oxides, nanocomposites and conducting polymers in terms of their processing, functionality, and applications in sensing the harmful chemicals. With addition, the recent literatures have been reviewed on the basis of morphology, structure, and physiochemical properties of TiO_2 and ZnO nanostructured semiconductors with brief description on the recent literatures of their sensing applications. TiO_2 and ZnO nanostructures based chemiresistors have shown comparable sensing performances. It has been noticed that the sensing performance are considerably affected by the preparation, morphology, and the electrical properties of semiconducting metal oxide.

1.2 Semiconducting Metal Oxide Nanostructures for Chemiresistor

1.2.1 Prospective Electrode of TiO₂ Nanotube Arrays for Sensing Phenyl Hydrazine

The inorganic metal oxide materials in nanoscale have recently received a great deal of interest owing to their unique structures, electrical, and catalytic properties [14, 15]. The nanostructures of titania (TiO₂) are one of most versatile metal oxides, exhibiting exotic inert surface and the optical properties. The tailoring of multidimensional TiO₂ nanostructures to 1D is playing a significant role for determining the physiological and electrical properties. One-dimensional TiO₂ nanomaterials are reported to display the large surface to volume area as compared to the bulk materials [16, 17]. Among various 1D TiO₂ nanostructures, TiO₂ NTs generally exhibits the large surface area [18], outstanding charge transport properties [19], excellent electronic, mechanical, and chemical stability properties [20]. In particular, TiO₂ NTs with highly uniform morphology and unique-orientated growth properties are promising for the applications in gas sensors and biosensors [21]. Recently, TiO₂ nanostructures with high surface area are extensively utilized for the detection of harmful chemicals through sensing. Kwon *et al.* studied the enhanced ethanol sensing properties over the surface of TiO₂ NTs electrode based sensors [22]. Chen *et al.* fabricated a room temperature hydrogen sensor with TiO₂ NT arrays based electrode [23]. Ameen *et al.* [24] have grown TiO₂ NT arrays on Ti foil substrate by simple electrochemical anodic oxidation and utilized as the working electrode for the fabrication of a highly sensitive, reliable, and reproducible chemical sensor for the detection of harmful phenyl hydrazine chemical.

The grown TiO₂ on Ti substrate displays highly ordered and self-assembled NT arrays, as shown in Figure 1.1(a). At high magnification (Figure 1.1(b)), a uniform and closely packed TiO₂ NT arrays are seen. Moreover, the grown TiO₂ NT arrays present distinguishable diameter distribution. The average diameter and wall thickness of TiO₂ NT arrays are observed as 100 ± 20 nm and 20 ± 5 nm, respectively. The inset of Figure 1.1(a) depicts the cross-sectional FESEM image of grown TiO₂ NT arrays which exhibits the average length of ~ 15 μ m. Figure 1.1(c, d) shows the transmission electron microscopy, high resolution (HR) TEM, and selected area electron patterns (SAED) of TiO₂ NT arrays. A hollow tubular morphology could be seen in the TEM image of grown TiO₂ NT arrays (Figure 1.1(c)), which is consistent with the FESEM results. The TiO₂ NT arrays exhibit the average diameter

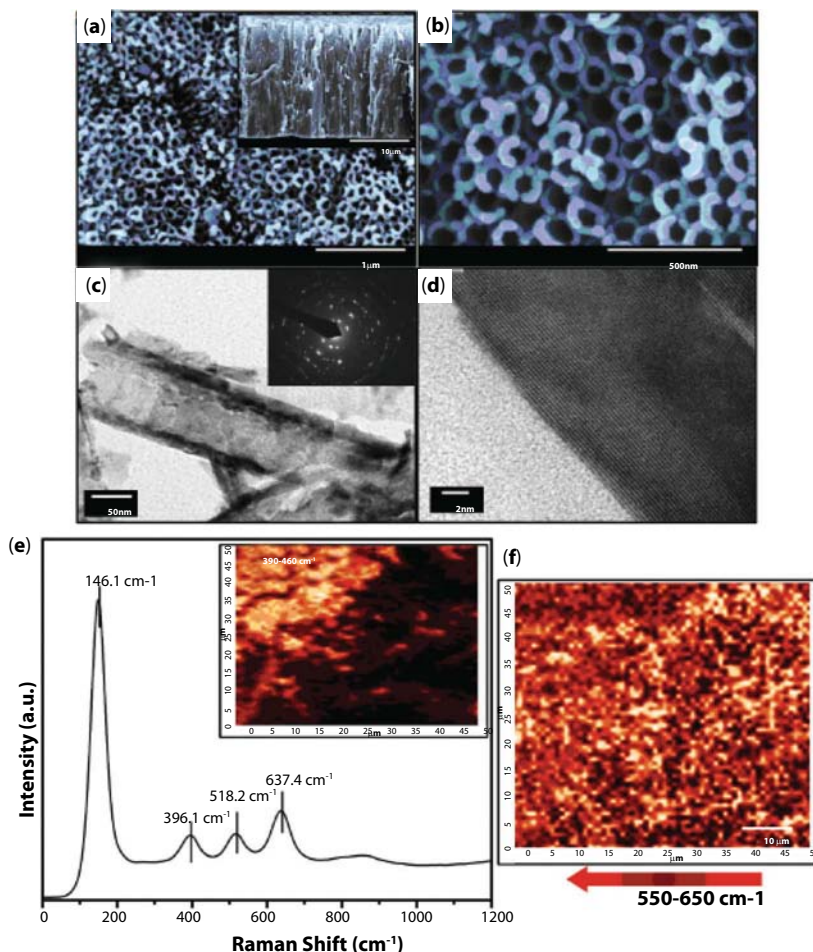


Figure 1.1 FESEM images of TiO₂ NT arrays at low (a) and high (b) magnifications. Inset of (a) shows cross section image of TiO₂ NT arrays, TEM image (c), and HRTEM image (d) of TiO₂ NT arrays. Inset of (c) shows SAED patterns of TiO₂ NT arrays, (e) Raman spectrum and inset of (e) shows the corresponding Raman mapping images in 390–460 cm⁻¹, and (f) the corresponding Raman mapping images 550–650 cm⁻¹ of TiO₂ NT arrays. Reprinted with permission from Ameen, *App. Phys. Lett.* 103(2013) 061602. © 2013, American Institute of Physics Ltd.

and wall thickness of 100 ± 20 and 20 ± 5 nm, respectively. The SAED pattern of TiO₂ NT arrays (inset of Figure 1.1(c)) shows polycrystalline phases in the anatase TiO₂. The HRTEM image of TiO₂ NT arrays (Figure 1.1(d)) shows well-resolved lattice fringes of crystalline TiO₂ NT arrays with plane spacing of ~ 0.35 nm, which corresponds to anatase TiO₂ (101). These observations considerably deduce the good crystallinity of grown TiO₂ NT

arrays. The phase composition and structural properties of TiO_2 NT arrays are investigated by Raman scattering spectroscopy and the corresponding mapping, as shown in Figure 1.1(e, f). The grown TiO_2 NT arrays obtain three active Raman modes at ~ 396.1 , ~ 518.2 , and $\sim 637.4 \text{ cm}^{-1}$ which correspond to the active Raman modes of anatase phase with symmetries of $B_{1g(1)}$, $(B_{1g(2)} + A_{g(1)})$, and E_{g3} , respectively, and match with the Raman modes of anatase TiO_2 [25, 26]. Consequently, Raman spectrum does not exhibit any Raman mode at $\sim 445 \text{ cm}^{-1}$, indicating that no rutile phase exist in the grown TiO_2 NT arrays. The inset of Figure 1.1(e) shows the Raman mapping in the range of $\sim 390\text{--}460 \text{ cm}^{-1}$ and reveals the larger dark part which corresponds to the peak at $\sim 396.1 \text{ cm}^{-1}$ whereas Figure 1.1(f) shows the Raman mapping in the range of $\sim 550\text{--}650 \text{ cm}^{-1}$ which exhibits highly uniform surface, suggesting that the grown TiO_2 NT arrays are in good quality of anatase TiO_2 phase.

The typical amperometric plot is shown in Figure 1.2(a). In the beginning, the electrochemical experiment is performed in PBS without phenyl hydrazine for stabilizing the background current. The successive addition of phenyl hydrazine has shown the linear increase in the current, exhibiting a linear relationship between the current and phenyl hydrazine concentrations. Figure 1.2(b) depicts the linear plot of current versus concentration of phenyl hydrazine for TiO_2 NT arrays electrode which again confirms the linear relationship between current and concentration of phenyl hydrazine. These observations infer that the TiO_2 NT arrays electrode is highly effective catalyst to detect the sensing response of phenyl hydrazine at very low concentration which might attribute to the good electrocatalytic, and direct electron transfer or fast electron exchange behavior of TiO_2 NT arrays. The current (I)–voltage (V) characteristics are measured for evaluating the sensing properties (sensitivity, detection limit, and correlation coefficient) of the fabricated phenyl hydrazine chemical sensor over TiO_2 NT arrays electrode. The current response is measured from 0.0–2.5 V, and the time delaying and response times are 1.0 and 10 s, respectively. The detailed sensing parameters of the fabricated phenyl hydrazine chemical sensor based on TiO_2 NT arrays electrode are evaluated by measuring a series of I–V characteristics with various concentrations of phenyl hydrazine (0.25 μM –0.10 mM). From Figure 1.2(c), the current has continuously increased with the increase of the phenyl hydrazine concentrations from 0.25 μM –0.10 mM, suggesting the good sensing response toward phenyl hydrazine chemical by TiO_2 NT arrays electrode. The enhancement in current might due to the better electrocatalytic behavior, generation of large number of ions, and the increase of ionic strength of the solution with the addition of phenyl hydrazine. The sensing parameters such as sensitivity,

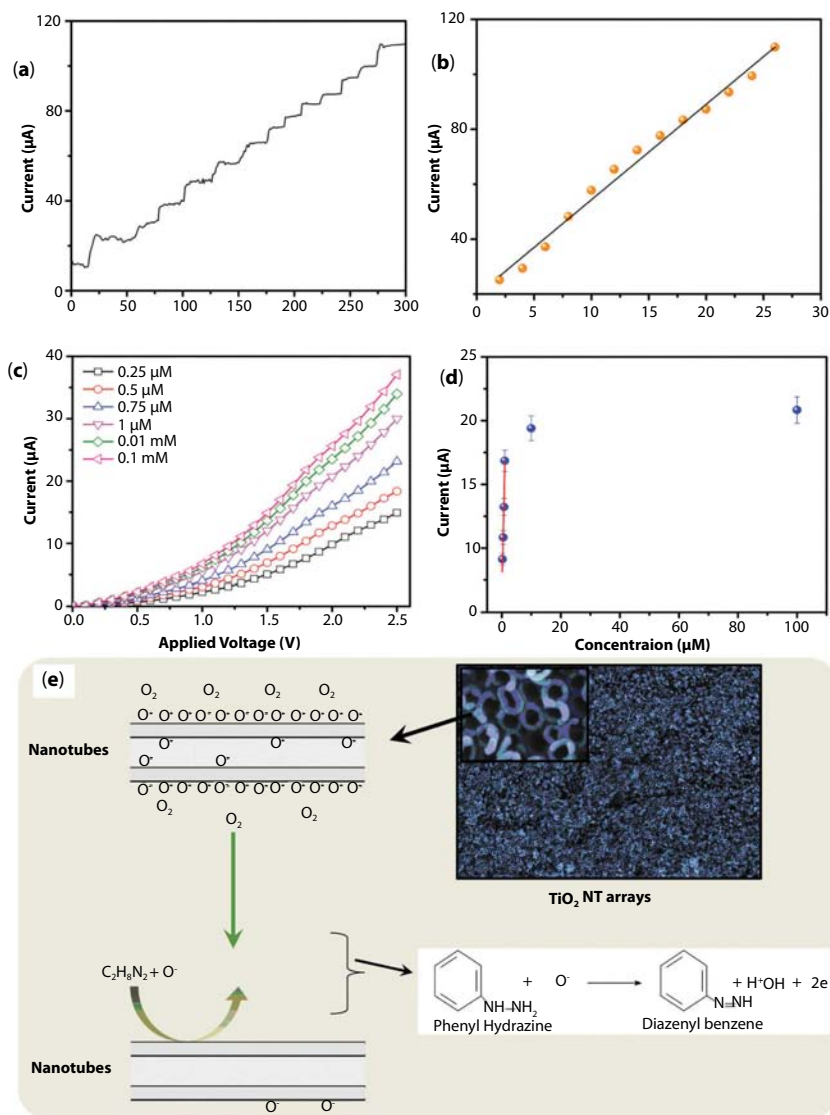


Figure 1.2 (a) Typical amperometric plot and (b) linear plot of current versus concentration of phenyl hydrazine of TiO_2 NT arrays based chemical sensor. (c) The I-V characteristics and (d) the calibration curve of current versus phenyl hydrazine concentration of TiO_2 NT arrays electrode based chemical sensor at different phenyl hydrazine concentrations (0.25 μM –0.10 mM) in 10ml of 0.1M PBS, and (e) schematic illustration of proposed mechanism of phenyl hydrazine chemical sensors over the surface of TiO_2 NT arrays based electrode. Reprinted with permission from Ameen, *App. Phys. Lett.* 103 (2013) 061602. © 2013, American Institute of Physics Ltd.

detection limit, and correlation coefficient are calculated by a calibration curve of current versus phenyl hydrazine concentration of the fabricated phenyl hydrazine chemical sensor. Figure 1.2(d) presents the plot of calibration current versus phenyl hydrazine concentration which reveals that the current increases linearly up to the phenyl hydrazine concentration of $\sim 1 \mu\text{M}$ and afterwards achieve a saturation level in the calibrated plot. The saturation point occurs due to the less availability of free active sites on the surface of TiO_2 NT arrays electrode for phenyl hydrazine chemical at higher concentration ($>10 \mu\text{M}$) in PBS. The fabricated phenyl hydrazine chemical sensor based on TiO_2 NT arrays electrode exhibits significantly high and reproducible sensitivity of $\sim 40.9 \mu\text{A} \cdot \text{mM}^{-1} \cdot \text{cm}^{-2}$ and the detection limit of $\sim 0.22 \mu\text{M}$ with correlation coefficient (R) of ~ 0.98601 and short response time of 10 s. Importantly, the fabricated phenyl hydrazine chemical sensor based on TiO_2 NT arrays electrode displays a good linearity in the range of $0.25 \mu\text{M}$ – $1 \mu\text{M}$. Thus, TiO_2 NT arrays electrode provides suitable surface for the oxidation of phenyl hydrazine and determines the sensing responses by increasing the current values. The reusability and reproducibility of the fabricated phenyl hydrazine chemical sensor based on TiO_2 NT arrays electrode were elucidated by measuring the sensing responses with the I–V characteristics for three consecutive weeks. The sensing parameters or properties showed the negligible drops in the fabricated phenyl hydrazine chemical sensor based on TiO_2 NT arrays electrode, which deduces the long term stability of the fabricated phenyl hydrazine chemical sensor. Thus, TiO_2 NT arrays with anatase phase and good crystal quality are promising and effective working electrode for the detection of phenyl hydrazine chemical or other hazardous chemicals.

1.2.2 Aligned ZnO Nanorods with Porous Morphology as Potential Electrode for the Detection of p-Nitrophenylamine

Aniline and its derivatives are the main constituents in various manufacturing industries of polymers, dyes, pesticides, pharmaceutical, rubber chemicals, explosives, and paintings [27, 28]. The excess release of aniline and its derivatives severely disturbs the water ecosystem and clean environment because it easily adsorbs on the colloidal organic matter and moves from soil to the groundwater [29]. The metal oxide semiconductors such as SnO_2 [30], TiO_2 [31], ZnO [32], Fe_2O_3 [33], In_2O_3 [34], CeO_2 [35], and WO_3 [36] have been utilized as efficient electron mediator electrode materials for the detection of harmful chemicals. ZnO semiconductors with wide band gap of $\sim 3.37 \text{ eV}$ are the most exotic and versatile

materials owing to its high exciton, binding energy, biocompatibility, better electrochemical activities, non-toxicity, chemical and photochemical stability and high electron communication features [37–39]. In particular, ZnO nanomaterials based electrode shows good electrochemical activities toward chemicals, biomolecules and gases owing to their high electron transfer characteristics with high electrochemical and photochemical stability [40, 41]. The changes in the surface and morphological properties of ZnO materials display significant impact on the performances of electrochemical system [42, 43]. Recently, 1D ZnO nanostructures such as nanobelts (NBs), nanowires (NWs), nanotubes (NTs), and NRs are extensively studied due to their sufficiently high surface-to-volume ratio and good electrical characteristics which are essential for fabricating various electrochemical and photoelectrochemical devices [44, 45]. Among 1D ZnO nanomaterials, aligned ZnO NRs are the highly explored material especially, in the fabrication of optoelectronic, electrochemical, photoelectrochemical and solar devices because of its unique electronic and high surface-to-volume ratio [46]. Recently, J.J. Hassan fabricated the high-sensitivity room temperature hydrogen gas sensor based on oblique and vertical ZnO nanorod arrays [47]. Ameen *et al.* reported the synthesis of vertically aligned ZnO NRs by low temperature solution process for the detection of hydrazine chemical via chemical sensor based on aligned ZnO NRs and demonstrated the high sensitivity [44]. Y. Lv *et al.* prepared ZnO NRs by a simple solution route for the fabrication of triethylamine gas sensor. Umar *et al.* fabricated the electrochemical sensor for the detection of hydroquinone chemical by Ce doped ZnO NRs electrode [48]. The synthesis of aligned nanoporous ZnO NRs thin film for the selective detection of p-nitrophenylamine (p-NPA) chemical was reported by Ameen *et al.* [49]. The synthesized aligned nanoporous ZnO NRs were characterized in terms of morphological, structural, optical, electrochemical and sensing properties. The fabricated aligned nanoporous ZnO NRs electrode based chemical sensor showed the rapid detection of p-NPA with high sensitivity of $\sim 184.26 \mu\text{A} \cdot \text{mM}^{-1} \cdot \text{cm}^{-2}$ and good reproducibility.

Figure 1.3 shows the FESEM images of aligned nanoporous ZnO NRs thin film. The cross section of ZnO thin film, as shown in Figure 1.3(a) describes highly dense and well aligned nanoporous ZnO NRs with the average length of $\sim 3\text{--}4 \mu\text{m}$. The low magnification surface image, as shown in Figure 1.3(b, c) displays uniform growth of aligned ZnO NRs with nanoporous surface. The average diameter of each hexagonal ZnO NRs is estimated as $\sim 200\text{--}300 \text{ nm}$, as shown in the inset of Figure 1.3(c). To check the elemental composition, the EDX spectrum (Figure 1.3(d)) reveals that the grown aligned nanoporous ZnO NRs exhibit good aspect ratio of Zn

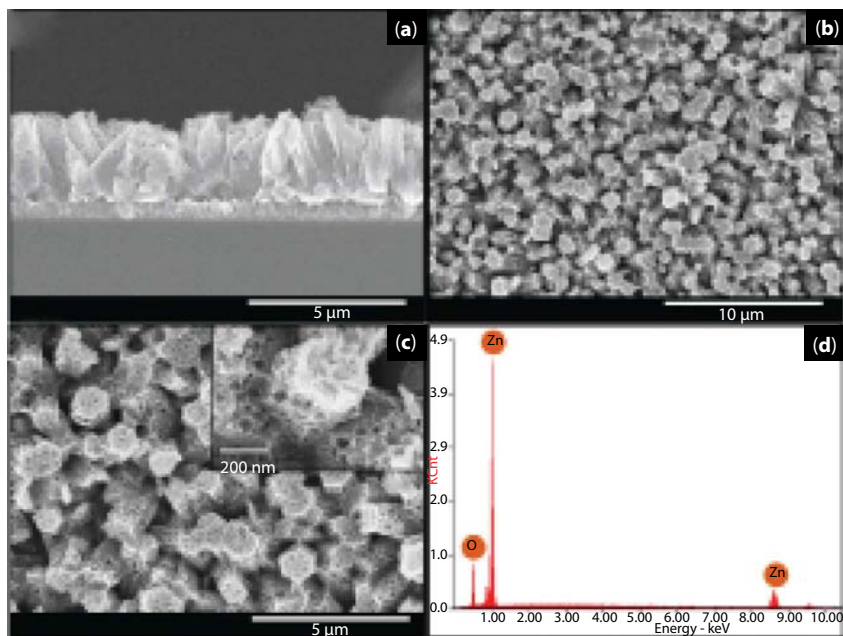


Figure 1.3 (a) Cross-section view and (b, c) surface view FESEM images and (d) the EDX spectrum of aligned nanoporous ZnO NRs. Inset shows the surface image at high magnification of aligned nanoporous ZnO NRs. Reprinted with permission from Ameen, *Appl. Catal. A: Gen.* 470 (2014) 271. © 2014, Elsevier Ltd.

and O elements in terms of atomic weight percentage. No other peak has been seen in the EDX spectrum, indicating the purity of the synthesized aligned nanoporous ZnO NRs.

The UV-DRS and room temperature PL analysis were used to investigate the optical properties of grown aligned nanoporous ZnO NRs thin film. Figure 1.4(a) shows the UV-DRS spectrum and derived band energy plot of aligned nanoporous ZnO NRs thin film (as shown in the inset of Figure 1.4(a)). An intense absorption edge at ~ 384 nm near UV region is recorded by the grown aligned nanoporous ZnO NRs thin film, which usually originates from a charge transfer process from the valence band to conduction band of ZnO [50–52]. From UV-DRS graph, the band gap of aligned nanoporous ZnO NRs thin film is calculated as ~ 3.23 eV which is approximately same to the band gap of bulk ZnO nanomaterials [53, 54]. This indicates that the grown aligned nanoporous ZnO NRs thin film actively absorbs the UV light as normal bulk ZnO materials. Figure 1.4(b) depicts the room temperature PL spectrum of grown aligned nanoporous ZnO NRs thin film. Two emission PL peaks are observed in which an

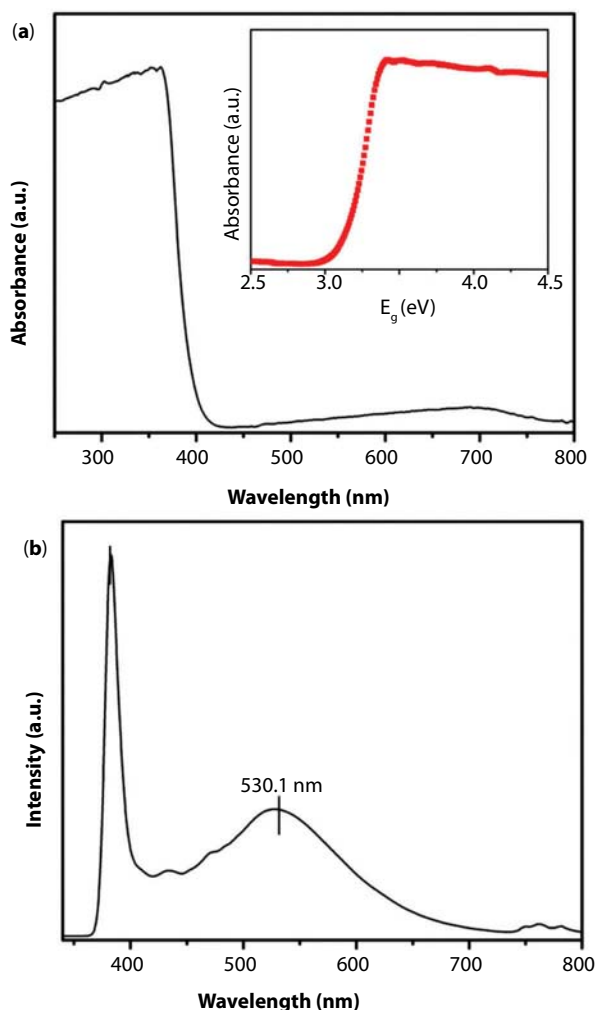


Figure 1.4 UV-DRS (a) and room temperature PL spectra (b) of aligned nanoporous ZnO NRs. Reprinted with permission from Ameen, *Appl. Catal. A: Gen.* 470 (2014) 271. © 2014, Elsevier Ltd.

intensive sharp UV emission at ~ 383.2 nm occurs due to the free exciton emission from the wide band gap of aligned nanoporous ZnO NRs thin film, while a broader green emission at ~ 530.1 nm is attributed to the recombination of electrons in single occupied oxygen vacancies and structural defects in the aligned nanoporous ZnO NRs [55]. Generally, the broad green emission is originated from the increased concentration of singly ionized oxygen vacancies and generation of non-stoichiometric

phase structure in the grown ZnO nanomaterials. The intense UV emission with weak broad green emission suggests the good optical properties and high quality of aligned nanoporous ZnO NRs grown on FTO substrate. This result is in consistent with the UV-DRS studies.

The cyclovoltametry (CV) analysis was performed to elucidate the electrochemical properties of aligned nanoporous ZnO NRs thin film electrode toward p-NPA chemical. The CV measurements were performed using three electrode systems comprising of aligned nanoporous ZnO NRs thin film as working electrode, Pt wire as cathode and reference Ag/AgCl electrode. The electrochemical system without p-NPA chemical in phosphate buffer solution (PBS, pH = 7.0) depicted very low oxidation or anodic current, while a significant increment in the oxidation current occurred after the addition of p-NPA (5 μM) in PBS. This change indicated that the aligned nanoporous ZnO NRs electrode executed quick sensing response toward p-NPA chemical which might result from the good electrocatalytic surfaces of aligned nanoporous ZnO NRs. Moreover, the typical CV of aligned nanoporous ZnO NRs electrode with a series of p-NPA concentrations (5–150 μM) in 0.1 M PBS at the scan rate of 50 mVs^{-1} was performed. With the increase of p-NPA concentration, the oxidation current substantially increased and reached to the highest current of $\sim 239.8 \mu\text{A}$ at highest concentration of p-NPA (150 μM), which was 4 factors higher than the oxidation current at lowest p-NPA concentration (5 μM). In general, the high height of the oxidation peak is related to the faster electron transfer reaction in the electrochemical system and represented the high electrocatalytic behavior of the electrode [56]. Herein, aligned nanoporous ZnO NRs electrode exhibited increased oxidation current which might due to the high electrocatalytic behavior toward p-NPA chemical in PBS.

To investigate the detailed sensing parameters of aligned nanoporous ZnO NRs electrode, I–V measurements was performed in 10 ml of 0.1 M PBS solution without and with a series of p-NPA concentrations at room temperature. Figure 1.5(a) shows the I–V characteristics of aligned nanoporous ZnO NRs electrode without and with p-NPA (5 μM) in 10 ml of 0.1 M PBS solution. It is seen that the low current value is detected without p-NPA, but it is drastically increased after the addition of p-NPA, suggesting the quick sensing response to p-NPA chemical. Furthermore, Figure 1.5(b) exhibits the typical I–V response of aligned nanoporous ZnO NRs thin film electrode at various concentrations of p-NPA (5–150 μM) into 0.1 M PBS solution (pH = 7.0)). A continuous increase in the current with the increase in the concentrations of p-NPA from 5–150 μM is seen which suggests the generation of large number of ions and the increase of ionic strength of the solution with the addition

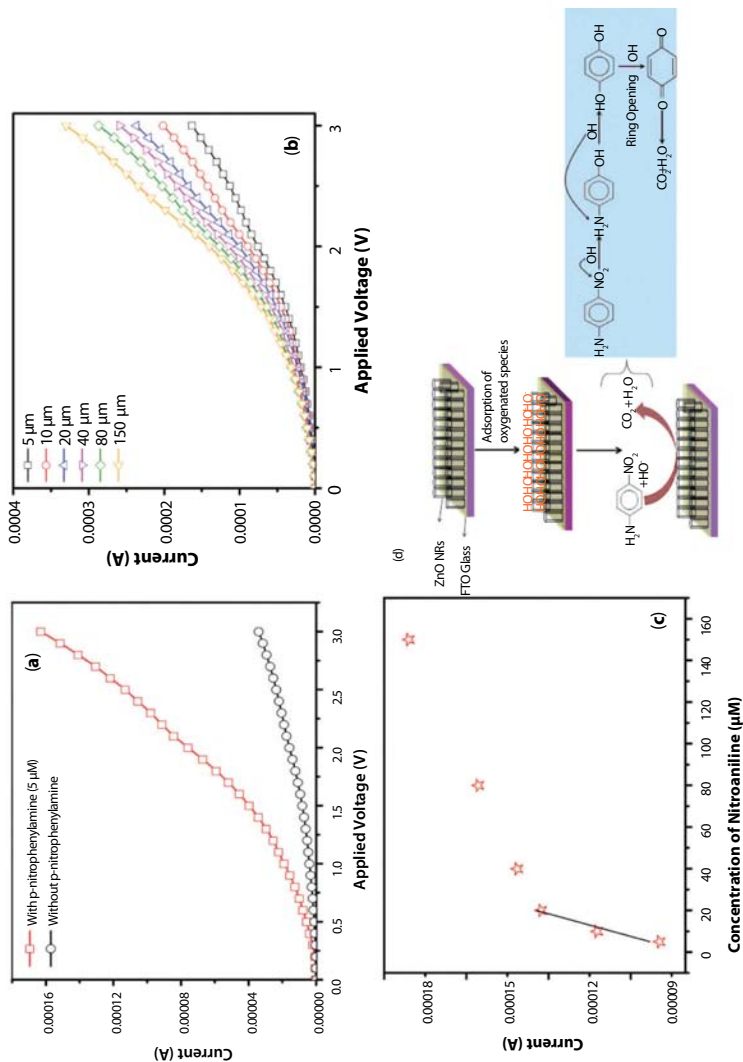


Figure 1.5 (a) The I–V characteristics of aligned nanoporous ZnO NR electrode without and with p-NPA (5 μM) in 10 ml of 0.1 M PBS solution, (b) I–V responses of aligned nanoporous ZnO NR electrode at various concentrations of p-NPA (5 μM–150 μM) in 0.1 M PBS (pH = 7.0), (c) plot of calibrated current and the wide range of p-NPA concentrations, and (d) proposed mechanism of p-NPA during the electrochemical reaction. Reprinted with permission from Ameen, *Appl. Catal. A: Gen.* 470 (2014) 271–281, Elsevier Ltd.

of different concentrations of p-NPA. On the basis of these results, highly active electrocatalytic surface of the grown aligned nanoporous ZnO NRs electrode favors the efficient detection of p-NPA. The sensitivity and other sensing parameters are evaluated by the plot of calibrated current and the wide range of p-NPA concentrations, as shown in Figure 1.5(c). The current increases with the increase in the concentrations of p-NPA up to $\sim 40 \mu\text{M}$ and then, the saturation starts after increasing the concentration of p-NPA. The fabricated p-NPA chemical sensor based on aligned nanoporous ZnO NRs electrode shows considerably high sensitivity of $\sim 184.26 \mu\text{A} \cdot \text{mM}^{-1} \cdot \text{cm}^{-2}$ and reasonable limit of detection (LOD) of $\sim 53.7 \mu\text{M}$ with response time of 10 s. A good linear dynamic range (LDR) from $5\text{--}20 \mu\text{M}$ and the correlation efficient of $R = \sim 0.97569$ are obtained. Importantly, the fabricated p-NPA chemical sensor based on aligned porous ZnO NRs electrode demonstrates highly reliable and reproducible sensitivity. An illustration of sensing response for p-NPA chemical over the surface of aligned nanoporous ZnO NRs electrode is presented in Figure 1.5(d). In the beginning, p-NPA chemical is chemisorbed over the surface of ZnO NRs electrode due to presence of active sites. These active sites on ZnO NRs generates by the easy interaction of atmospheric oxygen or oxygenated species through the transfer of electrons from the conduction band of ZnO to the adsorbed oxygen atoms [57]. The oxygenated species are generally present in the form of HO^- , O^- , O_2^- , etc. After the addition of p-NPA, the oxygenated species (like HO^-) on ZnO NRs get combined with p-NPA and oxidizes into CO_2 and H_2O after passing through several intermediate reactions as presented in Figure 1.5(d). The aligned porous ZnO NRs electrode exhibits reasonably good surface area of $\sim 74.8 \text{ m}^2/\text{g}$, which might helpful in the large generation of active sites over the surface of ZnO NRs. The quick and enhanced sensing properties could be explained by the nanoporous surface of aligned nanoporous ZnO NRs electrode which might provide large number of active sites surface for the detection of p-NPA. The high sensitivity and the good linearity of aligned nanoporous ZnO NRs electrode based chemical sensor are attributed to the excellent adsorption ability and high electrocatalytic and electrochemical activities of aligned nanoporous ZnO NRs thin film, as described in CV and amperometry results. The stability of p-NPA chemical sensor was analyzed by measuring the sensing performances via the I-V characteristics for three consecutive weeks. It was seen that no significant fall was observed in the sensing parameters of the fabricated p-NPA chemical sensor, confirming the long term stability of the fabricated aligned nanoporous ZnO NRs electrode based chemical sensor.

1.2.3 ZnO Nanotubes as Smart Chemiresistor for the Effective Detection of Ethanolamine Chemical

Unique wide band gap semiconductor called ZnO is highly explored and promising nanomaterial for a series of applications in field-effect transistors, lasers, photodiodes, sensors, and photovoltaics [58–60]. Due to excellent dielectric, ferroelectric, piezoelectric and pyroelectric properties, the ZnO nanomaterial find numerous applications particularly in photocatalysis, chemical sensors, memory resistors and photovoltaics [61, 62]. ZnO nanostructures in one dimension (1D) such as nanorods, nanobelts, nanowires and nanotubes show high surface-to-volume ratio, slow electron-hole recombination rate and good electrical characteristics [63]. Recently, the electrochemical method is adopted as the most acceptable technique to fabricate high performance chemical sensor. This system displays several advantages of high sensitivity, wide linear range, economical, rapid response, portability, and ease of operating procedure [64], but still facing the major problems of electron loss and low electron transfer rate over the surface of sensor's working electrode. Effective modifications of the working electrodes are necessitated to increase the electron transfer rate and the stability of chemical sensors for the reliable detection of harmful chemicals [65]. Ameen *et al.* fabricated a hydrazine chemical sensor using vertically aligned ZnO NRs electrode and demonstrated the high sensitivity toward hydrazine chemical [66]. Similarly, Ibrahim *et al.* reported the Ag doped ZnO nanoflowers based sensor for the detection of phenyl hydrazine chemical via electrochemical system [67]. So far, various chemical sensors are fabricated for the detection of harmful chemicals such as ethanol, propanol, phenol and nitroaniline, etc [68, 69]. In continuation, the ethanolamine chemical is one of the most useable chemicals at laboratory level but its excess discharge is a big threat to the environment. The inhalation or insertion of ethanolamine might affect the respiratory system, creates drowsiness, skin irritation and fatal to central nervous system. Ameen *et al.* [70] synthesized the aligned ZnO nanotubes (NTs) thin films on FTO substrate by low temperature solution method and extensively utilized as smart and effective working electrode for ethanolamine chemical sensor. The fabricated chemical sensor based on aligned ZnO NTs thin film electrode showed the rapid detection of ethanolamine with the high sensitivity of $\sim 37.4 \times 10^{-4} \text{ mA} \cdot \text{mM}^{-1} \cdot \text{cm}^{-2}$, good linearity of $\sim 0.05 \text{ mM}^{-1} \text{ mM}$ and the detection limit of $\sim 19.5 \text{ } \mu\text{M}$.

The morphological properties are shown in Figure 1.6(a, b). The vertically arranged tubular morphology of ZnO on FTO substrate is observed (Figure 1.6(a)). At high magnification image (Figure 1.6(b)), each ZnO NT

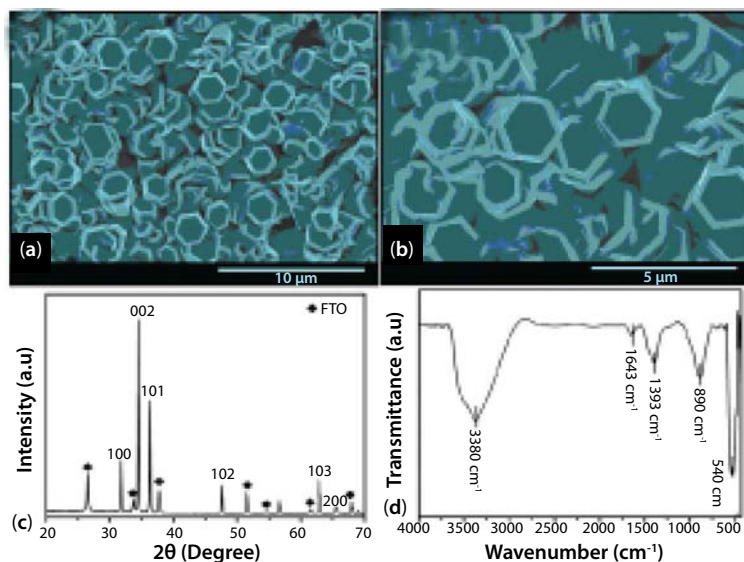


Figure 1.6 FESEM images at low (a) and high (b) magnifications, XRD patterns (c) and FTIR spectrum (d) of aligned ZnO NTs thin film. Reprinted with permission from Ameen, *Mater. Lett.* 106 (2013) 254. © 2013, Elsevier Ltd.

exhibits the hexagonal hollow morphology with the average diameter of $\sim 700\text{--}900$ nm and the outer thickness of $\sim 60\text{--}100$ nm. It is also seen that the aligned ZnO NTs are in the form of nanograins which have few developed free surfaces as well as grain boundaries and interfaces. The presence of these grain boundaries in aligned ZnO NTs might define the good optical and physical properties of nanograined ZnO NTs [71]. The aligned ZnO NTs thin film is further characterized by X-rays diffraction patterns to investigate the crystalline nature of grown nanomaterials, shown in Figure 1.6(c). The aligned ZnO NTs thin film shows the diffraction peaks at 31.8° (100), 34.5° (002), 36.3° (101), 47.8° (102), 56.7° (110), 63.1° (103), and 65.6° (200), corresponding to the wurtzite structure of ZnO crystals [72] and are well indexed to JCPDS No. 36-1451. The diffraction peak at 34.5° (002) displays much higher intensity, suggesting the preferential growth direction due to the instability of polar (002) plane [73]. The other diffraction peaks are associated to FTO substrate [74]. The occurrence of these grain boundaries in ZnO NTs is explained by the formation of invisible amorphous superficial and intergranular layers in between ZnO NTs [62]. The structural and purity of aligned ZnO NTs thin film are further analyzed by Fourier transform infrared, as shown in Figure 1.6(d). A strong IR band at $\sim 540\text{ cm}^{-1}$ is observed which corresponds to the typical Zn-O

group of ZnO nanomaterials [75]. The IR peaks at ~ 3380 , ~ 1643 , and ~ 890 cm^{-1} are associated to OH stretching mode, water scissoring vibration and bending vibration of nitrate, respectively [76]. Therefore, the grown NTs are pure and well crystalline ZnO along with few impurities.

The sensing behavior of aligned ZnO NTs electrode was demonstrated toward the concentration of ethanolamine chemical. Figure 1.7(a) depicts the illustration of the fabricated ethanolamine chemical sensor based on aligned ZnO NTs electrode. Typically, the sensor comprises of two electrode electrochemical system using aligned ZnO NTs as working electrode and Pt wire as a cathode in a fixed amount of phosphate buffer solution (PBS, 0.1 M, 10 ml, pH 7) as an electrolyte. A low current is detected when the electrochemical system does not contain ethanolamine chemical, as shown in Figure 1.7(a). After the addition of ethanolamine (0.05 mM), a drastic increase in the current is observed, suggesting that aligned ZnO NTs electrode shows quick sensing response toward the low concentration (0.05 mM) of ethanolamine. The detail sensing parameters of the fabricated ethanolamine chemical sensor were investigated by performing a series of I–V characteristics (Figure 1.7(b)) with various ethanolamine concentrations ranging from 0.05–10 mM in 0.1 M PBS. The current increases continuously with the increase of ethanolamine concentrations from 0.05–10 mM. These increments represent the generation of large number of ions and the increase of ionic strength of the solution with the addition of different concentrations of ethanolamine chemical. Figure 1.7(c) shows the plot of calibrated current versus ethanolamine concentrations to evaluate the sensitivity of the fabricated ethanolamine chemical sensor. The current increases linearly with the increase of ethanolamine concentrations up to 1 mM and afterwards, a saturation level is recorded in the calibrated plot which might due to the unavailability of free active sites over aligned ZnO NTs electrode for ethanolamine adsorption at the higher concentration (>1 mM). The fabricated aligned ZnO NTs electrode based ethanolamine chemical sensor shows significantly high, reliable and reproducible sensitivity of $\sim 37.4 \times 10^{-4} \text{ mA} \cdot \text{mM}^{-1} \cdot \text{cm}^{-2}$, and the detection limit of $\sim 19.5 \mu\text{M}$ with good linearity of ~ 0.05 – 1 mM, correlation coefficient (R) of ~ 0.9850 and a short response time (10 s). To investigate the reproducibility of the sensor, the I–V characteristics of the fabricated ethanolamine chemical sensor were measured for three consecutive weeks and found that the sensor did not show any significant decrease in the sensitivity and other sensing parameters. These results deduced the long term stability of the fabricated ethanolamine chemical sensor based on aligned ZnO NTs electrode. Moreover, the high sensitivity is determined by the presence of large number of oxygenated species on the surface of aligned ZnO NTs electrode

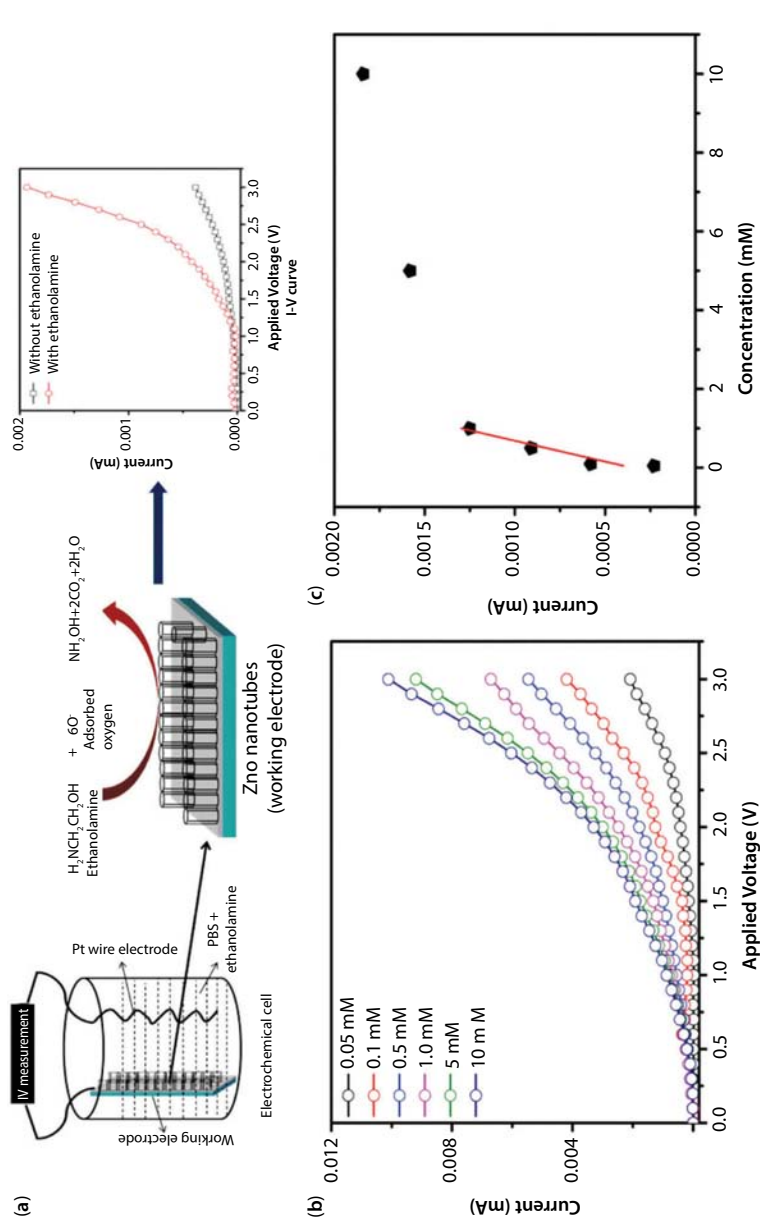


Figure 1.7 Schematic illustration of the fabricated ethanolamine chemical sensor (a), the I-V characteristics of aligned ZnO NTs thin film modified chemical sensor in ethanolamine concentrations in 10 ml PBS solution (b) and corresponding calibration curve of current versus ethanolamine concentrations (c). Reprinted with permission from Ameen, *Mater. Lett.* 106 (2013) 254. © 2013, Elsevier Ltd.

which might considerably create large number of active sites for the conversion of ethanolamine to less harmful products. Thus, the aligned ZnO NTs electrode could be a promising electrode for fabricating the advanced chemical sensor to detect the harmful chemicals.

1.3 Conducting Polymers Nanostructures for Chemiresistors

1.3.1 Sea-Cucumber-Like Hollow Polyaniline Spheres as Efficient Electrode for the Detection of Aliphatic Alcohols

Sensor technology is popularly known for the detection of volatile organic compounds (VOCs) such as alcohols, ethers, esters, halocarbons, ammonia, NO_2 , and warfare agent stimulants [77, 78]. Among various chemicals, ethanol is the commonly used highly corrosive essential chemical which is easily miscible with water or several other organic solvents [79, 80]. In particular, ethanol is extensively used chemical in perfumes or fragrances, colorings and medicinal industries and as feeding solvent for the synthesis of several organic products on a large scale [81]. Due to aforementioned causes, a reliable, simple, economical, highly sensitive, rapid and accurate method or technology is required for the early detection of ethanol. Conjugated polymers offer unique electronic properties owing to their good electrical conductivity, low energy optical transitions, low ionization potential and high electron affinity [82]. PANI shows unique electrical and electronic properties which could be easily changed either by the oxidation of PANI chain or by the protonation of imine nitrogen polymer backbone [83, 84]. S.S. Barkadea *et al.* prepared PANI/Ag nanocomposites electrode for analyzing ethanol vapor sensing [85]. A. Choudhury *et al.* fabricated the modified electrode of PANI thin film and demonstrated the sensing properties of alcohol vapor [84]. Additionally, M.H.H. Jumali and co-workers studied the influence of PANI on ZnO thin films for methanol sensing properties [86]. Ameen *et al.* [87] reported the sea-cucumber-like hollow PANI sphere through template free method, where the existence of the hydrogen bond between OH group of salicylic acid and amine group of polymer chain was a driving force to form self-assembled hollow PANI spheres. The fabricated ethanol chemical sensor based on sea-cucumber-like hollow PANI spheres electrode exhibited an ultrahigh sensitivity of $\sim 426.5 \mu\text{A}\cdot\text{cm}^{-2}\cdot\text{mM}^{-1}$ with a correlation coefficient (R) of ~ 0.90157 .

The morphology of synthesized PANI nanostructures is studied by FESEM images, as shown in Figure 1.8. The synthesized PANI nanostructures possess sea-cucumber-like morphology with a hollow open mouth which is much similar to the real image of sea-cucumber (Holothuroids), as shown in inset of Figure 1.8(a). The average diameter of each sea-cucumber-like hollow PANI sphere is in the range of $\sim 1\text{--}2\ \mu\text{m}$ (Figure 1.8(b)). Noticeably, the shell of PANI sphere is of thickness $\sim 100\text{--}200\ \text{nm}$, consisting uniformly distributed nanofibers which assemble into the morphology of sea-cucumber-like hollow PANI spheres. From Figure 1.8(c, d), the FESEM images of sea-cucumber-like hollow PANI sphere electrode (pellet) displays the highly compact and uniform morphology with few voids. The high magnification image of the electrode depicts the non-damaging hollow PANI spheres, indicating the stability of sea-cucumber-like hollow PANI morphology.

Figure 1.9 shows the TEM images of sea-cucumber-like hollow PANI spheres. The morphology of PANI nanostructures has not changed under the electron beam and exhibits the similar sea-cucumber-like

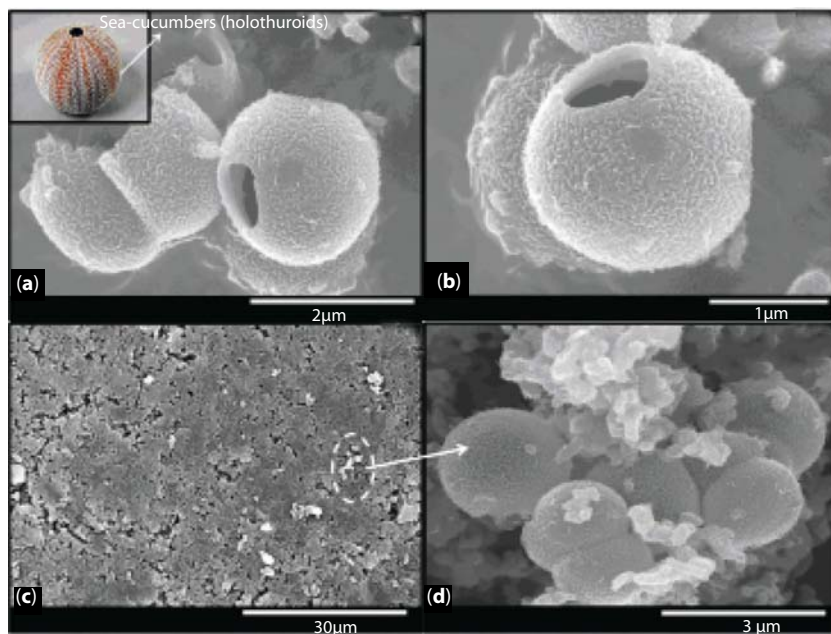


Figure 1.8 FESEM images at low (a) and high resolution (b) of sea-cucumber-like hollow PANI spheres and surface morphology of sea-cucumber-like hollow PANI spheres electrode at (c) low and (d) high magnification. Reprinted with permission from Ameen, *RSC Adv.* 3 (2013) 10460. © 2013, RSC Pub.

hollow spheres morphology, as shown in Figure 1.9(a). The single hollow sphere is of the average diameter of $\sim 1\text{--}2\ \mu\text{m}$ and the shell of the hollow spheres is comprised of sea-cucumber-like nanostructures, as shown in Figure 1.9(b). The element mapping images of sea-cucumber-like hollow PANI spheres have been analyzed to elucidate the elemental compositions of the synthesized PANI nanostructures. The elements mapping images of sea-cucumber-like hollow PANI spheres for carbon (C), nitrogen (N), and sulfur (S) elements are shown in Figure 1.10. The sea-cucumber-like hollow PANI sphere exhibits the major distribution of C and N element which indicates that the synthesized PANI is composed of C and N atoms. However, some assays of S are also detected which might present due to the use of oxidant during polymerization. Thus, the majorly distributed C and N elements in the synthesized PANI confirm the formation of sea-cucumber-like hollow PANI spheres.

The Raman scattering spectrum of sea-cucumber-like hollow PANI spheres is shown in Figure 1.11. The synthesized sea-cucumber-like hollow

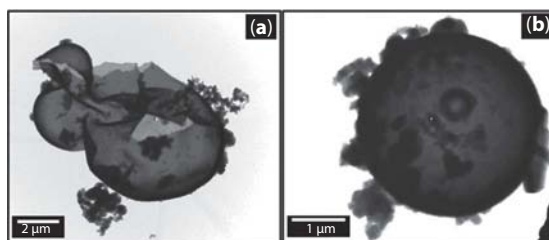


Figure 1.9 TEM images at low (a) and high resolution (b) of sea-cucumber-like hollow PANI spheres. Reprinted with permission from Ameen, *RSC Adv.* 3 (2013) 10460. © 2013, RSC Pub.

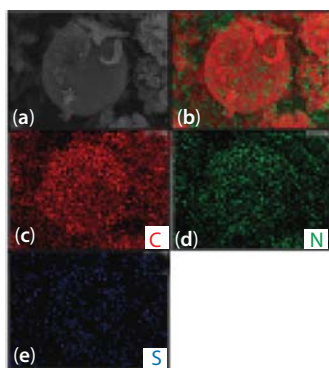


Figure 1.10 Elemental mapping images of (a) surface view, (b) mixed view, (c) C, (d) N, and (e) S elements of sea-cucumber-like hollow PANI spheres. Reprinted with permission from Ameen, *RSC Adv.* 3 (2013) 10460. © 2013, RSC Pub.

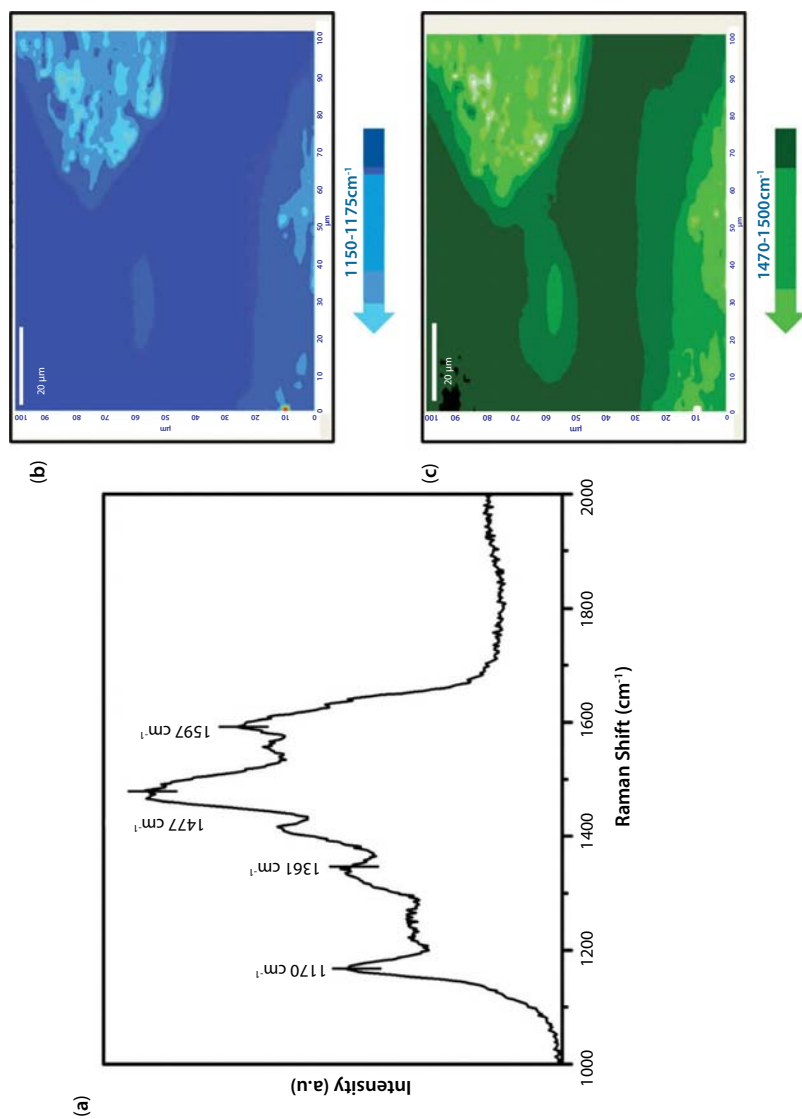


Figure 1.11 Raman spectrum (a) and its corresponding Raman mapping in 1150–1175 cm^{-1} (b) and 1470–1500 cm^{-1} (c) of sea-cucumber-like hollow PANI spheres. Reprinted with permission from Ameen, *RSC Adv.* 3 (2013) 10460. © 2013, RSC Pub.

PANI spheres obtain the Raman bands at 1170, 1477, and 1597 cm^{-1} , corresponding to the C–H bending vibration of semi quinonoid rings (cation-radical segments), N–H deformation vibration associated with the semiquinonoid structures and C=C stretching vibration in the quinonoid ring, respectively [88, 89]. A Raman band at 1361 cm^{-1} provides the information of C–N⁺ vibration of delocalized polaronic structures in the synthesized sea-cucumber-like hollow PANI spheres [90]. These structural characterizations reveal that the synthesized PANI nanostructures possess the typical structure of PANI. Figure 1.11(b, c) shows the Raman mapping by selecting the two ranges of $\sim 1150\text{--}1175 \text{ cm}^{-1}$ and $\sim 1470\text{--}1500 \text{ cm}^{-1}$. A Raman shift at $\sim 1170 \text{ cm}^{-1}$ in the range of $\sim 1150\text{--}1175 \text{ cm}^{-1}$ is assigned to the C–H bending vibration of the semi-quinonoid rings (shown in Figure 1.11(a)), as expressed by the light blue color in the mapping image (Figure 1.11(b)). The Raman mapping image in the range of $\sim 1470\text{--}1500 \text{ cm}^{-1}$ (Figure 1.11(c)) significantly exhibits the N–H deformation vibration which is associated with the semiquinonoid structures in sea-cucumber-like hollow PANI spheres. The corresponding Raman mapping clearly indicates the composition of sea-cucumber-like hollow PANI spheres with uniform distribution of C–H bending vibration and N–H deformation vibration of semiquinonoid rings in sea-cucumber-like hollow PANI spheres.

Figure 1.12 shows the CV analysis to investigate the electrocatalytic activity of sea-cucumber-like hollow PANI spheres electrode toward the detection of ethanol. Figure 1.12(a) shows the typical cyclic voltammogram (CV) of sea-cucumber-like hollow PANI spheres electrode without and with ethanol in 0.1 M phosphate buffer solution (PBS, pH=7.0) at the scan rate of 100 mVs^{-1} . The CV in 0.1 M PBS (pH=7.0) without ethanol exhibits very low redox current density in the range of -0.6 to 1.0 V . The introduction of ethanol in 0.1 M PBS (pH=7.0) increases the redox current density. It is noticed that the oxidation peak of CV is prominent with maximum anodic current $\sim 5.56 \times 10^{-4} \text{ A}$ at 0.33 V , indicating the oxidation process of ethanol over the sea-cucumber-like hollow PANI spheres electrode. However, the electrochemical response of ethanol is reversible and the cathodic peak (I_c) of $\sim -4.65 \times 10^{-4} \text{ A}$ at $\sim -0.04 \text{ V}$ is observed. Thus, the unique morphology of sea-cucumber-like hollow PANI spheres significantly involves the high electron transfer process via high electrocatalytic activity of electrode which might efficiently detect ethanol. Figure 1.12(b) shows CV responses of sea-cucumber-like hollow PANI spheres electrode at various scan rates from 10–200 mVs^{-1} in 0.1 M PBS buffer solution with 25 μM ethanol. The anodic current linearly increases with the increase of scan rates from 10–200 mVs^{-1} which suggests the oxidation process

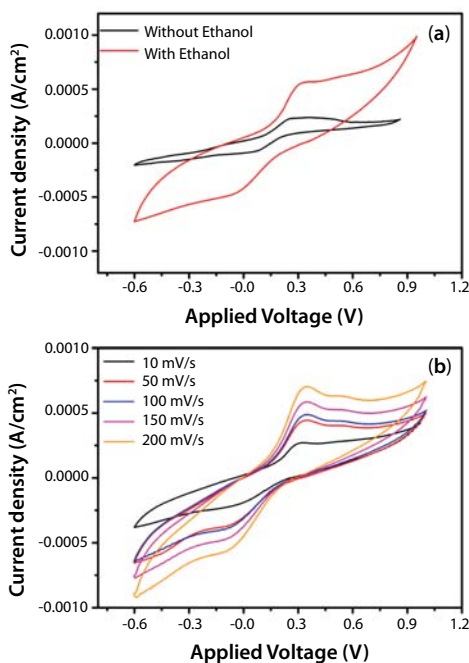


Figure 1.12 (a) Typical CV curve without and with ethanol (25 μM) in 10 ml of 0.1 M PBS solution and (b) CV sweep curves at different scan rates of sea-cucumber-like hollow PANI spheres. Reprinted with permission from Ameen, *RSC Adv.* 3 (2013) 10460. © 2013, RSC Pub.

through the controlled diffusion. In other words, the increased anodic current at highest scan rate also suggests the favorable electro-oxidation of ethanol with the potential sweep. Moreover, the high anodic current is usually attributed to a faster electron transfer reaction in the electrochemical system by the high electrocatalytic behavior of the electrode [91]. Herein, the electrode based on unique sea-cucumber-like hollow PANI spheres might accomplish the faster electron transfer reaction and the electrocatalytic activity at high scan rate of 200 mV s^{-1} .

The electrochemical behavior of the modified electrode based on sea-cucumber-like hollow PANI spheres was further characterized by electrochemical impedance (EIS). Figure 1.13 shows the EIS plots of the sea-cucumber-like hollow PANI spheres electrode in 0.1 M PBS (pH = 7.0) with the different concentrations of ethanol (25 μM –10 mM) at a frequency range from 100 kHz–1 Hz. Figure 1.13(a–e) shows the EIS behavior, where the depressed semicircle in the high frequency region is observed which typically attributes to the parallel combination of the charge transfer

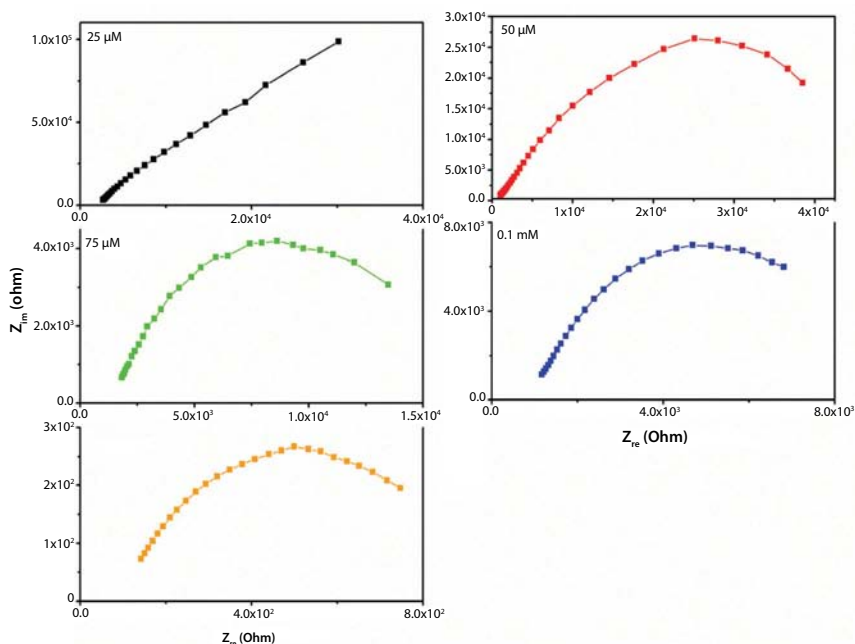


Figure 1.13 EIS plots of sea-cucumber-like hollow PANI spheres based electrode at different concentration of ethanol. Reprinted with permission from Ameen, *RSC Adv.* 3 (2013) 10460. © 2013, RSC Pub.

resistance (R_{CT}) of the electrochemical reaction and the double layer capacitance (C_{dl}) at the interface of the PANI film/electrolyte [92]. It is reported that signal response for sensing is determined by the values of R_{CT} at the interfaces of the PANI electrode and different concentrations of ethanol in PBS [93]. The sea-cucumber-like PANI hollow spheres electrode shows the significant decrease in the R_{CT} with the increased concentration of ethanol in PBS. The recorded R_{CT} values are in the following order of ~ 135.9 k Ω (25 μ M) $>$ ~ 40.12 k Ω (50 μ M) $>$ ~ 13.07 k Ω (75 μ M) $>$ ~ 6.636 k Ω (0.1 mM) $>$ ~ 0.667 k Ω (10 mM). In general, the higher R_{CT} value results to the low charge transfer rate at the interface of PANI electrode/electrolyte in the electrochemical system [94]. Moreover, the R_{CT} also depends on dielectric and the insulating features at the electrode/electrolyte interface [95]. At higher ethanol concentration (10 mM), the sea-cucumber-like hollow PANI electrode displays the smallest R_{CT} value of ~ 0.667 k Ω , indicating the higher charge transfer rate and high sensing response toward ethanol chemical. In other words, the unique morphology of PANI and the concentration of ethanol significantly favor the high ions transport or charge transfer at the electrode and the solution (ethanol in PBS) interfaces.

Furthermore, the detailed sensing behavior of the fabricated ethanol sensor with sea-cucumber-like hollow PANI spheres electrode was further elucidated by measuring a series of current (I)–voltage (V) characteristics with various concentration of ethanol ranging from 25 μM –10 mM in 0.1 M PBS. The current successively increased with the increase of ethanol concentration from 25 μM –10 mM in PBS, which might explain by the generation of large number of ions with the addition of different ethanol concentration, resulting in the increased ionic strength of the solution. The calibration curve of current versus concentration showed the sensitivity of the fabricated ethanol sensor with sea-cucumber-like hollow PANI spheres electrode. The current increased with the increase of ethanol concentration up to ~ 1 mM and then reaches a saturation level, which was consistent with CV and EIS results. The saturation point occurred due to the unavailability of free active sites over the surface of sea-cucumber-like hollow PANI spheres electrode for the adsorption of ethanol chemical at the higher concentration (>1 mM). Using the calibration curve, the sensitivity of ethanol was evaluated by taking the slope and divided by an active area of the electrode (0.5 cm^2). The high and the reproducible sensitivity of $\sim 426.5 \mu\text{A}\cdot\text{mM}^{-1}\cdot\text{cm}^{-2}$ with a correlation coefficient (R) of ~ 0.90157 was obtained by the sea-cucumber-like hollow PANI spheres electrode based chemical sensor toward the detection of ethanol. The fabricated ethanol chemical sensor showed the reasonable detection limit of $\sim 515.7 \mu\text{M}$ and a short response time (10 s). A good linearity in the range of 25 μM –0.1 mM was achieved with the sea-cucumber-like hollow PANI spheres electrode based ethanol chemical sensor. For stability and reproducibility or reversibility, the fabricated ethanol chemical sensor was monitored by measuring the I–V characteristics for three consecutive weeks. No significant fall was detected in the sensing parameters or properties, suggesting the long term stability or durability of the fabricated ethanol chemical sensor based on sea-cucumber-like hollow PANI spheres electrode. This remarkably high sensitivity might explain due to the unique hollow morphology of PANI nanostructures, good optical/electronic behaviors, strong electrocatalytic activity and strong adsorptive properties of electrode toward the ethanol chemical. Furthermore, the sensing response of sea-cucumber-like hollow PANI spheres electrode to ethanol chemical was determined by steady state current–time measurements. At first, the electrochemical experiment was performed in PBS (10 ml) solution without ethanol to stabilize the background current. Thereafter, the ethanol solution (3 μM) was added successively drop by drop in 10 ml of PBS by the peristaltic pump after every 30 s. The steady state current–time responses of sea-cucumber-like hollow PANI spheres electrode to ethanol chemical showed that after every

addition of ethanol chemical into PBS in the amperometric measurements significantly increases the current.

In order to check the selectivity of alcohols, a series of experiments have been performed using various alcohols such as methanol, propanol and butanol and the sensing parameters of each system were determined. Figure 1.14(a) shows the I–V characteristics of different alcohol sensors at $25\ \mu\text{M}$ in 10 ml PBS. Among different alcohols, the ethanol chemical sensor exhibits the maximum current of $\sim 2.62 \times 10^{-5}\ \text{A}$, indicating the highest sensing response with sea-cucumber-like hollow PANI spheres

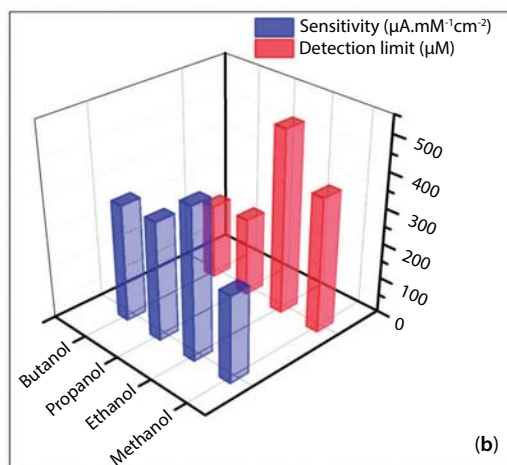
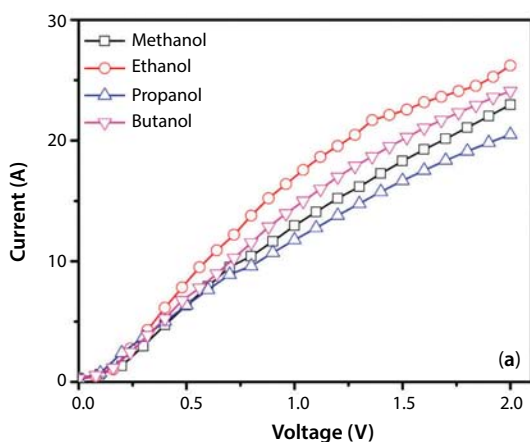


Figure 1.14 (a) I–V characteristics of different alcohols (methanol, ethanol, propanol, and butanol) sensors at $25\ \mu\text{M}$ in 10 ml PBS and (b) histograms of sensitivity and detection limit versus different alcohol sensors based on sea-cucumber-like hollow PANI spheres electrode. Reprinted with permission from Ameen, *RSC Adv.* 3 (2013) 10460. © 2013, RSC Pub.

electrode. Figure 1.14(b) represents the comparative studies of sensitivities and the detection limit toward different alcohols in PBS over the sea-cucumber-like hollow PANI spheres electrode. The order of sensitivities of different alcohols are as ethanol ($\sim 426.5 \mu\text{A.mM}^{-1}.\text{cm}^{-2}$) > propanol ($\sim 335.5 \mu\text{A.mM}^{-1}.\text{cm}^{-2}$) > butanol ($\sim 331.6 \mu\text{A.mM}^{-1}.\text{cm}^{-2}$) > methanol ($\sim 246.2 \mu\text{A.mM}^{-1}.\text{cm}^{-2}$) and the detection limits are in the order of ethanol ($\sim 515.7 \mu\text{M}$) > methanol ($\sim 379.6 \mu\text{M}$) > propanol ($\sim 222.4 \mu\text{M}$) > butanol ($\sim 213.1 \mu\text{M}$). On the other hand, the ethanol chemical sensing responses are also determined in different buffer solutions such as acetic acid and citric acid buffers to elucidate the suitability of PBS. The ethanol chemical sensor in acetic acid and citric acid buffers demonstrate the relatively low sensitivities of ~ 299.8 and $\sim 349.0 \mu\text{A.mM}^{-1}.\text{cm}^{-2}$ whereas, the sensitivity of $\sim 426.5 \mu\text{A.mM}^{-1}.\text{cm}^{-2}$ in PBS is highest toward ethanol chemical. This experiment clearly suggests that ethanol and phosphate buffer is highly suitable chemical and buffer to obtain the good sensing response of alcohols. Inclusively to check the selectivity other than aliphatic alcohols, the sensing performances of sea-cucumber-like hollow PANI spheres electrode toward amine (ethylamine) and thiol (ethanethiol) chemicals have been evaluated. The ethylamine and ethanethiol chemical sensors show lower sensitivities of ~ 80.7 and $\sim 103.6 \mu\text{A.mM}^{-1}.\text{cm}^{-2}$ in phosphate buffer as compared to aliphatic alcohols chemical sensors. Thus, the sea-cucumber-like hollow PANI spheres electrode is a promising active electrocatalytic electrode for the effective detection of ethanol chemical.

1.3.2 The Sensing Properties of Layered Polyaniline Nanosheets toward Hazardous Phenol Chemical

Phenol and phenolic compound are widely used chemicals in plastics, fertilizers, paints, rubber, adhesives, paper, and soap industries [96]. It is also used as an antiseptic, a topical anesthetic for sore throat lozenges and sprays as a skin exfoliant [97]. The excess concentration of phenol and phenolic compounds is an issue of environmental concern due to their toxicity and persistence or high adsorptive nature in the environment [98]. The detection, identification and the quantification of phenol and its compounds are very important for clean environment. Various PANI nanostructures display the improved optical, structural, electronic and electrical properties which might act as useful candidate for the application in electrochemical, electrochromic, biosensors and chemical sensors devices [99, 100]. Recently, PANI nanomaterials have gained a great attention in the field of sensors including gas sensor, biosensor and chemical sensors [101]. In

context of PANI based sensors, A.L. Kukla *et al.* prepared PANI thin films for detecting ammonia [102]. Y. Bo *et al.* explained the electrochemical DNA biosensor by PANI nanowires modified graphene electrode [103]. Recently, P. Kunzo *et al.* fabricated the hydrogen sensor based on unique oxygen plasma treated PANI thin film [104]. Till date, very few reports are available on phenol sensor using PANI nanomaterials. An amperometric phenol biosensor based on PANI electrode was studied in the aspects of optical and electrochemical properties [105]. J. Zhang *et al.* designed the composite electrode of PANI-ionic liquid-carbon nanofiber for the fabrication of highly sensitive amperometric biosensors toward phenols [106]. H.K. Seo *et al.* [107] synthesized the layered PANI nanosheets through the chemical polymerization and applied directly for the fabrication of phenol chemical sensor. The fabricated phenol sensor based on layered PANI nanosheets exhibited a high sensitivity of $\sim 1485.3 \mu\text{A} \cdot \text{mM}^{-1} \cdot \text{cm}^{-2}$ and very low detection limit of $\sim 4.43 \mu\text{M}$ with correlation coefficient (R) of ~ 0.9981 and short response time (10 s).

Figure 1.15 shows the topographic and three-dimensional (3D) AFM images of layered PANI nanosheets. The layered morphology of the synthesized PANI is visibly recorded in the topographic mode, as shown in Figure 1.15(a). The 3D AFM image (Figure 1.15(b)) has confirmed the same layered morphology, as detected in the topographic mode. The roughness of layered PANI nanosheets is estimated from AFM images by taking the value of the root mean roughness (R_{rms}). The layered PANI nanosheets exhibit relatively the high roughness of $\sim 52.3 \text{ nm}$. It is known that the electrode materials with large roughness factor display higher electrochemical behavior or the electrocatalytic activity [108]. The high

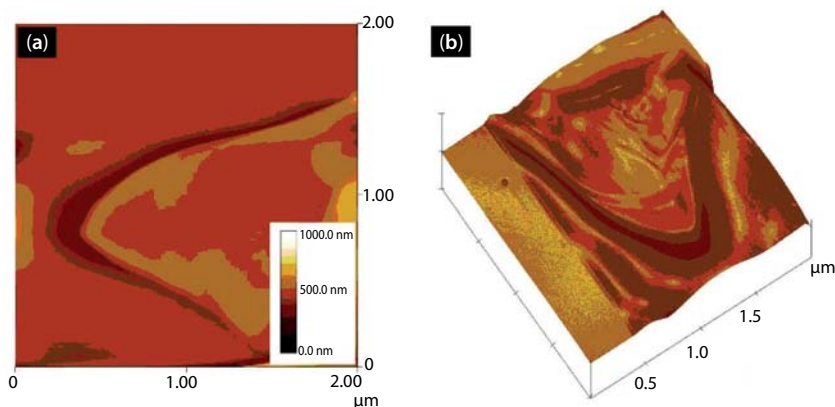


Figure 1.15 Topographic (a) and 3D (b) AFM images of layered PANI nanosheets. Reprinted with permission from Ameen, *Talanta* 104 (2013) 219. © 2013, Elsevier Ltd.

roughness of layered PANI nanosheets might improve the electrochemical behavior toward the detection of phenol.

Figure 1.16(a) shows the X-rays diffraction (XRD) patterns of layered PANI nanosheets. Typically, two diffraction peaks at 19.3° and 25.1° are recorded, corresponding to the periodicity parallel and perpendicular to the polymer chain, respectively. These peaks are also assigned to emeraldine structure of PANI. The recorded XRD patterns are similar to PANI sheets or matrix [108]. The element composition of the layered PANI nanosheets is analyzed by taking the line scan element mapping through EDS. Figure 1.16(b, c) shows the line scan element mapping image and pie profile of the elements. The C and N elements are majorly distributed in the line scan mapping however, the traces of Cl and S elements are also detected, as seen in the corresponding pie bar graph shown in Figure 1.16(c). The uniform distribution of C and N elements confirm the formation of layered PANI nanosheets.

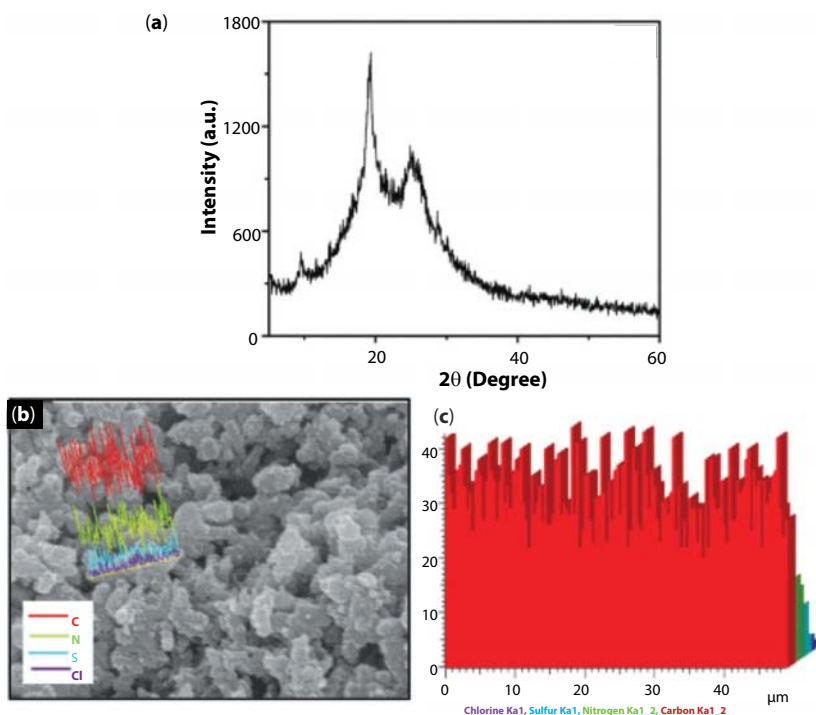
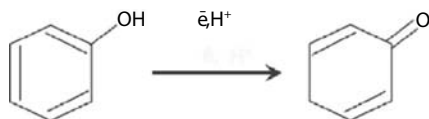


Figure 1.16 (a) XRD patterns, (b) line scanning elemental mapping image, and (c) the corresponding pie bar graph of layered PANI nanosheets. Reprinted with permission from Ameen, *Talanta* 104 (2013) 219. © 2013, Elsevier Ltd.

The electrocatalytic activity of layered PANI nanosheets electrode toward the detection of phenol was examined by the CV analysis. Figure 1.17 shows the typical CV of layered PANI nanosheets electrode without and with a series of phenol concentrations (20 μM –0.32 mM) in 0.1 M phosphate buffer (pH = 7.0) at the scan rate of 100 mVs^{-1} . The layered PANI nanosheets electrode shows the relatively low redox current in the absence of phenol, as shown in Figure 1.17(a). Importantly, the prominent oxidation peak with the maximum anodic current of $\sim 1.1 \times 10^{-4}$ A at ~ 0.37 V is obtained with the addition of lowest phenol concentration (20 μM), indicating the significant sensing response and high electrocatalytic activity over the surface of layered PANI nanosheets. The weak reduction peak with low cathodic current of -4.67×10^{-5} A is also observed in the CV curve. The electrochemical behavior with prominent oxidation peak along with weak reduction peak is quite similar to the reported literatures [109] and thus, the following reaction could be proposed for phenol



A series of CV plots have been carried out with various phenol concentrations ranging from 20 μM –0.32 mM in 0.1 M PBS to further examine the electrochemical properties of layered PANI nanosheets electrode. Figure 1.17(b) shows the typical quasi-reversible redox peaks to the electrochemical reaction of layered PANI nanosheets electrode toward the

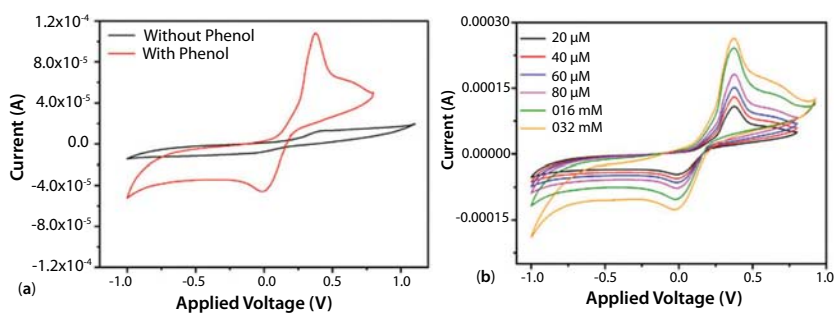


Figure 1.17 (a) Typical CV curve of fabricated phenol chemical sensor based layered PANI nanosheets electrode without and with phenol (20 μM) in 10 ml of 0.1 M PBS solution and (b) CV sweep curves in phenol concentrations of 20 μM –0.32 mM in 10 ml of 0.1 M PBS solution. Reprinted with permission from Ameen, *Talanta* 104 (2013) 219. © 2013, Elsevier Ltd.

phenol chemical in PBS. The oxidation peak gradually increases with the increase of phenol concentration from 20 μM –0.32 mM. It is reported that the high height of oxidation peak and the high anodic current are referred to the faster electron transfer reaction in the electrochemical system via high electrocatalytic behavior of the working electrode [110]. The highest anodic current is obtained at the highest concentration of phenol (0.32 mM), which is about 2 times larger than the lowest phenol concentration 20 μM . The considerable increased of the anodic current demonstrates that the electrochemical activity of layered PANI nanosheets electrode is remarkably promoted for the detection of phenol chemical and thus, confirms the involvement of high electrons transfer process via high electrocatalytic activity of the electrode.

The fabricated phenol chemical sensor is illustrated in Figure 1.18(a), which is comprised of layered PANI nanosheets electrode as working electrode and Pt wire as cathode electrode in PBS. The measurements of current (I)–voltage (V) characteristics (Figure 1.18(b)) are performed for evaluating the sensing properties such as sensitivity, detection limit and correlation coefficient of layered PANI nanosheets electrode toward phenol chemical. After the addition of phenol (20 μM), the sudden increase in the current of $\sim 67.3 \mu\text{A}$ is observed by the fabricated phenol chemical sensor however, a low current ($\sim 11.1 \mu\text{A}$) is recorded without phenol based chemical sensor. A series of the I–V characteristics have been established to elucidate the sensing parameters of the fabricated phenol chemical sensor with layered PANI nanosheets electrode, as shown in Figure 1.18(b). It is seen that the current has continuously increased with the increase of the phenol concentrations ($\sim 20 \mu\text{M}$ –0.32 mM), suggesting the good sensing response toward the phenol chemical by the layered PANI nanosheets electrode based phenol chemical sensor. This phenomenon might originate by the generation of large number of ions and the increase of ionic strength of the solution with the addition of different concentration of phenol. A calibration curve of current versus phenol concentration (Figure 1.18(c)) is plotted to calculate the sensitivity of the fabricated phenol chemical sensor. The calibrated current linearly increases up to the increase of the phenol concentrations $\sim 80 \mu\text{M}$ and then attains a saturation level in the calibrated plot. The occurrence of the saturation point might due to the unavailability of free active sites over the layered PANI nanosheets electrode for phenol adsorption at higher concentration ($>80 \mu\text{M}$). The fabricated phenol chemical sensor with layered PANI nanosheets electrode achieves high, and the reproducible sensitivity of $\sim 1485.3 \mu\text{A}\cdot\text{mM}^{-1}\cdot\text{cm}^{-2}$ and the detection limit of $\sim 4.43 \mu\text{M}$ with correlation coefficient (R) of ~ 0.9981 and short response time (10 s). A good linearity in the range of 20–80 μM is detected

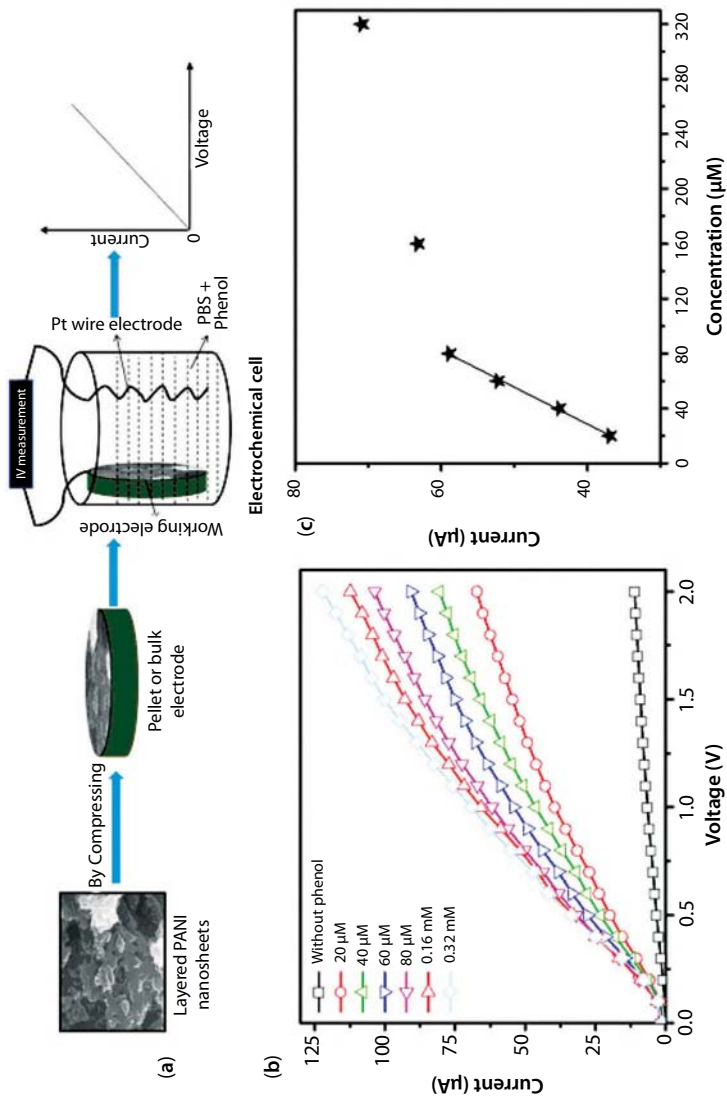


Figure 1.18 (a) Schematic illustration of the fabricated phenol chemical sensor, (b) I–V characteristics of layered PANI nanosheets based phenol chemical sensor at different phenol concentrations (20 μM - 0.32 mM) in 10 ml of 0.1 M PBS and (c) the calibration curve of current versus phenol concentration of the fabricated chemical sensor. Reprinted with permission from Ameen, *Talanta* 104 (2013) 219. © 2013, Elsevier Ltd.

by the fabricated phenol chemical sensor with layered PANI nanosheets electrode. However, the layered PANI nanosheets electrode shows less sensing response toward catechol chemical with the sensitivity of $\sim 41.4 \mu\text{A}\cdot\text{mM}^{-1}\cdot\text{cm}^{-2}$ and the detection limit of $19.4 \mu\text{M}$. The sensitivity toward catechol chemical with layered PANI nanosheets electrode is comparable to other catechol sensor [111]. For reproducibility and the stability of fabricated phenol chemical sensor, the sensing response by the I–V characteristics was measured for three consecutive weeks. It was found that the fabricated phenol chemical sensor did not show any significant decrease in the sensing parameters or properties, which deduced the long term stability of the fabricated phenol sensor based on layered PANI nanosheets electrode. Herein, the achieved sensitivity, detection limit and the correlation coefficient of the fabricated phenol chemical sensor are superior to those of reported literatures on phenol sensor with PANI electrodes [111–113]. Thus, the unique layered morphology of PANI nanosheets is promising and effective as working electrode for the detection of phenol chemical.

1.3.3 Prospective Electrode of Polypyrrole Nanobelts for the Detection of Aliphatic Alcohols

The major environment pollutants like CO_2 , CO , SO_2 , and VOCs are usually produced by the consumption of commonly used chemicals such as ammonia (NH_3), ethanol ($\text{C}_2\text{H}_5\text{OH}$), methanol (CH_3OH), and other aliphatic alcohols [114]. Moreover, the excessive use of VOCs such as aliphatic alcohols and ketones are continuously polluting the environment and causes the health problems [115]. Methanol is highly used as automotive fuel in motor vehicles and in making dyes and perfumes [116]. The surplus exposure of methanol to human could cause blindness, metabolic acidosis and might lead to death [117]. Conjugated polymers are known as p-type semiconductors with unique electronic properties due to their reasonable electrical conductivity, low energy optical transitions, low ionization potential, and high electron affinity [118]. These polymers could be easily synthesized through simple chemical or electrochemical processes and their conductivities could be altered by modifying the electronic structures through doping or de-doping procedures [119]. Therefore, conducting polymers could suitably work as an effective working electrode and might offer the fast response toward the detection of various harmful chemicals [120]. In general, the good selectivity, wide linear range, rapid response, portability, and the room temperature working abilities are the basic requirements for the efficient working of chemical sensors [121]. PPy, a conducting polymer, is much explored material because it shows high

electrical conductivity, high stability in air and aqueous media and thus, an extremely useful material for actuators, electric devices and for the efficient detection of the harmful chemicals [122, 123]. Few literatures are reported on the sensor performances of PPy nanostructure based electrodes for the detection of aliphatic alcohols S.J. Hong *et al.* studied nitro vinyl substituted PPy as a unique reaction-based chemosensor for cyanide anion [124]. C.W. Lin *et al.* prepared the composite electrode of PPy-poly vinyl alcohol (PVA) by electrochemical method for the detection of methanol and ethanol vapor [125, 126]. L. Jiang *et al.* prepared the composite films of PPy-PVA by in situ vapor state polymerization method and demonstrated the methanol sensing behavior based on the thickness of PPy-PVA film electrodes [127]. Recently, M. Babaei *et al.* determined the residual methanol content in the biodiesel samples by developing new PPy-ClO₄ electrodes via electrodeposition on interdigital electrodes [128]. The roughness and morphology of the PPy greatly influence the responses for the detection of harmful chemicals [129]. In this context, the unique and effective working electrode based on PPy nanobelts has been utilized for the fabrication of highly sensitive and reproducible aliphatic alcohols chemical sensor by Ameen *et al.* [130]. The unique PPy nanobelts were simply synthesized by the in situ chemical polymerization of pyrrole monomer and were directly applied as working electrode for the efficient detection of aliphatic alcohols using simple current (I)–voltage (V) characteristics.

The morphology of the synthesized PPy nanomaterials is analyzed by FESEM and TEM images, as shown in Figure 1.19. From FESEM images (Figure 1.19(a, b)), the synthesized PPy nanomaterials possess smooth and the uniform belt like morphology. Each PPy nanobelt presents the average thickness of ~100 nm and width of ~400 nm, as shown in Figure 1.19(b). The morphology of the synthesized PPy has been further characterized by the TEM analysis (Figure 1.19(c)). Similar morphology and the dimensions are observed in TEM image, which is consistent with the FESEM results. Interestingly, the morphology of PPy nanobelts has not changed under high energy electron beam, indicating the stability of PPy nanobelts.

The topographic and 3D AFM images of synthesized PPy nanobelts showed the nanobelts morphology was visibly seen in the AFM images. The synthesized PPy nanobelts showed the reasonable root mean roughness (R_{ms}) of ~18.1 nm. In our case, the PPy nanobelts with reasonable R_{ms} value might deliver the electrochemical behavior toward the detection of aliphatic alcohols.

The elemental compositions of the synthesized PPy nanobelts are estimated by the element line scan image through EDS, as depicted in Figure 1.20. The line scan image and pie profile (Figure 1.20(a, b)) display

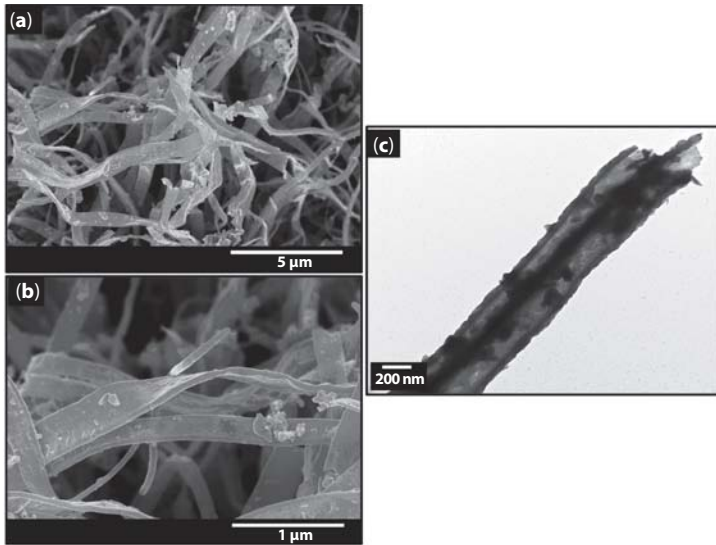


Figure 1.19 FESEM images at low (a) and high (b) resolution and TEM image (c) of PPy nanobelts. Reprinted with permission from Ameen, *Appl. Catal. B: Environ.* 144 (2014) 665. © 2014, Elsevier Ltd.

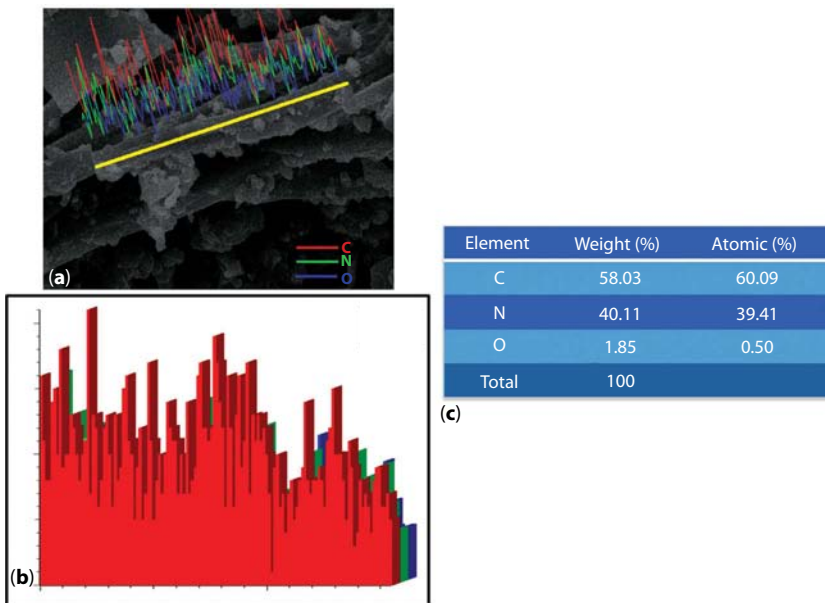


Figure 1.20 Line scanning elemental mapping image (a), corresponding pie bar graph (b), and summary of elemental mapping of PPy nanobelts (c). Reprinted with permission from Ameen, *Appl. Catal. B: Environ.* 144 (2014) 665. © 2014, Elsevier Ltd.

that the synthesized PPy nanobelts are largely composed of carbon and nitrogen elements. Few traces of oxygen elements are also recorded which might due to surface moisture or atmospheric oxygen on the surface of nanobelts. Figure 1.20(c) summarizes the existing elements of PPy nanobelts in weight percentage (wt%) and atomic percentage (at%). The synthesized PPy nanobelts are consisted of uniformly distributed carbon and nitrogen with at% of ~ 60.09 and ~ 39.41 , respectively. The detection of C, N and O elements confirm the formation of synthesized PPy nanobelts.

The electrochemical impedance spectroscopy (EIS) measurements were performed for the fabricated aliphatic alcohols chemical sensors based on novel PPy nanobelts electrode to explain the electrocatalytic activity of the electrodes. Figure 1.21 shows the EIS plots of the fabricated aliphatic alcohols chemical sensors based on novel PPy nanobelts electrode using 0.1 M phosphate sulfate solution (PBS) with methanol, propanol and butanol at similar concentration of $20 \mu\text{M}$. All EIS measurements are carried out at a frequency range from 100 kHz–1 Hz. From Figure 1.21, the fabricated aliphatic alcohols chemical sensor displays two semicircles, in which the large semicircle in the high frequency region is attributed to the parallel combination of the charge transfer resistance (R_{CT}) of the electrochemical reaction and the double layer capacitance (C_{dl}) at the interface of the PPy electrode/PBS electrolyte [131]. R_{CT} of sensor device defines the electron transfer kinetics of the redox probe at the electrode interface [131]. In general, the signal response for sensing device is determined by the values of R_{CT} at the interfaces of the PPy electrode and different concentrations of alcohol in PBS [132]. Herein, all electrochemical alcohol chemical sensors

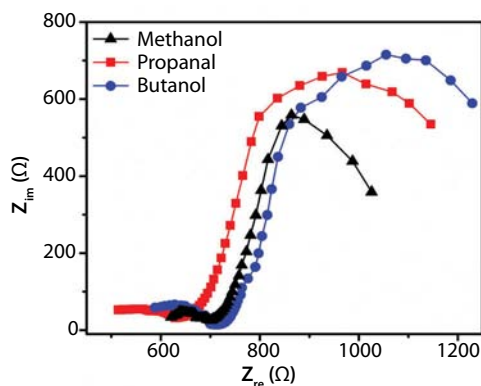


Figure 1.21 EIS plots of fabricated different aliphatic alcohol sensors based on PPy nanobelts electrode. Reprinted with permission from Ameen, *Appl. Catal. B: Environ.* 144 (2014) 665. © 2014, Elsevier Ltd.

present similar nature of EIS plots in 10 ml of PBS (0.1 M) with different alcohols at the same concentration of 20 μM . A relatively low R_{CT} value ($\sim 353 \Omega$) is obtained by the fabricated methanol chemical sensor based on PPy nanobelts electrode, however, the propanol and butanol chemical sensors show the high R_{CT} values of ~ 507 and $\sim 597 \Omega$, respectively. Generally, the low charge transfer rate at the interface of electrode/electrolyte in the electrochemical system is originated from high R_{CT} value [133]. This result suggests that the fabricated methanol chemical sensor based on PPy nanobelts electrode presents the better charge transfer rate and the electrocatalytic activity toward the methanol chemical, resulting to the high sensing response on the surface of PPy nanobelts electrode. Whereas, other aliphatic alcohols based chemical sensors are quite inferior to methanol chemical sensor.

The detailed sensing properties including the detection limit, linearity, correlation coefficient and sensitivity were extensively evaluated by the two electrodes I–V characteristics measurements where PPy nanobelts electrodes was used as working electrode while the Pt wire was applied as cathode. All I–V characteristics were measured with the applied voltage ranging from 0–2.5 V. The typical fabricated alcohol chemical sensor depicted the aliphatic alcohol sensing mechanism over the surface of PPy nanobelts. The fabricated aliphatic alcohol chemical sensor was performed in PBS with and without alcohols and the sensing behavior was simply explained by the I–V characteristics. It was noticed that the drastic increase in current was observed after the addition of aliphatic alcohols (20 μM) in all the fabricated chemical sensors as compared to chemical sensor without alcohol. The addition of methanol chemical (20 μM) in PBS displayed the highest current of $\sim 60.4 \mu\text{A}$ while the lower currents of ~ 58.7 and $\sim 55.4 \mu\text{A}$ were obtained with the addition of propanol and butanol chemicals in PBS, respectively. This gradual increase in the current indicated the rapid sensing response of PPy nanobelts electrode toward the detection of methanol, propanol and butanol chemicals, which might result from the better electrocatalytic or electrochemical behavior and the fast electron exchange of PPy nanobelts electrode. The I–V responses of PPy nanobelts electrode with various concentration of aliphatic alcohols ranging from 20 μM –1 mM in 10 ml of 0.1 M PBS were measured to investigate the detailed sensing behavior of PPy nanobelt electrode. The I–V characteristics of the fabricated methanol chemical sensor with various concentrations of methanol chemical (20 μM –1 mM) in 0.1 M PBS solution of pH 7. When PPy nanobelts based electrode was exposed to methanol, the current drastically increased with the increase of the methanol concentrations, exhibited the good sensing response to methanol chemical. The typical calibration curve

showed that the fabricated methanol chemical sensor based on PPy nanobelts electrode is reproducible, reliable and exhibits the highest sensitivity of $\sim 205.64 \mu\text{A} \cdot \text{mM}^{-1} \cdot \text{cm}^{-2}$ with the linearity of $20 \mu\text{M}$ – 0.16 mM , detection limit of $\sim 6.92 \mu\text{M}$ and correlation coefficient (R) of ~ 0.98271 . However, the fabricated propanol and butanol chemical sensors based on PPy nanobelts electrode showed the low sensitivities of ~ 190.76 and $\sim 146.34 \mu\text{A} \cdot \text{mM}^{-1} \cdot \text{cm}^{-2}$ and moderate detection limits of ~ 13.7 and $\sim 12.06 \mu\text{M}$, respectively. All aliphatic alcohol sensors displayed the same response time of 10 s. As compared to other aliphatic alcohols, the highest current response and sensitivity were observed for methanol chemical sensing which might suggest the high electron mobility and electrochemical activity over the surface of PPy nanobelts electrode, as described in EIS results.

Figure 1.22 depicts the schematic illustration of the proposed mechanism of aliphatic alcohol chemical sensors over the surface of PPy nanobelts electrode. The detection of aliphatic alcohol chemicals in liquid phase is generally obtained by the adsorption of oxygenated species in PBS to the surface of PPy nanobelts electrode. These adsorbed oxygenated species change the concentration of oxygen species due to surface reactions and thus, develops a potential barrier and enhances the resistance of the material [134]. Further, the chemisorbed oxygen reacts with alcohols over the PPy nanobelts electrode and forms a weak hydrogen bonding, which is due to the generation of an ion-dipole between $-\text{HN}^{+}$ of PPy and neutral molecule (alcohols) [135]. A hydroxyl terminated PPy is generated by the substitution of adsorbed alcohol on PPy nanobelts electrode [136]. Thus, the terminated hydroxyl might have electrons from the surface of PPy nanobelts to produce the highly reactive oxygenated species, resulting in the decrease of conductance. The releasing of electrons (\bar{e}) might significantly dissociate the adsorbed alcohols into CO_2 and H_2O by the electrocatalytic behavior of PPy nanobelts electrode. These electrons are back to the surfaces of PPy nanobelts and again increase the conductance of electrode. Herein, the differences in the sensing response of PPy nanobelts based electrode for different aliphatic alcohols could attribute to the variations in the concentration of adsorbed oxygen species which might considerably affect their sensing reaction and conductance of PPy nanobelts electrode. Additionally, the interference study has been performed to understand the high sensing response of methanol chemical through the fabricated chemical sensor based on PPy nanobelt electrode, as shown in Figure 1.22(c). The methanol, propanol and butanol are consecutively added into PBS to evaluate the sensing response. From the amperometric results (Figure 1.22(c)), a rapid response current is seen after the addition of methanol while propanol and butanol have shown weak response

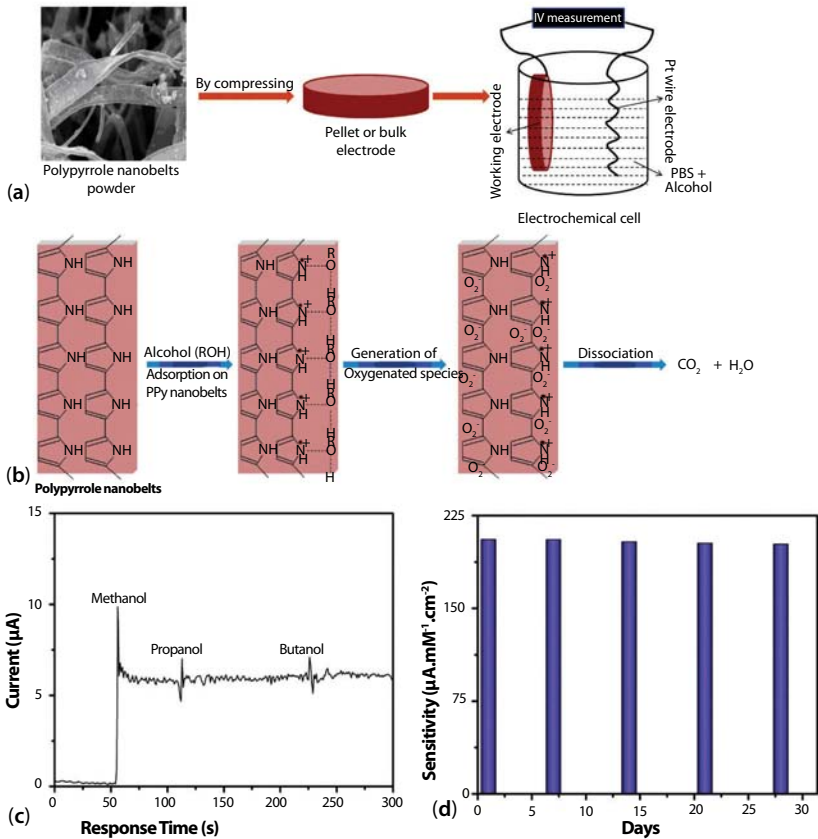


Figure 1.22 (a) Schematic illustration of electrochemical system and (b) proposed mechanism of aliphatic alcohol chemical sensors over the surface of PPy nanobelts electrode. (c) Interference tests of the fabricated aliphatic alcohol sensors upon addition of methanol ($5 \mu\text{M}$), propanol ($5 \mu\text{M}$), and butanol ($5 \mu\text{M}$) in PBS (pH 7) and (d) plot of sensitivity versus time interval (days) of the fabricated aliphatic alcohol sensor. Reprinted with permission from Ameen, *Appl. Catal. B: Environ.* 144 (2014) 665. © 2014, Elsevier Ltd.

current. This phenomenon clearly indicates that the fabricated chemical sensor based PPy nanobelt electrode is sensitive to methanol chemical as compared to other aliphatic alcohols.

Figure 1.23(A) shows the FTIR spectra of PPy nanobelts electrode before and after the sensing measurements. Before the sensing measurements, the main IR peaks at ~ 1560 and $\sim 1480 \text{ cm}^{-1}$ are observed for PPy nanobelts electrode corresponding to C=C antisymmetric and symmetric stretching vibration in PPy ring, respectively [137]. Another main IR peak at $\sim 3206 \text{ cm}^{-1}$ presents the N-H stretching in the PPy ring. After the

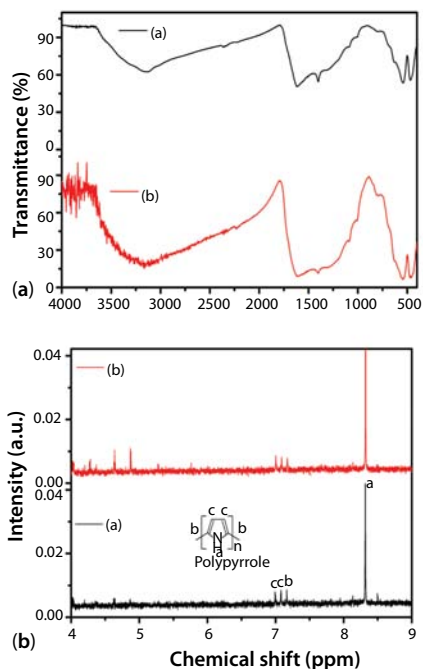


Figure 1.23 (A) FTIR and (B) $^1\text{H-NMR}$ spectra of PPy nanobelts electrode before (a) and after (b) the sensing measurements. Reprinted with permission from Ameen, *Appl. Catal. B: Environ.* 144 (2014) 665. © 2014, Elsevier Ltd.

sensing measurements, PPy nanobelts electrode shows almost similar IR spectrum with the peaks of high intensities, indicating that no structural changes have occurred after the sensing measurements. The increase in IR peak's intensity might attribute to the partial interaction between the OH group of alcohols and NH group of PPy nanobelts electrode. Noticeably, no effects or damages have been observed in the structural properties of PPy nanobelts after the sensing measurements in PBS electrolyte with various concentrations of aliphatic alcohols. Therefore, the prepared PPy nanobelts electrode is highly stable in aqueous medium and could be reused for other sensing measurements. The $^1\text{H-NMR}$ spectra of PPy nanobelts electrode before and after the sensing measurements in DMSO solvent is shown in Figure 1.23(B). The $^1\text{H-NMR}$ spectra of PPy nanobelt displays the peaks (a, b, c) in the range of 7.0–8.5 ppm, which are assigned to proton of NH group and the aromatic protons on pyrrole ring. After the sensing measurements, two NMR peaks are seen at 5.0–4.5 ppm, indicating the interaction of aliphatic alcohols on PPy nanobelts surface. The NMR peaks at 5.0–4.5 ppm correspond to the protons of carbon, attached with

OH group (alcoholic group). The existence of these peaks might suggest that the aliphatic alcohol first interact with the surface of PPy nanobelts through NH group during the sensing measurement, which is proposed in the illustrated mechanism. This result is fully consistent with FTIR results of PPy nanobelts electrode. The superior sensitivity and other sensing parameters of PPy nanobelt electrode toward aliphatic alcohol chemical might impute to the excellent adsorption ability and high electrocatalytic/electrochemical activities of PPy nanobelts. Therefore, PPy nanobelts are the excellent and novel working electrode materials for the fabrication of aliphatic alcohol chemical sensors.

1.4 Semiconducting Nanocomposites for Chemoresistors

1.4.1 Hydrazine Chemical Sensing by Modified Electrode of Polyaniline/Graphene Nanocomposite Thin Film

Hydrazine and its derivatives are commonly known fuels in explosives, antioxidants, rocket propellants, blowing agents, photographic chemical, corrosion inhibitor, insecticides, and plant growth regulators [138]. In spite of these, it is commonly known as a neurotoxin, carcinogenic, mutagenic and hepatotoxic [139]. The exposure of high level of hydrazine causes the irritation of eyes, nose, throat, temporary blindness, dizziness, nausea, pulmonary edema and coma, which might be lethal to the liver, kidneys, and central nervous system in humans [140]. The flat carbon nanosheets of sp^2 -bonded carbon atoms called graphene (Gr), has recently attracted viable attention due to its high electrical conductivity [141], large specific surface area (theoretically $2630 \text{ m}^2/\text{g}$) [142], low manufacturing cost and good mechanical properties [143]. Gr composites with metal oxide and organic semiconductors show the fascinating applications in electrochemical sensors and biosensors [144, 145]. The Gr composites are usually produced by incorporating Gr into other materials which could enhance the electrochemical properties by the synergic effects. PANI is known organic semiconductor or conducting polymer and is promising host material for various inorganic semiconductors and carbon materials because of relatively high conductivity, excellent chemical and the electrochemical stability [146, 147]. Recently, the composites of PANI and Gr exhibit tremendous applicability in many electronic, optical, electrochemical and biosensors [148, 149]. The PANI/Gr composites display significant electrical conductivity and electrochemical properties toward

various electrochemical, electrochromic and biosensing devices [150]. Although, PANI/Gr composites have been explored for several promising applications but still, the studies based on chemical sensor using PANI/Gr composites are limited. Recently, L.A. Mashat *et al.* demonstrated the hydrogen sensing properties of PANI/Gr composites [151]. Y. Bo group reported the electrochemical DNA biosensor by PANI nanowires modified Gr electrode [152]. The voltammetric determination of 4-aminophenol by the PANI/Gr composite modified electrode was studied by Y. Fan *et al.* [153]. The in situ electrochemical synthesis of aniline monomer with Gr to prepare PANI/Gr composite thin film electrode for the detection of hydrazine was reported by Ameen *et al.* [154]. The fabricated hydrazine sensor showed very high sensitivity of $\sim 32.54 \times 10^{-5} \text{ A.cm}^{-2} \text{ mM}^{-1}$ and high detection limit $\sim 15.38 \text{ mM}$. The in situ electrochemical synthesis of PANI/Gr composites modified electrode was effective for the rapid detection of hydrazine through simple current (I)-voltage (V) characteristics.

Figure 1.24 shows the FESEM and TEM images of Gr and PANI/Gr composite. The surface of Gr thin film (Figure 1.24(a)) exhibits layered morphology like the crumpled waves with the average thickness of several

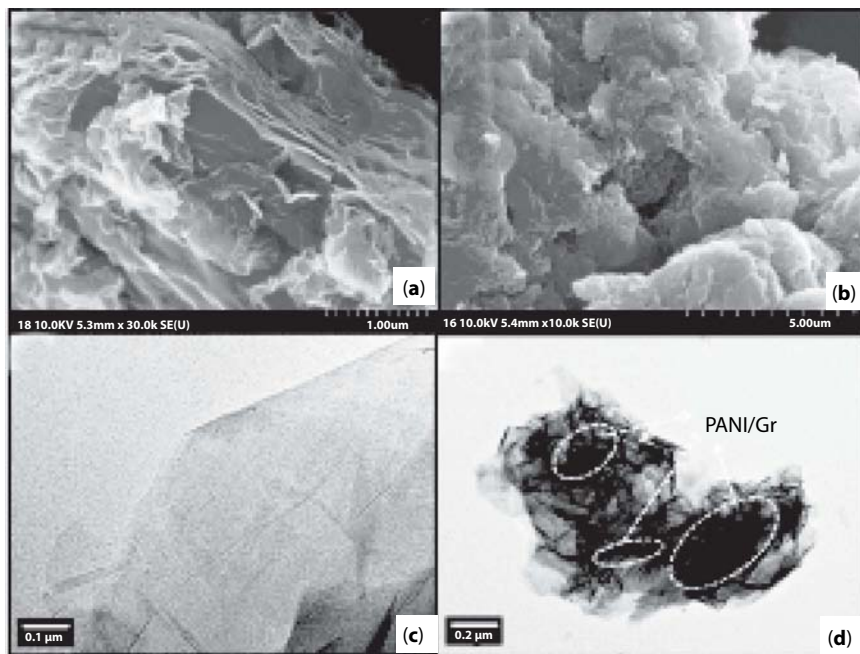


Figure 1.24 FESEM images of (a) Gr and (b) PANI/Gr composites. TEM images of (c) Gr and (d) PANI/Gr composites. Reprinted with permission from Ameen, *Sens. Act. B* 173 (2012) 177. © 2012, Elsevier Ltd.

hundred nanometers. The in situ electrochemically deposited PANI/Gr composites film (Figure 1.24(b)) manifests the mixed morphology of the layered Gr covered by PANI molecules obtained by the polymerization of aniline monomer in HCl. It is seen that during the polymerization of aniline in electrochemical process, PANI molecules have uniformly covered the Gr sheets. Similarly, the TEM images present the transparent layered sheet morphology of Gr which is stable under the electron beam, as shown in Figure 1.24(c). On the other hand, the transparent morphology along with aggregated clusters is observed in PANI/Gr composite, shown in Figure 1.24(d). The transparent edges and black parts are ascribed to Gr sheet and PANI in PANI/Gr composites, respectively.

Figure 1.25(a) shows the FTIR spectra of Gr and PANI/Gr composites. Typically, Gr sheets obtain the IR bands at ~ 1716 , ~ 1596 , ~ 1211 cm^{-1} / 1046 cm^{-1} which are ascribed to the characteristics of C=O, C=C, and C-O in C-O-C/C-O-H groups, respectively [155]. The IR bands at ~ 1592 , ~ 1501 , ~ 1304 , ~ 1231 , and 1147 cm^{-1} are recorded in the FTIR spectrum of PANI/Gr composites and these peaks are slightly shifted from the pristine PANI (not shown here) [151]. Particularly, the shifting in the IR band at ~ 1592 cm^{-1} indicates the interaction between Gr and PANI through π - π^* interactions by partial hydrogen bonding. Thus, it could be deduced that PANI/Gr composites possess the partial hydrogen bonding between O=C-O⁻ of Gr and PANI backbone during the in situ electrochemical polymerization. The UV-vis spectrum of Gr sheets and PANI/Gr composites, as shown in Figure 1.25(b) displays the optical properties and the interaction between Gr and PANI. A single absorbance peak at ~ 271 nm in Gr sheet is observed which attributes to π - π^* transitions of the C-C bonds in hexagonal ring [156]. The PANI/Gr composites exhibit three absorbance bands at ~ 278 , ~ 324 , and ~ 641 nm, corresponding to the characteristics bands of Gr sheet and PANI and the two absorption bands at ~ 324 and ~ 641 nm in the PANI/Gr composite are assigned to π - π^* and n - π^* transitions of PANI, respectively [157]. Importantly, a slight shift to higher absorption edge has been observed in the Gr absorption band in PANI/Gr composites which might indicate the π - π^* interaction between PANI and Gr in the PANI/Gr composites [158]. This result is fully consistent with FTIR results.

The sensing mechanism of hydrazine is generally explained by the concentration of electrolyte solution and the nature of the electrodes. It could be demonstrated by determining of intermediate in the oxidation process [159]. The CV was carried out for the PANI/Gr modified electrode without and with 0.1 μM hydrazine in 0.1 M PBS (pH = 7) at the scan rate of 100 mV/s to define the oxidation process. It is reported that the electrolyte solution with pH 7 shows the improved electrocatalytic oxidation

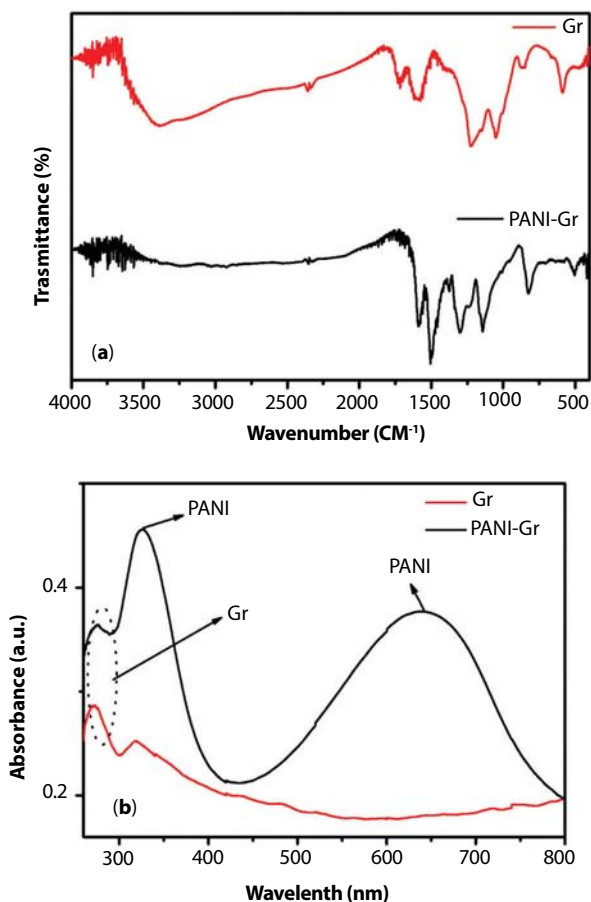


Figure 1.25 FTIR spectra (a) and UV-vis spectra (b) of Gr and PANI/Gr composites. Reprinted with permission from Ameen, *Sens. Act. B* 173 (2012) 177. © 2012, Elsevier Ltd.

of hydrazine [160]. From CV with hydrazine using the PANI/Gr modified electrode, the oxidation process started from -0.25 V and reached the maximum anodic current of $6.2 \mu\text{A}$ at 0.35 V. No cathodic current was displayed which indicated the irreversible electrochemical response toward hydrazine. The PANI/Gr modified electrode with hydrazine exhibited the higher current than that of without hydrazine system, indicated the effective oxidative detection of hydrazine. The calibration curve of current versus concentration elucidated the sensitivity of the fabricated hydrazine sensor. From this calibration plot, it was seen that the current increased with the increase of the concentrations up to 0.1 mM and afterwards, a saturation level was reached, which might due to the unavailability of free

active sites over PANI/Gr composite modified electrode for hydrazine adsorption at the higher concentration of hydrazine (>0.1 mM) [161]. In general, the sensitivity of hydrazine was calculated from the slope of calibration plot and divided by active area of electrode (0.25 cm²). The fabricated PANI/Gr composite based hydrazine chemical sensor showed reasonably high and reproducible sensitivity of $\sim 32.54 \times 10^{-5}$ A.cm⁻². mM⁻¹ in the linear dynamic range of 0.01 μ M to 0.1 mM. Moreover, a good linearity of ~ 0.78578 and the detection limit of ~ 15.38 mM with a short response time (10 s) were estimated from the I–V characteristics of hydrazine chemical sensor. To elucidate the stability of hydrazine chemical sensor, the I–V characteristics were measured for three consecutive weeks and no significant decrease was observed in the I–V properties of the fabricated PANI/Gr composite based hydrazine chemical sensor, indicated the fabricated hydrazine sensor shows long term stability. Interestingly, the sensitivity value and other parameters from I–V characteristics of the fabricated PANI/Gr composite based hydrazine chemical sensor are superior to other reported hydrazine chemical sensor [162–165]. The enhancement of sensing properties might due to the attractive features of Gr sheet and PANI layer containing subtle electronic behaviors and strong adsorptive capability [166, 167]. Additionally, some electrostatic interaction between Gr and hydrazine might occur through positively charged nitrogen atoms of hydrazine which results to increase the sensing properties.

1.5 Conclusions and Outlook

In summary, this chapter provides a comprehensive review on the morphological, structural, crystalline, optical, electrical and electrochemical properties of semiconducting metal oxides particularly TiO₂, ZnO, conducting polymers, and nanocomposites for the utilization of fabricating effective chemiresistors. The synthesis procedures and compositions of nanomaterials and nanocomposites considerably affect the optical, electrical, and electrochemical properties of the fabricated thin film electrode. The metal oxides semiconducting nanomaterial with different morphologies and sizes show the enhanced surface-to-volume ratio for efficient detection of harmful chemicals. The tailoring of multidimensional nanostructures to 1D is playing a significant role for determining the physiological and electrical properties. Particularly, 1D metal oxides nanomaterials are promising and effective for detecting various toxic chemicals through chemiresistors. The preparation and modifications of the working electrodes with different inorganic and organic nanomaterials could be promising electrodes for

the reliable and effective detection of harmful chemicals by electrochemical tools. On the other hand, a unique organic p-type semiconducting polymer like, PANI and PPy are highly stable polymer with good electrical conduction, high environmental stability, and ease of fabrication and thus, highly promising for detecting the toxic chemicals. Needless to say, due to the tremendous research efforts and the space limitations, this chapter is unable to cover all the exciting works reported in this field. Future research would be focused on the preparation of nanomaterials by exploring new and advanced techniques to achieve the highly advanced and sensitive materials for working electrodes. The optimization of working electrode in terms of thickness and electrical conductivity of metal oxide, conducting polymers, and nanocomposites could also provide the high performance of chemiresistors and biosensors.

Acknowledgments

Dr. Sadia Ameen acknowledges the Research Funds of Chonbuk National University in 2012. This work is fully supported by NRF Project # 2014R1A2A2A01006525. This work is also supported by “Leaders in Industry-University Cooperation Project” (2015), supported by the Ministry of Education, Science & Technology (MEST) and the National Research Foundation of Korea (NRF).

References

1. X.S. Fang, Y. Bando, U.K. Gautam, C.H. Ye and D. Golberg, *Journal of Materials Chemistry*, Vol. 18, p. 509, 2008.
2. T. Zhai, X. Fang, M. Liao, X. Xu, H. Zeng, B. Yoshio and D. Golberg, *Sensors*, Vol. 9, p. 6504, 2009.
3. R.K. Pandey and V. Lakshminarayanan, *Applied Catalysis B: Environmental*, Vol. 125, p. 271, 2012.
4. L.A. Mashat, H.D Tran, W. Wlodarski, R.B. Kaner and K. ZadehK. *Sensors and Actuators B: Chemical*, Vol. 134, p. 826, 2008.
5. K.E. Sapslord, M.M. Ngundi, M.H. Moore, M.E. Lassman, L.L.C. Shriver, C.R. Taitt and F.S. Ligler, *Sensors and Actuators B: Chemical*, Vol. 8113, p. 599, 2006.
6. K.T.C. Chai, P.A. Hammond and D.R.S. Cumming, *Sensors and Actuators B: Chemical*, Vol. 111, p. 305, 2005.
7. T. Hyodo, T. Mori, A. Kawahara, H. Kalsuki, Y. Shimizu and M. Egashira, *Sensors and Actuators B: Chemical*, Vol. 877, p. 41, 2001.

8. E. Chow, E.L.S. Wong, T. Bocking, O.T. Nguyen, D.B. Hibber and J.J. Gooding, *Sensors and Actuators B: Chemical*, Vol. 11, p. 540, 2005.
9. S.S. Bozkurl, E. Merdivan and Y. Benibol, *Microchimica Acta*, Vol. 168, p. 141, 2010.
10. A. Umar, M.M. Rahman and Y.B. Hahn, *Electrochemistry Communications*, Vol. 11, p. 1353, 2009.
11. Z. Jiang, J. Wang, L. Meng, Y. Huang and L. Liu, *Chemical Communications*, Vol. 47, p. 6350, 2011.
12. H.J. Zhang, J.S. Huang, H.O. Hou and T.Y. You, *Electroanalysis*, Vol. 21, p. 1869, 2009.
13. L. Zheng and J.F. Song, *Talanta*, Vol. 79, p. 319, 2009.
14. S. Ameen, M.S. Akhtar, Y.S. Kim and H.S. Shin, *Applied Catalysis B: Environmental*, Vol. 103, p. 136, 2011.
15. S. Ameen, M.S. Akhtar, M. Song and H.S. Shin, *ACS Applied Materials & Interfaces*, Vol. 4, p. 4405, 2012.
16. S.M. Lee, S.N. Cho and J. Cheon, *Advanced Materials*, Vol. 15, p. 441, 2003.
17. S.J. Limmer, T.P. Chou and G.Z. Cao, *Journal of Materials Science*, Vol. 39, p. 895, 2004.
18. L. Sun, J. Li, C.L. Wang, S.F. Li, Y.K. Lai, H.B. Chen and C.J. Lin, *Journal of Hazardous Material*, Vol. 171, p. 1045, 2009.
19. P.M. Perillo and D.F. Rodriguez, *Sensors and Actuators B: Chemical*, Vol. 171, p. 639, 2012.
20. H. Xu, Q. Zhang, C. L. Zheng, W. Yan and W. Chu, *Applied Surface Science*, Vol. 257, p. 8478, 2011.
21. Q. Wang, Y.Z. Pan, S.S. Huang, S.T. Ren, P. Li and J.J. Li, *Nanotechnology*, Vol. 22, p. 025501, 2011.
22. Y. Kwon, H. Kim, S. Lee, I.J. Chin, T.Y. Seong, W.I. Lee and C. Lee, *Sensors and Actuators B: Chemical*, Vol. 173, p. 441, 2012.
23. K.S. Chen, K. Xie, X.R. Feng, S.F. Wang, R. Hu, H.S. Gu and Y. Li, *International Journal of Hydrogen Energy*, Vol. 37, p. 13602, 2012.
24. S. Ameen, M.S. Akhtar, H.K. Seo and H.S. Shin, *Applied Physics Letters*, Vol. 103, p. 061602, 2013.
25. J. Wang and Z.Q. Lin, *Chemistry of Materials*, Vol. 20, p. 1257, 2008.
26. J.L. Zhao, X.H. Wang, R.Z. Chen and L.T. Li, *Solid State Communications*, Vol. 134, p. 705, 2005.
27. H.T. Gomes, P.V. Samant, P. Serp, P. Kalck, J.L. Figueiredo and J.L. Faria, *Applied Catalysis B: Environmental*, Vol. 54, p. 175, 2004.
28. M. Torres, A.M.T. Silva, F.J. Maldonado-Hódar, B.F. Machado, A.F. Pérez-Cadenas, J.L. Faria, J.L. Figueiredo and F. Carrasco-Marín, *Applied Catalysis B: Environmental*, Vol. 105, p. 86, 2011.
29. R. Levi, M. Milman, M.V. Landau, A. Brenner and M. Herskowitz, *Environmental Science & Technology*, Vol. 42, p. 5165, 2008.
30. M.L. Olvera and R. Asomoza, *Sensors and Actuators B: Chemica*, Vol. 45, p. 49, 1997.

31. R.K. Sharma, M.C. Bhatnagar and G.L. Sharma, *Sensors and Actuators B: Chemical*, Vol. 45, p. 209 1997.
32. F. Boccuzzi, A. Chiorino, S. Tsubota and M. Haruta, *Sensors and Actuators B: Chemical*, Vol. 24, p. 540, 1995.
33. E.T. Lee, G.E. Jang, C.K. Kim and D.H. Yoon, *Sensors and Actuators B: Chemical*, Vol. 77, p. 221, 2001.
34. S.R. Kim, H.K. Hong, C.H. Kwon, D.H. Yun, K. Lee and Y.K. Sung, *Sensors and Actuators B: Chemical*, Vol. 66, p. 59, 2000.
35. R. Bene, I.V. Perczel, F. Re^{ti}, F.A. Meyer, M. Fleisher and H. Meixner, *Sensors and Actuators B: Chemical*, Vol. 71, p. 36, 2000.
36. F. Bender, C. Kim, T. Mlsn and J.F. Vetelino, *Sensors and Actuators B: Chemical*, Vol. 77, p. 281, 2001.
37. A. Umar, S.H. Kim and Y.B. Hahn, *Current Applied Physics*, Vol. 8, p. 793, 2008.
38. A. Umar, M.S. Chauhan, S. Chauhan, R. Kumar, G. Kumar, S.A. Al-Sayari, S.W. Hwang and A. Al-Hajry, *Journal of Colloid and Interface Science*, Vol. 363, p. 521, 2011.
39. P.K. Samanta, *Science of Advanced Materials*, Vol. 4, p. 219, 2012.
40. S. Baskoutas and G. Bester, *The Journal of Physical Chemistry C*, Vol. 115, p. 15862, 2011.
41. S. Chrissanthopoulos, N. Baskoutas, V. Bouropoulos, P. Dracopoulos, S.N. Pouloupoulos and Yannopoulos, *Photonics and Nanostructures*. Vol. 9, p. 132, 2011.
42. O. Lupan, V.V. Ursaki, G. Chai, L. Chow, G.A. Emelchenko, I.M. Tiginyanu, A.N. Gruzintsev and A.N. Redkin, *Sensors and Actuators B: Chemical*, Vol. 144, p. 56, 2010.
43. D.S. Kang, S.K. Han, J.H. Kim, S.M. Yang, J.G. Kim, S.K. Hong, D. Kim and H. Kim, *Journal of Vacuum Science & Technology B*, Vol. 27, p. 1667, 2009.
44. S. Ameen, M.S. Akhtar and H.S. Shin, *Talanta*, Vol. 100, p. 377, 2012.
45. E. Galoppini, J. Rochford, H.H. Chen, G. Saraf, Y.C. Lu, A. Hagfeldt and G. Boschloo, *The Journal of Physical Chemistry B*, Vol. 110, p. 16159, 2006.
46. A. Hu, F. Wu, J. Liu, J. Jiang, R. Ding, X. Li, C. Cheng, Z. Zhu and X. Huang, *Journal of Alloys and Compounds*, Vol. 507, p. 261, 2010.
47. J.J. Hassan, M.A. Mahdi, C.W. Chin, H. Abu-Hassan and Z. Hassan, *Sensors and Actuators B: Chemical*, Vol. 176, p. 360, 2013.
48. G.N. Dar, A. Umar, S.A. Zaidi, A.A. Ibrahimd, M. Abaker, S. Baskoutas and M.S. Al-Assiri, *Sensors and Actuators B: Chemical*, Vol. 173, p. 72, 2012.
49. S. Ameen, M.S. Akhtar, H.K. Seo and H.S. Shin *Applied Catalysis A: General*, Vol. 470, p. 271, 2014.
50. R.J. Wu, D.J. Lin, M.R. Yu, M.H. Chen and H.F. Lai, *Sensors and Actuators B: Chemical*, Vol. 178, p. 185, 2013.
51. R.J. Wu, Y.C. Huang, M.R. Yu, T.H. Lin and S.L. Hung, *Sensors and Actuators B: Chemical*, Vol. 134, p. 213, 2008.

52. N. Izu, W. Shin and N. Murayama, *Sensors and Actuators B: Chemical*, Vol. 87, p. 99, 2002.
53. J.H. Sun, S.Y. Dong, J.L. Feng, X.J. Yin and X.C. Zhao, *Journal of Molecular Catalysis A: Chemical*, Vol. 335, p. 145, 2011.
54. P. Pouloupoulos, S. Baskoutas, S.D. Pappas, C.S. Garoufalidis, S.A. Droulias, A. Zamani and V. Kapaklis, *Journal of Physical Chemistry C*, Vol. 115, p. 14839, 2011.
55. S. Baskoutas, P. Pouloupoulos, V. Karoutsos, M. Angelakeris and N.K. Flevaris, *Chemical Physics Letters*, Vol. 417, p. 461, 2006.
56. K. Vanheusden, W.L. Warren, C.H. Seager, D.R. Tallant, J.A. Voigt and B.E. Gnade, *Journal of Applied Physics*, Vol. 79, p. 7983, 1996.
57. C. Roy, S. Byrne, E. McGlynn, J.P. Mosnier, E. dePosada, D.O. Mahony, J.G. Lunney, M.O. Henry, B. Ryan and A.A. Cafolla, *Thin Solid Films*, Vol. 436, p. 273, 2003.
58. R. Chakravarty and C. Periasamym. *Science of Advanced Materials*, Vol. 3, p. 276, 2011.
59. M. Vafaei and M.S. Ghamsari, *Materials Letters*, Vol. 61, p. 3265, 2007.
60. G.H. Lee, *Materials Letters*, Vol. 73, p. 53, 2010.
61. P.K. Samanta, *Science of Advanced Materials*, Vol. 4, p. 219, 2012.
62. B. Straumal, A. Mazilkin, S. Protasova, A. Myatiev, P. Straumal, E. Goering and B. Baretzky, *Physica Status Solidi (b)*, Vol. 248, p. 1581, 2011.
63. Y.F. Gao, M. Nagai, T.C. Chang and J.J. Shyue, *Crystal Growth & Design*, Vol. 7, p. 2467, 2007.
64. H.J. Zhang, J.S. Huang, H.Q. Hou and T.Y. You, *Electroanalysis*, Vol. 21, p. 1869, 2009.
65. H.K. Seo, S. Ameen, M.S. Akhtar and H.S. Shin, *Talanta*, Vol. 104, p. 219, 2013.
66. S. Ameen, M.S. Akhtar and H.S. Shin, *Talanta*, Vol. 100, p. 377, 2012.
67. A.A. Ibrahim, G.N. Dar, S.A. Zaidi, A. Umar, M. Abaker, H. Bouzid and S. Baskoutas, *Talanta*, Vol. 93, p. 257, 2012.
68. S. Ameen, M.S. Akhtar and H.S. Shin, *Sensors and Actuators B: Chemical*, Vol. 173, p. 177, 2012.
69. S. Ameen, M.S. Akhtar and H.S. Shin, *RSC Advances*, 2013; DOI: 10.1039/C3RA00016H.
70. S. Ameen, M.S. Akhtar and H.S. Shin, *Materials Letters*, Vol. 106, p. 254, 2013.
71. B.B. Straumal, A.A. Mazilkin, S.G. Protasova, A.A. Myatiev, P.B. Straumal, E. Goering and B. Baretzky, *Thin Solid Films*, Vol. 520, p. 1192, 2011.
72. A. Al-Hajry, A. Umar, Y.B. Hahn and D.H. Kim, *Superlattices and Microstructures*, Vol. 45, p. 529, 2009.
73. R.A. Laudise, E.D. Kolb and A.J. Caporason, *Journal of the American Ceramic Society*, Vol. 47, p.9, 1964.
74. S. Ameen, M.S. Akhtar, Y.S. Kim, O.B. Yang and H.S. Shin, *Electrochimica Acta*, Vol. 56, p. 1111, 2011.
75. S. Ameen, M.S. Akhtar and H.S. Shin, *Chemical Engineering Journal*, Vol. 195, p. 307, 2012.

76. R.M. Silverstein, F.X. Webster. *Spectrometric Identification of Organic Compounds*, John Wiley & Sons, New York, NY, USA, 1998
77. (a) C.E. Collins and L.J. Buckley, *Synthetic Metals*, Vol. 78, p. 93, 1996. (b) M. Abaker, G.N. Dar, A. Umar, S.A. Zaidi, A.A. Ibrahim, S. Baskoutas and A. Al-Hajry, *Science of Advanced Materials*, Vol. 4, p. 893, 2012. (c) A.A. Ibrahim, G.N. Dar, S.A. Zaidi, A. Umar, M. Abaker, H. Bouzid and S. Baskoutas, *Talanta*, Vol. 93, p. 257, 2012.
78. (a) M.S. Freund and N.S. Lewis, *Proceedings of the National Academy of Sciences U.S.A.*, Vol. 92, p. 2652, 1995. (b) G.N. Dar, A. Umar, S.A. Zaidi, S. Baskoutas, S.W. Hwang, M. Abaker, A. Al-Hajry and S.A. Al-Sayari, *Talanta*, Vol. 89, p. 155, 2012. (c) M. Abaker, A. Umar, S. Baskoutas, G.N. Dar, S.A. Zaidi, S.A. Al-Sayari, A. Al-Hajry, S.H. Kim and S.W. Hwang, *Journal of Physics D: Applied Physics*, Vol. 44, p. 425401, 2011.
79. R. Phathaitep, G. Atcharawan, C. Torranin, M. Pongsri, M. Nikorn and C. Supab, *Ceramics International*, Vol. 35, p. 649, 2009.
80. (a) Z. Jiang, J. Wang, L. Meng, Y. Huang and L. Liu, *Chemical Communications*, Vol. 47, p. 6350, 2011. (b) G.N. Dar, A. Umar, S.A. Zaidi, S. Baskoutas, S.H. Kim, M. Abaker, A. Al-Hajry and S.A. Al-Sayari, *Science of Advanced Materials*, Vol. 3, p. 901, 2011.
81. A. Umar, F. Al-Hazmi, G.N. Dar, S.A. Zaidi, R.M. Al-Tuwirqi, F. Alnowaiser, A.A. Al-Ghamdi and S.W. Hwang, *Sensors and Actuators B: Chemical*, Vol. 166, p. 97, 2012.
82. S. Ameen, M.S. Akhtar and M. Husain, *Science of Advanced Materials*, Vol. 2, p. 441, 2010.
83. S. Ameen, S.G. Ansari, M. Song, Y.S. Kim and H.S. Shin, *Superlattices and Microstructures*, 2009, 46, 745.
84. A. Choudhury, *Sensors and Actuators B: Chemical*, Vol. 138, p. 318, 2009.
85. S. Barkade, J.B. Naik and S.H. Sonawane, *Colloids and Surfaces A: Physicochemical and Engineering Aspects*, Vol. 378, p. 94, 2011.
86. M.H.H. Jumali, N. Ramli, I. Izzuddin, M.M. Salleh and M. Yahaya, *Sains Malaysiana*, Vol. 40, p. 203, 2011.
87. S. Ameen, M.S. Akhtar and H.S. Shin, *RSC Advances*, Vol. 3, p. 10460, 2013.
88. M.I. Boyer, S. Quillard, G. Louarn, G. Froyer and S. Lefrant, *The Journal of Physical Chemistry B*, Vol. 104, p. 8952, 2000.
89. M. Cochet, G. Louarn, S. Quillard, M.I. Boyer, J.P. Buisson and S. Lefran, *Journal of Raman Spectroscopy*, Vol. 31, p. 1029, 2000.
90. R. Mazeikiene, A. Statino, Z. Kuodis, G. Niauras and A. Malinauska, *Electrochemistry Communications*, Vol. 8, p. 1082, 2006.
91. S. Ameen, M.S. Akhtar and H.S. Shin, *Sensors and Actuators B: Chemical*, Vol. 173, p. 177, 2012.
92. P. Fiordiponti and G. Pistoia, *Electrochimica Acta*, Vol. 34, p. 215, 1989.
93. T. Yang, N. Zhou, Q. Li, Q. Guan, W. Zhang and K. Jiao, *Colloids and Surfaces B: Biointerfaces*, Vol. 97, p. 150, 2012.
94. M.A. Vorotyntsev, J.P. Badiali and G. Inzelt, *Journal of Electroanalytical Chemistry*, Vol. 472, p. 7, 1999.

95. R. Khan, A. Kaushik, P.R. Solanki, A.A. Ansari, M.K. Pandey and B.D. Malhotra, *Analytica Chimica Acta*, Vol. 616, p. 207, 2008.
96. S.G. Burton, *Current Organic Chemistry*, Vol. 7, p. 1317, 2003.
97. D. Perićin, V. Krimer, S. Trivi and L. Radulovi, *Food Chemistry*, Vol. 113, p. 450, 2009.
98. S.C. Atlow, L.B. Aporo and A.M. Klibanov, *Biotechnology and Bioengineering*, Vol. 26, p. 599, 1984.
99. S. Ding, D. Chao, M. Zhang and W. Zhang, *Journal of Applied Polymer Science*, Vol. 107, p. 3408, 2008.
100. P. Alexander, O. Nikolay, K. Alexander and S. Galina, *Progress in Polymer Science*, Vol. 28, p. 1701, 2003.
101. S. Ameen, M.S. Akhtar and H.S. Shin, *Sensors and Actuators B: Chemical*; DOI: org/10.1016/j.snb.2012.06.065.
102. A.L. Kukla, Y.M. Shirshov and S.A. Piletsky, *Sensors and Actuators B: Chemical*, Vol. 37, p. 135, 1996.
103. Y. Bo, H. Yang, Y. Hu, T. Yao and S. Huang, *Electrochimica Acta*, Vol. 56, p. 2676, 2011.
104. P. Kunzo, P. Lobotka, M. Micusik and E. Kovacova, *Sensors and Actuators B: Chemical*, Vol. 171, p. 838, 2012.
105. P. Wang, M. Liu and J. Kan, *Sensors and Actuators B: Chemical*, Vol. 140, p. 577, 2009.
106. J. Zhang, J. Lei, Y. Liu, J. Zhao, H. Ju, J. Zhang, J. Lei, Y. Liu, J. Zhao and H. Ju, *Biosensors and Bioelectronics*, Vol. 24, p. 1858, 2009.
107. H.K. Seo, S. Ameen, M.S. Akhtar and H.S. Shin, *Talanta*, Vol. 104, p. 219, 2013.
108. (a) Z. Dai, G. Wei, X. Xinghu and C. Hongyuan, *Chinese Science Bulletin*, Vol. 51, p. 19, 2006. (b) S. Hasim, S.C. Raghavendra, M. Revanasiddappa, K.C. Sajjan, M. Lakshmi and M. Faisal, *Bulletin of Materials Science*, Vol. 34, p. 1557, 2011.
109. M. Del, P.T. Sotomayor, A.A. Tanaka and L.T. Kubota, *Journal of Electroanalytical Chemistry*, Vol. 536, p. 71, 2002.
110. A. Umar, M.M. Rahman, S.H. Kim and Y.B. Hahn, *Chemical Communications*, p. 166, 2008.
111. H. Xuev and Z. Shen, *Talanta*, Vol. 57, p. 289, 2002.
112. Y. Fan, J.H. Liu, C.P. Yang, M. Yuv and P. Liu, *Sensors and Actuators B: Chemical*, Vol. 157, p. 669, 2011.
113. J. Adamski, P. Nowak and J. Kochana, *Electrochimica Acta*, Vol. 55, p. 2363, 2010.
114. M. Consales, A. Cutolo, M. Penza, P. Aversa, M. Giordano and A. Cusano, *Journal of Sensors*, Vol. 2008, p. 1 (Article ID: 936074), 2008. (b) S.C. Kim and W.G. Shim, *Applied Catalysis B: Environmental*, Vol. 98, p. 180, 2010.
115. P.C. Lekha, M. Balaji, S. Subramanian and D.P. Padiyan, *Current Applied Physics*, Vol. 10, p. 457, 2010.

116. P. Pandey, J.K. Srivastava, V.N. Mishra and R. Dwivedi, *Journal of Natural Gas Chemistry*, Vol. 20, p. 123, 2011.
117. M.A Medinsky and D.C Dorman, *Toxicology Letters*, Vol. 82, p. 707, 1995.
118. S. Ameen, M.S. Akhtar and M. Husain, *Science of Advanced Materials*, Vol. 2, p. 441, 2010. (b) R.K. Pandey and V. Lakshminarayanan, *Applied Catalysis B: Environmental*, Vol. 125, p. 271, 2012.
119. L.A. Mashat, H.D. Tran, W. Wlodarski, R.B. Kaner and K.K. Zadeh, *Sensors and Actuators B: Chemical*, Vol. 134, p. 826, 2008.
120. C.L. Zhu, Y.J. Chen, R.X. Wang, L.J. Wang, M.S. Cao and X.L. Shi, *Sensors and Actuators B: Chemical*, Vol. 140, p. 185, 2009.
121. S. Pirsá and N. Alizadeh, *Sensors and Actuators B: Chemical*, Vol. 147, p. 461, 2010.
122. (a) S. Pirsá and N. Alizadeh, *IEEE Sensors Journal*, Vol. 11, p. 3400, 2011. (b) R. Aydın and H.Ö. Dogan and F. Köleli, *Applied Catalysis B: Environmental*, Vol. 140, p. 478, 2013.
123. S.J. Hong and C.H. Lee, *Tetrahedron Letters*, Vol. 53, p. 3119, 2012.
124. M. Şenel and C. Nergiz, *Current Applied Physics*, Vol. 12, p. 1118, 2012.
125. C.W. Lin, B.J. Hwang and C.R. Lee, *Materials Chemistry and Physics*, Vol. 55, p. 139, 1998.
126. C.W. Lin, B.J. Hwang and C.R. Lee, *Journal of Applied Polymer Science*, Vol. 73, p. 2079, 1999.
127. L. Jiang, H.K. Jun, Y.S. Hoh, J.O. Lim, D.D. Lee and J.S. Huh, *Sensors and Actuators B: Chemical*, Vol. 105, p. 132, 2005.
128. M. Babaei and N. Alizadeh, *Sensors and Actuators B: Chemical*, Vol. 183, p. 617, 2013.
129. F. Quadrifoglio and V. Crescenzi, *Journal of Colloid and Interface Science*, Vol. 35, p. 447, 1971.
130. S. Ameen, M.S. Akhtar, H.K. Seo and H.S. Shin, *Applied Catalysis B: Environmental*, Vol. 144, p. 665, 2014.
131. P. Fiordiponti and G. Pistoia, *Electrochimica Acta*, Vol. 34, p. 215, 1989.
132. C.M. Li, C.Q. Sun, W. Chen and L. Pan, *Surface and Coatings Technology*, Vol. 198, p. 474, 2005.
133. M.A. Vorotyntsev, J.P. Badiali and G. Inzelt, *Journal of Electroanalytical Chemistry*, Vol. 472, p. 7, 1999.
134. P. Feng, Q. Wan and T.H. Wang, *Applied Physics Letters*, Vol. 87, p. 213111, 2005.
135. M. Hara and A. Eisenberg, *Macromolecules*, Vol. 17, p. 1335, 1984.
136. L.T. Sein, *The Journal of Physical Chemistry A*, Vol. 112, p. 598, 2008.
137. L.J. Bellamy. *The Infrared Spectra of Complex Molecules*, 2, 2nd ed., Chapman and Hall, London, 1980.
138. A. Umar, M.M. Rahman, S.H. Kim and Y.B. Hahn, *Chemical Communications*, Vol. 2, pp. 166–168, 2008.
139. S.M. Golabi and H.R. Zare, *Journal of Electroanalytical Chemistry*, Vol. 465, pp. 168–176, 1999.

140. American Conference of Governmental Industrial Hygienists, Documentation of Threshold Limit Values and Biological Exposure Indices, ACGIH, Cincinnati, OH, 1999.
141. X. Du, I. Skachko, A. Barker and E.Y. Andrei, *Nature Nanotechnology*, Vol. 3, pp. 491–495, 2008.
142. M.D. Stoller, S. Park, Y. Zhu, J. An and R.S. Ruoff, *Nano Letters*, Vol. 8, p. 3498, 2008.
143. C. Lee, X. Wei, J.W. Kysar and J. Hone, *Science*, Vol. 3, p. 385, 2008.
144. Y. Shao, J. Wang, H. Wu, J. Liu, I.A. Aksay and Y. Lin, *Electroanalysis*, Vol. 22, p. 1027, 2010.
145. M. Pumera, A. Ambrosi, A. Bonanni, E.L.K. Chng and H.L. Poh, *Analytical Chemistry*, Vol. 29, p. 954, 2010.
146. S. Ameen, M.S. Akhtar and M. Husain, *Science of Advanced Materials*, Vol. 2, p. 441, 2010.
147. S. Ameen, M.S. Akhtar, Y.S. Kim and H.S. Shin, *Chemical Engineering Journal*, Vol. 181, p. 806, 2012.
148. P. Alexander, O. Nikolay, K. Alexander and S. Galina, *Progress in Polymer Science*, Vol. 28, p. 1701, 2003.
149. S. Ding, D. Chao, M. Zhang and W. Zhang, *Journal of Applied Polymer Science*, Vol. 107, p. 3408, 2008.
150. T. Kuilla, S. Bhadra, D. Yao, N.H. Kim, S. Bose and J.H. Lee, *Progress in Polymer Science*, Vol. 35, p. 1350, 2010.
151. L.A. Mashat, K. Shin, K.K. Zadeh, J.D. Plessis, S.H. Han, R.W. Kojima, R.B. Kaner, D. Li, X. Gou, S.J. Ippolito and W. Wlodarski, *The Journal of Physical Chemistry C*, Vol. 114, p. 16168, 2010.
152. Y. Bo, H. Yang, Y. Hu, T. Yao and S. Huang, *Electrochimica Acta*, Vol. 56, p. 2676, 2011.
153. Y. Fan, J.H. Liu, C.P. Yang, M. Yu and P. Liu, *Sensors and Actuators B: Chemical*, Vol. 157, p. 669, 2011.
154. S. Ameen, M.S. Akhtar and H.S. Shin, *Sensors and Actuators B: Chemical*, Vol. 173, p. 177, 2012.
155. H. Wang, Q. Hao, X. Yang, L. Lu and X. Wang, *Electrochemistry Communications*, Vol. 11, p. 1158, 2009.
156. S. Goswami, U.N. Maiti, S. Maiti, S. Nandy, M.K. Mitra and K.K. Chattopadhyay, *Carbon*, Vol. 49, p. 2245, 2011 .
157. D. Han, Y. Chu, L. Yang, Y. Liu and Z. Lv, *Colloids and Surfaces A: Physicochemical and Engineering Aspects*, Vol. 259, p. 179, 2005.
158. H. Wang, Q. Hao, X. Yang, L. Lu and X. Wang, *ACS Applied Materials & Interfaces*, Vol. 2, p. 821, 2010.
159. X. Cao, B. Wang and Q. Su, *Journal of Electroanalytical Chemistry*, Vol. 361, p. 211, 1993.
160. E.F. Perez, G.O. Neto, A.A. Tanaka and L.T. Kubota, *Electroanalysis*, Vol. 10, p. 111, 1998.

161. S.G. Ansari, Z.A. Ansari, H.K. Seo, G.S. Kim, Y.S. Kim, G. Khang and H.S. Shin, *Sensors and Actuators B: Chemical*, Vol. 132, p. 265, 2008.
162. D. Jayasri and S.S. Narayanan, *Journal of Hazardous Materials*, Vol. 144, p. 348, 2007.
163. H.R. Zare and N. Nasirizadeh, *Electrochimica Acta*, Vol. 52, p. 4153, 2007.
164. M. Revenga-Parra, E. Lorenzo and F. Pariente, *Sensors and Actuators B: Chemical*, Vol. 107, p. 678, 2005.
165. S. Ivanov, U. Lange, V. Tsakova and V.M. Mirsky, *Sensors and Actuators B: Chemical*, Vol. 150, p. 271, 2010.
166. M. Hirata, T. Gotou, S. Horiuchi, M. Fujiwara and M. Ohba, *Carbon*, Vol. 42, p. 2929, 2004.
167. W.S. Hummers and R.E. Offeman, *Journal of the American Chemical Society*, Vol. 80, p. 1339, 1958.

The Synthetic Strategy for Developing Mesoporous Materials through Nanocasting Route

Rawesh Kumar and Biswajit Chowdhury*

*Department of Applied Chemistry; Indian School of Mines, Dhanbad,
Jharkhand, India*

Abstract

Nanocasting is a powerful methodology for creating ordered mesoporous materials that are more difficult to synthesize by conventional processes. Synthesis starts with fabrication of inorganic/carbon precursors inside the nanospaces of a mesoporous hard template, which is used as a true mold to produce the mesoporous materials with controllable pore size, morphology of the network. After fabrication inside the nanospaces, the template framework is selectively removed and the mesoporous ordered inorganic/organic material is obtained. In this chapter, a comprehensive literature survey for fabrication of mesoporous materials via mesoporous hard template, e.g., SBA-15, KIT-6, and mesoporous carbon, is presented. First two sections are limited to the basic understanding of nanocasting methodology. The later three sections comprise a review of works based on mesoporous silica/carbon template, which has been nurturing till date. A wide range of studies for synthesis of several inorganic compounds range from metal oxides, metal sulfides, metal carbide phosphate, and ceramics is covered.

Keywords: Nanomaterials, functional metal oxides, mesoporous, nanocasting.

2.1 Introduction to Nanocasting

The fabrication of porous materials, especially the creation of mesoporous materials, has been extensively investigated over the last few years. The worldwide large interest in mesoporous materials is due to its accessibility

*Corresponding author: biswajit_chem2003@yahoo.com

to extremely complex structures, [1] strong curvatures in solid state chemistry, interesting mass transport facilities, [2] confinement effect [3–5] and error tolerant (tend to reorganize spontaneously) capacity. Mesoporous materials are widely achieved by two processes namely soft templating and hard templating. Soft-templating is a surfactant based methodology where variety of organic surfactant forms mold and around which the inorganic/organic frameworks are weaved. Finally removal of these surfactant results in a cavity which retains the same morphology and structure of the organic surfactant. In soft-templating processes, the sol-gel [3,4] and evaporation induced self-assembly (EISA) processes [8–11] are typically involved in the synthesis of ordered mesoporous materials. In sol gel process, the assembly of surfactant and inorganic/organic widely depends on matching of charge density between them at interface [5, 6]. In basic medium, assembly of inorganic/organic anions (I^-) would match with surfactant cations (S^+) through coulomb forces (S^+I^-) whereas in acid medium, assembly of inorganic/organic cations would match with surfactant anions through coulomb force (S^-I^+). If both surfactant and inorganic/organic have same type of charge then a bridging counter ions is required to balance the coulombic interaction as ($S^-X^+I^-$) or ($S^+X^-I^+$). In strong acid medium, the interaction initiates through coulomb forces as $S^+X^-I^+$ that gradually transforms to the $(IX)^- S^+$ interaction. In EISA processes, a volatile solution of inorganic/organic precursor and surfactant is allowed to form surfactant–inorganic/organic interface. As well as solvent evaporates, precursors hydrolyze and cross-link to each other and high-content surfactants form liquid-crystal phases. In this way, inorganic/organic materials accumulate around the voids of liquid-crystalline phase and so a mesostructured hybrid is formed. Finally, ordered mesophases are solidified to form a rigid inorganic framework. Afterwards, the surfactants can be removed by calcinations and in this way high ordered mesoporous solids are synthesized. The mesoporous structure that coming out from soft-templating is generally difficult to predict because self-assembly and solvent induced assembly depends upon many parameter like temperature, solvent, concentration, hydrophobic/hydrophilic properties, interface interaction and ionic strength.

Another process named “hard templating” seems to be one of the most promising synthetic pathways to create porous materials, especially if materials with ordered porosity are the goal. Hard templates are molds in which ordered hollow cavity (pores) can be filled by precursors solution and allowed these to polymerize inside, i.e., MCM-41, SBA-15, KIT-6, etc. After digesting the hard template, ordered porous material having one-to-one replica can be created. In case of microporous materials, it is not easy

to achieve a one-to-one replica due to the lack of understanding for the template function in micropores. In case of ordered mesoporous, the synthesis indeed corresponds to a direct templating mechanism, where a relatively precise replica of the template is created. This replication process can be so perfect that one is tempted to use the term “nanocasting or casting process on the nanometer scale” to describe this process. It implies that the template is actually used as a true mold to produce the mesoporous materials with controllable pore size, morphology, distribution, properties and composition of the network. The application of the nanocasting technique to the fabrication of inorganic/carbon compounds implies that the fabrication of these products take place in the nanospaces of mesoporous hard template. After the synthesis of the material, the template framework is selectively removed and the inorganic/organic ordered mesoporous product is obtained. Due to the fact that the synthesis takes place in a confined nanospace, the sintering of the particles is restricted and the preparation of high surface area nanostructures or nanoparticles is achieved. Moreover, this synthetic strategy clearly suggests that the structure of the synthesized compounds can be tailored depending on the pore characteristics of the selected template. Mesoporous structures that coming out from hard template where fixed nanoscale pore architectures can be easily predicted. The pore walls of the replicas coming from hard templates can range from amorphous (such as carbon), to semi-crystalline (such as TiC) as well as single-crystalline (in most cases) whereas it is mostly amorphous in case of soft templating.

2.2 Steps of Nanocasting

Basically, the nanocasting route comprises in three steps: (i) Infiltration or introduction of precursor, (ii) The casting step or heat treatment under a controlled atmosphere of the impregnated template to convert the infiltrated precursor into the inorganic material, and (iii) Template removal by dissolution (i.e., silica) or by oxidation at high temperatures (i.e., carbon). A generalized scheme of nanocasting for getting mesoporous structures is summarized in Figure 2.1.

2.2.1 Infiltration

During nanocasting infiltration step is governed by four sub-steps, named (1) Selection of precursors, (2) Selection of solvent, (3) Selection of template, and (4) Infiltration of precursor solution/gas into the pores of template.

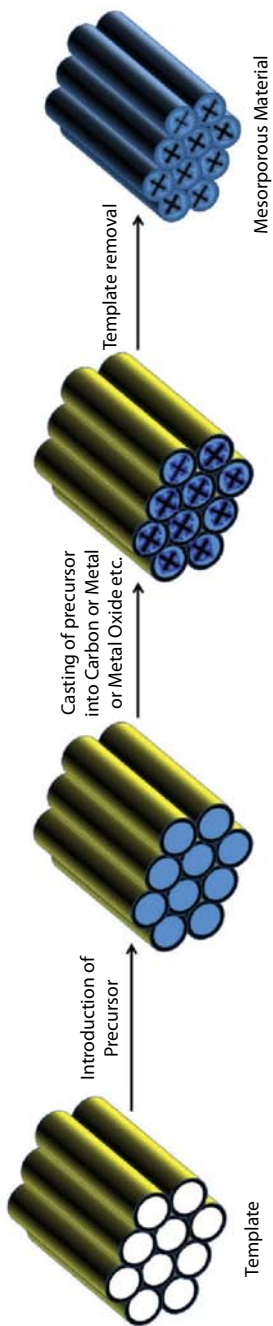


Figure 2.1 A generalize scheme of nanocasting for getting mesoporous structures.

2.2.1.1 Selection of Precursors

Selection of metal precursor has of prime importance in nanocast mesoporous metal oxide preparation. The weak acid salts like acetate, citrates and oxalates have low volume yield as well as high coordination ability which inhibit transportation of metal ion. Metal precursor should have high volume yield as heteropoly acid (e.g., phosphotungstic acid or phosphomolybdic acid) has 90% volume yield. But unfortunately apart from tungsten and molybdenum, this kind of heteropolyacid is rare. Nitrate metal precursors are easily decomposable and have highest mesoscopic regularity. In spite of its low volume yield, these salts are mostly reported due to low formation energy and fast transportation of ion inside the pore of template, e.g., Co_3O_4 [7].

The metal precursors; which have lower melting point than its decomposition temperature, can be directly grinded with template and further left for heating treatment. With rise in temperature above melting point, metal precursor melts and then impregnates into the mesochannels of the silica template through capillary force [15–17]. As for example to prepare nanocasted mesoporous NiO, $\text{Ni}(\text{NO}_3)_2 \cdot 6\text{H}_2\text{O}$ metal precursor is taken which have melting point (56.7°C) that is much lower than its decomposition temperature ($>110^\circ\text{C}$). At a temperature higher than 57°C , the liquid $\text{Ni}(\text{NO}_3)_2 \cdot 6\text{H}_2\text{O}$ easily moves into the mesopores channels of silica [15, 8]. This method is known as solid–liquid method. Metal precursor which have higher melting point should impregnate with solvent assistant.

Some group select low cost metal chloride precursor for infiltration into the mesopores channel. In this particular case, ammonia exposure is required before calcinations for conversion of metal chloride to metal hydroxide [9, 10]. A solution of copper nitrate infiltration into the mesochannels generally results into poor solution infiltration. So, again here ammonia exposure is required to make a good infiltration into mesochannels [11].

2.2.1.2 Selection of Solvent

Apart from above discussed, solvent cooperation with metal precursor is required for improving pore occlusion. The volatile solvent should have high dissolving activity, low coordination ability and weak interaction with silica surface (hydrogen bonding interaction). The highly soluble precursor (in suitable solvent) is allowed to impregnate into mesopores channels upon solvent evaporation. Enhanced filling efficiency of precursor in the template can be done by “two-solvent” nanocasting method in which metal precursor dissolved in water is allowed to impregnate into

mesopores of n-hexane mixed silica template. Amine or vinyl group functionalized silica surfaces (template) have positive charge that can induce electrostatic interaction with negative charged precursor ions and facilitate mass transportation of precursors into mesopores of template [22–24]. Generally, microwave digestion of silica template in presence of nitric acid and hydrogen peroxide is carried out to complete removal of organic surfactant. At the same time, interaction is played between abundant silanols inside the mesopore channels and metal precursors resulting better pore occupation [12, 13].

2.2.1.3 Selection of Template

The mesopore system of the hard template has a significant influence on the size and structure of resultant cast replicas. The pore connectivity of the hard template affects the mesoporous replica structures directly. The first ordered mesoporous silica MCM-41 contains hexagonal ordered cylindrical pores (space group $p6mm$) [14, 15] having no connecting channels in between the pores that results into disordered nanorods were obtained after the template removal. Interestingly, interconnected pore system of SBA-15 generate $p6mm$ replica after the template removal as indicated in Figure 2.2 [16].

SBA-16 and FDU-12 have caged pores structures. The caged mesoporous silica templates have perfect spherical pore structure; the resulting

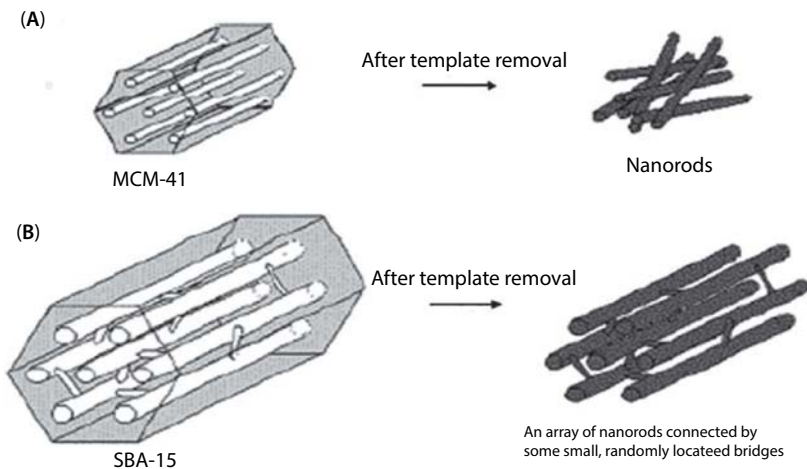


Figure 2.2 Schematic illustration of formation of (A) disordered structure using MCM-41 having disconnected pores system and (B) ordered structures using SBA-15 having an interconnected pore system [29].

replicas can be dispersed as spherical nanoparticles. A disk-shaped 2D hexagonal mesoporous silica known as INC-2 [17] was used as template to get mesoporous disk shaped replica recently.

The structure of the mesopores in KIT-6, similar to MCM-48, [18] is body-centered cubic (space group $Ia\bar{3}d$). Additionally, it consists of a pair of interpenetrating bicontinuous pores. Using KIT-6 as a template, the morphology of a proposed porous oxide is exact replica if the crystals of oxide can extend from one pore to another. Otherwise, only one of the pores would be replicated. The SBA-16 material has a body-centered cubic structure (space group $Im\bar{3}m$) and FDU-12 is face-centered cubic (space group $Fm\bar{3}m$). Unlike SBA-15 and KIT-6 in which the basic building unit of pores is cylindrical, both FDU-12 and SBA-16 consist of spherical nanocavities linked together by very short nanochannels or windows [32–34]. When porous crystals of oxides are made using FDU-12 and SBA-16 as templates, we expect that the final products have nanospheres connected by short nanorods having exact replica of their parent template. The Schematic illustration of formation of different ordered structure using different mesoporous template is summarized in Figure 2.3.

2.2.1.4 *Infiltration of Precursor Solution/Gas into the Pores of Template*

Impregnation, chemical vapor deposition (CVD), chemical vapor infiltration, and electrochemical deposition methods are generally used to infiltrate the precursor into the mesopores of hard template. In all these, impregnation is most popular way of infiltration. Five methods of impregnation have been developed called solid–liquid method, one-step nanocasting method, evaporation method, dual-solvent method and surface modification method.

In solid–liquid method, a metal-containing precursor is grinded with a mesoporous silica template, and is expected to move into the pores of silica after melting. In one-step nanocasting method, [19] the precursor nitrate is directly added into the synthetic system of mesoporous silica, forming highly ordered single crystals during a thermal treatment, and the organic surfactant is removed simultaneously. The advantage of this method is solvent-free and simplicity. Its limitation, on the other hand, is that the precursor must have a melting point lower than the decomposition temperature [18]. The evaporation method is simple and has been used by several groups [14, 25]. The mesoporous silica template is mixed with a selected metal nitrate in ethanol. The nitrate precursor is expected to migrate into the pores by a capillary action during the evaporation process

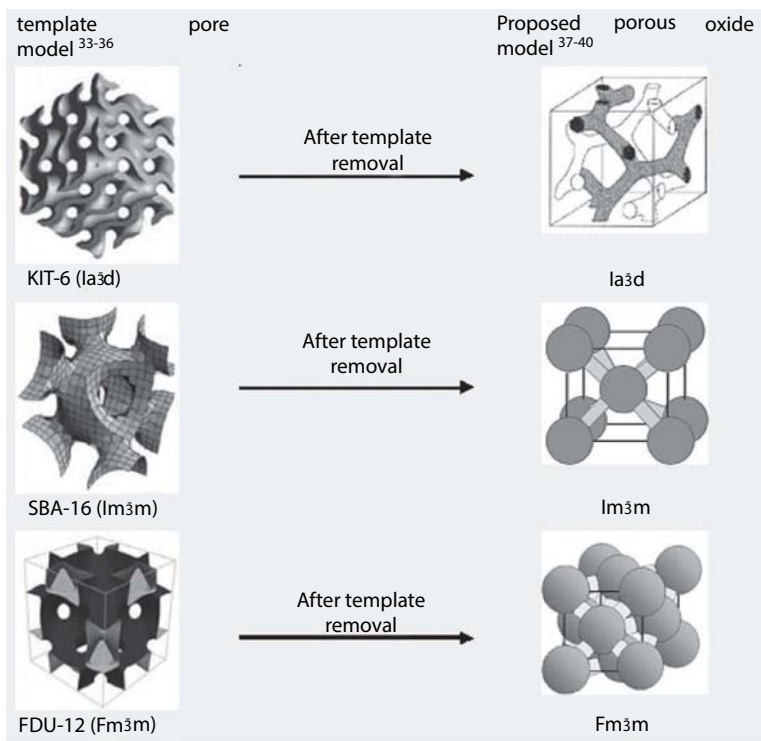


Figure 2.3 Schematic illustration of formation of Ia $\bar{3}$ d ordered structure using KIT-6, Im $\bar{3}$ m ordered structures using SBA-16 and Fm $\bar{3}$ m ordered structures with FDU-12

of ethanol. In the dual-solvent method, a suspension of mesoporous silica in dry hexane is mixed with an aqueous solution of metal nitrate. The nitrate precursor will be pushed into pores as much as possible by hexane during an overnight stirring [20]. The volume of solution should equal to the silica pore volume to maximize the impregnation quantity and prevent the growth of metal oxides out of the pores [21].

In the surface modification method, the inner wall of a silica template is functionalized with different silanes, i.e., aminosilylation using aminopropyltriethoxysilane (APTS). The driving force of the migration of the precursor molecules (i.e., heteropolyacidic precursor as $\text{H}_2\text{Cr}_2\text{O}_7$ and $\text{H}_3\text{PW}_{12}\text{O}_{40}$) is mainly ionic attraction [23, 22]. The ionic interaction between the functional group inside the pores and the anions of $\text{Cr}_2\text{O}_7^{2-}$ is stronger than the capillary force in the other conventional methods. The loading level of the precursor is very high in the present case, resulting in the large particles of porous Cr_2O_3 and where the original morphologies of the template particles could be maintained. Yang *et al.* showed that within

10 min, ethanol solution of H_2PtCl_6 or HAuCl_4 can be sucked up into the *N*-trimethoxysilylpropyl-*N,N,N*-trimethylammonium chloride functionalized SBA-15 due to the strong electrostatic interaction between cationic heteropolyacids group and anionic metal precursor [23]. This group also found interesting results about the morphology change of metal inside the template. Disk-shaped Pt nanoparticles in Pt/SBA-15 are attached on the pore wall of SBA-15 channels, where as spherical Au nanoparticles exist in the channels of Au/SBA-15. Subsequent Pt incorporation into Au/SBA-15 generates the coexistence of large Au nanoparticles and small Pt nanoparticles inside the channels of SBA-15.

Apart from impregnation, CVD and electrochemical deposition are also frequently used technique for metal precursor infiltration in mesoporous template. Vapors of precursor molecule are being infiltrated in the CVD process to fill the mesopore voids of template [24, 25]. Both diffusion and capillary forces play very important roles to incorporate metal component into the porous matrix. The “counter-force” corresponds to the deposition rate of precursor compounds. If the diffusion rate is higher compare to the deposition rate, an imperfect replication occurs due to low loading of precursors. However there is limitation of CVD process, generally in CVD process the mesopore entrances of a template are easily blocked, and a remarkable amount of precursor can be found outside of the mesopores.

2.2.2 The Casting Step

The formation of crystalline materials within the porosity of the hard template takes place according to a nucleation and growing mechanism. If the concentration of the inorganic species is high and the template has interconnected pores, the crystallites contain framework-confined pores that replicate the template scaffold. On the other hand, when the concentration of the infiltrated inorganic species is low or the template exhibits a non-connected porosity, the inorganic compound obtained will be formed by the aggregation of non-porous nanoparticles. It should be mentioned that when a homogeneously impregnated template is heat-treated to obtain an inorganic compound, the ionic species migrate towards the nucleation seeds. This migration results in the formation of numerous disconnected crystallites embedded in the porosity of the hard template. Once the template framework is removed, the resulting crystallites are retrieved. Obviously, they have a particle size that is much lower than that of the template.

Nanocasted mesoporous crystal size can be governed by long distance transportation of metal oxides inside the pore. During decomposition of

metal nitrate precursor into oxide, Nitrogen oxides are released as byproducts [26]. Nitrogen oxide can react with residual water to form nitric or nitrous acid that makes the residual solution acidic. As for example in the case of iron oxide, if the acid is too strong, the formed Fe_2O_3 can redissolve and be converted back to iron nitrate. A quasi-equilibrium is stabilized between formation and dissolving of Fe_2O_3 . Slow escape of water and nitrogen oxide shift the equilibrium to Fe_2O_3 crystal growth direction during calcination. On the other hand, fast escape of water causing solidification prior to decomposition that inhibits the long-distance transportation of the iron species and thus only isolated nanoparticles are formed.

2.2.3 Template Removal by Dissolution or by Oxidation at High Temperatures

Generally, template removal is carried out by NaOH or HF for getting nanocasted mesoporous metal oxide. The concentration of NaOH or HF should be select carefully. At a 2 mol L⁻¹ NaOH or 10% HF solution dissolved the CuO nanostructure and silica template completely in a short time whereas 0.1 mol L⁻¹ of hot NaOH solution (60–80°C) dissolve the silica template only [27]. When metal oxides are amphoteric in nature (as weak amphoteric oxides CuO and TiO_2) then it can be dissolved in NaOH and HF. This time use of NaOH or HF can never be suggested. The use of carbon family as template is an alternative template option especially if mesoporous amphoteric oxide preparation is target. It does not require NaOH or HF for template removal and can be easily removed by calcinations [28]. Temperature hot spots during calcinations can damage the ordered structure of the obtained silica as in the case of nanocasting silicates no.-1 (NCS-1). In this particular case; in lieu of calcinations, the carbon can be removed in a fluidized bed reactor in flowing air to avoid temperature hot spots [29].

2.3 Porous Silica as Template for Inorganic Compounds

Hard templates whose porosity is made up of non-connected pores (i.e., MCM-41 silica or anodic aluminum oxide membranes) will produce solids without framework-confined pores (called nanoparticulate materials). The first ordered mesoporous silica MCM-41 contains hexagonal-ordered cylindrical pores without connecting channels. So, the fabrication of three

dimensional networks of crystalline nanowires is difficult with MCM-41. This material can be used as a hard template for preparing linear nanowires and nanoparticles. Again in MCM-48, there are no interconnections between two mesochannels. A structures transformation from these templates gives the lower symmetry (from Ia $\bar{3}$ d to I4 $_1$ 32 or lower) and so finally nonconnected set of nanowires are obtained. Mesopores like SBA-15, KIT-6, and FUD-12 have cylindrical pores connected by small channels, body centre cubic with interpenetrating bicontinuous pores and face centre cubic spherical nanocavities linked together by some very short nanochannels respectively. When porous crystals of oxides are made using SBA-15 as templates, the final products are an array of nanorods connected by some small, randomly located bridges whereas FDU-12 and SBA-16 as templates, the final products are nanospheres connected by short nanorods. It should be more explained through examples.

The mesoporous Co $_3$ O $_4$ material is a reversed replica of spherical pores (fcc FDU-12 and bcc SBA-16) [16]. The morphology of a proposed porous oxide with KIT-6 as template is something different. If two pores of KIT-6 are connected to each other by some channels, the crystals of oxide can extend from one pore to another (bicontinuous pore), e.g., Co $_3$ O $_4$. Otherwise, only one of the pores would be replicated, e.g., Cr $_2$ O $_3$ [15, 25, 42] Using CeCl $_3$.7H $_2$ O as precursor over bicontinuous cubic KIT-6 template, the cubic mesoporous CeO $_2$ replica with symmetry Ia $\bar{3}$ d was obtained [19, 30]. Cubic crystal as Co $_3$ O $_4$ [31], CeO $_2$ [18, 25, 53, 32] NiO, [15, 18, 25] and In $_2$ O $_3$ [18, 25, 41, 33] can grow inside the pore of FDU-12 and SBA-16 that truly replicate the 3D mesostructure. Cr $_2$ O $_3$, Fe $_2$ O $_3$, WO $_3$ and MnO $_2$ can replicate the 3D mesostructure whenever the template is SBA-15 and KIT-6 whereas noncubic Cr $_2$ O $_3$ (rhombohedral), [15, 23, 25, 42] Fe $_2$ O $_3$ (rhombohedral), [25, 42, 34] WO $_3$, [22, 44, 53] and MnO $_2$ (tetragonal) [25, 35, 36] cannot replicate the 3D mesostructure inside FDU-12 and SBA-16. The hexagonally ordered **ferrihydrite nanowires** [37] can be obtained by both SBA-15 and KIT-6 template in which previous one has large low temperature coercivity. Interestingly, Mn(NO $_3$) $_2$.6H $_2$ O precursor inside the channels of FDU-12 template transforms different symmetry metal oxide at different temperature, i.e., tetragonal symmetry (less replicative) at 500°C and cubic symmetry (well replicative) at higher temperature [18]. These results indicate confined growth easily occurs between metal oxides and hard templates with similar structures. In Figure 2.4, different morphologies of porous crystals oxides (NiO) by using same precursor but various mesopores template has been summarized to have a glimpse on the crystal structure for different case.


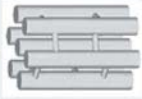
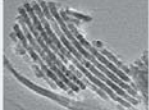

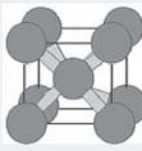
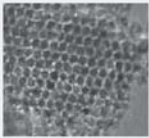

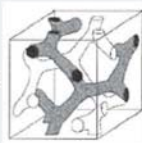
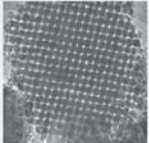


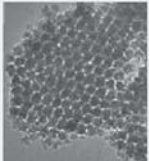
Precursor	Mesopores template (only pore model is shown)	Thermal treatment (110° C) & silica etching	Expected Mesostructures	Meso-structure found	Ref
$\text{Ni}(\text{NO}_3)_2 \cdot 6\text{H}_2\text{O}$	 SBA-15, p6mm	→		 NiO, p6mm	Error! Book mark not defined
$\text{Ni}(\text{NO}_3)_2 \cdot 6\text{H}_2\text{O}$	 SBA-16, Im3m	→		 NiO, Im3m	8
$\text{Ni}(\text{NO}_3)_2 \cdot 6\text{H}_2\text{O}$	 KIT-6, Ia3d	→		 NiO, Ia3d	Error! Book mark not defined
$\text{Ni}(\text{NO}_3)_2 \cdot 6\text{H}_2\text{O}$	 FDU-12, Fm3m	→		 NiO, Fm3m	8

Figure 2.4 Different morphologies of porous crystals oxides (NiO) by using same precursor but different mesopores template (only pore model of template) are shown.

The pore size and wall thickness of nanocasted mesoporous metal oxides can be controlled by varying different synthesis condition of template especially hydrothermal temperature and calcinations temperature. Rumpelcker *et al.* synthesized a series of mesoporous Co_3O_4 with wall thicknesses from 4 to 10 nm, pore size from 3 to 10 nm using different KIT-6 templates obtained under different hydrothermal treatment

temperatures [38]. Similar study was used to prepare β - MnO_2 having pore size varying between pore sizes between 3 and 11 nm, wall thicknesses between 4.7 and 10.1 nm [39]. By varying calcinations temperature of KIT-6 in the range of 500°C and 1000°C, Y. Ren *et al.* synthesized a series of mesoporous Co_3O_4 , with pore size in the range of 3.7–11.9 nm and wall thickness in the range of 2.2–8.2 nm [40]. Yue *et al.* used KIT-6 as a hard template to synthesize mesoporous rutiles with different pore sizes (4.9–7.2 nm) by variation of the rutile crystallization temperatures between 100°C and 600°C.

2.3.1 Nanocast Cobalt Oxides, Cerium Oxide, and Copper Oxide

Ordered cobalt oxides have been successfully prepared by a nanocasting route using mesoporous KIT-6 silica as a hard template and cobalt nitrate as metal precursor [41]. Yanqin Wang *et al.* prepared mesostructured Co_3O_4 with Ia $\bar{3}$ d symmetry from cubic Ia $\bar{3}$ d mesoporous vinylsilica [24]. Co_3O_4 derived from KIT-6 have high surface area and oxygen adspecies concentrations, good low-temperature reducibility and high-quality 3D ordered mesoporous architecture of KIT-6 than Co_3O_4 derived from SBA-15 [42]. Additionally, it has interesting magnetic properties if the pore system can be filled with another ferromagnetic material that brings useful catalytic application [43]. Nanocasted mesoporous CoO was synthesized by mild reduction of Co_3O_4 using glycerol results into decreasing pore parameters having surface area from 113 to 55 m^2g^{-1} and pore volume from 0.184 to 0.138 cm^3g^{-1} than nanocasted Co_3O_4 [44, 45]. Nanostructured CoO has attracted much attention due to exhibit superparamagnetism or weak ferromagnetism [46].

Different ordered structures of CeO_2 was synthesized by using different mesoporous template as indicated in TEM image in Figure 2.5. The mesoporous CeO_2 showed a higher catalytic activity than normal CeO_2 powder at a relatively low temperature [54]. Vasconcelos *et al.* infiltrate the aqueous solution of $\text{Ce}(\text{NO}_3)_3 \cdot 6\text{H}_2\text{O}$ or $\text{ZrOCl}_2 \cdot 8\text{H}_2\text{O}$, or $\text{Ti}(\text{BuO})_4$ into well dispersed SBA-15 in n-hexane [47]. Further, calcination at 600°C and etching by HF results into formation of mesoporous high surface area CeO_2 , ZrO_2 , TiO_2 , and CeO_2 - ZrO_2 in which binary oxide CeO_2 - ZrO_2 have moderate basicity. It is also a proof of cooperative acid–base character in the $\text{Ce}_{0.8}\text{Zr}_{0.2}\text{O}_2$ phase. Begon̄a Puertolas *et al.* prepared mesoporous cerium oxide templated by KIT-6 and found that low aging temperature (40°C) samples does not undergo proper etching where as aging at 80°C undergoes proper etching on NaOH application [52]. S. Sun *et al.* prepared

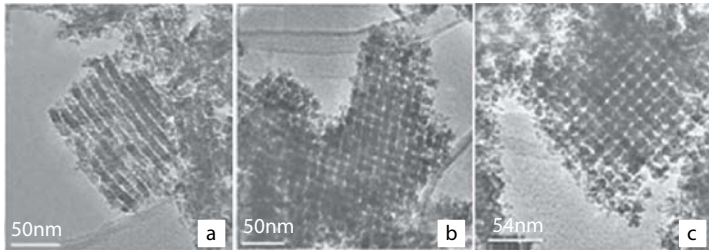


Figure 2.5 TEM images of porous CeO_2 templated by (a) SBA-15, (b) KIT-6, and (c) FDU-12, respectively [15, 18].

mesoporous Co_3O_4 oxides from KIT-6 at different aging temperature [48]. Mesoporous Co_3O_4 oxides prepared from KIT-6 aged at low temperature (300°C) have uncoupled sub-frameworks while mesoporous Co_3O_4 oxides prepared from KIT-6 aged at high temperature (500°C) possess coupled sub-frameworks. Co_3O_4 replicas with uncoupled sub-frameworks possess higher surface area and more open pore system and exhibit better performance for CO oxidation than Co_3O_4 replicas with coupled sub-frameworks. Chunyan Ma *et al.* prepared metal precursor solution by stirring $\text{HAuCl}_4 \cdot 3\text{H}_2\text{O}$ (adjusted with 1 M NaOH solution to pH 7 and dispersed in ethanol) and solid $\text{Co}(\text{NO}_3)_2 \cdot 6\text{H}_2\text{O}$ for 2 h [49]. Subsequently, SBA-15 was added in the mixture and ethanol was removed by the evaporation at 70°C for 12 h. Finally calcinations and etching of the composite resulted into mesoporous $\text{Au}/\text{Co}_3\text{O}_4\text{-CeO}_2$ catalysts composed of Co_3O_4 spinel and CeO_2 fluorite crystalline phase domains. Mesostructured $\text{Co}_3\text{O}_4\text{-CeO}_2$ (with the Co/Ce ratio of 16/1) prepared by using template KIT-6 and metal nitrate precursor possesses larger quantities of surface hydroxyl groups and surface oxygenated species [50]. J. Zhu *et al.* prepared mesoporous CuCo_2O_4 spinel replica by infiltrating metal nitrate solutions into the pores of SBA-15 (dispersed in n-hexane), drying in air, calcination at 653 K and etching with NaOH. In the same way this group also prepared mesoporous MnCo_2O_4 and NiCo_2O_4 spinel replicas [51]. These replicas have high specific surface areas ($91\text{--}129\text{ m}^2\text{g}^{-1}$) and large pore volumes ($0.35\text{--}0.41\text{ cm}^3\text{g}^{-1}$) and mainly present in form of Co(II)/Co(III), Cu(II), Mn(III)/Mn(IV), and Ni(II). Treating a lithium source with as-made Co_3O_4 (templated from SBA-15 and KIT-6), porous crystalline LiCoO_2 was made which has a superior capacity retention on cycling compared with the normal LiCoO_2 because of its large surface areas [52].

Using mixed solution of metal nitrate precursor in ethanol and KIT-6 template, J. Zhu *et al.* prepared a mesoporous copper cerium bimetal oxide [53]. Intimate contact between the copper species and ceria matrices

enhanced the synergistic interactions and redox properties between catalysts and supports. Using mixed solution of Cu(II) nitrate and Ru (III) chloride as precursor (in ethanol) and KIT-6 template, X. Cui *et al.* prepared mesoporous CuO/RuO₂ bimetal oxides [54].

2.3.2 Nanocast Chromium Oxides

Jiao *et al.* prepared mesoporous Cr₂O₃ replicas (sphere-like particles) by using KIT-6 as a hard template and Cr(NO₃)₃·9H₂O as a precursor via “two-solvent” method [42]. Selected area electron diffractogram (SAED) patterns display that the whole particle belongs to the same single-crystal, although the material is constituted by curly Cr₂O₃ nanowires according to the Ia $\bar{3}$ d symmetry. The mesostructure and the crystals of Cr₂O₃ have a 6-fold axis in [111] direction and HRTEM images along [100] directions are close to a square pattern as shown in Figure 2.6. Dupont *et al.* prepared mesoporous Cr₂O₃ by infiltration of chromium (III) nitrate nonahydrate ethanol solution into the mesopores of KIT-6 followed by solvent evaporation at 40°C, calcinations at 550°C and etching by HF [55]. Y. Xia *et al.* [56] showed that ultrasound-assisted dispersion at 40°C for 100 min after infiltration of chromium nitrate precursor into KIT-6 template results into improve mesoporosity quality of the chromia materials. Ioannis Tamiolakis prepared highly ordered mesoporous Cr₂O₃-phosphomolybdic acid by ultrasonication of ethanol solution containing SBA-15, Cr(NO₃)₃·9H₂O and quantitative amount of H₃PMo₁₂O₄₀·26H₂O followed by calcinations and etching of silica by HF [57]. P. M. Rao *et al.* prepared mesoporous Cs_xH_{3-x}PW₁₂O₄₀ by using aqueous solutions of Cs₂CO₃ and H₃PW₁₂O₄₀ as precursor (Cs_x/W₁₂ = 1.5 and 2.5) and SBA-15 as template [58]. Nanocasted cesium salt of phosphotungstic heteropolyacid materials are stable against leaching and colloidization in polar solvents and shows higher catalytic activity by a factor of 2–3 than that of the standard Cs_{2.5}H_{0.5}PW₁₂O₄₀ material in isopropanol dehydration reactions.

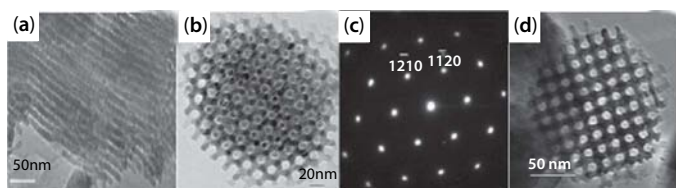


Figure 2.6 (a) TEM image of porous single-crystal of Cr₂O₃ casted from SBA-15 [25]. (b) TEM image of porous single-crystal of Cr₂O₃ casted from KIT-6 and viewed down along [111] direction. (c) The corresponding SAED pattern indexed onto the rhombohedral unit cell of Cr₂O₃ crystal. (d) TEM image of porous single-crystal of Cr₂O₃ casted from KIT-6 and viewed down along [100] [42].

2.3.3 Nanocast Indium Oxides and Nickel Oxide

Haffer *et al.* prepared mesoporous In_2O_3 by infiltration of metal nitrate salt precursor into KIT-6 or SBA-15, drying at ambient temperature, heating at 300°C to convert nitrate salt into Indium oxide and finally etching by NaOH [59]. A mesoporous silica matrix with lower pore interconnectivity (SBA-15) may therefore be expected to lead to a less well-defined spherical In_2O_3 particle shape. The morphologies of the In_2O_3 particles were not related to those of the silica templates. Uniform In_2O_3 morphology can be explained by the growth mechanism inside the silica pores in the nanometer scale, which is governed by the formation of (presumably) liquid droplets of precursor species prior to oxide formation. Hence, uniform In_2O_3 particles can be obtained even without paying attention to morphological control during the synthesis of the silica matrices. A new one-step nanocasting method is introduced over silica monolith in which Indium nitrate precursors is buried inside the mesopores channels in the hydrophilic domain of triblock copolymers due to the coordination function, and can be transformed into continuous frameworks during heat treatment [41, 60]. Upon triblock copolymer removal, Indium nitrate reduces into metal and aggregates inside the pore channels (due to its low melting point) to form nanowires. During calcination, metal is oxidized into In_2O_3 and finally, In_2O_3 nanowires arrays are obtained upon silica template removal. TEM image of indium oxide nanowire arrays nanocasted by the mesoporous silica with the bicontinuous cubic is shown in Figure 2.7.

Moises Cabo prepared mesoporous NiCo_2O_4 spinel by using cobalt nitrate and nickel nitrate precursor (in ratio 2:1) and SBA-15 or KIT-6 template [61]. However, formation of the stoichiometric NiCo_2O_4 compound can only be guaranteed for calcinations temperatures below than 400°C otherwise partial decomposition into NiO occurs [62]. Cobalt ions migration rate on the silica surface is much higher than that of Ni ions. Hence, while Co_3O_4 nanowires are easily formed within silica channels, NiO tends to form nanoparticles or nanorods making it difficult to retain the ordered mesostructure after template removal [63]. So, the NiO and

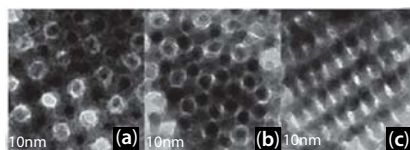


Figure 2.7 TEM images of the indium oxide nanowire arrays nanocasted by the mesoporous silica with the bicontinuous cubic (Ia $\bar{3}$ d) structure, viewed along the characteristic directions: (a) [100], (b) [111], and (c) [311] [41].

Co_3O_4 templated by SBA-15 have randomly oriented nanorods and hexagonally arranged nanowires morphology. Interestingly a halfway morphology was observed for the NiCo_2O_4 sample, which showed larger wires than NiO replica but less perfectly arranged than in Co_3O_4 replica [64]. Using mixed nitrate solutions of Co, Ni and Al as precursor and SBA-15 as template, Francisco F. de Sousa prepared nanostructured Ni-containing spinel oxides as NiAl_2O_4 , and $\text{CeO}_2\text{-NiAl}_2\text{O}_4$ [65].

2.3.4 Nanocast Molybdenum and Manganese Oxide

V. Yifeng Shi *et al.* synthesized highly ordered crystallized tetragonal phase mesoporous MoO_2 having surface area $66 \text{ m}^2\text{g}^{-1}$ and pore volume $0.29 \text{ cm}^3\text{g}^{-1}$ with a 3D bicontinuous cubic symmetry by using phosphomolybdic acid ($\text{H}_3\text{PMo}_{12}\text{O}_{40}$) as a precursor and KIT-6 as template [66]. Compared to the XRD pattern of KIT-6, the diffraction peaks of mesoporous MoO_2 are slightly shift to higher angles, indicating a small shrinkage of the mesostructure after replication however the structural regularity of mesoporous MoO_2 is only slightly lower than that of its template KIT-6 (Figure 2.8).

Tian *et al.* prepared SBA-15 templated porous Mn_xO_y composed of MnO_2 , Mn_2O_3 , and Mn_3O_4 using the evaporation method [25]. Escax *et al.* prepared MnO_2 and characterized with different technique and reached to the conclusion that elongated and monophasic MnO_2 nanoparticles can be generated within the pores of SBA-15 silicas, the thermal reduction of

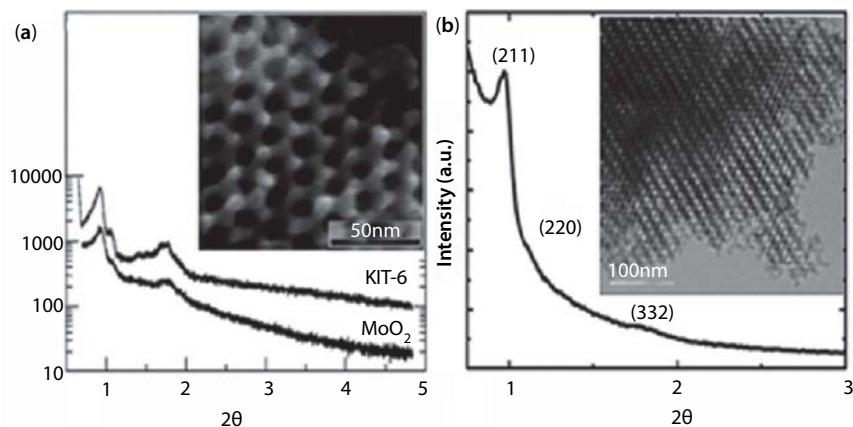


Figure 2.8 (a) Small-angle XRD patterns of mesoporous silica template KIT-6 and its replica mesoporous MoO_2 materials. Inset has high resolution SEM images of mesoporous MoO_2 materials [88]. (b) Low-angle XRD pattern of mesoporous, $\beta\text{-MnO}_2$ and inset has TEM images of mesoporous, $\beta\text{-MnO}_2$ viewed down [210] plane [58].

these nanoparticles lead to mixtures of Mn_2O_3 and Mn_3O_4 and significantly affected by the mesopore diameters of the silica template [67]. Above the 600°C temperature, a size induced structural modifications, associated with changes in structural parameters and thermal dilation properties of Mn_2O_3 nanoparticle have been observed.

M. A. Wolfovich *et al.* prepared nanocasted Mn–Ce-oxide catalyst having surface area $316\text{ m}^2/\text{g}$ at Mn/Ce=1.8 by internal gelation of corresponding metal chlorides into tubular mesopores of SBA-15, crystallization of oxide layer at 700°C and finally removal of silica by NaOH [68]. T. Valdés-Solis *et al.* prepared spinel ferrite (MnFe_2O_4) nanoparticles by using respective metal hydrated nitrate as precursors (Mn/Fe=1/2) and mesoporous silica gel as template [69]. Zhou *et al.* prepared MnO_2 through evaporation method by using KIT-6 template [22] and manganese nitrate precursor. J. Y. Luo *et al.* prepared ordered mesoporous $\beta\text{-MnO}_2$ having surface area $0.38\text{ cm}^3\text{g}^{-1}$, pore volume $0.01\text{ cm}^3\text{g}^{-1}$ and pore size distribution centered at 4.9 and 18.2 nm [58].

2.3.5 Nanocast Iron Oxide

Jiao F. *et al.* prepared the low density and low quality of the small inter-pore channels Fe_2O_3 using SBA-15 template through the surface modification method [70]. Tian B. Z. *et al.* prepared low crystallinity porous Fe_2O_3 with negative replication using same template by the evaporation method [44]. Feng Jiao *et al.* prepared mesoporous $\alpha\text{-Fe}_2\text{O}_3$ by using metal nitrate precursor dissolved in ethanol and KIT-6 template. It would be noted that calcination at 500°C for 3 h, results into mesoporous $\alpha\text{-Fe}_2\text{O}_3$ with disordered walls where as calcinations at 600°C for 6 h results into mesoporous $\alpha\text{-Fe}_2\text{O}_3$ with ordered walls [56]. This change in ordering is sufficient to make a profound influence on the magnetic behavior. Mesoporous ordered $\alpha\text{-Fe}_2\text{O}_3$ was employed for reduction by heating at 350°C for 1 h under a 5% H_2 –95% Ar atmosphere which results the transformation from the hexagonal close packed oxide sub-array of $\alpha\text{-Fe}_2\text{O}_3$ (corundum structure) to the cubic close packed sub-array of Fe_3O_4 spine [71]. Further, mesoporous Fe_3O_4 was undergone to oxidation by heating at 150°C for 2 h in air which resulted into the transformation from Fe_3O_4 spinel to $\gamma\text{-Fe}_2\text{O}_3$ phase as shown in Figure 2.9. H. Tuysuz *et al.* prepared ordered mesoporous two-line ferrihydrite by infiltrating metal nitrate precursor into SBA-15 or KIT-6 template, calcinations to 200°C , re-impregnated under the same conditions and followed by calcination at 200°C for 6 h [59]. However to get ordered mesoporous ferrihydrite, template needs to be impregnated at least twice. At 250°C , the ferrihydrite phase is obtained, but at 300°C ,

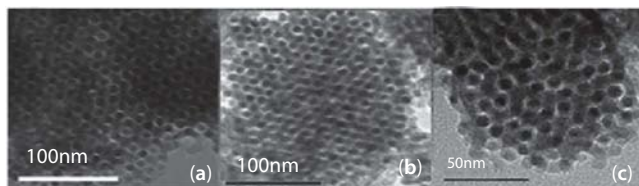


Figure 2.9 TEM images recorded along the direction for mesoporous (a) α - Fe_2O_3 , (c) Fe_3O_4 , and (e) γ - Fe_2O_3 [93].

the formation of hematite is observed. Ferrihydrite corresponds to that of hematite [72] in which Fe^{3+} ions are octahedrally coordinated within a hexagonal unit cell, whereas the Fe^{3+} ions located on the surface (about 30%) have a tetrahedral coordination [73].

2.3.6 Nanocast Tungsten Oxide

Bin Yue *et al.* used aminosilylized 3D mesoporous SBA-15 as the template for better filling of tungstophosphoric acid in the pores [44]. The bridges between the nanorods not only connect the nanorods inside the channels but also help the crystal growth in the neighboring mesopores. Some bridges are in the same scale as that of the nanorods which makes the crystal mechanically stronger. So, finally after heat treatment and etching, 3D mesoporous tungsten oxide single crystals are obtained. E. Rossinyol *et al.* prepared mesoporous tungsten oxides by phosphotungstic acid as tungsten precursor and KIT-6 as template [53]. WO_3 replica prepared from KIT-6 template have larger surface area and retained mesostructure than replica from SBA-15 [74, 75]. Chromium incorporation in mesoporous WO_3 leads to increase the number of oxygen vacancies.

2.3.7 Nanocast Tin Oxide

G. Satishkumar *et al.* prepared tin oxide nanoparticles by using metal chloride precursor and hexane dispersed SBA-15 as template [76]. At 250°C in air tin oxide nanoparticle (5 nm) with well defined cassiterite structure were formed inside the SBA-15 matrix mesopores. After calcinations in air at 700°C , the sintering and arrangement of SnO_2 nanoparticle resulted in the formation of nanowires. The small angle XRD patterns and HRTEM micrographs of SnO_2 (in Figure 2.10) shows that hexagonal order is retained by SnO_2 NP even after silica etching. This group also prepared tin oxide nanowires by using same precursor and chloride grafted SBA-15 and shows that only 16% tin was loaded than 28% tin loading over non-grafted

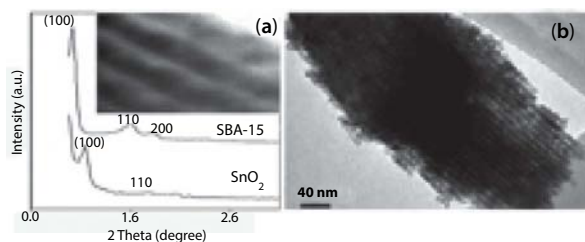


Figure 2.10 (a) Low-angle XRD patterns of SBA-15 and SnO_2 obtained after removal of silica from composite calcined in air at 700°C and inset have HRTEM micrographs of SnO_2 NP obtained after silica removal [98]. (b) TEM images of as-prepared mesoporous BiVO_4 [100].

SBA-15 or silanol rich SBA-15. J.-H. Smatt *et al.* prepared SnO_2 and ZrO_2 sphere by using metal chloride salt as precursor and spherical mesoporous silica particles as the mold [77]. The replicas have the same size distribution as the starting silica spheres (positive replicas). On the other hand, the internal porosity can still be regarded as a negative replica of the silica mesopore structure on the nanometer length scale.

2.3.8 Nanocast BiVO_4 and B_4C

G. Li *et al.* synthesized ordered mesoporous bismuth vanadate (BiVO_4) crystals having a surface area $59\text{ m}^2\text{g}^{-1}$ and a pore volume $0.12\text{ cm}^3\text{g}^{-1}$ by using bismuth nitrate hydrate and ammonia metavanadate as bismuth and vanadium sources and KIT-6 as a template [78] (Figure 2.10). Conventional BiVO_4 had a much larger crystal size than mesoporous BiVO_4 , ranging from 100 to 200 nm. This was due to uncontrolled crystal growth in the absence of ordered mesoporous channels and so, long-range order mesoporous structure could not be found. It is probably attributed to the collapse of the BiVO_4 pore wall located in the channels of silica during the silica etching process.

Another interesting material, Boron carbide (B_4C) can be synthesized by wet infiltration technique [79]. As reported in literature, SBA-15 was infiltrated with bisdecaboranyl-hexane precursor solution in ethanol and left overnight for evaporation. It is now heated from room temperature to 573 K at 150 K h^{-1} , then 5 h at 573 K , followed by heating to 973 K at 30 K h^{-1} . After 973 K was reached, the sample was heated to the pyrolysis temperature (1273 K) at 120 K h^{-1} and maintained for 2 h . Finally, after silica etching by the mixture of $\text{EtOH}/\text{H}_2\text{O}/40\%\text{ HF}$ solution, ordered mesoporous B_4C having pore diameter 3.7 nm , surface areas $705\text{ m}^2/\text{g}$ and pore volumes $0.57\text{ cm}^3/\text{g}$ was obtained.

2.3.9 Nanocast Metal

Porous metal-nanowire thin films are obtained by depositing Pt, Au, Ni, and Cu inside the mesoporous silica thin films coated on a conductive substrate by electrodeposition method [102–105]. In spite of better pore occupation, the non-conductive silica thin film produces lower deposition current which increases the deposition time resulting into lower yield. Reduction of metallic precursor into metal (**Au, Ni, Cu**) inside pore channels by reducing agent in solution would be better method than electrodeposition method [80, 81].

The presence of platinum Pt inside the mesopores of silica thin film (Pt@mesoporous silica thin films) behaves as nucleation sites for Ni electroplating solution. So, Zhang *et al.* immersed Pt@mesoporous silica thin films into nickel electroplating solution. After etching silica, ordered mesoporous Ni nanowire arrays are obtained. The key issue is that the nucleation site of the deposited metals (as Pt here) should locate inside mesochannels. Otherwise the metals (Ni) would deposit, nucleate and grow outside the mesopores [99]. If the target is to find gold nanowires, Pd@mesoporous silica thin films should be immersed into gold plating bath followed by silica removal by HF [107]. In Figure 2.11(a) it can be seen that gold nanowires (in dark color) have been filled into the channels of SBA-15 mesoporous thin films and shaped into a nanostructure with its morphology complementary to that of template. Morphology of unsupported gold nanowires after silica removal is shown in Figure 2.11(b) which is again identical to that of the pore channels. The nanobridges between the two adjacent nanowires can be clearly seen as highlighted by arrows in the Figure 2.11(b) and enlarged in Figure 2.11(c) which is the reflection of interconnections between pore channels in mesoporous thin film template. Lattice fringes across the width of the entire nanowire, with interplanar

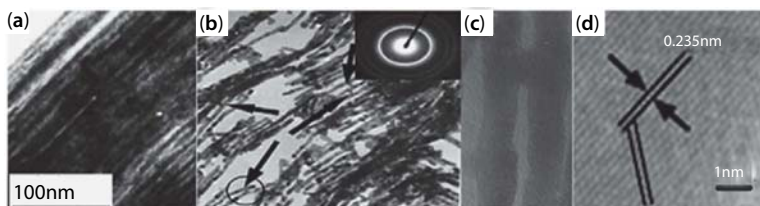


Figure 2.11 (a) TEM image of gold nanowires fully incorporated into the pore channels of MTFs. (b) TEM image of unsupported gold nanowires by removal of silica matrix. The arrows highlight the bridges between the nanowires. The inset shows select-area electron diffraction. (c) The enlarged image of ellipse portion of image (b) HRTEM image of gold nanowire [107].

spacings of ca. 0.24 and 0.2 nm is shown in Figure 2.11(d) similar to those of face-centered gold also indicating the synthesized gold nanowires are locally single crystalline in nature.

In a solid salt occlusion technique, metal precursor (i.e., AgNO_3) and hard template (SBA-15) are grounded and heated at 250°C for 12 h followed by subsequent heating at 300°C for 2 h to get **silver nanowire array**/SBA-15 [82]. In impregnation method, $\text{Pt}(\text{NH}_3)_4(\text{NO}_3)_2$ are introduced inside the straight mesopores of MCM-41 followed by subsequent heating in oxidizing and reducing environment to get Pt seeds containing MCM-41. The repeated impregnation and reduction several times results into Pt nanowires/MCM-41 material. After removing silica template, **Pt nanowire** having length 10 to 100 nm and diameter 3 nm are found with lack of mesostructural regularity due to absence of support among nanowire as CMK-1. The crystal plane of Pt nanowires is parallel to the pore-wall surface of the silica template and pore diameter is close to pore diameter of MCM-41 [83]. Using SBA-15 as template, porous Pt nanowires arrays are found where two nanowires are supported by Pt nanorods as CMK-3 [84]. Using MCM-48 as template, only one set of mesopores is nanocast among the two sets of bicontinuous pores in some domain, resulting decreasing symmetry (I4132) as CMK-2. However, Ryoo and co-worker synthesized ordered 3D bicontinuous Pt nanowire framework by using MCM-48 as template [85]. Using ultraviolet irradiation as alternative reducing technique and ethane functionalized mesopores silica as template; **Pt**, **Pt-Ru**, and **Pt-Pd** necklace nanowires are obtained due to increasing surface hydrophobicity of silica hard template. With phenyl functionalized mesopores silica is used as template, similar morphology can be obtained even under H_2 reduction [112–114]. Interestingly by using $\text{Os}_3(\text{CO})_{12}$ as precursor and MCM-48 as template, a low structural mesostructural regularity or **Os replica** is obtained [86]. Chemical vapor infiltration technique is a solvent less technique where a low temperature is adopted to convert metallic precursor to metallic phase. Vapor of organometallic compound (as precursor) is first infiltrated inside the mesochannels of silica hard template where precursor is reduced by simply heating to get Pd nanowire/Silica hard template. After template removal, dispersed **Pd nanowires** or nanowire arrays are produced depending on template used MCM-41 or SBA-15 type.

2.3.10 Nanocast Metal Sulfides

A proper metal precursor is required to introduce metal ion into the mesopore of silica. The subsequent treatment with alkali metal sulphide (Na_2S , K_2S) converts the metal ions into metal sulphide but the Ksp value

of sulphide are low that lead easy precipitation and hence block the pore orifice. Introducing Cu^{+2} , Ni^{+2} , Cd^{+2} , Zn^{+2} , Hg^{+2} , and Ag^{+2} into the mesopores of cation functionalized (such as CTA^+) MCM-41 and then subsequent treatment with H_2S is a way of getting mesopores [87]. In the same way mercapto functionalized SBA-15 can absorb Pb^{+2} and Cd^{+2} inside the pore channel [88, 89]. But heterogenous and discrete dispersion of precursors inside the pore channel is a major drawback for this methodology due to which mesopores replica is not obtained. Metal nitrate-ethanol solution with thiourea would be a better option of filling into mesopores. In fact at 170°C , thiourea decomposes and then react with metal ion and after microwave digestion of mesopores silica, 2D mesopores CdS , ZnS , and In_2S_3 are obtained [90]. But this method is limited to metal sulfides with a low sulfuration temperature. For Metal sulphide with a high sulfuration temperature as WS_2 and MoS_2 , phosphotungstic acid phosphomolybdic acid (have high yield 96 wt.%) is a good metal precursor. Due to hydrogen bonding interaction between heteropoly acid (PTA) molecules and the silanol groups on the template, PTA molecule is easily incorporated into SBA-15. After sulfurization by H_2S gas and etching silica template, highly ordered 2D hexagonal and 3D bicontinuous cubic mesostructured WS_2 and MoS_2 nanocrystal array are obtained (Figure 2.12) [91].

WS_2 have a layered structure (grow along the nanospaces, both cylindrical mesochannels and mesotunnels) which contains a tungsten metal layer sandwiched by two sulfur layers. M. Remskar found that due to lack of S or W atom at edges, high energy dangling bonds makes the surface unstable or it can be said fewer the edges, more thermodynamic WS_2 crystal are [92]. The search of precursor having both metal ion and S was started with $[\text{Cd}_{10}\text{S}_{16}\text{C}_{32}\text{H}_{80}\text{N}_4\text{O}_{28}]$ that can be thermally decomposed to CdS at 160°C with high volume yield. With SBA-15 as template, CdS nanowires supported by randomly connected nanorods having surface area $150\text{ m}^2\text{g}^{-1}$ is formed as like as CMK-3 [93]. Summary of preparation layout for nanocast metal sulfides is shown in Table 2.1.

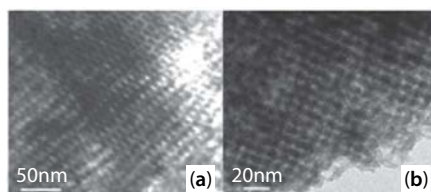


Figure 2.12 TEM images of (a) cubic mesoporous WS_2 replicated from the KIT-6 hard template with the Ia $\bar{3}$ d symmetry along the [331], (b) mesoporous MoS_2 prepared from the KIT-6 [120].

Table 2.1 Summary of preparation layout for nanocast metal sulfides.

Nanocast Materials	Precursor	Template	Method Sequence	Ref
Metal sulphide	Cu^{+2} , Ni^{+2} , Cd^{+2} , Zn^{+2} , Hg^{+2} , Ag^{+2} salts	Cation functionalized MCM-41	Impregnation and subsequent H_2S treatment	[119]
Metal sulphide	Pb^{+2} , Cd^{+2} salts	Mercapto functionalized SBA-15	Impregnation and subsequent Heating	[117, 118]
CdS , ZnS and In_2S_3	Cd^{+2} , Zn^{+2} and In^{+3} nitrate-ethanol solution with thiourea	SBA-15	Impregnation and subsequent Heating	[119]
WS_2 and MoS_2	Phosphotungstic acid Phosphomolybdic acid	SBA-15	Impregnation and subsequent H_2S treatment	[120]
CdS nanowires array	$\text{Cd}_{10}\text{S}_{16}\text{C}_{32}\text{H}_{80}\text{N}_4\text{O}_{28}$	SBA-15	Impregnation and subsequent Heating	[122]

2.3.11 Nanocasted Ceramics

Deposition of SiC into mesoporous silica channels by the chemical vapor infiltration method is insufficient to get true ordered mesoporous SiC due to blocking of pore beyond a complete filling [46]. Polycarbonsilane (PCS) and polysilane as precursor can easily be filled in the void space of silica sphere as template having diameter range 20 to 100 nm. It is decomposed into SiC after heating at 1000–1400°C. Finally after etching silica template, disordered mesoporous SiC having surface area 400–600 m²g⁻¹ under the heat treatment at 1400°C and surface area 200 m²g⁻¹ by heating at 100°C are obtained respectively. Using SBA-15 or KIT-6 as template and xylene or benzene dissolved polycarbonsilane precursor followed by a series of thermal treatments, 2D hexagonal and 3D bicontinuous highly ordered mesopores SiC are obtained respectively [94]. Ordered Mesoporous SiC prepared from different PCS and operation processes have different surface area as reported in literature (Figure 2.13) [95,96].

The task of forming mesoporous metal nitrides by metal nitrides precursors is very difficult only due to extremely low volume conversion of precursor into metal nitrides and due to this nanoparticles of GaN and TiN were obtained instead of nanowire using MCM-41 and SBA-15 template [126–128]. Yang *et al.* synthesized disordered GaN nanorods with short length even using SBA-15 as template due to lack of connected nanorods between the two adjacent nanowires [97]. It is easier to get ordered mesoporous metal oxide through nanocasting and then convert metal oxide into metal nitride by ammonia treatment at a certain high temperature. On this basis, ordered hexagonal mesoporous CoN nanowires array having surface area 89 m²g⁻¹ and pore volume 0.20 cm³g⁻¹ is synthesized (Figure 2.13) [98].

In most of the cases, ammonia nitridation temperature of metal oxide is so large that it disturbs the ordered mesostructure. The second possible way is sectional introduction of metal and sulfide precursors (atmosphere-assisted in-situ reaction). The loading amount of the metal

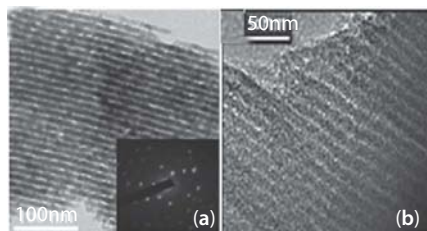


Figure 2.13 Mesoporous CoN replica [130] mesoporous SiC material [124] templated from SBA-15.

oxide should be high enough due to inoccupation of nitrogen precursor and large volume shrinkage during the replacement of oxygen with nitrogen. The nitrogen atoms are then introduced by the solid-gas reaction of metal oxide and ammonia under high temperature. But the problem starts from formation of silicon oxynitride by silicon template itself above 700°C. At high temperature leads to high nitrogen content [131–134]. A specified temperature ramp can be adopted to obtain the mesoporous structures. As for example, Cr_2O_3 @SBA-15 nanocomposites are heated to 950°C in ammonia atmosphere and maintained for 5000 min first to ensure deep nitration of Cr_2O_3 and the silica template. Further, temperature is slowly decreased to 700°C with a ramp of $0.5^\circ\text{C min}^{-1}$ so, that silica template will not react further. After etching template, self-supported CrN having surface area $78 \text{ m}^2\text{g}^{-1}$ and pore volume about $0.2 \text{ cm}^3\text{g}^{-1}$ is obtained [130]. Also by using tri(methylamino)borazine as precursor, nonordered mesostructure BN having surface area $140 \text{ m}^2\text{g}^{-1}$, pore volume $0.16 \text{ cm}^3\text{g}^{-1}$ and pore size 2.9 nm, is obtained [99, 100]. Using polymerized ethylenediamine and carbon tetrachloride as precursor inside pore channel of SBA-15, mesoporous carbon nitride (CN) having surface area $140 \text{ m}^2\text{g}^{-1}$ and pore volume $0.16 \text{ cm}^3\text{g}^{-1}$ is obtained [101].

2.3.12 Nanocasted Mesoporous YPO_4

Preparation of metal phosphate through nanocasting route is somewhat difficult due to precipitation of metal salt and phosphate during infiltration of yttrium nitrate salt and phosphoric acid into the pore channels of mesoporous templates that can block the pore channel of template, resulting in the formation of disordered YPO_4 nanoparticles. Qiuling Luo *et al.* had used concentrate nitric acid to dissolve the precipitated YPO_4 and finally a homogenous solution ($\text{Y}(\text{NO}_3)_3$ /phosphate/ HNO_3) system is successfully infiltrated into the pore channels of KIT-6 dispersed in n-hexane, followed by air dried, calcined (650°C) and etching by 5% HF solution [102]. This group also synthesized lanthanides doped YPO_4 which possess a high surface area, large pore volume and uniform pore size distribution, and exhibit intrinsically tunable photoluminescence properties without grafting or doping of external fluorophore species.

2.3.13 Potential Application

Mesoporous Co_3O_4 nanocasted from KIT-6 have high surface area, three dimensional ordered mesoporous architecture as well as high oxygen adspecies concentrations. So why, it shows excellent catalytic performance

towards CO oxidation reaction [64]. Additionally, it has interesting magnetic properties if the pore system can be filled with another ferromagnetic material that brings useful catalytic application [65]. Ordered cobalt oxides nanocasted by KIT-6 shows high catalytic activity in the total oxidation of propane and toluene, much higher than a conventional Co_3O_4 prepared by simple evaporation of cobalt nitrate [63]. When it is used as support for gold, simultaneous presence of Au^{++} and Au° over the surface enhances the catalytic activity for total oxidation of propane and toluene [103]. Mesoporous cerium oxide catalyst templated by KIT-6 have more compact cerium oxide framework with a higher degree of interconnectivity among the networks. It shows an exceptionally high total oxidation of naphthalene performance both in terms of activity and stability [52]. Mesoporous ordered $\text{CeO}_2\text{-ZrO}_2$ synthesized by J. S. Vasconcelos showed moderate basicity and demonstrate excellent performance towards gas-phase dehydration of glycerol [69]. Mesostructured $\text{Co}_3\text{O}_4\text{-CeO}_2$ ($\text{Co/Ce} = 16/1$) synthesized by C. Ma *et al.* have larger quantities of surface hydroxyl groups and surface oxygenated species that was found to be an effective catalytic material for the complete oxidation of benzene [72]. $\text{Au/Co}_3\text{O}_4\text{-CeO}_2$ have Co_3O_4 (110) facets composed mainly of Co^{+3} which adsorb and activate formaldehyde on the Co_3O_4 surface whereas surface active oxygen species are generate easier over supported gold catalyst that improve the activity of formaldehyde oxidation [71]. High specific surfaces of spinel cobaltite replicas such expose more active sites for catalytic oxidation of CO and their interconnecting pore structure favor the adsorption of reactants and desorption of products. Among these CuCo_2O_4 and MnCo_2O_4 catalysts exhibit high activities and robust stabilities toward the reaction of CO oxidation [73]. Synergic interaction between mesoporous copper and ceria matrices enhanced the catalytic performance towards CO oxidation [68] whereas ruthenium bimetallic component is responsible for both high conversion of NH_3 and high selectivity for N_2 [76]. Three dimensional ordered mesoporous Cr_2O_3 was curiously fitted for as negative electrode in lithium batteries [70]. It has low temperature reducibility which is responsible for the excellent catalytic performance oxidation of typical volatile organic compounds such as formaldehyde, acetone, and methanol [78]. $\text{Cr}_2\text{O}_3\text{-PMA}$ nanocomposites exhibit high catalytic activity and durability in oxidation of 1-phenylethanol using H_2O_2 as an oxidant [79].

5 wt.% mesoporous NiO milled together with MgH_2 shows faster H_2 desorption rates (7 times faster) together with slightly lower sorption activation energies compared with pure MgH_2 . It opens a new perspective in hydrogen storage material [86]. NiAl surface interactions and reconstruction in nanostructured Ni-containing spinel oxides as NiAl_2O_4 , and

$\text{CeO}_2\text{-NiAl}_2\text{O}_4$ shows better catalytic behavior for dry reforming of methane [87]. Ordered mesoporous In_2O_3 templated from KIT-6 exhibited significantly improved ethanol sensitivity due to its large surface area with enough sensing active sites, proper pore distribution for sufficient gas diffusion and appropriate particle size for effective electron depletion [104]. The Mesoporous MoO_2 templated by KIT-6 exhibits a typical metallic conductivity with low resistivity and a reversible capacity as high as 750 mAhg^{-1} at C/20 (41.9 mA g^{-1}) after 30 cycles, rendering it as a promising anode material for lithium ion batteries [88]. MnO_2 derived from KIT-6 have high surface area, oxygen adspecies concentrations, good low-temperature reducibility and high-quality 3D ordered mesoporous architecture of KIT-6 than MnO_2 derived from SBA-15. It account for the excellent catalytic performance of MnO_2 for toluene oxidation [64]. The ordered thin wall mesoporous $\beta\text{-MnO}_2$ would be a promising cathode material in rechargeable lithium-ion batteries. The mesoporous structure act as a buffer layer to alleviate the volume expansion of the electrode materials during lithiation/delithiation. Mesopores structures also provide larger specific surface area leading to higher current density and fast transport of electrolyte with lithium ion whereas thin pore wall reduces the lithium ion diffusion path [58]. Spinel ferrite (MnFe_2O_4) nanoparticles ($\text{Mn/Fe} = 1/2$) is suitable candidate for the removal of pollutants in wastewaters by means of the Fenton heterogeneous reactions [91]. A. H. M. Batista *et al.* synthesized nanostructured mesoporous MAl_2O_4 ($\text{M} = \text{Cu, Ni, Fe or Mg}$) spinels by using SBA-15 template and different meal precursor and investigated in the dehydrogenation of ethylbenzene in the presence of CO_2 [105]. NiAl_2O_4 is highly selective for the production of toluene whereas the selectivities in the dehydrogenation of ethylbenzene with CO_2 showed that styrene was the predominant product for FeAl_2O_4 catalyst due to the continuous oxidation of Fe^{3+} sites by the CO_2 . Additionally, FeAl_2O_4 is stable over the timescale of the reaction. Mesoporous BiVO_4 however lack the long range order but it possesses a large surface area and a small crystal size, resulting in excellent visible light photocatalytic activity [100].

2.4 Porous Silica as Template for Mesoporous Carbon

2.4.1 CMK Family

MCM-41 has 1D porous channels lacking of micropores and mesopores in the wall. So, it is not suitable for the preparation of mesoporous carbon replica [29]. Interestingly, when MCM-41 is treated with microwave digestion

to remove surfactant template, more silanol group appear providing strong binding sites for carbon precursor which facilitates the structural transformation of MCM-41 to its carbon replica with interconnected microporous and mesoporous tunnels [106]. The synthesis of ordered mesoporous carbons **CMK-1**, **CMK-2**, **CMK-3** can be performed by impregnating carbon precursor (as sucrose or furfuryl alcohol or resorcinol or formaldehyde) over different support MCM-48, SBA-1, and SBA-15 respectively followed by thermal treatment and subsequent removal of silica mold [50, 107, 108]. Carbon precursor should have high carbon yield on thermal treatment so that pore of the template remains filled to a larger extent. If sucrose is selected for carbon precursor over MCM-48 (symmetry Ia $\bar{3}$ d), subsequent thermal treatment and silica removal yield a carbon replica of uniform pore distribution but lower symmetry (I4 $\bar{1}$ 32) named CMK-1 whereas poly(divinylbenzene) as precursor over silylated MCM-48 shows much better structural regularity [36, 109]. It is also depicted in Figure 2.14(a) that the removal of the silica wall caused a new peak to appear in XRD, which corresponded to the position of the (110). This change indicates the structure transformation of the resultant carbon to a new ordered structure that allowed this reflection such as cubic I4132 or another. CMK-1 displayed high capacitance due to the remarkable microporous while the mesopores allow easier ion diffusion to the active surface [110]. Interestingly, XRD pattern shows that hexagonal structural order is retained in CMK-3 but having weak diffraction intensities than MCM-48, due to incomplete cross linking of the carbon frameworks (Figure 2.14(b)). As inset TEM images of Figure 2.14(b) shows, the structure of the CMK-3 carbon is exactly an inverse replica of SBA-15.

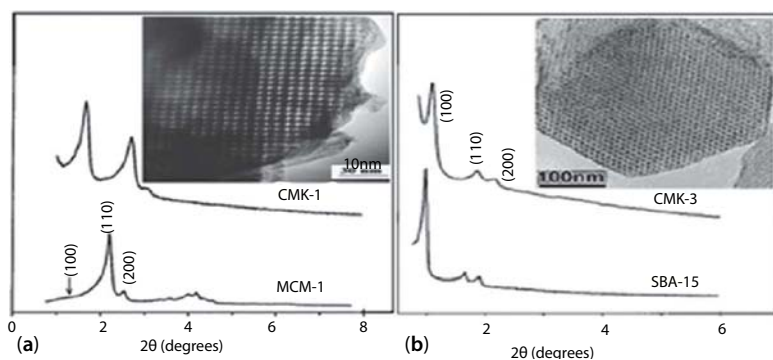


Figure 2.14 Changes in powder X-ray diffraction patterns during synthesis of the carbon molecular sieve: (a) CMK-1 with its silica template MCM-48, the inset figure shows TEM of the ordered carbon molecular sieve CMK-1 [143]; (b) CMK-3 with its silica template SBA-15, the inset figure shows TEM of ordered carbon molecular sieve CMK-3 [50].

The morphology of CMK-3 nanocasted by an organic polymer as polystyrene [111] corresponds to rod-like shapes of the original SBA-15 whereas excellent example of SBA-15 replication is achieved by a CVD process with acetonitrile [112]. The aromatic naphthalene, anthracene or pyrene impregnation or CVD for benzene over MSU-H template followed by carbonization and template removal results into a CMK-3 type OMC [113]. The pore diameter of CMK-1, CMK-3, poly(methyl methacrylate) coated CMK-1, and CMK-3 are 3.9, 2.7, 3.4, and 2.5 nm, respectively. These can be good option for adsorption of those molecules which have effective size lower than pore diameter. These ranges of pore size can invite the adsorption of molecules that have effective size lower than pore diameter [150–154].

The mesoporous carbon replica with exact Ia $\bar{3}$ d symmetry (**CMK-4**) is achieved by CVD process with acetylene over MCM-48 template [36]. If pore system of Al-SBA-15 is only coated by the carbon precursor instead of completely filling it, a surface-templated mesoporous carbon, named **CMK-5** having surface area 2500 m²g⁻¹ and pore volume about 2 cm³g⁻¹ and an array of hollow carbon tubes is obtained [114]. Here again, the lower intensity of the (100) reflection in comparison to that for the (110) reflection was found which is attributed to the diffraction interference between the pipe walls and the spacers interconnecting adjacent pipes. High-resolution TEM images of the CMK-5 sample are shown in Figure 2.15(a)&(b). Figure 2.14 shows a hexagonally ordered array of circles and can be interpreted as a projection of the CMK-5 structure Figure 2.15(c) in the direction parallel to the pore channels.

The removal of the silica mold results in two different types of pores in the CMK-5 matrix. One type of pores is generated in the inner part of the channels which are not filled with carbon precursor. The other types of pores are obtained after silica template removal in the spaces where the silica walls of the SBA-15 are present previously. Pyrolyzing polyfurfuryl alcohol under vacuum atmosphere over Al-SBA-15 resulted in the formation of high quality CMK-5 [115]. It can also be synthesized by varying

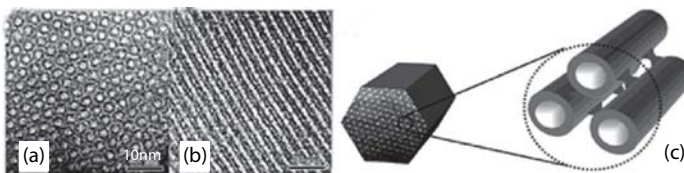


Figure 2.15 TEM images of CMK-5 [155] (a) the channel direction and (b) perpendicular to it (c) Schematic illustration of the Structure of CMK-5 Carbon

concentration of furfuryl alcohol as precursor and oxalic acid as catalyst even over SBA-15 [116] and by varying catalytic CVD time over Co-SBA-15 [117]. The thickness of tubular nanorods can be controlled with the lowest value of 106 nm by using Al as the catalyst [118]. The pore sizes of carbons from the CMK-series till discussed are below about 4.0 nm. The carbon replicas obtained from liquid-phase process using sucrose solution over MCM-41 and SBA-15 templates displaying essentially shrunk and distorted structure with thinner framework elements compared to the gas-phase chemical vapor infiltration (CVI) based replicas [119].

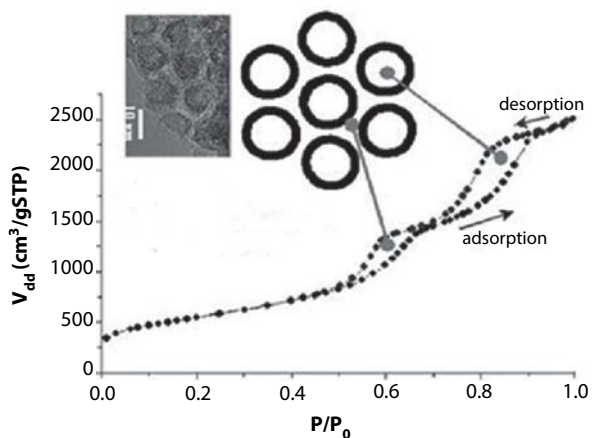
If sucrose as carbon precursor and KIT-6 as template is used, the resulting rod like mesoporous carbon is **CMK-8** material. In the same way, tube like mesoporous carbon **CMK-9** is formed by dispersing furfuryl alcohol over KIT-6 material. The pore size of these templates can be easily tuned from 4 to 12 nm range. Bimodal porous carbon can be synthesized by using binary templates (mixing of mesoporous silica and silica colloid) [120, 121]. The pore size of resulting carbon can be tuned by choosing different silica colloid particle and mesoporous silica during binary template formation. Rayoo and coworkers have used mixed CTAB and polyoxyethylenehexadecylether surfactant to prepare hexagonal mesoporous silica under acidic conditions [122, 123]. By decreasing CTAB/C₁₆EO₈ ratio, wall thickness of resultant silica could be increased from 1.4 to 2.2 nm. By using it as template, ordered mesoporous carbons replica (tunable pore size range 2.2 to 3.3 nm) is formed. The precise information about the precursor, mesopores template and mesostructures is presented in Table 2.2.

2.4.2 NCC-1, UF-MCN, SNU-1, MCF, and MCCF

The search of mesostructured carbons becomes true with discovery of nanocast carbon number 1 (**NCC-1**), mesocellular carbon foam (**MCCF**) and large pore nanocast mesoporous carbon. The preparation condition is somewhat different from CMK-5 as relatively low concentration of furfuryl alcohol (25 vol %), at high aging temperature as well as higher carbonation temperature is required. Undoped or aluminum doped SBA-15 aged at 140°C for 3 days is selected as template to prepare NCC-1 material resulting into an array of connected nanotubes of hexagonal order with high-pore-volume and bimodal pore size distribution. The isotherms of such carbons have a pronounced double hysteresis loop which indicates the existence of the bimodal pore system. In the adsorption-desorption, the step at lower relative pressure corresponding to the pores left by the silica template and the step at higher pressure to the pores in the inner part of the nanotubes are observed (Figure 2.16) [124]. NCC-1 has high pore

Table 2.2 Selected carbon precursor, used mesopores template for nanocasting, and final mesostructures with symmetry.

Precursor	Mesopores Template (symmetry)	Thermal Treatment & silica etching	Mesostructures
Sucrose	MCM-48 (Ia $\bar{3}$ d)	—————>	CMK-1 (I41/a or lower)
Sucrose	SBA-1 (Pm $\bar{3}$ n)	—————>	CMK-2 (Unknown cubic)
Polystyrene or acetonitrile (by CVD process)	SBA-15 (p $\bar{6}$ mm)	—————>	CMK-3 (p $\bar{6}$ mm)
Acetylene (by CVD process)	MCM-48 (Ia $\bar{3}$ d)	—————>	CMK-4 (Ia $\bar{3}$ d)
Furfuryl alcohol coating	Al-SBA-15 or Co-SBA-15	—————>	CMK-5 (p $\bar{6}$ mm)
Sucrose	KIT-6 (Ia $\bar{3}$ d)	—————>	CMK-8 (rod like)
Furfuryl alcohol	KIT-6 (Ia $\bar{3}$ d)	—————>	CMK-9 (tube like).

**Figure 2.16** Nitrogen sorption isotherm of the mesoporous carbon NCC-1 and inset has pore-size distribution and TEM images [165].

volume (up to $4 \text{ cm}^3\text{g}^{-1}$) and a bimodal pore-size distribution where one pore have average diameter 5 nm and another pore that are in the inner part of nanotube having average pore diameter 10 nm.

The precursor gel containing formaldehyde mixed urea was added with INC-2 template at 363 K for 9 h to initiate polymerization and the formaldehyde-INC-2 nanocomposite was obtained [125]. The obtained nanocomposite was carbonized at 873 K for 6 h under 50 ml/min of N_2 flow. After carbonization, 5 wt.% HF aqueous solutions was used for removing silica, followed by filtration and overnight drying at 110°C to obtain mesoporous disk shaped “**Urea Formaldehyde well-ordered Mesoporous Carbon Nitride (UF-MCN)** replica.” These materials have highly ordered 1D mesopore structures with a 2D hexagonal arrangement with short 1D ordered mesopore channels of submicrometer length (100–300 nm). The channel directions are perpendicular to the larger surface of hexagonal platelet and parallel to the thickness. J. Lee *et al.* synthesized a mesoporous carbon named SNU-1 (Seoul National University-1) nanocasted material from Al-MCM-48 by using phenol-resin as the carbon precursor [126, 127]. This mesoporous carbon is not a real negative replica of the MCM-48 silica, but similar to CMK-1. It exhibits periodical 3D interconnected mesopores with diameter of 2 nm. A. B. Fuertes *et al.* synthesized different carbon mesopores having pore size in 3–8 nm range casted by SBA-16 template and polyfurfuryl alcohol carbon precursor [128]. The short pore length nanocasted mesoporous carbons have enhanced electrolyte accessibility as well as rapid ion diffusion [129].

Poly-(ethylene oxide)-poly(propylene oxide)-poly(ethyleneoxide) (PEO-PPO-PEO) triblock copolymer have been well known to create a well defined mesoporous silica material SBA-15. When very low concentration of TMB is added to a PEO-PPO-PEO templated system, the hexagonally packed pore structure is maintained. Upon increasing the oil-polymer ratio, a new **Mesocellular foam** (MCF) phase is obtained. The MCF phase possesses a system of interconnected pores with diameters of 220–420 Å [130]. Further; aluminum can be incorporated into the silicate framework to generate strong acid catalytic sites. Now, Al incorporated mesocellular silicate foam (AIMCF) can be used as a template for getting MCCF. Jinwoo Lee *et al.* [131] incorporate excess of phenol into the pores of AIMCF by heating a mixture of AIMCF and phenol at 140°C under static vacuum. The resulting phenol-incorporated AIMCF and formaldehyde polymerized was put in an autoclave at 130°C for 2 days to yield the phenol-resin/AIMCF nanocomposite. Further, heating at 1 K min^{-1} to 160°C and held

at that temperature for 5 h under nitrogen flowing then at 5 K min⁻¹ to 850°C and held at that temperature for 7 h is applied to carbonize phenol resin inside the pores of AlMCF to get the carbon/AlMCF nanocomposite. Finally, The dissolution of the AlMCF template using 1 N NaOH in a 1:1 mixture of EtOH and H₂O generated MCCF having surface area 1037 m²g⁻¹ and pore volume 1.66 cm³g⁻¹. Magnetic MCCF was fabricated by using mesocellular silica as a template, divinylbenzene (DVB) as the carbon precursor and Fe(NO₃)₃·9H₂O as the magnetic source via then a nanocasting process [132]. Schematic illustration for the synthesis of MCCF is shown in Figure 2.17.

Large pore nanocast mesoporous carbon having tunable entrances in the range of 4–9 nm sizes and interconnected network can be prepared by using sucrose as carbon precursor and FDU-12 as template results into synthesis of large pore nanocast mesoporous carbon having tunable entrances in the range of 4–9 nm sizes and interconnected network [34].

2.4.3 Hollow Mesoporous Carbon Sphere/Prism

Impregnation of phenol and paraformaldehyde over core-shell silica@mesoporous silica, initiates polymerization inside the mesopores channels at 200°C. After leaching silica template, hollow mesoporous carbon sphere having surface area 1200 cm²g⁻¹ and pore volume 1.47 cm³g⁻¹ were found [133]. The inner hollow diameter and outer-shell thickness are dependent on the diameter of stober silica sphere and the thickness of the mesoporous silica shell respectively.

It should be noted that, core-shell silica@mesoporous silica (stober sphere) was formed by coating of mesoporous silica layer by co-condensation of octadecyltrimethoxysilane and TEOS over uniform silica spheres. The Schematic illustration for synthesis of hollow mesoporous carbon spheres and their SEM and TEM with different inner and outer sizes is shown in Figure 2.18.

Hyeon's group synthesized gold nanoparticles encapsulated in hollow mesoporous carbon sphere by using gold nanoparticles encapsulated silica sphere (as reported by Liz-Marzan *et al.* [134]) in place of stober sphere [135]. This product has great potential in catalysis because carbon shell can prevent the aggregation and deactivation of gold nanoparticles. If mesoporous silicalite-1 zeolite is used in place of stober sphere, hollow mesoporous carbon prisms was formed [136, 137]. By using mesoporous aluminosilica sphere [138] as template and sucrose as carbon precursor, hollow mesoporous carbon spheres having surface area 1800 cm²g⁻¹ and pore volume 1 cm³g⁻¹ with bicontinuous cubic structure



Figure 2.17 Schematic illustration for the synthesis of MCCF [172].

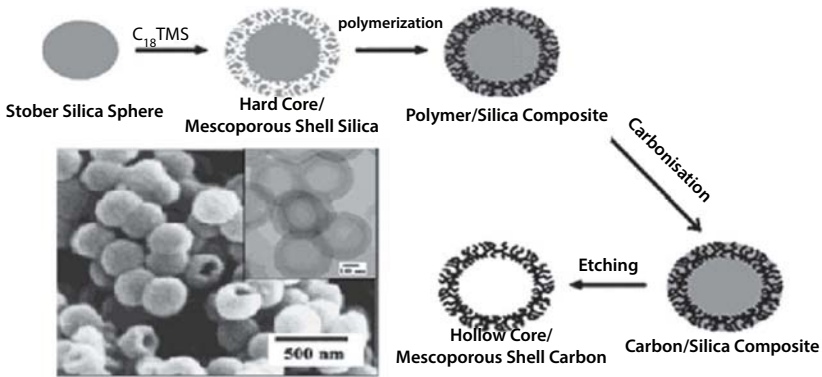


Figure 2.18 Schematic illustration for synthesis of hollow mesoporous carbon sphere [174]. SEM and TEM (inset) images for hollow mesoporous carbon spheres with different inner and outer sizes: inner diameter of 220 nm, thickness of mesoporous carbon shell of 50 nm.

(Ia3d symmetry) was synthesized [139]. Its unique 3D bicontinuous cubic mesopore structure can facilitate the mass transportation. The above procedure of getting hollow mesoporous carbon sphere is quite complex and shows poor regularity. Mokaya and coworkers prepared a 2D hexagonal hollow mesoporous carbon sphere with regularity as same as mother template by filling the carbon precursor (styrene) over SBA-15 through CVD, followed by heat treatment over 950°C and silica etching [32, 140, 141]. The cell parameter (10.5 nm) in CVD process is larger than that in impregnation process (9.1 nm) due to closer packing of carbon precursors inside mesochannels by CVD than impregnation. Summary for preparation layout of hollow mesoporous carbon sphere/prism is shown in Table 2.3.

2.4.4 Ordered Mesopores Carbon with Surface Grafted Magnetic Particles

Infiltration by carbon precursor into magnetic nanoparticle deposited SBA-15 followed by thermal treatment and subsequent removal of silica mold resulting into “Ordered Mesopores Carbon with Surface Grafted Magnetic Particles.” The Schematic Illustration of the synthesis procedure of ordered mesopores carbon with surface grafted magnetic particles is shown in Figure 2.19 [142].

It is cleared from above that before infiltration by carbon precursor; magnetic nanoparticle grafted template is required. For grafting magnetic particle in template, two sub-steps arrive; one named deposition of cobalt

Table 2.3 Summary for preparation layout of hollow mesoporous carbon sphere/prism.

Nanocast Materials	Precursor	Template	Method Sequence	Ref.
Hollow mesoporous carbon sphere	Phenol and paraformaldehyde	Core-shell silica@mesoporous silica	Impregnation and subsequent heating	[174]
Hollow mesoporous carbon sphere	Phenol and paraformaldehyde	Gold nanoparticles encapsulated silica sphere	Impregnation and subsequent heating	[176]
Hollow mesoporous carbon prisms	Phenol and paraformaldehyde	Mesoporous silicalite-1 zeolite sphere	Impregnation and subsequent heating	[178]
Hollow mesoporous carbon sphere	Sucrose	Mesoporous aluminosilica sphere	Impregnation and subsequent heating	[180]
Hollow mesoporous carbon sphere	Styrene	SBA-15	CVD	[181]

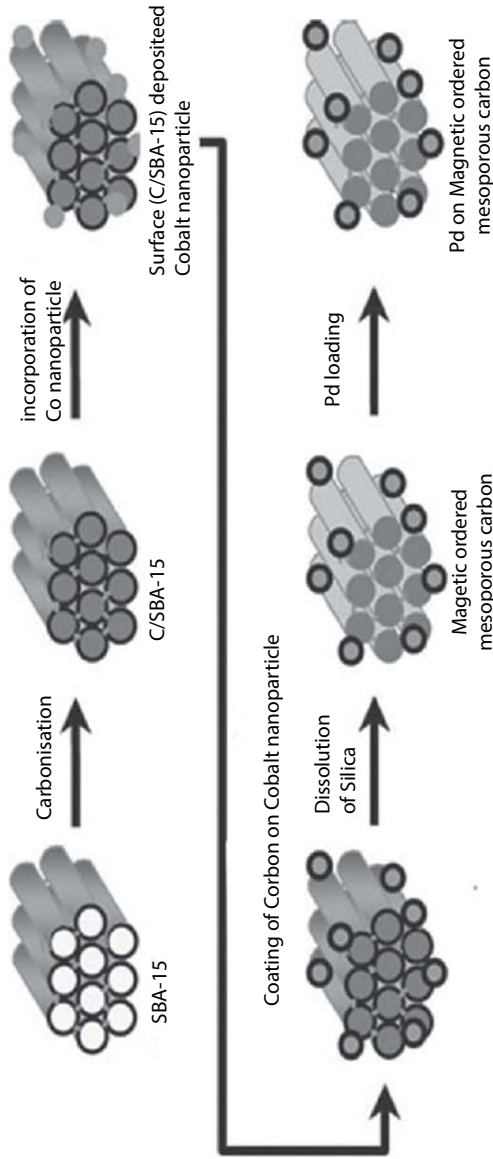


Figure 2.19 Illustration of the synthesis procedure [183].

nanoparticles into SBA-15 and another protection by a nanometer thick carbon layer [183]. To protect the deposition of magnetic nanoparticles inside the pore of SBA-15, PMMA (a thermally decomposable polymer) filled SBA-15 is taken as template and cobalt nanoparticle suspended in toluene is allowed to impregnate over. Further, the composite is wetted with furfuryl alcohol containing oxalic acid and heated to 850°C under argon in order to convert the furfuryl alcohol into a thin carbon coating on the surface of the cobalt nanoparticles. Simultaneously, heat treatment to carbonize the poly-FA, the PMMA in the pores of the SBA-15 was performed to restore the accessible pore system. In this way, magnetic carbon and silica can be fabricated with magnetic anchors grafted to the outer surface while maintaining an open pore systems. Now, this magnetic nanoparticle deposited SBA-15 can be used as new template waiting for new carbon precursor.

The low-angle X-ray powder diffraction (XRD) pattern of the resultant Co-OMC shows well-resolved reflections (Figure 2.20a), thus indicating an ordered structure. This is consistent with the TEM observation (Figure 2.20b).

In the same way magnetic nanoparticles deposited MCM-48 template was synthesized by filling MCM-48 with cobalt nitrate solution and further applied to calcination and subsequent reduction. Finally, to get Cobalt (2–3 nm size range) containing CMK-1, cobalt deposited MCM-48 was chosen as a hard template in which sucrose solution was infiltrated; followed by carbonization and removal of silica [143]. Using similar methodology, woo and coworkers [144] prepared CMK-3 with Pt nanoparticle (1–5 nm) embedded in the carbon wall whereas Li *et al.* [145] introduced sucrose and nickel nitrate hexahydrate repeatedly into the pores of SBA-15. At 15.2 wt.% of Ni, the NiO-CMK-3 composite have surface area 1000 m²g⁻¹ and pore volume of 0.91 cm³g⁻¹. As the pyrolysis

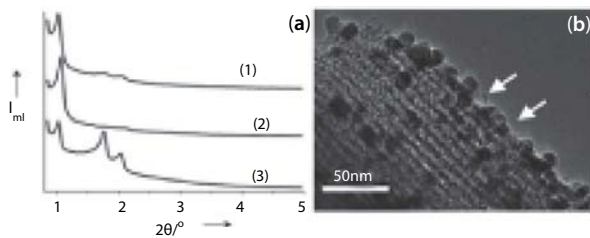


Figure 2.20 (a) Low angle XRD patterns of different Co-OMC Types of mesoporous carbons: (1) magnetic CMK-3, (2) magnetic polyacrylonitrile (PAN)-based OMC, and (3) magnetic CMK-5. (b) TEM images of Co-OMC at different magnification: high magnification. Arrows indicate hollow carbon shells left after the leaching procedure [183].

temperature increases, the specific surface area and pore volume was increased. Li *et al.* developed “cross linking PAN incorporated SBA-15” by incorporation of PAN and their subsequent oxidation. Now, this composite was immersed into aqueous solution of Pd (NO₃)₂ where Pd cations are adsorbed by nitrogen groups of PAN. Further, pyrolysis and etching of silica lead to the formation of Pd-OMC material [146]. At pyrolysis temperature above than 650°C, no visible Pd particles was found either on the external surface of carbon supports or in the carbon wall. By using Copper (II) phthalocyanine-tetrasulfonic acid tetrasodium salt as precursor under 600°C pyrolysis temperature, stable nanocast carbon was obtained. However, carbon, copper sulfur compound or large copper particles is more evident in the carbon framework above 600°C [147]. Complete inclusion of metal (Pd, Pt, Ru) precursors in β -cyclodextrin could be infiltrated into 3D polystyrene sphere, followed by toluene immersion and heat treatment. This procedure lead the formation of metal incorporated hierarchically [148, 149]. The summary for preparation layout of ordered mesopores carbon with surface grafted magnetic particles is shown in Table 2.4.

2.4.5 Surface Modified Mesoporous Nitrogen Rich Carbon by Nanocasting

Nitrogen containing groups can be introduced by directly using suitable nitrogen-rich precursor to the mesoporous carbon. Using PAN as the carbon source, 2,2'-azobisisobutyronitrile as initiator and SBA-15 as template, N-containing nanocast mesoporous carbons with monomodal or bimodal pore-size distribution were synthesized [150]. Its pore structures is tunable simply by changing the stabilization temperature and carbonization temperature (specific surface area and pore volumes ranging from 500 to 800 m²g⁻¹ and from 0.55 to 1.2 cm³g⁻¹) where as the connectivity between the adjacent pores are improved (in bimodal pore size distribution) due to randomly distributed incompletely coated pore walls. The nitrogen content and type of nitrogen species present in the material can be controlled by treatment temperature. As well as temperature increases, the nitrogen content in the resultant sample decreases and at the same time pyridine like nitrogen species changes to pyridinium ions [80]. When ammoxidation was carried out before carbonization, the amount of incorporated nitrogen was high up to 8 wt.%, whereas only 1.6 wt.% nitrogen can be detected in a sample prepared from carbonization prior to ammoxidation [151].

Table 2.4 Summary for preparation layout of ordered mesopores carbon with surface grafted magnetic particles.

Nanocast materials	Precursor	Template	Method Sequence	Ref.
Co-CMK-3 Co-PAN-based OMC, Co-CMK-5	Different carbon precursors	Magnetic nanoparticle deposited SBA-15	Impregnation and subsequent heating	[183]
Co-CMK-1	Sucrose solution	Cobalt (magnetic nanoparticle) deposited MCM-48	Impregnation and subsequent heating	[184]
Pt-CMK-3	Sucrose and nickel nitrate hexahydrate	SBA-15	Impregnation and subsequent heating	[185]
NiO-CMK-3	Nickel nitrate hexahydrate	SBA-15	Impregnation and subsequent pyrolysis	[186]
Pd-OMC	Pd (NO ₃) ₂	Cross linking PAN incorporated SBA-15	Impregnation and subsequent pyrolysis	[187]
Co-OMC	Copper (II) phthalocyanine-tetrasulfonic acid tetrasodium salt	SBA-15	Impregnation and subsequent pyrolysis	[188]

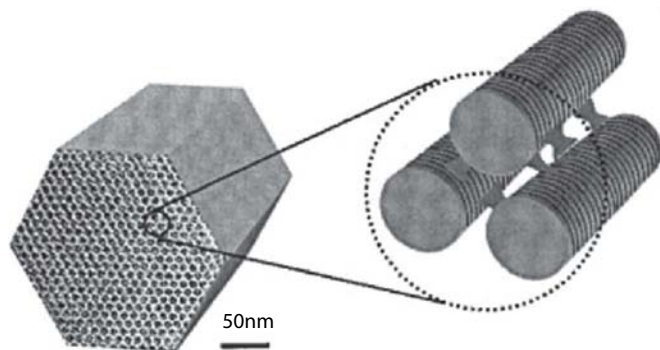


Figure 2.21 Carbonization of aromatic sources in an aluminosilicate mesoporous template yields mesoporous carbon materials with highly graphitic framework structures and excellent mechanical strength and thermal stability [189].

Using pyrrole as carbon precursor and ferric chloride as oxidant [191] or acetonitrile as precursor [152, 153] N-incorporated nanocast mesoporous carbon materials is synthesized by CVD over SBA-15 template. Polymerization of pyrrole vapor (carbon precursor) over Fe (III) SBA-15 template followed by carbonization and template removal results into nitrogen containing OMC [154]. In the same way, acenaphthene polymerizes over AlCl_3 treated silica template (SBA-15, MCM-41) give mesoporous carbon with a graphitic skeleton [155] (Figure 2.21).

When Furfuryl alcohol is selected as carbon precursor and mesoporous aluminosilicate oxynitride (OMASON) as template, the nitrogen atoms from template were partially transferred to carbon framework during pyrolysis process and the resulted carbon replica having specific surface area about $1600 \text{ m}^2\text{g}^{-1}$ and pore volume $1.6 \text{ cm}^3\text{g}^{-1}$ has nitrogen content in the range of 1.4 to 3.1 wt.% which is decreased with increasing carbonization temperatures from 700–900°C [156]. By using melamine-formaldehyde resin as carbon precursor and commercial fumed silica (Aerosil-200) as hard template, nitrogen-enriched mesoporous carbon sphere [157] and other carbon replica made from aniline [158] quinoline-polymerized pitch [159] as carbon precursor is also reported. Summary of preparation layout for nitrogen rich OMC is shown in Table 2.5.

2.4.6 Potential Application

Palladium nanoparticles deposited inside the pores of CMK-3 analogue shows enhance performance than conventional one in Sonogashira reaction [160]. Molecular level dispersed and encapsulated Pd on the mesoporous

Table 2.5 Summary for preparation layout of nitrogen rich OMC.

	Precursor	Template	Method Sequence	Ref.
Nitrogen rich OMC	PAN, 2,2'-azobisisobutyronitrile	SBA-15	Impregnation and subsequent heating	[191]
	Pyrrole ferric chloride	SBA	CVD	[191]
	Acetonitrile	SBA	CVD	[193]
	Pyrrole	Fe (III) SBA-15	CVD	[195]
	Acenaphthene	AlCl ₃ treated silica template	CVD	[196]
	Furfuryl alcohol	OMASON	Impregnation and subsequent heating	[197]
				Dissolution of silica

carbon support (Pd-OMC) exhibits remarkably high selectivity for alcohol (benzyl alcohol, 1-phenylethanol and cinnamyl alcohol) oxidation to the corresponding aldehydes while at the same time had relatively high activity [187]. Mesostructured CN templated by disk-shaped 2D hexagonal mesoporous silica (INC-2) and urea/formaldehyde as carbon and nitrogen precursors is utilized in the metal-free oxidation of cyclic olefins with hydrogen peroxide where conversion for cyclopentene, cyclohexene and cis-cyclooctene is obtained in the range of 65–80% and selectivities onto epoxides were 40–90%, respectively [166]. The Pt(50)-Ru(50) catalyst dispersed on nanocast carbons with a spherical cavity shows 10–15% increase in methanol oxidation activity as compared to that of the corresponding commercially available Pt-Ru alloy catalyst [161].

CMK-3 oxidized with nitric acid bears large number of functional groups like $-\text{COOH}$ and $\text{C}-\text{OH}$ that produce pseudo-capacitance resulting in an increase in capacitance [162] whereas pyridine containing mesoporous carbon exhibits excellent capacitive properties due to an enhanced, fast and reversible faradaic redox reaction [192]. 10.0–30.7 wt.% of RuO_2 in CMK-3 dramatically leads to an increased capacitance highest value reached was 633 F g^{-1} due to large surface area of CMK-3 and the pseudo-capacitance of amorphous RuO_2 [163] whereas SnO_2 nanoparticles supported mesoporous carbon shows improved specific capacity [164]. 6 wt.% of birnessite-type MnO_2 in porous carbon template form 3D assemblies of silica spheres shows remarkably enhance the capacitance as high as 660 F g^{-1} and even 490 F g^{-1} capacitance is maintained after 500 cycles [165]. Up to 60% Pt nanoparticles (particle size: 3 nm) uniformly dispersed on mesoporous carbons templated from SBA-15 and phenanthrene carbon source shows lower sheet resistance than sucrose carbon source [166].

L. Calvillo *et al.* prepared Pt impregnated surface-oxygen-rich-CMK-3 and tested it as electrode for PEM fuel cell [167]. Surface oxygen decomposes during the reduction stage of metal precursor which facilitates the mobility of platinum particle and favoring the agglomeration of Pt particle. There is an electronic interaction between the surface groups of the support and the Pt atoms which favors the electron transfer from catalytic sites to the conductive carbon electrode. It results into better electrocatalytic performance than the commercial Pt-carbon black on carbon cloth electrode. Baizeng Fang *et al.* synthesized hollow core/mesoporous shell carbon which has uniform particle size, well-developed three-dimensionally interconnected bimodal porosity, and large specific surface area and pore volume suited for using as anode catalyst support in low temperature fuel cells. So, hollow core/mesoporous shell carbon supported Pt50Ru50 (60 wt.%) has exhibited almost two times the power density in direct formic acid

fuel cell than delivered by the commonly used Pt or Pt alloy supported on carbon black Vulcan XC-72 [168]. Nanocast mesoporous carbons, using modified glass carbon as an electrode, showed a high catalytic activity to the electro-oxidation of nicotinamide adenine dinucleotide (NADH) and H_2O_2 [169] and the electrochemical oxidation of hydroquinone [170]. Such ability of nanocast mesoporous carbons is effective low-potential amperometric biosensing of glucose and electrochemical sensors for the detection of hydroquinone due to its very low detection limit. Ordered mesoporous carbon-supported PtBi nanoparticles in the size range of 3 nm exhibits the robust mass activity for formic acid oxidation in direct formic acid fuel cell anode [171]. Hollow core mesoporous shell carbon supported Pt nanoparticles showed significant enhancement in the electrocatalytic activity toward oxygen reduction reaction as well as an enhancement of 91–128% in power density compared with that of Pt/Vulcan in direct methanol fuel cells [172].

The stability of carbon materials at high temperature, their acid tolerance and low affinity for water has unique advantage over silicate molecular sieves. For adsorption of bulky molecule like enzymes, vitamins, proteins or other organic molecules, acid tolerable biocompatible mesopores like CMK families are needed. It was found that the adsorption amount depends significantly on the pH of the solution. The maximum adsorption is close to the isoelectric point of the enzyme [150]. For adsorption of Vitamin E, CMK-3 was better option than CMK-1 and activated carbon where a non-polar solvent such as n-heptane is more preferred than polar n-butanol [152]. Again for vitamin B_{12} (effective size 2.09 nm), CMK-3 having larger pore diameter 3.9 nm was found to be most suited than CMK-1 which have 2.7 nm pore diameter [153]. However, on coating with poly(methyl methacrylate), pore diameter of CMK-3 reduces to 3.4 nm but increased interaction between the carbonyl group of poly(methyl methacrylate) and amino group of vitamin B_{12} through hydrogen bonding shows higher adsorption capacity than noncoated carbons. Vinu *et al.* reported the largest adsorption capacity of cytochrome *c* on CMK-3 was only 229 mg/g [150] and Sevilla *et al.* reported the largest amount of lysozyme immobilized by porous carbon was 510 mg/g [173] whereas The FeNi/C composite templated from SBA-15 using metal nitrates and furfuryl alcohol as precursor shows cytochrome *c* adsorption up to 732 mg/g and lysozyme adsorption up to 790 mg/g [174]. CMK-3 showed a larger amount of L-histidine adsorption as compared to SBA-15 due to the stronger hydrophobic interaction between the non-polar side chains of amino acids and the hydrophobic surface of the mesoporous carbon as compared to mesoporous silica. Apart from the mesoporous silica, it has more his adsorption than the conventional adsorbent, namely activated carbon [175]. Yong Tian

et al. synthesized Ni-containing ordered mesoporous carbons (Ni/OMCs) and found that methyl orange desorption rate increased with the increasing of pore sizes for the carbon materials [176]. Ajayan Vinu *et al.* synthesized novel large pore cage type mesoporous carbons by using sucrose and sulfuric acid solution as precursor and KIT-6 template which exhibit unusual adsorption capacity of catechin in aqueous solution and higher adsorption capabilities of amino acid (histidine), vitamin (vitamin E, α -tocopherol), endocrine disrupter (nonylphenol), and enzyme (lysozyme) as compared with the CMK-3 mesoporous carbon [177]. Katsuhiko Ariga *et al.* prepared carbon nanocage by using KIT-6 as template and sucrose as carbon source which exhibit larger adsorption capacity for tannic acid with a two-step adsorption, while CMK-3 showed lower capacity in single-step mode. Only poor adsorption capacity was detected for activated carbon powder and SBA-15 [178].

2.5 Porous Carbon as Template for Inorganic Compound

It has been noted that some oxides may react with silica when mesoporous silica is used as template, leading to some difficulties in crystal growth in the confined pores (i.e., **MgO**). The silica source (from template) can participate in reaction during $\text{Mg}(\text{NO}_3)_2 \cdot 6\text{H}_2\text{O}$ decomposition process. Additionally, ammonia silica reactions are more prominent during nitridation of metal oxide to metal nitride inside the silica template at high temperature. Also during template removal by HF and NaOH solution, some amphoteric oxides like CuO, ZnO and Al_2O_3 may react with HF or NaOH. So, silica cannot be removed during preparation of the other oxides. This problem can be overcome by using mesoporous carbon, e.g., CMK family [50] as an alternative template. The mesoporous metal oxide can be easily obtained by simply removing carbon template with thermal treatment. So, during the synthesis of these metal oxides, two steps of nanocasting are involved, i.e., starting from silica to carbon family ending up with metal oxide. Thus this process is also called “repeat nanocasting” in the literature. Schematic illustration of the repeat nanocasting process is shown in Figure 2.22.

2.5.1 Nanocasted Silica by Porous Carbon Template

Extending this thinking, mesoporous/microporous silica can also be nanocasted from mesoporous carbon family. CMK-1 or carbon replica (which is itself casted from MCM-48) have a lower symmetry (I41/a) can

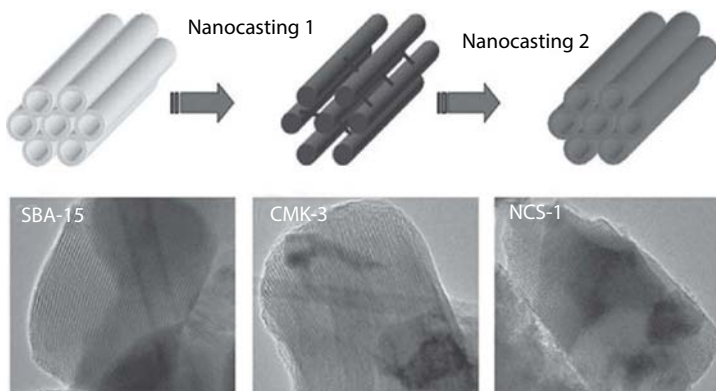


Figure 2.22 Schematic illustration of the repeat nanocasting process [179] and TEM observations of SBA-15, CMK-3, and NCS-1 [180].

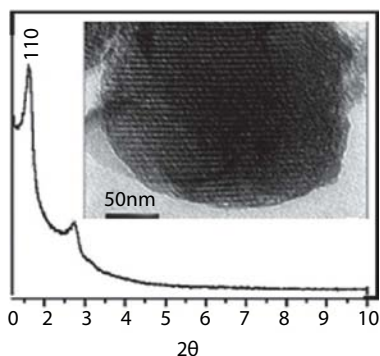


Figure 2.23 The XRD pattern of the HUM-1 and inset shows its TEM image [222].

also used as template for siliceous precursors and results into formation of Hannam University Mesostructure-1 (HUM-1) having more lower or new cubic phase symmetry of pore arrangement [222–224]. The XRD pattern and TEM image of the HUM-1 indicates a long-range structural order characteristic of silica materials with periodically ordered mesopores (Figure 2.23) Using tetraethoxysilane (TEOS) as siliceous precursor and tetrapropylammonium hydroxide as hydrolysis agent along with mesoporous carbon template, a new class of ordered mesoporous aluminosilicates with crystallized zeolite pore walls are obtained as RMMs casted from CMK-1 template, RMMs casted from CMK-3, OMZ-1 from CMK-5 [225–227]. By using Na_2SiO_3 solution to impregnate in mesopores of CMK-3 followed by water and HCl vapor treatment as polymerization initiator, Nanocasted

silica NCS-1 is formed [51, 181]. NCS-1 may be casted by using TEOS as siliceous source by incipient-wetness impregnation from CMK-3 [221]. In the same way SBA-15 (space group of $p6mm$) can be casted by chemical vapor infiltration technique from CMK-3 [182]. But all these structures have low hydrothermal stability due to the absence of crystalline pore walls, which hinders its practical applications. Long impregnation period (48 h at 40°C) of siliceous precursor and higher temperature HCl vapor treatment (160–240°C) during preparation leads a highly hydrothermally stable nanocasted SBA-15 [183].

2.5.2 Nanocasted Alumina and Nanocasted MgO

Using carbon aerogel as a hard template and aluminum nitrate as a precursor, a glassy amorphous mesoporous alumina has been yielded by nanocasting [184]. The generated alumina exhibits small transparent granules (diameter 3–6 mm) and inherits the 3D network structure of the carbon template. The pore diameters can be varied from 5 to 30 nm by variation of the template and the loading amount of the alumina precursor. At high loadings, the obtained glassy alumina clearly has a bimodal pore-size distribution in the mesopore range. The mesopore surface area of the alumina can be as high as 365 m²g⁻¹, and the pore volume reaches about 1.55 cm³g⁻¹.

Ethanol solution of aluminum nitrate is used as precursor to improve the wettability of relatively hydrophobic template CMK-3. Ammonia was adopted to hydrolyze the aluminum oxide precursor. The filling and hydrolysis steps were repeated at least four times to ensure that the template pores were fully filled with the aluminum oxide precursor. Finally, a stepwise calcination procedure was applied to transform the amorphous framework walls into a crystalline ordered mesoporous γ -Al₂O₃ (named

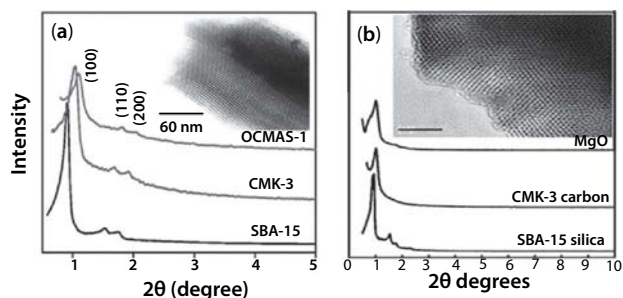


Figure 2.24 (a) Low-angle XRD patterns for SBA-15, CMK-3 and OCAMS-1 and TEM images of OCAMS-1 [232]. (b) Powder XRD patterns of mesoporous MgO and “parent” CMK-3 and SBA-15, and the TEM image of MgO [234].

OCAMS-1) under an inert atmosphere and subsequently to remove the carbon template in air. The wide-angle XRD pattern of OCAMS-1 shows four weak diffraction peaks in accordance with the γ - Al_2O_3 phase (JCPDS card no. 10-0425), implying the presence of crystalline framework walls [185] as depicted in Figure 2.24(a).

Spherical interconnected 3D mesoporous MgO having surface area $150 \text{ m}^2\text{g}^{-1}$ and pore volume $0.73 \text{ cm}^3\text{g}^{-1}$ is prepared by using carbon aerogel as hard template and magnesium nitrate as metal oxide precursor [186]. However, it cannot be defined as “repeat nanocasting” because carbon aerogel is synthesized by drying resorcinol / formaldehyde polymer under ambient pressure instead using, any primary template. Magnesium nitrate infiltration over CMK-3 (which is itself nanocasted by SBA-15) followed by vacuum drying and heating to 300°C under air (to convert the metal nitrate into oxide) forms MgO@CMK-3 composite as final product. Repeating this procedure three times, MgO loading increases such that mass ratio of CMK-3 and MgO is found 1: 1 ratio which is confirmed by thermal analysis [187, 188]. After carbon template removal at 800°C in air, a periodically ordered uniform narrow mesoporous MgO having surface area $306 \text{ m}^2\text{g}^{-1}$ pore volume $0.51 \text{ cm}^3\text{g}^{-1}$ and pore diameter 5.6 nm is formed. The basic properties of the catalysts needed be activated by calcination at 700°C so that all chemisorbed species such as OH, H, CO_2 can be removed. It has smaller pore diameter and thicker pore walls than the SBA-15 because the wall thickness in CMK-3 is always lower than the pore diameter in the parent SBA-15 [36]. The low-angle XRD patterns of SBA-15, CMK-3 and OCAMS-1 or MgO as depicted in Figure 2.24(b), shows the hexagonal symmetry mesostructure. The broadening of the 100 reflection peaks reveals some degradation in structural regularity. TEM images of OCAMS-1 display the hexagonally ordered mesopores and the evenly spaced parallel channels, indicating a well-developed long-range order which is consistent with the XRD results. The TEM image of MgO displays a long-range periodic ordering with hexagonal symmetry.

2.5.3 Nanocasted CeO_2 and ZnO

Mesopores CeO_2 with crystalline pore walls and large specific surface area (up to $148 \text{ m}^2\text{g}^{-1}$) can be prepared by using CMK-3 carbon as a hard template and saturated aqueous solution $\text{Ce}(\text{NO}_3)_3$ as the precursor. CeO_2 product exhibits 2D hexagonal periodic arrangement with uniform pores with a diameter of $\sim 5 \text{ nm}$ [189]. Tsoncheva *et al.* deposited iron (III) containing nanoparticles over nanocasted CeO_2 and obtained pronounced

positive effect over Fe/CeO_2 catalyst towards methanol decomposition. This is probably due to the intensive electron exchange at the interface between the Fe_2O_3 species and the CeO_2 support, as well as by the formation of methoxy group intermediates on the CeO_2 surface [190]. Zhang Huili *et al.* reported mesoporous ceria-supported gold catalyst by the colloidal deposition method [191]. X. Lai *et al.* prepared indium oxide by infiltrating method. The indium nitrate precursor was infiltrated into the pore of SBA-15 by ultrasonic wave and vacuum followed by heating at 400°C to convert precursor into indium oxide and combustion at 550°C [192]. The SAED patterns of CeO_2 show the atomic-scale crystallinity of the porous materials. Interestingly wide angle XRD pattern indicates that CeO_2 is crystalline and the pore walls are polycrystalline in nature. The SAED pattern, TEM images and wide angle XRD patterns of (a) mesoporous CeO_2 is shown in Figure 2.25(a).

To prepare mesoporous ZnO, $\{\text{H}_3\text{CZnO}(\text{CH}_2)_2\text{OCH}_3\}_4$ was taken as a precursor which is infiltrated by vacuum for 5 h into PAN-based CMK-3. Collected product is further treated at a relative humidity of 50% to hydrolyze the ZnO precursor and calcined in pure oxygen at 370°C to prepare ordered **mesoporous ZnO** having surface areas $200\text{ m}^2\text{g}^{-1}$ [21, 191]. However, the structure of ZnO is less ordered than in the original carbon template. To prepare hexagonally arranged improved periodic ZnO, CMK-3 carbon was taken as template and a solution of $\text{Zn}(\text{NO}_3)_2$ in THF is taken as a precursor [193] followed by thermal treatment under air at 300°C and finally the removal of the carbon matrix by heating under air at 700°C . Nanocast mesoporous ZnO shows a higher sensitivity to carbon monoxide and nitrogen dioxide as compared to the bulk sensor [194]. The SAED patterns of ZnO shows a single spot superimposed on diffuse rings indicate that the pore walls consist of ZnO crystalline domains. The SAED patterns and TEM images of ZnO is shown in Figure 2.25(b).

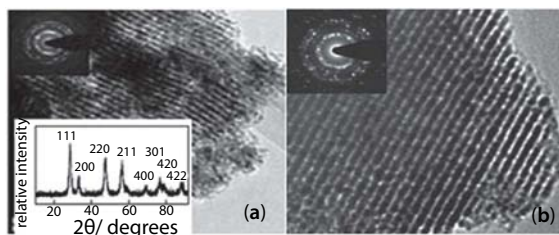


Figure 2.25 (a) SAED pattern, TEM images and wide angle XRD patterns of mesoporous CeO_2 [236] (b) TEM images of ZnO and SAED patterns [240].

2.5.4 Nanocasted CuO

Impregnation of copper nitrate (repeated twice) over CMK-3 template under vacuum, subsequent heating to 300°C (to decompose copper nitrate to CuO) and finally calcination leads the formation of 2D hexagonal (p6mm) structure mesoporous CuO having pore wall thickness of about 4–5 nm, a mean pore size of 5.5 nm, specific surface area 149 m²g⁻¹ and total pore volume 0.22 cm³g⁻¹ (Figure 2.26) [195]. These results once again indicate the perfect replications from silica (SBA-15) to carbon (CMK-3) and further from carbon (CMK-3) to CuO. B. Solsona *et al.* reported mesoporous cobalt-supported gold catalyst by a deposition–precipitation method.

2.5.5 Nanocasted Other Metal Oxide

Mesopores inorganic materials such as alumina, zirconia, titania, etc. can also be synthesized from the CMK-3 by using the nano-replication synthetic strategy [196]. The CMK-3 was impregnated with aqueous solution of metal precursors (Na₂SiO₃, TiCl₄, ZrOCl₂, and NaAlO₂) by wetness method using a rotary evaporator, and subsequently the sample was hydrothermally treated under acidic or basic conditions to obtain the fully condensed inorganic framework (mesoporous SiO₂, TiO₂, ZrO₂, and Al₂O₃). The materials have well-crystalline tetragonal-ZrO₂, γ-Al₂O₃ and rutile-TiO₂ frameworks, respectively but their mesoscopic orders are not in good qualities compared with that of the silica material.

Metal (Al and Ti) alkoxide as precursor in ethanol solution was allowed to infiltrate in the pore of hollow mesoporous carbon sphere (that is itself prepared by using spherical SBA-15 silica as the template via a CVD of acetonitrile) [197, 198]. The hydrolysis of the alkoxides in the carbon mesopore channels was initiated by exposing the mixture in air. Afterwards, the removal of the carbon (by calcination at 500–600°C) results in porous metal oxides as with predominantly hollow sphere morphology. Finally,

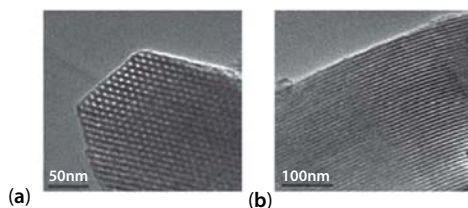


Figure 2.26 TEM images of the mesoporous copper oxide recorded along the (a) [001] and (b) [110] directions [242].

mesopores $\gamma\text{-Al}_2\text{O}_3$, titania (anatase), MgTiO_3 and $\text{MgO-Al}_2\text{O}_3$ are formed that do not exhibit ordered mesostructure probably due to the less-ordered structure of the carbon template used here, resulting in the random growth of metal oxide crystals.

2.5.6 Mesoporous Sphere of Metal Oxide and Phosphate

A. Dong *et al.* prescribed a general procedure for synthesis of mesoporous sphere of metal oxide and phosphate and synthesized TiO_2 and ZrO_2 sphere composed of particulate nanocrystals, whereas mesoporous Al_2O_3 spheres composed of interesting lath-shaped nanoparticles [244]. The desired precursor such as alkoxides or inorganic salts (dissolved in organic solvent) is chosen to impregnate into the pore of carbon sphere template. After removing the redundant precursor by centrifugation, the hydrolysis of precursor was initiated by exposure to the moisture in air. The mesoporous inorganic spheres were finally obtained by crystallization or polymerization of inorganic species at 600°C (or 950°C for rutile-type Titania formation) in nitrogen for 6 h, coupled with removal of carbon at 550°C in air for 8 h. The precursor became more hydrophobic with the hexane and cyclohexane (1:1, v/v) and therefore could fill all the parts of carbon template leading to solid ZrO_2 spheres. Interestingly only ethanol solution of ZrCl_4 was somewhat hydrophilic and face difficulty to infiltrate the inner parts of the carbon spheres, resulting in hollow ZrO_2 spheres after calcination. On the contrary, it indicates the effect of polarity of precursor on the final product morphologies due to the hydrophobic nature of carbon template. These hollow metal oxide spheres grow randomly on less ordered carbon template. So, they do not exhibit ordered mesostructures. The size of the replicated sphere (i.e., diameter of TiO_2 sphere = 500–600 nm) is somewhat smaller than that of the original carbon spheres (i.e., diameter of carbon sphere = 800–900 nm) and much less than that of the silica parent due to volume shrinkage. The surface areas of $\gamma\text{-Al}_2\text{O}_3$, Titania, MgTiO_3 and $\text{MgO-Al}_2\text{O}_3$ are 212, 100, 154, and $322\text{ m}^2\text{g}^{-1}$, respectively. The TEM images of (A) mesoporous $\gamma\text{-Al}_2\text{O}_3$ spheres and mesoporous Al_2O_3 hollow spheres are shown in Figure 2.27.

2.5.7 Nanocast Ceramics

Using carbon CMK-3 as a template and trimethylaminoborazine (MAB) as precursor infiltration was done [135, 199]. Simple calcination in air for carbon removal was restricted in this case due to sensitiveness of boron compounds to air and moisture. So, the synthesis was done under a protective atmosphere of argon using standard Schlenk techniques. The carbon

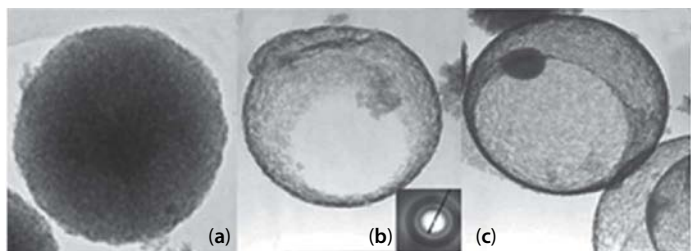


Figure 2.27 TEM images of (a) mesoporous γ - Al_2O_3 spheres, [244] (b) & (c) mesoporous Al_2O_3 hollow spheres [245].

template was eliminated by ammonia treatment at 1000°C . Finally, the hexagonal mesostructure of CMK-3 was transferred to the **BN** replica and so, ordered mesoporous BN having specific surface area of $\sim 540\text{ m}^2\text{g}^{-1}$, pore volume of $\sim 0.27\text{ cm}^3\text{g}^{-1}$ and pore-size distribution \sim centered at 4.4 nm is found as depicted in Figure 2.28(a). It is found that the mesostructure of BN is better retained by a two-step procedure, ceramization followed by template elimination using hydrogenation, rather than a one-step procedure of ceramization and template hydrogenation simultaneously [200]. The cubic ordered mesoporous carbon (CMK-8) was also used for further replication of mesoporous BN which exhibits cubic mesostructure and the pore diameter is concentrated at 4.7 nm [201].

Nanocasted mesoporous carbon CMK-3 was immersed in xylene containing polycarbosilane (PCS) precursor under stirring until the xylene nearly evaporated [202]. The thermal treatment of PCS-carbon composites was carried out under nitrogen flow in a tube furnace with a multi-step temperature program starting from room temperature to 350°C at 5°C rpm , then to 700°C at 1°C rpm then 1500°C at 2°C rpm . The final temperature 1500°C is maintained for 30 min, and then it is cooled to room temperature for getting SiC-C composite. Further reactive gases including air and ammonia were employed simultaneously to incorporate O or N into SiC ceramics and to oxidize or reduce the carbon template. At 1000°C under high purity nitrogen, ammonia gas is blown over SiC-C composite to find ordered mesoporous SiCN as presented in Figure 2.28(c). Mesostructured SiOC can be obtained by the calcination of SiC-C composite at 500°C under air atmosphere in a muffle oven (Figure 2.28(b)). The ordered mesoporous SiOC and SiCN ceramics have large surface areas of $200\text{--}400\text{ m}^2\text{g}^{-1}$, pore volumes of $0.4\text{--}0.8\text{ cm}^3\text{g}^{-1}$ and narrow pore-size distributions (4.9–10.3 nm). Alternatively, polyvinylsilazane diluted in toluene to obtain 60 wt.% solution can also be used as a SiCN ceramic precursor over CMK-3 and CMK-8 template [203]. At thermal treatment (1400°C)

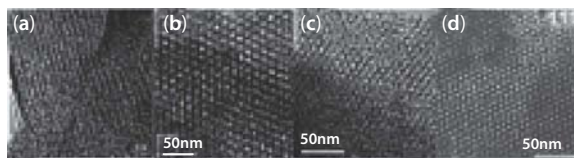


Figure 2.28 TEM images of mesoporous (a) BN [135] (b) SiOC [249] (c) SiCN [249] (d) SiN [251].

under nitrogen atmosphere, SiCN–C composite is formed. Afterwards air combustion was carried out to find mesoporous SiCN. The surface area of SiCN is $247 \text{ m}^2\text{g}^{-1}$ whenever it is casted from CMK-3 whereas surface area is $472 \text{ m}^2\text{g}^{-1}$, when it is casted from CMK-8. It is cleared that using cubic rather than hexagonal mesoporous carbon as template results into formation of SiCN having large surface area.

PCS precursor was filled into the channels of CMK-8 by solvent evaporation- induced impregnation [204]. The resultant composites were then heated to 900°C under an ammonia atmosphere to produce silicon nitride carbon composites. A further treatment at 1400°C in an N_2 atmosphere was carried out before removal of carbon template by ammonia at 1000°C . Finally, ordered mesoporous **silicon nitride** of 3D bicontinuous cubic mesostructure (Ia $\bar{3}$ d) having surface area $384 \text{ m}^2\text{g}^{-1}$, pore volume $0.71 \text{ cm}^3\text{g}^{-1}$ and large pore size 5.7 nm is found (Figure 2.28(d)). Its nitrogen content can reach as high as 32 wt.%. Elemental analysis shows that the Si, N, O, and C contents are 54, 32, 11, and 2.0 wt.%, respectively. The stoichiometric composition can be described as $\text{Si}_1\text{N}_{1.18}\text{O}_{0.36}\text{C}_{0.09}$.

2.5.8 Mesoporous Hydroxyapatite and Phosphates

Hydroxyapatite-calcium is a highly demanding biocompatible material which have excellent bond forming ability with living bone issue. Zhiguo Xia *et al.* synthesized ordered mesoporous hydroxyapatite by infiltrating the solution of $\text{CaCl}_2/(\text{NH}_4)_2\text{HPO}_4$ ($\text{Ca}/\text{P} = 1.67$) aqueous solution to the mesopores channel of CMK-3 at pH 10–11 for 24 h, followed by drying and calcination. Finally, a white and rod like morphology (as confirmed by TEM), mesoporous (confirmed by surface area and porosity measurement) and hexagonal (as confirmed by (002), (211), and (300) peaks in XRD) hydroxy apatite is obtained [205]. P. Połrołniczak *et al.* synthesized temperature resistant ordered mesoporous tin phosphate by using CMK-3 as hard template and $\text{SnCl}_4 \cdot 5\text{H}_2\text{O}$ and H_3PO_4 in 1:1 molar ratio as precursor [206].

2.5.9 Potential Application

Mesoporous TS-1 templated from CMK-3 shows improved catalytic performance for thiophene oxidation and is able to catalyze oxidation of bulky sulfur containing molecule such as dimethyldibenzothiophene [207]. An enhanced catalytic activity for CO oxidation was observed over ordered mesoporous ceria oxides (template by CMK-3) supported gold catalyst; possibly due to the nano-sized particle and narrow pore size of the ordered mesoporous ceria [238]. C. L. Lima *et al.* prepared mesoporous $\text{SnO}_2\text{-ZrO}_2$, $\text{SnO}_2\text{-MnO}_2$, and $\text{SnO}_2\text{-TiO}_2$ by carbon template (itself prepared by SBA-15) among which small-sized Sn Ti is a promising catalyst for the gas phase dehydration of glycerol [208]. Acidic sites plays cooperativity between Sn and Ti and favors the production of acrolein and 1-hydroxyacetone in glycerol dehydration. The presence of crystalline SnO_2 as a separate phase increased the catalytic performance, whereas the catalytic performance of ZrO_2 or MnO_2 associated with tin oxide was poor due to the major acidity and/or basicity enhancement.

2.6 Future Prescriptive

PtRu (nanocatalysts) deposited mesoporous carbon thin film (template from SBA-15) as a novel electrode materials is an attempt toward high-performance fuel cell electrodes with designed nanostructures that allow improvements of the catalytic surfaces and the molecular transport at the same time with an integrated architecture [209]. Graphitic-CN ($\text{g-C}_3\text{N}_4$) inside the channel of CMK-3 ($\text{g-C}_3\text{N}_4\text{@CMK-3}$ nanorods) is low-cost, metal free oxygen reduction reaction electrocatalyst, which exhibited extremely high electrocatalytic activity and efficiency and a promising candidate for the next generation of highly efficient oxygen reduction reaction electrocatalysts particularly for methanol alkaline fuel cells [210]. Phosphorus-doped ordered mesoporous carbons (templated by SBA-15) specially which having short channel length is found to have superior electrochemical performances for metal free oxygen reduction reaction, coupled with much enhanced stability and alcohol tolerance compared to those of platinum via four-electron pathway in alkaline medium [211]. Last two examples are metal free oxygen reduction reaction in fuel cell that indicates a hope in future nanocasting fuel cell technology. CMK-1 type mesoporous carbon nanoparticle material was successfully synthesized by using a MCM-48 template and utilized for the delivery of membrane impermeable chemical agents inside of eukaryotic cells by Tae-Wan Kim *et al.* [212].

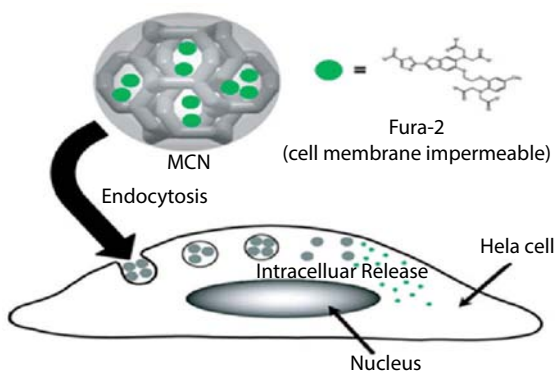


Figure 2.29 Schematic representation of the endocytosis of mesoporous carbon nanoparticles and the intracellular release of Fura-2 Molecules [259].

It has high inhibitory concentration ($>50 \mu\text{g}/\text{mL}$ per million cells) and serve as a transmembrane carrier for delivering Fura-2 (membrane impermeable fluorescence dye) through the cell membrane to release these molecules inside of live HeLa cells (Figure 2.29). Qiuling Luo *et al.* synthesized lanthanide-doped yttrium phosphates ($\text{YPO}_4:\text{Ln}^{3+}$, $\text{Ln}^{3+} = \text{Eu}^{3+}$, Tb^{3+} , and Ce^{3+}) by using KIT-6 have both the mesoporous properties for the storage of biological actives and photoluminescence properties for the online monitoring of carrier, resulting in a potential application as a new generation of drug delivery vehicles in biomedicine [138].

Mesoporous materials are defect tolerant and may undergo self-healing processes but surprisingly behavior of nanocasted mesoporous materials under irradiation has not been yet studied [213]. Use of biosynthesized polymers as hard template as Natural rubber latex [214] for getting mesoporous structures opens the future prescriptive for researcher working in the area. In post nanocasting process, Suk Bon Yoon *et al.* work for recrystallization transformation of the sacrificial silica template into more useful functional nanostructured silica offers an attractive alternative to the problem of handling silica waste and toxic etchants [215].

2.7 Limitation

Nanocasting method is more complex than the conventional hydrothermal methods. As well as steps of nanocasting increases from one step to two steps, the partial loss of structural order is more prominent, i.e.,

mesoporous metal/non-metal oxide casted from CMK family have less structural order than silica family templates. Less structural order is claimed to less surface area of mesoporous casted material [253] that is definitely not good for the field where high surface area mesoporous are in demand. The functionalization of the mesoporous support is generally attributed to good interaction between function group and deposited metal oxide but at the same while electrical conductivity decreases in the fuel cell. Functionalization could accelerate the electrochemical corrosion of the support reducing the durability of the fuel cell [208]. These drawbacks limit the use functionalized mesoporous template in fuel cell. K. Xia *et al.* showed that hydrogen uptake is attributed to the micropores with pore sizes smaller than 1 nm [154] where as Tse's group in theoretical calculation showed that pore size distribution in the range of 0.6–0.75 nm should best suited [216]. So, due to fewer amounts of micropores in mesopores system, nanocasted carbons are less preferred for gas storage. Unsupported ordered mesoporous metal oxide had also limitation than supported one in catalysis, i.e.,

Wojciech Gac synthesized mesoporous cobalt nanostructured oxides by using MCM-48 template and ethanol solution of cobalt nitrate as precursor, [217] followed by titling of silica by NaOH. It is found that cobalt impregnated MCM-48 is more active towards ethanol conversion than nanocasted mesoporous cobalt oxide. Ethanol conversion approached 100% at 420°C for supported and 66% for unsupported cobalt catalysts, respectively. The activity of silica supported catalysts was related to the large surface area of silica support and the enhancement of the redox processes by small cobalt species.

2.8 Conclusion

In a nutshell the review could eventually establish the role of hard template, i.e., mesoporous silica for synthesizing variety inorganic compounds ranges from metal oxides, metal sulfides, metal carbide phosphate, and ceramics. Interesting strategic approach to exploit the orderliness of the mesoporous silica for designing ordered nanocrystalline inorganic material was surveyed thoroughly. The synthesis of metal oxides by “repeat nanocasting” via mesoporous carbon can be a simple approach where soft templating methodology was found difficult. The high throughput research on nanocasting methodology is desired to be more focused for developing advanced material.

Acknowledgments

RK would like to acknowledge Indian School of Mines for providing junior research fellowship. BC would like to acknowledge DST, Govt. of India for funding (SB/S1, PC-10/2012).

References

1. M. Antonietti and G. A. Ozin, *Chem.-Eur. J.*, Vol. 10, p. 28, 2004.
2. D. R. Rolison, *Science*, Vol. 299, p. 1698, 2003.
3. U. Ciesla and F. Schuth, *Microporous Mesoporous Mater.*, Vol. 27, p. 131, 1999.
4. J. Y. Ying, C. P. Mehnert and M. S. Wong, *Angew. Chem. Int. Ed.*, Vol. 38, p. 56, 1999.
5. Q. S. Huo, D. I. Margolese, U. Ciesla, D. G. Demuth, P. Y. Feng, T. E. Gier, P. Sieger, A. Firouzi, B. F. Chmelka, F. Schuth and G. D. Stucky, *Chem. Mater.*, Vol. 6, p. 1176, 1994.
6. Q. S. Huo, D. I. Margolese, U. Ciesla, P. Y. Feng, T. E. Gier, P. Sieger, R. Leon, P. M. Petroff, F. Schuth and G. D. Stucky, *Nature*, Vol. 368, p. 317, 1994.
7. C. Dickinson, W. Z. Zhou, R. P. Hodgkins, Y. F. Shi, D. Y. Zhao and H. Y. He, *Chem. Mater.*, Vol. 18, p. 3088, 2006.
8. W. B. Yue and W. Z. Zhou, *J. Mater. Chem.*, Vol. 17, p. 4947, 2007.
9. S. C. Laha and R. Ryoo, *Chem. Commun.*, p. 2138, 2003.
10. R. L. Bao, K. Jiao, H. Y. He, J. H. Zhuang and B. Yue, *Stud. Surf. Sci. Catal.*, Vol. 165, p. 267, 2006.
11. S. Polarz, A. V. Orlov, F. Schuth and A. H. Lu, *Chem.-Eur. J.*, Vol. 13, p. 592, 2007.
12. B. Tian, X. Liu, H. Yang, S. Xie, C. Yu, B. Tu and D. Zhao, *Adv. Mater.*, Vol. 15, p. 1370, 2003.
13. C. Yu, Y. Yu and D. Zhao, *Chem. Commun.*, p. 575, 2000.
14. C. T. Kresge, M. E. Leonowicz and W. J. Roth, *Nature*, Vol. 359, p. 710, 1992.
15. J. S. Beck, J. C. Vartuli, W. J. Roth, M. E. Leonowicz, C. T. Kresge, K. D. Schmitt, C. T. W. Chu, D. H. Olson and E. W. Sheppard, *J. Am. Chem. Soc.*, Vol. 114, p. 10834, 1992.
16. R. Ryoo, S. H. Joo, M. Kruk and M. Jaroniec, *Adv. Mater.*, Vol. 13, p. 677, 2001.
17. Sujandi, S.-E. Park, D.-S. Han, S.-C. Han, M.-J. Jin and T. Ohsuna, *Chem. Commun.*, p. 4131, 2006.
18. A. Monnier, F. Schuth, and Q. Huo, *Science*, Vol. 261, p. 1299, 1993.
19. H. Yang, Q. Shi, B. Tian, Q. Lu, F. Gao, S. Xie, J. Fan, C. Yu, B. Tu and D. Zhao, *J. Am. Chem. Soc.*, Vol. 125, p. 4724, 2003.

20. K. Jiao, B. Zhang, B. Yue, Y. Ren, S. X. Liu, S. R. Yan, C. Dickinson, W. Z. Zhou and H. Y. He, *Chem. Commun.*, p. 5618, 2005.
21. M. Imperor-Clerc, D. Bazin, M. D. Appay, P. Beaunier and A. Davidson, *Chem. Mater.*, Vol. 16, p. 1813, 2004.
22. B. Yue, H. Tang, Z. Kong, K. Zhu, C. Dickinson, W. Zhou and H. He, *Chem. Phys. Lett.*, Vol. 407, p. 83, 2005.
23. C.-M. Yang, P.-H. Liu, Y.-F. Ho, C.-Y. Chiu and K.-J. Chao, *Chem. Mater.*, Vol. 15, p. 275, 2003.
24. P. Krawiec, C. Weidenthaler and S. Kaskel, *Chem. Mater.*, Vol. 16, p. 2869, 2004.
25. K. B. Lee, S. M. Lee and J. Cheon, *Adv. Mater.*, Vol. 13, p. 517, 2001.
26. X. Sun, Y. Shi, P. Zhang, C. Zheng, X. Zheng, F. Zhang, Y. Zhang, N. Guan, D. Zhao, and G. D. Stucky, *J. Am. Chem. Soc.*, Vol. 133, p. 14542, 2011.
27. Y. Ren, PhD thesis, University of St Andrews, 2010.
28. S. Jun, S. H. Joo, R. Ryoo, M. Kruk, M. Jaroniec, Z. Liu, T. Ohsuna and O. Terasaki, *J. Am. Chem. Soc.*, Vol. 122, p. 10712, 2000.
29. M. Kang, S. H. Yi, H. Lee, J. E. Yie and J. M. Kim, *Chem. Commun.*, p. 1944, 2002.
30. B. Puertolas, B. Solsona, S. Agouram, R. Murillo, A. M. Mastral, A. Aranda, S. H. Taylor and T. Garcia., *Appl. Catal. B*, Vol. 93, p. 395, 2010.
31. E. Rossinyol, J. Arbiol, F. Peiró, A. Cornet, J. R. Morante, B. Tian, T. Bo and D. Zhao, *Sens. Actuators B. Chem.*, Vol. 109, p. 57, 2005.
32. W. H. Shen, X. P. Dong and Y. F. Zhu, *Microporous Mesoporous Mater.*, Vol. 85, p. 157, 2005.
33. B. Tian, X. Liu, L. A. Solovyov, Z. Liu, H. Yang, Z. Zhang, S. Xie, F. Zhang, B. Tu, C. Yu, O. Terasaki and D. Zhao, *Chem. Soc.*, Vol. 126, p. 865, 2004.
34. F. Jiao, A. Harrison, J.-C. Jumas, A. V. Chadwick, W. Kockelmann and P. G. Bruce, *J. Am. Chem. Soc.*, Vol. 128, p. 5468, 2006.
35. Q. Zhou, X. Li and Y. G. Li, *Chin. J. Chem.*, Vol. 24, p. 835, 2006.
36. J. Y. Luo, J. J. Zhang and Y. Y. Xia, *Chem. Mater.*, Vol. 18, p. 5618, 2006.
37. H. Tuysuz, E. L. Salabas, C. Weidenthaler and F. Schuth, *J. Am. Chem. Soc.*, Vol. 130, p. 280, 2008.
38. A. Rumplecker, F. Kleitz, E. L. Salabas and F. Schuth, *Chem. Mater.*, Vol. 19, p. 485, 2007.
39. Y. Ren, A. R. Armstrong, F. Jiao and P. G. Bruce, *J. Am. Chem. Soc.*, Vol. 132, p. 996, 2010.
40. Y. Ren, F. Jiao and P. G. Bruce, *Microporous Mesoporous Mater.*, Vol. 121, p. 90, 2009.
41. T. Garcia, S. Agouram, J. F. Sánchez-Royo, R. Murillo, A. M. Mastral, A. Aranda, I. Vázquez, A. Dejoz and B. Solsona, *Appl. Catal. A*, Vol. 386, p. 16, 2010.
42. Yucheng Du, Qi Meng, Jinshu Wang, Jing Yan, Haiguang Fan, Yuxi Liu and Hongxing Dai, *Microporous Mesoporous Mater.*, Vol. 162, p. 199, 2012.

43. T. Wagner, J. Roggenbuck, C. D. Kohl, M. Fréchet and M. Tiemann, *Stud. Surf. Sci. Catal.*, Vol. 165, p. 347, 2007.
44. H. Tüysüz, C. W. Lehmann, H. Bongard, B. Tesche, R. Schmidt and F. Schüth, *J. Am. Chem. Soc.*, Vol. 130, p. 11510, 2008.
45. H. Tuysuz, Y. Liu, C. Weidenthaler and F. Schüth, *J. Am. Chem. Soc.*, Vol. 130, p. 14108, 2008.
46. V. Skumryev, S. Stoyanov, Y. Zhang, G. Hadjipanayis, D. Givord and J. Nogues, *Nature*, Vol. 423, p. 850, 2003.
47. S. J. S. Vasconcelos, C. L. Lima, J. M. Filho, A. C. Oliveira, E. B. Barros, F. F. de Sousa, M. G. C. Rocha, P. Bargiela and A. C. Oliveira, *Chem. Eng. J.*, Vol. 168, p. 656, 2011.
48. S. Sun, Q. Gao, H. Wang, J. Zhu and H. Guo, *Appl. Catal. B*, Vol. 97, p. 284.
49. C. Ma, D. Wang, W. Xue, B. Dou, H. Wang and Z. Hao, *Environ. Sci. Technol.*, Vol. 45, p. 3628, 2011.
50. C. Ma, Z. Mu, C. He, P. Li, J. Li and Z. Hao, *J. Environ. Sci.*, Vol. 23, p. 2078, 2011.
51. J. Zhu and Q. Gao, *Microporous/Mesoporous Mater.*, Vol. 124, p. 144, 2009.
52. F. Jiao, K. M. Shaju and P. G. Bruce, *Angew. Chem. Int. Ed.*, Vol. 44, p. 6550, 2005.
53. J. Zhu, Q. Gao and Z. Chen, *Appl. Catal. B*, Vol. 81, p. 236, 2008.
54. X. Cui, J. Zhou, Z. Ye, H. Chen, L. Li, M. Ruan and J. Shi, *J. Catal.*, Vol. 270, p. 310, 2010.
55. L. Dupont, S. Laruelle, S. Grugeon, C. Dickinson, W. Zhou and J.-M. Tarascon, *J. Power Sources*, Vol. 175, p. 502, 2008.
56. Y. Xia, H. Dai, L. Zhang, J. Deng, H. He and C. T. Au, *Appl. Catal. B Environ.*, Vol. 100, p. 229, 2010.
57. Ioannis Tamiolakis, Ioannis N. Lykakis, Alexandros P. Katsoulidis, Manolis Stratakis and Gerasimos S. Armatas, *Chem. Mater.*, Vol. 23, p. 4204, 2011.
58. P. M. Rao, P. Goldberg-Oppenheimer, S. Kababya, S. Vega and M. V. Landau, *J. Mol. Catal. A Chem.*, Vol. 275, p. 214, 2007.
59. Stefanie Haffer, Thomas Waitz, and Michael Tiemann, *J. Phys. Chem. C*, Vol. 114, p. 2075, 2010.
60. G. Li, S. Bhosale, T. Wang, Y. Zhang, H. Zhu and J. H. Fuhrhop, *Angew. Chem. Int. Ed.*, Vol. 42, p. 3818, 2003.
61. M. Cabo, E. Pellicer, E. Rossinyol, O. Castell, S. Suriñach and M. D. Baró, *Cryst. Growth Des.*, Vol. 9, p. 4814, 2009.
62. Y. Kobayashi, X. Ke, H. Hata, P. Schiffer and T. E. Mallouk, *Chem. Mater.*, Vol. 20, p. 2374, 2008.
63. A. H. Lu, D. Zhao and Y. Wan, *Nanocasting. A Versatile Strategy for Creating Nanostructured Porous Materials*. 1st ed. UK: RSC Publishing; 2010.
64. M. Cabo, S. Garroni, E. Pellicer, C. Milanese, A. Girella, A. Marini, E. Rossinyol, S. Suriñach, and M. D. Baró, *Int. J. Hydrogen Energy*, Vol. 36, p. 5400, 2011.

65. F. F. de Sousa, H. S. A. de Sousa, A. C. Oliveira, M. C. C. Junior, A. P. Ayala, E. B. Barros, B. C. Viana, J. M. Filho and A. C. Oliveira, *Int. J. Hydrogen Energy*, Vol. 37, p. 3201, 2012.
66. Y. Shi, B. Guo, S. A. Corr, Q. Shi, Y.-S. Hu, K. R. Heier, L. Chen, R. Seshadri and G. D. Stucky, *Nano Lett.*, Vol. 9, p. 4215, 2009.
67. V. Escax, M. Impéror-Clerc, D. Bazin and A. Davidson, *C. R. Chimie*, Vol. 8, p. 663, 2005.
68. M. Abecassis-Wolfovich, M. V. Landau, A. Brenner and M. Herskowitz, *J. Catal.*, Vol. 247, p. 201, 2007.
69. T. Valdés-Solís, P. Valle-Vigón, S. Álvarez, G. Marbán and A. B. Fuertes, *Catal. Commun.*, Vol. 8, p. 2037, 2007.
70. F. Jiao, B. Yue and K. K. Zhu, *Chem Lett.*, Vol. 32, p. 770, 2003.
71. F. Jiao, J.-C. Jumas, M. Womes, A. V. Chadwick, A. Harrison and P. G. Bruce, *J. Am. Chem. Soc.*, Vol. 128, p. 12905, 2006.
72. J. Jambor and J. Dutrizac, *Chem. Rev.*, Vol. 98, p. 2549, 1998.
73. J. Zhao, F. E. Huggins, Z. Feng and G. P. Huffman, *Clays Clay Miner.*, Vol. 42, p. 737, 1994.
74. L. G. Teoh, Y. M. Hon, J. Shieh, W. H. Lai and M. H. Hon, *Sens. Actuators B*, Vol. 96, p. 219, 2003.
75. E. Rossinyol, A. Prim, E. Pellicer, J. Arbiol, F. H. Ramirez, F. Peiro, A. Cornet, J. R. Morante, L. A. Solovyov, B. Tian, T. Bo and D. Y. Zhao, *Adv. Funct. Mater.*, Vol. 17, p. 1801, 2007.
76. G. Satishkumar, L. Titelman, M. V. Landau, *J. Solid State Chem.*, Vol. 182, p. 2822, 2009.
77. J. H. Smått, N. Schüwer, M. Järn, W. Lindner and M. Lindén, *Microporous Mesoporous Mater.*, Vol. 112, p. 308, 2008.
78. G. Li, D. Zhang and J. C. Yu, *Chem. Mater.*, Vol. 20, p. 3983, 2008.
79. J. Li, S. Bernard, V. Salles, C. Gervais and P. Miele, *Chem. Mater.*, Vol. 22, No. 16, p. 4660, 2010.
80. Z. Zhang, S. Dai, D. A. Blom and J. Shen, *Chem Mater.*, Vol. 14, p. 965, 2002.
81. J. Gu, J. Shi, L. Xiong, H. Chen, L. Li and M. Ruan., *Solid State Sci.*, Vol. 6, p. 747, 2004.
82. L. M. Worboys, P. P. Edwards and P. A. Anderson, *Chem. Commun.*, p. 2894, 2002.
83. Z. Liu, Y. Sakamoto, T. Ohsuna, K. Hiraga, O. Terasaki, C. H. Ko, H. J. Shin and R. Ryoo, *Angew. Chem. Int. Ed.*, Vol. 39, p. 3107, 2000.
84. Y.-J. Han, J. M. Kim and G. D. Stucky, *Chem. Mater.*, Vol. 12, p. 2068, 2000.
85. A. Fukuoka, Y. Sakamoto, S. Guan, S. Inagaki, N. Sugimoto, Y. Fukushima, K. Hirahara, S. Iijima and M. Ichikawa, *J. Am. Chem. Soc.*, Vol. 123, p. 3373, 2001.
86. K. Lee, Y.-H. Kim, S. B. Han, H. Kang, S. Park, W. S. Seo, J. T. Park, B. Kim and S. Chang, *J. Am. Chem. Soc.*, Vol. 125, p. 6844, 2003.
87. Z. T. Zhang, S. Dai, X. D. Fan, D. A. Blom, S. J. Pennycook and Y. Wei, *J. Phys. Chem. B*, Vol. 105, p. 6755, 2001.

88. F. Gao, Q. Lu, X. Liu, Y. Yan, and D. Zhao, *Nano Lett.*, Vol. 1, p. 743, 2001.
89. F. Gao, Q. Y. Lu and D. Y. Zhao, *Chem. Phys. Lett.*, Vol. 360, p. 585, 2002.
90. X. Y. Liu, B. Z. Tian, C. Z. Yu, B. Tu, Z. Liu, O. Terasaki and D. Y. Zhao, *Chem. Lett.*, Vol. 32, p. 824, 2003.
91. Y. Shi, Y. Wan, R. Liu, B. Tu and D. Zhao, *J. Am. Chem. Soc.*, Vol. 129, p. 9522, 2007.
92. M. Remskar, *Adv. Mater.*, Vol. 16, p. 1497, 2004.
93. F. Gao, Q. Y. Lu and D. Y. Zhao, *Adv. Mater.*, Vol. 15, p. 739, 2003.
94. Y. F. Shi, Y. Meng, D. H. Chen, S. J. Cheng, P. Chen, H. F. Yang, Y. Wan and D. Y. Zhao, *Adv. Funct. Mater.*, Vol. 16, p. 561, 2006.
95. J. Yan, A. Wang and D.-P. Kim, *J. Phys. Chem. B*, Vol. 110, p. 5429, 2006.
96. P. Krawiec, D. Geiger and S. Kaskel, *Chem. Commun.*, p. 2469, 2006.
97. C. T. Yang and M. H. Huang, *J. Phys. Chem. B*, Vol. 109, p. 17842, 2005.
98. Y. F. Shi, Y. Wan, R. Y. Zhang and D. Y. Zhao, *Adv. Funct. Mater.*, Vol. 18, p. 2436, 2008.
99. P. Dibandjo, L. Bois, F. Chassagneux, D. Cornu, J. M. Letoffe, B. Toury, F. Babonneau and P. Miele, *Adv. Mater.*, Vol. 17, p. 571, 2005.
100. P. Dibandjo, F. Chassagneux, L. Bois, C. Sigala and P. Miele, *J. Mater. Chem.*, Vol. 15, p. 1917, 2005.
101. A. Vinu, K. Ariga, T. Mori, T. Nakanishi, S. Hishita, D. Golberg and Y. Bando, *Adv. Mater.*, Vol. 17, p. 1648, 2005.
102. Q. Luo, S. Shen, G. Lu, X. Xiao, D. Mao and Yanqin Wanga, *J. Mater. Chem.*, Vol. 19, p. 8079, 2009.
103. B. Solsona, E. Aylón, R. Murillo, A. M. Mastral, A. Monzonis, S. Agouram, T. E. Davies, S. H. Taylor and T. Garcia, *J. Hazard Mater.*, Vol. 187, p. 544, 2011.
104. X. Sun, H. Hao, H. Ji, X. Li, S. Cai, and C. Zheng, *ACS Appl. Mater. Interfaces*, Vol. 6(1), p. 401, 2014.
105. A. H. de M. Batistaa, F. S. O. Ramosa, T. P. Bragaa, C. L. Limab, F. F. de Sousab, E. B. D. Barrosh, J. M. Filhob, A. S. de Oliveirac, J. R. de Sousac, A. Valentinia, and A. C. Oliveiraa, *Appl. Catal. A Gen.*, Vol. 382, p. 148, 2010.
106. B. Z. Tian, S. N. Che, Z. Liu, X. Y. Liu, W. B. Fan, T. Tatsumi, O. Terasaki and D. Y. Zhao, *Chem. Commun.*, p. 2726, 2003.
107. R. Ryoo, S. H. Joo and S. Jun, *J. Phys. Chem. B*, Vol. 103, p. 7743, 1999.
108. R. Ryoo, S. H. Joo, S. Jun, T. Tsubakiyama and O. Terasaki, *Stud. Surf. Sci. Catal.*, Vol. 135, p. 150, 2001.
109. S. B. Yoon, J. Y. Kim and J. S. Yu, *Chem. Commun.*, p. 559, 2001.
110. K. Jurewicz, C. V. Guterl, E. Frackowiak, S. Saadallah, M. Reda, J. Parmentier, J. Patarin and F. Beguin, *J. Phys. Chem. Solids*, Vol. 65, p. 287, 2004.
111. M. Choi and R. Ryoo, *Nat. Mater.*, Vol. 2, p. 473, 2003.
112. Y. Xia, Z. Yang and R. Mokaya, *Chem. Mater.*, Vol. 18, p. 140, 2006.
113. C. H. Kim, D.-K. Lee and T. J. Pinnavaia, *Langmuir*, Vol. 20, p. 5157, 2004.
114. S. H. Joo, S. J. Choi, I. Oh, J. Kwak, Z. Liu, O. Terasaki and R. Ryoo, *Nature*, Vol. 412, p. 169, 2001.

115. M. Kruk, M. Jaroniec, T. W. Kim and R. Ryoo, *Chem. Mater.*, Vol. 15, p. 2815, 2003.
116. A. H. Lu, W. Li, W. Schmidt, W. Kiefer and F. Schuth, *Carbon*, Vol. 42, p. 4303, 2004.
117. W. H. Zhang, C. H. Liang, H. J. Sun, Z. Q. Shen, Y. J. Guan, P. L. Ying and C. Li, *Adv. Mater.*, Vol. 14, p. 1776, 2002.
118. S. N. Che, K. Lund, T. Tatsumi, S. Iijima, S. H. Joo, R. Ryoo and O. Terasaki, *Angew. Chem. Int. Ed.*, Vol. 42, p. 2182, 2003.
119. J. Parmentier, L. A. Solovyov, F. Ehrburger-Dolle, J. Werckmann, O. Ersen, F. Bley, and J. Patarin, *Chem. Mater.*, Vol. 18, p. 6316, 2006.
120. K. P. Gierszal and M. Jaroniec, *Chem. Commun.*, p. 2576, 2004.
121. H. I. Lee, C. Pak, C. H. Shin, H. Chang, D. Seung, J. E. Yie and J. M. Kim, *Chem. Commun.*, p. 6035, 2005.
122. J. S. Lee, S. H. Joo and R. Ryoo, *J. Am. Chem. Soc.*, Vol. 124, p. 1156, 2002.
123. J. S. Lee, S. H. Joo and R. Ryoo, *Stud. Surf. Sci. Catal.*, Vol. 146, p. 33, 2003.
124. A. Lu, W. Schmidt, B. Spliethoff and F. Schuth, *Adv. Matter.*, Vol. 15, p. 1602, 2003.
125. B. H. Min, M. B. Ansari, Y. H. Mo and S. E. Park, *Catal. Today*, Vol. 204, p. 156, 2013.
126. J. Lee, S. Yoon, T. Hyeon, S. M. Oh and K. B. Kim, *Chem. Commun.*, p. 2177, 1999.
127. S. Yoon, J. Lee, T. Hyeon and S. M. Oh, *J. Electrochem. Soc.*, Vol. 147, p. 2507, 2000.
128. A. B. Fuertes, G. Lota, T. A. Centeno and E. Frackowiak, *Electrochim. Acta*, Vol. 50, p. 2799, 2005.
129. H. Q. Li, J. Y. Luo, X. F. Zhou, C. Z. Yu and Y. Y. Xia, *J. Electrochem. Soc.*, Vol. 154, p. 731, 2007.
130. J. S. Lettow, Y. J. Han, P. Schmidt-Winkel, P. Yang, D. Y. Zhao, G. D. Stucky and J. Y. Ying, *Langmuir*, Vol. 16, p. 8291, 2000.
131. J. Lee, K. Sohn and T. Hyeon, *J. Am. Chem. Soc.*, Vol. 123, p. 5146, 2001.
132. J. Lee, D. Lee, E. Oh, J. Kim, Y. P. Kim, S. Jin, H. S. Kim, Y. Hwang, J. H. Kwak, J. G. Park, C. H. Shin, J. Kim and T. Hyeon, *Angew. Chem. Int. Ed.*, Vol. 44, p. 7432, 2005.
133. S. B. Yoon, K. Sohn, J. Y. Kim, C. H. Chin, J. S. Yu and T. Hyeon, *Adv. Mater.*, Vol. 14, p. 19, 2002.
134. L. M. LizMarzan, M. Giersig and P. Mulvaney, *Langmuir*, Vol. 12, p. 4329, 1996.
135. M. Kim, K. Sohn, H. B. Na and T. Hyeon, *Nano Lett.*, Vol. 2, p. 1383, 2002.
136. G. S. Zhu, S. L. Qiu, J. H. Yu, Y. Sakamoto, F. S. Xiao, R. R. Xu and O. Terasaki, *Chem. Mater.*, Vol. 10, p. 1483, 1998.
137. J. S. Yu, S. B. Yoon, Y. J. Lee and K. B. Yoon, *J. Phys. Chem. B*, Vol. 109, p. 7040, 2005.
138. Y. S. Li, J. L. Shi, Z. L. Hua, H. R. Chen, M. L. Ruan and D. S. Yan, *Nano Lett.*, Vol. 3, p. 609, 2003.

139. Y. S. Li, Y. Q. Yang, J. L. Shi and M. L. Ruan, *Microporous Mesoporous Mater.*, Vol. 112, p. 597, 2008.
140. Y. D. Xia and R. Mokaya, *Adv. Mater.*, Vol. 16, p. 886, 2004.
141. D. Y. Zhao, J. L. Feng, Q. S. Huo, N. Melosh, G. H. Fredrickson, B. F. Chmelka and G. D. Stucky, *Science*, Vol. 279, p. 548, 1998.
142. A. H. Lu, W. Schmidt, N. Matoussevitch, H. Bönemann, B. Spliethoff, B. Tesche, E. Bill, W. Kiefer and F. Schüth, *Angew. Chem. Int. Ed. Engl.*, Vol. 43, p. 4303, 2004.
143. S. M. Holmes, P. Foran, E. P. L. Roberts and J. M. Newton, *Chem. Commun.*, p. 1912, 2005.
144. W. C. Choi, S. I. Woo, M. K. Jeon, J. M. Sohn, M. R. Kim and H. J. Jeon, *Adv. Mater.*, Vol. 17, p. 446, 2005.
145. H. Li, S. Zhu, H. Xi and R. Wang, *Microporous Mesoporous Mater.*, Vol. 89, p. 196, 2006.
146. A. H. Lu, W. C. Li, Z. Hou and F. Schuth, *Chem. Commun.*, p. 1038, 2007.
147. A. H. Lu, H. Tuysuz and F. Schuth, *Microporous Mesoporous Mater.*, Vol. 111, p. 117, 2008.
148. Y. Zhou, S. H. Yu, A. Thomas and B. H. Han, *Chem. Commun.*, p. 262, 2003.
149. B. H. Han, S. Polarz and M. Antonietti, *Chem. Mater.*, Vol. 13, p. 3915, 2001.
150. A. H. Lu, A. Kiefer, W. Schmidt and F. Schuth, *Chem. Mater.*, Vol. 16, p. 100, 2004.
151. N. D. Kim, W. Kim, J. B. Joo, S. Oh, P. Kim, Y. Kim and J. Yi, *J. Power Sources*, Vol. 180, p. 671, 2008.
152. Y. Xia, Z. Yang and R. Mokaya, *J. Phys. Chem. B*, Vol. 108, p. 19293, 2004.
153. Y. Xia and R. Mokaya, *Chem. Mater.*, Vol. 17, p. 1553, 2005.
154. C.-M. Yang, C. Weidenthaler, B. Spliethoff, M. Mayanna and F. Schüth, *Chem. Mater.*, Vol. 17, p. 355, 2005.
155. T. W. Kim, I. S. Park and R. Ryoo, *Angew. Chem. Int. Ed. Engl.*, Vol. 42, p. 4375, 2003.
156. J. Wang and Q. Liu, *J. Phys. Chem. C*, Vol. 111, p. 7266, 2007.
157. W. Li, D. Chen, Z. Li, Y. Shi, Y. Wan, G. Wang, Z. Jiang and D. Y. Zhao, *Carbon*, Vol. 45, p. 1757, 2007.
158. A. Vinu, P. Srinivasu, T. Mori, T. Sasaki, A. Asthana, K. Ariga and S. Hishita, *Chem. Lett.*, Vol. 36, p. 770, 2007.
159. M. Kodama, J. Yamashita, Y. Soneda, H. Hatori, K. Kamegawa and I. Moriguchi, *Chem. Lett.*, Vol. 35, p. 680, 2006.
160. P. Handa, T. Witula, P. Reis and K. Holmberg, *ARKIVOC*, p. 107, 2008.
161. G. S. Chai, S. B. Yoon, J. S. Yu, J. H. Choi and Y. E. Sung, *J. Phys. Chem. B*, Vol. 108, p. 707, 2004.
162. H. Li, H. Xi, S. Zhu, Z. Wen and R. Wang, *Microporous Mesoporous Mater.*, Vol. 96, p. 357, 2006.
163. H. Li, R. Wang and R. Cao, *Microporous Mesoporous Mater.*, Vol. 111, p. 32, 2008.

164. F. Su, X. S. Zhao, Y. Wang, J. Zeng, Z. Zhou and J. Y. Lee, *J. Phys. Chem. B*, Vol. 109, p. 20200, 2005.
165. Y. Lei, C. Fournier, J. L. Pascal and F. Favier, *Microporous Mesoporous Mater.*, Vol. 110, p. 167, 2008.
166. S. H. Joo, C. Pak, D. J. You, S. A. Lee, H. I. Lee, J. M. Kim, H. Chang and D. Seung, *Electrochim. Acta*, Vol. 52, p. 1618, 2006.
167. L. Calvillo, M. Gangeri, S. Perathoner, G. Centi, R. Moliner, and M. J. Lázaro, *Int. J. Hydrogen. Energy*, Vol. 36, p. 9805, 2011.
168. B. Fang, M. Kim and J.-S. Yu, *Appl. Catal. B Environ.*, Vol. 84, p. 100, 2008.
169. M. Zhou, L. Shang, B. Li, L. Huang and S. Dong, *Biosens. Bioelectron.*, Vol. 24, p. 442, 2008.
170. Y. Hou, L. Guo and G. Wang, *J. Electroanal. Chem.*, Vol. 617, p. 211, 2008.
171. X. Ji, K. T. Lee, R. Holden, L. Zhang, J. Zhang, G. A. Botton, M. Couillard and L. F. Nazar, *Nature Chemistry*, Vol. 2, p. 286, 2010.
172. J. H. Kim, B. Fang, S. B. Yoon, J.-S. Yu, *Appl. Catal. B Environ.*, Vol. 88, p. 368, 2009.
173. M. Sevilla, P. V.-Vigón, P. Tartaj, A. B. Fuertes, *Carbon*, Vol. 47, p. 2519, 2009.
174. Z. Wang, X. Liu, M. Lv, J. Meng, *Carbon*, Vol. 48, p. 3182, 2010.
175. A. Vinu, K. Z. Hossain, G. Satish Kumar, K. Ariga, *Carbon*, Vol. 44, p. 530, 2006.
176. Y. Tian, X. Wang, Y. Pan, *J. Hazard. Mater.*, Vol. 213–214, p. 361, 2012.
177. A. Vinu, M. Miyahara, T. Mori, K. Ariga, *J. Porous Mater.*, Vol. 13, p. 379, 2006.
178. K. Ariga, A. Vinu, M. Miyahara, J. P. Hill and T. Mori, *J. Am. Chem. Soc.*, Vol. 129, p. 11022, 2007.
179. An-Hui Lu, Dongyuan Zhao and Ying Wan, *Nanocasting a Versatile Strategy for Creating Nonosturctured Porous Materials*, ISBN: 978-0-85404-188-6, ISSN: 1757-7136.
180. A. H. Lu, W. Schmidt, B. Spliethoff and F. Schuth, *Chem. Eur. J.*, Vol. 10, p. 6085, 2004.
181. F. Schuth, *Angew. Chem. Int. Ed.*, Vol. 42, p. 3604, 2003.
182. J. Parmentier, C. Vix-Guterl, S. Saadallah, M. Reda, M. Iliescu, J. Werckmann and J. Patarin, *Chem. Lett.*, Vol. 32, p. 262, 2003.
183. L. Wang, K. Lin, Y. Di, D. Zhang, C. Li, Q. Yang, C. Yin, Z. Sun, D. Jiang and F. S. Xiao, *Microporous Mesoporous Mater.*, Vol. 86, p. 81, 2005.
184. W. Li, A. H. Lu, W. Schmidt and F. Schuth, *Chem. Eur. J.*, Vol. 11, p. 1658, 2005.
185. Q. Liu, A. Wang, X. Wang and T. Zhang, *Chem. Mater.*, Vol. 18, p. 5153, 2006.
186. W. Li, A. H. Lu, C. Weidenthaler and F. Schuth, *Chem. Mater.*, Vol. 16, p. 5676, 2004.
187. J. Roggenbuck and M. Tiemann, *J. Am. Chem. Soc.*, Vol. 127, p. 1096, 2005.
188. J. Roggenbuck, G. Koch and M. Tiemann, *Chem. Mater.*, Vol. 18, p. 4151, 2006.

189. J. Roggenbuck, H. Schafer, T. Tsoncheva, C. Minchev, J. Hanss and M. Tiemann, *Microporous Mesoporous Mater.*, Vol. 101, p. 335, 2007.
190. T. Tsoncheva, J. Roggenbuck, M. Tiemann, L. Ivanova, D. Paneva, I. Mitov and C. Minchev, *Microporous Mesoporous Mater.*, Vol. 110, p. 339, 2008.
191. Z. Huili, Y. Xiaojie, and L. Wencui, *Chin. J. Catal.*, Vol. 30, p. 1085, 2009.
192. X. Lai, H. Wang, D. Mao, N. Yang, J. Yao, C. Xing, D. Wang and X. Li, *Mater. Lett.*, Vol. 62, p. 3868, 2008.
193. T. Waitz, M. Tiemann, P. J. Klar, J. Sann, J. Stehr and B. K. Meyer, *Appl. Phys. Lett.*, Vol. 90, p. 123108, 2007.
194. T. Wagner, T. Waitz, J. Roggenbuck, M. Froba, C. D. Kohl and M. Tiemann, *Thin Solid Films*, Vol. 515, p. 8360, 2007.
195. X. Lai, X. Li, W. Geng, J. Tu, J. Li and S. Qiu, *Angew. Chem. Int. Ed.*, Vol. 46, p. 738, 2007.
196. M. Kang, D. Kim, S. Hwan Yi, J. U. Han, J. E. Yie and J. M. Kim, *Catal. Today*, Vol. 93–95, p. 695, 2004.
197. A. Dong, N. Ren, Y. Tang, Y. Wang, W. Hua and Z. Gao, *J. Am. Chem. Soc.*, Vol. 125, p. 4976, 2003.
198. Y. Xia and R. Mokaya, *J. Mater. Chem.*, Vol. 15, p. 3126, 2005.
199. P. Dibandjo, F. Chassagneux, L. Bois, C. Sigala and P. Miele, *J. Mater. Chem.*, Vol. 19, p. 1917, 2005.
200. P. Dibandjo, L. Bois, F. Chassagneux, J. M. Letoffe and P. Miele, *J. Porous Mater.*, Vol. 15, p. 13, 2008.
201. P. Dibandjo, F. Chassagneux, L. Bois, C. Sigala and P. Miele, *Microporous Mesoporous Mater.*, Vol. 92, p. 286, 2006.
202. Y. F. Shi, Y. Wan, Y. Zhai, R. Liu, Y. Meng, B. Tu and D. Y. Zhao, *Chem. Mater.*, Vol. 19, p. 1761, 2007.
203. J. Yan, A. Wang and D. P. Kim, *Microporous Mesoporous Mater.*, Vol. 100, p. 128, 2007.
204. Y. F. Shi, Y. Wan, B. Tu and D. Y. Zhao, *J. Phys. Chem. C.*, Vol. 112, p. 112, 2008.
205. Z. Xia, L. Liao and S. Zhao, *Mater. Res. Bull.*, Vol. 44, p. 1626, 2009.
206. P. Pórolniczak and S. Kowalak, *J. Porous Mater.*, Vol. 18, p. 703, 2011.
207. Y. Fang and H. Hu, *Catal. Commun.*, Vol. 8, p. 817, 2007.
208. C. L. Lima, S. J. S. Vasconcelos, J. M. Filho, B. C. Neto, M. G. C. Rocha, P. Bargiela and A. C. Oliveira, *Appl. Catal. A Gen.*, Vol. 399, p. 50, 2011.
209. M.-L. Lin, C.-C. Huang, M.-Y. Lo and C.-Y. Mou, *J. Phys. Chem. C*, Vol. 112, p. 867, 2008.
210. Y. Zheng, Y. Jiao, J. Chen, J. Liu, J. Liang, A. Du, W. Zhang, Z. Zhu, S. C. Smith, M. Jaroniec, G. Qing (Max) Lu, and S. Z. Qiao, *J. Am. Chem. Soc.*, Vol. 133, p. 20116, 2011.
211. D.-S. Yang, D. Bhattacharjya, S. Inamdar, J. Park and J.-S. Yu, *J. Am. Chem. Soc.*, Vol. 134, p. 16127, 2012.
212. T.-W. Kim, P.-W. Chung, I. I. Slowing, M. Tsunoda, E. S. Yeung and V. S.-Y. Lin, *Nano Lett.*, Vol. 8, p. 3724, 2008.

213. P. Makowski, X. Deschanel, A. Grandjean, D. Meyer, G. Toquer and F. Goettmann, *New J. Chem.*, Vol. 36, p. 531, 2012.
214. Y. Maa, M. Zenga, J. Hea, L. Duana, J. Wanga, J. Li, J. Wanga, *Appl. Catal. A Gen.*, Vol. 396, p. 123, 2011.
215. S. B. Yoon, J.-Y. Kim, S.-K. Park, J. H. Kim, M.-S. Kim, and J.-S. Yu, *Ind. Eng. Chem. Res.*, Vol. 50, p. 7998, 2011.
216. S. Patchkovskii, J. S. Tse, S. N. Yurchenko, L. Zhechkov, T. Heine and G. Seifert, *PNAS*, Vol. 102, p. 10439, 2005.
217. W. Gac, W. Zawadzki, B. Tomaszewska, *Catal. Today*, Vol. 176, p. 97, 2011.

Spray Pyrolysis of Nano-Structured Optical and Electronic Materials

Nurdan Demirci Sankir*, Erkan Aydin,
Esmâ Ugur, and Mehmet Sankir

*Department of Materials Science and Nanotechnology Engineering,
TOBB University of Economics and Technology, Ankara, Turkey*

Abstract

This chapter focuses on the fundamentals of the spray pyrolysis (SP) technology, the formation of oxide nano powders, nano rods and nanocrystalline thin films, and the performance/manufacturing condition relationships of these materials. Specific application areas such as photovoltaic, energy storage, and sensors will also be given in a subsection of the chapter. Moreover, our approach to building nanocrystalline chalcopyrite semiconductor thin films for photovoltaic applications is given. Chalcopyrite semiconductors are good alternatives to silicon-based photovoltaic devices because of their appropriate band gap energy, high absorption coefficient, and stability. Although selenium-based chalcopyrite materials have very high energy conversion efficiencies in photovoltaics, sulfur-based semiconductors have been quickly replacing them due to the non-toxicity of the sulfur-containing materials. This chapter gives information on the nanocrystalline thin-film deposition of both selenium- and sulfur-based chalcopyrite semiconductors via SP. Applications of these materials in the photovoltaic area are also discussed. Furthermore, our very recent work on the SP of copper-based photovoltaic devices on flexible substrates is summarized. Usage of flexible substrates, polymers, and metal foils, which combine the advantages of being very lightweight with mechanical robustness, is discussed. Therefore, spray-pyrolyzed materials can be used in flexible electronic applications or in the areas where the weight/volume ratio is crucial like unmanned air vehicles.

Keywords: Spray pyrolysis, nanostructured oxides, chalcopyrite semiconductors, photovoltaic, energy storage devices, sensors, flexible electronics

*Corresponding author: dnurdan@yahoo.com

3.1 Introduction

Nanostructured materials, such as nanoparticles, nanoporous materials, nanopillars, nanorods, and nanocrystalline thin films, have huge potential in various application fields including energy related devices, sensors, and optics. In general, nanomaterials have the advantage of large surface-to-volume ratio and tailoring of the physical and chemical properties by varying the size. Hence, many researchers have been focused on the new, efficient and cost effective nanomaterial manufacturing methods. Although spray pyrolysis (SP) technique has been used to build functional materials since 1960s, the application fields and variety of the spray-pyrolyzed materials has increased dramatically since then. Therefore, we would like to introduce this important technique to the readers, who do not aware of. Moreover, researchers in the SP area will find detailed information about the various nanostructured materials produced via numerous different SP technologies in this chapter.

Furthermore, there will be the information about the copper based chalcopyrite and chalcogenide semiconductors produced by our research group using ultrasonic SP method in this chapter. As explained in the following sections ultrasonic SP is superior to other pyrolysis techniques due to its very high material yield and low energy requirement. Also for the first time in literature, our group has been used ultrasonic SP technique to build functional materials on flexible substrates such as polyimide and stainless steel foils.

Section 3.2 gives information about the basis of the SP method. It is important to have knowledge about the fundamentals of the technology, since the material type and properties strongly depends on the manufacturing conditions. Section 3.2 explains the flame and SP methods, also the atomization techniques, which are the heart of the spraying process. Then the some cutting edge examples of the nanoparticles, nanopillars-nanoporous materials, and nanocrystalline thin films are given in sections 3.3, 3.4, and 3.5, respectively. These sections focus on the most commonly used oxides, chalcopyrites, and chalcogenides. The relationship between manufacturing conditions and the materials properties is discussed via summarizing the recent and most efficient works in the literature.

3.2 Spray Pyrolysis Technology

The SP technique is one of the simplest forms of the chemical deposition techniques. It has been applied to deposit a wide variety of thin films, nano

powders, and three-dimensional nano-structured films. These products were used in various applications such as solar cells [1–3], sensors [4–6], energy storage devices [7–9], and biomedical applications [10, 11].

Chemical precursors, usually appropriate salts in solution or nanoparticle suspensions are used as starting materials in SP process. This method involves the generation of the droplets by nebulization or atomization of the solution. Moreover, evaporation of the solvent, diffusion of the solute, drying, precipitation, reaction between precursors and surrounding gas, pyrolysis, or sintering occur in the furnace or on the hot plate during the formation of the final product. Typical SP equipment consists of an atomizer, pump, substrate heater, and temperature controller. SP technique is superior to other wet chemical and vacuum based manufacturing techniques due to some unique advantages, listed below:

- This technique allows to use very large choice of precursors including water and/or alcohol soluble chlorides, nitrates, and metal-organic salts.
- It is appropriate for in-line production with high throughput.
- This method is a robust process and can be easily scaled-up.
- It allows high material utilization, and low material waste.
- SP requires neither high quality substrates nor vacuum at any stage (except the low-pressure spray pyrolysis (LPSP)), which is a great advantage in terms of equipment and production cost.
- It is possible to build functional materials at moderate temperature (100–500°C).
- It is very easy to tailor the properties of product by simply adjusting the precursor solution composition.
- Compositional gradient and layered films or core/shell structures can be easily obtained by changing composition of the spray solution during the spray process.

Hence, many researchers have been focused on manufacturing functional structures including functional nanocrystalline thin films, nano powders and three-dimensional nano-structures using SP technologies.

In a general manner, pyrolysis process starts when the droplets of the precursor solution are generated by any kind of excitation technique. During the aerosol transport process, droplets are carried to the hot substrate or to the hot furnace and they starts to lose their solvent. Finally, decomposition occurs when the droplet lose its solvent completely. If this

occurs just before reaching the substrate usually non-adherent nanopowders are formed. If droplets decompose on the heated substrates it forms a film. All mentioned processing parameters take part during this period and affect the physical properties of the final products. Influence of the preparation conditions will be discussed later in the text. Figure 3.1 shows the modification of droplets during the SP process. As can be seen this figure, two models could be suggested for which the droplet moves towards the substrate. First one assumes the constant initial droplet size [12]. While increasing the substrate temperature droplets starts to evaporate before reaching the substrate and nanoparticle formation occurs. In the second model temperature of the substrate is assumed as constant [13]. Early evaporation of the solvent occurs when the droplet size decreases.

Following subsection gives very brief information about the flame spray pyrolysis (FSP), which is generally used to form nanoparticles. Then the various mist generation technologies will be introduced to the reader in order to build a bridge between production mechanism and the form of the material. In other words it is possible to build nanoparticles, nanoporous, or nanocrystalline thin films of the same material via using different spray technologies or manufacturing conditions. Each technology has its unique advantage in terms of the nature of the deposited material.

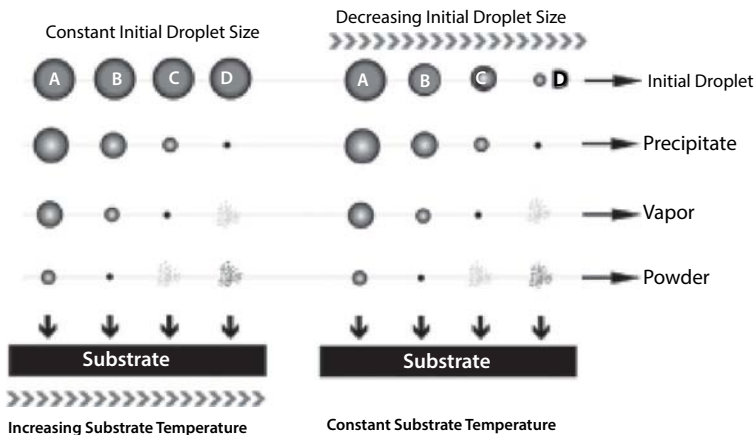


Figure 3.1 Modification of generated droplets while they are transported from the atomizing surface to the substrate. If the temperature or the initial droplet size is varied, there are four defined paths which the droplet can take as it moves towards the substrate (A–D).

3.2.1 Flame Spray Pyrolysis

FSP has been applied for the production of wide variety of high purity nanopowders ranging from single metal oxides like alumina to more complex mixed oxides, metals, and catalyst systems [14]. FSP allows production of powders with controlled characteristics at a high rate. In this technique a liquid, which contains precursor materials, is fed into the spraying nozzle, where oxidizing gas pass through the flame zone (Figure 3.2). The spray is combusted and the precursors are converted into nano sized metal or metal oxide particles, depending on the material and the operating conditions. The technique is flexible and allows the use of a wide range of precursors, solvents and process conditions. Thus it provides control over the particle size and the composition. FSP systems are generally comprised of three main experimental parts: an atomizer, a burner and a collecting system. Figure 3.2 shows the sketch of the simplified FSP system. In literature, numerous types of materials have been successfully produced for optical and electrical applications via the FSP method such as simple metal oxide nanoparticles – γ - Fe_2O_3 [15], Al_2O_3 [16], SiO_2 [17], β - Bi_2O_3 [18], ZnO [19], and CuO [20].

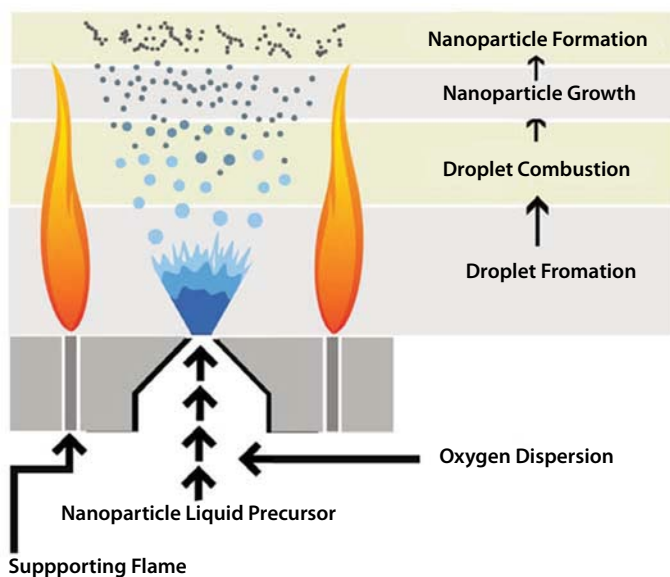


Figure 3.2 Nanoparticle synthesis by FSP system.

3.2.2 Mist Generation Technologies

Conventionally, SP technologies are classified by the way of atomization. The average size and the size distribution of the final particles can be roughly determined from the diameter (or the volume) of the atomized droplet and the initial concentration of the starting solution [21]. Therefore, atomization technique has a control over the material properties [22]. Various atomization techniques have been employed for mist generation including air blast [23] (liquid is exposed to a stream of air), ultrasonic (ultrasonic frequencies produce the short wavelengths necessary for the fine atomization) [22], and electrostatic (liquid is exposed to a high electric field) [24]. These atomizers differ in droplet size, rate of atomization and the droplet velocity. These factors affect the heating rate and residence time of the droplet during SP. For any atomizer, the particle characteristics, including particle size distribution, homogeneity, and the phase composition, depend on the type of the precursor and solvent, concentration, pH, viscosity, and the surface tension. On the other hand, droplet size depends on the type of the nozzle, flow rate, feed pressure, and spray pattern. The following section summarizes the commonly used atomization technologies.

3.2.2.1 Air Blast

In principle, the air blast atomizer functions in exactly the same way as the air assist atomizer. Both employ the kinetic energy of a flowing airstream to shatter the solution into mist. Air blast nozzles can generate different spray patterns, such as flat fan, full cone, and hollow cone sprays [25]. In this type of nozzles, pressurized liquid is fed through the orifice in the nozzle. Finally, with the help of the compressed air flow atomization of droplets is obtained. The air blast nozzle is shown schematically in Figure 3.3(a).

The atomizing nozzle from a spray pyrolysis process can be simulated using random number distributions for the generated size of the droplet, the initial droplet velocity, and the droplet direction as it leaves the atomizer. The radius of a droplet, formed from a liquid which is forced through a thin circular outlet is given by;

$$r = \left(\frac{3r_n\gamma}{2\rho_d g} \right)^{1/3} \quad (3.1)$$

where r_n is the outlet radius, ρ_d is the liquid density, g is the gravitational acceleration, and γ is the liquid-gas surface tension. The radius of the droplet could be tailored via changing one of the variables given in Eqn. (3.1).

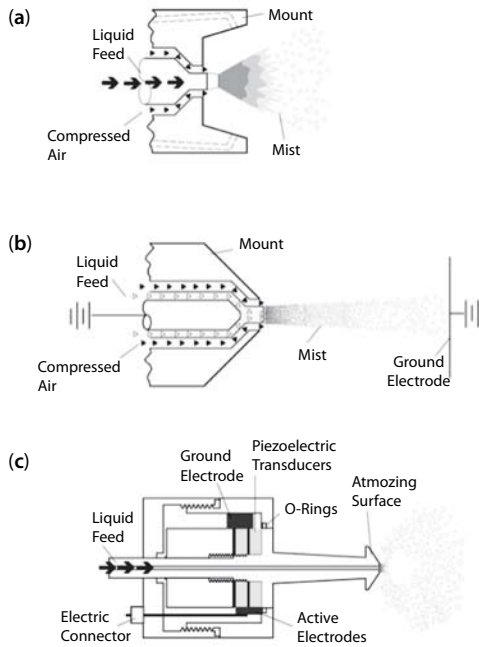


Figure 3.3 Schematic illustrations of (a) air blast, (b) electric field assisted, and (c) ultrasonic nozzles.

3.2.2.2 Electric Field

In this atomization technique, the fluid is exposed to an intense electric field while travelling through the atomizer to the substrate. An electric charge is induced onto the surface of the liquid to be atomized. Then the electric charge having opposite sign is induced on the impact surface. The like charges created on the liquid surface severely increase its surface tension, causing the film to break into ligaments. As the charge is continuously applied, the ligaments atomize into droplets. The schematic illustration of the electric field assisted nozzles is shown in Figure 3.3(b). The charge transfers to the fluid and repulsive forces between the atomizer and the fluid tear the droplets from the atomizer and send them toward the substrate surface. Electrostatic nozzles are particularly advantageous because their droplet sizes are more uniform than any other type of nozzles. Besides, they offer a greater degree of the control on the droplet size.

Droplet size calculation in the presence of electric field can be done using additional force, provided by an electric field. The relationship between the droplet diameter d and its charge has been measured by Hendricks *et al.* [26]. They showed that there is a relation between charge and the

droplet diameter, $qa d^n$, where the exponent n is varying between 1.5 and 2.3 while the poly disperse droplet size distribution is ranging between 0.1 and 10 μm .

3.2.2.3 Ultrasonic Generation

Ultrasonic vibration is superior to the other techniques due to the lower energy requirement and smaller droplet size formation [27]. Ultrasonic atomization uses mechanical vibrations generated via a piezoceramic element, which distributes the liquid without applying pressure or compressed air (Figure 3.3(c)). The energy from the vibrations gets transferred to the liquid, creating capillary waves. Once enough energy is transferred, these capillary waves will no longer be able to remain stable, and this causes the liquid stream to break into small droplets. Ultrasonic nozzles are primarily used in the biomedical industry for coating purposes [28]. Ultrasonic generators are capable of creating very fine droplets, which travels at a relatively low velocity. They also do not consume a lot of fluid. This greatly reduces the amount of the energy needed for the atomization. Average droplet size generated by ultrasonic nozzles is inversely proportional to the excitation frequency as in the following equation:

$$d_p = 0.34 \left(\frac{8\pi\sigma}{\rho f^2} \right) \quad (3.2)$$

where d_p is the droplet size, σ is the surface tension, ρ is the density of the solution, and f is the excitation frequency [29, 30].

3.3 Nanoparticles Created via Spray Pyrolysis Method

Size reduction of the particles in nanometer range gives occasion to be superior to the performance of surface atoms due to higher surface-to-volume ratio. Other size reduction effect in nano scale is the constraint of movement of electrons – quantum confinement effect. This leads to the different chemical and physical behavior of nano materials from their bulk form. Material properties could be tailored for specific applications with controlling the dimensions and composition of the structures. Nanoparticles, in which electrons are confined in all three dimensions, are ultra fine particles with sizes between 1 and 100 nanometers.

Nanostructures like rods and particles have become the most promising research material because of their attractiveness for very large range of optical and electronic applications. Wide band gap oxide nanorod arrays, which have far greater surface area (over 100 times more) than thin films, have great advantages in applications where surface area plays a critical role.

Mechanical attrition/ball milling, microwave plasma reactions, laser ablation, solid-state reactions, aerosol, etc. processes have been used for synthesis of ultrafine particles [31–36]. Several physical aerosol and chemical methods have been reported to synthesize the ceramic nanoparticles. Vapor condensation techniques: sputtering, laser vaporization, thermal evaporation [37–39], chemical vapor condensation (CVC) methods: flame processes [40–42], chemical methods: sol-gel, low-temperature wet-chemical, etc. [43, 44] can be sorted as metal oxide nanoparticle synthesis methods. One of the aerosol processing is SP, liquid-phase method with advantages of being a simple, continuous and cost effective production [21]. Metal oxide nanoparticles can be synthesized with various types of SP methods such as electrospray, low-pressure, salt-assisted (SAD) and liquid flame spray (LFS or FSP) pyrolysis [21, 45]. For various applications including thin-film solar cells, gas sensors, display devices, optoelectronic devices, frost-resistant surfaces and battery applications, nanorod arrays of ZnO [46], ZnS [47], SnO₂ [48], FTO [49], and nanostructured thin films, such as TiO₂ [50] and LiMn₂O₄ [51] have been synthesized by SP technique.

SP method allows continuous synthesis of nanoparticles with adjustable sizes, a significant parameter. It also results narrow size distribution with highly crystalline and having desired stoichiometry of the nanoparticles. Ultrafine particles could be produced using electrospray pyrolysis. In this method, applied voltage onto the capillary tube leads to conical shape of meniscus of a spray solution. With the continuous breakup of a jet, stable droplets are formed in the range of nanometers to micrometers [21]. FSP method used to synthesize noble metal and metal oxide nanoparticles for various types of applications [52, 53]. Small variations of process conditions make alterations to property and quality of the nanoparticles. Herein flame and spray characteristics and gas phase reactions could be controlled in order to determine the quality of the particles [53]. LPSP is another method used for nanometer-ordered oxide materials [21, 54]. LPSP system is composed of three components; two-fluid nozzle for dispersing a liquid, a porous glass filter, and a vacuum pump [21]. A thin liquid film on the glass filter surface is obtained by spraying a liquid through a pneumatic nozzle by a carrier gas. This liquid film and carrier gas pass through the filter pores aided by the carrier gas and are expanded into a low-pressure chamber. The size and morphology of the particles prepared by the LPSP

process was different from those produced by ultrasonic SP. The ZnO particles were in nanometer size fabricated by LPSP. Conversely, submicron size ZnO particles were produced in the case of ultrasonic SP.

Oxide nanoparticles have a huge potential to use in sensor [4], antireflective coatings [55], energy storage [56], and photovoltaics applications [57]. These oxides could be easily synthesized via SP methods. Following subsections summarize the nanoparticle oxides, which can be produced via SP method.

3.3.1 Copper Oxides

Copper oxide (CuO) and cuprous oxide (Cu_2O) are semiconductor materials with promising use for electronic and optoelectronic devices. CuO generally used in gas sensing applications [58], and electronic devices such as, field emitters [59], high T_c superconductors [60]. Biological applications are also very promising for copper oxides [61]. Synthesis of CuO nanoparticles have been reported by Chiang *et al.* for photoelectrochemical (PEC) water splitting application using copper (II) nitrate aqueous solution as a precursor for FSP. It can be stated that the main advantage of this method is the high production rate at a relatively low cost [17, 62]. Particle size and size distribution are strongly in dependence with precursor concentration and the flame conditions such as, gas flow rate, temperature and collection of particles at different heights. Figure 3.4 shows the transmission electron microscopy (TEM) images of the CuO nanoparticles produced at various manufacturing conditions [62]. As can be seen in this figure, particle size is directly related with the sintering temperature and sintering process time. Chiang *et al.* first synthesized the CuO nanoparticles via FSP, and then they obtained the thin films on ITO coated glass substrates by spin coating technique. They also reported the effect of the particle size distribution on the PEC water splitting performance. It was observed that increasing the sintering temperature and duration has increased crystallinity of the CuO films. Hence, the photocurrent density of the PEC cell increased also [63].

3.3.2 Indium Oxide

Indium oxide (In_2O_3), n-type semiconductor with band gap 3.6 eV, has been widely used as microelectronic device materials such as in solar cells, sensors, flat displays and/or architectural glasses [57]. As some metals, such as zinc and tin, doped indium oxide materials have been employed as transparent conductive oxides (TCO) for the device applications in optics. Tin-doped

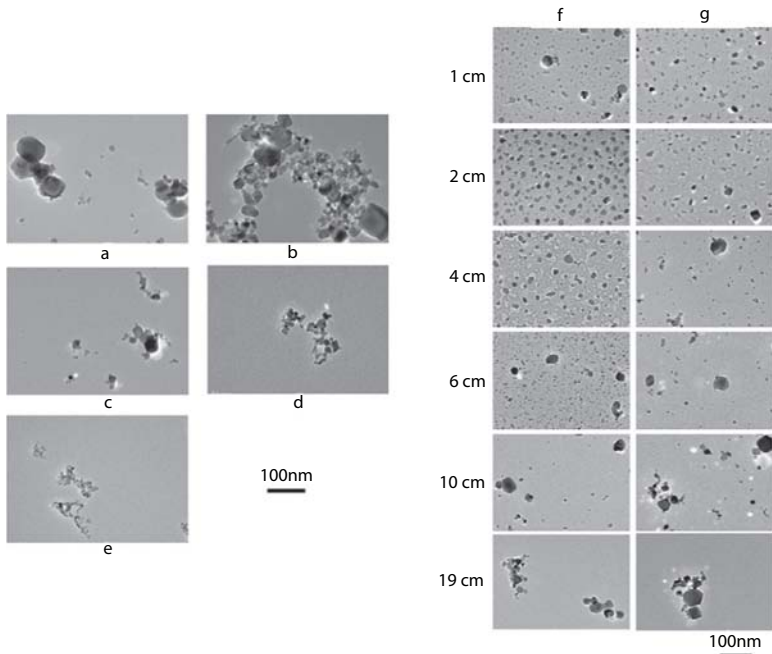


Figure 3.4 TEM micrograph for CuO nanoparticles based on different precursor concentrations: (a) 35%, (b) 25%, (c) 17%, (d) 5%, and (e) 0.5% and collected at different heights for flame conditions: (f) 13.8 L/min total gas flow rate, 2185 K adiabatic flame temperature, and (g) 6.1 L/min total gas flow rate, 2383 K adiabatic flame temperature [62] (Reprinted with permission from Elsevier, doi:10.1016/ijhydee.2011.10.033).

indium oxide (ITO) and zinc-doped indium oxide (IZO) nanoparticles could be synthesized via SP using precursor containing metal chlorides. Ogi *et al.* reported that low pressure SP system with two-fluid nozzle was used for ITO and IZO nanoparticle synthesis for OLED, solar cell and infrared reflection in energy-saving window technologies [64]. TEM figures proved that synthesized TCO nanoparticles have highly ordered lattice fingers, which has proved highly crystallized TCO nanoparticles could be obtained via low pressure SP (Figure 3.5). On the other hand, volume resistivity of LPSP-prepared ITO nanoparticles had resistivity on the order of $10^{-4} \Omega\text{m}$, which is lower than the resistivity of the pellet made from commercial ITO nanoparticles, $10^{-2} \Omega\text{m}$ [64]. Relation between resistivity and the particle size has been reported in previous study of T. Ogi *et al.* [64]. Reducing the particle size has increased the conductivity of ITO thin films derived from LPSP synthesized ITO nanoparticles.

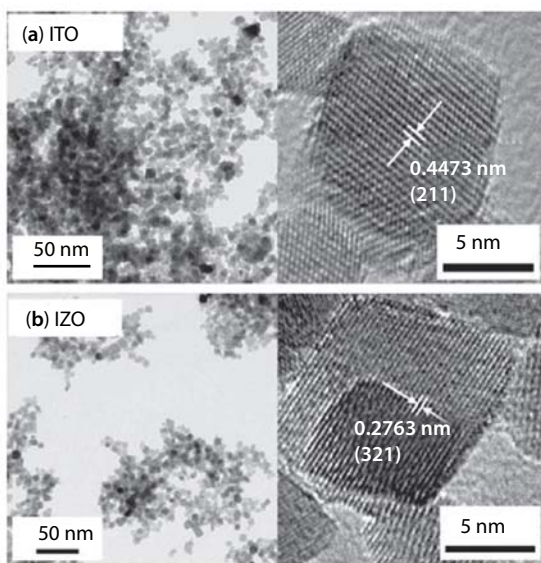


Figure 3.5 Low and high-magnification TEM images of various transparent conductivity oxide nanoparticles including (a) ITO and (b) IZO [64] (Reprinted with permission from Elsevier, doi:10.1016/j.appt.2008.09.002).

3.3.3 Tin Oxide

Tin oxide (SnO_2) has been used in solid-state gas sensors, oxidation catalyst systems and transparent conductor technology due to its physical and chemical properties. Combination of the high electrical conductivity and optical transparency make SnO_2 an important material for optoelectronic applications [65]. Additionally, SnO_2 has been the most frequently used material for sensor applications since surface chemical activity has a close relationship with gas sensitivity [65]. Various kinds of nanostructures of SnO_2 have been studied such as SnO_2 nanobelts [66], SnO nanodiskettes [67], and other nanoscopic materials [68]. SnO_2 nanoparticles utilized into various applications will be the focus of this subsection.

Sahm *et al.* reported that SnO_2 nanoparticles were synthesized via FSP for gas sensing applications [4]. In this study, tin source was dissolved in ethanol for precursor solution and the precursor was dispersed by oxygen gas. It should be noted here that premixed methane/oxygen flamelet ring was used to maintain the spray flame and additional oxygen flow was applied for assuring enough oxidant for complete conversion of the reactants. The nanopowders are collected on a filter with the help of a vacuum pump. To investigate the sensing properties of tin oxide nanoparticles for CO , NO_2 , and propanal gases, sensor structure was fabricated by drop coating on alumina substrates with interdigitated Pt electrodes

and DC electrical measurements was performed. It could be concluded that NO_2 gas results in increase in the sensor resistance while propanal and CO results decrease in the sensor resistance. Lower signals for CO were observed even at higher concentrations. On the other hand, the sensor signals of propanal and CO are higher in dry air than in humid at low operating temperatures ($<300^\circ\text{C}$). For NO_2 and propanal, Sahn *et al.* reported that sensors gave fast and stable responses and showed the expected power law behavior compared to the state-of-the-art SnO_2 thick film sensors. Moreover, Figure 3.6 underlines the typical behavior of undoped SnO_2 nanoparticles for CO sensing since small signals were observed.

It is expected that nanoparticle form of SnO_2 has facilitated to increase the sensitivity, faster response and recovery time of gas sensors since responding depends on the surface reaction between metal oxide and gas molecules. Franke *et al.* gave an overview of the relationship between particle size and gas-sensing sensitivity and response [69]. It could be concluded that sensing properties of metal oxide materials have been improved with reducing particle size. In literature, various characterization tools have performed particle size detection. For this reason reported particle size values are not directly comparable each other.

3.3.4 Titanium Dioxide

Titanium dioxide (TiO_2) is also known as titania which is a wide band gap semiconductor. When irradiated with light, TiO_2 could produce electron-hole pairs. Therefore, TiO_2 has been utilized for various applications. When the TiO_2 synthesized in nano scale, it has more attractive properties compared with the bulk TiO_2 . For example, photoactivity of TiO_2 particles has

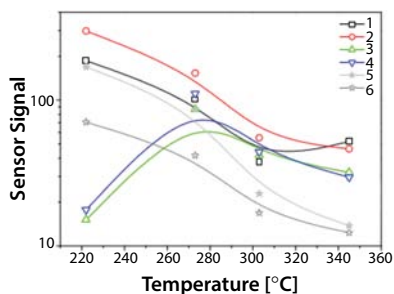


Figure 3.6 Sensor signal (to 150 ppm propanal) dependence on operating temperature of the sensors in dry air (1, 2, and 5) and at 50% relative humidity (3, 4, and 6), 1–4: FSP SnO_2 ; 5 and 6: commercially available SnO_2 [4] (Reprinted with permission from Elsevier, doi:10.1016/j.snb.2003.10.003).

been enhanced with increasing surface area due to increased light absorption rate and photo induced carrier density [70]. Increased surface area of the titanium dioxide materials have been utilized in solar cell applications. Chiba *et al.* have obtained 11.2% photo conversion efficiency using the TiO_2 nanocrystalline electrodes in dye sensitized solar cells [71]. TiO_2 could also be part of photocatalytic fuel generation reactions, mainly including H_2 production and CO_2 reduction. In literature, there are comprehensive reviews on TiO_2 as a photocatalyst material [72, 73]. Furthermore, TiO_2 materials could be employed for purification of pollutants [74], photocatalytic self-cleaning [75], photo-induced super hydrophilicity [76], and photosynthesis [77].

Titania nanoparticles, which have various functional shape and structure, could be synthesized by several methods such as sputtering [78], hydrothermal route [79], sol-gel [80], solvothermal route [81] precipitation methods [82] etc. SP is also one of the most promising techniques for synthesizing titania nanoparticles. H. Teisala *et al.* reported the synthesis of TiO_2 nanoparticles via liquid FSP method using titanium tetraisopropoxide as a precursor to deposit nanoparticles directly on paperboard due to their hydrophilic property [83]. M. Aromaa *et al.* also reported the superhydrophilic TiO_2 nanoparticles obtained using FSP method (Figure 3.7) [84].

SP synthesis of TiO_2 nanoparticles, used in photocatalytic applications, has been reported which included doped and/or composite structures to improve the photocatalytic performance of nanoparticles. To investigate the vanadium (V) doping effect on photocatalytic

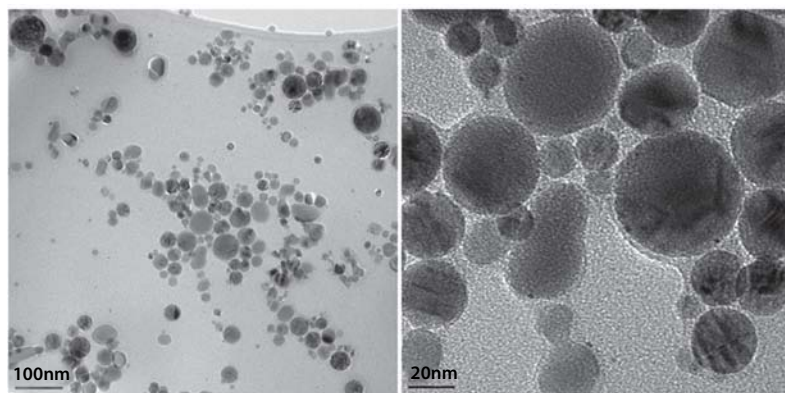


Figure 3.7 TEM images with different magnifications for spray pyrolyzed TiO_2 nanoparticles [84] (Reprinted with permission from Elsevier, doi:10.1016/j.jaerosci.2012.04.009).

properties of TiO_2 nanoparticles, Tian's group has reported FSP synthesized nanoparticles smaller than 50 nm [85]. Since it is well known that metal doping can change the crystal structure, morphology, particle size etc. B. Tian *et al.* also reported that degradation rate of 1%V- TiO_2 is two times higher than that over undoped TiO_2 nanoparticles where 2,4-dichlorophenol (DSP) was selected as a target pollutant under visible light illumination [85].

3.3.5 Zinc Oxide

Electrode and/or antireflection coating for solar cells and photocatalysts are main application areas of the zinc oxide (ZnO) [86, 19]. Also it could be possible to tailor the optical and electrical properties of ZnO with doping such as aluminum and gallium doping. Although, some ZnO nanoparticle synthesis methods have been reported in literature [87–89], SP is one of the set up commercial processes to make easy and inexpensive metal oxide nanoparticles [19]. FSP and LPSP could be used to synthesize the ultrafine ZnO nanoparticles [19, 64] since SP based production is promising method with availability of broad variety of precursors for powder synthesis [19]. Figure 3.8 shows that higher solution rates have resulted rod-like shape particles. Besides, decreasing the solution rates in FSP process results very small ZnO particles of about 10 nm [19]. For ZnO nanoparticle formation, Okuyama *et al.* reported that tailoring the operating pressure and the aerosol formation mechanism might cause difference in size and morphology of the particles [21]. Concerning the evolution of the particle morphology, solid (dense)-spherical particles and hollow or fragmented particles are often formed.

Ogi *et al.* have also reported the LPSP method for synthesizing the aluminum and gallium doped ZnO (AZO and GZO, respectively) nanoparticles using acetate and nitrate precursor solutions [64]. Highly crystalline AZO and GZO nanoparticles have been obtained with the resistivity 2.7×10^4 and $2.2 \times 10^4 \Omega\text{m}$ for AZO and GZO, respectively [64]. Volume resistivity of zinc oxide-based TCOs was higher than indium oxide-based ones (indium oxide section). Hence, doped indium-oxide based transparent electrodes have been predominant in optical and electrical properties. However, indium is a rare material and many researchers currently work on the increase in electrical conductivity of the ZnO. AZO films have small crystallite size and therefore more grain boundaries. This results in electron scattering on boundaries and increase in the electrical resistivity [64].

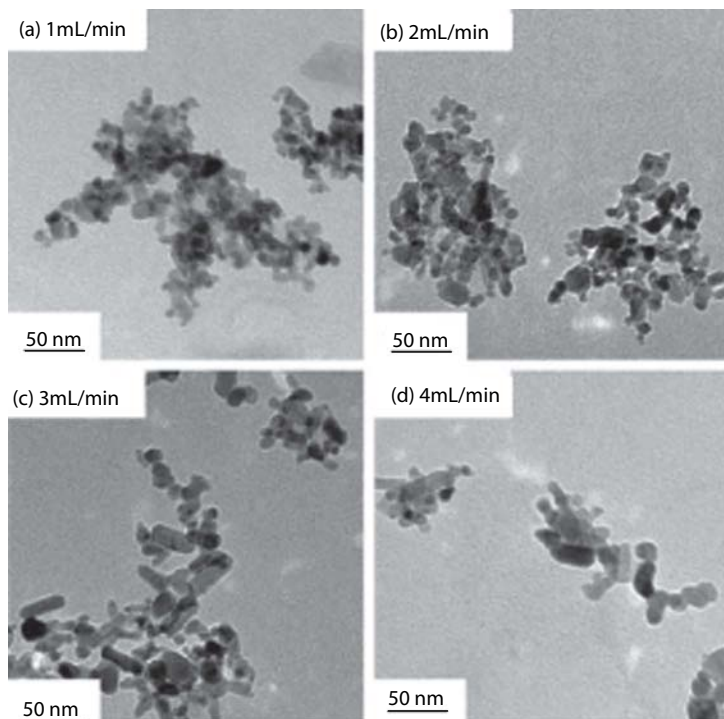


Figure 3.8 Transmission electron microscopic images of the FSP-made ZnO particles. The primary particle size increased in the order (a), (b), (c), and (d), corresponding to the precursor solution feed rate of 1, 2, 3, and 4 ml/min, respectively [19] (Reprinted with permission from Springer, doi:10.1023/A:1021153419671).

3.4 Nanopillars and Nanoporous Structures

In general, nanostructured or nanoscale materials can be recognized as solid materials with nanoscale dimensions. Nanoparticles have been discussed in Section 3.3. In this section we will introduce the spray-pyrolyzed materials having nanosize dimensions at least one-direction, such as nanopillars and nanoporous materials. In other words, materials with nanoscale in all dimensions (x , y , z) are called 0D materials. Nanoparticles and quantum dots are classified under 0D materials. On the other hand, nanowires, nanorods, nanotubes are confined in two-dimension and classified as 1D nanomaterials. However, a nanomaterial must have at least one dimension below 100 nm.

Nanoporous materials are structures of combined holes with diameter less than approximately 100 nm. Well-known naturally existing nanoporous structure aluminosilicate based zeolite has been used as catalyst for

decades [90]. Vertically standing nanostructures pave the way for significantly greater surface areas than flat surfaces. This phenomenon leads to enhance in device active area, making device more efficient, for instance in solar cell and/or sensor applications.

Vertically standing nanostructures, for example nanowires, nanopillars, pave the way for significantly greater surface areas than flat surfaces. This phenomenon leads to enhance in device active area and makes device more efficient. Vertically aligned nanostructures differ from nanoporous structures with their shape and function. Nanoporous materials, which have the pores less than 100 nm, consist of a regular organic or inorganic framework supporting the main structure. However, nanopillars are pillar shaped nanostructures, which has diameters in nanoscale (<100 nm). Nanopillar structures could be applied various materials with numerous deposition techniques. Some examples reported in literature include electrodeposited ZnO/Cu₂O heterostructure nanopillars [91], ITO nanopillars synthesized by RF magnetron sputtering [92], alumina nanopillars obtained by chemical etching of alumina films [93], electrodeposited SnO₂ nanowires obtained by using highly ordered porous anodic alumina template [68]. 1D nanostructure based materials have huge variety of applications such as sensor, solar cell and PEC cell technology, display devices and optoelectronic devices.

Most commonly used highly ordered nanoporous material is alumina, since it has been used as template for synthesizing nanopillars, nanorods, etc. It is well known that pore size could be controlled easily by changing the experimental parameters [94]. Further, metal oxide nanoporous materials have been used in dye synthesized solar cell, sensor and PEC cell applications [95–97]. SP method could be the easiest and most inexpensive way to produce these 1D nano-structures and nanoporous materials. We will continue our discussion based on the SP of the metal oxide nanopillar and nanoporous structures such as nanoporous TiO₂ thin films, nanoporous hematite (α -Fe₂O₃) thin films, ZnO nanorods, and SnO₂ nanorods.

3.4.1 Hematite (α -Fe₂O₃)

Iron oxide (hematite) is a material with 2.2 eV band gap, which can be used water splitting in PEC cells [98]. Iron oxide (α -Fe₂O₃) is a world abounded and inexpensive material. Also it has good chemical stability in a wide pH range and environmental compatibility [99–101]. Although, PEC performance of hematite is not very high, it is possible to improve performance of α -Fe₂O₃ by using nano-scale hematite and/or doping with selective atoms [102, 103]. For more efficient transport and collection of photogenerated

charge carriers several strategies have been introduced to overcome the limitations of the hematite. Modification of the film morphology is another way to increase the device performance [98]. SP has been used to obtain nanoporous Ti doped hematite thin films, reported by S. Kumari *et al.* for PEC cell application [98]. Figure 3.9 shows the scanning electron microscopy images of the undoped and Ti doped spray pyrolyzed hematite thin films.

Spray pyrolyzed Ti doped nanoporous $\alpha\text{-Fe}_2\text{O}_3$ thin films have been deposited on ITO glass substrates at 350°C [98]. With Ti doping, up to 1.4% photo conversion efficiency was observed. S. Kumari *et al.* explained the reason of the enhanced photo-response as the increased donor density by doping and modified nanoporous surface morphology [98].

In an another study, Cesar *et al.* have studied the water splitting performance of the ultrasonic spray pyrolyzed nanoporous iron oxide photoanodes as a function of the silicon doping [104]. With the help of silicon doping, they have improved the photoresponse of nanocrystalline $\alpha\text{-Fe}_2\text{O}_3$ films compared to that of the films reported earlier [105].

Doping of n-type iron oxide photoanodes has tremendous effect on the poor conductivity and short hole diffusion length, which results in a high electron-hole recombination rate. With this motivation, doping of n-type iron oxide thin films with various metals including lithium, titanium, chrome, nickel, indium, tin and zinc has been studied by Sartoretti *et al.* [106]. To investigate the influence of annealing, they have annealed the photoelectrodes in air at 550°C for 60 min before being rapidly cooled under a flow of nitrogen for 5–10 min. Figure 3.10 summarizes the change of photocurrent as a function of the dopants, doping ratios and annealing temperature. It can be seen that, in most cases, the addition of dopants had a detrimental effect on the performance of the electrodes. However, large

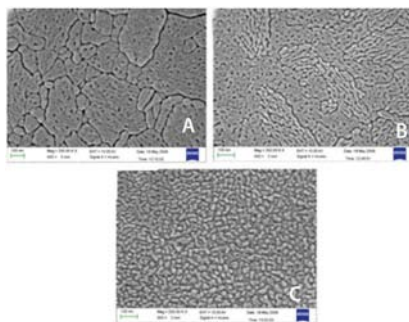


Figure 3.9 FE-SEM images of (a) undoped, (b) 0.02 M, and (c) 0.05 M Ti^{+4} doped $\alpha\text{-Fe}_2\text{O}_3$ thin films [98] (Reprinted with permission from Elsevier, DOI: 10.1016/j.ijhydene.2010.01.101).

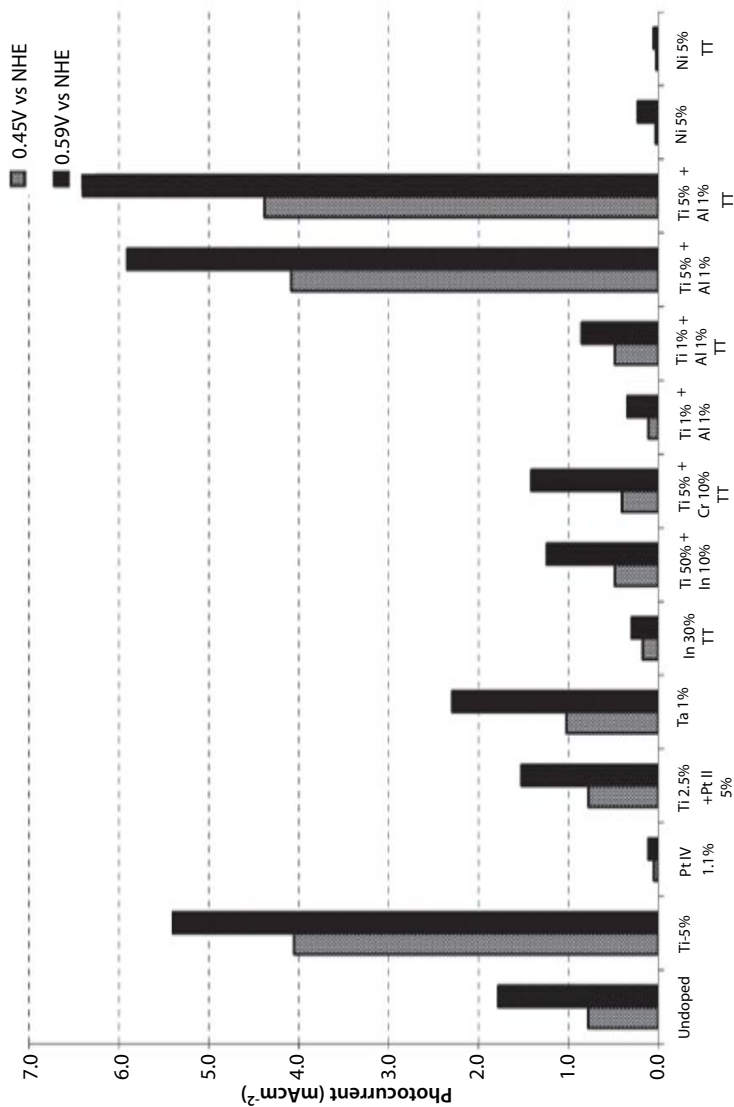


Figure 3.10 Comparison of the effect of dopants and annealing (labeled “TT”) [106] (Reprinted with permission from ACS Publications, DOI: 10.1021/jp051546g).

photocurrents were observed following the addition of either Al^{3+} (1%) or Zn^{2+} (4%) in conjunction with Ti^{4+} (5%). In particular, the $\text{Zn}^{2+}/\text{Ti}^{4+}$ doping of ferric oxide seems to affect the hole diffusion length. This leads to a favorable negative shift of the photocurrent onset potential. A clear link could be established between the extents of crystallinity of the films, monitored by Raman spectroscopy, with their photoactivity.

3.4.2 Tin Oxide (SnO_2)

1D metal oxide materials such as SnO_2 , ZnO , and In_2O_3 have shown high potential for optoelectronic devices, gas sensors and solar energy devices [48, 107]. However, there are very limited studies in literature on the SP of SnO_2 nanostructures. Among these studies, Bakrania *et al.* and Liu *et al.* reported the preparation of SnO_2 nanorods via the FSP [108, 109]. Although, low yield and not well controlled morphology of SnO_2 was reported by Bakrania *et al.*, J. Liu *et al.* adopted the flame approach for continuous, rapid and scalable synthesis of single-crystalline SnO_2 nanorods using Fe doping and adjusting flame residence time [108, 109]. In another study, F. Paraguay-Delgado *et al.* reported the spray pyrolyzed SnO_2 nanorods for sensor applications [48]. Figure 3.11 shows the scanning electron microscopy images of the spray pyrolyzed SnO_2 nanorod arrays and one nanorod.

3.4.3 Titanium Dioxide

Nanu *et al.* reported the spray pyrolyzed nanoporous TiO_2 thin films for copper indium sulfide (CIS) based solar cell applications [110]. Anatase- TiO_2 structure has been used as electrode for CIS nanocomposite 3D solar cell concept [110]. Nanu *et al.* has reported the 4% energy conversion efficiency for 3D solar cells with extremely thin absorber (ETA) layer [110].

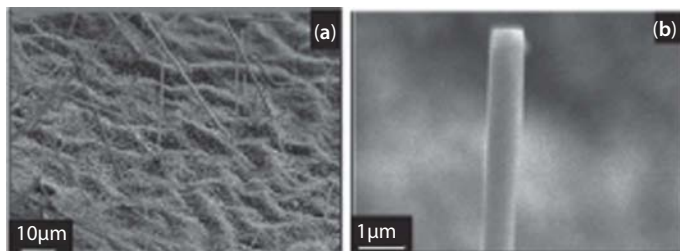


Figure 3.11 SEM images from the SnO_2 production: (a) 500 \times (showing the inside surface of the tube) and (b) 10 000 \times (where the details of the top of a SnO_2 nanorod, grown on the glass surface can be seen) micrographs [48] (Reprinted with permission from IOP Science, doi:10.1088/0957-4484/16/6/011).

Nanostructured titania thin films, obtained using flame aerosol method, could be used also for water splitting applications [111]. Figure 3.12 shows the 3D solar cell structures deposited on the ITO coated glass substrates.

It is known that process parameters have an influence on the performance of the materials used in various applications such as water splitting and dye-synthesized solar cells. Thimsen *et al.* reported that TiO₂ nanostructures were obtained under sets of process parameters of total argon, oxygen, and methane flow rates of 4.0, 2.7, and 0.9 lpm, respectively and the burner to substrate distance of 4.1 cm were vet proper to use these materials in water-splitting application [111]. On the other hand, for dye-synthesized solar cell applications, flow rates were reported as 6.0, 4.0, and 1.35 lpm for argon, oxygen, and methane, respectively and burner to substrate distance was 1.7 cm [111]. This underlines the affect of the process condition on the device performances. As can be seen in Figure 3.13, depending on the film thickness and the morphology, columnar and granular water-splitting performance varies.

Columnar morphology showed highly crystalline structures and for this morphology, nanoparticles were deposited onto FTO substrate out of flame [111]. It could be said that highly crystalline columnar TiO₂ nanostructured films showed higher performances than granular form for both applications [111]. For the case of dye-synthesized solar cell performance, cell with 6.9 μm columnar film resulted 6% efficiency because of the higher light absorption [111] (Figure 3.14).

3.4.4 Zinc Oxide

Zinc oxide (ZnO) nanorods are another very attractive material used in various applications such as, antireflection coating, window layer in solar

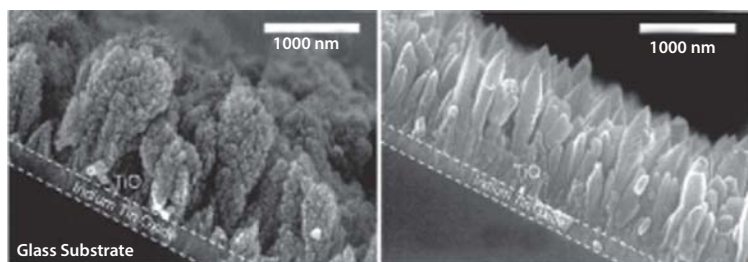


Figure 3.12 Side-view SEM image of a granular film deposited at a burner–substrate distance of 4.1 cm and columnar film deposited at a burner–substrate distance of 1.7 cm [111] (Reprinted with permission from ACS Publications, DOI: 10.1021/jp710422f).

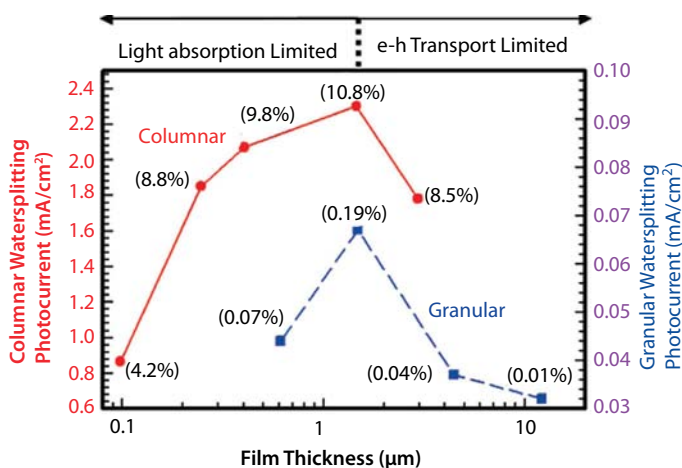


Figure 3.13 Water splitting photocurrent as a function of film thickness for the columnar films deposited at a burner–substrate distance of 1.7 cm (red); and granular films deposited at 4.1 cm (blue). The hydrogen conversion efficiency is in parenthesis next to each point [111] (Reprinted with permission from ACS Publications, DOI: 10.1021/jp710422f).

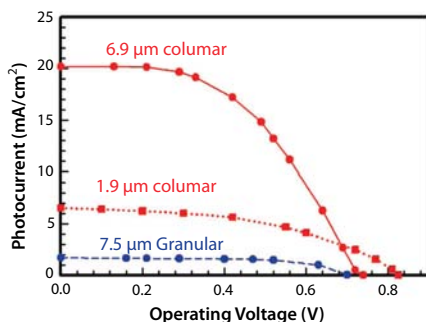


Figure 3.14 Dye-sensitized solar cell performance characteristics – photocurrent as a function of operating voltage for a 1.9 μm columnar film (dotted-red), 6.9 μm columnar (solid-red) and a 7.5 μm granular film (dashed-blue) [111] (Reprinted with permission from ACS Publications, DOI: 10.1021/jp710422f).

cells, and electrode for dye-synthesized solar cells [112–114]. Although, various methods, such as VLS, CVD and MOCVD have been used to prepare ZnO nanorod arrays, [115–117], SP of ZnO nanostructures have the advantages of low manufacturing cost and ease of production [47]. Zinc chloride based precursor solutions and different micro-structured ITO glasses were reported for ZnO nanorod synthesis [47]. It could be noted that substrate temperature and microstructure of ITO substrates have strong effect on ZnO morphology.

Spray pyrolyzed ZnO nanorods arrays have been used in solar cell applications by Krunk *et al.* [118]. They have fabricated ETA layer solar cell using SP processes in all deposition steps. The maximum obtained solar cell efficiency was 4.17% for ZnO_{rod}/In₂S₃/CuInS₂ solar cells. These cells have relatively small contact area, 1.0–1.5 mm², and were attained by the combination of several nanocells produced on the ZnO nanorods with length of 600 nm [118]. Figure 3.15 shows the cross-sectional scanning electron microscopy picture of the nanostructured solar cells [118].

It has been reported in the same study that the solar cell efficiency is related with the length of the ZnO nanorods [118]. In other words, the maximum photo conversion was observed for the ZnO nanorod type solar cell with 600 nm rod length. As can be seen from Figure 3.16, open circuit voltage and short circuit current values were 441 mV and 15.7 mA/cm², respectively. ZnO_{rod}/In₂S₃/CuInS₂ solar cell with 600 nm ZnO nanorod length had 4.17% efficiency with contact area 1.50 mm². On the other hand, 1µm-long ZnO nanorods caused much lower current density than expected [118]. It should be noted here that local thickness of the component layers decreased with increment in ZnO nanorod length under the constant deposition conditions. Moreover, these significantly lower local thicknesses on longer

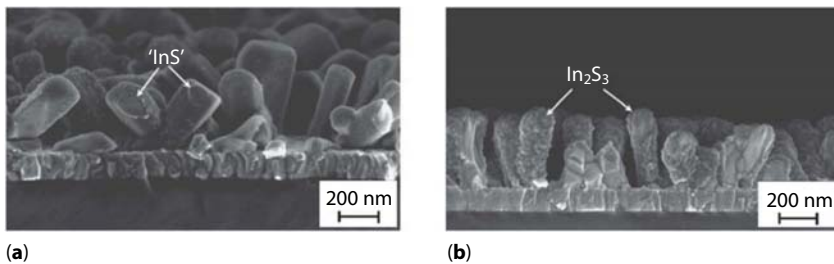


Figure 3.15 SEM micrographs of ZnO nanorods covered with (a) 'In-S' and (b) In₂S₃ layers [118] (Reprinted with permission from Elsevier, doi:10.1016/j.solmat.2010.02.036).

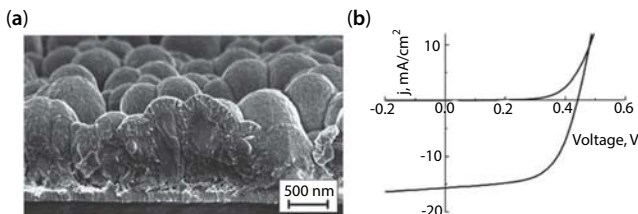


Figure 3.16 SEM cross-sectional micrograph (a) before applying back contact, and current-voltage characteristics (b) of the best solar cell ZnO_{rod}/In₂S₃/CuInS₂ [118] (Reprinted with permission from Elsevier, doi:10.1016/j.solmat.2010.02.036).

rods could be responsible for the decrease in cell performance. This may be because of the increased recombination losses with enhanced leakage [118]. M. Krunk *et al.* also claimed that ZnO nanorods longer than a critical value may cause the short problem between back and front contacts, since ZnO nanorods were directly deposited onto TCO covered glass.

Spray pyrolyzed ZnO nanorods could be used also for sensing applications such as H₂S sensing [119]. Shinde *et al.* was reported hexagonal pillar shaped ZnO nanorods with different thicknesses synthesized via SP method [119]. Although, many gases were tested for various temperatures, vertically aligned ZnO nanorod based sensors showed the highest selectivity to H₂S gas at temperature lower than 50°C [119].

3.5 Nanocrystalline Thin Film Deposition by Spray Pyrolysis

Even though there is now a clear understanding on the role of the different process parameters involved in the SP technique on the film properties [18, 120] many details regarding the deposition mechanisms are not fully understood and are still discussed in the literature. For the first time in literature, Sears *et al.* have proposed chemical vapor deposition-like SP mechanism [121]. In this model, the film is grown from the vapor formed by the droplets arriving in the vicinity of the high temperature substrate. One of the disadvantages of this model is not being considered the spreading of the droplets on the substrate, which significantly contribute to the film growth in the SP process. Another model proposed by Beckel *et al.* explaining the precipitation of the precursor from the droplet before impact [122]. This followed by spreading the droplet on the heated substrate. Finally, subsequent stacking of the precipitates is being observed. In this model, decomposition of precursor was not defined. The complete model includes the precursor atomization, droplet transport towards the heated substrate, the evaporation of the residual solvent, droplet hitting the substrate and spreading, the salt decomposition, and finally the nucleation and growth of particles was proposed by Gallage *et al.* Nanocrystalline chalcopyrite and kesterite thin films are the most popular semiconducting thin films, which will be discussed in the following subsections [123].

3.5.1 Nanocrystalline Cu-Based Chalcopyrite Thin Films

Chalcopyrite materials, which are used for photovoltaic devices, are of great research interest in recent years due to their leading low cost energy

production. In chalcopyrite structure, each atom has four neighbors arranged at the corners of a regular tetrahedron bonded by sp^3 bonds (Figure 3.17). The tetrahedral structure of the chalcopyrites can be considered as a superlattice structure of the sphalerite or zinc blende structure, which has a diamond like structure. The Bravais lattice of the chalcopyrite is body centered tetragonal. Each S (or Se) atom in the lattice is at the center of the tetrahedron with four cations at each corner.

As researchers continue to work on classical methods to fabricate chalcopyrite based photovoltaics, they have been looking to new approaches, such as the use of nanotechnology, to improve the device performances. Future photovoltaic devices employ nanotechnology to accelerate the fabrication of cost-effective and highly efficient devices. The exceptional properties of nanocrystalline materials are determined by the three features of their nature: (i) grain size spatially confined to less than 100 nm, (ii) significant number of grain boundaries with a typical concentration of about 10^{20} cm^{-3} , and (iii) variations in composition between the grains and grain boundaries [124]. Photovoltaic devices, which include nanocrystalline materials, have been proposed to improve the efficiency of the photon conversion (intermediate band solar cell) and provide sites for excitation dissociation and pathways for electron transport [125].

Numerous type of nanostructures have been applied to solar cells including nanocrystalline thin films [126], nanocomposites [110], quantum wells [127], quantum dots [128], nanowire and nanotubes [129], nanoparticles [130] for various functions and performance enhancement strategies [125]. Chalcopyrite thin films produced by SP technique are usually in nanocrystalline form due to nature of the SP technique. Low

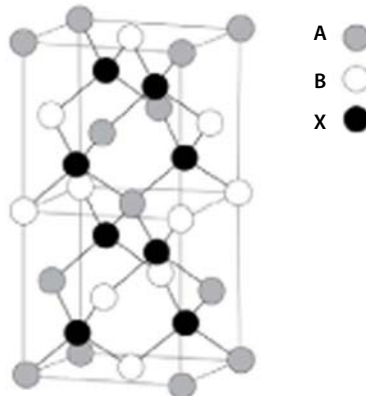


Figure 3.17 Crystal structure of chalcopyrite lattice.

temperature processing conditions and short nucleation and growth times result with nano sized grains.

In literature, some ternary and quaternary nanocrystalline chalcopyrite thin films have been fabricated by SP technique. Sharma *et al.* have been fabricated the nanocrystalline thin films of copper indium sulfide (CuInS_2) on glass substrates using the SP technique [131]. They have prepared an aqueous mixture of solutions using copper chloride (CuCl_2), indium chloride (InCl_3) and thiourea ($\text{CS}(\text{NH}_2)_2$) as copper, indium and sulfur sources, respectively. XRD calculations show that the crystallite size of the films ranges from 8 nm to about 15 nm. The nanocrystalline nature of the films was also confirmed by the TEM [131].

In another study, Khan *et al.* have also been deposited CuInS_2 thin films by SP technique [132]. They have used following stoichiometric ratio for spraying solution; CuCl_2 : InCl_3 : $\text{CS}(\text{NH}_2)_2 = 1:1:3$. They have confirmed single-phase nano-sized (12–15 nm) particles of CuInS_2 using field emission scanning electron (Figure 3.18(a)) and field emission transmission microscopy techniques (Figure 3.18(b)). In these semiconductor thin films, there are additional energy levels in the band gap, which are localized and close to either the conduction or the valence band. Due to nanocrystalline nature of the spray pyrolyzed films, they have showed the activated variable range hopping in the localized states near the Fermi level.

Nanocrystalline metallic precursor alloys can also be spray pyrolyzed by using precursor solution having some metallic salts. These precursors could be converted into some functional devices. Yoon *et al.* has demonstrated the first example of carbon- and oxygen-free $\text{Cu}(\text{In,Ga})(\text{SSe})_2$ (CIGSSe) absorber layers prepared by electro spraying a CuInGa (CIG) precursor followed by annealing, sulfurization, and selenization at elevated temperature for solar cell applications [133]. In this study, they have deposited the CuInGa (CIG) thin films on Mo coated soda lime glass substrates. They

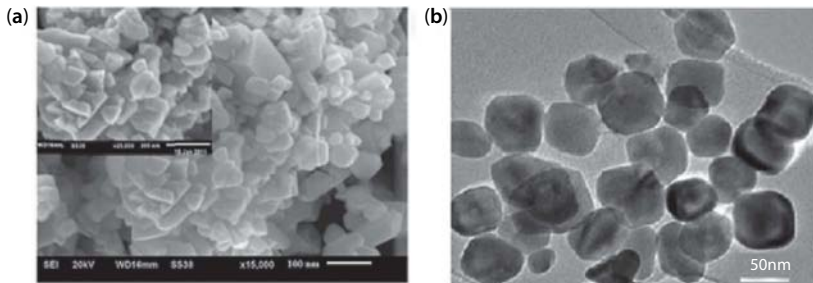


Figure 3.18 (a) FESEM and (b) FETEM images of spray pyrolyzed CuInS_2 thin films [132] (Reprinted with permission from Elsevier, doi:10.1016/j.matlet.2011.11.033).

have obtained chalcopyrite structure by sulfurization and selenization of the precursors. For this study, the optimal post-treatment temperature was reported as 300°C for annealing and 500°C for both sulfurization and selenization steps. The carbon impurities in the precursor film were removed by air annealing, and oxide that was formed during annealing was removed by sulfurization. The fabricated CIGS_{Se} solar cell showed a conversion efficiency of 4.63% for a 0.44 cm² area, with $V_{oc} = 0.4$ V, $J_{sc} = 21$ mA/cm², and $FF = 0.53$. The carbon- and oxygen-free approaches introduced in this study clearly helped to improve the efficiency.

In SP technique, nanocrystalline particles could be added into the solution to improve the crystallinity of the films. Cai *et al.* have been introduced the copper-rich (CuS) nanoparticles into an aqueous solution of CuCl₂, InCl₃ and CS(NH₂)₂ [134]. These particles take role as nucleation sites, which accelerate the grain growth. After selenization process at 480–500°C, the grain size of CISSe films were increased by a factor of seven in the presence of the nanoparticles of copper sulfide and indium sulfide. Figure 3.19(a) and (b) show the cross-sectional scanning electron microscopy images of CuInS₂ and CuIn(S,Se)₂ films, respectively. As can be seen from these figures, crystallinity of CuIn(S, Se)₂ films drastically increased with nanoparticle contribution in solution. Hence, the power conversion efficiency of 6.2%, which is 85% higher than the device without nanoparticle contribution, is observed.

In recent years, Cu-based chalcopyrites are of great research interest as p-type photocathode for PEC water splitting. Their appropriate band levels for water reduction and long-term stabilities have already been confirmed in solar cell applications. It has been proved that p-n junction formation between the p-type chalcopyrite and appropriate n-type semiconductors improved the water splitting properties of Cu-based chalcopyrites. Spray pyrolyzed CIS and gallium incorporated copper indium sulfide (CIGS),

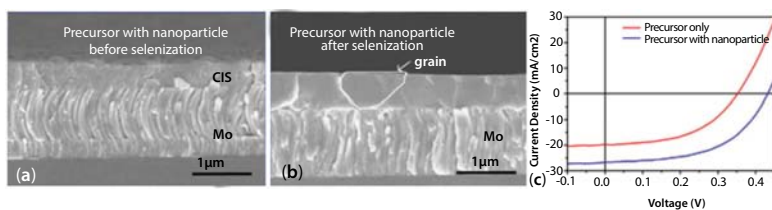


Figure 3.19 Cross-sectional FESEM image of the absorber layer from nanoparticle incorporated precursor (a) before and (b) after selenization. (c) IV curve of device fabricated from nanoparticle incorporated precursor (blue) film and precursor film without nanoparticle (red). The active area of both devices was 0.08 cm² [134] (Reprinted with permission from ACS Publications, DOI: 10.1021/am303057z).

which are cost-efficient alternatives for PEC applications, have been studied by Ikeda *et al.* [135]. They have deposited nanocrystalline CIS and CIGS thin films by SP technique. However, in order to take the advantage of more efficient charge transport the sprayed CIS and CIGS films was then annealed under sulfur-rich environment at 600°C for 10 min. For improved efficiency, PEC water splitting measurements were performed by using CdS-modified CIS and CIGS films as photocathodes and a RuO₂ counter electrode. With the help of formation a p–n junction, appreciable improvements of PEC properties of Cu(In,Ga)Se₂ photocathodes have also been demonstrated by Yokoyama *et al.* CIS and CIGS chalcopyrites worked as photocathode for PEC water splitting with applied bias potential of 0.65 V [136]. By using the p–n junction formation, PEC water splitting whilst applying relatively low bias potentials has been introduced.

Our research group has also been introduced the cost efficient approach for high quality nanocrystalline Cu-based chalcopyrites using ultrasonic impact nozzles. Very low material consumption, in other words high deposition yield is very important for cost efficient fabrication of the thin film photovoltaics on large scale. In our recent study, we have reported high quality CuInS₂ thin films with solution consumption up to 1/12 of the literature [27]. Furthermore, we have obtained very high electrical mobility, which is 40.1 cm²/V s, at 1.52 ml/cm² loading. Figure 3.20 indicates the schematic of our SP system and a real picture of CIS thin film deposited on glass substrate.

Cu-based quaternary chalcopyrites are novel materials for efficient photovoltaics. However, current efficient chalcopyrite photovoltaics suffer from highly toxic selenization and/or sulfurization process steps. Moreover, they also require again highly toxic KCN etching process to remove Cu based secondary phases from the surface of absorber layers. Our group has introduced an improvement on the properties of spray pyrolyzed nanocrystalline Cu-based chalcopyrites by conventional and rapid thermal annealing. Annealing procedures have been performed without using any toxic gases such as H₂S and H₂Se. Although, grain size of the CuInGaS₂ thin films were improved via annealing process all deposited films had nanocrystalline nature. Maximum electrical mobility of 30.9 cm²/Vs was observed for the annealed sample at 600°C for 30 min. This value is very high compare to the mobility values of CuInGaS₂ thin films reported in literature [137].

Flexible solar cells have unique advantages compare to the conventional rigid substrate based solar cells including the possibility of roll-to-roll manufacturing, mechanical robustness and lightweight. However, SP of thin films on flexible films have some difficulties. The major obstacle for SP of the thin films on flexible polymer foils is deformation of the substrate under

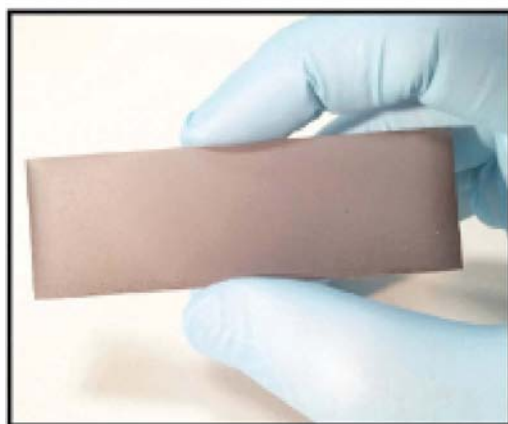
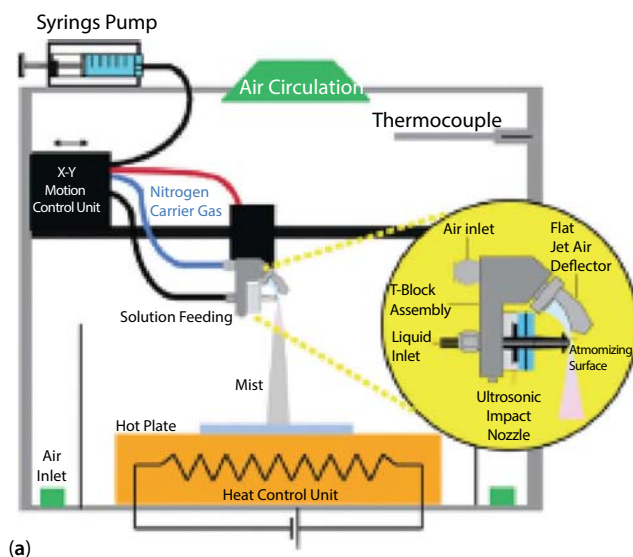


Figure 3.20 (a) Schematic illustration of USP system, (b) picture of CuInS_2 films deposited using 1.52 ml/cm^2 solution loading [27] (Reprinted with permission from Elsevier, doi:10.1016/j.solener.2013.05.024).

thermal shock provided by impact of liquid droplets on substrate at elevated temperatures. This impact of droplets generally resulted the fast cooling of the substrate, and therefore, defect formation occurred on the surface of the films. Finally, thin films peeled from the substrates. Our research group has developed a new method to deposit Cu-based chalcopyrite thin films

on flexible polyimide and stainless steel foils. Moreover, we introduced the first prototype of spray pyrolyzed Cu-based chalcopyrite photovoltaics. Figure 3.21 shows some primary flexible samples on Upilex® foil. First prototype films showed efficiency close to 1%. The relatively low efficiency values could be attributed to different recombination mechanisms and the inefficient charge collection due to non-optimized processing conditions.

Currently, we are also working on novel Cu-based nanocrystalline chalcopyrite thin films solar cells on flexible stainless steel foils. Stainless steel foils have some advantages when compared to counterpart deposited on Upilex® foils. It allows high temperature processing and post-annealing treatments (up to $\sim 700^\circ\text{C}$). Moreover, the coefficient of the thermal expansion of the stainless steel is very close to molybdenum, which is used as back contact. However, diffusion of iron or other undesired metals to the absorber layer cause deficiency of the performance of the solar cells. For this reason, they require a diffusion barrier layer between the back contact and stainless steel foil. These issues should be took care during the processing of the solar devices on stainless steel foils. The first prototype of this kind of solar cells, which have 200 nm alumina barrier layer and spray pyrolyzed nanocrystalline CIS absorber layer, showed 0.47% efficiency over 0.73 cm^2 active area (Figure 3.22). According to our best knowledge neither polyimide nor stainless steel has been used as the substrate material in the spray pyrolyzed thin film solar cells.

3.5.2 Nanocrystalline Kesterite Thin Films

Although, the thin film of $\text{Cu}(\text{In,Ga})(\text{S,Se})_2$, (CIGSSe), and CdTe photovoltaic technologies are currently being manufactured to take advantage of

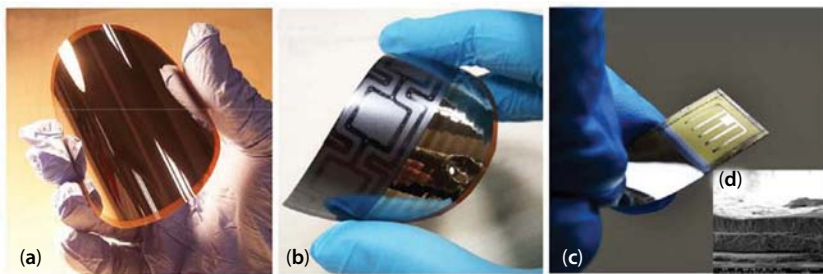


Figure 3.21 (a) Large area Mo back contact on Upilex® foil, (b) ultrasonically sprayed nanocrystalline CIS thin film on Mo coated Upilex® foil, (c) thin film solar cells having Upilex®/Mo/CIS/Ag-InS/ZnO/AZO-Ag-AZO/Ni/Al structure, and (d) cross-section SEM image of full structure device manufactured at TOBB University of Economics and Technology.



Figure 3.22 (a) Alumina coatings on stainless steel foil with different thickness values and (b) first prototype of flexible Stainless Steel/Mo/CIS/Ag-InS/ZnO/AZO-Ag-AZO/Ni/Al structure solar cells manufactured at TOBB University of Economics and Technology.

the high power conversion efficiencies, these approaches rely on elements that are either costly and/or rare in the earth's crust (e.g., In, Ga, Te). Toxic effects of the elements such as cadmium and selenium is another important issue restricting the usage of Cu(In,Ga)(S,Se)_2 , (CIGSSe) and CdTe. These factors potentially limit these technologies in terms of the future cost reduction and production growth [138]. Recently, there has been an effort to investigate the direct band gap $\text{Cu}_2\text{ZnSnS}_4$ (CZTS) thin films for photovoltaic applications. CZTS are particularly attractive because tin and zinc are naturally abundant in the Earth's crust and sulfur has relatively low toxicity.

The deposition of CZTS thin films by using SP technique in ambient environment was reported first time by Nakayama and Ito in 1997 [139]. They have fabricated CZTS films on soda lime glass substrates using precursor solution including CuCl_2 , ZnCl_2 , SnCl_4 , and thiourea at suitable concentrations in deionized water/ethanol solvent mixture.

Valdés *et al.* have also been studied on the SP of the $\text{Cu}_2\text{ZnSnS}_4$ (CZTS) thin films on glass substrates using aqueous precursors [140]. They have changed the substrate temperatures from 325°C to 425°C to observe effect of substrate temperature on the film properties. They confirmed the nanocrystalline structure of the films by XRD method for all examined substrate temperatures. The optical band gaps of the films were ranged between 1.3 and 1.5 eV. In order to explore photovoltaic properties of the spray deposited CZTS films, they have employed photoelectrochemistry. P-type behavior of these materials has also been confirmed by PEC measurements. The observation of the photovoltage and photocurrent during photo excitation presents the potential of the spray pyrolyzed nanocrystalline CZTS thin films for photovoltaic applications even at low temperature depositions.

Daranfed *et al.* also investigated the influence of the substrate temperature on the growth of CZTS films [141]. XRD analysis indicated that the deposited films have nanocrystalline kesterite structure. The grain sizes vary in the range 30–52 nm with increasing substrate temperature. The optical band gap of the films was ranged from 1.45 to 1.6 eV. XRD analysis, SEM observation and refractive index measurements indicated that the film crystallinity has been improved with increasing the substrate temperature (Figure 3.23).

In another study, Espindola-Rodriguez *et al.* have been examined the compositional gradient of the spray pyrolyzed CZTS films by controlling the stoichiometry and post-annealing conditions [142]. In this study,

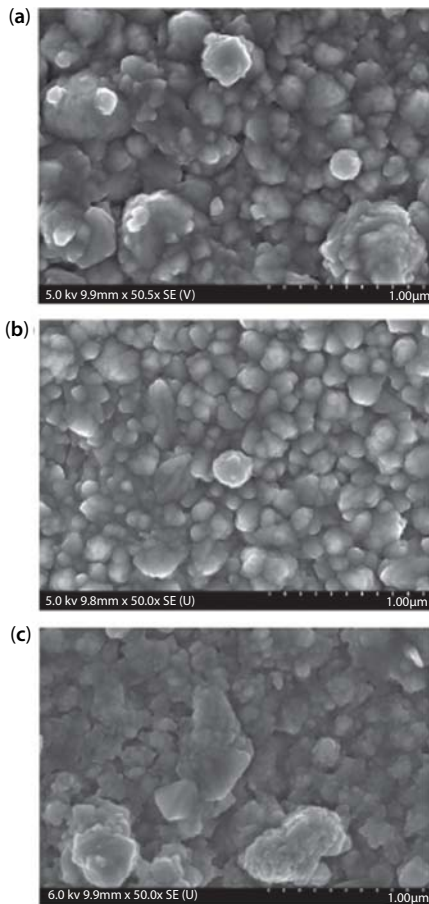


Figure 3.23 SEM images of CZTS thin films prepared at substrate temperature: (a) 280°C, (b) 320°C, and (c) 360°C [141] (Reprinted with permission from Elsevier, doi:10.1016/j.jallcom.2012.07.063).

they observed the structure of the as grown samples is nanocrystalline and this feature was independent on the sprayed solutions concentrations (Figure 3.24). They have concluded that composition have minor effects on grain size while the annealing temperature has more dominant influence on the crystallinity. Moreover, in order to correlate their optoelectronic properties with the chemico-physical, structural and electrical characteristics of the layers, solar cell prototypes were fabricated using a classical CZTS/CdS/i-ZnO/ZnO:Al structure. The obtained 0.49% efficiency is still under literature. When the optoelectronic parameters analyzed, it can be concluded that major problems come from the low shunt resistance (R_{sh}), which leads to low open circuit voltage (V_{OC}) and the consequent deterioration of F.F. and efficiency. It can be concluded that the compositional issues are not the main origin of the low V_{OC} . These results showed that, even if the small grain sizes are achieved in the annealed layers (of the

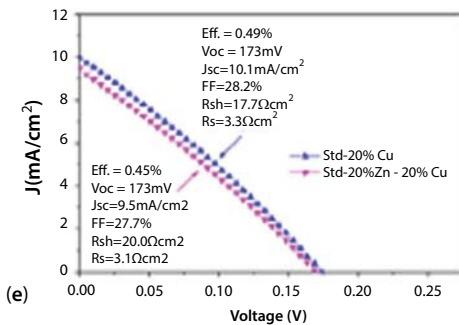
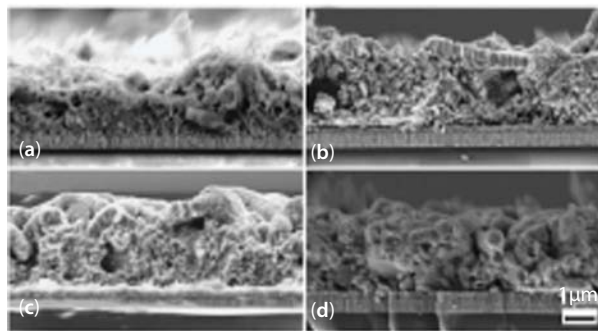


Figure 3.24 Cross sectional SEM micrographs for CZTS (a) +20% Zn; -20% Cu as grown, (b) -20% Cu annealed at 550°C, (c) +20% Zn; -20% Cu annealed at 550°C, and (d) -20% Cu annealed at 580°C. (e) Illuminated J–V curves (AM1.5) and optoelectronic parameters of the best cells obtained [142] (Reprinted with permission from Elsevier, doi:10.1016/j.tsf.2012.12.082).

order of hundreds of nanometers), the need for an optimization of the annealing procedures.

Zeng *et al.* have been demonstrated the potential of kesterite structure solar cells fabricated by SP followed by the high temperature selenization [143]. Nanocrystalline films have been obtained by deposition of $\text{Cu}_2\text{ZnSnS}_4$ in atmospheric condition with substrate temperature of 280°C . As deposited CZTS films were annealed under selenium vapor at 520°C for 12 min. This resulted with 300–500 nm grain size. Figure 3.25 shows the solar cell performances under illumination. Efficiency, open current voltage, short circuit current and fill factor of these devices are 5.1%, 370 mV, 27.3 mA/cm^2 and 50.6%, respectively (Figure 3.25). For low-selenium samples, 5.1% efficiency was obtained with higher $V_{\text{oc}} = 426 \text{ mV}$ and lower $J_{\text{sc}} = 24.2 \text{ mA/cm}^2$ as compared to the control cell. This is most probably due to the larger band gap, lower carrier mobility and carrier lifetime of CZTS obtained at low selenization values [144, 145].

It is well known that CZTS absorber layers have been derived from CuInSe_2 material by replacing scarce In(III) by abundant elements Zn(II) and Sn(IV) in the ratio 50%:50%. The conduction band of CZTS is higher than the H^+ reduction potential, so it is an appropriate photocathode material for solar hydrogen production. Additionally, cost efficient and large area fabrication of CZTS films by SP technique could be a key factors for the development of PEC applications. With this motivation, Huang *et al.* have demonstrated the PEC application of spray pyrolyzed CZTS films [146]. Nanocrystalline CZTS films deposited using ultrasonic SP system and annealed in tube furnace at different temperature values between 350°C and 500°C . PEC measurements have been performed in $0.5 \text{ M Na}_2\text{SO}_4$ electrolyte solution. Under illumination, all of the CZTS thin films exhibit a cathodic photocurrent, which suggests that the CZTS films are p-type

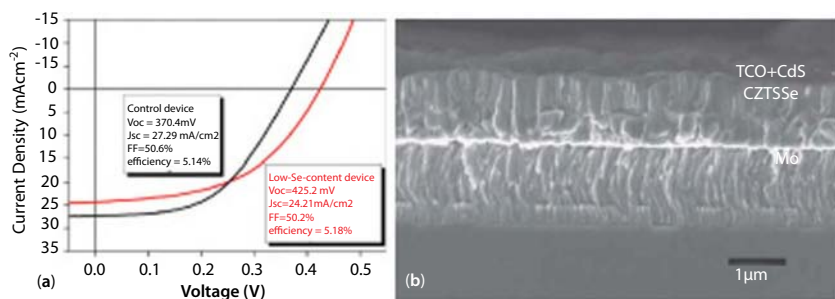


Figure 3.25 (a) Light J–V curve of control cell (black) and low-Se-content cell (red) (inset device parameter) and (b) cross-section of the full device on Mo coated glass [143] (Reprinted with permission from Elsevier, doi:10.1016/j.solmat.2014.01.029).

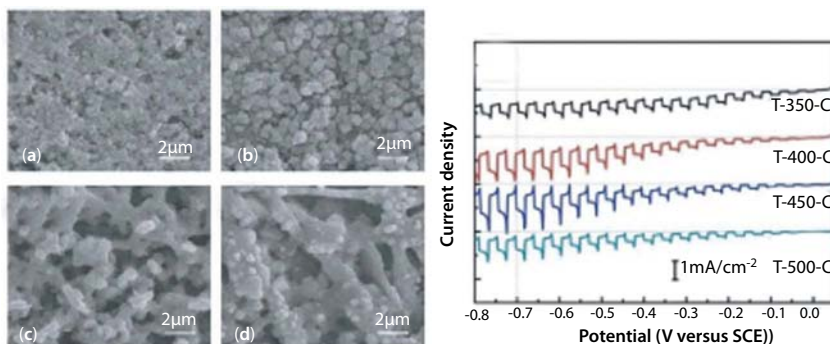


Figure 3.26 Surface SEM images of the CZTS thin films prepared at different substrate temperatures and after annealing in sulfur vapour at 510°C for 1 h: (a) 350°C, (b) 400°C, (c) 450°C, and (d) 500°C. (e) PEC properties of the CZTS films at different substrate temperatures and after annealing in sulfur vapour at 510°C for 1 h [146] (Reprinted with permission from IOP Science, doi:10.1088/0022-3727/46/23/235108).

semiconductors. At a potential -0.7 V SCE, the films at 400°C exhibit the best photocurrent of 0.77 mAcm^{-2} and a similar photocurrent is obtained for the sample at 450°C. The photocurrent of the samples at 400°C and 450°C is much higher than that of the sample at 350°C, maybe due to better crystallinity. Figure 3.26 shows the change in morphology and the PEC performance with the process temperature. Moreover, obvious transient photocurrent is observed in all the samples. This suggests the undesirable surface recombination at the interface of the solid/electrolyte. The photocurrent can be improved by surfacetreatment or electrocatalyst modification [146].

3.5.3 Nanocrystalline Metal Oxide Thin Films

Up to now we have been discussing the spray pyrolyzed semiconductors having narrow and mid band gap energy for solar cell applications. In this subsection we will mention about the spray pyrolyzed oxide materials, which can be utilized into touch-screen sensors, smart windows, and photovoltaics. Unlike the sections 3.2 and 3.3, here the nanocrystalline thin film of the oxides will be discussed briefly.

3.5.3.1 Tin Oxide

Transparent and conductive coatings have been widely used in optoelectronic applications such as touch-screen sensors, liquid crystal display (LCD) devices, plasma and organic light emitting diode (OLED) displays, smart windows, and photovoltaics-including inorganic, organic devices and dye-sensitized solar cells [147]. Doped tin oxide materials could also

be used as TCO. Kumara *et al.* has reported the air-atomized SP method to produce fluorine-doped SnO_2 (FTO) thin films using tin chloride and ammonium fluoride [148]. They reported that substrate temperature and deposition time affected the crystallinity of FTO films. It was demonstrated that nanocrystalline FTO thin films deposited at 450°C had high potential for transparent electrodes. Additionally they reported the 10.4% efficiency for dye-sensitized solar cell with spray pyrolyzed FTO layer.

Tin oxide is also one of the most favorable materials for sensor applications due to its low operating temperatures, high sensitivities, mechanical simplicity of sensor design, and low manufacturing costs [149]. Varying the structural parameters of the films, such as effective size of grains, crystallographic structure, and orientation of grains, has affected the sensor performance. For instance, metal doping of SnO_2 has influenced the gas sensing performance, since film morphology and bulk electro-physical properties of SnO_2 could be tailored by doping [150]. Also nanocrystalline SnO_2 films have more sensitivity than that of the films having higher crystallite sizes [151]. Brinzari *et al.* reported that minimization of the area of inter grain contacts became essential for achievement of maximum gas sensitivity. Therefore, structural modification of thin films could be the solution for this task. Such an optimization can be seen in Figure 3.27.

3.5.3.2 Titanium Dioxide

Like tin oxide, titanium dioxide (TiO_2) is very promising material with wide range of application areas such as Li-ion battery [152], dye sensitized solar cell [153–155], sensors [156], and photocatalytic reactions [72]. Natarajan *et al.* reported the spray pyrolyzed TiO_2 thin films for lithium ion batteries as anode material [152]. They also reported the effects of the experimental parameters on continuous film formation and crystallinity of the TiO_2 . It was also noted that infuse rate (more than 10 ml/min) affected the film formation adversely and polycrystalline anatase form of TiO_2 was

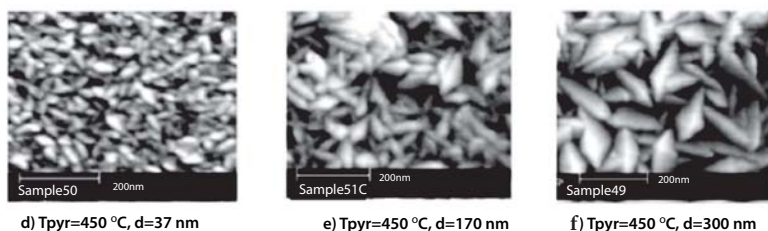


Figure 3.27 The SEM images of SnO_2 films deposited by the SP method with various thicknesses [151] (Reprinted with permission from Elsevier, doi:10.1016/S0040-6090(01)00978-6).

observed for substrate temperature above 300°C. The resulted discharge capacity of 65 mAh/g was reported for nanocrystalline TiO₂ anode based batteries where TiO₂ films were deposited at 400°C.

A. M. More *et al.* reported the web-like structured TiO₂ thin films via SP method for LPG sensing [157]. Ti (III) chloride solution was used as precursor and substrate temperature was kept constant at 375°C. They noted that before testing the LPG gas sensing, films were annealed at 500°C for 24 hours. Maximum sensor response of 35.8% was reported for LPG sensing with spray pyrolyzed TiO₂ thin films (Figure 3.28).

Alternatively, influence of doping of TiO₂ thin films for better LPG sensing has been studied [158]. Nickel doping of TiO₂ films could be achieved by just adding of nickel chloride into the titanium chloride precursor with appropriate stoichiometry.

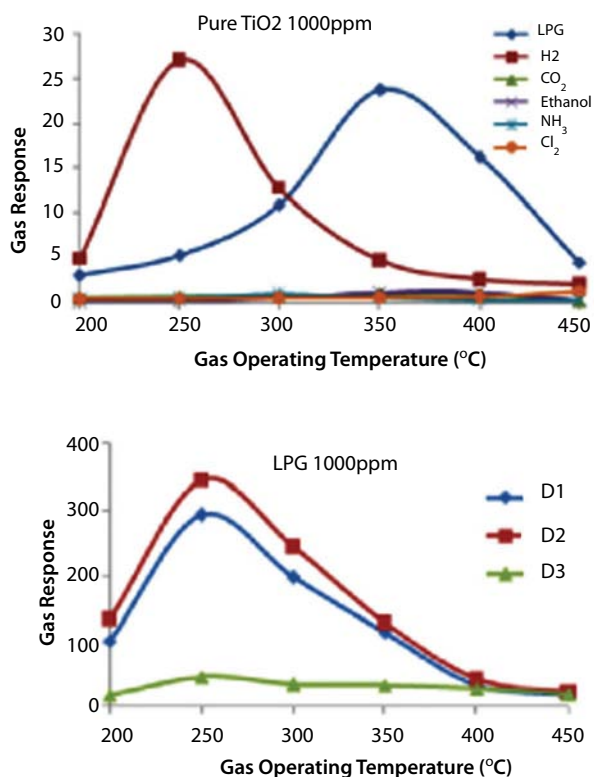


Figure 3.28 Variation of gas responses of pure TiO₂ thin film (top) and LPG sensing response of Ni doped TiO₂ thin films with preparation conditions (Ni:Ti) = 1:99 (D1), 2.5:97.5 (D2), 5:95 (D3), respectively [158] (Reprinted with permission from Elsevier, doi:10.1016/j.snb.2012.08.030).

Titanium dioxide was also used as transparent electrode for dye synthesized solar cells [153]. TiO_2 colloidal suspension was used to prepare transparent titania electrodes on FTO glass. Among the air-atomized SP, hand spray and doctor-blade methods, air-atomized spray pyrolyzed TiO_2 thin films with 10 μm thickness had more than 80% transparency [153]. Moreover, the conversion efficiency of 8.2% was reported for solar cell (Figure 3.29).

3.5.3.3 Zinc Oxide

Zinc oxide (ZnO) thin films could be deposited via various techniques, such as sputtering [159], sol-gel [160], chemical bath deposition [161], reactive electron beam evaporation [162], and electrodeposition [163]. Among these SP is one of the most commonly used method for deposition of the ZnO thin films [164–167]. Pure and doped ZnO thin films have gained attention due to their physical, optical and electrical properties. ZnO transparent electrodes should meet the needs low electrical resistivity and high optical transparency [168]. Moreover, for next generation optical and electronic devices, these electrodes should be flexible, lightweight, cost effective, and compatible with large area production. It is known that SP method allows the large area manufacturing with relatively low costs [165, 169, 170]. The optical and electrical properties of ZnO and aluminum doped ZnO (AZO) have been studied [170]. The type of the precursor has a huge influence on the structural and morphological characteristics of the films. For example, the resistivities of the films from zinc acetate and zinc nitrate precursors were 14 and 5300 Ωcm , respectively. Also, as deposition time for Zn acetate precursor was increased, as-grown samples became highly nanostructured (Figure 3.30).

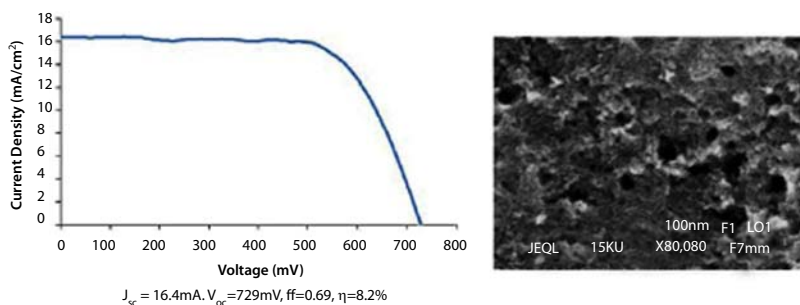


Figure 3.29 I–V characteristics of the films, with 0.25 cm^2 surface area, fabricated using TiO_2 transparent electrode (right: SEM images of nanocrystalline TiO_2 electrode) [153] (Reprinted with permission from Elsevier, doi:10.1016/j.electacta.2011.07.119).

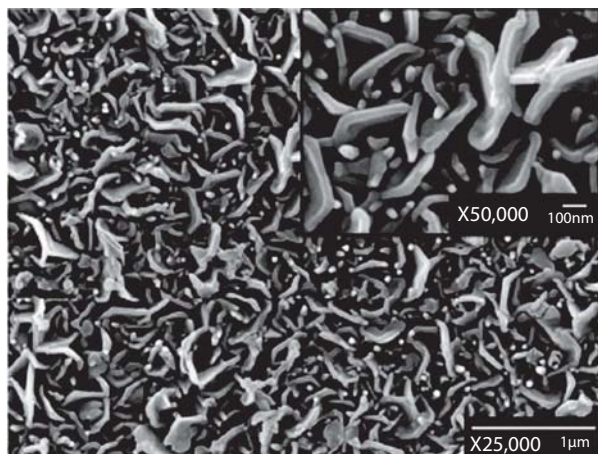


Figure 3.30 SEM image of a ZnO film with deposition time 60 min and with precursor 0.5 M aqueous solution of zinc acetate [170] (Reprinted with permission from Elsevier, doi:10.1016/j.tsf.2013.10.015).

To observe high transparency and low resistivity in ZnO films, aluminum doping has been studied. Doping of aluminum has been achieved by adding aluminum metal salt into the precursor solution [170, 171]. Gallium doping has also been studied for especially optoelectronic device applications [172].

LPG and H₂S gas sensing of spray pyrolyzed ZnO thin films were reported [173, 174]. Nanocrystalline ZnO thin film with smaller grain sizes resulted with high responses for LPG sensing (max 31% at operation temperature 400°C for ZnO films obtained using 0.10M zinc nitrate solution). It is known that determination of gas sensing of metal oxides is obtained by the interactions between a target gas and the surface of the sensors [173]. Besides H₂S sensing responses of ZnO films with different thicknesses have been investigated [174]. Shewale *et al.* stated that increasing film thickness made grain size increase from 15 to 28 nm (Figure 3.31) [174].

3.5.4 Nanocrystalline Chalcogenide Thin Films

The crystal structure of chalcogenide materials consists of at least one chalcogen anion and an electropositive element. Even though all group 16 elements of the periodic table are defined as chalcogens, the term chalcogenide is more commonly reserved for sulfides, selenides, and tellurides. In literature, sulfides, selenides, and tellurides of indium, cadmium, copper, zinc and tin are most commonly studied chalcogenide nanocrystalline thin films. These thin films have been utilized in various optical and electrical applications.

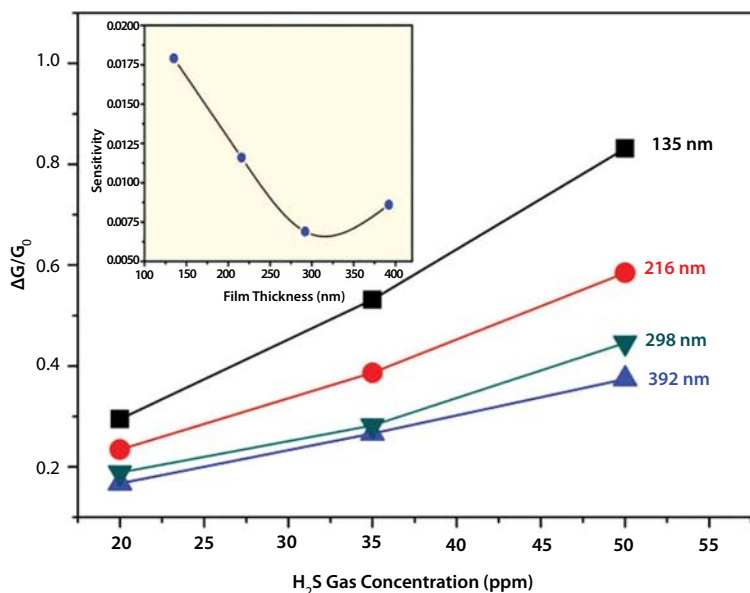


Figure 3.31 The variation of gas response as a function of H_2S gas concentration. The inset shows the variation of sensitivity as a function of ZnO film thickness [174] (Reprinted with permission from Elsevier, doi:10.1016/j.snb.2012.11.076).

Cadmium chalcogenides, a II–VI semiconductor compound, with appropriate band gap energy have been attracting a great deal of attention because of their potential applications in optoelectronic devices such as solid-state lasers and detectors, solar cells, and optical memories. Currently, the most efficient thin film photovoltaic technologies have been using chemical bath deposited cadmium sulfide thin films [175, 176]. However, chemical bath deposition process leaves very large amount of highly toxic chemicals to nature. On the other hand, SP technique allows reducing solution consumption and risks about the environmental issues. In literature various studies have been conducted to understand the impact of deposition parameters on the film properties of nanocrystalline cadmium sulfide [177–179].

Alternatively, nanocrystalline indium sulfides thin films are very popular materials among possible chalcogenides prepared for optoelectronic and photovoltaic applications due to its stability, wider band gap and good photoconductive behavior [180]. Moreover, this material eliminates toxic effects of cadmium and improves the light transmission in the blue wavelength region. In literature, effects of deposition conditions on the film properties of indium sulfide have been studied extensively [181–184]. S. Buecheler *et al.* has reported 12.4% efficiency using spray pyrolyzed

nanocrystalline indium sulfide thin films as a buffer layer in solar cell application. Recently, our group has introduced high quality indium sulfide thin films prepared via ultrasonic SP with very low solution consumption [185]. We have also observed that silver incorporation enhanced the light sensitization of the In_2S_3 thin films. The photosensitivity of the films, which is a measure of change in resistivity with illumination, with 20% silver was about 2×10^3 . This was ten times higher than the photosensitivity of the undoped samples, which could be the key parameter to utilize indium sulfide as a buffer layer for thin film solar cell applications [185].

Zinc sulfide (ZnS) has drawn considerable interest with its physical, optical and electrical properties for applications such as photocatalysis [186], electroluminescent device technology [187], and photovoltaic [188]. Highly crystalline wurtzite ZnS thin films could be obtained using SP method with deposition temperature of 310°C [143]. Zeng *et al.* noted that surface morphology and preferential crystal growth of ZnS thin films were changed with various spray rates. Moreover, Zn/S molar ratio in solution could affect the structure of spray pyrolyzed ZnS. Dedova *et al.* has studied several molar ratios as 1/1, $\frac{1}{2}$, and $\frac{1}{3}$ to fabricate ZnS thin films at deposition temperatures ranging from 400°C to 600°C [47]. They reported that 1/1 molar ratio ZnS films deposited at 500°C resulted cubic structure. The molar ratio of $\frac{1}{2}$ at 500°C was reported as the optimum deposition condition.

Finally copper sulfide is a p-type semiconductor material with suitable band gap varying from 1.2 to 2.35 eV for absorber layer in solid-state solar cells [189, 190] and also photocatalyst [191]. Spray pyrolyzed copper sulfide absorber layers have been investigated by L. Isac *et al.* [189, 190]. Additionally, nanocomposite solar cells with Cu_xS absorber layer showed efficiency about 6% [192]. The diode behavior of these absorbers has also been studied and stated that I–V characteristic could be correlated with film thickness. SP method allows controlling the Cu_xS film morphology with adjusting the precursor solution and deposition parameters; therefore, optimization of Cu_xS film properties could enhance the diode performance [189].

3.6 Conclusion

The SP technique has a tremendous potential to form functional nanocrystalline thin films, nano powders and three-dimensional nano-structures for various applications including energy storage, biomedical, and photovoltaic devices. The SP technique is appropriate for in-line production with high throughput. This method is a robust process and can be easily scaled-up. Hence, many researchers have been focused on manufacturing

functional structures using SP technologies. Deposition conditions such as substrate temperature, solution stoichiometry, and solvent type affect the material's properties. Controlling the deposition conditions also makes it possible to tailor the physical properties of the functional materials depending on the application.

Deposition of nano-structured oxides via SP is a very active area of research due to several unique advantages such as low manufacturing cost, high performance, and very wide range of applications. Nanoparticles, nano rods or nanocrystalline thin films of zinc oxide, titanium dioxide, lithium oxide and many other oxides have a large potential in reflectors, sunscreens, photovoltaics and energy storage devices. Another very important application of spray pyrolyzed metal oxides is sensors. Porous tin oxide and tin oxide-manganese (III) oxide mixed films have been used as Taguchi type hydrogen sensors. Spray pyrolyzed metal oxides has also been utilized in carbon monoxide, hydrocarbon, and humidity sensors.

Acknowledgement

Authors would like to thanks to Republic of Turkey Ministry of Science, Industry and Technology for their support under contract number 01072. STZ.2011-2.

References

1. X. Zeng, K. F. Tai, T. Zhang, C. W. J. Ho, X. Chen, A. Huan, T. C. Sum, L. H. Wong, $\text{Cu}_2\text{ZnSn}(\text{S},\text{Se})_4$ kesterite solar cell with 5.1% efficiency using spray pyrolysis of aqueous precursor solution followed by selenization, *Sol. Energy Mater. Sol. Cells* 124 (2014) 55–60.
2. T. T. John, M. Mathew, C. S. Kartha, K. P. Vijayakumar, T. Abe, Y. Kashiwaba, $\text{CuInS}_2/\text{In}_2\text{S}_3$ thin film solar cell using spray pyrolysis technique having 9.5% efficiency, *Sol. Energy Mater. Sol. Cells* 89 (2005) 27–36.
3. E. Karber, A. Abass, S. Khelifi, M. Burgelman, A. Katerski, M. Krunks, Electrical characterization of all-layers-sprayed solar cell based on ZnO nanorods and extremely thin CIS absorber, *Sol. Energy* 91 (2013) 48–58.
4. T. Sahm, L. Mädler, A. Gurlo, N. Barsan, S. E. Pratsinis, U. Weimar, Flame spray synthesis of tin dioxide nanoparticles for gas sensing, *Sensors Actuat. B* 98 (2004) 148–153.
5. C. M. Ghimbeu, J. Schoonman, M. Lumbreras, M. Siadat, Electrostatic spray deposited zinc oxide films for gas sensor applications, *App. Surf. Sci.* 253 (2007) 7483–7489.

6. V. R. Shinde, T. P. Gujar, C. D. Lokhande, LPG sensing properties of ZnO films prepared by spray pyrolysis method: Effect of molarity of precursor solution *Sensors Actuat. B* 120 (2007) 551–559.
7. S. N. Karthick, S. R. P. Gnanakan, A. Subramania, H. J. Kim, Nanocrystalline LiMn_2O_4 thin film cathode material prepared by polymer spray pyrolysis method for Li-ion battery, *J. Alloy. Compd.* 489 (2010) 674–677.
8. V. R. Shinde, S. B. Mahadik, T. P. Gujar, C. D. Lokhande, Supercapacitive cobalt oxide (Co_3O_4) thin films by spray pyrolysis, *App. Surf. Sci.* 252 (2006) 7487–7492.
9. T. P. Gujar, V. R. Shinde, C. D. Lokhande, Woo-Young Kim, Kwang-Deog Jung, Oh-Shim Joo, Spray deposited amorphous RuO_2 for an effective use in electrochemical supercapacitor, *Electrochem. Commun.* 9 (2007) 504–510.
10. P. Tartaj, M. P. Morales, S. Veintemillas-Verdaguer, T. Gonzalez-Carreno, C. J. Serna, The preparation of magnetic nanoparticles for applications in biomedicine, *J. Phys. D: Appl. Phys.* 36 (2003) R182–R197.
11. P. Tartaj, M. P. Morales, T. Gonzalez-Carreno, S. Veintemillas-Verdaguer, C. J. Serna, Advances in magnetic nanoparticles for biotechnology applications, *J. Magn. Magn. Mater.* 290–291 (2005) 28–34.
12. J. C. Viguie and J. Spitz, Chemical vapor deposition at low temperatures, *J. Electrochem. Soc.* 122 (4) (1975) 585–588.
13. W. Siefert, Properties of thin In_2O_3 and SnO_2 films prepared by corona spray pyrolysis, and a discussion of the spray pyrolysis process, *Thin Solid Films* 120 (4) (1984) 275–282.
14. W. Y. Teoh, R. Amala, Lutz Madler, Flame spray pyrolysis: An enabling technology for nanoparticles design and fabrication, *Nanoscale* 2 (2010) 1324–1347.
15. S. Grimm, M. Schultz, S. Barth, R. Muller, Flame pyrolysis – A preparation route for ultrafine pure $\gamma\text{-Fe}_2\text{O}_3$ powders and the control of their particle size and properties, *J. Mater. Sci.* 32 (1997) 1083–1092.
16. A. I. Y. Tok, F. Y. C. Boey, X. L. Zhao, Novel synthesis of Al_2O_3 nano-particles by flame spray pyrolysis, *J. Mater. Process. Tech.* 178 (2006) 270–273.
17. R. Mueller, L. Madler, S. E. Pratsinis, Nanoparticle synthesis at high production rates by flame spray pyrolysis, *Chem. Eng. Sci.* 58 (2003) 1969–1976.
18. L. Madler and S. E. Pratsinis, Bismuth oxide nanoparticles by flame spray pyrolysis, *J. Am. Ceram. Soc.* 85 (7) (2002) 1713–1718.
19. T. Tani, L. Madler, S. E. Pratsinis, Homogeneous ZnO nanoparticles by flame spray pyrolysis, *J. Nanoparticle. Res.* 4 (2002) 337–343.
20. R. N. Kailash, A. W. Sandeep, Optical and gas sensing properties of CuO nanoparticles grown by spray pyrolysis of cupric nitrate solution, *Int. J. Mater. Sci. Eng.* 2 (2014) 63–66.
21. K. Okuyama, I. W. Lenggoro, Preparation of nanoparticles via spray route, *Chem. Eng. Sci.* 58 (2003) 537–547.
22. E. Aydin, N. D. Sankir, Ultrasonic spray deposition of CuInS_2 absorber thin films: effect of nozzle frequency, *J. Optoelectron. Adv. M.*, 15 (1–2) (2013) 14–21.

23. D. Perednis, O. Wilhelm, S. E. Pratsinis, L. J. Gauckler, Morphology and deposition of thin yttria-stabilized zirconia films using spray pyrolysis, *Thin Solid Films* 474 (2005) 84–95.
24. D. Zaouk, Y. Zaatar, R. Asmarb, J. Jabbour, Piezoelectric zinc oxide by electrostatic spray pyrolysis, *Microelectr. J.* 37(2006) 1276–1279.
25. M. Ctoupeau, B. Prunet-Foch, Electrostatic spraying of liquids: Main functioning modes, *J. Electrostat.* 25 (2) (1990) 165–184.
26. C. D. Hendricks Jr., Charged droplet experiments, *J. Colloid Sci.* 17(3) (1962) 249–259.
27. N. D. Sankir, E. Aydin, H. Unver, E. Uluer, M. Parlak, Preparation and characterization of cost effective spray pyrolyzed absorber layer for thin film solar cells, *Sol. Energy* 95 (2013) 21–29.
28. C. S. Tsai, R. W. Mao, S. K. Lin, N. Wanga, S. C. Tsai, Miniaturized multiple Fourier-horn ultrasonic droplet generators for biomedical applications, *Lab. Chip.* 10 (2010) 2733–2740.
29. K. A. Ramisetty, A. B. Pandit, P. R. Gogate, Investigations into ultrasound induced atomization, *Ultrason. Sonochem.* 20 (2013) 254–264.
30. R. J. Lang, Ultrasonic atomization of liquids, *J. Acoust. Soc. Am.* 34(1) (1962) 6–8.
31. C. Lam, Y. F. Zhang, Y. H. Tang, C. S. Lee, I. Bello, S. T. Lee, Large-scale synthesis of ultrafine Si nanoparticles by ball milling, *J. Cryst. Growth* 220 (2000) 466–470.
32. B. Gunther, A. Kumpmann, Ultrafine oxide powders prepared by inert as evaporation, *Nanostruct. Mater.* 1(1) (1992) 27–30.
33. D. Vollath, K. E. Sickafus, Synthesis of nanosized ceramic oxide powders by microwave plasma reactions, *Nanostruct. Mater.* 1(5) (1992) 427–437.
34. G. F. Gaertner, H. Lydtin, Review of ultrafine particle generation by laser ablation from solid targets in gas flows, *Nanostruct. Mater.* 4(5) (1994) 559–568.
35. F. Li, X. Yu, H. Pan, M. Wang, X. Xin, Syntheses of MO_2 ($M = \text{Si}, \text{Ce}, \text{Sn}$) nanoparticles by solid-state reactions at ambient temperature, *Solid State Sci.* 2 (2000) 767–772.
36. Y. Lu, H. Fan, A. Stump, T. L. Ward, T. Rieker, C. J. Brinker, Aerosol-assisted self-assembly of mesostructured spherical nanoparticles, *Nature* 398 (1999) 223–226.
37. M. S. El-Shall, W. Slack, W. Vann, D. Kane, D. Hanley, Synthesis of nanoscale metal oxide particles using laser vaporization/condensation in a diffusion cloud chamber, *J. Phys. Chem.* 98(12) (1994) 3067–3070.
38. C. G. Granqvist, R. A. Buhrman, Ultrafine metal particles, *J. Appl. Phys.* 47 (1996) 2200.
39. H. Hahn, R. S. Averback, The production of nanocrystalline powders by magnetron sputtering, *J. Appl. Phys.* 67 (1990) 1113.
40. G. D. Ulrich, J. W. Rieh, Aggregation and growth of submicron oxide particles in flames, *J. Colloid. Interface Sci.* 87 (1982) 257–265.
41. D. Lindackers, C. Janzena, B. Rellinghaus, E. F. Wassermann, P. Roth, Synthesis of Al_2O_3 and SnO_2 particles by oxidation of metalorganic

- precursors in premixed $H_2/O_2/Ar$ low pressure flames, *Nanostruct. Mater.* 10(8) (1998) 1247–1270.
42. G. Skandan, Y-J. Chen, N. Glumac, B. H. Kear, Synthesis of oxide nanoparticles in low pressure flames, *Nanostruct. Mater.* 11(2) (1999) 149–158.
 43. V. R. Palkar, Sol-gel derived nanostructured γ -alumina porous spheres as an adsorbent in liquid chromatography, *Nanostruct. Mater.* 11(3) (1999) 369–374.
 44. L. Gao, H. Z. Wang, J. S. Hong, H. Miyamoto, K. Miyamoto, Y. Nishikawa, S. D. D. L. Torre, SiC-ZrO₂(3Y)-Al₂O₃ nanocomposites superfast densified by spark plasma sintering, *Nanostruct. Mater.* 11(1) (1999) 43–49.
 45. J. M. Makela, H. Keskinen, T. Forsblom, J. Keskinen, Generation of metal and metal oxide nanoparticles by liquid flame spray process, *J. Mater. Sci.* 39 (2004) 2783–2788.
 46. M. Krunk, A. Katerski, T. Dedova, I. O. Acik, A. Mere, Nanostructured solar cell based on spray pyrolysis deposited Zn nanorod array, *Sol. Energy Mater. Sol. Cells* 92 (2008) 1016–1019.
 47. T. Dedova, M. Krunk, I. Gromyko, V. Mikli, I. Sildos, K. Utt, and T. Unt, Effect of Zn:S molar ratio in solution on the properties of ZnS thin films and the formation of ZnS nanorods by spray pyrolysis, *Phys. Status Solidi A* (2014) 1–8.
 48. F. Paraguay-Delgado, W. Antunez-Flores, M. Miki-Yoshida, A. Aguilar-Elguezabal, P. Santiago, R. Diaz and J. A. Ascencio, Structural analysis and growing mechanisms for long SnO₂ nanorods synthesized by spray pyrolysis, *Nanotechnology* 16 (2005) 688–694.
 49. B. Russo, G. C. Zao, Fabrication and characterization of fluorine-doped thin oxide thin films and nanorod arrays via spray pyrolysis, *Appl. Phys. A* 90 (2008) 311–315.
 50. M. O. Abou-Helal, W. T. Seeber, Preparation of TiO₂ thin films by spray pyrolysis to be used as a photocatalyst, *App. Surf. Sci.* 195 (2002) 53–62.
 51. Z. Bakenov, M. Wakihara, I. Taniguchi, Battery performance of nanostructured lithium manganese oxide synthesized by ultrasonic spray pyrolysis at elevated temperature, *J. Solid State Electrochem.* 12 (2008) 57–62.
 52. R. Strobel, J. Grunwaldt, A. Camenzind, S. E. Pratsinis, A. Baiker, Flame-made alumina supported Pd–Pt nanoparticles: Structural properties and catalytic behavior in methane combustion, *Catal. Lett.* 104 (2005) 9–19.
 53. M. Eslamian and M. C. Heine, Characteristics of spray flames and the effect of group combustion on the morphology of flame-made nanoparticles, *Nanotechnology* 19 (2008) 045712.
 54. I. W. Lenggoro, Y. Itoh, N. Iida, K. Okuyama, Control of size and morphology in NiO particles prepared by a low-pressure spray pyrolysis, *Mater. Res. Bull.* 38 (2003) 1819–1827.
 55. K. C. Krogman, T. Druffel, M. K. Sunkara, Anti-reflective optical coatings incorporating nanoparticles, *Nanotechnology* 16 (2005) 338–343.

56. Y. Jiang, P. Wang, X. Zang, Y. Yang, A. Kozinda, L. Lin, Uniformly embedded metal oxide nanoparticles in vertically aligned carbon nanotube forest as pseudocapacitor electrodes for enhanced energy storage, *Nano Lett.* 13 (2013) 3524–3530.
57. W. S. Seo, H. H. Jo, K. Lee, J. T. Park, Preparation and optical properties of highly crystalline, colloidal, and size-controlled indium oxide nanoparticles, *Adv. Mat.* 15 (2003) 795–797.
58. P. Samarasekara, N. T. R. N. Kumara, N. U. S. Yapa, Sputtered copper oxide (CuO) thin films for gas sensor devices, *J. Phys. Condens. Matter* 18 (2006) 2417–2420.
59. A. Z. Liao, W. D. Zhu, J. B. Chen, X. Q. Zhang, C. W. Wang, Vertically aligned single-crystalline ultra-thin CuO nanosheets: Low-temperature fabrication, growth mechanism, and excellent field emission, *J. Alloy. Compd.* 609 (2014) 253–261.
60. S. E. Sebastian, N. Harrison, F. F. Balakirev, M. M. Altarawneh, P. A. Goddard, R. Liang, D. A. Bonn, W. N. Hardy, G. G. Lonzarich, Normal-state nodal electronic structure in underdoped high- T_c copper oxides, *Nature* 511 (2014) 61–64.
61. G. Ren, D. Hu, E. W. C. Cheng, M. A. Vargas-Reus, P. Reip, R. P. Allaker, Characterisation of copper oxide nanoparticles for antimicrobial applications, *Int. J. Antimicrob. Agents* 33 (2009) 587–590.
62. C. Y. Chiang, K. Aroh, S. Ehrman, Copper oxide nanoparticle made by flame spray pyrolysis for photoelectrochemical water splitting – Part I. CuO nanoparticle preparation, *Int. J. Hydrogen Energ.* 37 (2012) 4871–4879.
63. C. Y. Chiang, K. Aroh, N. Franson, V. R. Satsangi, S. Dass, S. Ehrman, Copper oxide nanoparticle made by flame spray pyrolysis for photoelectrochemical water splitting – Part II. Photoelectrochemical study, *Int. J. Hydrogen Energ.* 36 (2011) 15519–15526.
64. T. Ogi, D. Hidayat, F. Iskandar, A. Purwanto, K. Okuyama, Direct synthesis of highly crystal in transparent oxide nanoparticles by low pressure spray pyrolysis, *Adv. Powder Technol.* 20 (2009) 203–209.
65. M. Batzill, U. Diebold, The surface and materials science of tin oxide, *Prog. Surf. Sci.* 79 (2005) 47–154.
66. E. Comini, G. Faglia, G. Sberveglieri, D. Calestani, L. Zanotti, M. Zha, Tin oxide nanobelts electrical and sensing properties, *Sensors Actuat. B* 111–112 (2005) 2–6.
67. Z. R. Dai, Z. W. Pan, Z. L. Wang, Growth and structure evolution of novel tin oxide diskettes, *J. Am. Chem. Soc.* 124 (2002) 8673–8680.
68. A. Kolmakov, Y. Zhang, G. Cheng, M. Moskovits, Detection of CO and O₂ using tin oxide nanowire sensors, *Adv. Mater.* 15 (2003) 997–1000.
69. M. E. Franke, T. J. Koplín, U. Simon, Metal and metal oxide nanoparticles in chemiresistors: Does the nanoscale matter? *Small* 2 (2006) 36–50.

70. Y. Lan, Y. Lu, Z. Ren, Mini review on photocatalysis of titanium dioxide nanoparticles and their solar applications, *Nano Energy* 2 (2013) 1031–1045.
71. Y. Chiba, A. Islam, Y. Watanabe, R. Komiya, N. Koide, L. Han, Dye-sensitized solar cells with conversion efficiency of 11.1%, *Jpn. J. Appl. Phys.* 45 (2006) 638–640.
72. A. Fujishima, T. N. Rao, D. A. Tryk, Titanium dioxide photocatalysis, *J. Photoch. Photobio. C Photochem. Rev.* 1 (2000) 1–21.
73. A. Wold, Photocatalytic properties of titanium dioxide (TiO₂), *Chem. Mater.*, 1993, 5 (3), 280–283.
74. R. L. Pozzo, M. A. Baltanás, A. E. Cassano, Supported titanium oxide as photocatalyst in water decontamination: State of the art, *Catal. Today*, 39 (1997) 219–231.
75. I. P. Parkin, R. G. Palgrave, Self-cleaning coatings, *J. Mater. Chem.*, 15 (2005) 1689–1695.
76. K. Hashimoto, H. Irie, A. Fujishima, TiO₂ photocatalysis: A historical overview and future prospects, *Jpn. J. Appl. Phys.*, 44 (2005) 8269–8285.
77. O. Carp, C. Huisman, A. Reller, Photoinduced reactivity of titanium dioxide, *Prog. Solid State Chem.*, 32(2004) 33–177.
78. L. Dreesen, J-F. Colomer, H. Limage, A. Giguère, Stéphane Lucas, Synthesis of titanium dioxide nanoparticles by reactive DC magnetron sputtering, *Thin Solid Films* 518 (2009) 112–115.
79. Z. Li, B. Hou, Y. Xu, D. Wu, Y. Sun, Hydrothermal synthesis, characterization, and photocatalytic performance of silica-modified titanium dioxide nanoparticles, *J. Colloid Interf. Sci.* 288 (2005) 149–154.
80. N. Wetchakun, S. Phanichphant, Effect of temperature on the degree of anatase–rutile transformation in titanium dioxide nanoparticles synthesized by the modified sol–gel method, *Curr. Appl. Phys.* 8 (2008) 343–346.
81. C. S. Kim, B. K. Moon, J-H. Park, S. T. Chung, S-M. Son, Synthesis of nanocrystalline TiO₂ in toluene by a solvothermal route, *J. Cryst. Growth* 254 (2003) 405–410.
82. X. Peng, A. Chen, Aligned TiO₂ nanorod arrays synthesized by oxidizing titanium with acetone, *J. Mater. Chem.* 14 (2004) 2542–2548.
83. H. Teisala, M. Tuominen, M. Aromaa, J. M. Mäkelä, M. Stepien, J. J. Saarinen, M. Toivakka, J. Kuusipalo, Development of superhydrophobic coating on paperboard surface using the Liquid Flame Spray, *Surf. Coat. Tech.* 205 (2010) 436–445.
84. M. Aromaa, A. Arffman, H. Suhonen, J. Haapanen, J. Keskinen, M. Honkanen, J. Nikkanen, E. Levanen, M. E. Messing, K. Deppert, H. Teisala, M. Tuominen, J. Kuusipalo, M. Stepien, J. J. Saarinen, M. Toivakka, J. M. Makela, Atmospheric synthesis of superhydrophobic TiO₂ nanoparticle deposits in a single step using Liquid Flame Spray, *J. Aerosol Sci.* 52 (2012) 57–68.

85. B. Tian, C. Li, F. Gua, H. Jianga, Y. Hua, J. Zhang, Flame sprayed V-doped TiO_2 nanoparticles with enhanced photocatalytic activity under visible light irradiation, *Chem. Eng. J.* 151 (2009) 220–227.
86. W. Ohm, W. Riedel, Ü. Askünger, M. D. Heinemann, C. A. Kaufmann, J. L. Garcia, V. Izquierdo, X. Fontané, T. Goislard, M. C. Lux-Steiner, S. Gledhill, An overview of technological aspects of $\text{Cu}(\text{In,Ga})\text{Se}_2$ solar cell architectures incorporating ZnO nanorod arrays, *Phys. Status Solidi A* (2014) 1–12.
87. A. Becheri, M. Dürr, P. L. Nostro, P. Baglioni, Synthesis and characterization of zinc oxide nanoparticles: Application to textiles as UV-absorbers, *J. Nanopart. Res.* 10 (2008) 679–689.
88. M. L. Kahn, M. Monge, V. Collière, F. Senocq, A. Maisonnat B. Chaudret, Size- and shape-control of crystalline zinc oxide nanoparticles: A new organometallic synthetic method, *Adv. Func. Mater.* 15 (2005) 458–468.
89. L. Wang, M. Muhammed, Synthesis of zinc oxide nanoparticles with controlled morphology, *J. Mater. Chem.* 9 (1999) 2871–2878.
90. M. M. J. Treacy, J. M. Newsam, Two new three-dimensional twelve-ring zeolite frameworks of which zeolite beta is disordered intergrowth, *Nature* 332 (1988) 249–251.
91. G. Guerguerian, F. Elhordoy, C. J. Pereyra, R. E. Marotti, F. Martin, D. Leinen, J. R. Ramos-Barrado, E. A. Dalchiale, $\text{ZnO}/\text{Cu}_2\text{O}$ heterostructure nanopillar arrays: Synthesis, structural and optical properties, *J. Phys. D Appl. Phys.* 45 (2012) 245301 (10pp).
92. J. W. Cho, S. J. Park, J. Kim, W. Kim, H. K. Park, Y. R. Do, B. K. Min, Bulk heterojunction formation between indium tin oxide nanorods and CuInS_2 nanoparticles for inorganic thin film solar cell applications, *ACS Appl. Mater. Interfaces* 4 (2012) 849–853.
93. Z. Yuan, H. Huang, S. Fan, Regular alumina nanopillar arrays, *Adv. Mater.* 14 (2002) 303–306.
94. S. Chu, K. Wada, S. Inoue, M. Isogai, A. Yasumori, Fabrication of ideally ordered nanoporous alumina films and integrated alumina nanotube arrays by high-field anodization, *Adv. Matter.* 17 (2005) 2115–2119.
95. M. Okuya, K. Shiozaki, N. Horikawa, T. Kosugi, G. R. A. Kumara, J. Madarasz, S. Kaneko, G. Pokol, Porous TiO_2 thin films prepared by spray pyrolysis deposition (SPD) technique and their application to UV sensors, *Solid State Ionics* 172 (2004) 527–531.
96. H. E. Prakasam, O. K. Varghese, M. Paulose, G. K. Mor, C. A. Grimes, Synthesis and photoelectrochemical properties of nanoporous iron (III) oxide by potentiostatic anodization, *Nanotechnology* 17 (2006) 4285–4291.
97. O. K. Varghese, D. Gong, W. R. Dreschel, K. G. Ong, C. A. Grimes, Ammonia detection using nanoporous alumina resistive and surface acoustic wave sensors, *Sens. Actuat. B* 94 (2003) 27–35.

98. S. Kumari, A. P. Singh, Sonal, D. Deva, R. Shrivastav, S. Dass, V. R. Satsangi, Spray pyrolytically deposited nanoporous Ti^{4+} doped hematite thin films for efficient photoelectrochemical splitting of water, *Int. J. Hydrogen Energy* 35 (2010) 3985–3990.
99. A. B. Murphy, P. R. F. Barnes, L. K. Randeniya, I. C. Plumb, I. E. Grey, M. D. Horne, Efficiency of solar water splitting using semiconductor electrodes, *Int. J. Hydrogen Energy* 31 (2006) 1999–2017.
100. R. Shinar, J. H. Kennedy, Photoactivity of doped $\alpha\text{-Fe}_2\text{O}_3$ electrodes, *Sol. Energy Mater.* 6 (1982) 323–335.
101. K. L. Hardee, A. J. Bard, Semiconductor electrodes, V. The application of chemically vapor deposited iron oxide films to photosensitized electrolysis, *J. Electrochem. Soc.* 123 (1976) 1024–1026.
102. V. M. Aroutiounian, V. M. Arakelyan, G. E. Shahnazaryan, H. R. Hovhannisyanyan, Heli Wang, John A. Turner, Photoelectrochemistry of tin-doped iron oxide electrodes, *Sol. Energy* 81 (2007) 1369–1376.
103. Y. S. Hu, A. Kleiman-Shwarscstein, A. J. Forman, D. Hazen, J. N. Park, E. W. McFarland, Pt-doped $\alpha\text{-Fe}_2\text{O}_3$ thin films active for photoelectrochemical water splitting, *Chem. Mater.* 20 (2008) 3803–3805.
104. I. Cesar, A. Kay, J. A. G. Martinez, M. Grätzel, Translucent thin film Fe_2O_3 photoanodes for efficient water splitting by sunlight: Nanostructure-directing effect of Si-doping, *J. Am. Chem. Soc.* 128 (2006) 4582–4583.
105. A. Duret, M. Grätzel, Visible light-induced water oxidation on mesoscopic $\alpha\text{-Fe}_2\text{O}_3$ films made by ultrasonic spray pyrolysis, *Phys. Chem. B* 109 (2005) 17184–17191.
106. C. J. Sartoretti, B. D. Alexander, R. Solarska, I. A. Rutkowska, J. Augustynski, Photoelectrochemical oxidation of water at transparent ferric oxide film electrodes, *J. Phys. Chem. B* 109 (2005) 13685–13692.
107. K. R. Han, C. S. Kim, K. T. Kang, H. J. Koo, D. I. Kang, H. Jingwen, Study on sensing properties of tin oxide CO gas sensor with low power consumption, *Sens. Actuat. B Chem.* 81 (2002) 182–186.
108. S. D. Bakrania, C. Perez, M. S. Wooldridge, Methane-assisted combustion synthesis of nanocomposite tin dioxide materials, *P. Combust. Inst.* 31 (2007) 1797–1804.
109. J. Liu, F. Gu, Y. Hu, C. Li, Flame synthesis of tin oxide nanorods: A continuous and scalable approach, *J. Phys. Chem. C* 114 (2010) 5867–5870.
110. M. Nanu, J. Schoonman, A. Goossens, Nanocomposite three-dimensional solar cells obtained by chemical spray deposition, *Nano Lett.* 5 (2005) 1716–1719.
111. E. Thimsen, N. Rastgar, P. Biswas, Nanostructured TiO_2 films with controlled morphology synthesized in a single step process: Performance of dye-sensitized solar cells and photo watersplitting, *J. Phys. Chem. C* 112 (2008) 4134–4140.

112. J. Y. Chen, K. W. Sun, Growth of vertically aligned ZnO nanorod arrays as antireflection layer on silicon solar cells, *Sol. Energy Mater. Solar Cells* 94 (2010) 930–934.
113. Q. Zhang, C. S. Dandeneau, X. Zhou, G. Cao, ZnO Nanostructures for dye-sensitized solar cells, *Adv. Mater.* 21 (2009) 4087–4108.
114. E. Galoppini, J. Rochford, H. Chen, G. Saraf, Y. Lu, A. Hagfeldt, G. Boschloo, Fast electron transport in metal organic vapor deposition grown dye-sensitized ZnO nanorod solar cells, *J. Phys. Chem. B* 110 (2006) 16159–16161
115. H. Huang, O. K. Tan, Y. C. Lee, T. D. Tran, M. S. Tse, X. Yao, Semiconductor gas sensor based on tin oxide nanorods prepared by plasma-enhanced chemical vapor deposition with post plasma treatment, *Appl. Phys. Lett.* 87 (2005) 163123.
116. G. Yi, C. Wang, W. I. Park, ZnO nanorods: Synthesis, characterization and applications, *Semicond. Sci. Technol.* 20 (2005) 22–34.
117. J. Y. Park, I. O. Jung, J. H. Moon, B. Lee, S. S. Kim, Temperature induced shape change of highly aligned ZnO nanocolumns, *J. Cryst. Growth* 282 (2005) 353–358.
118. M. Krunk, E. Karber, A. Katerski, K. Otto, I. O. Acik, T. Dedova, A. Mere, Extremely thin absorber layer solar cells on zinc oxide nanorods by chemical spray, *Sol. Energy Mater. Sol. Cells* 94 (2010) 1191–1195.
119. S. D. Shinde, G. E. Patil, D. D. Kajale, V. B. Gaikwad, G. H. Jain, Synthesis of ZnO nanorods by spray pyrolysis for H₂S gas sensor, *J. Alloy. Compd.* 528 (2012) 109–114.
120. E. Arca, K. Fleischer, I. V. Shvets, Influence of the precursors and chemical composition of the solution on the properties of ZnO thin films grown by spray pyrolysis, *J. Phys. Chem. C* 113(50) (2009) 21074–21081.
121. W. M. Sears, M. A. Gee, Mechanics of film formation during the spray pyrolysis of tin oxide, *Thin Solid Films* 165(1) (1988) 265–77.
122. D. Beckel, A. Dubach, A. Studart, L. Gauckler, Spray pyrolysis of La_{0.6}Sr_{0.4}Co_{0.2}Fe_{0.8}O_{3-δ} thin film cathodes, *J. Electroceram.*, 16(3) (2006) 221–228.
123. R. Gallage, A. Matsuo, T. Watanabe, N. Matsushita, M. Yoshimura, Fabrication of transparent ceria films by spray deposition without post firing, *J. Electroceram.* 22(1) (2009) 33–39.
124. I. Kosacki, H. U. Anderson, Microstructure – Property relationships in nanocrystalline oxide thin films, *Ionics* 6 (2000) 294–311.
125. L. Tsakalagos, Nanostructures for photovoltaics, *Mater. Sci. Eng. R* 62 (2008) 175–189.
126. S. L. Castro, S. G. Bailey, R. P. Raffaele, K. K. Banger, A. F. Hepp, Nanocrystalline chalcopyrite materials (CuInS₂ and CuInSe₂) via low-temperature pyrolysis of molecular single-source precursors, *Chem. Mater.* 15 (2003) 3142–3147.
127. M. Mazzer, K. W. J. Barnham, I. M. Ballard, A. Bessiere, A. Ioannides, D. C. Johnson, M. C. Lynch, T. N. D. Tibbits, J. S. Roberts, G. Hill, C. Calder, Progress in quantum well solar cells, *Thin Solid Films* 511–512 (2006) 76–83.

128. R. P. Raffaele, S. L. Castro, A. F. Hepp, S. G. Bailey, Quantum dot solar cells, *Prog. Photovolt. Res. Appl.* 10 (2002) 433–439.
129. S. Phok, S. Rajaputra, V. P. Singh, Copper indium diselenide nanowire arrays by electrodeposition in porous alumina templates, *Nanotechnology* 18 (2007) 475601.
130. D. Derkacs, S. H. Lim, P. Matheu, W. Mar, E. T. Yu, Improved performance of amorphous silicon solar cells via scattering from surface plasmon polaritons in nearby metallic nanoparticles, *Appl. Phys. Lett.* 89 (2006) 093103.
131. A. K. Sharma, P. Rajaram, Nanocrystalline thin films of CuInS_2 grown by spray pyrolysis, *Mater. Sci. Eng. B* 172 (2010) 37–42.
132. M. A. M. Khan, S. Kumar, M. Ahamed, M. S. AlSalhi, Structural and electrical properties of spray deposited thin films of CuInS_2 nanocrystals, *Mater. Lett.* 68 (2012) 497–500.
133. H. Yoon, S. H. Na, J. Y. Choi, M. W. Kim, H. Kim, H. S. An, B. K. Min, S. Ahn, J. H. Yun, J. Gwak, K. Yoon, S. S. Kolekar, M. F. A. M. van Hest, S. S. Al-Deyab, M. T. Swihart, S. S. Yoon, Carbon- and oxygen-free Cu(InGa)(SSe)_2 solar cell with a 4.63% conversion efficiency by electrostatic spray deposition, *ACS Appl. Mater. Interfaces* 6 (2014) 8369–8377.
134. Y. Cai, J. C. W. Ho, S. K. Batabyal, W. Liu, Y. Sun, S. G. Mhaisalkar, L. H. Wong, Nanoparticle-induced grain growth of carbon-free solution processed CuIn(S,Se)_2 solar cell with 6% efficiency, *ACS Appl. Mater. Interfaces* 5 (2013) 1533–1537.
135. S. Ikeda, M. Nonogaki, W. Septina, G. Gunawan, T. Harada, M. Matsumura, Fabrication of CuInS_2 and Cu(In,Ga)S_2 thin films by a facile spray pyrolysis and their photovoltaic and photoelectrochemical properties, *Catal. Sci. Technol.*, 3 (2013) 1849–1854.
136. D. Yokoyama, T. Minegishi, K. Maeda, M. Katayama, J. Kubota, A. Yamada, M. Konagai, K. Domen, Photoelectrochemical water splitting using a Cu(In,Ga)Se_2 thin film, *Electrochem. Commun.* 12 (2010) 851–853.
137. E. Aydin, M. Sankir, N. D. Sankir, Conventional and rapid thermal annealing of spray pyrolyzed copper indium gallium sulfide thin films, *J. Alloy. Compd.* 615 (2014) 461–468.
138. David B. Mitzi, Oki Gunawan, Teodor K. Todorov, Kejia Wang, Supratik Guha, The path towards a high-performance solution-processed kesterite solar cell, *Sol. Energy Mater. Sol. Cells*, 95 (2011) 1421–1436.
139. N. Nakayama, K. Ito, Sprayed films of stannite $\text{Cu}_2\text{ZnSnS}_4$, *App. Surf. Sci.* 92 (1996) 171–175.
140. M. Valdés, G. Santoro, M. Vázquez, Spray deposition of $\text{Cu}_2\text{ZnSnS}_4$ thin films, *J. Alloy. Compd.* 585 (2014) 776–782.
141. W. Daranféd, M. S. Aida, N. Attaf, J. Bougdira, H. Rinnert, $\text{Cu}_2\text{ZnSnS}_4$ thin films deposition by ultrasonic spray pyrolysis, *J. Alloy. Compd.* 542 (2012) 22–27.
142. M. Espindola-Rodríguez, M. Placidi, O. Vigil-Galán, V. Izquierdo-Roca, X. Fontané, A. Fairbrother, D. Sylla, E. Saucedo, A. Pérez-Rodríguez,

- Compositional optimization of photovoltaic grade $\text{Cu}_2\text{ZnSnS}_4$ films grown by pneumatic spray pyrolysis, *Thin Solid Films* 535 (2013) 67–72.
143. X. Zeng, K.F. Tai, T. Zhang, C.W.J. Ho, X. Chen, A. Huan, T.C. Sum, L.H. Wong, $\text{Cu}_2\text{ZnSn}(\text{S},\text{Se})_4$ kesterite solar cell with 5.1% efficiency using spray pyrolysis of aqueous precursor solution followed by selenization, *Solar Energy Materials and Solar Cells*, 124 (2014) 55–60.
 144. I. Repins, C. Beall, Nirav Vora, C. DeHart, D. Kuciauskas, P. Dippo, B. To, J. Mann, W-C. Hsu, A. Goodrich, R. Noufi, Co-evaporated $\text{Cu}_2\text{ZnSnSe}_4$ films and devices, *Sol. Energy Mater. Sol. Cells*, 101 (2012) 154–159.
 145. T. Washio, T. Shinji, S. Tajima, T. Fukano, T. Motohiro, K. Jimbo, H. Katagiri, 6% Efficiency $\text{Cu}_2\text{ZnSnS}_4$ -based thin film solar cells using oxide precursors by open atmosphere type CVD, *J. Mater. Chem.* 22 (2012) 4021–4024.
 146. S. Huang, W. Luo and Z. Zou, Band positions and photoelectrochemical properties of $\text{Cu}_2\text{ZnSnS}_4$ thin films by the ultrasonic spray pyrolysis method, *J. Phys. D: Appl. Phys.* 46 (2013) 235108.
 147. D. S. Ginley, H. Hosono, D. C. Paine, Handbook of Transparent Conductors, Springer: New York, 2010.
 148. G. R. A. Kumara, C. S. K. Ranasinghe, E. N. Jayaweera, H. M. N. Bandara, M. Okuya, R. M. G. Rajapakse, Preparation of fluoride-doped tin oxide films on soda–lime glass substrates by atomized spray pyrolysis technique and their subsequent use in dye-sensitized solar cells, *J. Phys. Chem. C* 118 (2014) 16479–16485.
 149. V. M. Jimenez, A. R. Gonzalez-Elipe, J. P. Espinos, A. Justo, A. Fernandez, Synthesis of SnO and SnO_2 nanocrystalline powders by the gas phase condensation method, *Sens. Actuat. B* 31 (1996) 29–32.
 150. G. Korotcenkov, I. Boris, V. Brinzari, S. H. Han, B. K. Cho, The role of doping effect on the response of SnO_2 -based thin film gas sensors: Analysis based on the results obtained for Co-doped SnO_2 films deposited by spray pyrolysis, *Sens. Actuat. B* 182 (2013) 112–124.
 151. V. Brinzari, G. Korotcenkov, V. Golovanov, Factors influencing the gas sensing characteristics of tin dioxide films deposited by spray pyrolysis: Understanding and possibilities of control, *Thin Solid Films* 391 (2001) 167–175.
 152. C. Natarajan, N. Fukunaga, G. Nogami, Titanium dioxide thin film deposited by spray pyrolysis of aqueous solution, *Thin Solid Films* 322 (1998) 6–8.
 153. H. M. N. Bandara, R. M. G. Rajapakse, K. Murakami, G. R. R. A. Kumara, G. Anuradha Sepalage, Dye-sensitized solar cell based on optically transparent TiO_2 nanocrystalline electrode prepared by atomized spray pyrolysis technique, *Electrochem. Acta* 56 (2011) 9159–9161.
 154. P. J. Cameron, L. M. Peter, Characterization of titanium dioxide blocking layers in dye-sensitized nanocrystalline solar cells, *J. Phys. Chem. B* 10 (2003) 14394–14400.
 155. U. Bach, D. Lupo, P. Comte, J. E. Moser, F. Weissörtel, J. Salbeck, H. Spreitzer, M. Gratzel, Solid-state dye-sensitized mesoporous TiO_2 solar cells with high photon-to-electron conversion efficiencies, *Nature* 395 (1998) 583–585.

156. A. Rothschild, F. Edelman, Y. Komem, F. Cosandey, Sensing behavior of TiO_2 thin films exposed to air at low temperatures, *Sens. Actuat. B* 67 (2000) 282–289. A. Watanabe, H. Kozuka, Photoanodic properties of sol-gel-derived Fe_2O_3 thin films containing dispersed gold and silver particles, *J. Phys. Chem. B* 107 (2003) 12713–12720.
157. A. M. More, J. L. Gunjekar, C. D. Lokhande, Liquefied petroleum gas (LPG) sensor properties of interconnected web-like structured sprayed TiO_2 films, *Sens. Actuat. B* 129 (2008) 671–677.
158. L. A. Patil, D. N. Suryawanshi, I. G. Pathan, D. M. Patil, Nickel doped spray pyrolyzed nanostructured TiO_2 thin films for LPG gas sensing, *Sens. Actuat. B* 176 (2013) 514–521.
159. R. Ondo-Ndong, F. Pascal-Delannoy, A. Boyer, A. Giani, A. Foucaran, Structural properties of zinc oxide thin films prepared by r.f. magnetron sputtering, *Mater. Sci. Eng. B* 97 (2003) 68–73.
160. J. Lee, K. Ko, B. Park, Electrical and optical properties of ZnO transparent conducting films by the sol-gel method, *J. Cryst. Growth* 247 (2003) 119–125.
161. Z. Y. Wu, J. H. Cai, G. Ni, ZnO films fabricated by chemical bath deposition from zinc nitrate and ammonium citrate tribasic solution, *Thin Solid Films* 516 (2008) 7318–7322.
162. R. Al Asmar, G. Ferblantier, F. Mailly, P. Gall-Borrut, A. Foucaran, Effect of annealing on the electrical and optical properties of electron beam evaporated ZnO thin films, *Thin Solid Films* 473 (2005) 49–53.
163. T. Pauporté, D. Lincot, Electrodeposition of semiconductors for optoelectronic devices: results on zinc oxide, *Electrochim. Acta* 45 (2000) 3345–3353.
164. E. Bacaksiz, M. Parlak, M. Tomakin, A. Özçelik, M. Karakız, M. Altunbaş, The effects of zinc nitrate, zinc acetate and zinc chloride precursors on investigation of structural and optical properties of ZnO thin films, *J. Alloy. Compd.* 466 (2008) 447–450.
165. M. Krunk, T. Dedova, I. Oja Açıık, Spray pyrolysis deposition of zinc oxide nanostructured layers, *Thin Solid Films* 515 (2006) 1157–1160.
166. R. Romero, D. Leinen, E. A. Dalchiele, J. R. Ramos-Barrado, F. Martín, The effects of zinc acetate and zinc chloride precursors on the preferred crystalline orientation of ZnO and Al-doped ZnO thin films obtained by spray pyrolysis, *Thin Solid Films* 515 (2006) 1942–1949.
167. T. V. Vimalkumar, N. Poornima, C. Sudha Kartha, K. P. Vijayakumar, Effect of precursor medium on structural, electrical and optical properties of sprayed polycrystalline ZnO thin films, *Mater. Sci. Eng. B* 175 (2010) 29–35.
168. T. Minami, Transparent conducting oxide semiconductors for transparent electrodes, *Semicond. Sci. Technol.* 20 (2005) 35–44.
169. M. Kaelin, D. Rudmann, A. N. Tiwari, Low cost processing of CIGS thin film solar cells, *Sol. Energy* 77 (2004) 749–756.
170. G. Kenanakis, N. Katsarakis, E. Koudoumas, Influence of precursor type, deposition time and doping concentration on the morphological, electrical

- and optical properties of ZnO and ZnO:Al thin films grown by ultrasonic spray pyrolysis, *Thin Solid Films* 555 (2014) 62–67.
171. F. Z. Bedia, A. Bedia, M. Aillerie, N. Maloufi, F. Genty, B. Benyoucef, Influence of Al-doped ZnO transparent contacts deposited by a spray pyrolysis technique on performance of HIT solar cells, *Energy Procedia* 50 (2014) 853–861.
 172. S. S. Shinde, P. S. Shinde, Y. W. Oh, D. Haranath, C. H. Bhosale, K. Y. Rajpure, Structural, optoelectronic, luminescence and thermal properties of Ga-doped zinc oxide thin films, *App. Surf. Sci.* 258 (2012) 9969–9976.
 173. V. R. Shinde, T. P. Gujar, C. D. Lokhande, LPG sensing properties of ZnO films prepared by spray pyrolysis method: Effect of molarity of precursor solution, *Sens. Actuat. B* 120 (2007) 551–559.
 174. P. S. Shewale, G. L. Agawane, S. W. Shin, A. V. Moholkar, J. Y. Lee, J. H. Kim, M. D. Uplane, Thickness dependent H₂S sensing properties of nanocrystalline ZnO thin films derived by advanced spray pyrolysis, *Sens. Actuat. B* 177 (2013) 695–702.
 175. A. Chirila, P. Reinhard, F. Pianezzi, P. Bloesch, A. R. Uhl, C. Fella, L. Kranz, D. Keller, C. Gretener, H. Hagendorfer, D. Jaeger, R. Erni, S. Nishiwaki, S. Buecheler, A. N. Tiwari, Potassium-induced surface modification of Cu(In,Ga)Se₂ thin films for high-efficiency solar cells, *Nat. Mater.* 12 (2013) 1107–1111.
 176. I. Repins, M. A. Contreras, B. Egaas, C. DeHart, J. Scharf, C. L. Perkins, B. To, R. Noufi, 19.9%-Efficient ZnO/CdS/CuInGaSe₂ solar cell with 81.2% fill factor, *Prog. Photovoltaics: Res. Appl.* 16 (2008) 235–239.
 177. A. A. Yadav, E. U. Masumdar, Photoelectrochemical investigations of cadmium sulphide (CdS) thin film electrodes prepared by spray pyrolysis, *J. Alloy. Compd.* 509 (2011) 5394–5399.
 178. P. Raji, C. Sanjeeviraja, K. Ramachandran, Thermal and structural properties of spray pyrolysed CdS thin film, *Bull. Mater. Sci.* 28 (2005) 233–238.
 179. D. R. Acosta, C. R. Magan, A. I. Martinez, A. Maldonado, Structural evolution and optical characterization of indium doped cadmium sulfide thin films obtained by spray pyrolysis for different substrate temperatures, *Sol. Energy Mater. Sol. Cells* 82 (2004) 11–20.
 180. L. Bhira, H. Essaidi, S. Belgacem, G. Couturier, J. Salardenne, N. Barreaux, J. C. Bernede, *Phys. Stat. Sol. (a)* 181 (2000) 427–435.
 181. E. Kärber, K. Otto, A. Katerski, A. Mere, M. Krunks, Raman spectroscopic study of In₂S₃ films prepared by spray pyrolysis, *Mater. Sci. Semicond. Process.* 25 (2014) 137–142.
 182. R. Jayakrishnan, T. T. John, C. S. Kartha, K P Vijayakumar, T. Abe, Y. Kashiwaba, Defect analysis of sprayed β-In₂S₃ thin films using photoluminescence studies, *Semicond. Sci. Technol.* 20 (2005) 1162–1167.
 183. M. Calixto-Rodriguez, A. Tiburcio-Silver, A. Ortiz, A. Sanchez-Juarez, Optoelectronic properties of indium sulfide thin films prepared by spray pyrolysis for photovoltaic applications, *Thin Solid Films* 480–481 (2005) 133–137.

184. S. Buecheler, D. Corica, D. Guettler, A. Chirila, R. Verma, U. Müller, T. P. Niesen, J. Palm, A. N. Tiwari, Ultrasonically sprayed indium sulfide buffer layers for $\text{Cu}(\text{In,Ga})(\text{S,Se})_2$ thin-film solar cells, *Thin Solid Films* 517 (2009) 2312–2315.
185. E. Aydin, M. Sankir, N. D. Sankir, Influence of silver incorporation on the structural, optical and electrical properties of spray pyrolyzed indium sulfide thin films, *J. Alloy. Compd.* 603 (2014) 119–124.
186. J. H. Bang, R. J. Hehnich and K. S. Suslick, Nanostructured ZnS:Ni^{2+} photocatalysts prepared by ultrasonic spray pyrolysis, *Adv. Mater.* 20 (2008) 2599–2603.
187. S. H. Sohn, Y. Hamakawa, Excitation and deexcitation of ac-driven thin-film ZnS electroluminescent devices, *J. Appl. Phys.* 72 (1992) 2492–2504.
188. Y. P. Fu, N. A. Allsop, S. E. Gledhill, T. Kohler, M. Kruger, R. Saez-Araoz, U. Block, M. C. Lux-Steiner, C. H. Fischer, ZnS nanodot film as defect passivation layer for $\text{Cu}(\text{In,Ga})(\text{S,Se})_2$ thin-film solar cells deposited by spray-ILGAR (ion-layer gas reaction), *Adv. Energy Mater.* 1 (2011) 561–564.
189. L. Isac, I. Popovici, A. Enesca, A. Duta, Copper sulfide (Cu_xS) thin films as possible p-type absorbers in 3D solar cells, *Energy Procedia* 2 (2010) 71–78.
190. L. Isac, A. Duta, A. Kriza, S. Manolache, M. Nanu, Copper sulfides obtained by spray pyrolysis – Possible absorbers in solid-state solar cells, *Thin Solid Films* 515 (2007) 5755–5758.
191. L. Andronic, L. Isac, A. Duta, Photochemical synthesis of copper sulphide/titanium oxide photocatalyst, *J. Photochem. Photobiol. A Chem.* 221 (2011) 30–37.
192. L. Reijnen, B. Meester, A. Goossens, J. Schoonman, Nanoporous $\text{TiO}_2/\text{Cu}_{1.8}\text{S}$ heterojunctions for solar energy conversion, *Mater. Sci. Eng. C* 19 (2002) 311–314.

Multifunctional Spinel Ferrite Nanoparticles for Biomedical Application

Noppakun Sanpo¹, Cuie Wen², Christopher C. Berndt^{1,3} and James Wang^{*,1}

¹*Faculty of Science, Engineering and Technology, Swinburne University of Technology, Hawthorn, Victoria, Australia*

²*Aerospace and Manufacturing Engineering, RMIT University, Bundoora, Victoria, Australia*

³*Materials Science and Engineering, Stony Brook University, Stony Brook, NY, USA*

Abstract

This chapter is organized into six major parts. The first part introduces the synthesis of transition metal-substituted cobalt ferrite nanoparticles, the use of citric acid (CA) as a chelating agent in the sol-gel method, and applications of spinel ferrite nanoparticles in biomedical fields. The second part provides an overview of the structure and magnetism of spinel ferrites. The third part examines the sol-gel synthesis of ceramic nanoparticles. The fourth part presents a summary of organic acid chelating agents, with special reference to CA. The fifth part looks at the preparation of cobalt ferrite and transition metal-substituted cobalt ferrite nanoparticles ($\text{Co}_{0.5}\text{X}_{0.5}\text{Fe}_2\text{O}_4$ with $X = \text{Cu, Zn, Mn or Ni}$) by sol-gel methods. The final section highlights the influence of transition metal substitution on the physical and antibacterial properties of cobalt ferrite nanoparticles. A discussion on the biocompatibility of spinel ferrite nanoparticles is presented.

Keywords: Spinel ferrite, biocompatibility, antibacterial properties, sol-gel, transition metals, nanoparticles

4.1 Introduction

Metal-oxide nanoparticles are of interest because of their unique optical, electronic and magnetic properties. Cobalt ferrite (CoFe_2O_4) nanoparticles have high permeability, good saturation magnetization and no preferred

*Corresponding author: jawang@swin.edu.au

direction of magnetization. They are magnetically “soft”, being easily magnetized and demagnetized, and electrically insulating [1]. These properties, along with their physical and chemical stability, make them suitable for magnetic recording applications, such as audio and video tapes, and high-density digital recording disks [2]. The magnetic character of the particles used for recording media depends crucially on the size, shape and purity of the nanoparticles [3]. The coercivity of Fe_3O_4 nanoparticles, which strongly influences the recording performance, has been enhanced by doping cobalt into these nanoparticles [4] or forming a cobalt coating [5]. The substitution of the Co^{2+} ion that is present in cobalt ferrite with Zn^{2+} , Ni^{2+} , Cr^{2+} or Cu^{2+} allows variations in their properties that can be tuned to specific applications.

Vaidyanathan *et al.* [6] demonstrated that when Co^{2+} was substituted with Zn^{2+} in CoFe_2O_4 , the new $\text{Co}_x\text{Zn}_{(1-x)}\text{Fe}_2\text{O}_4$ nanoparticles exhibited enhanced properties; e.g. excellent chemical stability, high corrosion resistance, magneto-crystalline anisotropy, magnetostriction and magneto-optical characteristics. Singhal *et al.* [7] studied nickel-substituted cobalt ferrite nanoparticles produced by an aerosol route. The results showed that the lattice parameter of nanoparticles decreased linearly with an increase in nickel concentration, which could be attributed to the smaller ionic radius of Ni^{2+} compared to Co^{2+} . Moreover, the increase in nickel concentration decreased the saturation magnetization because the relatively high orbital contribution of the Ni^{2+} to the magnetic moment of Co^{2+} induces large anisotropy.

Paulsen *et al.* [8] studied manganese-substituted cobalt ferrite magnetostrictive materials for magnetic stress sensor applications. The measurement indicated that substituting manganese for some of the iron in the cobalt ferrite can lower the Curie temperature of the material while maintaining suitable magnetostriction for stress sensing applications. These results demonstrated the possibility of optimizing the magnetomechanical hysteresis of cobalt ferrite-based composites for stress sensor applications through control of the Curie temperature.

Jadhav *et al.* [9] synthesized zinc-substituted cobalt ferrite nanoparticles by using a wet chemical coprecipitation technique. They found that all the samples exhibit ferromagnetic behavior, which decreases with the substitution of Zn^{2+} ions. Curie temperature decreases with the increasing substitution of Zn^{2+} ions, which is attributed to a decrease in magnetic linkages between tetrahedral and octahedral sites.

Magnetic iron oxide nanoparticles are the subject of much research because of their possible application in areas such as biomedical engineering and diagnostics [10]. In the last three decades, the application of some magnetic iron oxide nanoparticles (maghemite, $\gamma\text{-Fe}_2\text{O}_3$ or magnetite,

Fe_3O_4) in the topical area of *in vitro* diagnostics has increased. The stabilization of the ferrofluid is achieved by optimizing the electrostatic repulsions of similarly charged surfaces. Coating of the magnetic nanoparticles with biocompatible polymers has drawn recent interest [11] with the aim to form a stable non-toxic aqueous dispersion of magnetic iron oxide nanoparticles. However, using such magnetic nanoparticles for biological and medical purposes remains a challenge.

The magnetic nanoparticles need modification to increase the biocompatibility and bacterial activity before implementation for drug delivery applications. For example, coating a silver thin film onto Fe_3O_4 nanoparticles can improve bacterial activity; as well as benefiting the paramagnetic properties of the nanostructures so that they can be recovered and recycled from the site of action by means of an external magnetic field [12]. Moreover, oleic acid was used as a surfactant coating for Fe_3O_4 nanoparticles, followed by an adsorption-coating with four different antibiotics (cephalosporins) [13]. The nanofluid only acts as a carrier for the antibiotic. Moreover, the small size of the magnetic nanoparticles allows delivery of an antibiotic when targeting organs such as the brain and kidney.

Iconaru *et al.* [14] investigated the biocompatibility of magnetic iron oxide nanoparticles doped with dextran thin films that were produced by the spin coating deposition of a solution. It was established that osteoblast cells adhered very well to dextran thin films obtained from targets containing 1 and 5 wt.% maghemite and exhibited a normal actin cytoskeleton, which suggested that these cells underwent normal cell cycle progression. The data strongly suggested the potential use of iron oxide-dextran nanocomposites as a potential marker for biomedical applications.

Li *et al.* [15] studied the biocompatibility of the core-shell $\text{Fe}_3\text{O}_4/\text{Au}$ composite magnetic nanoparticles, which have potential applications in tumour hyperthermia. The results showed that $\text{Fe}_3\text{O}_4/\text{Au}$ composites appear to be highly biocompatible and safe nanoparticles according to the evaluation of toxicity *in vivo* and *in vitro*. Considering that some of the Food and Drug Administration-approved MRI contrast agents are made of Fe_3O_4 ; $\text{Fe}_3\text{O}_4/\text{Au}$ composites have potential as safe optical and thermal agents; allowing the combination of cancer detection and cancer-specific hyperthermic treatment. The results of this study provided an experimental foundation for further clinical research and evaluation of this promising material.

Chen *et al.* [16] demonstrated the concept of hollow core/shell structured mesoporous nanocapsules as multifunctional drug delivery systems (DDSs). Ellipsoidal $\text{Fe}_3\text{O}_4\text{-mSiO}_2$ nanocapsules were used as an example of a promising platform for simultaneous drug delivery and cell imaging.

Chelating agents are used in inorganic chemistry to prevent particle agglomeration by reducing condensation reactions in liquid phase synthesis. They have been proven to control the cobalt ferrite phase in sol-gel chemical synthesis [17]. Chelating agents can function as good selective flocculants because of their metal specificity and selectivity. From the synthesis point of view, chelating agents present advantages over conventional mineral processing in terms of metal selectivity. There are many reagents that may be used with chelating agents in specific applications because of the variation in major donor atoms which are sulphur, nitrogen, oxygen and phosphorus. It is important to understand the chemical behaviour of donors to predict the properties of chelating groups. Normally the choice of a chelating agent or a group is made on the basis of its function in analytical metal separations.

Most of the chelating groups form the necessary chemical complexes with almost all of the transition and many non-transition metals and, therefore, specificity is not as qualified as for selective adsorption on minerals. The selectivity is determined by consideration of differences in stability constants and chelate formation under various solution conditions. Moreover, the contribution from the donor atoms as they are located in the mineral lattice has to be considered in obtaining the selectivity. Also, the solubility of the mineral, in addition to that of the metal chelate, has a pronounced influence on the selectivity and the collection power of the chelating agent.

Sol-gel techniques offer enhanced control over homogeneity, elemental composition and powder morphology. As well, uniformly nano-sized metal clusters can be achieved, which are crucial for enhancing the properties of the nanoparticles. These advantages make the sol-gel route a favourable alternative to other conventional methods for the preparation of ceramic oxide composites [18].

Therefore, the objectives of this chapter are fourfold. The first objective is to develop novel multifunctional magnetic iron-based nanoparticles that also exhibit biocompatible and antibacterial properties to fulfil the requirements of a DDS. The second is to synthesize transition metal-substituted cobalt ferrite nanoparticles ($\text{Co}_{0.5}\text{X}_{0.5}\text{Fe}_2\text{O}_4$ with $\text{X} = \text{Cu}, \text{Zn}, \text{Mn}$ or Ni) by the sol-gel process using citric acid (CA) as the chelating agent. The third is to investigate the effect of substitution of these transition metals on surface morphology, size distribution and antibacterial properties of the synthesized transition metals-substituted cobalt ferrite nanoparticles. The last objective is to discuss the biocompatibility of spinel nanoparticles and explore their future applications.

4.2 Ferrites

Ferrites are well-known ferrimagnetic materials that consist mainly of ferrimagnetic oxides and, therefore, are electrically insulating. Ferrites are widely used in high-frequency applications because an alternating current field does not induce undesirable eddy currents in an insulating material [19].

Ferrites have two structural symmetries that are determined by the size and charge of the metal ions, which balance the charge of the oxygen ions and their relative amount [20].

4.2.1 Cubic Ferrites

Cubic ferrite has the general formula $MO.Fe_2O_3$ where M is a divalent metal ion. These ferrites crystallize in the spinel structure and the spinel lattice is composed of a close packed oxygen arrangement in which 32 oxygen ions form the unit cell. These anions are packed in a face centred cubic (FCC) arrangement leaving two types of space between anions: tetrahedrally coordinated sites (A), surrounded by four nearest oxygen atoms; and octahedrally coordinated sites (B), surrounded by six nearest neighbour oxygen atoms. These are illustrated in Figure 4.1. In total, there are 64 tetrahedral sites and 32 octahedral sites in the unit cell, of which only 8 tetrahedral sites and 16 octahedral sites are occupied, resulting in a structure that is electrically neutral [20].

The localization of ions either in the A or B sites depends fundamentally on the ion and lattice sizes, as well as the temperature and the orbital preference for specific coordination. In general, divalent ions are larger than trivalent ions (Table 4.1). The trivalent ion nuclei produce greater

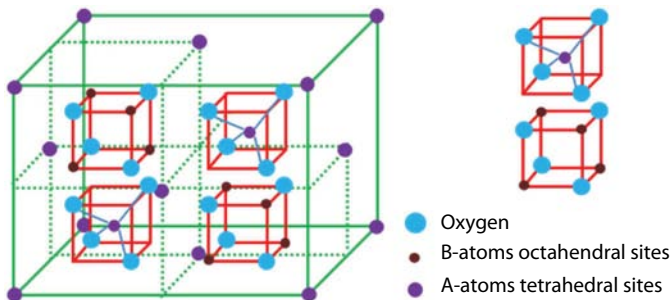


Figure 4.1 The unit cell structure of spinel ferrite.

electrostatic attraction, hence their electron orbits contract. The octahedral sites are larger than the tetrahedral sites and, thus, the divalent ions are localized in the octahedral sites whereas trivalent ions are located in the tetrahedral sites [20].

Some properties of the ferrites can be enhanced by incorporation of divalent metallic ions inside their structure. In the case of cobalt ferrite, the incorporation of cobalt ions results in an increase in coercivity due to an increased magnetocrystalline anisotropy resulting from the coupling of the spins of the cobalt and iron ions [2]. Cobalt ferrite (CoFe_2O_4) is a cubic ferrite with an inverse spinel structure where Co^{2+} ions are located in B sites and Fe^{3+} in the A and B sites. This ferrite is characterized by having an anisotropy constant higher than ferrites such as magnetite and maghemite, Table 4.2. The anisotropy constant of bulk cobalt ferrite is in the range of $1.8\text{--}3.0 \times 10^6$ erg/cm³ and the saturation magnetization is 80.8 emu/g at room temperature and 93.9 emu/g at 5 K [21].

It has been observed that the magnitude of magnetic properties depends on the particle size. A decrease in particle size results in a decrease in coercivity and saturation magnetization, whereas the susceptibility and anisotropy constant have been reported to increase [22].

Table 4.1 Radii of metal ions commonly involved in spinel ferrites.

Ion	Ionic Radius (Å)
Fe^{2+}	0.83
Fe^{3+}	0.67
Co^{2+}	0.82
Zn^{2+}	0.74
Ni^{2+}	0.78
Mn^{3+}	0.70

Table 4.2 Anisotropy constants of some ferrites [20].

Ferrite	Anisotropy Constant K_1 (erg/cm ³)
FeFe_2O_4	-1.1×10^3
$\text{Co}_{0.8}\text{Fe}_{2.2}\text{O}_4$	3.9×10^6
MnFe_2O_4	-28×10^3
$\text{Co}_{0.3}\text{Mn}_{0.4}\text{Fe}_2\text{O}_4$	1.1×10^6

4.2.2 Hexagonal Ferrites

Hexagonal ferrites are widely used as permanent magnets and are characterized by possessing a high coercivity [23]. Their general formula is $MO.6Fe_2O_3$, where M can be Ba, Sr or Pb. The hexagonal ferrite lattice is similar to the spinel structure, with the oxygen ions closely packed, but some layers include metal ions, which exhibit similar ionic radii as the oxygen ions. This lattice has three different sites occupied by metals: tetrahedral, octahedral and trigonal bipyramid.

4.3 The Sol–Gel Method

4.3.1 The Sol–Gel Processing Method

Sol–gel processing is a chemical engineering technique to manufacture ceramic powders, especially oxides. The term *sol* refers to the initial solution of the chemical components from which the final powder will eventually be derived. *Gel* is a term used to describe the final product of the ceramic material. The methods are based on mixing solutions that enable reactions for the formation of distinct particles. It is important to note that the particles are not precipitated from solution; rather, the mechanism of particle production is based on colloidal science in which the particles are suspended in the liquid. Typical ceramic powders that are produced by this technique include chromia [24], alumina [25], cobalt ferrite [17] and ceramic alloys of stabilized zirconia [26].

The most broadly used synthetic technique for bulk metal oxides is the ceramic method that is based on the direct reaction of powder mixtures. The diffusion of the atomic or ionic species is controlled through the reactants and products. These solid state processes require high temperature and small particle sizes to bring the reaction partners sufficiently close together and to provide high mobility. The reaction conditions lead to thermodynamically stable phases, preventing the formation of metastable solids. There are various products that can be collected from the sol–gel process (Figure 4.2) and these depend on the synthesizing route.

Sol–gel procedures were successful in the preparation of bulk metal oxides (e.g. ceramics, glasses, films and fibres) [27] and, therefore, they have been applied for nanoparticle synthesis. Liquid-phase routes represent the most promising alternatives for the size- and shape-controlled synthesis of nanoparticles [28]. The number of oxide nanoparticles obtained by sol–gel chemistry is small compared to the variety of compounds obtained *via* powder routes [18].

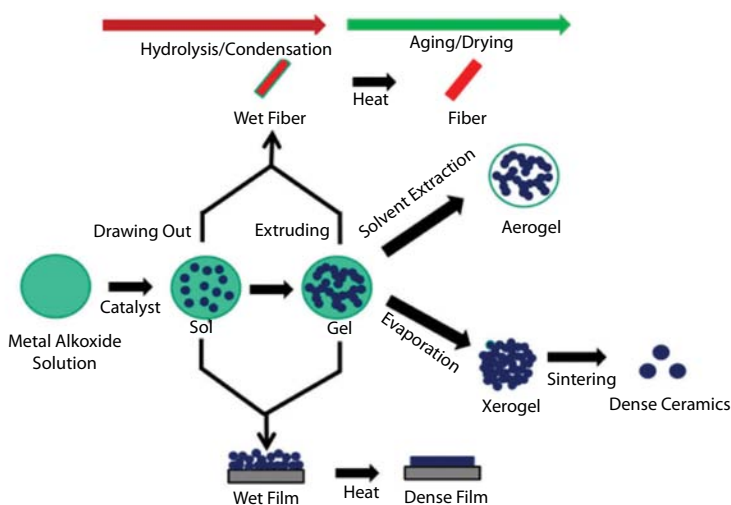


Figure 4.2 Various steps in the sol-gel process to control the final morphology of the product. The steps can be grouped into (i) hydrolysis/condensation and (ii) aging/drying stages.

A synthesis protocol developed for a bulk metal oxide may not be directly accommodated to its corresponding counterpart on the nanoscale. The reasons for this observation are manifold. Aqueous sol-gel chemistry is complex due to the high reactivity of the metal oxide precursors towards water and the double role of water as ligand and solvent. On the other hand, there are many reaction parameters that must be controlled (e.g. hydrolysis and condensation rate of the metal oxide precursors, the pH and temperature, the method of mixing, the rate of oxidation and the nature and concentration of anions) to provide good reproducibility of the synthesis protocol [29].

Another fundamental problem of aqueous sol-gel chemistry is that the as-synthesized precipitates are generally amorphous. The required post-synthetic annealing step to induce the crystallization process prevents fine control over crystal size and shape. These limitations play a minor role for the preparation of bulk oxides; however, they are major issues in the case of nanoparticle synthesis.

Nonaqueous (or non-hydrolytic) sol-gel processes in organic solvents are able to overcome some of the major limitations of aqueous systems [30]. The advantages are a direct consequence of the role of the organic components in the reaction system that act as (i) a solvent, (ii) an organic ligand of the precursor molecule, (iii) a surfactant that enables chemical

reaction or (iv) permits the *in situ* formation of organic condensation products. The organic components behave as an oxygen supplier for oxide formation and determine strongly the particle size and shape as well as the surface properties due to their coordination properties. However, they moderate reactivity of the oxygen to carbon bond, which results in slower reaction rates.

The nonaqueous synthesis routes yield metal oxide nanoparticles with uniform, yet complex crystal morphologies with crystallite sizes of just a few nanometres, and good dispersibility in the organic phase. Another important point is the fact that the chemistry of the oxygen-carbon bond is well-known from organic chemistry. This aspect is significant considering the fundamental role of organic reaction pathways in nonaqueous sol-gel chemistry. In parallel to the formation of the inorganic nanoparticles, the organic species undergo transformation reactions [31]. It is possible to correlate the processes leading to these organic species by analyzing the growth mechanisms of the oxide nanoparticles.

4.3.1.1 Processing Steps for the Sol-Gel Route

The sol-gel process consists of the following 6 prime steps (Figure 4.3).

- i. Preparation of a homogeneous solution either by dissolution of metal organic precursors in an organic solvent that is miscible with water, or by dissolution of inorganic salts in water.
- ii. Conversion of the homogeneous solution into a sol by treatment with a suitable reagent that is generally water with, or without, an acid base.
- iii. Aging of the solution.
- iv. Shaping of the gel.
- v. Thermal treatment or sintering of the final product.
- vi. Classification into appropriate particle size for the intended application.

Step (i) – The components are placed into solution. The liquid component is usually water or an alcohol. The solute is either an inorganic nitrate chloride or based on metal-organic compounds. These components allow thorough mixing of the species on the atomic scale, explaining the excellent homogeneous compositions that are obtained. This solution is often referred to as the “precursor” since it is the basis of the following steps that lead to the final powder.

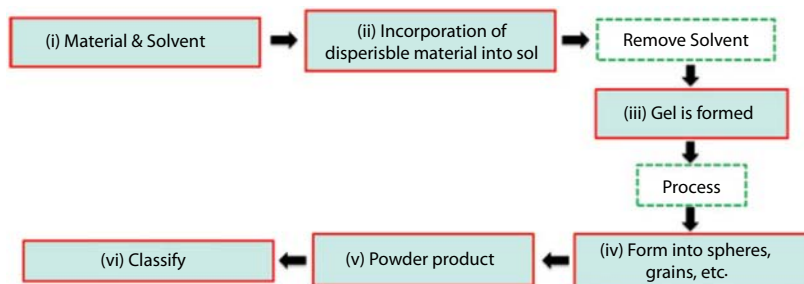


Figure 4.3 The production steps for a sol-gel production route.

Step (ii) – The above solution, if it is not already a sol, is converted to a sol. A sol is a colloidal dispersion (or a dispersed solid phase) that contains particles smaller than about 150 nm (0.15 μm or 5.9×10^{-8} in.). The sol can be made stable by pH adjustment. Otherwise, the particles will grow to agglomerates that may precipitate and, thereby, not enable the unique powder chemistries to be obtained.

Step (iii) – The gelation step occurs next. This is essentially a step to remove most of the solvent (water or alcohol) so that a rigid body of well-defined chemistry is formed. The gel is still quite plastic or highly viscous. The processing variables are pH, temperature and time.

Step (iv) – The gel is shaped to the required morphology. This may be as spheres, fibres or coatings. Thermal spray powders of spherical morphology are produced by a process called spray drying. These morphologies may also be produced by controlling the gelation stage in the conventional process.

Step (v) – The remaining solvent is removed and the gel is calcined to form the final powder. This final temperature is significantly lower than the temperatures of conventional processing methods. For example, silica can be calcined from 600°C to 1,000°C (1,110°F to 1,830°F) rather than 1,300°C to 1,400°C.

Step (vi) – Conventional sieving is performed to obtain the required particle size distribution for the intended application.

4.3.1.2 Controlling the Properties of the Gel

The control of the gel properties can be listed into four distinct areas:

- (i) The pore structure, specific surface area, micropore volume and other features that control density.
- (ii) The elemental composition of the gel. Possibilities of incorporating metal, metal-oxide or non-metal functional modifiers.

- (iii) The morphology of the product; for example, the synthesis of monolithic pieces, spheres, layers, coverings, foams and membranes.
- (iv) Regulating macroscopic properties such as opacity, density and fracture resistance.

The issue of tailoring the pore volume and specific surface area of the sol-gel process is complex because there are several specific factors that control the properties of final products; e.g. temperature, pressure, pH, water-to-Si ratio, ageing and drying time. The above process variables are related to the hydrolysis and condensation reactions arising during the sol-gel process. Fast condensation leads to compact, dense, low-area structures; while rapid hydrolysis accompanied by moderate condensation speed gives rise to open, irregular, porous matrices. Any of the synthesis parameters may act as an effective modifier factor as long as it changes the absolute or relative rates of these two competing reactions.

Jones *et al.* [32] performed a comprehensive study on the dependence of pore characteristics on the preparation conditions of sol-gel derived aluminosilicates. Their method was to take a default tetraethylorthosilicate (TEOS)-based acid catalyzed hydrolysis reaction, and synthesis a series of gels changing one parameter a time. They found that if the Al-to-Si ratio increases, the solvent (ethanol) content or the pH results in a decrease in the specific surface area of the products. Increasing the H₂O-to-Si ratio, on the other hand, results in higher BET surfaces. In addition, porosity and total pore volume change in line with the BET surface. However, micropore volume seems to follow the opposite trend: the lower the surface area, the higher the contribution of micropores to the total pore volume. Moreover, increasing the size of the alkyl group of the solvent alcohol or the number of -OH groups per molecule increases the BET area, pore volume and porosity, but decreases the micropore volume.

Toba *et al.* [33] studied the properties of titanosilicates prepared by various synthesis techniques. They found that the complexing agent (1,6-hexanediol) produced the most homogeneous samples and offered (chiefly *via* changing the Ti/Si ratio) the greatest control over pore system characteristics.

The ageing step during the sol-gel process is the key factor to predict the properties of the final products. Ageing is identified when a gel is maintained in pores and its structure and properties continue to change long after the gel point. Four processes can occur during ageing: (i) polycondensation, (ii) syneresis, i.e. shrinkage of the gel accompanied by the expulsion of liquid from the gel pores, (iii) coarsening and (iv) phase transformation.

The optimization and mechanism of the ageing process are poorly understood [27].

The next important step in sol-gel synthesis is drying, which can be performed either under supercritical conditions, at elevated temperatures, or decreased pressures. Scherer *et al.* [34] discovered a co-operative effect between the synthesis pH and the drying parameters (e.g. solvent type, washing solvent type) of aerogels. They found that surface area, pore size and pore volume decreased as the surface tension of the liquid to be removed from base-catalyzed aerogels increased. On the other hand, micropore surface area and pore volume increase considerably in the case of acid-catalyzed gelation steps. They explained this phenomenon by pointing out that the higher the surface tension at the liquid-vapour interface, then the higher the capillary pressure within the pore. When the pressure exceeds a certain threshold value, the gel network loses its integrity. Acid catalyzed gels are less highly cross-linked than base catalyzed ones; therefore, the same surface tension values correspond to the breaking of different pores in their case.

The last step in a typical sol-gel process is a high temperature treatment called densification or calcination. It is considered one of the most important factors that controls the morphology and the particle size of the final product. The calcination rate depends on maximum temperature, heating rate and atmosphere (inert or oxidizing). In the first stage of the heating process (up to 300–400°C) water and volatile organics are removed from the gel. This process is generally accompanied by an increase in the specific surface area. Surface area diminishes in the second stage (up to 800–1000°C) because of capillary contraction, condensation and sintering. This change is caused by the gel-to-glass transition, which is driven by the higher free energy of gels. In the final stage, once the gel-to-glass transition is complete, the structure and properties of the material are indistinguishable from those of a conventional melt-derived glass [35].

4.3.2 Applications

Sol-gel derived ceramics are useful for heterogeneous catalytic applications since they have replaced commercial catalysts such as amorphous sol-gel silica instead of normal silica, silica-alumina composites instead of zeolites and so on. Although such common examples do not claim scientific attention; they can be of interest because their pore system or their morphological features are special.

Sol-gel derived mixed oxides, on the other hand, have been prepared successfully; for example, oxides such as alumina-silica, titania-silica, $\text{Fe}_2\text{O}_3\text{-SiO}_2$,

$\text{ZrO}_2\text{-SiO}_2$, $\text{BaO-Al}_2\text{O}_3$ and $\text{La}_2\text{O}_3\text{-Al}_2\text{O}_3$ [36]. Even though the objectives of these studies are quite different, their common feature is that they use the control over homogeneity, elemental composition and sample morphology offered by the sol-gel technique. Final products are usually compared to those synthesized by conventional methods such as co-precipitation and the sol-gel materials are often superior in certain respects.

The achievement of manufacturing very small and uniform metal cluster sizes [18] endows the sol-gel process as a favourable alternative to conventional two-step impregnation methods for the preparation of metal/metal-oxide composites. Mixing can be performed at the atomic level; therefore, the resulting materials are of considerable interest to the nano-industry. New materials can be prepared by the non-metallic functionalization of sol-gel derived oxide matrices. Heteropoly acids, amino acids and carbohydrates can be anchored onto the walls of the pores, offering possibilities for the heterogenization of traditionally homogeneous reactions and performing delicate tasks such as molecular recognition [37] and chiral separation [38].

4.4 Chelating Agents

Chelating agents are chemical compounds that can form stable metal complexes that are characterized by ring structures, as illustrated in Figure 4.4.

Figure 4.4(a) shows the first case of chelating agents in which the metal is coordinated to the four nitrogens of two molecules of ethylene diamine, giving rise to a charged double ringed complex with a chloride ion neutralizing the two charges. Figure 4.4(b) presents chelating agents that create an intra-molecular hydrogen bridge. Figure 4.4(c) exhibits the chelating agents that involve polynuclear halogen bridges.

4.4.1 Mineral Processing Examples of Using Chelating Agents

Normally the choice of a chelating agent or a group is made on the basis of its function in well-known analytical metal separations. Several researchers have studied the application of using chelating agents in mineral processing [39].

The separation of minerals by flotation and flocculation depends on the selective adsorption of surfactants and polymers onto them. Reagents with chelating functional groups have received increasing attention for analytical separations in recent years since these were known to exhibit excellent metal selectivity. Some chelating agents have been tried as collectors for

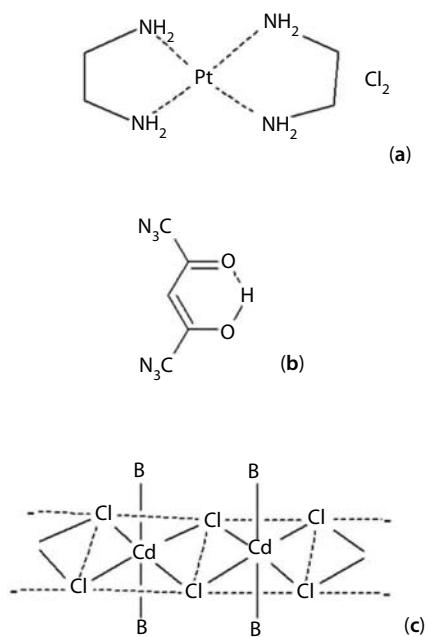


Figure 4.4 General structure of chelating agents.

various mineral systems and excellent separations have been obtained in certain cases. The various possible hypotheses of the interactions between a mineral and a chelating group are, however, not adequately understood; although there is evidence to suggest that some form of a metal complex is created at the surface. In particular, the different mechanisms at the mineral surface versus those in the bulk are not fully recognized and, as a result, the development of collectors based on their use in analytical separations is not achieved easily. It is reported that chelating collectors seldom form the specific structure with metal or mineral and the properties of both the chelating agents and the mineral are important in determining their collecting action. The donor atoms on the chelating agents, as well as those associated with the mineral species, play an important role in their interactions on the surface.

Somasundaran *et al.* [40] studied the application of using chelating agents in mineral processing systems; the basis of the donor properties of the chelating groups and the metal species; and recent approaches to understand the chelation. Moreover, emphasis was given to the criteria for selection of chelating agents as collectors for various minerals and the predictability of the behaviour of a chelating agent for a given mineral system. It was found that although chelating agents can be used effectively for the

flotation of ores, they do not possess absolute specificity towards minerals species. Moreover, the chemical interaction between chelating agents and mineral species in the bulk and on the surface becomes more essential for understanding the mechanism. Finally, it was concluded that the rule of surface chemical alterations, due to either changes in oxidation state of surface species or precipitation of various dissolved mineral species, will have to be considered in actual mineral processing systems.

There are books, reviews and technical papers dealing with the in-depth chemistry of chelating compounds and their functions [41]. There are 3 terms that define the sol-gel processing route of minerals: chelated, sequestered and complexed. In order for a compound to fulfil the requirement of being a true chelating agent, it must have certain chemical characteristics. This chelating compound must consist of at least two sites capable of donating electrons to the metal it chelates. Moreover, the donating atom(s) must also be in a position within the chelating molecule so that the formation of a ring with the metal ion can occur. The term sequestered deals more with the action of chelation or complexing, not the actual chemical arrangement. Meanwhile, the term “complexed” originates from combinations of minerals and organic compounds that do not meet the requirement of a true chelate.

Most of the chelating groups form complexes with almost all of the transition and many non-transition metals and, therefore, specificity is not as absolute as is required for their selective adsorption on minerals [42]. The selectivity is determined by consideration of differences in stability constants and chelate formation under various solution conditions. Moreover, the contribution from the donor atoms as they are located in the mineral lattice has to be considered in obtaining the selectivity. Also, the solubility of the mineral, in addition to that of the metal chelate, has a pronounced influence on the selectivity and the collection power of the chelating agent.

Chelating agents can be classified either on the basis of donor atoms involved (O-O, N-O, N-N, S-O, S-S, S-N), ring size (4-, 5- or 6-membered), charge on the complex (anion, cation, neutral), number of bonds to the metal for every chelating molecule. However, there are five categories of compounds that are commonly mixed with minerals and that have been used in manufacturing. These chelating agents are (i) synthetic chelates, (ii) lignosulfonates, (iii) humic or fulvic acids, (iv) organic acids and (v) amino acids.

Each type of chelating agent exhibits a different chemical structure, physical properties and chelated mechanism to the minerals. This book chapter will only focus on the organic acid group since CA was used in the sol-gel synthesis.

4.4.2 Organic Acids

Organic acids compounds are essential for the transportation and solubility of divalent elements (Zn^{2+} , Mn^{2+} , Fe^{2+} and Cu^{2+}) in plants [43]. On the other hand, the organic acids can be called “anionic organic acids” because of their negative charge. One of the most popular organic acids used for manufacturing and agriculture is CA, which is considered a weak organic acid. It is produced as a white crystalline powder and the chemical structure is presented in Figure 4.5.

The first discovery of CA was credited to Islamic alchemist Jabir bin Hayyan in the 8th century [44]. Later, in the 13th century, medieval scholars in Europe were aware of the acidic nature of lemon and lime juices. CA was first extracted from the medium in 1784 by the Swedish chemist Carl Wilhelm Scheele [45] who crystallized it from lemon juice. Industrial-scale CA production began in 1890 and was based on the Italian citrus fruit industry.

From the chemical structure point of view, CA shares the properties of other carboxylic acids. It decomposes through the loss of carbon dioxide and water when heated above $175^{\circ}C$. The acidity of CA is slightly stronger than other typical carboxylic acids because the anion can be stabilized by intermolecular hydrogen-bonding from other protic groups.

CA is a useful ingredient in the food and beverage industries. The examples of the products that are produced using CA are jams, jellies, candies, preserved food and frozen foods. It is also added in gelatin and fruit-based desserts as well as in canned vegetables and meat products. CA is recognized as being safe for use in food by all major national and international food regulatory agencies. It is naturally present in almost all forms of life, and excess CA is readily metabolized and eliminated from the body. CA has the ability to chelate with several metals, which makes it useful in soaps and laundry detergents. When CA chelates with metals in hard water, it allows these cleaners to produce foam and work more efficiently without the need for water softening.

Similarly, CA is used to regenerate the ion exchange materials used in water softeners by stripping off the accumulated metal ions as citrate complexes. It is used in the biotechnology and pharmaceutical industry to passivate high purity process piping as a substitute to using nitric acid. Nitric

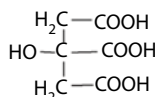


Figure 4.5 Chemical structure of CA.

acid presents a hazardous disposal issue once it is used for this purpose, while CA does not.

CA is also used to chelate copper in formulations used to kill algae in reservoirs and natural waters [46]. The CA chelates the copper, then slowly releases it resulting in an extended time of effectiveness. Although organic acids do not directly chelate monovalent elements (single positive charge: K^+ , Na^+), they are associated in plant systems by loosely held ionic attractions. In foliar applications [47], these anionic (negatively charged) organic acids play an important role in converting cationic (positively charged) minerals into non-ionic (neutral) compounds for increased leaf penetration and movement into the plant. Plants have the ability to manufacture many types of organic acids such as citric, malic, fumaric, succinic and others. Some of these acids are used to transport minerals in the plant. Others are excreted from the roots to solubilize and take needed minerals into the plant system.

4.5 Approach and Methodology

The prior background discussion has indicated the importance and need for focussed studies concerning the influence of chelating agents on materials formed from nanoparticles such as spinel ferrites. Therefore, spinel ferrite nanoparticles were prepared *via* a sol-gel route using CA and poly vinyl alcohol (PVA) as a chelating agent. The influence of chelating agents on physical properties and antibacterial properties of these nanoparticles against *Escherichia coli* (*E. coli*) and *Staphylococcus aureus* (*S. aureus*) was investigated. The following sections document the efficacy of such an approach with the intent to develop potentially therapeutic agents.

4.5.1 Fabrication of Spinel Ferrite Nanoparticles

The chelating agent, which is CA gel, was prepared by dissolving CA powders in distilled water (5% w/v) at 70°C. The chelating agent solutions were kept at 70°C for 5 h or until the solution became clear. Cobalt nitrate ($Co(NO_3)_2 \cdot 6H_2O$), iron nitrate ($Fe(NO_3)_3 \cdot 9H_2O$), copper nitrate ($Cu(NO_3)_2 \cdot 6H_2O$), nickel nitrate ($Ni(NO_3)_2 \cdot 6H_2O$), chromium nitrate ($Mn(NO_3)_2 \cdot 4H_2O$) and zinc nitrate ($Zn(NO_3)_2 \cdot 6H_2O$) powders with Fe:Co:(Zn, Cu, Ni, Mn) mole ratios of 2:0.5:0.5 were dissolved into the chelating agent solution under magnetic stirring. The sol-gel reaction was continued for 3 h and then the temperature increased to 80°C for 10 h or until the gel dried into powder form. Finally, all samples were sintered at

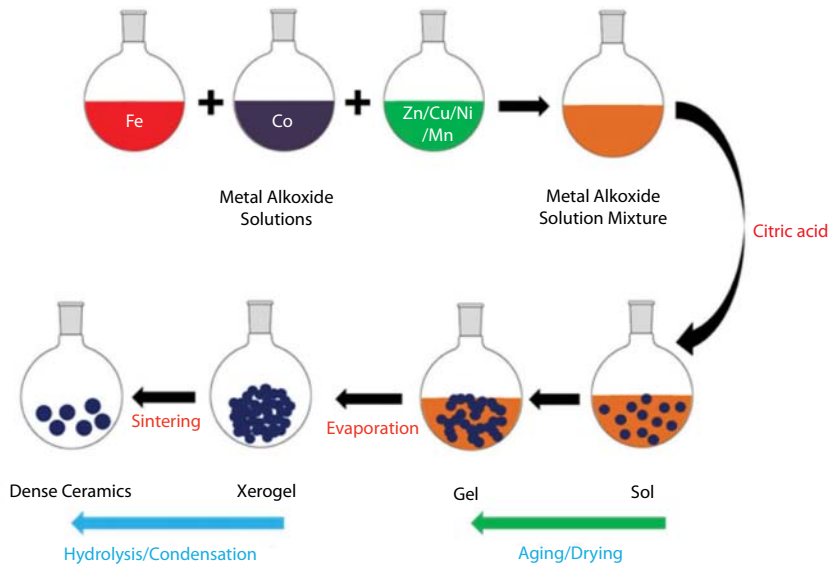


Figure 4.6 The preparation of spinel ferrite and transition metals-substituted spinel ferrite nanoparticles.

800°C for 4 h and then ground using a mortar and pestle to form a nanoparticle. Figure 4.6 diagrams the method employed.

4.5.2 Analytical Techniques Employed

Elemental composition analyses of the nanoparticles were carried out using energy dispersive X-ray spectroscopy (EDX). Phase analyses of cobalt ferrite nanoparticles were conducted using X-ray diffraction (Bruker AXS D8 Advance XRD). Surface wettability, an indicator of the surface interaction of the metal oxide with a given solvent and an important measure for bio-medical applications, was measured using the water contact angle technique (WCA-FTA200). The morphology (i.e. homogeneity and particle size) of the materials was observed using a field emission scanning electron microscope (ZEISS SUPRA 40 VP SEM). Particle size characterization of nanoparticles was performed using a 90 Plus Particle Size Analyzer (Brookhaven Instrument Corp., USA). The antimicrobial activity of cobalt ferrite nanoparticles was tested against gram negative bacteria, *E. coli*, and gram positive bacteria, *S. aureus*.

4.5.3 Biocompatibility Study

4.5.3.1 Cell Culture

Osteoblast-like cells (SaOs-2, Sarcoma osteogenic) (Barwon Biomedical Research, Geelong Hospital, Victoria, Australia), a human osteosarcoma cell line with osteoblastic properties, were cultured in minimum essential media (MEM) (Gibco, Invitrogen, Mulgrave, VIC, Australia) supplemented with 10% foetal bovine serum (Bovogen Biologicals, Essendon, VIC, Australia), 1% non-essential amino acid (Sigma-Aldrich, Castle Hill, NSW, Australia), 10,000 units/mL penicillin–10,000 µg/mL streptomycin (Gibco), and 0.4% amphostat B (In Vitro Technologies, Auckland, New Zealand) at 37°C in a humidified atmosphere of 5% CO₂ in air. The culture medium was changed every 3 days.

4.5.3.2 Cytotoxicity

The cytotoxicity of all transition metal-substituted cobalt ferrite nanoparticles was evaluated by use of the media extracts of the samples (International Organization for Standardization, 1999). Transition metal-substituted cobalt ferrite nanoparticles were mixed with the media at a concentration of 0.22 g/mL. All samples of nanoparticles with media were incubated in a humidified atmosphere of 5% CO₂ in air at 37°C for 72 h. The nanoparticle mixture was filter-sterilized with a 0.22 µm filter (Falcon, BD Biosciences, San Jose, CA, USA) to obtain the extracts. Cells were also seeded into wells containing only the media and incubated for 72 h as a negative control. SaOs-2 cells were seeded into negative controls and extracts from the nanoparticles at a density of 10,000 cells per well. After cell culture for 5 days, cells were harvested with 0.1% Trypsin-5 mM EDTA (Sigma-Aldrich) and collected. Cell counts were obtained by the trypan blue exclusion method, whereby dead cells are stained blue and live cells remained clear. The cell viability was determined by the ratio of live cells to the total number of cells per sample [48].

4.5.3.3 Statistical Analysis

The values are expressed as means ± one standard deviation (SD). All of the experiments were conducted in triplicate. A one-way ANOVA (SPSS 14.0 for Windows software) method was used to determine the differences observed among the groups; $p < 0.05$ was considered significant.

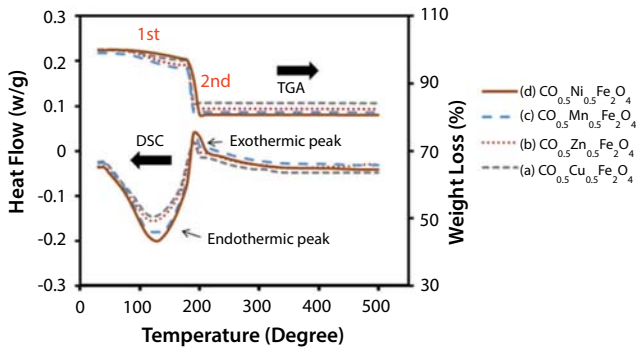


Figure 4.7 DSC/TGA curves of synthesized transition metal-substituted cobalt ferrite nanoparticles: (a) $\text{Co}_{0.5}\text{Cu}_{0.5}\text{Fe}_2\text{O}_4$, (b) $\text{Co}_{0.5}\text{Zn}_{0.5}\text{Fe}_2\text{O}_4$, (c) $\text{Co}_{0.5}\text{Mn}_{0.5}\text{Fe}_2\text{O}_4$ and (d) $\text{Co}_{0.5}\text{Ni}_{0.5}\text{Fe}_2\text{O}_4$.

4.6 Experimental Results

4.6.1 Differential Scanning Calorimetry and Thermo Gravimetric Analyses

Differential scanning calorimetry (DSC) and thermogravimetric analysis (TGA) curves of synthesized transition metal-substituted cobalt ferrite nanoparticles, (a) $\text{Co}_{0.5}\text{Cu}_{0.5}\text{Fe}_2\text{O}_4$, (b) $\text{Co}_{0.5}\text{Zn}_{0.5}\text{Fe}_2\text{O}_4$, (c) $\text{Co}_{0.5}\text{Mn}_{0.5}\text{Fe}_2\text{O}_4$ and (d) $\text{Co}_{0.5}\text{Ni}_{0.5}\text{Fe}_2\text{O}_4$ obtained from CA as a chelating agent are shown in Figure 4.7. The TGA curve exhibits two distinct weight loss steps and the DSC curve presents one exothermic and endothermic peak over 25–500°C.

The first weight loss step in the range of 25–150°C, which was accompanied by an endothermic broad peak around 150°C in the DSC curve, arises due to the loss of residual moisture in the powder. The second weight loss step in the range of 200°C and the sharp exothermic peak around 200°C is associated with the combustion of nitrates and the oxidation of carbon from the CA to form carbon dioxide. No weight loss was observed above 300°C, implying the presence of transition metal-substituted cobalt ferrite nanoparticles in this temperature range [49].

4.6.2 Raman Analyses

Synthesized transition metal-substituted cobalt ferrite nanoparticles have been investigated for phase characterization using Raman analyses. Cobalt ferrite has a cubic inverse spinel structure belonging to the $O_h^7 (Fd3m)$ space group. The metallic cations can occupy two types of positions: either

surrounded by six oxygen ions forming an octahedron or by four oxygen ions forming a tetrahedron. This structure gives rise to 39 normal modes among which five are Raman active ($A_{1g}+1E_g+3T_{2g}$) [50]. Figure 4.8 shows Raman spectra of synthesized transition metal-substituted cobalt ferrite nanoparticles: (a) CoFe_2O_4 , (b) $\text{Co}_{0.5}\text{Cu}_{0.5}\text{Fe}_2\text{O}_4$, (c) $\text{Co}_{0.5}\text{Zn}_{0.5}\text{Fe}_2\text{O}_4$, (d) $\text{Co}_{0.5}\text{Mn}_{0.5}\text{Fe}_2\text{O}_4$ and (e) $\text{Co}_{0.5}\text{Ni}_{0.5}\text{Fe}_2\text{O}_4$. The spectrum of CoFe_2O_4 (Figure 4.8(a)) consists of broad bands at 311, 470, 571, 619 and a strong band at 693 cm^{-1} [51]. In cobalt ferrite, the octahedral site is occupied by cobalt and iron ions and the tetrahedral site is occupied by only the iron ion. Due to the difference in ionic radii of cobalt and iron ions in CoFe_2O_4 , the Fe–O and Co–O bond distances redistribute themselves between both sites and result in a doublet-like structure. It has been observed that Raman bands at 690 and 619 cm^{-1} are assigned to $A_{1g}(1)$ and $A_{1g}(2)$ modes reflecting the stretching vibration of Fe^{3+} and O^{2-} ions in octahedral sites (*O-site*), while low frequency bands at 571, 470 and 311 cm^{-1} are assigned to $T_{2g}(3)$, $T_{2g}(2)$ and E_g modes, respectively, which reflect the vibration at the tetrahedral sites (*T-site*) [52].

All transition metal-substituted cobalt ferrite nanoparticles present almost the same pattern of Raman spectra. Some changes of the spectra labelled on spectra (a) in Figure 4.8 are noticed when transition metals (Cu, Zn, Mn and Ni) become incorporated into the cobalt ferrite cubic structure.

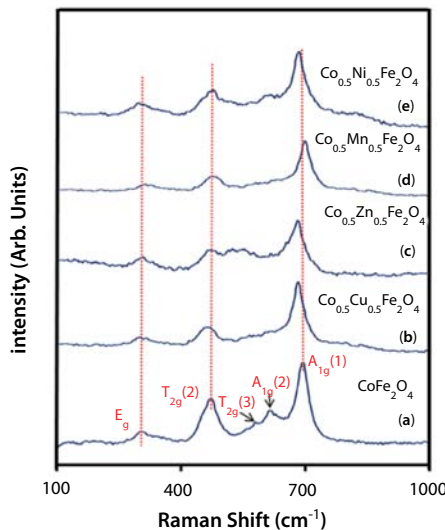


Figure 4.8 Raman spectra of the synthesized transition metal-substituted cobalt ferrite nanoparticles: (a) CoFe_2O_4 , (b) $\text{Co}_{0.5}\text{Cu}_{0.5}\text{Fe}_2\text{O}_4$, (c) $\text{Co}_{0.5}\text{Zn}_{0.5}\text{Fe}_2\text{O}_4$, (d) $\text{Co}_{0.5}\text{Mn}_{0.5}\text{Fe}_2\text{O}_4$ and (e) $\text{Co}_{0.5}\text{Ni}_{0.5}\text{Fe}_2\text{O}_4$.

There is some observable decrease in intensity of the 690 cm^{-1} tetrahedral Raman band and all the peaks are shifted towards the lower wave number side in Figure 4.8(b), (c) and (e). The Raman peaks in Figure 4.8(d) shift towards the higher wave number, which is called a blue shift. On other hand, the red shift, or movement of peaks to a lower wave number, is attributed to the higher atomic mass of zinc, copper and nickel compared to the cobalt ion. In a similar fashion to the spinel ferrite, the distribution of divalent and trivalent cations can change due to migration of metal ions from tetrahedral to octahedral sites and vice versa. These changes could arise from a high degree of cation disorder induced by Zn^{2+} , Cu^{2+} , Mn^{2+} and Ni^{2+} ion incorporation and/or a particle size effect [53].

4.6.3 Particle Size Analysis

Figure 4.9 shows the particle size distribution of synthesized transition metal-substituted cobalt ferrite nanoparticles: (a) CoFe_2O_4 , (b) $\text{Co}_{0.5}\text{Cu}_{0.5}\text{Fe}_2\text{O}_4$, (c) $\text{Co}_{0.5}\text{Zn}_{0.5}\text{Fe}_2\text{O}_4$, (d) $\text{Co}_{0.5}\text{Mn}_{0.5}\text{Fe}_2\text{O}_4$ and (e) $\text{Co}_{0.5}\text{Ni}_{0.5}\text{Fe}_2\text{O}_4$. All of these nanoparticles present a polydisperse particle size distribution.

The particle diameter range of synthesized transition metal-substituted cobalt ferrite nanoparticles: (a) CoFe_2O_4 , (b) $\text{Co}_{0.5}\text{Cu}_{0.5}\text{Fe}_2\text{O}_4$, (c) $\text{Co}_{0.5}\text{Zn}_{0.5}\text{Fe}_2\text{O}_4$, (d) $\text{Co}_{0.5}\text{Mn}_{0.5}\text{Fe}_2\text{O}_4$ and (e) $\text{Co}_{0.5}\text{Ni}_{0.5}\text{Fe}_2\text{O}_4$ are 11–90, 5–80, 18–90, 7–85 and 10–85 nm, respectively. Meanwhile, the average particle size of synthesized transition metal-substituted cobalt ferrite nanoparticles are 50, 43, 52, 45 and 46 nm, respectively.

The graphs in Figure 4.9 indicate that the average particle size of the nanoparticles increased in the order of $\text{Co}_{0.5}\text{Cu}_{0.5}\text{Fe}_2\text{O}_4 < \text{Co}_{0.5}\text{Mn}_{0.5}\text{Fe}_2\text{O}_4 < \text{Co}_{0.5}\text{Ni}_{0.5}\text{Fe}_2\text{O}_4 < \text{CoFe}_2\text{O}_4 < \text{Co}_{0.5}\text{Zn}_{0.5}\text{Fe}_2\text{O}_4$.

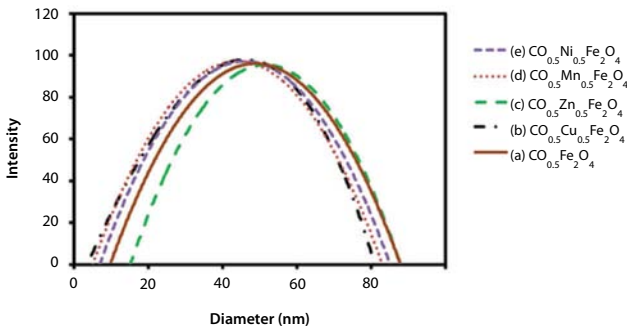


Figure 4.9 Particle size distribution of synthesized transition metal-substituted cobalt ferrite nanoparticles: (a) CoFe_2O_4 , (b) $\text{Co}_{0.5}\text{Cu}_{0.5}\text{Fe}_2\text{O}_4$, (c) $\text{Co}_{0.5}\text{Zn}_{0.5}\text{Fe}_2\text{O}_4$, (d) $\text{Co}_{0.5}\text{Mn}_{0.5}\text{Fe}_2\text{O}_4$ and (e) $\text{Co}_{0.5}\text{Ni}_{0.5}\text{Fe}_2\text{O}_4$.

4.6.4 Microstructure of Spinel Ferrite Nanoparticles

SEM micrographs were analyzed to investigate the grain structure of the nanoparticles and assist in understanding the development of the grain sizes. Figure 4.10 shows the SEM images of the synthesized cobalt ferrite and transition metal-substituted cobalt ferrite nanoparticles, (a) CoFe_2O_4 , (b) $\text{Co}_{0.5}\text{Cu}_{0.5}\text{Fe}_2\text{O}_4$, (c) $\text{Co}_{0.5}\text{Zn}_{0.5}\text{Fe}_2\text{O}_4$, (d) $\text{Co}_{0.5}\text{Mn}_{0.5}\text{Fe}_2\text{O}_4$ and (e) $\text{Co}_{0.5}\text{Ni}_{0.5}\text{Fe}_2\text{O}_4$. The CoFe_2O_4 nanoparticles, Figure 4.10(a), exhibit an angular morphology. Meanwhile, the nanoparticles synthesized with transition metal doping in Figure 4.10(b)–(e) present particles with irregular shapes and agglomeration where some particles form large clusters. The average sizes of 30 grains, measured by ImageJ (available from the National Institutes of Health, USA), for CoFe_2O_4 , $\text{Co}_{0.5}\text{Cu}_{0.5}\text{Fe}_2\text{O}_4$, $\text{Co}_{0.5}\text{Zn}_{0.5}\text{Fe}_2\text{O}_4$, $\text{Co}_{0.5}\text{Mn}_{0.5}\text{Fe}_2\text{O}_4$ and $\text{Co}_{0.5}\text{Ni}_{0.5}\text{Fe}_2\text{O}_4$ are 42.97 ± 0.5 , 40.14 ± 0.4 , 44.18 ± 0.6 , 40.26 ± 0.2 and 41.01 ± 0.5 nm, respectively [49].

The elemental compositions of synthesized cobalt ferrite and transition metal-substituted cobalt ferrite nanoparticles ($\text{Co}_{0.5}\text{X}_{0.5}\text{Fe}_2\text{O}_4$ with $X = \text{Cu}$,

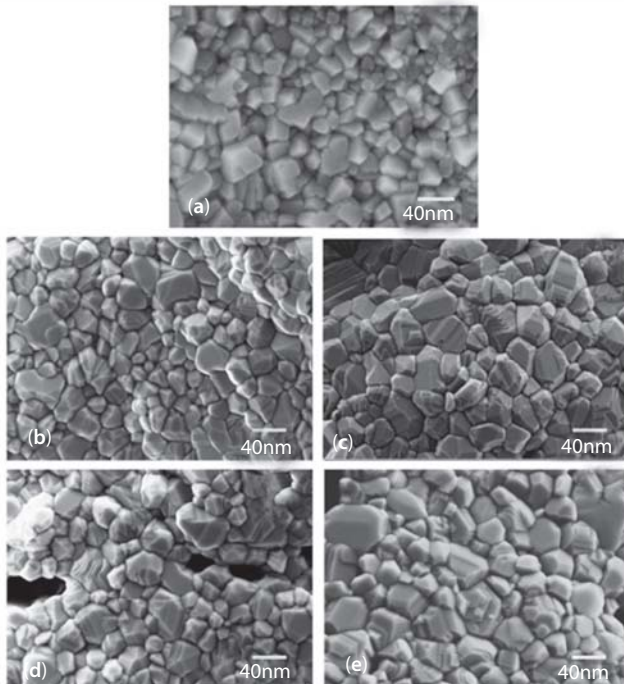


Figure 4.10 SEM images of synthesized transition metal-substituted cobalt ferrite nanoparticles: (a) CoFe_2O_4 , (b) $\text{Co}_{0.5}\text{Cu}_{0.5}\text{Fe}_2\text{O}_4$, (c) $\text{Co}_{0.5}\text{Zn}_{0.5}\text{Fe}_2\text{O}_4$, (d) $\text{Co}_{0.5}\text{Mn}_{0.5}\text{Fe}_2\text{O}_4$ and (e) $\text{Co}_{0.5}\text{Ni}_{0.5}\text{Fe}_2\text{O}_4$.

Table 4.3 The elemental composition of synthesized cobalt ferrite and transition metal-substituted cobalt ferrite nanoparticles.

Ferrite Composition	At. %						
	Co	Cu	Zn	Mn	Ni	Fe	O
CoFe ₂ O ₄	14.49	–	–	–	–	28.54	56.97
Co _{0.5} Cu _{0.5} Fe ₂ O ₄	7.38	7.43	–	–	–	28.31	56.88
Co _{0.5} Zn _{0.5} Fe ₂ O ₄	7.36	–	7.40	–	–	28.46	56.78
Co _{0.5} Mn _{0.5} Fe ₂ O ₄	7.32	–	–	7.51	–	28.35	56.82
Co _{0.5} Ni _{0.5} Fe ₂ O ₄	7.34	–	–	–	7.48	28.37	56.81

Zn, Mn and Ni) are listed in Table 4.3. These results indicate that the ratio of “Co/transition metal/Fe” for all of the synthesized nanoparticles is almost the same as that of the ideal transition metal-substituted cobalt ferrite (Co_{0.5}X_{0.5}Fe₂O₄ with X = Cu, Zn, Mn and Ni) structure, which could confirm that no organic chelating agents remained in the system [49].

4.6.5 XRD Analysis

X-ray diffraction patterns of synthesized cobalt ferrite and transition metal-substituted cobalt ferrite nanoparticles, (a) CoFe₂O₄, (b) Co_{0.5}Cu_{0.5}Fe₂O₄, (c) Co_{0.5}Zn_{0.5}Fe₂O₄, (d) Co_{0.5}Mn_{0.5}Fe₂O₄ and (e) Co_{0.5}Ni_{0.5}Fe₂O₄, obtained from sol-gel methods using CA as the chelating agent and calcined at 800°C for 4 h are shown in Figure 4.11.

The peaks at 30.12°, 35.54°, 37.12°, 43.13°, 53.41°, 56.89° and 62.62° are indexed as the reflection planes of (220), (311), (222), (400), (422), (511) and (440), respectively. Analysis of the XRD patterns of all samples confirmed the formation of the cubic spinel structure [54] as the main characteristic peak. Moreover, no XRD peaks corresponding to the other phases such as α-Fe₂O₃, CoO, ZnO, NiO, MnO₂, Co₂O₃ or Co₃O₄ were detected, which indicates that transition metals were completely substituted into the cobalt ferrite lattice synthesized by calcination of the precursor and chelating agent derived from the sol-gel process. These results are in good agreement with Zi *et al.* [55].

The crystallite size *D* was calculated according to the Scherrer equation [56]:

$$D = \frac{0.9\lambda}{\beta \cos\theta} \quad (4.1)$$

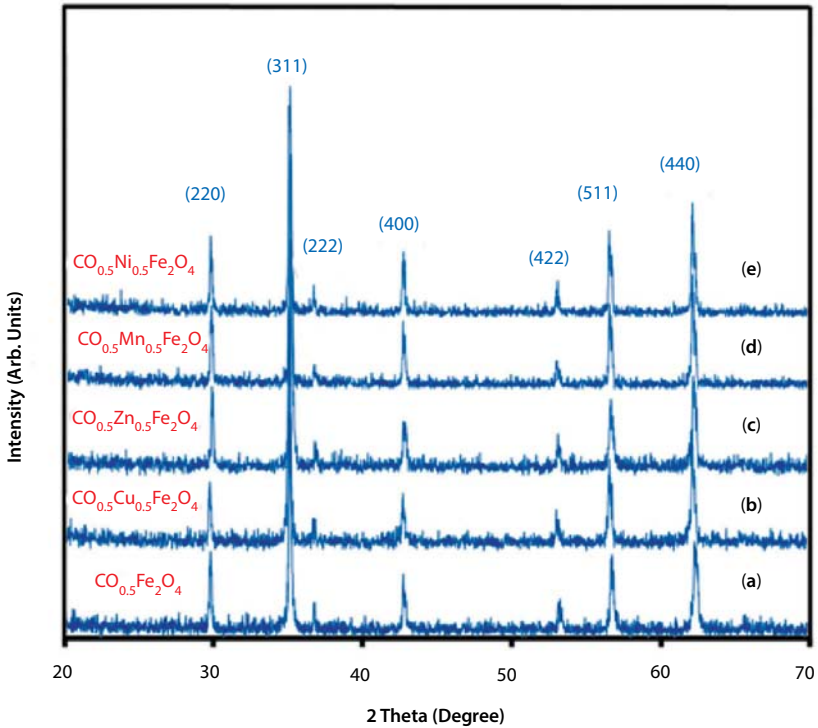


Figure 4.11 X-ray diffraction patterns of synthesized transition metal-substituted cobalt ferrite nanoparticles: (a) CoFe_2O_4 , (b) $\text{Co}_{0.5}\text{Cu}_{0.5}\text{Fe}_2\text{O}_4$, (c) $\text{Co}_{0.5}\text{Zn}_{0.5}\text{Fe}_2\text{O}_4$, (d) $\text{Co}_{0.5}\text{Mn}_{0.5}\text{Fe}_2\text{O}_4$ and (e) $\text{Co}_{0.5}\text{Ni}_{0.5}\text{Fe}_2\text{O}_4$.

where λ is the wavelength of the radiation, θ is the diffraction angle and β is the full width at half maximum (FWHM) of the diffraction peak. The lattice parameter was calculated according to the formula:

$$a = d_{hkl} \sqrt{(h^2 + k^2 + l^2)} \quad (4.2)$$

The reflection plan (311) was used to calculate the crystallite size and lattice constant since this crystallographic plane exhibited the maximum diffraction intensity. The crystallite size and lattice constant of the cobalt ferrite and transition metal-substituted cobalt ferrite nanoparticles ($\text{Co}_{0.5}\text{X}_{0.5}\text{Fe}_2\text{O}_4$ with $X = \text{Cu}, \text{Zn}, \text{Mn}$ and Ni) have been summarized in Table 4.4. The calculated lattice constant a (using the d value and respective hkl (311) parameters) increased from 8.385 to 8.401 Å for the samples calcined at 800°C with zinc substitution. Meanwhile, the lattice constant

Table 4.4 The crystallite size and lattice constant of the synthesized cobalt ferrite and transition metal-substituted cobalt ferrite nanoparticles.

Ferrites Composition	Lattice Parameter (Å)	Crystallite Size (nm)
CoFe_2O_4	8.385	42.97
$\text{Co}_{0.5}\text{Cu}_{0.5}\text{Fe}_2\text{O}_4$	8.361	40.14
$\text{Co}_{0.5}\text{Zn}_{0.5}\text{Fe}_2\text{O}_4$	8.401	44.18
$\text{Co}_{0.5}\text{Mn}_{0.5}\text{Fe}_2\text{O}_4$	8.309	40.26
$\text{Co}_{0.5}\text{Ni}_{0.5}\text{Fe}_2\text{O}_4$	8.356	40.01

decreased to 8.361, 8.309 and 8.356 Å with copper, manganese and nickel substitution, respectively. The relationship between transition metals substitution and lattice parameter can be explained by Vegard's law [57]. According to this law, the increase of the lattice parameter results from the difference in the Zn^{2+} (0.74 Å) and Co^{2+} (0.72 Å) ionic radii [58]. On the other hand, a decrease of the lattice parameter results from the smaller ionic radii of Cu^{2+} , Mn^{2+} and Ni^{2+} compared with Co^{2+} . Moreover, the crystallite size of cobalt ferrite and transition metal-substituted cobalt ferrite nanoparticles determined by taking the FWHM of the (311) peak was found to lie in the range of 40–50 nm. The values agree well with those measured by ImageJ [49].

Zinc and copper systems have been selected for further calculation when altering the substitution concentration from 30, 50, 70 and 100%. The calculated lattice constant a (using the d value and respective hkl (311) parameters) increased from 8.385 Å to 8.401 Å for the samples calcined at 800°C with increasing zinc substitution from 0 to 1. The relationship between zinc substitution and lattice parameter is near linear as shown in Figure 4.12. According to Vegard's law [57], the linear relationship implies the formation of homogeneous $\text{Co}_{(1-x)}\text{Zn}_x\text{Fe}_2\text{O}_4$ solid solutions. The increase of the lattice parameter results from the difference in the Zn^{2+} (0.74 Å) and Co^{2+} (0.72 Å) ionic radii [58]. Moreover, the crystallite size of cobalt ferrite and zinc-substituted cobalt ferrite nanoparticles determined by taking the FWHM of the (311) peak was found to lie in the range of 40–50 nm; values that agree well with those measured from ImageJ [51].

Some small shifts of the peak positions in the XRD were noticed and the calculated lattice constant (using a d value and respective hkl (311) parameters) was found to decrease from 8.385 to 8.361 Å for the samples calcined at 800°C with increasing copper substitution from 0 to 1. The

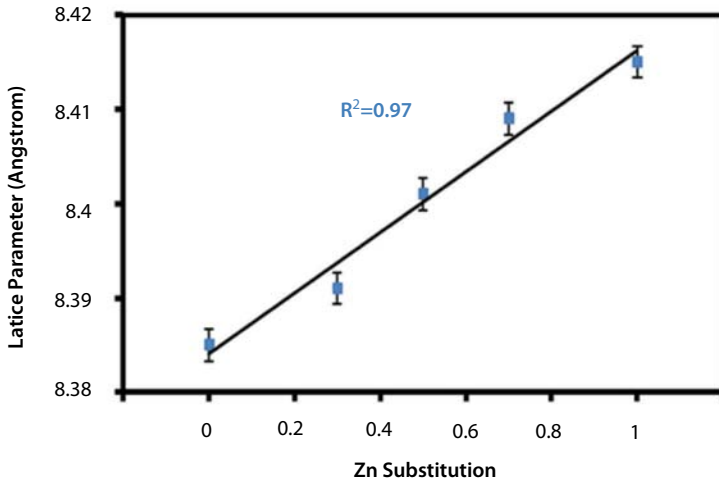


Figure 4.12 Dependence of the lattice parameter, determined from XRD peak positions, upon the extent of zinc doping. The R^2 value represents the goodness of fit for a straight line.

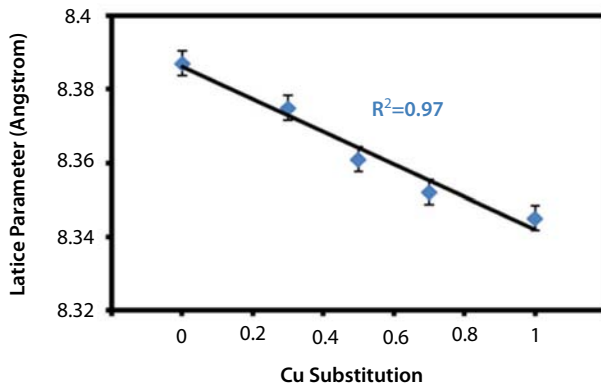


Figure 4.13 Dependence of the lattice parameter, determined from XRD peak positions, upon of the extent of copper doping. The R^2 value represents the goodness of fit for a straight line.

relationship between copper substitution and lattice parameter is close to linear as shown in Figure 4.13. The lattice parameter decreased linearly with copper concentration due to the smaller ionic radius of Cu^{2+} compared to Co^{2+} . Moreover, the crystallite sizes of cobalt ferrite and copper-substituted cobalt ferrite nanopowders calculated by taking the FWHM of the (311) peak were in the range of 35–45 nm. These XRD-determined values agree well with the values measured from SEM images [59].

4.6.6 Contact Angle Measurement and Roughness Parameters

The hydrophilicity and surface roughness are presented in Table 4.5. The surface of cobalt ferrite and transition metal-substituted cobalt ferrite nanoparticles were hydrophilic since the water contact angle was less than 90. The results indicate that cobalt ferrite nanoparticles are marginally more hydrophilic than those derived from transition metal-substituted cobalt ferrite nanoparticles. Significant differences in the type of substitution transition metal ions have been noticed with respect to the contact angles of the transition metal-substituted cobalt ferrite nanoparticles. The water contact angles increase with the substitution of zinc, manganese, copper and nickel, respectively. In terms of the surface roughness of nanoparticles, nickel-substituted cobalt ferrite presents the smoothest surface followed by copper, manganese, pure cobalt ferrite and zinc. These results are in good agreement with the previous XRD results in Table 4.4 that revealed nickel-substituted cobalt ferrite exhibits the smallest crystallite nanoparticle size [49].

4.6.7 Antibacterial Activities of the Spinel Ferrite Nanoparticles

The antibacterial activities of the transition metal-substituted cobalt ferrite nanoparticles against *E. coli* and *S. aureus* are shown in Figure 4.14. All tests were repeated ten times after culture incubation at 37°C overnight. The concentration of cobalt ferrite nanoparticles was fixed at 1 g/L. Compared to the control (the sample of bacteria solution without adding nanoparticles), cobalt ferrite and transition metal-substituted cobalt

Table 4.5 Surface wettability and roughness parameters for synthesized cobalt ferrite and transition metal-substituted cobalt ferrite nanoparticles.

Samples	Water Contact Angle (degree)	Surface Roughness Ra (μm)
CoFe ₂ O ₄	61 ± 0.2	3.54
Co _{0.5} Cu _{0.5} Fe ₂ O ₄	65 ± 0.3	2.97
Co _{0.5} Zn _{0.5} Fe ₂ O ₄	64 ± 0.3	3.95
Co _{0.5} Mn _{0.5} Fe ₂ O ₄	65 ± 0.1	3.28
Co _{0.5} Ni _{0.5} Fe ₂ O ₄	66 ± 0.2	2.58

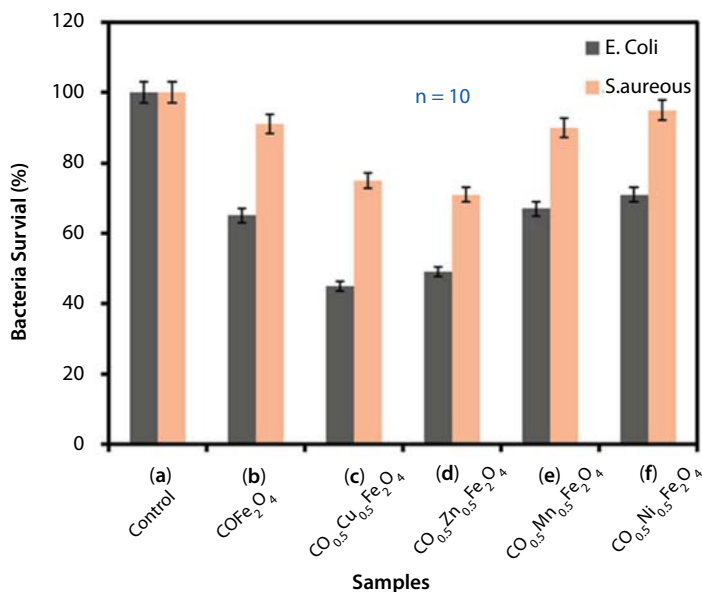


Figure 4.14 Antibacterial activities against *E. coli* and *S. aureus* of synthesized transition metal-substituted cobalt ferrite nanoparticles: (a) without cobalt ferrite nanoparticles, (b) CoFe_2O_4 , (c) $\text{Co}_{0.5}\text{Cu}_{0.5}\text{Fe}_2\text{O}_4$, (d) $\text{Co}_{0.5}\text{Zn}_{0.5}\text{Fe}_2\text{O}_4$, (e) $\text{Co}_{0.5}\text{Mn}_{0.5}\text{Fe}_2\text{O}_4$ and (f) $\text{Co}_{0.5}\text{Ni}_{0.5}\text{Fe}_2\text{O}_4$.

ferrite nanoparticles inhibit the growth of both *E. coli* and *S. aureus*, and the *E. coli* killing rate of all ferrite composite nanoparticles is higher than the *S. aureus* killing rate. The antibacterial properties of manganese and nickel-substituted cobalt ferrite nanoparticles are lower than the pure cobalt ferrite nanoparticles. However, their antibacterial abilities became more dominant when copper and zinc were substituted into cobalt ferrite nanoparticles.

There are several possible mechanisms for the antibacterial action of zinc and copper ferrite nanoparticles. Studies suggested that when *E. coli* is treated with copper nanoparticles, changes take place in its cell membrane morphology. These nanoparticles adhere to the bacterial cell wall and penetrate through the cell membrane as presented in Figure 4.15 [60]. Copper ions cause destruction of the bacterial cell wall, degradation and lysis of the cytoplasm; leading to cell death. Moreover, high concentrations of copper nanoparticles demonstrate complete cytotoxicity against *E. coli* [61]. Nanoparticles have a large surface area, thus their bactericidal efficacy is enhanced compared to large sized particles. Hence, nanoparticles are believed to impart cytotoxicity to microorganisms. Copper nanoparticles exhibit a large surface-to-volume ratio, which enhances their

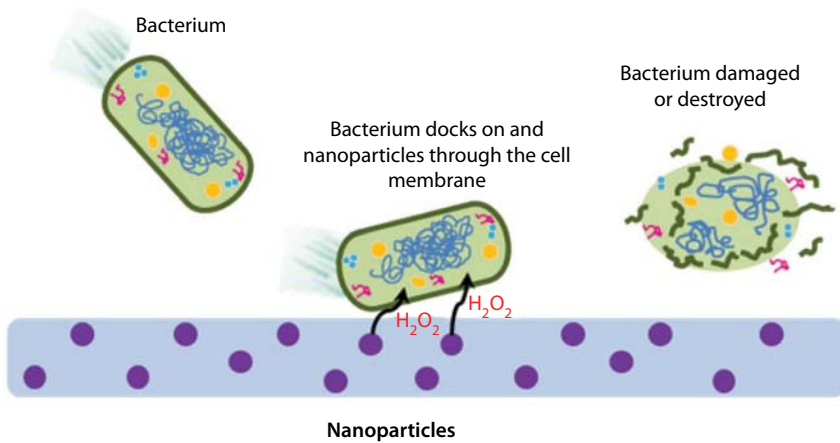


Figure 4.15 The mechanisms for the antibacterial action of spinel ferrite nanoparticles (adapted from Yamamoto *et al.* [64]).

bioactivity and makes them effective bactericidal agents [62]. For the zinc nanoparticle system, studies showed that zinc binds to the membranes of microorganisms, similar to mammalian cells, prolonging the lag phase of the growth cycle and increasing the generation time of the organisms so that it takes each organism more time to complete cell division [63].

Another proposition maintained that the main chemical species contributing to the occurrence of the antibacterial activity were assumed to be active oxides; for example, hydrogen peroxide (H_2O_2) and super-oxide (O_2^-), generated from the surface of the zinc ceramics [64]. These active oxides readily penetrate the cell wall of bacteria and cause cell destruction. The penetration rate of active oxides through the bacteria cell wall plays an important role in the killing rate of zinc ferrite nanoparticles against bacteria. Furthermore, the structure and chemical composition of the cell walls are quite different between *E. coli* and *S. aureus*. The *E. coli* cell wall consists of lipid A, lipopolysaccharide and peptidoglycan; whereas the cell wall of *S. aureus* consists mainly of peptidoglycan. The results indicate that active oxides generated from transition metal-substituted cobalt ferrite have more capability to penetrate the cell wall and decrease the cell division of *E. coli* rather than *S. aureus*. However, the precise mechanism of interaction between bacteria (*E. coli* and *S. aureus*) and transition metal-substituted cobalt ferrite nanoparticles needs to be investigated further.

4.6.8 Biocompatibility of Spinel Ferrite Nanoparticles

The synthesized cobalt ferrite and transition metal-substituted cobalt ferrite nanoparticles ($Co_{0.5}X_{0.5}Fe_2O_4$ with $X = Cu, Zn, Mn$ and Ni) showed

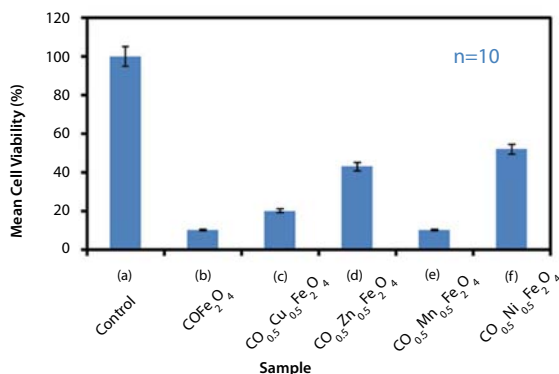


Figure 4.16 The percentage of mean cell viability of synthesized transition metal-substituted cobalt ferrite nanoparticles: (a) control, (b) CoFe_2O_4 , (c) $\text{Co}_{0.5}\text{Cu}_{0.5}\text{Fe}_2\text{O}_4$, (d) $\text{Co}_{0.5}\text{Zn}_{0.5}\text{Fe}_2\text{O}_4$, (e) $\text{Co}_{0.5}\text{Mn}_{0.5}\text{Fe}_2\text{O}_4$ and (f) $\text{Co}_{0.5}\text{Ni}_{0.5}\text{Fe}_2\text{O}_4$.

different degrees of cytotoxicity after cell culture for 5 days (Figure 4.16). The control group (cells seeded into wells containing only media) was considered biocompatible. The spinel ferrite nanoparticles could also be considered biocompatible if the cell viability on the nanoparticles was equivalent to or greater than that of the control group. The percentage of mean cell viability for CoFe_2O_4 , $\text{Co}_{0.5}\text{Cu}_{0.5}\text{Fe}_2\text{O}_4$, $\text{Co}_{0.5}\text{Zn}_{0.5}\text{Fe}_2\text{O}_4$, $\text{Co}_{0.5}\text{Mn}_{0.5}\text{Fe}_2\text{O}_4$ and $\text{Co}_{0.5}\text{Ni}_{0.5}\text{Fe}_2\text{O}_4$ was 10%, 20%, 43%, 11% and 52%, respectively, compared with that of the control group, which was 100%. It could be concluded that the biocompatibility of spinel ferrite nanoparticles decreased in the order of $\text{CoFe}_2\text{O}_4 < \text{Co}_{0.5}\text{Mn}_{0.5}\text{Fe}_2\text{O}_4 < \text{Co}_{0.5}\text{Cu}_{0.5}\text{Fe}_2\text{O}_4 < \text{Co}_{0.5}\text{Zn}_{0.5}\text{Fe}_2\text{O}_4 < \text{Co}_{0.5}\text{Ni}_{0.5}\text{Fe}_2\text{O}_4$. Moreover, this biocompatibility test needs further study to find the suitable concentration before being employed in biomedical applications.

4.7 Concluding Remarks

This work initially reviews the inter-relationships between spinel nanoparticles and transition metals substitution. It is emphasized that significant advances in material developments for many industries; i.e. mining, agricultural and biomedical, have been implemented. Against this backdrop, a case is made concerning cobalt ferrite nanoparticles that have been modified by substitution of transition metals using citric acid (CA) as a chelating agent. A sol-gel technique for synthesizing transition metal-substituted cobalt ferrite nanoparticles that employs CA as a chelating agent was developed. Transition metal-substituted cobalt ferrite nanoparticles formed a cubic spinel structure and exhibited irregular

morphology with a crystallite size in the range of 40–50 nm. The substitution of zinc and copper in cobalt ferrite nanoparticles significantly improved antibacterial activity against *E. coli* and *S. aureus*. Copper-substituted cobalt ferrite nanoparticles have the most effective contact biocidal property among all of the nanoparticles.

The biocompatibility of zinc and nickel-substituted cobalt ferrite nanoparticles are higher than the other nanoparticles. The antibacterial activity of transition metal-substituted cobalt ferrite nanoparticles against *E. coli* was higher than for *S. aureus*. Zinc and nickel-substituted cobalt ferrite nanoparticles could be used in drug delivery systems as well as complement other biomedical and biotechnology applications.

Acknowledgements

The authors acknowledge financial support for this research through the Australia-India Strategic Research Fund (AISRF) ST060048. Mr. Sanpo acknowledges support from Swinburne University of Technology in the form of post graduate scholarship.

References

1. V. L. Calero-DdelC and C. Rinaldi, *Journal of Magnetism and Magnetic Materials*, Vol. 314, p. 60, 2007.
2. V. Pillai and D. O. Shah, *Journal of Magnetism and Magnetic Materials*, Vol. 163, p. 243, 1996.
3. R. Skomski, *Journal of Physics Condensed Matter*, Vol. 15, p. R841, 2003.
4. E. Koster, *IEEE Transactions on Magnetics*, Vol. 8, p. 428, 1972.
5. S. Umeki, S. Saitoh, and Y. Imaoka, *IEEE Transactions on Magnetics*, Vol. 10, p. 655, 1974.
6. G. Vaidyanathan and S. Sendhilnathan, *Physica B: Condensed Matter*, Vol. 403, p. 2157, 2008.
7. S. Singhal, J. Singh, S. K. Barthwal, and K. Chandra, *Journal of Solid State Chemistry*, Vol. 178, p. 3183, 2005.
8. J. A. Paulsen, A. P. Ring, C. C. H. Lo, J. E. Snyder, and D. C. Jiles, *Journal of Applied Physics*, Vol. 97, p. 044502, 2005.
9. S. S. Jadhav, S. E. Shirsath, S. M. Patange, and K. M. Jadhav, *Journal of Applied Physics*, Vol. 108, p. 093920, 2010.
10. S. M. Moghimi, A. C. Hunter, and J. C. Murray, *Pharmacological Reviews*, Vol. 53, p. 283, 2001.
11. J. M. Wilkinson, *Medical Device Technology*, Vol. 14, p. 29, 2003.

12. S. Sun, H. Zeng, D. B. Robinson, S. Raoux, P. M. Rice, S. X. Wang, and G. Li, *Journal of the American Chemical Society*, Vol. 126, p. 273, 2004.
13. A. S. Buteică, D. E. Mihaiescu, A. M. Grumezescu, B. Ş. Vasile, A. Popescu, O. M. Mihaiescu, and R. Cristescu, *Digest Journal of Nanomaterials and Biostructures*, Vol. 5, p. 927, 2010.
14. S. L. Iconaru, E. Andronescu, C. S. Ciobanu, A. M. Prodan, P. le Coustumer, and D. Predoi, *Digest Journal of Nanomaterials and Biostructures*, Vol. 7, p. 399, 2012.
15. Y. Li, J. Liu, Y. Zhong, J. Zhang, Z. Wang, L. Wang, Y. An, M. Lin, Z. Gao, and D. Zhang, *International Journal of Medicine*, Vol. 6, 2805, 2011.
16. Y. Chen, H. Chen, D. Zeng, Y. Tian, F. Chen, J. Feng, and J. Shi, *ACS Nano*, Vol. 4, p. 6001, 2010.
17. N. Sanpo, C. C. Berndt, and J. Wang, *Journal of Applied Physics*, Vol. 112, p. 084333, 2012.
18. G. De, G. Mattei, P. Mazzoldi, C. Sada, G. Battaglin, and A. Quaranta, *Chemistry of Materials*, Vol. 12, p. 2157, 2000.
19. W. D. Callister, *Materials science and engineering: An introduction*, John Wiley & Sons, USA, 2007.
20. A. Goldman, *Modern ferrite technology*, Springer Science & Business Media Incorporated, 2006.
21. L. D. Tung, V. Kolesnichenko, D. Caruntu, N. H. Chou, C. J. Oconnor, and L. Spinu, *Journal of Applied Physics*, Vol. 93, p. 7486, 2003.
22. N. Moumen and M. P. Pileni, *The Journal of Physical Chemistry*, Vol. 100, p. 1867, 1996.
23. N. A. Spaldin, *Magnetic materials: Fundamentals and device applications*, Cambridge University, 2003.
24. M. Chatterjee, B. Siladitya, and D. Ganguli, *Materials Letters*, Vol. 25, p. 261, 1995.
25. M. Crişan, M. Zaharescu, V. D. Kumari, M. Subrahmanyam, D. Crişan, N. Drăgan, M. Răileanu, M. Jitianu, A. Rusu, G. Sadanandam, and J. Krishna Reddy, *Applied Surface Science*, Vol. 258, p. 448, 2011.
26. C. Viazzi, A. Deboni, J. Zoppas Ferreira, J.-P. Bonino, and F. Ansart, *Solid State Sciences*, Vol. 8, p. 1023, 2006.
27. L. L. Hench and J. K. West, *Chemical Reviews*, Vol. 90, p. 33, 1990.
28. I. H. Gul and A. Maqsood, *Journal of Alloys and Compounds*, Vol. 465, p. 227, 2008.
29. J. Livage, M. Henry, and C. Sanchez, *Progress in Solid State Chemistry*, Vol. 18, p. 259, 1988.
30. M. Niederberger, *Accounts of Chemical Research*, Vol. 40, p. 793, 2007.
31. M. Niederberger and G. Garnweitner, *Chemistry – A European Journal*, Vol. 12, p. 7282, 2006.
32. S. D. Jones, T. N. Pritchard, and D. F. Lander, *Microporous Materials*, Vol. 3, p. 419, 1995.
33. M. Toba, F. Mizukami, S. I. Niwa, T. Sanoa, K. Maedaa, A. Annila, and V. Komppa, *Journal of Molecular Catalysis*, Vol. 91, p. 277, 1994.

34. G. W. Scherer and D. M. Smith, *Journal of Non-Crystalline Solids*, Vol. 189, p. 197, 1995.
35. C. J. Brinker, G. W. Scherer, and E. P. Roth, *Journal of Non-Crystalline Solids*, Vol. 72, p. 345, 1985.
36. M. Chai, M. Machida, K. Eguchi, and H. Arai, *Journal of Membrane Science*, Vol. 96, p. 205, 1994.
37. F. Mizukami, H. Izutsu, and T. Osaka, *Advanced Materials*, Vol. 6, p. 854, 1994.
38. F. Mizukami, Y. Akiyama, and H. Izutsu, *Supramolecular Science*, Vol. 5, p. 433, 1998.
39. B. K. Parekh and J. D. Miller, *Advances in flotation technology*, Society for Mining Metallurgy & Exploration Incorporated, 1999 .
40. P. Somasundaran and D. R. Nagaraj, "Chemistry and applications of chelating agents in floatation and flocculation", in M. J. Jones and R. Oblatt, eds., *Reagents in minerals industry*, IMM, London, pp. 209–219, 1984.
41. S. K. Singh, Ramprakash, S. Kumari, and B. S. Duhan, *Annals of Biology*, Vol. 29, p. 15, 2013.
42. I. V. Raspertova, V. A. Ovchynnikov, O. V. Shishkin, and R. D. Lampeka, *Transition Metal Chemistry*, Vol. 37, p. 607, 2012.
43. R. Millaleo, M. Reyes- Diaz, A. G. Ivanov, M. L. Mora, and M. Alberdi, *Journal of Soil Science and Plant Nutrition*, Vol. 10, p. 470, 2010.
44. H. Flack, *Acta Crystallographica Section A*, Vol. 65, p. 371, 2009.
45. F. H. Verhoff, *Citric acid: Ullmann's encyclopedia of industrial chemistry*, Wiley-VCH Verlag GmbH & Co. KGaA, 2000 .
46. A. Fraise, J. Y. Maillard, and S. Sattar, *Russell, Hugo and Ayliffe's principles and practice of disinfection, preservation and sterilization*, Wiley, 2012 .
47. G. Gershuny, *Start with Soil*, Rodale Press, 1998 .
48. P. F. Kruse and M. K. Patterson, *Tissue culture: Methods and applications*, Academic Press, 1973 .
49. N. Sanpo, C. C. Berndt, C. Wen, and J. Wang, *Acta Biomaterialia*, Vol. 9, p. 5830, 2013.
50. T. Yu, Z. X. Shen, Y. Shi, and J. Ding, *Journal of Physics Condensed Matter*, Vol. 14, p. L613, 2002.
51. N. Sanpo, C. C. Berndt, and J. Wang, *Journal of Applied Physics*, Vol. 112, p. 084333, 2012.
52. D. Varshney, K. Verma, and A. Kumar, *Journal of Molecular Structure*, Vol. 1006, p. 447, 2011.
53. S. Ayyappan, G. Panneerselvam, M. P. Antony, N. V. Rama Rao, N. Thirumurugan, A. Bharathi, and J. Philip, *Journal of Applied Physics*, Vol. 109, p. 084303, 2011.
54. K. E. Sickafus, J. M. Wills, and N. W. Grimes, *Journal of the American Ceramic Society*, Vol. 82, p. 3279, 1999.
55. Z. Zi, Y. Sun, X. Zhu, Z. Yang, J. Dai, and W. Song, *Journal of Magnetism and Magnetic Materials*, Vol. 321, p. 1251, 2009.
56. J. Robertson, *Acta Crystallographica Section A*, Vol. 35, p. 350, 1979.

57. I. P. Parkin, *Applied Organometallic Chemistry*, Vol. 14, p. 227, 2000.
58. Y. Köseoğlu, A. Baykal, M. S. Toprak, F. Gözüak, A. C. Başaran, and B. Aktaş, *Journal of Alloys and Compounds*, Vol. 462, p. 209, 2008.
59. N. Sanpo, J. Wang, and C. C. Berndt, *Journal of Nano Research*, Vol. 22, p. 95, 2013.
60. C.-H. Hu and M.-S. Xia, *Applied Clay Science*, Vol. 31, p. 180, 2006.
61. M. Raffi, S. Mehrwan, T. M. Bhatti, J. I. Akhter, A. Hameed, W. Yawar, and M. M. Ul Hasan, *Annals of Microbiology*, Vol. 60, p. 75, 2010.
62. P. K. Stoimenov, R. L. Klinger, G. L. Marchin, and K. J. Klabunde, *Langmuir*, Vol. 18, p. 6679, 2002.
63. L. L. Radke, B. L. Hahn, D. K. Wagner, and P. G. Sohnle, *Clinical Immunology and Immunopathology*, Vol. 73, p. 344, 1994.
64. O. Yamamoto and J. Sawai, *Bulletin of the Chemical Society of Japan*, Vol. 74, p. 1761, 2001.

Heterostructures Based on TiO_2 and Silicon for Solar Hydrogen Generation

Dilip Kumar Behara, Arun Prakash Upadhyay, Gyan Prakash Sharma,
B.V. Sai Krishna Kiran, Sri Sivakumar* and Raj Ganesh S. Pala*

*Department of Chemical Engineering, Indian Institute of Technology Kanpur,
Kanpur, UP, India*

Abstract

Renewable and pollution-free energy sources seem to be essential ingredients for long-term socioeconomic stability. Solar-based hydrogen production from water-splitting reaction is a fascinating and promising process that can meet this niche if implemented on a large scale. Contemporary research focuses on the development of semiconductor photocatalysts that work under visible region of solar spectrum for efficient hydrogen production. As most of the water-splitting photocatalysts have severe limitations in their performance, the development and efficacy of these photomaterials are still in its preliminary stage. Titanium di-oxide (TiO_2) and Silicon (Si) based materials are two most promising systems for photocatalysis (PC) and photoelectrocatalytic (PEC) applications among existing semiconductor materials owing to their abundance, nontoxicity, stability, and cost. Heterostructures based on these materials can be designed to gainfully utilize the functionalities of individual phases. Further, the interface of such heterojunctions plays a major role in charge carrier separation and enhancement in photon absorption cross section. This chapter presents a comprehensive overview of heterostructures based on TiO_2 and silicon for PC/PEC applications. Additionally, it addresses some challenging issues, unresolved critics, and pros/cons in development of heterostructures for solar energy application.

Keywords: Silicon, titanium di-oxide, photocatalysis, heterostructures, solar energy

*Corresponding authors: rpala@iitk.ac.in; srisiva@iitk.ac.in

5.1 Introduction

Growing energy demands depends considerably on generation of solar based fuels and chemicals. Central to such approaches are materials that are capable of capturing solar energy and converting them to a more utilizable form of energy. In the area of solar hydrogen, wherein solar energy is utilized for splitting water into hydrogen and oxygen, materials like TiO_2 , Si, Fe_2O_3 , ZnO , WO_3 , and BiVO_4 have been promising [1–9]. However, the development and efficacy of these photomaterials is still in its preliminary stage due to poor absorption cross section, charge carrier recombination and surface electrochemical reactivity. Several attempts such as doping, sensitization and addition of sacrificial agents have been tried to alleviate these shortcomings [6, 10, 11]. In spite of several efforts made for the improvement in single-phase materials, the most promising and generic approach resides in the use of composite/heterostructured systems, in which materials of same or different phases form an interface/heterojunction. Contemporary reports indicate that the heterojunctions formed at the interface promote the interfacial charge-transfer and improve the photocatalytic activity compared to individual counter parts [12–17]. This book chapter provides a state-of-the-art review on research activities that focus on the role of heterointerface, charge transfer mechanisms and synthetic strategies in photocatalysis (PC)/photoelectrocatalytic (PEC) applications. This review is limited to TiO_2 and Si heterostructures.

This chapter is divided into six sections. The first section serves as a broad introduction. The second section outlines the motivation and the need of heterostructures/junctions in the rational design of photocatalysts/photoelectrocatalysts. Moreover, this section provides overall classification, extensive discussion and some challenging issues regarding processing of heterostructures. The third section addresses TiO_2 polymorphic junctions like Degussa P25 (which is a heterojunction between anatase and rutile TiO_2), some important metal-semiconductor junctions, core-shell, and Janus systems. This section also covers other TiO_2 polymorphic heterojunctions, e.g., anatase-rutile, rutile-brookite, and brookite-anatase. The fourth section describes silicon based heterostructures, its classification and performance comparison against multijunctions. The fifth section provides an overview of some of the key issues addressed insufficiently in the context of heterostructures for solar hydrogen generation. The concluding section summarizes important issues of heterostructure assemblies in the context of Si and TiO_2 based materials for sustainable solar energy applications.

5.2 Overview of Heterostructures

5.2.1 Motivation/Importance of Heterostructured Nanomaterials

In the context of PC/PEC applications, the properties of nanoparticles distinctly differ from their bulk and molecular counterparts due to three main differences (1) surface/volume ratio, (2) quantum confinement effect, and (3) enhanced electrodynamic interactions [18, 19]. Prerequisite of any semiconductor material (nanoparticle and/or bulk) is to have efficient charge separation upon light excitation [20–22]. Upon light absorption, the created excitons (which are a bound electron–hole pair) have to be “split” so that the charge carriers can become mobile (or “free”). The mobile electrons and holes so created should not recombine and have to reach the surface to facilitate corresponding redox reactions. An interface formed between semiconductors facilitates splitting of exciton, provided that two semiconductors, constituting the interface have appropriate electron affinity and ionization potential [23]. In principle, migration and diffusion can provide the driving force for the electrons and holes to reach the surface. The typical diffusion length of electrons/holes is less than 10 nm before they recombine with holes/electrons, respectively [24]. Considering these factors, the concept of heterojunctions was introduced, in which junction formed between electron donating and accepting materials [25, 26], showed better efficiency of photocatalytic reactions by enhancing electron–hole splitting upon optical absorption cross section [27–35].

5.2.1.1 *What Is Heterojunction/Heterostructure?*

A heterojunction is an interface formed between regions of dissimilar materials (metals, semiconductors or insulators) in contrast to a homojunction, wherein the interface is formed between similar materials (metal-metal or semiconductor-semiconductor). A heterostructure can be defined as the combination of multiple heterojunctions together in a system or a device [36]. The properties of the homo/heterojunction nanostructures are sensitive to the shape and size of the heteronanostructures involved [37]. Such system plays a key role in the development of nanoscale devices owing to its influence on the properties like ohmic contact, schottky barrier and thermal stability [38, 39]. Furthermore, properly designed heterostructures typically involve modification of the electronic structure at the interface that facilitates optical absorption, charge separation, and enhances the kinetics of surface reaction [14], as illustrated in Figure 5.1(A).

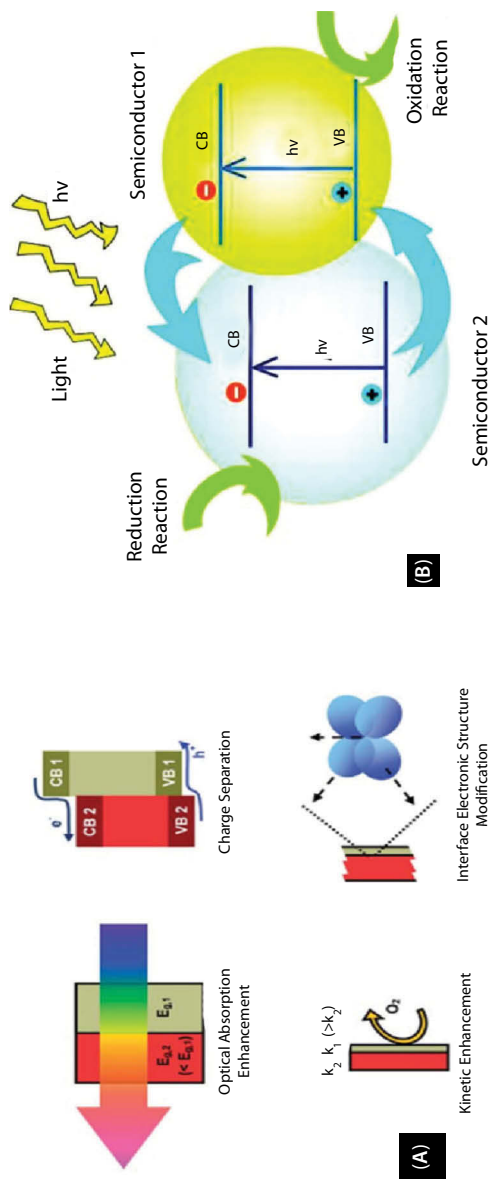


Figure 5.1 (A) Schematic illustration of primary processes responsible for performance enhancement in heterostructure systems, (B) charge transfer in a coupled semiconductor-semiconductor system. Reprinted with permission from Refs. [14] and [40]. Copyright © 2011, Royal Society of Chemistry and Copyright © 2010, American Chemical Society.

When two materials/phases/particles are coupled, the driving force for electrons and holes transport depends on their band edge positions [40] (Figure 5.1(B)). In contrast to single-phase materials, hybrids of two or more components seem to possess better energy conversion efficiencies [41]. Moreover, heterojunction nanomaterials not only improve the incident photon to current conversion efficiency but also increase the photochemical stability by avoiding contact between the narrow bandgap semiconductors and the electrolytes [42].

5.2.1.2 *Conditions for Forming Heteronanostructures*

The following three important aspects are essential in forming heterostructures. (1) Uniform size of the individual components, (2) smooth and defect free interfaces, and (3) good stability [13]. The interface and interfacial strain between two phases plays a major role in heterostructure formation [43]. Different degrees of interfacial strain are correlated to different type of heterostructures, e.g., (1) A well matched lattice parameters of crystalline phases lead to core/shell heterostructures formation [44], (2) anisotropic heterostructures (dimers or oligomers) are formed if there is overall lattice mismatch along certain miller indices with existence of coincident site lattices (i.e., systems with reduced symmetry compared to symmetric core-shell structures) [45].

5.2.2 **Classification of Heterostructures**

Heterostructures are broadly classified based on band alignments, charge transfer mechanisms, coupling of different domains and morphological effects. These classifications are elaborated below.

5.2.2.1 *Heterostructures Based on Band Alignment*

Based on the band alignment at the core-shell interface, semiconductor core-shell nanostructures are categorized into type-I, reverse type-I and type-II configurations (schematically elaborated in Figure 5.2). In type-I core-shell nanocrystals, the band gap of the core is narrower than band gap of shell. The shell material is utilized to improve the optical properties by passivation of the core (e.g., CdSe core/ZnS shell nanocrystals) [46]. In such systems, bright and stable luminescence is due to confinement of electron-hole (e^-h^+) pair in the core. In the inverse type-I system, the band gap of core is broader than the band gap of shell which permits both the charge carriers to reside in the shell (ZnSe core/CdSe shell

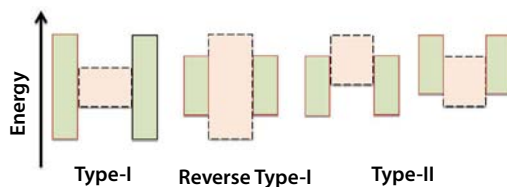


Figure 5.2 Schematic representation of the energy-level alignment in different core/shell systems. Pale yellow portions of the rectangles represent core (center) and pale green portions of the rectangles represent shell (outer) materials, respectively.

nanocrystals) [47]. In type-II system, the valence and conduction band (CB) of core lies below the valence and CB of shell, respectively, or vice-versa. Such staggered band alignment results in smaller effective band gap than each of individual constituent, minimizes the energy need for electron hole pair separation. The examples of such classification are CdTe/ZnTe and CdS/ZnSe [35], which have applications in photovoltaics.

5.2.2.2 Heterostructures Based on Charge Transfer Mechanisms

Depending on the charge transfer mechanisms, Liu *et al.* classified the heterostructures into the six categories (1) traditional charge transfer mechanism, (2) sensitization, (3) indirect Z-scheme, (4) direct Z-scheme, (5) vectorial electron transfer, and (6) co-catalyst coupling [48]; (schematically elaborated in Table T.1). In traditional charge-carrier transfer mechanisms, the photogenerated charge carriers move from one phase to another, depending upon the alignment of band edges. The most renowned example for such mechanism is TiO₂/CdS heterostructure [49]. Likewise, CdS quantum dots (QDs) with nanosized TiO₂ belongs to this category [50, 51]. Sensitization photochemical systems consist of a sensitizer which is bound to the semiconductor and has its lowest unoccupied molecular orbital (LUMO) above the CB of the semiconductor. In such systems, the charge injection from the LUMO of the sensitizer to CB of semiconductor minimizes the e⁻-h⁺ pair recombination. Examples for these systems are listed in the Table T.1 [52, 53]. Indirect Z-scheme systems contain two isolated semiconductor moieties and a redox mediator. Such systems have advantage of keeping charge carriers with stronger oxidation/reduction abilities on different semiconductor moieties. Examples for such system are rutile/anatase TiO₂ [54] and RuO₂/WO₃ [55]. Direct Z-scheme and vectorial transfer systems have one common merit in their mechanism wherein the charge carriers are isolated on different semiconductors. An example for direct Z-scheme based systems is ZnO-CdS [56].

Table T.1 Classification of heterostructures based on charge transfer mechanisms proposed by Liu *et al.*, reproduced from Ref. [48].

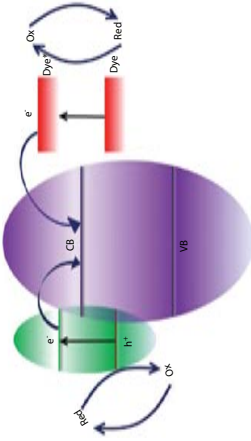
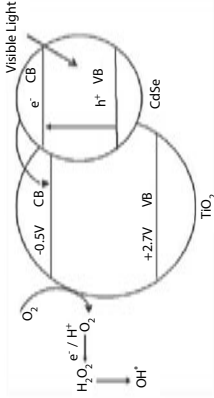
S. No.	Name of the mechanism	Pictorial representation	Representative cartoon in literature	Reference
1	Traditional charge-carrier transfer			CdS/TiO ₂ [49] Bi ₂ S ₃ /TiO ₂ [62] PbS/TiO ₂ [63]

Figure T.1 A2 Example for traditional charge-carrier transfer CdS/TiO₂, reprinted with permission from Ref. [49], Copyright © 2008, American Chemical Society.

Figure T.1 A1 Schematic diagram representing traditional charge transfer mechanism.

(Continued)

Table T.1 (Cont.)

S. No.	Name of the mechanism	Pictorial representation	Representative cartoon in literature	Reference
2	Sensitization	 <p>Figure T.1 B1 Schematic diagram representing sensitization.</p>	 <p>Figure T.1 B2 Schematic diagram representing the inter-particle charge transfer process in a CdSe/TiO₂ coupled system, Reprinted with permission from Ref. [65], Copyright © 2006, Elsevier.</p>	CdS/TiO ₂ [52] N719/TiO ₂ [53] Cu ₂ O/TiO ₂ [64] CdSe/TiO ₂ [65]

<p>3</p>	<p>Indirect Z-scheme</p>		<p>Figure T.1 C1 Schematic diagram representing indirect Z-scheme.</p>		<p>Figure T.1 C2 Proposed reaction mechanism for overall photocatalytic water splitting using IO_3^-/I^- redox mediator and a mixture of Pt-TiO_2-anatase and TiO_2-rutile photocatalysts, reprinted with permission from Ref. [54], Copyright © 2001, Elsevier.</p>	<p>Rutile/Anatase TiO_2 [54] RuO_2/WO_3 [55] $\text{Pt-WO}_3/$ Pt-SrTiO_3 [66] together with redox mediators</p>
----------	--------------------------	--	---	--	--	---

(Continued)

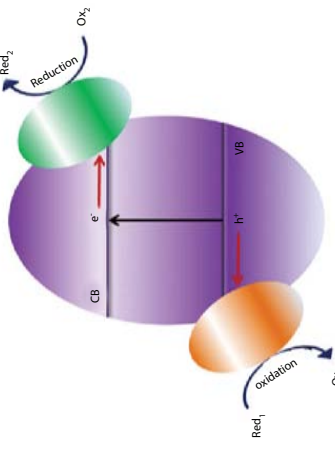
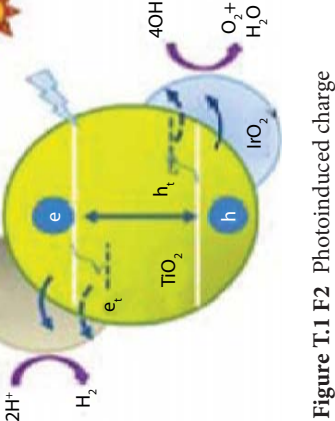
Table T.1 (Cont.)

S. No.	Name of the mechanism	Pictorial representation	Representative cartoon in literature	Reference
4	Direct Z-scheme			ZnO/CdS [56] WO ₃ /dye-sensitized TiO ₂ [67]
		<p>Figure T.1 D1 Schematic diagram representing direct Z-scheme.</p>	<p>Figure T.1 D2 Schematic of band structures in the Z-scheme mechanism in ZnO/CdS heterostructures, reprinted with permission from Ref. [56], Copyright © 2009, Royal Society of Chemistry.</p>	

<p>5</p>	<p>Vectorial electron transfer</p>		<p>Figure T.1 E1 Schematic diagram representing vectorial electron transfer.</p>
<p>$\text{TiO}_2\text{-Au-CdS}$ [57] $\text{Bi}_2\text{S}_3\text{-TiO}_2$ [68]</p>		<p>Figure T.1 E2 Energy band diagram of CdS-Au-TiO_2 system, reprinted with permission from Ref. [57], Copyright © 2006, Rights Managed by Nature Publishing Group.</p>	

(Continued)

Table T.1 (Cont.)

S. No.	Name of the mechanism	Pictorial representation	Representative cartoon in literature	Reference
6	Co-catalyst coupling	 <p>The diagram shows a semiconductor with a conduction band (CB) and a valence band (VB). A green co-catalyst is positioned above the CB, and an orange co-catalyst is positioned below the VB. An arrow labeled 'e-' points from the CB to the green co-catalyst, with 'Red_s' and 'Reduction' written above it. Another arrow labeled 'h+' points from the VB to the orange co-catalyst, with 'Ox_s' and 'Oxidation' written below it.</p>	 <p>The cartoon shows a green TiO₂ particle with a Pt co-catalyst on the left and an IrO₂ co-catalyst on the right. A sun icon indicates light excitation. An arrow labeled 'e-' points from the valence band to the conduction band, and another arrow labeled 'h+' points from the conduction band to the valence band. Below the Pt, an arrow shows '2H⁺' being converted to 'H₂'. Below the IrO₂, an arrow shows '4OH' being converted to 'O₂ + H₂O'.</p>	<p>IrO₂/TiO₂ [61] Pt, RuO₂, NiO, Rh-Cr₂O₃, MoS₂ [69]</p>
		<p>Figure T.1 F1 Schematic diagram representing co-catalyst coupling.</p>	<p>Figure T.1 F2 Photoinduced charge separation in a TiO₂ semiconductor particle coupled to Pt and IrO₂ co-catalysts, reprinted with permission from Ref. [61], Copyright © 2011, American Chemical Society.</p>	

In systems like TiO_2 -Au-CdS [57], excitation of both semiconductors TiO_2 and CdS leads to simultaneous vectorial electron transfer from $\text{TiO}_2 \rightarrow \text{Au} \rightarrow \text{CdS}$, which results in significant reduction of recombination rate. In such systems, CdS acts as the reduction site for the overall system and the reversal of electron transfer from CdS to TiO_2 is a minor pathway, which strongly supports vectorial transfer system. When such heterostructures are coupled with a co-catalyst their photocatalytic efficiency increases due to availability of redox reaction sites on the co-catalyst surface. Noble metals like Pt, Ru, Rh, Pd and metal oxides like NiO, RuO_2 , and CeO_2 are most widely used co-catalysts. Some good examples for this system are Au/ TiO_2 [58], Ag/ TiO_2 [59], Pt/ TiO_2 [60], and IrO_2 / TiO_2 [61].

5.2.2.3 Heterostructures Based on Effective Coupling of Different Domains

The electronic and optical properties of heteronanostructures can be efficiently controlled by not only tuning the individual components, sizes, shapes but also coupling of these individual domains. Feng *et al.* [13] classified the metal and/or semiconductor heterojunctions into the following three classes: (1) core-shell heterojunctions, (2) segmented heterojunctions, and (3) branched heterojunctions as shown in Figure 5.3. All these three classes can be achieved using metal-metal, semiconductor-semiconductor and metal-semiconductor heterojunctions.

A variety of core-shell metal-metal heterojunctions like $\text{Au}_{\text{core}}/\text{Ag}_{\text{shell}}$, $\text{Au}_{\text{core}}/\text{Pt}_{\text{shell}}$ [70], $\text{Rh}_{\text{core}}/\text{Pt}_{\text{shell}}$ have been reported for electrical, optical, catalytic and magnetic properties enhancement. On the other hand, segmented Au/Co heterojunctions [71] synthesized by the group of Chaudret and Pd-Au segmented heterojunctions [72] synthesized by the group of Xia falls under segmented heterojunctions. Au/Pt branched heterojunctions

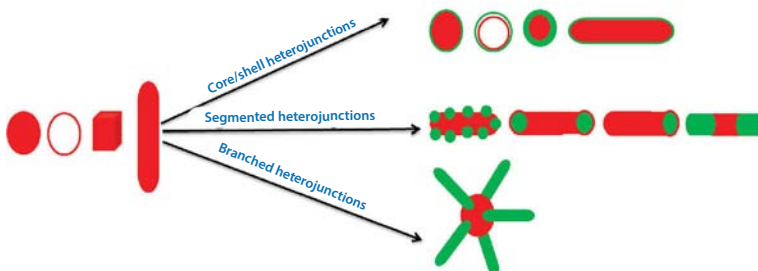


Figure 5.3 Schematic illustration of formation of metal and/or semiconductor heterojunction nanomaterials, Reproduced from Ref. [13].

reported by Guo *et al.* [73] and Wang *et al.* [74] falls under class of branched heterojunctions.

With respect to semiconductor-semiconductor heterojunctions, we have already discussed core-shell classification under section 5.2.1.1. The next classification of semiconductor-semiconductor heterojunctions, e.g., $\text{Cu}_2\text{S}/\text{In}_2\text{S}_3$ [75], $\text{CdS}/\text{Ag}_2\text{S}$ [76], and $\text{CdS}/\text{Cu}_2\text{S}$ [77] reported fall under segmented heterojunctions. Lastly, branched heterojunctions, e.g., CdTe/CdSe , CdTe/CdS , CdSe/CdS were extensively studied by group of Alivisatos [78] fall under the branched heterostructure category.

Metal-semiconductor heterojunctions with core-shell configuration, e.g., Au/ZnO [79], Au/SnO_2 [80] and $\text{Cu}_2\text{S}/\text{Au}$ [81] have been widely employed for improving optical, electronic, catalytic, magnetic and surface passivation properties. In addition to core-shell classification, segmented metal-semiconductor heterojunctions (e.g., Ag/ZnO [82], Ag/TiO_2 [83], and Ag/MoO_3 [84]) and branched heterojunctions (e.g., Pt/MWCNT [85], PbS/Au [86], and $\text{Cu}/\text{Cu}_x\text{S}$ [87]) have been extensively studied for various photocatalytic and photoelectrochemical applications.

5.2.2.4 Heterostructures Based on Morphology (1D Nanomaterials)

It is well known fact that morphology of nanoparticles plays a very important role in exploiting their properties for several applications. Aneta *et al.* [88] classified 1D heterojunctions as segmented (or end-to-end), core-shell (co-axial), angled cross junctions (or sometimes called as T-junctions), hyper-branched and other multi branched (usually called as nanobrushes) heterojunctions as shown in Figure 5.4. Further, Tong *et al.* [11] classified 1D nanoheterostructures into three types as (1) axial heteronanostructures, (2) radial heteronanostructures, and (3) hierarchical heteronanostructures.

5.2.3 Discussion on Other Heterostructure Classifications

Beyond the above mentioned classifications, heterostructures are also classified on the basis of nature (insulators, metals and semiconductors) and availability of materials. In this context, Zheng *et al.* [89] and Buonsanti *et al.* [90] listed a variety of heterojunctions forming heterostructures as metal-metal junctions [91], metal-polymer junctions [92], inorganic semiconductor junctions [93], inorganic semiconductor-metal junctions [94], inorganic-organic semiconductor junctions [95], and semiconductor-carbon nanotube junctions [96]. Inorganic semiconductor-insulator hybrid structures like CdSe/ZnS core/shell [97] and CdSe QDs embedded into TiO_2 matrix QDs [98] are extensively used for bio labeling. Additionally,

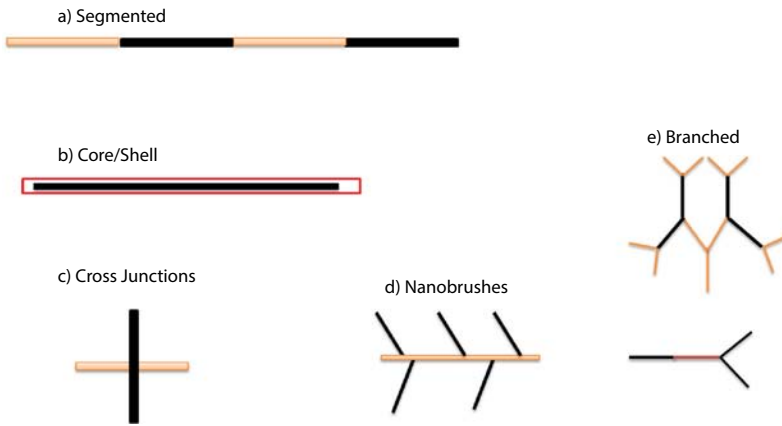


Figure 5.4 Schematic illustration of different types of 1D heterojunctions, reproduced from Ref. [88].

inorganic semiconductor-metal heterostructures like CdTe-Ag [99], CdS-Au [100], and CdSe-Au [101] were exploited for photocatalytic and photo-electronic applications.

5.2.4 Challenges/Key Issues in Forming Heterostructures

Some key issues pointed out by Liu *et al.* [48] are:

1. In case of sensitization, issues like stability, contact, high surface area, availability of suitable band edge sensitizers and electrolytes are to be clarified.
2. In case of indirect Z-scheme, prominent issues are availability of suitable redox mediators in solution and semiconductor surface availability for redox reactions.
3. In case of direct Z-scheme, the major issues are in identifying appropriate pair of semiconductor, making proper contact between two phases and effective interfacial carrier transfer.
4. In case of vectorial transfer mode, design of semiconductor-metal-semiconductor framework with appropriate electronic/geometric structure is a challenging task.
5. In case of co-catalyst systems, major issues like ohmic/Schottky contact, optical absorption cross section enhancement of photocatalysts are important.

Although, some of the above mentioned key issues have been addressed by research communities, it is a challenge to design and develop simple synthesis procedures for the fabrication of high quality heterojunctions. There are limited reports on efficient control of nucleation and growth of heterostructure formations. Furthermore, controlled modification of suitable semiconductors for proper band electronic structure and interfacial atomic structure is still a challenging task.

In this book chapter, we focused only on heterostructures that contain inorganic semiconductor or metal excluding organic, polymeric or biological components. Further, we have not addressed issues related to the synthesis and growth mechanisms involved in the formation of these heterostructures. However, readers can refer to the reviews by Casavola *et al.* [102] and Luigi *et al.* [103], for further information on these issues.

5.3 TiO₂ Heterostructures

This section briefly covers: (1) P25 degussa, a heterostructure of anatase-rutile TiO₂ particles, (2) other TiO₂ polymorphic heterojunctions like anatase-brookite/brookite-rutile/brookite-anatase, anatase TiO₂-(B), (3) TiO₂ coupled with metals (i.e., metal-semiconductor junctions and the role of plasmonic metals in enhancement of photocatalytic activity), (4) core-shell structures, and (5) Janus systems.

5.3.1 Heterojunctions of TiO₂ Polymorphic Phases

5.3.1.1 Anatase-Rutile Heterojunctions: P25 Degussa

P25 Degussa, a commercial product from Evonik Degussa Corporation, Germany consists of ~4:1 w/w ratio of anatase and rutile (i.e., 75–80% anatase and rest of rutile) as constitutive components. Due to the “intimate” co-existence of these two phases and the formation of anatase-rutile interfaces/surface states, it is observed that P25 Degussa is more effective than a system consisting of pure Rutile or Anatase [104]. The effective nature of P25 is believed to be the “synergistic effect” between Rutile and Anatase. However, the limited understanding of the “synergistic effect” has prevented extensive exploitation of this effect.

Several models, e.g., antenna model [105] and interfacial band model [106] support the “synergistic effect.” However, no report provides a detailed rationale for its 80%-20% anatase-rutile composition and high photoactivity. Qualitatively, the probable reason may be the specific

combination and morphology of anatase/rutile phases enhances the e^-h^+ pair transport and thereby decreases the rate of recombination [107]. Alexander *et al.* [108] and Agrios *et al.* [109] proposed tightly interwoven anatase crystallites with rutile which are responsible for difference in surface reactions on Degussa P25 leads to unique adsorption sites. Moreover, Hurum *et al.* [110] and Tzab *et al.* [111] reaffirmed that the promising photocatalytic activity of P25 Degussa is due to interfacial electron transfer.

Apart from synergistic effect, several presumptions exist in literature for P25 Degussa to show high activity. For example, electrons selectively migrate either to rutile [112] or anatase [105], leading to excess holes in other phase. From the TEM images, Roger *et al.* [113] predicted that P25 consists amorphous mixture of anatase and rutile where few anatase particles are covered with rutile phase particles. Later, these results were supported by Ohno *et al.* [114]. On the other hand, HRTEM analysis of Abhaya *et al.* [115] confirmed that individual catalyst particle is single-phase (either rutile or anatase) without presence of any amorphous material (i.e., any amorphous phase is confined to at most a monolayer). Figure 5.5(A) confirms the absence of amorphous states exists in P25 Degussa and Figure 5.5(B) confirms amorphous nature of P25 Degussa.

In spite of several presumptions like synergistic effect, tightly interwoven structures of anatase and rutile particles, the origin of the high photocatalytic activity of P25 Degussa is still unclear and underlying mechanism needs to be understood in a much broader sense. However, all in all, based on above discussions and arguments from literatures on P25 Degussa, we can say that this TiO_2 polymorphic phases of anatase and rutile, as the first heterostructures that have been explored extensively in context of PC application.

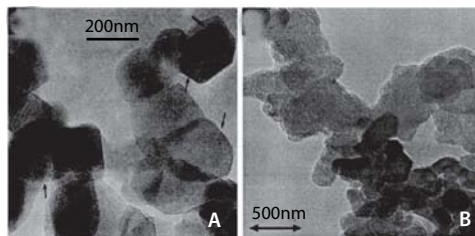


Figure 5.5 (A) Confirming no amorphous phase in P25, (B) Amorphous phase presence confirmed by Ohno *et al.* Reprinted with permission from Refs. [115, 114], Copyright © 1995, Elsevier, Copyright © 2001, Elsevier.

5.3.1.2 Other TiO₂ Polymorphic Phase Heterojunctions

Recently, heterojunctions of TiO₂ polymorphic phases (anatase-rutile/rutile-brookite/brookite-anatase) has shown significant improvement in comparison to the performance of individual phases. There is no clarity and confirmative proof on band edge location of TiO₂ polymorphic phases. However, the interfacial charge carrier transport in TiO₂ polymorphic heterojunctions can be explained in two main pathways: (1) Due to lower CB minimum, rutile phase acts as a passive electron sink and captures electrons from anatase phase [116], (2) transport of electrons from the rutile to anatase occurs *via* lower energy electron trapping sites of anatase phase [105, 110]. Figure 5.6 shows two models of electron transfer from anatase to rutile and vice-versa [105, 117]. However, there is a certain possibility that both pathways are operational simultaneously and contribution of individual modes depend on the particle size, surface energy, localized electronic states and structural interface in the bandgap of anatase/rutile phases.

Pablo *et al.* [17] studied the photoactivity of anatase-rutile bi layer films, consisting of an anatase layer of variable thickness. The enhanced photoactivity of such system is attributed to heterojunction formed *via* buried anatase-rutile. Furthermore, Kawahara *et al.* [112] also proved the electron transfer from CB of anatase to rutile in the patterned anatase/rutile bi layer-type photocatalyst system and achieved highest photodecomposition of CH₃CHO by such bi layers than pure anatase or rutile photocatalysts. Similarly, Zhang *et al.* [118] confirmed the surface junctions play a

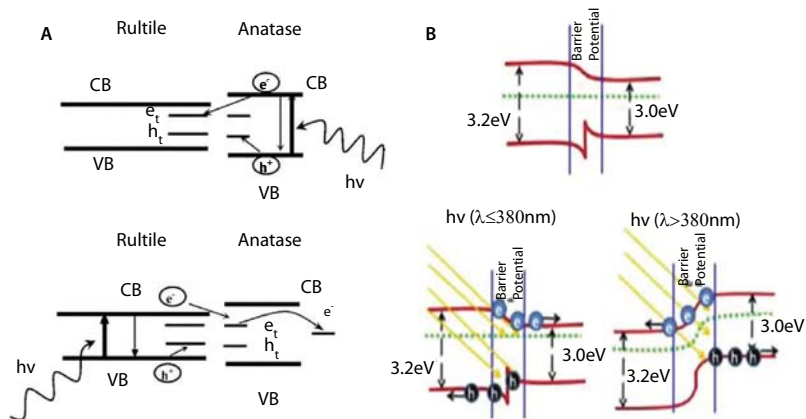


Figure 5.6 (A) Model for charge separation in mixed phase TiO₂, and (B) Interfacial model of Anatase/Rutile systems, Reprinted with permission from Refs. [105, 117], Copyright © 2003, American Chemical Society, Copyright © 2011, Elsevier.

key role in enhancement of water splitting reaction. They observed higher hydrogen evolution rate (nearly four times compared to pure phases) at a temperature of 700–750°C, where a mixture of rutile and anatase exists, than either at 400°C (pure anatase) or at 800°C (pure rutile). TEM images of Figure 5.7 confirm core-shell structure formation of anatase-rutile systems.

A limited numbers of articles are available on heterojunctions of anatase-rutile, rutile-brookite and brookite-anatase TiO₂ polymorphic phases, e.g., anatase core-rutile shell [119], rutile core-anatase shell [120, 121], brookite core-anatase shell [16]. Figure 5.8(A) shows the electron transfer from anatase to rutile [122] and Figure 5.8(B) illustrates the electron transfer from brookite to anatase [123]. Apart from anatase/rutile heterojunctions, limited reports on heterojunctions of other phases of titania like anatase/TiO₂-(B) [16], anatase/brookite [123], and rutile/brookite [124] are available in literature.

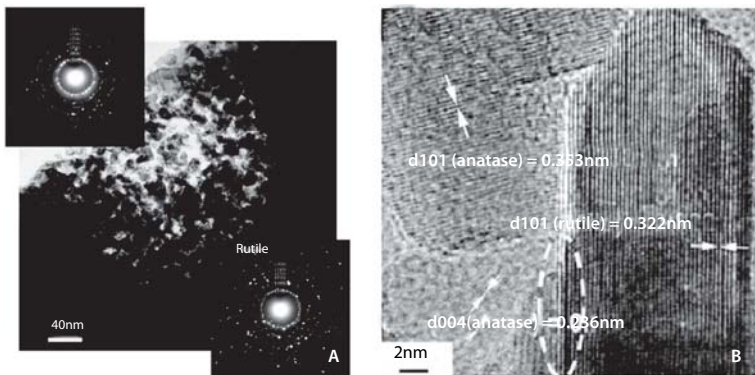


Figure 5.7 (A) TEM image confirming anatase core-rutile shell, (B) TEM image confirmation of rutile core-anatase shell, reprinted with permission from Refs. [119, 121], Copyright © 2006, American Chemical Society, Copyright © 2012 The American Ceramic Society.

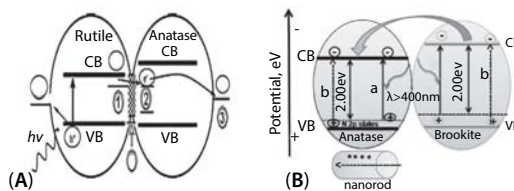


Figure 5.8 (A) Charge carrier transfer from anatase to rutile and (B) Schematic representation of energy band diagram, band alignment and charge transfer from brookite to anatase, reprinted with permission from Ref. [122], Copyright © 2013, Elsevier and Reproduced from Ref. [123].

5.3.2 TiO₂ Heterojunctions with Metals (Metal-Semiconductor Junctions)

Metal nanostructures are often coupled with semiconductor matrices to form hybrid structures which have novel optical, electronic, magnetic, catalytic and biological applications [125, 126]. These metal-semiconductor composite materials are effective in separating charge carriers [127–133] upon photoexcitation. The main objective of either metal-metal or metal-semiconductor composites formation is to improve the charge rectification in the original system. However, the catalytic efficiency of single component systems are low (<5%) because of charge carrier recombination [134]. In metal-semiconductor coupled systems, irradiation of light causes the excitation of the electrons from VB to the CB in semiconductor which is quickly transferred to the metal nanoparticle in the vicinity of the semiconductor. Metals can also act as a reservoir for photoinduced charge carriers to improve the charge transfer process by decreasing the recombination rate. Some important metal-semiconductor composites reported in the literature are Au/TiO₂ [58], Ag/TiO₂ [59], Pt/TiO₂ [60], Cu-TiO₂ [135], Ru-TiO₂ [136], and Ir-TiO₂ [137] are listed in Table T.2.

5.3.2.1 Role of Plasmonic Metals in Metal-Semiconductor Coupled Systems

Surface plasmon resonance (SPR) in noble metals like Au, Ag, and Pt that are coupled to semiconductor systems improves the charge carrier separation as well as the photon absorption [58, 183, 184]. The SPR effect is a result of coherent oscillation of the free electrons on the surface of nanomaterials, induced by visible light irradiation which enhances the localized electric field in the proximity of the metal particles for the facile formation of e⁻-h⁺ pairs in the vicinity of the semiconductor [159, 185–187].

Plasmonic PC has been rationalized *via* two different mechanisms. In the first mechanism, the noble metal NPs absorb the visible light which leads to generation of photocarriers, separated at the metal-semiconductor interface. As a result of this, redox reactions take place on the surface of the plasmonic photocatalyst. This mechanism relies on the transfer of photogenerated electrons and/or holes from the noble metal NPs to semiconductors [188]. Along these lines, Figure 5.9 shows the SPR effect enhances the photoactivity of the system, when gold is irradiated with visible light [189]. However, in second mechanism, the SPR-induced electric field can enhance the rate of e⁻-h⁺ pair formation, especially by localizing electromagnetic energy close to semiconductor surfaces. This

Table T.2 List of some important metal-semiconductor junctions (heterostructures of TiO₂ with metals other than gold).

S. No.	System	Synthesis method	Remarks/applications	Reference
1	Pt-TiO ₂			
	Pt-TiO ₂	Co-sputter deposition	Photoelectrochemical applications	[138]
		Photoreduction method	Catalytic/photocatalytic applications	[60, 139–141]
2	Cu-TiO ₂			
	Cu doped TiO ₂	Sol-gel method/magnetron sputtering	Photocatalytic applications	[135, 142–145]
	Cu doped TiO ₂	Sol-gel synthesis	Hydrogen production	[146]
	Cu doped TiO ₂	Sol-gel synthesis	Photophysical/catalytic applications	[135, 143, 147–151]
3	Ag-TiO ₂			
	Ag-TiO ₂	Layer by layer assembly/ reduction of Silver salts/sol-gel routes	Dispersion studies/charge separation at interface/catalysis applications	[59, 152–156]
	Ag-TiO ₂	Chemical Reduction	Core-shell nanofibers for photoinduced electron storage and PC applications	[157]
	Ag-TiO _{2-x} N _x	Doping followed by deposition with silver nitrate	Visible light PC applications	[158]

(Continued)

Table T.2 (Cont.)

S. No.	System	Synthesis method	Remarks/applications	Reference
	Ag-N-TiO ₂	Chemical Reduction method/ N doping followed by Polyol process	Optical simulations have been done	[159, 160]
4	Ru-TiO₂			
	Ru-TiO ₂	Sol-gel synthesis	Tested for Johnson-Mehl-Avrami model	[136]
5	Ir-TiO₂			
	Ir-TiO ₂	Vapor phase selective hydrogenation	Selective hydrogenation of crotonaldehyde	[137, 161]
6	Graphene-TiO₂ heterojunctions			
	Graphene-TiO ₂ nanocomposites	Precipitation and deposition/ molecular grafting/	Photocatalytic/photoelectrical/ environmental/pollutants removal/ Li-ion battery applications	[162–181]
	Graphene-TiO ₂ nanocomposites	Sol-gel method	Water splitting reaction	[182]

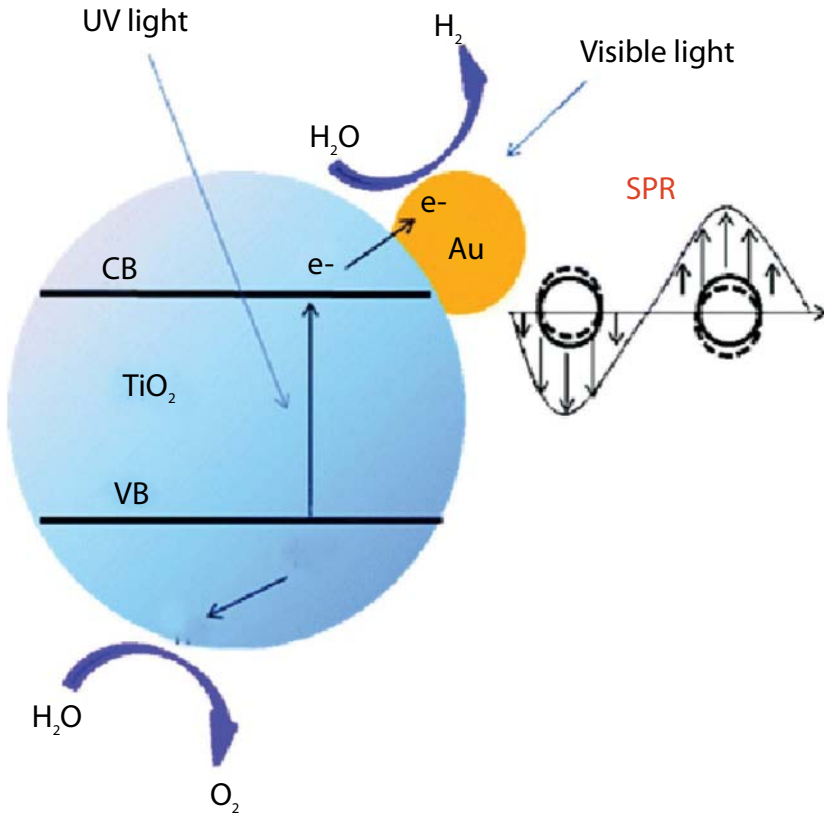


Figure 5.9 SPR effect of Gold when irradiated with visible light in enhancing the photoactivity, adapted from gold loaded TiO₂ for water splitting by SPR effect, reprinted with permission from Ref. [189], Copyright © 2011, American Chemical Society.

electric field interacts with neighboring semiconductor and induces the formation of charge carriers which migrate to perform surface redox reactions [190]. However, only few reports are available which supports this mechanism [191].

5.3.2.1.1 Au-TiO₂ Nanocomposites

Gold NPs are frequently used in solar energy applications because it extends photon absorption from UV to visible region due to SPR effect. Fermi level equilibration is a key phenomenon that dictates the storage/discharge capacity of metal NPs [192–194]. The electron storage in metal NPs shifts the Fermi level of the system to more negative potentials and making it more reductive [195]. Group of Tatsuma [196] has first studied the Au-SPR in Au-TiO₂ for methanol/ethanol oxidation system. Liu *et al.* [197] firstly reported sixty six fold improvement in water splitting activity

after addition of Au on TiO_2 material as compared to only TiO_2 . Silva *et al.* [198] reported the photocatalytic activity of the Au- TiO_2 plasmonic photocatalyst for generation of H_2 and O_2 from water and demonstrated that Au NPs act as light harvesters and gas evolution centers. The mechanism of charge carrier/electron transfer in coupled systems of noble metals with semiconductors is demonstrated by group of Kamat [58, 195, 199–204], group of Linic [190] and group of Myung-hwan [188]. In particular photo induced charge transfer processes in Au- TiO_2 nanocomposites have been extensively studied by the group of Kamat. Table T.3 lists some important Au- TiO_2 composites synthesized *via* different routes.

5.3.2.1.2 Ag- TiO_2 Nanocomposites

After gold, silver occupies the next position as an important noble metal in PC. In fact, some articles report more SPR effect in Ag than Au because Ag has very small value (imaginary component) of dielectric constant, which leads to a large local field enhancement and relatively small loss of the surface-plasmon propagation [240]. The first work on Ag- TiO_2 reported by Gonzazelize *et al.* [241] explained the electron exchange between TiO_2 and Ag. The first work on Ag- TiO_2 core-shell structures formed by coating of TiO_2 onto metal nanoparticles was reported by Liz-marzan and co-workers using layer by layer assembly [153]. Several reports on Ag coupled plasmonic heterostructures/heterojunctions like Linic *et al.* [160], Yu *et al.* [242], Wang *et al.* [188], and Zhang *et al.* [243] are available in literature.

5.3.2.1.3 Pt- TiO_2 Nanocomposites

Platinum coupling with TiO_2 has been reported by several research groups for enhanced photoactivity [244, 245]. In contrast to Au and Ag, the SPR of Pt NPs remain relatively unexplored because the SPR of Pt NPs is typically below 450 nm, which makes it more difficult to probe due to the strong absorption of light by most solvents in the specified wavelength range [246]. The first work on Pt composites ($\text{Pt}/\text{Bi}_2\text{O}_3$) encompassing SPR effect is reported by Li *et al.* [247] *via* Pt NPs dispersion on the Bi_2O_3 substrate. Later, Zhai *et al.* [248] fabricated the plasmonic photocatalyst Pt- TiO_2 , for PC applications. Various reports are available on Pt coupled with TiO_2 or platinized TiO_2 as a photocatalyst for variety of reactions [249, 250]. However, all the reports confirm that Au shows higher catalytic activity and SPR effect than Ag and Pt [251].

5.3.2.1.4 Graphene- TiO_2 Nanocomposites

Graphene, an important conducting substrate, has gained significant importance in the field of catalysis. Large number of citations of a recent article “rise of graphene” reported in literature is indicative of the

Table T.3 List of heterostructures of TiO₂ with gold metal (some important journal articles comprising of composites in colloidal form, films, core-shell, and Janus schemes).

S. No.	System	Synthesis method	Remarks/applications	Reference
Metal-Semiconductor junctions				
Gold-TiO₂ heterojunctions				
1	Au-TiO ₂ nanocomposites	Reduction of gold salt followed by sol-gel technique	Charge distribution/Fermi level equilibration studies in metal-semiconductor interfaces	[58, 195, 199-203]
	Au-TiO ₂ nanocomposites	Electrochemical/evaporation Method	Photocatalytic water splitting	[197]
	Au-TiO ₂ nanocomposites	Flame spray pyrolysis	Water reduction	[205]
	Au-TiO ₂ nanocomposites	Co-polymer assisted sol-gel method	Water reduction, reduction of p-nitrophenol and optical sensor applications	[206-211]
	Au-TiO ₂ nanocomposites	Deposition-precipitation and self-assembly	Decomposition of RhB	[212, 213]
2	Au-TiO ₂ nanocomposites	Photochemical deposition	Photocatalytic applications	[198, 214, 215]
	Au-TiO ₂ films	Electrochemical way	Photocatalytic applications	[216]
	Au-TiO ₂ films	Sol-gel method	PC and gas sensing applications	[217]
	Au-TiO ₂ films	Coating by sono-electrochemical methods	Visible light PC	[218-221]

(Continued)

Table T.3 (Cont.)

S. No.	System	Synthesis method	Remarks/applications	Reference
3	Au/TiO ₂ core-shell	Complexation of a titania precursor with a positive polyelectrolyte, followed by hydrolysis (Layer by layer process)	Applications in catalysis and photonics	[162, 222–226]
4	Au-TiO ₂ Janus, eccentric core-shell, and concentric core-shell geometries.	Seed mediated growth followed by TiO ₂ coating	First paper showing energy calculations of Janus Au-TiO ₂ systems	[205, 207, 209–211]
5	Au-TiO ₂ Janus structures	Controlled hydrolysis in presence of gold NPs	Visible light Hydrogen generation	[227–229]
6	Au-TiO ₂ yolk structures	Modified sol-gel method prior to deposition	For photodegradation of RITC dye	[230]
7	Au-TiO ₂ Nanotube arrays	Layer by layer assembly	Tunable catalytic activities	[231, 232]
8	Au in TiO ₂ nanoreactors	Wet chemical method	Hollow core-shell Au-TiO ₂ nanocomposite system for photocatalytic applications	[233]
9	Au/ TiO ₂ /CNT	Self-assembly	Nanocomposites for photocatalytic applications	[234–237]
10	Au-TiO ₂ review articles	---	Environmental applications	[238, 239]

popularity of graphene [252]. Graphene oxide promotes the electron transfer in semiconductor-metal heterostructures through π - π network [162]. Graphene-modified TiO_2 heterostructures have received considerable importance and seem to be promising in the context of pollution control and photocatalytic applications. Yang *et al.* [253] presented the high photocatalytic properties exhibited by Graphdiyne and Graphene composites with TiO_2 (towards methylene blue degradation) experimentally and theoretically. Figure 5.10(A) graphene- TiO_2 composite systems used for photodegradation of methylene blue dye [254] and Figure 5.10(B) shows the charge transfer from Fe doped TiO_2 to Graphene network [255].

Multifunctional photocatalyst assemblies for water splitting reaction have been demonstrated recently by Hyoung *et al.* [256]. Further, they demonstrated the selective catalytic processes occurring at distinct sites on a single layer graphene or reduced graphene oxide sheet by the incorporation of more than two catalyst particles into the system. Graphene-based composites are also used in solar cells [257] and semiconductor PC [258]. Recent reviews confirm the utilization of these materials widely by research communities [259]. A complete list of TiO_2 coupled with different semiconductors (e.g., CdS, CdSe, and ZnS) *via* various multi junctions like metal-semiconductor-metal, semiconductor-metal-semiconductor is listed in Tables T.4 and T.5 for information. (The contents listed in this table covers some important reports from literature on heterojunctions)

5.3.3 Core-Shell Structures

The functional properties of nanomaterials are greatly improved by capping them with other compatible materials and such systems are referred to as “core-shell” nanostructures. The major criterion for core-shell

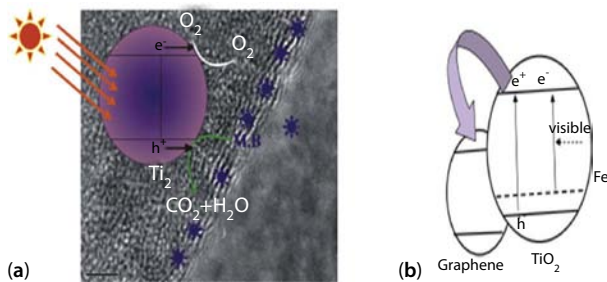


Figure 5.10 (A) Multi layers of Graphene- TiO_2 nanocomposites in photodegradation of methylene blue and (B) Fe doped TiO_2 -graphene nanocomposites for visible light PC. Reprinted with permission from Refs. [254, 255]. Copyright © 2013, Elsevier, Copyright © 2011, Elsevier.

Table T.4 List of some semiconductor-semiconductor junctions/heterostructures (only coupled with TiO_2 is listed).

Semiconductor-semiconductor junctions				
S. No.	System	Synthesis method	Remarks/applications	Reference
1	CdS-TiO₂ heterojunctions			
	CdS-TiO ₂	Precipitation methods	Photoluminescence applications/H ₂ from decomposition of H ₂ S	[260–262]
	CdS/TiO ₂	Sono synthesis	Core-shell structures without surfactants	[263–266]
	CdS/TiO ₂	Electrodeposition	Photoelectrochemical water decomposition	[267]
	CdS@TiO ₂	Two-step solvo-thermal method	Visible light PC	[268]
	CdS-TiO ₂ films	Hydrothermal synthesis	TiO ₂ films sensitized with CdS	[269]
	CdS@TiO ₂ CdS@Anatase@Rutile	Chemical routes	PEC applications	[270]
2	CdS-TiO ₂	Chemical vapor deposition	PEC applications	[271]
	CdSe-TiO₂			
	CdSe QDs-TiO ₂ films	Chemical deposition	Optical absorption studies of CdSe QDs deposited on TiO ₂ films	[272]

	CdSe-TiO ₂	Electrophoretic deposition	Photocatalytic applications	[273, 274]
	CdSe-N-doped TiO ₂	Sol-gel method	Solar energy conversion applications(PV&PEC)	[275]
3	ZnS-TiO₂			
	ZnS-TiO ₂	Solvothermal route	TiO ₂ capped ZnS nanowires for growth mechanism studies	[276]
4	SrTiO₃-TiO₂			
	TiO ₂ -SrTiO ₃	Electrochemical anodization/sol-gel method	DSSC/PEC water splitting/UV photodetector applications	[277, 278]
5	ZnO-TiO₂			
	TiO ₂ -ZnO nanocomposites	Two step solchemical method	Gas sensor applications	[279]
	ZnO-TiO ₂ -nanotubes	Electrochemical anodization	PC applications	[280]
6	SnO₂-TiO₂			
	SnO ₂ -TiO ₂	Precipitation and deposition method	Capped vs Couple system importance	[281-283]
7	Cu₂O-TiO₂			
	Cu ₂ O-TiO ₂	Anodic oxidation followed with cathodic deposition	Deposition kinetics	[284]

(Continued)

Table T.4 (Cont.)

Semiconductor-semiconductor junctions				
S. No.	System	Synthesis method	Remarks/applications	Reference
8	$\text{Cu}_2\text{O}/\text{TiO}_2$	In situ hydrolysis and crystallization method	Photodegradation of 4-nitrophenol	[285]
	$\text{Cu}_2\text{O}-\text{TiO}_2$	Alcohol-aqueous based chemical precipitation method	PC applications	[286]
	Pbs-TiO₂			
9	TiO_2 -Pbs	Colloidal hot-injection route	Visible light generation of hydrogen/ photovoltaic applications	[287]
	TiO_2 -Pbs QDs	layer-by-layer deposition	Solar cell applications	[288]
	ZrO₂-TiO₂			
	ZrO_2 - TiO_2 thin films	Sol-gel method	Used in UV detectors	[289]
10	ZrO_2 - TiO_2 - N_{2x}	Mesoporous	Coupled system for optical properties	[290]
	CoO-TiO₂			
	CoO/TiO_2	Pulsed laser deposition	Applications in spintronic devices	[291]

Table T.5 List of some semiconductor–metal–semiconductor junctions, metal–semiconductor–metal junctions and metal–insulator–semiconductor–insulator–metal junctions (only coupled with TiO_2 are listed).

Semiconductor–metal–semiconductor junctions				
S. No.	System	Synthesis method	Remarks/applications	Reference
1	$\text{TiO}_2/\text{WO}_3/\text{Au}/\text{MWCNT}$ composites	Chemical reduction followed by ultra-sonication	Hydrogen production–Advantages/drawbacks	[292]
2	$\text{CdS}-\text{Au}-\text{TiO}_2$	deposition–precipitation method	Solid state Z. scheme for photocatalytic applications	[57]
3	$\text{CdS}-\text{Pt}-\text{TiO}_2$	Hydrothermal synthesis	Photocatalytic hydrogen production	[293]
4	$\text{CdS}/\text{Pt}-\text{TiO}_2$	dipping and deposition technique	Photocatalytic bacterial (<i>E. coli</i>) applications	[294]
5	$\text{TiO}_2-\text{Pt}-\text{SiO}_2$	Photo assisted deposition and impregnation method	Catalytic applications	[295]
6	$\text{TiO}_2-\text{Ag}-\text{SiO}_2$	Photo assisted deposition and impregnation method	Catalytic applications	[296]
Metal–semiconductor–metal junctions				
1	$\text{Pt}/\text{Au}-\text{TiO}_2$ based MSM		UV photodetectors	[297]
2	$\text{Ni}-\text{TiO}_2$ based MSM	Sol–gel method	UV photodetectors	[298]
3	TiO_2 based MSM	Radio frequency magnetron sputtering	UV photodetectors	[299, 300]
Metal–insulator–semiconductor–insulator–metal junctions				
1	TiO_2 based MISIM junctions	Atomic layer deposition technique	UV photodetectors	[301]

structure formation is existence of coherent interfaces and negligible lattice mismatch between core and shell as discussed in previous sections. Figure 5.11(A) shows TEM images of Au-TiO₂ core-shell systems [228] and Figure 5.11(B) shows the TEM image of Ag-TiO₂ core-shell systems [302].

Further, these composite core-shell structures also increase the efficiency of photocatalytic reactions [303, 304]. This enhanced photocatalytic rate is due to decrease in charge carrier recombination rate and fast transport of electrons from one phase to another which are situated with proper band edge alignments. Figure 5.12 schematically shows the electron and hole transfer from anatase to rutile or vice-versa in core-shell structured systems with proper band edge alignments.

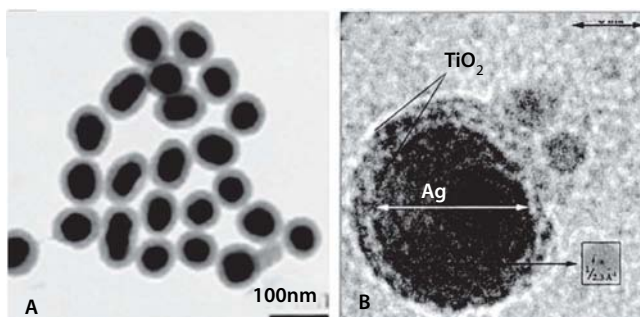


Figure 5.11 (A) Au@TiO₂ core-shell, Au as core and TiO₂ as shell and (B) TEM images confirming Ag as core and TiO₂ as shell, Reprinted with permission from Refs. [228, 302], Copyright © 2012 WILEY-VCH Verlag GmbH & Co. KGaA, Weinheim, Copyright © 2000, American Chemical Society.

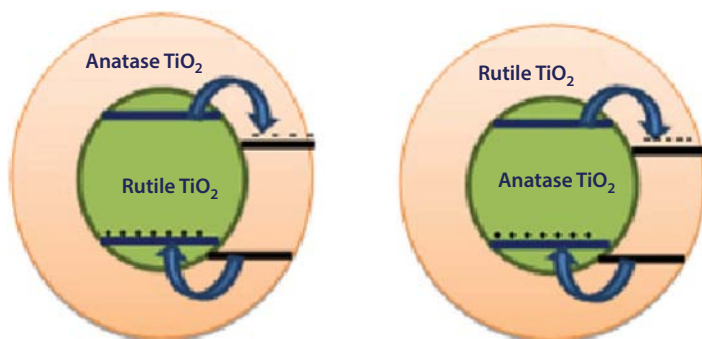


Figure 5.12 Schematic representation of charge transfer in core-shell TiO₂ anatase-rutile system, depending on band edge alignments between anatase and rutile TiO₂.

Depending on combination of materials (metal, semiconductor and/or insulator) as core or shell, various combinations of core/shell structures can be formed [305–307]. For example, semiconductor/semiconductor [308], semiconductor/metal [309], metal/semiconductor [310], metal/metal [311, 312], and metal/metal-oxide [313, 314] are well reported in literature. As discussed in section 5.2.1.1, these core–shell structures may fall in any of categories of type-I, II or reverse type-I. For example CdSe/ZnS [44, 307, 315], which fall under type-I, is used to enhance photoluminescence of CdSe nanocrystals. Most of the core–shell systems of TiO₂ coupled systems are listed in Table T.4 for information.

5.3.3.1 *Black TiO₂: A Crystalline Core and Amorphous/Disordered Shell TiO₂ Material*

Recently, “Black TiO₂” based materials with lesser “effective bandgap”, have been reported by the group of Samuel Mao and was prepared by hydrogenating/or incorporating hydrogen as a dopant into the TiO₂ lattice [316]. As a photocatalyst, black TiO₂ has shown promising results in improving visible and infrared optical absorption. The plausible reason for drastic decrease in bandgap upon hydrogenation of original/pristine TiO₂ material is due to disordered shell over crystalline core structure formation [316] which was confirmed from HRTEM images (nanocrystalline material as a core and a highly disordered surface layer as shell). Same group has also explored this material via DFT calculations and concluded that the incorporated hydrogen in the system induces or creates a disordered phase on the outside of crystalline anatase nanoparticle core. They also confirmed that Ti³⁺ centers in the system are responsible for formation of black color of the pristine material.

5.3.4 **Janus Structures**

Janus particles (named after the Roman god Janus) can be considered as a special type of “patchy particles” [317], with a patch covering only a fraction of the particle (Figure 5.13(A) shows optical image of black green photonic balls resembling Janus systems) [321]. “Patchy particles” can be defined as particles with one or more well-defined patches, displaying strongly anisotropic and directional interactions [317]. The specialty of these structures is in having different properties at opposite sides which enable these systems to mimic the behavior of surfactant molecules, leading to completely new self-assembled structures, with many more possibilities than those found in isotropic particles [317]. Janus

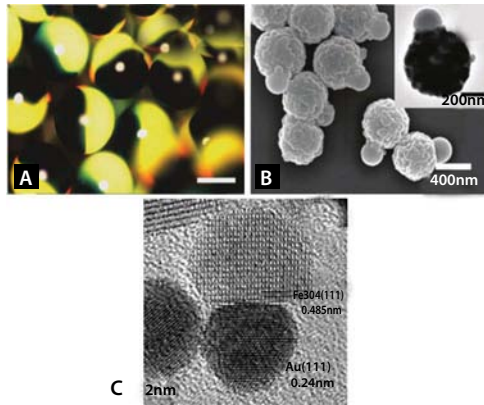


Figure 5.13 (A) Optical image of black green photonic balls, scale bars 200 μm , (B) SEM and TEM (inset) images of PS-SiO₂ Janus particles, and (C) Au-Fe₃O₄ Janus particles. Reprinted with permission from Refs. [321, 322, 323]. Copyright © 2008 WILEY-VCH Verlag GmbH & Co. KGaA, Weinheim, Copyright © 2011, American Chemical Society and Copyright © 2005, American Chemical Society.

structures emerged as important structures in PC field due to exposure of both phases for surface redox reactions. These sorts of possibilities rely on a strict control of growth processes in colloidal synthesis when they are utilized to form clusters with predefined size, shape and properties [318–320]. Figure 5.13(B) shows the SEM and TEM (inset) images of PS-SiO₂ Janus particles [322] and Figure 5.13(C) shows Au-Fe₃O₄ Janus particles [323].

Some early reports on concentric core–shell morphologies coupled with TiO₂ material are available in the literature [59, 154, 324]. Seh *et al.* developed anisotropic growth of TiO₂ onto gold nanoparticles to form eccentric Au-TiO₂ core–shell nanostructures [325] and anisotropic growth of TiO₂ onto gold nanorods to form a noncentrosymmetric Janus morphology, in which TiO₂ grows on one side of the gold nanorod leaving the other side exposed. They also calculated the theoretical energy to study the interfacial elastic energies in the TiO₂ coated gold nanorods and reported that the Janus and concentric morphologies are both energetically stable structures formed under different conditions [210]. Several other non centrosymmetric morphologies, that includes eccentric [224, 326], Janus [326–328], yolk-shell [329] and flower like [222] morphologies have also been reported in literature. Review articles by Wei *et al.* [330], Caruso *et al.* [239], and Eugenio *et al.* [331] published in recent time have addressed the utility of these nanostructures in PC.

5.4 Silicon Based Heterostructures

While a number of materials including semiconductors (Si [332], III-V [333], II-VI [334]), and metal oxide (TiO_2 [335], ZnO [336], Fe_2O_3 [337], WO_3 [338]) have gained considerable attention for harvesting the solar energy for chemical energy conversion, silicon being one of the cheapest, most abundant and important semiconductor material, is anticipated to have considerable potential for solar cells and PEC devices, especially if the devices can be made using fabrication methods not involving high vacuum. Silicon, having band gap of 1.12 eV, efficiently absorbs the solar light, but the higher valance band maximum (VBM) energy makes it thermodynamically impossible to participate in water oxidation. Moreover, it readily corrodes in aqueous medium. Therefore, use of silicon is quite challenging for photoelectrocatalysis. To overcome such limitation, a composite semiconductor electrode consisting semiconductor heterostructure, capable of absorbing different sections of solar spectrum is essential [339]. The major advantage of such systems is explained in sections 5.2 and 5.3, lies in feasible charge carrier transfer between the units that are coupled with proper band edge alignments.

5.4.1 Silicon Based Heterostructures for PEC Application

5.4.1.1 Silicon-Semiconductor Heterojunction

Silicon is coupled with semiconductors of proper choice for various PC/PEC applications. Hwang *et al.* [340] synthesized highly dense n-Si/ TiO_2 and p-Si/ TiO_2 core-shell nanowire (NW) arrays for photo-oxidative analysis. They have prepared highly oriented Si nanowires by electroless etching of silicon wafer followed by growth of TiO_2 over both n and p type Si nanowires by atomic layer deposition to form Si/ TiO_2 core-shell heteronanostructures. The observed photocurrent for core-shell structure is significantly higher than the planar Si/ TiO_2 system because core-shell structure has low reflectance and larger surface area.

As TiO_2 is transparent under visible light, e^- - h^+ pairs are created in both of n-Si/ TiO_2 and p-Si/ TiO_2 heterostructure. The photogenerated holes in TiO_2 moves towards TiO_2 electrolyte interface where OH^- is oxidized to form oxygen. On the other hand, electrons move towards electrode surface where they participate in surface redox reactions. Photogenerated electron in silicon moves toward counter electrode for reduction reaction. The generated holes in silicon move toward the semiconductor heterojunctions and recombine with photogenerated electrons of TiO_2 . Since the band

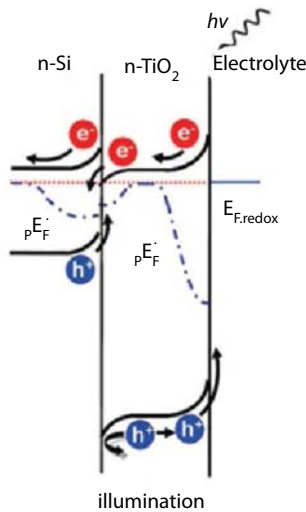


Figure 5.14 Schematic of band energy diagram and carrier transfer, reprinted with permission from Ref. [340], Copyright © 2009, American Chemical Society .

alignment at the interface helps in recombination reduction under illumination, a large increment in photocurrent is observed for this system.

Hongtao *et al.* [341] reported the fabrication of both n-Si NW/TiO₂ and p-Si NW/TiO₂ heterostructure by chemical vapor deposition of n type TiO₂ on Si NW of around 200 nm diameter. Both p and n type Si NW were prepared by chemical etching of p and n type of silicon wafers, respectively. In n-Si NW/TiO₂ heterostructure system, the larger band gap material (TiO₂) absorbs only UV radiation and allows visible light to pass through, which is absorbed on the smaller band gap n-Si NW. The photo-conversion efficiency enhances due the absorption of both UV and visible light at the heterojunction. In this process, TiO₂ behaves like a window for smaller band gap n-Si NW and hence the effect is known as “window effect” [342]. Enhanced photoelectrochemical activity of both heterostructures can be explained by schematic band diagram (Figure 5.15). Fermi level of n-TiO₂ is located nearer the CB which is more positive than n-Si NW. At the semiconductor interface, electrons from CB of n-Si NW moves to the CB of n-TiO₂ until the Fermi levels are equalized. In this process, energy band of Si NW bends downside and of TiO₂ bands bends upside resulting in decrement in valance band difference, ΔE_v . This difference is the barrier or driving force for the photogenerated hole transfer/injection from Si NW to the TiO₂ [343]. Once this barrier is overcome, transfer of the photogenerated holes takes place from Si NW to TiO₂ and will participate in the redox reactions subsequently with the generation

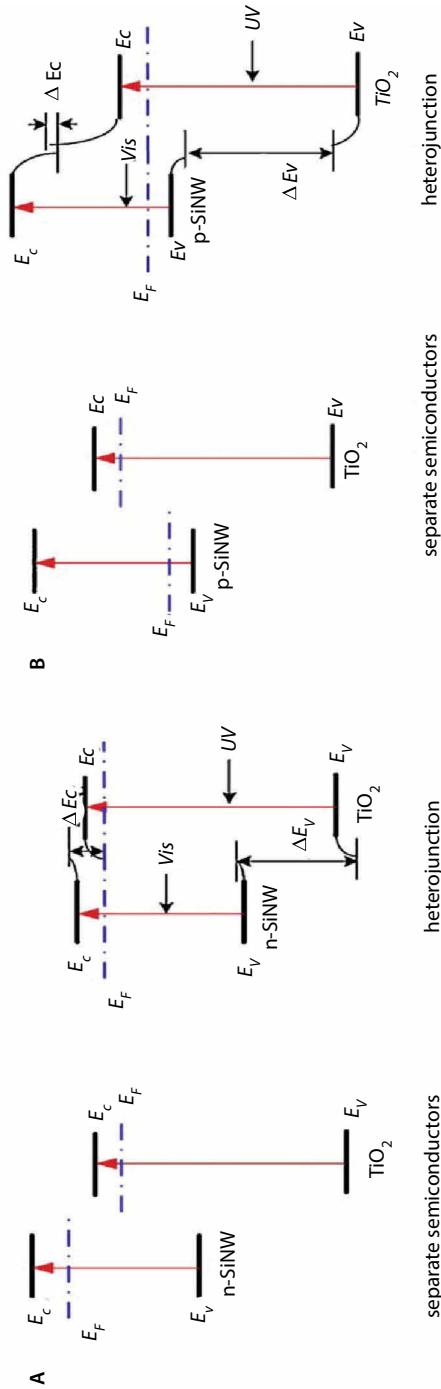


Figure 5.15 (A) Schematic of band energy diagram before forming heterostructure and (B) Schematic of band energy diagram after forming heterostructure, reprinted with permission from Ref. [34]. Copyright © 2009, Elsevier.

of holes in TiO_2 by UV light. In contrast of this, p-Si NW shows the increase in ΔE_v . Therefore, higher potential biasing is needed. However, dark current increases significantly at the biasing potential more than 2V which is lesser than ΔE_v . Hence, the visible light photoresponse is absent. Figure 5.15 shows schematic band energy diagram A) before and B) after forming heterostructure [341].

Betty *et al.* [344] reported highly stable and highly active heterostructure of porous silicon and nitrided TiO_2 (TiON) nanoparticles. Photoelectrodes were synthesized by electrochemically prepared porous silicon micro-channel with (TiON). Enhanced activity is due to efficient defect mediated charge transfer mechanism between porous silicon and TiON which is sluggish in polished Si/TiON heterostructures. The electrode prepared at 600°C was found to be highly active. Photocatalytic measurements in water-methanol system show strong dependency of activity on nitrogen concentration and prepared electrode was stable for more than six months of operation.

Sun *et al.* [345] reported a low cost p/n branched heterostructure by two step solution phase integration of Zinc oxide nanowire branches to Silicon nanowire backbone for solar water splitting. The size of nanowires, density and shape enhances the light absorption by minimizing the reflection and scattering. The lower CB of ZnO than Si facilitate the photogenerated electrons to move across the ZnO layer to the water reduction level, while the holes move to the back contact of the Si. The 3D Si/ZnO nanowire heterostructure shows enhanced photocathodic current density and better overall hydrogen production kinetics as compared to Si/ZnO planar heterostructure/Si NW/planar Si.

Quantum chemical calculations performed by Wang *et al.* [346] based on Density Function Theory (DFT) on Si/ WO_3 heterostructures demonstrated its possible limitation in Z-scheme application. They concluded the following:

- i. Heterointerface is formed by Si-O bonding preferentially.
- ii. There is no localized state produced in band gap because of fully saturated interfacial atoms.
- iii. Heterostructure formed has type-II band alignment with the CB of n- WO_3 more than the valance band of p-Si by 0.5 eV resulting in small schottky barrier.
- iv. Interfacial oxygen diffusion from WO_3 to Si is thermodynamically possible. However, this diffused oxygen takes the interstitial position in Si and has no influence on band alignment and electronic properties and thereby on photocatalytic water splitting performance.

Silicon/indium tin oxide (ITO) heterojunction gained considerable interest for solar water splitting because of its conductivity and transparency. Some of the properties of ITO and heterojunction formed with silicon are as follows [347]:

- i. ITO reduces series resistance losses in the overlayer due to its electronic degeneracy.
- ii. ITO adheres well to many substrates and quite resistive towards chemical attack.
- iii. ITO can be deposited at lower temperature so as to minimize interdiffusion.
- iv. The refractive index of ITO (~ 2.0) makes it partially antireflecting on silicon.
- v. The wide band gap of ITO (3.6 eV) absorbs minimum visible light in the oxide layer. Thus most of the light is available for junction area absorption.

Hodes *et al.* [347] reported Si/SiO_x/ITO hybrid heterostructure for PEC application by ITO layer deposition using spray pyrolysis on both n-Si and p-Si electrode. The smooth transition between Si and ITO layer caused by the SiO_x layer at the heterojunction minimizes the interfacial state densities formed due to geometric parameters (e.g., lattice mismatch). Additionally, SiO_x enhances the open circuit voltage by minimizing the leakage current. The electrodes were catalytically modified with either Pt or RuO₂ for PEC application. The synthesized electrodes show $\sim 40\%$ reduction in threshold voltage for water splitting due to facile electron transfer at the Schottky barrier between Si and ITO layer.

5.4.1.2 Semiconductor-Semimetal Heterojunction

Being a zero band gap material, graphene is a promising semimetal for fabrication of many semimetal-semiconductor heterojunctions in the context of electrode preparations. Owing to high surface area, high carrier mobility and high optical transparency, graphene can be considered as favorable material in comparison to metals [348]. Due to its fine structure constant, graphene absorbs only $2.3 \pm 0.1\%$ of white light with negligible reflectance ($< 0.1\%$) and hence responsible for its usage in preparation of optically transparent electrodes (stretchable/flexible/foldable electronics) [349, 350]. The usual methods for the fabrication of Si/graphene heterostructures are spin casting and chemical vapor deposition of graphene on top of silicon followed by drying [351]. However, stability is the major

issue in such methods because of weak interaction force between graphene and substrate. Kedi *et al.* [348] reported the synthesis of graphene silicon heterostructure using electrophoresis followed by annealing. Due to the efficient photogenerated charge separation promoted from the interfacial electrostatic field of graphene/Si heterostructure, the prepared photoelectrodes shows high photoresponse in aqueous solution.

Mechanism for photogenerated electron separation is shown in Figure 5.16. For isolated semiconductor, the Fermi level of graphene is above the Fermi level of p-Si. After the heterostructure formation, electrons flow from graphene to p-Si to equalize the Fermi levels resulting in an internal electric field at the interface. When this heterojunction is exposed to electromagnetic radiation, the incident photons induce photogenerated electron and hole in the sub layer silicon. These electrons and holes are facilitated by electric field at the interface to move towards graphene and Silicon, respectively. As the Fermi level of heterostructure is lesser than the reduction potential of water, a large number of photogenerated electrons have to move towards graphene through silicon. As a result of which, the Fermi level of graphene moves up enough to facilitate hydrogen generation. Figure 5.16 shows the schematic band diagram of (A) isolated materials, (B) heterojunctions in dark, (C) under xenon radiation, and (D) under xenon radiation with aqueous electrolyte [348].

5.4.2 Heterojunctions vs Multijunction Silicon

In contrast to the Si heterojunctions, multijunction amorphous silicon (a-Si) has gained considerable interest. Si based multi junctions (e.g., three junction amorphous cell) can be visualized in thin film amorphous silicon solar cells designed based on independent thin film cells deposited

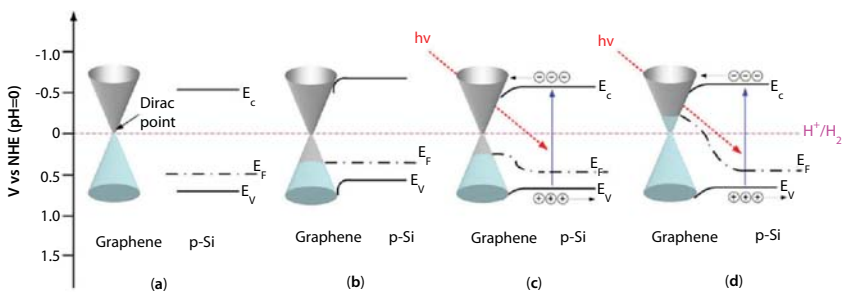


Figure 5.16 Schematic of band diagram of (A) isolated materials, (B) heterojunctions in dark, (C) under xenon radiation, and (D) under xenon radiation with aqueous electrolyte, reprinted with permission from Ref. [348], Copyright © 2011, Elsevier.

on top of each other [352]. It produces voltage up to 2.4 V. Each thin cell is designed to utilize different region of solar spectrum. This technique is known as “solar spectrum splitting” [353]. In such a cell, the top cell harnesses the energy in the range from 300 to 690 nm. Middle cell harnesses in the range of 450–750 nm and the bottom cell harnesses the energy in the range of 550–880 nm [354]. There are three main advantages of such multijunction solar water splitting cells: (1) sufficient water splitting voltage output, (2) high efficiency, and (3) low cost as compared to crystalline multijunction semiconductor cells. Triple junction amorphous silicon solar cells are exploited for making integrated photovoltaic-electrolysis devices in which the photocurrent generation equivalent to hydrogen generation can easily be measured.

Reece *et al.* [355] reported a solar water splitting cell consisting of earth abundant materials that operate in near neutral environment, both with wired and wireless (artificial leaf) configurations. The cell, consisting of triple junction amorphous silicon photovoltaic, is interfaced to hydrogen evolving catalyst, made from an alloy of earth abundant cheap metals and oxygen evolving catalysts of cobalt borate (Co-OEC). Both catalysts were interfaced directly through electro-deposition with a commercial triple junction amorphous silicon solar cell in wired and wireless configuration. Fabricated cell consists of three junction amorphous silicon deposited on a stainless steel substrate and layered with a 70 nm thick ITO [355].

The Co-OEC, interfaced with semiconductor, enhances the efficiency of solar driven water splitting [356–359]. The unique properties of Co-OEC is its self-assembly upon oxidation of Co^{2+} [360], self-healing [361], and it can be operated in buffered electrolyte with pure or neutral water at normal temperature [362, 363]. These properties are similar to OEC found naturally in photo synthetic systems.

To facilitate the catalyst activity at significant current densities, an electrolyte must have an excellent proton accepting behavior. Phosphate (Pi) electrolyte fulfils this criterion better than that of borate (Bi) and hence is well suited for water oxidation [364]. In addition, Pi acts as a local buffer to maintain the constant pH at high current density whereas Bi fails to support catalyst and loses its proton accepting behavior beyond certain pH. The working model of CoPi was proposed by Kanan *et al.* [365] shown in Figure 5.17. Co^{2+} is a high spin ion and result in the formation of low spin Co^{3+} upon oxidation which electrodeposits on the electrode under the influence of HPO_4^{2-} due to lesser solubility of HPO_4^{2-} in Co^{3+} against Co^{2+} . Co^{3+} again gets oxidize to produce Co^{4+} -oxo form which liberates O_2 and cobalt regains its +2 electronic state.

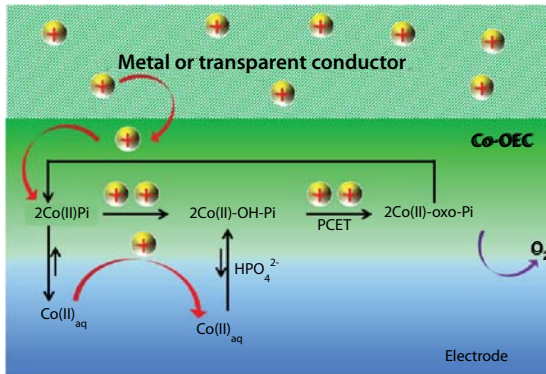


Figure 5.17 Working model of Co-Pi catalytic system, reproduced from Ref. [365].

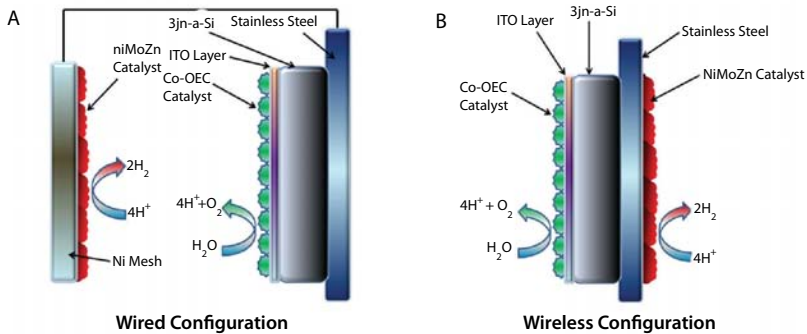


Figure 5.18 Schematic representation for (A) wired PEC configuration and (B) wireless PEC configuration, reproduced from Ref. [355].

Hydrogen evolving Ternary alloy NiMoZn was deposited on a Ni mesh substrate connected to a three junction solar cell through a wire in wired configuration, while the wireless configuration consists of direct deposition of ternary alloy on the opposite stainless steel surface of triple junction amorphous silicon solar cell [355] (Figure 5.18(A)).

The choice of metals in the ternary alloy is specific for hydrogen evolution. First metal catalyses the hydrogen formation from water *via* electrolysis. There is a range of metals which can be employed as hydrogen formation catalyst, e.g., Ni, Fe, Co, Cu, W, Mo, Ru, Rh, Pt, and Pd. The selection of second metal type is according to low association constant with an anionic species. Hence, it prohibits the deposition of anionic species on the electrode. The said anionic species (e.g., Pi and Bi) facilitates the formation of catalytic material on the counter electrode. Moreover, this species

is responsible for stability and/or operation of catalytic material in context of counter redox reaction. Third metal is chosen to increase the surface area of the catalytic material. The mechanism involves re-orientation or re-structuration of catalytic material upon the addition of third metal by induced repulsive interaction, resulting in agglomeration, nodule formation, precipitation and phase separation which subsequently enhance the surface area [366].

The un-optimized device performance gives 2.5% and 4.7% of solar to fuel efficiency for wireless and wired configuration when driven by 6.2% and 7.7% electricity efficient solar cell in borate electrolyte of pH 9.2. Wireless configuration was tested against stability and found to be stable up to 10 hours. The stability of the cell depends on the material and the method of preparation of the conductive oxide layer.

5.4.3 Pros/Cons in Improvement of Si Heterostructures for Energy Harvesting and Conversion

1. Although silicon is the most abundant and promising material of interest among other semiconductors available till date, the recurring problems of its photo-corrosion or dissolution in acidic mediums for prolonged time is still an unresolved issue.
2. The surface passivation techniques has to be explored more to utilize Silicon as photocatalytic/PEC material.
3. In spite of significant improvement in Si heterostructures, the basic underlying mechanism of growth of Si films on different substrates and the kinetics is still unclear.

5.5 Some Unaddressed Issues of Heterostructures in Relation to Photocatalysis

1. There are no clear reasons cited for the actual driving force for nucleation and growth in forming heterostructure systems like Au/CdSe synthesized by growing CdSe on the top of a crystalline Au core [101]. The synthesis and development of anisotropic nanomaterials is itself a complex process and mechanistic aspect of growth requires greater attention in understanding.
2. As the size of nanocrystals is a critical factor in determining the morphology of nanocrystal heterostructures, more

focused studies is required for elucidating the mechanism of heterojunction formation, which in turn is necessary in developing rational and controllable approaches for synthesis of nanocrystal-based multifunctional materials (i.e., more exploitation of the lattice strain induced by heterointerfaces is essential).

3. Till now, there is no report which addresses clear epitaxial relationships between different phases. The extent of defects in the interface has to be quantified as they can have detrimental effects on the overall properties of the system.
4. Limited reports on the stability of the semiconductor-metal/ semiconductor-semiconductor/ semiconductor-metal-semiconductor/metal-semiconductor-metal (MSM) interface during electrochemical/photo-electrochemical operations.

5.5.1 Measures to be Taken in Perspective of Photocatalysis of Heteronanostructures

1. Development of high quality materials for better understanding coupling phenomena between two units and properties of individual components that are synergistically coupled in forming heteronanostructures.
2. Search for new synthesis/fabrication techniques without the need of weak organic molecules as linkers.
3. Methods to form heterostructures without significant lattice strain being induced across the heterostructures in spite of the dissimilarity of the respective crystal-phases.
4. Prevention of metal nanoparticle oxidation at semiconductor interface which is predominant due to large surface/volume ratio of nanoparticles, i.e., there is no demarcation between surface oxide/bulk metal in nanomaterials.

5.6 Summary/Conclusions and Future Outlook

Silicon/TiO₂ heterostructures continues to be extensively explored due to its initial promise and evolutionary improvements in efficiencies. A more recent theme is in utilizing the nanostructures and heterojunctions to improve the efficiency. Comprehensive understanding of these areas has to involve greater understanding of band alignments/band structures in heteronanostructures, capacitance/flat-band potential measurements and its role in interfacial electron transfer kinetics. With greater certainty in the

molecular structure of these materials, greater utility of the reactivity indices developed in the area of surface electrochemistry can be made [367]. All this will enable deconvolution of the effects of photon absorption, electron–hole separation cum transport and surface reactivity, all of which play an important role in PEC. While many studies focus on improving efficiencies and factors affecting stability have to be unraveled, especially in the context of nanostructures. In fact, immense effort has been devoted in effective/efficient catalyst design for various applications in PC, PEC applications and photovoltaics. In this book chapter, we have presented an up-to-date review of the current achievements, methodologies and principles applied in building heteronanostructures for PC/PEC applications. Due to massive amount of research articles available in PC field, we are limited towards covering few representative contributions in PC field.

Rational design and synthesis of heterostructured nanocrystals/materials with a topologically controlled composition promises to disclose unprecedented horizons in the manipulation of the properties of many nano-sized metal, semiconductor and/or oxide material that is brought into contact with other materials. Future progress in this synthetic field will open up access to new breeds of colloidal nanoheterostructures, which could enable various optoelectronic, magnetic, biomedical, photovoltaic applications with a high level of performance. Even though many interesting aspects/controlling mechanisms in semiconductor-heterostructures have been identified, many phenomenological concepts of these heterostructured photocatalysts are still unclear. There is much science to be unraveled before we can categorically correlate the functional efficiencies to molecular and mesoscopic structure of the heterostructures.

Acknowledgment

The work was supported by the Technology System Development division of the Department of Science and Technology, Government of India via the grant **DST/ME/20110310**.

Notes on Contributors

Dilip Kumar Behara: Dilip Kumar Behara has done masters in chemical engineering and currently he is a PhD student in the department of chemical engineering, Indian Institute of Technology at Kanpur. Phone: 91-512-2596227, Fax: 91-512-2590104, E mail: dkbehara@iitk.ac.in

Arun Prakash Upadhyay: Arun Prakash Upadhyay has done masters in chemical engineering and currently he is a PhD student in the department of chemical engineering, Indian Institute of Technology at Kanpur. Phone: 91-512-2597895, Fax: 91-512-2594010, E mail: arunppch@iitk.ac.in.

Gyan Prakash Sharma: Gyan Prakash Sharma has done masters in chemical engineering and currently he is a PhD student in the department of chemical engineering, Indian Institute of Technology at Kanpur. Phone: 91-512-2596227, Fax: 91-512-2590104, E mail: gyanp@iitk.ac.in

B.V. Sai Krishna Kiran: B.V. Sai Krishna Kiran has done masters in Chemical engineering and currently working as Senior Executive-R&D at Flareum Solar Technologies Pvt. Ltd., Pune. Phone: 08960440380, 08866138144; E mail: bvskkiran@gmail.com

Dr. Sri Sivakumar: Sri Sivakumar is working as an assistant professor in the department of chemical engineering, Indian Institute of Technology at Kanpur. His research interests are synthesis of different nanomaterials for variety of applications in particular drug delivery, bio-imaging, solar hydrogen generation, catalytic reactions, and solid state lightings. Phone: 91-512-2597697, Fax: 91-512-2590104, E mail: srisiva@iitk.ac.in

Dr. Raj Ganesh S Pala: Raj Ganesh S Pala is working as an assistant professor in the department of chemical engineering, Indian Institute of Technology at Kanpur. His research focus is on the synthesis and characterization of nanomaterials for electro catalysis, fuel cells and photoelectrochemical systems. Phone: 91-512-2596143, Fax: 91-512-2590104, E mail: rpala@iitk.ac.in

References

1. K. Maeda and K. Domen, *Journal of Physical Chemistry Letters*, Vol. 1, pp. 2655–2661, 2010.
2. H. Tong, S.X. Ouyang, Y.P. Bi, N. Umezawa, M. Oshikiri, and J.H. Ye, *Advanced Materials*, Vol. 24, pp. 229–251, 2012.
3. H.L. Zhou, Y.Q. Qu, T. Zeid, and X.F. Duan, *Energy & Environmental Science*, Vol. 5, pp. 6732–6743, 2012.
4. K. Takanaabe and K. Domen, *Chemcatchem*, Vol. 4, pp. 1485–1497, 2012.
5. Y. Park, K.J. McDonald, and K.S. Choi, *Chemical Society Reviews*, Vol. 42, pp. 2321–2337, 2012.
6. R.M.N. Yerga, M.C.A. Galvan, F. del Valle, J.A.V. de la Mano, and J.L.G. Fierro, *Chemsuschem*, Vol. 2, pp. 471–485, 2009.

7. S.S. Mao, S.H. Shen, and L.J. Guo, *Progress in Natural Science – Materials International*, Vol. 22, pp. 522–534, 2012.
8. X.B. Chen, C. Li, M. Gratzel, R. Kostecki, and S.S. Mao, *Chemical Society Reviews*, Vol. 41, pp. 7909–7937, 2012.
9. A. Kubacka, M. Fernandez-Garcia, and G. Colon, *Chemical Reviews*, Vol. 112, pp. 1555–1614, 2012.
10. M.D. Hernandez-Alonso, F. Fresno, S. Suarez, and J.M. Coronado, *Energy & Environmental Science*, Vol. 2, pp. 1231–1257, 2009.
11. H. Tong, S. Ouyang, Y. Bi, N. Umezawa, M. Oshikiri, and J. Ye, *Advanced Materials*, Vol. 24, pp. 229–251, 2012.
12. H. Suk Joon, L. Seungok, J. Jum Suk, and L. Jae Sung, *Energy & Environmental Science*, Vol. 4, pp. 1781–1787, 2011.
13. X.M. Feng, G.Q. Hu, and J.Q. Hu, *Nanoscale*, Vol. 3, pp. 2099–2117, 2011.
14. C.X. Kronawitter, L. Vayssieres, S.H. Shen, L.J. Guo, D.A. Wheeler, J.Z. Zhang, B.R. Antoun, and S.S. Mao, *Energy & Environmental Science*, Vol. 4, pp. 3889–3899, 2011.
15. P.V. Kamat, *Journal of Physical Chemistry Letters*, Vol. 3, pp. 663–672, 2012.
16. B. Liu, A. Khare, and E. Aydil, *ACS Applied Materials & Interfaces*, Vol. 3, pp. 4444–4450, 2011.
17. P. Romero-Gomez, A. Borrás, A. Barranco, J. Espinos, and A. Gonzalez-Elipe, *Chemphyschem: A European Journal of Chemical Physics and Physical Chemistry*, Vol. 12, pp. 191–196, 2011.
18. G. Schmid, *Endeavour*, Vol. 14, pp. 172–178, 1990.
19. J. Kreuter, *Pharmaceutica Acta Helveticae*, Vol. 53, pp. 33–39, 1978.
20. G. Weiser, *Physical Review B*, Vol. 45, pp. 14076–14085, 1992.
21. P.G. Dacosta and E.M. Conwell, *Physical Review B*, Vol. 48, pp. 1993–1996, 1993.
22. J.M. Leng, S. Jeglinski, X. Wei, R.E. Benner, Z.V. Vardeny, F. Guo, and S. Mazumdar, *Physical Review Letters*, Vol. 72, pp. 156–159, 1994.
23. C.W. Tang, *Applied Physics Letters*, Vol. 48, pp. 183–185, 1986.
24. A.K. Ghosh and T. Feng, *Journal of Applied Physics*, Vol. 49, pp. 5982–5989, 1978.
25. J.J.M. Halls, C.A. Walsh, N.C. Greenham, E.A. Marseglia, R.H. Friend, S.C. Moratti, and A.B. Holmes, *Nature*, Vol. 376, pp. 498–500, 1995.
26. G. Yu, J. Gao, J.C. Hummelen, F. Wudl, and A.J. Heeger, *Science*, Vol. 270, pp. 1789–1791, 1995.
27. D. Gross, A. Sussha, T. Klar, E. Da Como, A. Rogach, and J. Feldmann, *Nano Letters*, Vol. 8, pp. 1482–1485, 2008.
28. J.R. Sohn and C.K. Lee, *Bulletin – Korean Chemical Society*, Vol. 28, pp. 2459, 2007.
29. X. Zong, H. Yan, G. Wu, G. Ma, F. Wen, L. Wang, and C. Li, *Journal of the American Chemical Society*, Vol. 130, pp. 7176–7177, 2008.
30. N. Serpone, P. Maruthamuthu, P. Pichat, E. Pelizzetti, and H. Hidaka, *Journal of Photochemistry and Photobiology A: Chemistry*, Vol. 85, pp. 247–255, 1995.

31. R. Beranek and H. Kisch, *Angewandte Chemie (International Ed. in English)*, Vol. 47, pp. 1320–1322, 2008.
32. A. Alivisatos, K. Johnsson, X. Peng, T.E. Wilson, C.J. Loweth, M.P. JR Bruchez, and P.G. Schultz, *Nature*, Vol. 382, pp. 609–611, 1996.
33. K.Y. Song, M.K. Park, Y.T. Kwon, H.W. Lee, W.J. Chung, and W.I. Lee, *Chemistry of Materials*, Vol. 13, pp. 2349–2355, 2001.
34. A. Hameed, T. Montini, V. Gombac, and P. Fornasiero, *Journal of the American Chemical Society*, Vol. 130, pp. 9658–9659, 2008.
35. S. Ivanov, A. Piryatinski, J. Nanda, S. Tretiak, K. Zavadil, W. Wallace, D. Werder, and V. Klimov, *Journal of the American Chemical Society*, Vol. 129, pp. 11708–11719, 2007.
36. Wikipedia. Available from: <http://en.wikipedia.org/wiki/Heterojunction>. 2004
37. J.H. Ahn, H.S. Kim, K.J. Lee, S. Jeon, S.J. Kang, Y.G. Sun, R.G. Nuzzo, and J.A. Rogers, *Science*, Vol. 314, pp. 1754–1757, 2006.
38. J.T. Hu, M. Ouyang, P.D. Yang, and C.M. Lieber, *Nature*, Vol. 399, pp. 48–51, 1999.
39. F. Leonard and J. Tersoff, *Physical Review Letters*, Vol. 84, pp. 4693–4696, 2000.
40. X.L. Hu, G.S. Li, and J.C. Yu, *Langmuir*, Vol. 26, pp. 3031–3039, 2010.
41. X.B. Chen, S.H. Shen, L.J. Guo, and S.S. Mao, *Chemical Reviews*, Vol. 110, pp. 6503–6570, 2010.
42. X.H. An, F.Z. Liu, Y.J. Jung, and S. Kar, *Nano Letters*, Vol. 13, pp. 909–916, 2013.
43. N. Lazarides, V. Paltoglou, P. Maniadis, G.P. Tsironis, and C. Panagopoulos, *Physical Review B*, Vol. 84, pp. 245428-1–245428-6, 2011.
44. M.A. Hines and P. Guyot-Sionnest, *Journal of Physical Chemistry*, Vol. 100, pp. 468–471, 1996.
45. K.W. Kwon and M. Shim, *Journal of the American Chemical Society*, Vol. 127, pp. 10269–10275, 2005.
46. X.N. Fei, G.Z. Jia, and J. Guo, *Optoelectronics and Advanced Materials – Rapid Communications*, Vol. 6, pp. 679–682, 2012.
47. X.H. Zhong, R.G. Xie, Y. Zhang, T. Basche, and W. Knoll, *Chemistry of Materials*, Vol. 17, pp. 4038–4042, 2005.
48. G. Liu, L.Z. Wang, H.G. Yang, H.M. Cheng, and G.Q. Lu, *Journal of Materials Chemistry*, Vol. 20, pp. 831–843, 2010.
49. W.T. Sun, Y. Yu, H.Y. Pan, X.F. Gao, Q. Chen, and L.M. Peng, *Journal of the American Chemical Society*, Vol. 130, pp. 1124–1125, 2008.
50. J.C. Kim, J. Choi, Y.B. Lee, J.H. Hong, J.I. Lee, J.W. Yang, W.I. Lee, and N.H. Hur, *Chemical Communications*, pp. 5024–5026, 2006.
51. H. Park, W. Choi, and M.R. Hoffmann, *Journal of Materials Chemistry*, Vol. 18, pp. 2379–2385, 2008.
52. J.C. Yu, L. Wu, J. Lin, P.S. Li, and Q. Li, *Chemical Communications*, pp. 1552–1553, 2003.

53. M.K. Nazeeruddin, R. Splivallo, P. Liska, P. Comte, and M. Gratzel, *Chemical Communications*, pp. 1456–1457, 2003.
54. R. Abe, K. Sayama, K. Domen, and H. Arakawa, *Chemical Physics Letters*, Vol. 344, pp. 339–344, 2001.
55. K. Sayama, R. Yoshida, H. Kusama, K. Okabe, Y. Abe, and H. Arakawa, *Chemical Physics Letters*, Vol. 277, pp. 387–391, 1997.
56. X.W. Wang, G. Liu, Z.G. Chen, F. Li, L.Z. Wang, G.Q. Lu, and H.M. Cheng, *Chemical Communications*, pp. 3452–3454, 2009.
57. H. Tada, T. Mitsui, T. Kiyonaga, T. Akita, and K. Tanaka, *Nature Materials*, Vol. 5, pp. 782–786, 2006.
58. V. Subramanian, E.E. Wolf, and P.V. Kamat, *Journal of the American Chemical Society*, Vol. 126, pp. 4943–4950, 2004.
59. T. Hirakawa and P. Kamat, *Journal of the American Chemical Society*, Vol. 127, pp. 3928–3934, 2005.
60. X. Wang, J. Yu, H. Yip, L. Wu, P. Wong, and S. Lai, *Chemistry*, Vol. 11, pp. 2997–3004, 2005.
61. B.H. Meekins and P.V. Kamat, *Journal of Physical Chemistry Letters*, Vol. 2, pp. 2304–2310, 2011.
62. Y. Bessekhoud, D. Robert, and J. Weber, *Journal of Photochemistry and Photobiology A – Chemistry*, Vol. 163, pp. 569–580, 2004.
63. R. Brahim, Y. Bessekhoud, A. Bouguelia, and M. Trari, *Journal of Photochemistry and Photobiology A – Chemistry*, Vol. 194, pp. 173–180, 2008.
64. M.K.I. Senevirathna, P. Pitigala, and K. Tennakone, *Journal of Photochemistry and Photobiology A – Chemistry*, Vol. 171, pp. 257–259, 2005.
65. W.K. Ho and J.C. Yu, *Journal of Molecular Catalysis A – Chemical*, Vol. 247, pp. 268–274, 2006.
66. K. Sayama, K. Mukasa, R. Abe, Y. Abe, and H. Arakawa, *Journal of Photochemistry and Photobiology A: Chemistry*, Vol. 148, pp. 71–77, 2002.
67. M. Gratzel, *Nature*, Vol. 414, pp. 338–344, 2001.
68. Y. Bessekhoud, D. Robert, and J. Weber, *Journal of Photochemistry and Photobiology A, Chemistry*, Vol. 163, pp. 569–580, 2004.
69. F.E. Osterloh, *Chemistry of Materials*, Vol. 20, pp. 35–54, 2008.
70. L.H. Lu, G.Y. Sun, H.J. Zhang, H.S. Wang, S.Q. Xi, J.Q. Hu, Z.Q. Tian, and R. Chen, *Journal of Materials Chemistry*, Vol. 14, pp. 1005–1009, 2004.
71. F. Wetz, K. Soulantica, M. Respaud, A. Falqui, and B. Chaudret, *Materials Science & Engineering C – Biomimetic and Supramolecular Systems*, Vol. 27, pp. 1162–1166, 2007.
72. P.H.C. Camargo, Y. Xiong, L. Ji, J.M. Zuo, and Y.N. Xia, *Journal of the American Chemical Society*, Vol. 129, pp. 15452–15453, 2007.
73. S.J. Guo, L. Wang, S.J. Dong, and E.K. Wang, *Journal of Physical Chemistry C*, Vol. 112, pp. 13510–13515, 2008.
74. S.Y. Wang, N. Kristian, S.P. Jiang, and X. Wang, *Nanotechnology*, Vol. 20, pp. 025605–025614, 2009.

75. W. Han, L.X. Yi, N. Zhao, A.W. Tang, M.Y. Gao, and Z.Y. Tang, *Journal of the American Chemical Society*, Vol. 130, pp. 13152–13161, 2008.
76. R.D. Robinson, B. Sadtler, D.O. Demchenko, C.K. Erdonmez, L.W. Wang, and A.P. Alivisatos, *Science*, Vol. 317, pp. 355–358, 2007.
77. B. Sadtler, D.O. Demchenko, H. Zheng, S.M. Hughes, M.G. Merkle, U. Dahmen, L.W. Wang, and A.P. Alivisatos, *Journal of the American Chemical Society*, Vol. 131, pp. 5285–5293, 2009.
78. D.J. Milliron, S.M. Hughes, Y. Cui, L. Manna, J.B. Li, L.W. Wang, and A.P. Alivisatos, *Nature*, Vol. 430, pp. 190–195, 2004.
79. K.K. Haldar, T. Sen, and A. Patra, *Journal of Physical Chemistry C*, Vol. 112, pp. 11650–11656, 2008.
80. G. Oldfield, T. Ung, and P. Mulvaney, *Advanced Materials*, Vol. 12, pp. 1519–1522, 2000.
81. X.G. Wen and S.H. Yang, *Nano Letters*, Vol. 2, pp. 451–454, 2002.
82. Y.H. Zheng, L.R. Zheng, Y.Y. Zhan, X.Y. Lin, Q. Zheng, and K.M. Wei, *Inorganic Chemistry*, Vol. 46, pp. 6980–6986, 2007.
83. B.M. Wen, C.Y. Liu, and Y. Liu, *Inorganic Chemistry*, Vol. 44, pp. 6503–6505, 2005.
84. W.J. Dong, Z. Shi, J.J. Ma, C.M. Hou, Q. Wan, S.H. Feng, A. Cogbill, and Z.R. Tian, *Journal of Physical Chemistry B*, Vol. 110, pp. 5845–5848, 2006.
85. S. Sun, D. Yang, G. Zhang, E. Sacher, and J.P. Dodelet, *Chemistry of Materials*, Vol. 19, pp. 6376–6378, 2007.
86. J. Yang, H.I. Elim, Q.B. Zhang, J.Y. Lee, and W. Ji, *Journal of the American Chemical Society*, Vol. 128, pp. 11921–11926, 2006.
87. Y.L. Liu and A.R.H. Walker, *Journal of Physical Chemistry C*, Vol. 114, pp. 4264–4271, 2010.
88. A.J. Mieszawska, R. Jalilian, G.U. Sumanasekera, and F.P. Zamborini, *Small*, Vol. 3, pp. 722–756, 2007.
89. H. Zheng, Y. Li, H. Liu, X. Yin, and Y. Li, *Chemical Society Reviews*, Vol. 40, pp. 4506–4524, 2011.
90. R. Buonsanti, M. Casavola, G. Caputo, and P.D. Cozzoli, *Recent Patents on Nanotechnology*, Vol. 1, pp. 224–232, 2007.
91. K. Liu, K. Nagodawithana, P. Searson, and C. Chien, *Physical Review B*, Vol. 51, pp. 7381–7384, 1995.
92. M. Bognitzki, H.Q. Hou, M. Ishaque, T. Frese, M. Hellwig, C. Schwarte, A. Schaper, J.H. Wendorff, and A. Greiner, *Advanced Materials*, Vol. 12, pp. 637–640, 2000.
93. J.M. Delia, M.H. Steven, C. Yi, M. Liberato, L. Jingbo, W. Lin-Wang, and A.P. Alivisatos, *Nature*, Vol. 430, pp. 190–195, 2004.
94. J.M. Aneta, J. Romaneh, U.S. Gamini, and P.Z. Francis, *Journal of the American Chemical Society*, Vol. 127, pp. 10822–10823, 2005.
95. Y. Guo, Q. Tang, H. Liu, Y. Zhang, Y. Li, W. Hu, S. Wang, and D. Zhu, *Journal of the American Chemical Society*, Vol. 130, pp. 9198–9199, 2008.
96. Y. Li, Y. Bando, and D. Golberg, *Advanced Materials*, Vol. 16, pp. 93–96, 2004.

97. D. Gerion, F. Pinaud, S.C. Williams, W.J. Parak, D. Zanchet, S. Weiss, and A.P. Alivisatos, *Journal of Physical Chemistry B*, Vol. 105, pp. 8861–8871, 2001.
98. M.A. Petruska, A.V. Malko, P.M. Voyles, and V.I. Klimov, *Advanced Materials*, Vol. 15, pp. 610–613, 2003.
99. Y.F. Wang, M.J. Li, H.Y. Jia, W. Song, X.X. Han, J.H. Zhang, B. Yang, W.Q. Xu, and B. Zhao, *Spectrochimica Acta Part a – Molecular and Biomolecular Spectroscopy*, Vol. 64, pp. 101–105, 2006.
100. P.V. Kamat and B. Shanhavi, *Journal of Physical Chemistry B*, Vol. 101, pp. 7675–7679, 1997.
101. T. Mokari, E. Rothenberg, I. Popov, R. Costi, and U. Banin, *Science*, Vol. 304, pp. 1787–1790, 2004.
102. M. Casavola, R. Buonsanti, G. Caputo, and P.D. Cozzoli, *European Journal of Inorganic Chemistry*, Vol. 2008, pp. 837–854, 2008.
103. L. Carbone and P.D. Cozzoli, *Nano Today*, Vol. 5, pp. 449–493, 2010.
104. N.T. Nolan, M.K. Seery, and S.C. Pillai, *Journal of Physical Chemistry C*, Vol. 113, pp. 16151–16157, 2009.
105. C.H. Deanna, G.A. Alexander, A.G. Kimberly, R. Tijana, and C.T. Marion, *The Journal of Physical Chemistry B*, Vol. 107, pp. 4545–4549, 2003.
106. M.A. Nadeem, M. Murdoch, G.I.N. Waterhouse, J.B. Metson, M.A. Keane, J. Llorca, and H. Idriss, *Journal of Photochemistry and Photobiology A: Chemistry*, Vol. 216, pp. 250–255, 2010.
107. D.C. Hurum, A.G. Agrios, K.A. Gray, T. Rajh, and M.C. Thurnauer, *Journal of Physical Chemistry B*, Vol. 107, pp. 4545–4549, 2003.
108. G.A. Alexander, A.G. Kimberly, and W. Eric, *Langmuir*, Vol. 19, pp. 1402–1409, 2003.
109. A. Agrios, K. Gray, and E. Weitz, *Langmuir: The ACS Journal of Surfaces and Colloids*, Vol. 20, pp. 5911–5917, 2004.
110. D. Hurum, K. Gray, T. Rajh, and M. Thurnauer, *The Journal of Physical Chemistry B*, Vol. 109, pp. 977–980, 2005.
111. R. Trejo-Tzab, J.J. Alvarado-Gil, P. Quintana, and T. Lopez, *Journal of Molecular Catalysis A – Chemical*, Vol. 281, pp. 113–118, 2008.
112. T. Kawahara, Y. Konishi, H. Tada, N. Tohge, J. Nishii, and S. Ito, *Angewandte Chemie (International Ed. in English)*, Vol. 41, pp. 2811–2813, 2002.
113. I.B. Roger, G.-C. Teresita, S.L. John, P. Leonardo, and J.D.T. Richard, *Journal of Solid State Chemistry*, Vol. 92, pp. 178–190, 1991.
114. T. Ohno, K. Sarukawa, K. Tokieda, and M. Matsumura, *Journal of Catalysis*, Vol. 203, pp. 82–86, 2001.
115. K.D. Abhaya, R. Georg, R.B. James, H. Min, and R.P. Michael, *Journal of Solid State Chemistry*, Vol. 115, pp. 236–239, 1995.
116. R.I. Bickley, T. Gonzalezcarreno, J.S. Lees, L. Palmisano, and R.J.D. Tilley, *Journal of Solid State Chemistry*, Vol. 92, pp. 178–190, 1991.
117. G.N. Ranjith, P. Samrat, and S.K. Samdarshi, *Solar Energy Materials and Solar Cells*, Vol. 95, pp. 1901–1907, 2011.

118. J. Zhang, Q. Xu, Z. Feng, M. Li, and C. Li, *Angewandte Chemie (International Ed. in English)*, Vol. 47, pp. 1766–1769, 2008.
119. S. Yun-Mo, L. Jin-Kyung, and C. Won-Seok, *Crystal Growth & Design*, Vol. 6, pp. 805–808, 2006.
120. L. Gang, Y. Xiaoxia, C. Zhigang, W. Xuewen, W. Lianzhou, L. Gao Qing, and C. Hui-Ming, *Journal of Materials Chemistry*, Vol. 19, pp. 6590–6596, 2009.
121. F.Z. Shi, Y.G. Li, Q.H. Zhang, and H.Z. Wang, *Journal of the American Ceramic Society*, Vol. 95, pp. 1927–1932, 2012.
122. V. Caratto, B. Aliakbarian, A. Casazza, and L. Setti, *Materials Research Bulletin*, Vol. 48, pp. 2095–2101, 2013.
123. L.G. Gai, X.Q. Duan, H.H. Jiang, Q.H. Mei, G.W. Zhou, Y. Tian, and H. Liu, *Crystengcomm*, Vol. 14, pp. 7662–7671, 2012.
124. J. Li and T. Ishigaki, *Acta Materialia*, Vol. 52, pp. 5143–5150, 2004.
125. Y. Yin and A. Alivisatos, *Nature*, Vol. 437, pp. 664–670, 2005.
126. P. Cozzoli, T. Pellegrino, and L. Manna, *Chemical Society Reviews*, Vol. 35, pp. 1195–1208, 2006.
127. A. Henglein, *Chemical Reviews*, Vol. 89, pp. 1861–1873, 1989.
128. A. Henglein, *The Journal of Physical Chemistry*, Vol. 97, pp. 5457–5471, 1993.
129. P.V. Kamat, *The Journal of Physical Chemistry B*, Vol. 106, pp. 7729–7744, 2002.
130. M. Matsumura, Y. Saho, and H. Tsubomura, *The Journal of Physical Chemistry*, Vol. 87, pp. 3807–3808, 1983.
131. Y. Nosaka, K. Yamaguchi, A. Kuwabara, H. Miyama, R. Baba, and A. Fujishima, *Journal of Photochemistry and Photobiology A: Chemistry*, Vol. 64, pp. 375–382, 1992.
132. J. Zhensheng, L. Qinglin, Z. Xinhua, X. Chanjuan, W. Chuanping, Z. Huqin, F. Liangbo, W. Hanqing, C. Zhengshi, and J. Zhicheng, *Journal of Photochemistry and Photobiology A: Chemistry*, Vol. 71, pp. 85–96, 1993.
133. A. Kudo and Y. Miseki, *Chemical Society Reviews*, Vol. 38, pp. 253–278, 2009.
134. P.V. Kamat, *Chemical Reviews*, Vol. 93, pp. 267–300, 1993.
135. G. Colon, M. Maicu, M.C. Hidalgo, and J.A. Navio, *Applied Catalysis B: Environmental*, Vol. 67, pp. 41–51, 2006.
136. J. Malek, A. Watanabe, and T. Mitsunashi, *Journal of Thermal Analysis and Calorimetry*, Vol. 60, pp. 699–705, 2000.
137. P. Chen, J.Q. Lu, G.Q. Xie, G.S. Hu, L. Zhu, L.F. Luo, W.X. Huang, and M.F. Luo, *Applied Catalysis A – General*, Vol. 433, pp. 236–242, 2012.
138. Y.M. Wang, X.J. Li, and S.J. Zheng, *Journal of Inorganic Materials*, Vol. 22, pp. 729–732, 2007.
139. T. Sasaki, N. Koshizaki, J.W. Yoon, S. Yamada, M. Koinuma, M. Noguchi, and Y. Matsumoto, *Electrochemistry*, Vol. 72, pp. 443–445, 2004.
140. C.J. Ren, L.N. Zhou, Y.W. Duan, and Y.Q. Chen, *Journal of Rare Earths*, Vol. 30, pp. 1106–1111, 2012.
141. D.J. Park, T. Sekino, S. Tsukuda, and S.-I. Tanaka, *Journal of the Ceramic Society of Japan*, Vol. 120, pp. 307–310, 2012.

142. J.M.G. Amores, V.S. Escribano, and V. Lorenzelli, *Journal of Materials Chemistry*, Vol. 4, pp. 965–971, 1994.
143. X. Baifu, W. Peng, D. Dandan, L. Jia, R. Zhiyu, and F. Honggang, *Applied Surface Science*, Vol. 254, pp. 2569–2574, 2008.
144. G. Blondeau, M. Froelicher, M. Froment, A. Hugot Le Goff, and J. Zerbino, *Journal of the Electrochemical Society*, Vol. 126, pp. 1592–1596, 1979.
145. Z. Wenjie, L. Ying, Z. Shenglong, and W. Fuhui, *Catalysis Today*, Vol. 93–95, pp. 589–594, 2004.
146. L.S. Yoong, F.K. Chong, and B.K. Dutta, *Energy*, Vol. 34, pp. 1652–1661, 2009.
147. R. Lopez, R. Gomez, and M.E. Llanos, *Catalysis Today*, Vol. 148, pp. 103–108, 2009.
148. H. Park, D. Kim, S. Kim, and K. Lee, *Journal of Alloys and Compounds*, Vol. 415, pp. 51–55, 2006.
149. P.M. Thibado and D.A. Bonnell, *Journal of the American Ceramic Society*, Vol. 80, pp. 1267–1273, 1997.
150. S. Wu, Y. Yin, F. He, and Y. Qin, *Photographic Science and Photochemistry*, Vol. 23, pp. 333–339 2005.
151. S.-X. Wu, Z. Ma, Y.-N. Qin, F. He, L.-S. Jia, and Y.-J. Zhang, *ACTA Physicochimica Sinica*, Vol. 19, pp. 967–969, 2003.
152. T. Hirakawa and P.V. Kamat, *Journal of the American Chemical Society*, Vol. 127, pp. 3928–3934, 2005.
153. P.-S. Isabel, S.K. Dmitry, A.M. Arif, G. Michael, A.K. Nicholas, and M.L.-M.n. Luis, *Langmuir*, Vol. 16, pp. 2731–2735, 2000.
154. H. Sakai, T. Kanda, H. Shibata, T. Ohkubo, and M. Abe, *Journal of the American Chemical Society*, Vol. 128, pp. 4944–4945, 2006.
155. Z. Dan, S. Ximing, Z. Rongwei, Z. Ming, and L. Fengqi, *European Journal of Inorganic Chemistry*, Vol. 2005, pp. 1643–1648, 2005.
156. A. Takai and P. Kamat, *ACS Nano*, Vol. 5, pp. 7369–7376, 2011.
157. Z. Peng, S. Changlu, Z. Zhenyi, Z. Mingyi, M. Jingbo, G. Zengcai, S. Yangyang, and L. Yichun, *Journal of Materials Chemistry*, Vol. 21, pp. 17746–17753, 2011.
158. V. Jurate and S.V. Rajender, *New Journal of Chemistry*, Vol. 34, pp. 1094–1096, 2010.
159. D. Ingram and S. Linic, *Journal of the American Chemical Society*, Vol. 133, pp. 5202–5205, 2011.
160. B.I. David, C. Phillip, L.B. Jonathan, and L. Suljo, *ACS Catalysis*, Vol. 1, pp. 1441–1447, 2011.
161. P. Chen, J.Q. Lu, G.Q. Xie, L. Zhu, and M.F. Luo, *Reaction Kinetics Mechanisms and Catalysis*, Vol. 106, pp. 419–434, 2012.
162. I. Lightcap, T. Kosel, and P. Kamat, *Nano Letters*, Vol. 10, pp. 577–583, 2010.
163. W. Graeme, S. Brian, and V.K. Prashant, *ACS Nano*, Vol. 2, pp. 1487–1491, 2008.
164. Z. Hao, L. Xiaojun, L. Yueming, W. Ying, and L. Jinghong, *ACS Nano*, Vol. 4, pp. 380–386, 2010.

165. N. Yun Hau, I. Akihide, J.B. Nicholas, K. Akihiko, and A. Rose, *Catalysis Today*, Vol. 164, pp. 353–357, 2011.
166. L. Rowan and W. Aidan, *Carbon*, Vol. 49, pp. 741–772, 2011.
167. Z. Liming, D. Shuo, N. Yufeng, Y. Kai, L. Nan, D. Boya, X. Qin, R. Alfonso, K. Jing, and L. Zhongfan, *Journal of the American Chemical Society*, Vol. 133, pp. 2706–2713, 2011.
168. J. Guodong, L. Zhifen, C. Chao, Z. Lihua, C. Qing, W. Nan, W. Wei, and T. Heqing, *Carbon*, Vol. 49, pp. 2693–2701, 2011.
169. M. Kiran Kumar, Z. Yong, Y. Yongli, and L. Kian Ping, *Advanced Functional Materials*, Vol. 19, pp. 3638–3643, 2009.
170. O. Akhavan, M. Abdollahad, and A. Esfandiari, *Journal of Physical Chemistry C*, Vol. 114, pp. 12955–12959, 2010.
171. F. Yang, H. Ke-Jing, N. De-Jun, Y. Chun-Peng, and J. Qiang-Shan, *Electrochimica Acta*, Vol. 56, pp. 4685–4690, 2011.
172. Z. Fei, Y. Yuan, C. Na, W. Liangzhuan, and Z. Jinfang, *Scripta Materialia*, Vol. 64, pp. 621–624, 2011.
173. Q. Yongcai, Y. Keyou, Y. Shihe, J. Limin, D. Hong, and L. Weishan, *ACS Nano*, Vol. 4, pp. 6515–6526, 2010.
174. Y. Nailiang, Z. Jin, W. Dan, C. Yongsheng, and J. Lei, *ACS Nano*, Vol. 4, pp. 887–894, 2010.
175. T. Yong-Bing, L. Chun-Sing, X. Jun, L. Zeng-Tao, C. Zhen-Hua, H. Zhubing, C. Yu-Lin, Y. Guodong, S. Haisheng, C. Limiao, L. Linbao, C. Hui-Ming, Z. Wen-Jun, B. Igor, and L. Shuit-Tong, *ACS Nano*, Vol. 4, pp. 3482–3488, 2010.
176. Z. Yanhui, T. Zi-Rong, F. Xianzhi, and X. Yi-Jun, *ACS Nano*, Vol. 4, pp. 7303–7314, 2010.
177. L. Jincheng, B. Hongwei, W. Yinjie, L. Zhaoyang, Z. Xiwang, and S. Darren Delai, *Advanced Functional Materials*, Vol. 20, pp. 4175–4181, 2010.
178. C. Chao, C. Weimin, L. Mingce, Z. Baoxue, W. Yahui, W. Deyong, and F. Yujie, *ACS Nano*, Vol. 4, pp. 6425–6432, 2010.
179. Z. Haijiao, X. Panpan, D. Guidong, C. Zhiwen, O. Kokyo, P. Dengyu, and J. Zheng, *Nano Research*, Vol. 4, pp. 274–283, 2011.
180. L. Yongye, W. Hailiang, C. Hernan Sanchez, C. Zhuo, and D. Hongjie, *Nano Research*, Vol. 3, pp. 701–705, 2010.
181. O. Akhavan and E. Ghaderi, *The Journal of Physical Chemistry C*, Vol. 113, pp. 20214–20220, 2009.
182. Z. Xiao-Yan, L. Hao-Peng, C. Xiao-Li, and L. Yuehe, *Journal of Materials Chemistry*, Vol. 20, pp. 2801–2806, 2010.
183. I. Paramasivam, J.M. Macak, and P. Schmuki, *Electrochemistry Communications*, Vol. 10, pp. 71–75, 2008.
184. T. Mokari, C.G. Sztrum, A. Salant, E. Rabani, and U. Banin, *Nature Materials*, Vol. 4, pp. 855–863, 2005.
185. K. Awazu, M. Fujimaki, C. Rockstuhl, J. Tominaga, H. Murakami, Y. Ohki, N. Yoshida, and T. Watanabe, *Journal of the American Chemical Society*, Vol. 130, pp. 1676–1680, 2008.

186. E. Thimsen, F. Le Formal, M. Grätzel, and S. Warren, *Nano Letters*, Vol. 11, pp. 35–43, 2011.
187. W. Hua, Y. Tingting, S. Weiwei, L. Jinghong, and G. Lin, *The Journal of Physical Chemistry C*, Vol. 116, pp. 6490–6494, 2012.
188. P. Wang, B. Huang, Y. Dai, and M.-H. Whangbo, *Physical Chemistry Chemical Physics: PCCP*, Vol. 14, pp. 9813–9825, 2012.
189. C. Jiun-Jen, C.S.W. Jeffrey, W. Pin Chieh, and T. Din Ping, *The Journal of Physical Chemistry C*, Vol. 115, pp. 210–216, 2011.
190. S. Linic, P. Christopher, and D. Ingram, *Nature Materials*, Vol. 10, pp. 911–921, 2011.
191. D.B. Ingram and S. Linic, *Journal of the American Chemical Society*, Vol. 133, pp. 5202–5205, 2011.
192. H. Arnim, H. Arnold, and M. Paul, *The Journal of Physical Chemistry*, Vol. 96, pp. 8700–8702, 1992.
193. W. Annabel, G. Michael, and M. Paul, *The Journal of Physical Chemistry B*, Vol. 105, pp. 8810–8815, 2001.
194. S. Vaidyanathan, E.W. Eduardo, and V.K. Prashant, *The Journal of Physical Chemistry B*, Vol. 107, pp. 7479–7485, 2003.
195. V. Subramanian, E. Wolf, and P. Kamat, *Journal of the American Chemical Society*, Vol. 126, pp. 4943–4950, 2004.
196. Y. Tian and T. Tatsuma, *Journal of the American Chemical Society*, Vol. 127, pp. 7632–7637, 2005.
197. Z. Liu, W. Hou, P. Pavaskar, M. Aykol, and S. Cronin, *Nano Letters*, Vol. 11, pp. 1111–1116, 2011.
198. C.G. Silva, J. Raquel, M. Tiziana, M. Raffaele, and G. Hermenegildo, *Journal of the American Chemical Society*, Vol. 133, pp. 595–602, 2011.
199. M. Jakob, H. Levanon, and P.V. Kamat, *Nano Letters*, Vol. 3, pp. 353–358, 2003.
200. D. Lahiri, V. Subramanian, T. Shibata, E.E. Wolf, B.A. Bunker, and P.V. Kamat, *Journal of Applied Physics*, Vol. 93, pp. 2575–2582, 2003.
201. V. Subramanian, E.E. Wolf, and P.V. Kamat, *Langmuir*, Vol. 19, pp. 469–474, 2003.
202. A. Dawson and P.V. Kamat, *Journal of Physical Chemistry B*, Vol. 105, pp. 960–966, 2001.
203. V. Subramanian, E. Wolf, and P.V. Kamat, *Journal of Physical Chemistry B*, Vol. 105, pp. 11439–11446, 2001.
204. P.V. Kamat, *Pure and Applied Chemistry*, Vol. 74, pp. 1693–1706, 2002.
205. J. Fang, S.W. Cao, Z. Wang, M.M. Shahjamali, S.C.J. Loo, J. Barber, and C. Xue, *International Journal of Hydrogen Energy*, Vol. 37, pp. 17853–17861, 2012.
206. A.A. Ismail, D.W. Bahnemann, and S.A. Al-Sayari, *Applied Catalysis A – General*, Vol. 431, pp. 62–68, 2012.
207. A.A. Ismail, A. Hakki, and D.W. Bahnemann, *Journal of Molecular Catalysis A – Chemical*, Vol. 358, pp. 145–151, 2012.

208. M.M. Khan, S. Kalathil, J. Lee, and M.H. Cho, *Bulletin of the Korean Chemical Society*, Vol. 33, pp. 1753–1758, 2012.
209. M.G. Manera, J. Spadavecchia, D. Buso, C.D. Fernandez, G. Mattei, A. Martucci, P. Mulvaney, J. Perez-Juste, R. Rella, L. Vasanelli, and P. Mazzoldi, *Sensors and Actuators B – Chemical*, Vol. 132, pp. 107–115, 2008.
210. S. Zhi Wei, L. Shuhua, Z. Shuang-Yuan, M.S. Bharathi, H. Ramanarayan, L. Michelle, S. Kwok Wei, Z. Yong-Wei, and H. Ming-Yong, *Angewandte Chemie International Edition*, Vol. 50, pp. 10140–10143, 2011.
211. S. Zhi Wei, L. Shuhua, Z. Shuang-Yuan, S. Kwok Wei, and H. Ming-Yong, *Chemical Communications*, Vol. 47, pp. 6689–6691, 2011.
212. N. Shin-ichi, I. Aimi, and T. Hiroaki, *Journal of the American Chemical Society*, Vol. 132, pp. 6292–6293, 2010.
213. K. Ewa, M. Orlando Omar Prieto, A. Ryu, and O. Bunsho, *Physical Chemistry Chemical Physics*, Vol. 12, pp. 2344–2355, 2010.
214. H.X. Li, Z.F. Bian, J. Zhu, Y.N. Huo, H. Li, and Y.F. Lu, *Journal of the American Chemical Society*, Vol. 129, pp. 4538–4539, 2007.
215. A. Primo, A. Corma, and H. Garcia, *Physical Chemistry Chemical Physics*, Vol. 13, pp. 886–910, 2011.
216. S. Kalathil, M.M. Khan, A.N. Banerjee, J. Lee, and M.H. Cho, *Journal of Nanoparticle Research*, Vol. 14, pp. 141051–141061, 2012.
217. D. Buso, J. Pacifico, and A. Martucci, *Advanced Functional Materials*, Vol. 17, pp. 347–354, 2007.
218. S.Y. Zhu, S.J. Liang, Q. Gu, L.Y. Xie, J.X. Wang, Z.X. Ding, and P. Liu, *Applied Catalysis B – Environmental*, Vol. 119, pp. 146–155, 2012.
219. J.J. Chen, H.L. Su, F. Song, W.J. Moon, Y.S. Kim, and D. Zhang, *Journal of Colloid and Interface Science*, Vol. 370, pp. 117–123, 2012.
220. T.C. Kuo, T.C. Hsu, Y.C. Liu, and K.H. Yang, *Analyst*, Vol. 137, pp. 3847–3853, 2012.
221. H.H. Mohamed, R. Dillert, and D.W. Bahnemann, *Chemistry – A European Journal*, Vol. 18, pp. 4314–4321, 2012.
222. X. Wu, H. Song, J. Yoon, Y. Yu, and Y. Chen, *Langmuir*, Vol. 25, pp. 6438–6447, 2009.
223. K.S. Mayya, D.I. Gittins, and F. Caruso, *Chemistry of Materials*, Vol. 13, pp. 3833–3836, 2001.
224. D.D. Lekeufack, A. Brioude, A. Mouti, J.G. Alauzun, P. Stadelmann, A.W. Coleman, and P. Miele, *Chemical Communications*, Vol. 46, pp. 4544–4546, 2010.
225. H. Song, Y.-T. Yu, and P. Norby, *Journal of Nanoscience and Nanotechnology*, Vol. 9, pp. 5891–5897, 2009.
226. Z. Nan, L. Siqi, F. Xianzhi, and X. Yi-Jun, *The Journal of Physical Chemistry C*, Vol. 115, pp. 9136–9145, 2011.
227. F. Xiaoning, L. Jun, Y. Hui, S. Jiuchuan, L. Xue, Z. Xiaokai, and J. Yuxi, *Materials Chemistry and Physics*, Vol. 130, pp. 334–339, 2011.

228. Z.W. Seh, S.H. Liu, M. Low, S.Y. Zhang, Z.L. Liu, A. Mlayah, and M.Y. Han, *Advanced Materials*, Vol. 24, pp. 2310–2314, 2012.
229. S. Pradhan, D. Ghosh, and S. Chen, *ACS Applied Materials & Interfaces*, Vol. 1, pp. 2060–2065, 2009.
230. B. Dai, F. Polzer, I. Hausler, and Y. Lu, *Zeitschrift Fur Physikalische Chemie – International Journal of Research in Physical Chemistry & Chemical Physics*, Vol. 226, pp. 827–835, 2012.
231. F.X. Xiao, *Journal of Physical Chemistry C*, Vol. 116, pp. 16487–16498, 2012.
232. M. Guo, C.F. Su, G.Q. Lu, X.F. Zhu, C.X. Wu, and L.Z. Wang, *Thin Solid Films*, Vol. 520, pp. 7066–7070, 2012.
233. L. Jing and Z. Hua Chun, *Angewandte Chemie*, Vol. 117, pp. 4342–4345, 2005.
234. Y.X. Zhang, B. Gao, G.L. Puma, A.K. Ray, and H.C. Zeng, *Science of Advanced Materials*, Vol. 2, pp. 503–513, 2010.
235. S. Cho, J.W. Jang, S. Hwang, J.S. Lee, and S. Kim, *Langmuir*, Vol. 28, pp. 17530–17536, 2012.
236. H.H. Wang, S.J. Dong, Y. Chang, and J.L. Faria, *Journal of Hazardous Materials*, Vol. 235, pp. 230–236, 2012.
237. X.D. Hao, Y.X. Zhang, J. Liu, M. Dong, M. Huang, Y. Yuan, X.L. Li, and J.M. Huang, *Nano*, Vol. 7, pp. 1250025–1250037, 2012.
238. M.R. Hoffmann, S.T. Martin, W.Y. Choi, and D.W. Bahnemann, *Chemical Reviews*, Vol. 95, pp. 69–96, 1995.
239. X.D. Wang and R.A. Caruso, *Journal of Materials Chemistry*, Vol. 21, pp. 20–28, 2011.
240. G. Hong-Mei, Z. Li, S. Xiong-Rui, X. Si, L. Shao-Ding, and W. Qu-Quan, *Advanced Functional Materials*, Vol. 19, pp. 298–303, 2009.
241. A.R. Gonzalezlope, J. Soria, and G. Munuera, *Journal of Catalysis*, Vol. 76, pp. 254–264, 1982.
242. J.G. Yu, J.F. Xiong, B. Cheng, and S.W. Liu, *Applied Catalysis B – Environmental*, Vol. 60, pp. 211–221, 2005.
243. H.J. Zhang, G.H. Chen, and D.W. Bahnemann, *Journal of Materials Chemistry*, Vol. 19, pp. 5089–5121, 2009.
244. J.G. Highfield and P. Pichat, *New Journal of Chemistry*, Vol. 13, pp. 61–66, 1989.
245. J.S. Lee and W.Y. Choi, *Environmental Science & Technology*, Vol. 38, pp. 4026–4033, 2004.
246. C.B. Nadja, H.r. Thomas, K. Markus, S. Paul, M.E. Lukas, and E.I. Alexander, *Nano Letters*, Vol. 8, pp. 4588–4592, 2008.
247. L. Renhong, C. Wenxing, K. Hisayoshi, and M. Chunxia, *Green Chemistry*, Vol. 12, pp. 212–215, 2010.
248. W.Y. Zhai, S.J. Xue, A.W. Zhu, Y.P. Luo, and Y. Tian, *Chemcatchem*, Vol. 3, pp. 127–130, 2011.
249. A. Henglein, B. Lindig, and J. Westerhausen, *Journal of Physical Chemistry*, Vol. 85, pp. 1627–1628, 1981.

250. D. Bahnemann, A. Henglein, J. Lilie, and L. Spanhel, *Journal of Physical Chemistry*, Vol. 88, pp. 709–711, 1984.
251. Z. Zhaoke, H. Baibiao, Q. Xiaoyan, Z. Xiaoyang, D. Ying, and W. Myung-Hwan, *Journal of Materials Chemistry*, Vol. 21, pp. 9079–9087, 2011.
252. A.K. Geim and K.S. Novoselov, *Nature Materials*, Vol. 6, pp. 183–191, 2007.
253. N.L. Yang, Y.Y. Liu, H. Wen, Z.Y. Tang, H.J. Zhao, Y.L. Li, and D. Wang, *ACS Nano*, Vol. 7, pp. 1504–1512, 2013.
254. A.A. Ismail, R.A. Geioushy, H. Bouzid, S.A. Al-Sayari, A. Al-Hajry, and D.W. Bahnemann, *Applied Catalysis B – Environmental*, Vol. 129, pp. 62–70, 2013.
255. N. Farhangi, R.R. Chowdhury, Y. Medina-Gonzalez, M.B. Ray, and P.A. Charpentier, *Applied Catalysis B – Environmental*, Vol. 110, pp. 25–32, 2011.
256. H.-I. Kim, G.-H. Moon, D.N. Monllor-Satoca, Y. Park, and W. Choi, *The Journal of Physical Chemistry C*, Vol. 116, pp. 1535–1543, 2012.
257. B. Tang and G.X. Hu, *Journal of Power Sources*, Vol. 220, pp. 95–102, 2012.
258. Q.J. Xiang, J.G. Yu, and M. Jaroniec, *Chemical Society Reviews*, Vol. 41, pp. 782–796, 2011.
259. X. Huang, X.Y. Qi, F. Boey, and H. Zhang, *Chemical Society Reviews*, Vol. 41, pp. 666–686, 2011.
260. L. Spanhel, M. Haase, H. Weller, and A. Henglein, *Journal of the American Chemical Society*, Vol. 109, pp. 5649–5655, 1987.
261. K.R. Gopidas, M. Bohorquez, and P.V. Kamat, *Journal of Physical Chemistry*, Vol. 94, pp. 6435–6440, 1990.
262. N. Serpone, E. Borgarello, and M. Gratzel, *Journal of the Chemical Society – Chemical Communications*, Vol. 6, pp. 342–344, 1984.
263. N. Ghows and M.H. Entezari, *Ultrasonics Sonochemistry*, Vol. 19, pp. 1070–1078, 2012.
264. D.R. Baker and P.V. Kamat, *Advanced Functional Materials*, Vol. 19, pp. 805–811, 2009.
265. R. Vogel, P. Hoyer, and H. Weller, *The Journal of Physical Chemistry*, Vol. 98, pp. 3183–3188, 1994.
266. S. Kohtani, A. Kudo, and T. Sakata, *Chemical Physics Letters*, Vol. 206, pp. 166–170, 1993.
267. A.S. Aliev, M.N. Mamedov, and M.T. Abbasov, *Inorganic Materials*, Vol. 45, pp. 965–967, 2009.
268. H.W. Wei, L. Wang, Z.P. Li, S.Q. Ni, and Q.Q. Zhao, *Nano-Micro Letters*, Vol. 3, pp. 6–11, 2011.
269. X.W. Wang, G. Liu, L.Z. Wang, J.A. Pan, G.Q. Lu, and H.M. Cheng, *Journal of Materials Chemistry*, Vol. 21, pp. 869–873, 2011.
270. J.T. Li, M.W.G. Hoffmann, H. Shen, C. Fabrega, J.D. Prades, T. Andreu, F. Hernandez-Ramirez, and S. Mathur, *Journal of Materials Chemistry*, Vol. 22, pp. 20472–20476, 2012.
271. J.S. Luo, L. Ma, T.C. He, C.F. Ng, S.J. Wang, H.D. Sun, and H.J. Fan, *Journal of Physical Chemistry C*, Vol. 116, pp. 11956–11963, 2012.

272. L.J. Diguna, Q. Shen, A. Sato, K. Katayama, T. Sawada, and T. Toyoda, *Materials Science & Engineering C – Biomimetic and Supramolecular Systems*, Vol. 27, pp. 1514–1520, 2007.
273. P. Brown and P.V. Kamat, *Journal of the American Chemical Society*, Vol. 130, pp. 8890–8891, 2008.
274. D. Liu and P. Kamat, *The Journal of Physical Chemistry*, Vol. 97, pp. 10769–10773, 1993.
275. T. Lopez-Luke, A. Wolcott, L.P. Xu, S.W. Chen, Z.H. Wcn, J.H. Li, E. De La Rosa, and J.Z. Zhang, *Journal of Physical Chemistry C*, Vol. 112, pp. 1282–1292, 2008.
276. M. Lei, Y.B. Zhang, X.L. Fu, Y.T. Huang, L. Zhang, and J.H. Xiao, *Materials Letters*, Vol. 65, pp. 3577–3579, 2011.
277. J. Zhang, J.H. Bang, C.C. Tang, and P.V. Kamat, *ACS Nano*, Vol. 4, pp. 387–395, 2009.
278. M. Zhang, H.F. Zhang, K.B. Lv, W.Y. Chen, J.R. Zhou, L. Shen, and S.P. Ruan, *Optics Express*, Vol. 20, pp. 5936–5941, 2012.
279. M.R. Vaezi, *Journal of Materials Processing Technology*, Vol. 205, pp. 332–337, 2008.
280. H. Yang, S. Yu, S. Lau, X. Zhang, D. Sun, and G. Jun, *Small (Weinheim an der Bergstrasse, Germany)*, Vol. 5, pp. 2260–2264, 2009.
281. K. Vinodgopal, I. Bedja, and P.V. Kamat, *Chemistry of Materials*, Vol. 8, pp. 2180–2187, 1996.
282. I. Bedja and P.V. Kamat, *Journal of Physical Chemistry*, Vol. 99, pp. 9182–9188, 1995.
283. K. Vinodgopal and P.V. Kamat, *Environmental Science & Technology*, Vol. 29, pp. 841–845, 1995.
284. L. Huang, F. Peng, H.J. Wang, H. Yu, W. Geng, J. Yang, S.Q. Zhang, and H.J. Zhao, *Materials Chemistry and Physics*, Vol. 130, pp. 316–322, 2011.
285. S. Chu, X.M. Zheng, F. Kong, G.H. Wu, L.L. Luo, Y. Guo, H.L. Liu, Y. Wang, H.X. Yu, and Z.G. Zou, *Materials Chemistry and Physics*, Vol. 129, pp. 1184–1188, 2011.
286. L. Huang, F. Peng, H.J. Wang, H. Yu, and Z. Li, *Catalysis Communications*, Vol. 10, pp. 1839–1843, 2009.
287. K.P. Acharya, N.N. Hewa-Kasakarage, T.R. Alabi, I. Nemitz, E. Khon, B. Ullrich, P. Anzenbacher, and M. Zamkov, *Journal of Physical Chemistry C*, Vol. 114, pp. 18291–18291, 2010.
288. L. Etgar, T. Moehl, S. Gabriel, S.G. Hickey, A. Eychmuller, and M. Gratzel, *ACS Nano*, Vol. 6, pp. 3092–3099, 2012.
289. H. Zhang, S. Ruan, C. Feng, B. Xu, W. Chen, and W. Dong, *Journal of Nanoscience and Nanotechnology*, Vol. 11, pp. 10003–10006, 2011.
290. X.C. Wang, J.C. Yu, Y.L. Chen, L. Wu, and X.Z. Fu, *Environmental Science & Technology*, Vol. 40, pp. 2369–2374, 2006.
291. L.H. Van, M.H. Hong, and J. Ding, *Science and Technology of Hybrid Materials*, Vol. 111, pp. 131–134, 2006.

292. Z. Pap, E. Karacsonyi, L. Baia, L.C. Pop, V. Danciu, K. Hernadi, K. Mogyorosi, and A. Dombi, *Physica Status Solidi B – Basic Solid State Physics*, Vol. 249, pp. 2592–2595, 2012.
293. H. Park, Y.K. Kirn, and W. Choi, *Journal of Physical Chemistry C*, Vol. 115, pp. 6141–6148, 2011.
294. Q. Kang, Q.Z. Lu, S.H. Liu, L.X. Yang, L.F. Wen, S.L. Luo, and Q.Y. Cai, *Biomaterials*, Vol. 31, pp. 3317–3326, 2010.
295. R.M. Mohamed, *Journal of Materials Processing Technology*, Vol. 209, pp. 577–583, 2009.
296. R.M. Mohamed and I.A. Mkhaliid, *Journal of Alloys and Compounds*, Vol. 501, pp. 301–306, 2010.
297. D. Cal skan, B. Butun, S. Ozcan, and E. Ozbay, *Journal of Vacuum Science & Technology B: Microelectronics and Nanometer Structures*, Vol. 31, pp. 20606, 2013.
298. X.Z. Kong, C.X. Liu, W. Dong, X.D. Zhang, C. Tao, L. Shen, J.R. Zhou, Y.F. Fei, and S.P. Ruan, *Applied Physics Letters*, Vol. 94, pp. 123502–123505, 2009.
299. H.L. Huang, W.F. Yang, Y.N. Xie, X.P. Chen, and Z.Y. Wu, *IEEE Electron Device Letters*, Vol. 31, pp. 588–590, 2010.
300. H.L. Xue, X.Z. Kong, Z.R. Liu, C.X. Liu, J.R. Zhou, W.Y. Chen, S.P. Ruan, and Q. Xu, *Applied Physics Letters*, Vol. 90, pp. 201118–201121, 2007.
301. W. Wang, C. Shan, H. Zhu, F. Ma, D. Shen, X. Fan, and K. Choy, *Journal of Physics D: Applied Physics*, Vol. 43, pp. 45102, 2010.
302. I. Pastoriza-Santos, D.S. Koktysh, A.A. Mamedov, M. Giersig, N.A. Kotov, and L.M. Liz-Marzan, *Langmuir*, Vol. 16, pp. 2731–2735, 2000.
303. A. Bard, *The Journal of Physical Chemistry*, Vol. 86, pp. 172–177, 1982.
304. A. Bard and M. Fox, *Accounts of Chemical Research*, Vol. 28, pp. 141–145, 1995.
305. N. Baccile, A. Fischer, B. Julian-Lopez, D. Grosso, and C. Sanchez, *Journal of Sol-Gel Science and Technology*, Vol. 47, pp. 119–123, 2008.
306. S. Jansat, K. Pelzer, J. Garcia-Anton, R. Raucoules, K. Philippot, A. Maisonnat, B. Chaudret, Y. Guari, A. Mehdi, C. Reye, and R.J.R. Corriu, *Advanced Functional Materials*, Vol. 17, pp. 3339–3347, 2007.
307. A.R. Kortan, R. Hull, R.L. Opila, M.G. Bawendi, M.L. Steigerwald, P.J. Carroll, and L.E. Brus, *Journal of the American Chemical Society*, Vol. 112, pp. 1327–1332, 1990.
308. B. Idriss and V.K. Prashant, *The Journal of Physical Chemistry*, Vol. 99, pp. 9182–9188, 1995.
309. K. Bernhard and J.B. Allen, *Journal of the American Chemical Society*, Vol. 100, pp. 4317–4318, 1978.
310. P. Kamat and B. Shanghavi, *The Journal of Physical Chemistry B*, Vol. 101, pp. 7675–7679, 1997.
311. J.L. Marignier, J. Belloni, M.O. Delcourt, and J.P. Chevalier, *Nature*, Vol. 317, pp. 344 – 345, 1985.

312. R.G. Freeman, B.H. Michael, C.G. Katherine, A.J. Michael, and J.N. Michael, *The Journal of Physical Chemistry*, Vol. 100, pp. 718–724, 1996.
313. L. Liz-Marzan, M. Giersig, and P. Mulvaney, *Langmuir*, Vol. 12, pp. 4329–4335, 1996.
314. Hardikar and Matijevic, *Journal of Colloid and Interface Science*, Vol. 221, pp. 133–136, 2000.
315. B.O. Dabbousi, J. RodriguezViejo, F.V. Mikulec, J.R. Heine, H. Mattoussi, R. Ober, K.F. Jensen, and M.G. Bawendi, *Journal of Physical Chemistry B*, Vol. 101, pp. 9463–9475, 1997.
316. X.B. Chen, L. Liu, P.Y. Yu, and S.S. Mao, *Science*, Vol. 331, pp. 746–750, 2011.
317. R.-F.N. Denis and M.L.-M.N. Luis, *Particle & Particle Systems Characterization*, Vol. 30, pp. 46–60, 2013.
318. J. Shan, C. Qian, T. Mukta, L. Erik, S.S. Kenneth, and G. Steve, *Advanced Materials*, Vol. 22, pp. 1060–1071, 2010.
319. C. Qian, B. Sung Chul, and G. Steve, *Nature*, Vol. 469, pp. 381–384, 2011.
320. Q. Chen, J. Whitmer, S. Jiang, S. Bae, E. Luitjen, and S. Granick, *Science*, Vol. 331, pp. 199–202, 2011.
321. S.H. Kim, S.J. Jeon, W.C. Jeong, H.S. Park, and S.M. Yang, *Advanced Materials*, Vol. 20, pp. 4129–4134, 2008.
322. Y.H. Wang, C.L. Zhang, C. Tang, J. Li, K. Shen, J.G. Liu, X.Z. Qu, J.L. Li, Q. Wang, and Z.Z. Yang, *Macromolecules*, Vol. 44, pp. 3787–3794, 2011.
323. H. Yu, M. Chen, P.M. Rice, S.X. Wang, R.L. White, and S.H. Sun, *Nano Letters*, Vol. 5, pp. 379–382, 2005.
324. P.-S. Isabel, S.K. Dmitry, A.M. Arif, G. Michael, A.K. Nicholas, and M.L.-M.N. Luis, *Langmuir*, Vol. 16, pp. 2731–2735, 2000.
325. Z. Seh, S. Liu, S.-Y. Zhang, K. Shah, and M.-Y. Han, *Chemical Communications (Cambridge, England)*, Vol. 47, pp. 6689–6691, 2011.
326. Z. Seh, S. Liu, M. Low, S.-Y. Zhang, Z. Liu, A. Mlayah, and M.-Y. Han, *Advanced Materials*, Vol. 24, pp. 2310–2314, 2012.
327. S. Zhi Wei, L. Shuhua, Z. Shuang-Yuan, M.S. Bharathi, H. Ramanarayan, L. Michelle, S. Kwok Wei, Z. Yong-Wei, and H. Ming-Yong, *Angewandte Chemie*, Vol. 123, pp. 10140–10143, 2011.
328. S. Zhi Wei, L. Shuhua, Z. Shuang-Yuan, S. Kwok Wei, and H. Ming-Yong, *Chemical Communications*, Vol. 47, pp. 6689–6691, 2011.
329. L. Ilkeun, J. Ji Bong, Y. Yadong, and Z. Francisco, *Angewandte Chemie*, Vol. 50, pp. 10208–10211, 2011.
330. Z. Seh, S. Liu, and M.-Y. Han, *Chemistry, an Asian Journal*, Vol. 7, pp. 2174–2184, 2012.
331. L. Armelao, D. Barreca, G. Bottaro, A. Gasparotto, S. Gross, C. Maragno, and E. Tondello, *Coordination Chemistry Reviews*, Vol. 250, pp. 1294–1314, 2006.
332. S.W. Boettcher, J.M. Spurgeon, M.C. Putnam, E.L. Warren, D.B. Turner-Evans, M.D. Kelzenberg, J.R. Maiolo, H.A. Atwater, and N.S. Lewis, *Science*, Vol. 327, pp. 185–187, 2010.

333. M. Szklarczyk and J.O. Bockris, *Journal of Physical Chemistry*, Vol. 88, pp. 5241–5245, 1984.
334. J. Hensel, G.M. Wang, Y. Li, and J.Z. Zhang, *Nano Letters*, Vol. 10, pp. 478–483, 2010.
335. S.U.M. Khan, M. Al-Shahry, and W.B. Ingler, *Science*, Vol. 297, pp. 2243–2245, 2002.
336. A. Wolcott, W.A. Smith, T.R. Kuykendall, Y.P. Zhao, and J.Z. Zhang, *Advanced Functional Materials*, Vol. 19, pp. 1849–1856, 2009.
337. I. Cesar, A. Kay, J.A.G. Martinez, and M. Gratzel, *Journal of the American Chemical Society*, Vol. 128, pp. 4582–4583, 2006.
338. W. Smith and Y.P. Zhao, *Catalysis Communications*, Vol. 10, pp. 1117–1121, 2009.
339. Khaselev and Turner, *Science*, Vol. 280, pp. 425–427, 1998.
340. Y. Hwang, A. Boukai, and P. Yang, *Nano Letters*, Vol. 9, pp. 410–415, 2009.
341. Y. Hongtao, C. Shuo, Q. Xie, Z. Huimin, and Z. Yaobin, *Applied Catalysis B: Environmental*, Vol. 90, pp. 242–248, 2009.
342. M. A.G., *Heterojunctions and Metal-Semiconductor Junctions*, Academic Press, Inc. 1972 .
343. C. Fulton, G. Lucovsky, and R. Nemanich, *Applied Physics Letters*, Vol. 84, pp. 580–582, 2004.
344. C.A. Betty, R. Sasikala, O.D. Jayakumar, T. Sakuntala, and A.K. Tyagi, *Progress in Photovoltaics: Research and Applications*, Vol. 19, pp. 266–274, 2011.
345. K. Sun, Y. Jing, C. Li, X.F. Zhang, R. Aguinaldo, A. Kargar, K. Madsen, K. Banu, Y.C. Zhou, Y. Bando, Z.W. Liu, and D.L. Wang, *Nanoscale*, Vol. 4, pp. 1515–1521, 2012.
346. W.C. Wang, S.Y. Chen, P.X. Yang, C.G. Duan, and L.W. Wang, *Journal of Materials Chemistry A*, Vol. 1, pp. 1078–1085, 2012.
347. G. Hodes, L. Thompson, J. DuBow, and K. Rajeshwar, *Journal of the American Chemical Society*, Vol. 105, pp. 324–330, 1983.
348. W. Kedi, Q. Wenying, Y. Hongtao, Z. Huimin, and C. Shuo, *Applied Surface Science*, Vol. 257, pp. 7714–7718, 2011.
349. R.R. Nair, P. Blake, A.N. Grigorenko, K.S. Novoselov, T.J. Booth, T. Stauber, N.M.R. Peres, and A.K. Geim, *Science*, Vol. 320, pp. 1308–1308, 2008.
350. D.H. Kim, J.H. Ahn, W.M. Choi, H.S. Kim, T.H. Kim, J.Z. Song, Y.G.Y. Huang, Z.J. Liu, C. Lu, and J.A. Rogers, *Science*, Vol. 320, pp. 507–511, 2008.
351. X. Li, C.Y. Li, H.W. Zhu, K.L. Wang, J.Q. Wei, X.M. Li, E.Y. Xu, Z. Li, S. Luo, Y. Lei, and D.H. Wu, *Chemical Communications*, Vol. 46, pp. 3502–3504, 2010.
352. X.M. Deng, X.B. Liao, S.J. Han, H. Povolny, and P. Agarwal, *Solar Energy Materials and Solar Cells*, Vol. 62, pp. 89–95, 2000.
353. T.G.S. David M. Peterson, *Inherent Spectrum-Splitting Photovoltaic Concentrator System*, General Dynamics Corporation, US4328389A, 1982 .
354. N.A. Kelly and T.L. Gibson, *International Journal of Hydrogen Energy*, Vol. 31, pp. 1658–1673, 2006.

355. S.Y. Reece, J.A. Hamel, K. Sung, T.D. Jarvi, A.J. Esswein, J.J.H. Pijpers, and D.G. Nocera, *Science*, Vol. 334, pp. 645–648, 2011.
356. A.S. Jason and C. Kyoung-Shin, *Chemistry of Materials*, Vol. 23, pp. 1105–1112, 2011.
357. E. Steinmiller and K.-S. Choi, *Proceedings of the National Academy of Sciences of the United States of America*, Vol. 106, pp. 20633–20636, 2009.
358. D. Zhong, J. Sun, H. Inumaru, and D. Gamelin, *Journal of the American Chemical Society*, Vol. 131, pp. 6086–6087, 2009.
359. D. Zhong and D. Gamelin, *Journal of the American Chemical Society*, Vol. 132, pp. 4202–4207, 2010.
360. Y. Surendranath, M. Kanan, and D. Nocera, *Journal of the American Chemical Society*, Vol. 132, pp. 16501–16509 .
361. D. Lutterman, Y. Surendranath, and D. Nocera, *Journal of the American Chemical Society*, Vol. 131, pp. 3838–3839, 2009.
362. Y. Surendranath, M. Dinca, and D. Nocera, *Journal of the American Chemical Society*, Vol. 131, pp. 2615–2620, 2009.
363. J.E. Arthur, S. Yogesh, Y.R. Steven, and G.N. Daniel, *Energy & Environmental Science*, Vol. 4, pp. 499–504, 2011.
364. Y. Surendranath, M. Dinca, and D.G. Nocera, *Journal of the American Chemical Society*, Vol. 131, pp. 2615–2620, 2009.
365. M.W. Kanan, Y. Surendranath, and D.G. Nocera, *Chemical Society Reviews*, Vol. 38, pp. 109–114, 2009.
366. A.J.E. Steven Y. Reece, Kinberly Sung, Zachary I. Green, Daneil G. Nocera, *Compositions, Electrodes, Methods, and Systems for Water Electrolysis and Other Electrochemical Techniques*, US 8361288 B2, Sun Catalytix Corporation, 2011 .
367. J.K. Norskov, T. Bligaard, J. Rossmeisl, and C.H. Christensen, *Nature Chemistry*, Vol. 1, pp. 37–46, 2009.

Studies on Electrochemical Properties of MnO_2 and CuO Decorated Multi-Walled Carbon Nanotubes as High-Performance Electrode Materials

Mohan Raja

*School of Engineering and Technology, Jagran Lakecity University,
Bhopal, Madhya Pradesh, India*

Abstract

Manganese oxide (MnO_2) and copper oxide (CuO) decorated multi-walled carbon nanotubes (MWCNTs) were synthesized by simple wet chemical method without surfactants and studied for their properties as electrode materials in energy storage applications such as supercapacitors. The prepared samples were characterized by using different analytical techniques such as X-ray diffraction (XRD), X-ray photoelectron spectroscopy (XPS), transmission electron microscopy (TEM), and surface area studies. The electrochemical properties of the metal oxide decorated MWCNTs were studied using cyclic voltammetry (CV) and galvanostatic charge-discharge studies. The MnO_2 -MWCNTs electrode showed more significant capacitive behavior than other electrode materials such as CuO -MWCNTs. The average specific capacitance of MnO_2 -MWCNTs and CuO -MWCNTs electrodes were found to be 282.60 and 180.41 F g^{-1} , respectively.

Keywords: Multi-walled carbon nanotubes, metal oxides, nanoparticles, wet chemical synthesis, transmission electron microscopy (TEM), electrochemical properties

6.1 Introduction

In recent years, the research has focused on developing new electrode materials for energy storage devices such as supercapacitors and batteries.

Corresponding author: mohanraja27@yahoo.com

Because of the environmental issues and depleting fossil fuels, interest in the development of alternative energy storage devices with high power and energy densities, has increased exponentially. For practical applications, supercapacitors must fulfill the following technical requirements: high specific capacitance, long cycle life and high charge–discharge rate. The supercapacitors have several advantages of high power density, long cycle life, short charge time, and safety over the battery and attracts great interests for energy storage devices [1].

Depending on charge storage mechanism, they are basically classified into two types: electric double layer capacitors (EDLCs) based on carbon electrodes and pseudocapacitors with certain metal oxides (RuO_2 , MnO_2 , and CuO) [2, 3]. Of all the transition-metal oxides studied as pseudocapacitor materials, in addition hydrated ruthenium oxide (RuO_2) has been found to be the most promising material in terms of energy density. However, the high cost of RuO_2 has prompted the research community to focus on other transition-metal oxides such as MnO_2 , and CuO , mainly because of cost-effectiveness. Moreover conducting polymers act as electrode materials [4]. Carbon materials with high specific surface area, such as activated carbon, activated carbon fibers, carbon aerogels/foams, and carbon nanotubes (CNTs) are the main electrode materials for supercapacitor application [5–7].

CNTs are attractive materials for electrodes of electrochemical energy storage devices due to their high conductivity, chemical stability, low mass density, and large surface area. CNTs are mainly classified in to two groups: single walled carbon nanotubes (SWCNTs) and multi-walled carbon nanotubes (MWCNTs). Both of them have been recognized as potential electrode materials for supercapacitors.

The capacitance of CNTs based supercapacitor electrodes can be enhanced by various techniques such as activating CNTs with acid treatment [8] modification of CNTs with conducting polymers [9] or with certain transition-metal oxides [10, 11]. Manganese dioxide (MnO_2) [12] and copper oxide (CuO) [13] are the candidates on account of their electrochemical behavior, low cost and environmental compatibility. However, the specific surface areas of these metal oxides in general are not high enough for high capacitance. The CNTs have been introduced to yield high conductivity and large specific surface area [14].

In this paper, the structural and electrochemical screening of dissimilar economical metal oxides such as MnO_2 and CuO decorated in MWCNTs using wet chemical method are studied. The main advantages of the wet chemical method are its flexibility and the level of experimental control so that a wide variety of materials can be introduced into the CNTs. The

behavior of supercapacitive of these metal oxides decorated electrodes have been studied using cyclic voltammetry (CV) and galvanostatic charge–discharge measurements and the results were discussed. However, based on developed knowledge, the supercapacitance properties of the MnO_2 and CuO nanoparticles decorated in MWCNTs have attracted great attentions.

6.2 Experimental

6.2.1 Materials

Commercial MWCNTs (Nanocyl[®]-7000, diameter 15–25 nm, length 1.5 μm) with specific surface area of 250–300 m^2/g were procured from Nano Best Corporation, South Korea. Copper chloride, manganese chloride, and sodium hydroxide were purchased from Aldrich Chemical Co. and used without further purification.

6.2.2 Preparation and Fabrication of Supercapacitor Cell

1 g of MWCNTs was dispersed in 100 ml of distilled water through ultrasonication. To this solution, 100 ml of 0.5 M manganese chloride solution was added with constant stirring at 60°C and following by sodium hydroxide solution (0.5 M) was added drop wise to the constantly stirred. To generate manganese hydroxide grafted CNTs, after the completion of reaction; solid products were collected by centrifuging and dried under vacuum at 100°C. MnO_2 grafted onto CNTs were reduced at 150°C. In another set of experiment, copper oxide (CuO) nanoparticles decorated CNTs were prepared as discussed below. 1 g of MWCNTs was dispersed in 100 ml of distilled water through ultrasonication. To this solution, 100 ml of 0.5 M Cu chloride solution was added with constant stirring at 80°C and following by sodium hydroxide solution (0.5 M) was added drop wise to the constantly stirred. After the completion of reaction, solid products were collected by centrifuging and dried under vacuum at 100°C. It is expected that during drying process, Cu hydroxide developed on the CNT surface get reduced to CuO nanoparticles and adhered on the surface by van der Waals force of interaction as discussed previously by earlier researchers [15].

The electrochemical properties and capacitance measurements of these electrodes were studied using a symmetric two-electrode system with 6 M KOH aqueous solution as electrolyte. A cathode as working electrode and

anode as counter electrode were prepared by the coating of a slurry composed of 98 wt% metal oxides decorated MWCNTs as the active material and 2 wt% polytetrafluoroethylene (PTFE) solution with ethanol on a nickel mesh. Two pieces of cellulose-based separator immersed in the electrolyte placed between the two electrodes were used.

6.3 Characterization

XRD measurements were performed using a Macscience X-ray diffractometer equipped with a Cu $K\alpha$ photon source (40 kV, 20 mA, $\lambda = 0.154$ nm). X-ray photoelectron spectroscopy (XPS) was carried out with a high-resolution ESCA-2000. Morphological characterization was performed at 400 keV using transmission electron microscopy (TEM) (JEOL 100C) using samples deposited on the carbon coated Cu grids. Brunauer Emmett and Teller (BET) specific surface area analysis was studied with Sorptomatic 1990 using the N_2 adsorption/desorption method. Structural characterization was done using Raman spectroscopy (RFS/100s, Bruker, Germany). CV and galvanostatic charge–discharge spectroscopy measurements were carried out using electrochemical workstation instrument (Autolab PGSTAT20, the Netherlands). Voltammetry testing was carried out at constant potentials scan rate of 5 mV/s between -0.4 and 0.4 V charge–discharge test was conducted at constant current scan rate of 10 mA/cm.

6.4 Results and Discussion

Figure 6.1 shows powder X-ray diffraction (XRD) patterns of MnO_2 -MWCNTs (a) and CuO-MWCNTs (b). The diffraction peaks at 2θ value of 25.80° were ascribed to the 002, reflections of the MWCNTs [16] while other peaks at 2θ values of 32.80° , 34.40° , 38.80° , 43.60° , 46.30° , and 65.50° were well indexed to the reflections of α - MnO_2 as indicated in Figure 6.1(a) (JCPDS card no. 14-0644). Similarly, CuO-MWCNTs shows major diffraction peaks at 28.4° , 32.32° , 39.5° , 47.6° , and 56.26° (Figure 6.1(b)) that are assigned to the (110), (111), (200), (220), and (311) reflections, similar to the reported values of face centered cubic CuO nanoparticles (JCPDS (5-0661)) [13] along with the diffraction peak due to (002) plane of MWCNTs. The average particle sizes of the MnO_2 and CuO nanoparticles decorated onto the CNTs are determined using Scherrer's equation [17], and it is observed to be 53 nm (MnO_2 -MWCNTs) and 60 nm (CuO-MWCNTs).

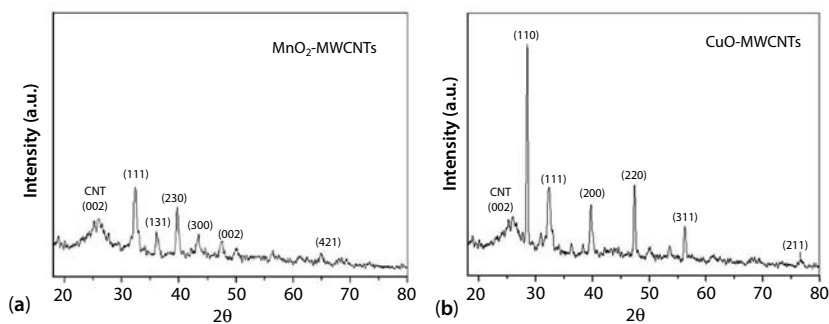


Figure 6.1 X-ray diffraction results of (a) MnO₂-MWCNTs and (b) CuO-MWCNTs.

The successful decoration of MnO₂ and CuO nanoparticles on the MWCNTs was confirmed by the XPS results shown in Figure 6.2. XPS results of pure CNTs exhibit a strong peak at 284.5 eV that corresponds to the carbon (C1s) peak [16]. The strong peaks at 642.2 and 653.5 eV can be corroborated to the Mn peaks (Mn2p spectra) in the case MnO₂-MWCNT with the appearance of peak at 529.6 eV that corroborates to the O1s spectra revealing the introduction of oxide. Similarly, new peak at 940 eV in the survey scan spectra of CuO-MWCNT corresponds to the Cu peak (Cu2p spectra) confirming the formation of CuO nanoparticles on the CNT surface in Figure 6.2. High-resolution spectra results of MnO₂ and CuO nanoparticles decorated onto CNTs were shown in Figure 6.3(a) and (b). MnO₂ nanoparticles decorated onto CNTs exhibits two strong peaks with binding energies of 642.2 and 653.5 eV that are due to Mn2p_{3/2} and Mn2p_{1/2}, respectively, consistent with those of MnO₂ as reported in the literature [18] indicating that the MWCNTs were successfully decorated with MnO₂ nanoparticles. Similarly, the high-resolution spectra of CuO nanoparticles decorated onto CNTs exhibits two strong peaks at 932.7 and 952.5 eV that are due to Cu2p_{3/2} and Cu2p_{1/2}, respectively (Figure 6.3(b)), revealing the successful formation of CuO nanoparticles on the MWCNT surface [19].

The decorating of metal oxide nanoparticles such as MnO₂ and CuO on the MWCNTs was further confirmed by the TEM results shown in Figure 6.4(a) and (b). It is obviously from the TEM images that the surface of CNT becomes irregular after the decoration of metal oxide nanoparticles on the surface. The average particle sizes of the decorated metal oxide nanoparticles onto the CNTs are observed to 50 nm. These results are further supported by the XRD results, which is used to characterize dimensions and structure of these nanomaterials.

Figure 6.5 shows Raman spectra of pure MWCNTs, MnO₂-MWCNTs, and CuO-MWCNTs measured less than 514.5 nm excitation over the

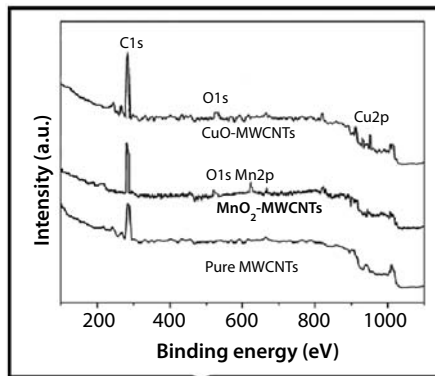


Figure 6.2 XPS survey scan results of MnO_2 and CuO nanoparticle decorated MWCNTs.

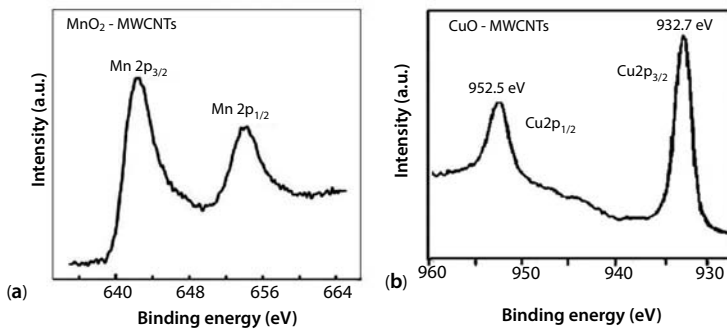


Figure 6.3 High-resolution spectra results of (a) MnO_2 -MWCNTs and (b) CuO -MWCNTs.

Raman shift interval of $1000\text{--}3000\text{ cm}^{-1}$. The D- and G-bands of MWCNTs at ~ 1290 and 1589 cm^{-1} , corresponding to defect and disorder induced modes and the in-plane E_{2g} zone centered mode, are clearly observed in pure MWCNT [16]. Decorating of Manganese oxide (MnO_2 -MWCNTs) result in the shift of tangential mode vibration (G band) to 1595 cm^{-1} from 1589 cm^{-1} clearly reveal the decrease in van der Waals force of interaction between the CNTs due to the introduction of the nanoparticles on the CNT surface. Similarly, in the case of CuO -MWCNTs, G-band shift to the higher frequency (1593 cm^{-1}), corroborating the decrease in van der Waals force of interaction between CNTs due to the grafting of copper oxide nanoparticles on CNTs through van der Waals force of interaction. The D- to G-band intensity ratio (ID/IG) of MnO_2 -MWCNTs is 0.167, lesser than that of pure MWCNTs (0.189). Similar trend observed in CuO -MWCNTs (ID/IG, 0.167).

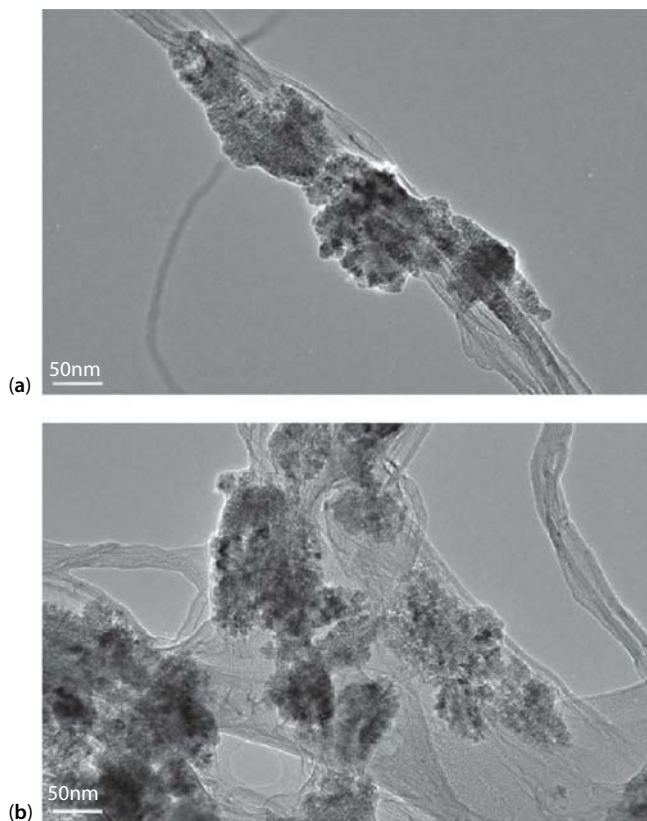


Figure 6.4 (a) TEM image of MnO₂ nanoparticles decorated carbon nanotubes (MnO₂-MWCNTs); (b) TEM image of CuO nanoparticles decorated carbon nanotubes (CuO-MWCNTs).

Slight reduction in ID/IG value may be attributed to the reduction in surface defects due to the decoration of nanoparticles on the surface of CNTs.

The surface area measurements of the metal oxide nanoparticles decorated CNTs were determined using nitrogen adsorption/desorption isotherms. The multilayer adsorption model developed by BET is fitted against isotherms to evaluate the surface area of the nanotubes. BET surface area result of pure MWCNTs and metal oxide nanoparticles decorated MWCNTs were shown in Table 6.1. Surface area values of metal oxide nanoparticles decorated CNTs are higher than pure MWCNTs. Higher surface area of metal oxide nanoparticles decorated onto CNTs results in better efficiency in electrochemically behavior, which could be further confirmed by CV.

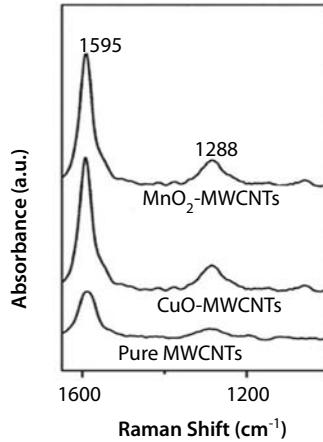


Figure 6.5 Raman spectra results of pure and metal oxide nanoparticles decorated MWCNTs.

Table 6.1 BET surface analysis results of MnO_2 and CuO nanoparticle decorated MWCNTs.

S. No.	Samples Name	S_{BET} (m^2/g)
1	Pure MWCNT	285.7
2	MnO_2 -MWCNT	678.9
3	CuO-MWCNT	515.3

The CV behavior of pure MWCNTs, MnO_2 and CuO nanoparticles decorated MWCNTs electrodes at a potential scan rate of 5 mV/s were shown in Figure 6.6. The result of pure MWCNTs reveals no current peaks and furthermore it is nearly symmetric with respect to the zero current line. This indicates that the electrodes have the characteristic of a capacitor with constant charging and discharging rates over a complete cycle. We can observe there are oxidation peaks for MnO_2 -MWCNTs and CuO-MWCNTs electrodes, which are attributed to redox reactions due to the functional groups on MWCNTs [20]. MnO_2 -MWCNT and CuO-MWCNT electrodes, the lack of symmetry to the curves is probably due to combination of double layer and pseudo capacitances contributing to the total capacitance [21]. The area of the curves increases in MnO_2 -MWCNTs compare to CuO-MWCNTs, which is indicating an improvement of the specific capacitance for dissimilar electrode materials. The CV curve for

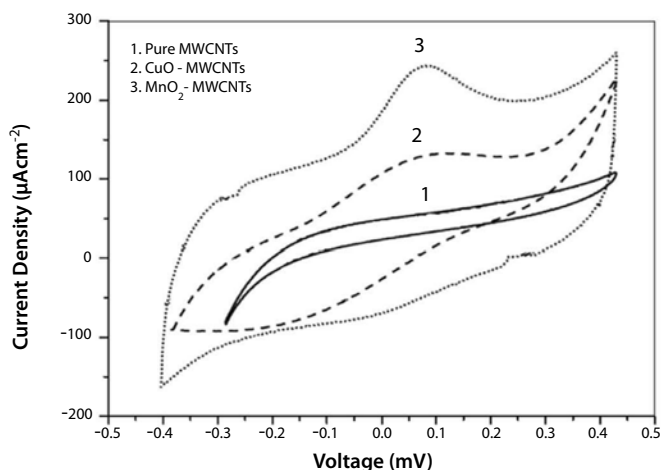


Figure 6.6 Cyclic voltammetry (CV) behavior of pure MWCNTs, MnO_2 and CuO nanoparticles decorated MWCNTs electrodes at a potential scan rate of 5 mV/s.

MnO_2 -MWCNTs electrode shows more rectangular shape and more significant capacitive behavior than CuO-MWCNTs electrode. This is due to higher pseudocapacitive behavior of MnO_2 than CuO. The CuO-MWCNTs curve had an oxidation peak approximately at 0.05 V and a reduction peak around -0.12 V; however, MnO_2 decorated in to MWCNTs, it was clearly found that larger oxidation peaks at 0.07 V and non significant reduction peaks around 0.0 V occurred. These affirmed that there were electrochemical oxidation and reduction on the CuO-MWCNTs and MnO_2 -MWCNTs electrodes when the supercapacitor was being charged or discharged.

The charge-discharge properties of CuO-MWCNTs and MnO_2 -MWCNTs electrodes were investigated by galvanostatic charge discharge in 6 M KOH solutions. The galvanostatic charge-discharge curves of the CuO-MWCNTs and MnO_2 -MWCNTs are shown in Figure 6.7. The symmetry of the charge and discharge characteristics showed good capacitive behavior of the CuO-MWCNTs and MnO_2 -MWCNTs electrodes. There is no iR drop is observed for all curves, which means that the electrodes have low internal resistance. In addition, the charge/discharge duration increases in the MnO_2 decorated MWCNTs and it has indicating the highest specific capacitance for MnO_2 -MWCNTs. The specific capacitance of the system has been evaluated using the formula [22]:

$$\text{Specific capacitance, } C \text{ (F/g)} = \frac{i\Delta t}{m \Delta v} \quad (6.1)$$

where i is the current used for charge/discharge, Δt is the time elapsed for the charge or discharge cycle, m is the mass of the active electrode, and Δv

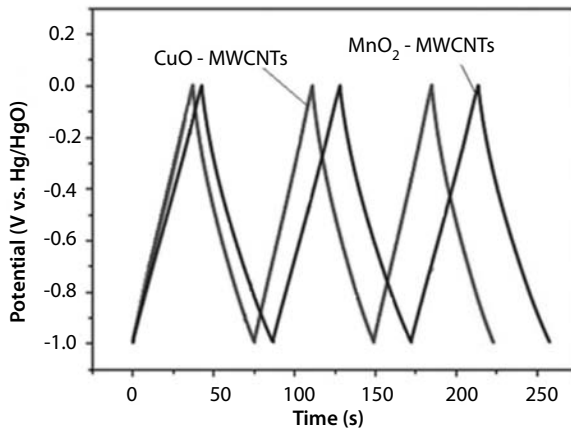


Figure 6.7 Galvanostatic charge–discharge curves of the CuO-MWCNTs and MnO₂-MWCNTs.

is the voltage interval of the charge or discharge. The specific capacitance of MnO₂-MWCNTs electrode is much higher than that CuO-MWCNT electrode at the same scan rates. The specific capacitance of 282.60 Fg⁻¹ is obtained at 10 mVs⁻¹ in 6 M KOH aqueous solution for MnO₂-MWCNTs electrode, compared to 180.41 Fg⁻¹ for CuO-MWCNTs electrode. The improvement of the specific capacitances accredited to the presence of CuO and MnO₂ decorated in the MCWNTs, which in turn amend the microstructure and morphology of MCWNTs, allowing the metal oxides to be obtainable for the electrochemical reactions and improves the efficiency of the electrodes. These imply further that MnO₂-MWCNTs electrode has excellent capacitive properties due to high conductivity of CNTs.

6.5 Conclusion

The transition-metal oxides such as CuO and MnO₂ were decorated MWCNTs with the same mass ratio by a simple wet chemical method. TEM images showed the distribution of CuO and MnO₂ particles of size of about 40–60 nm attached in the side of MWCNTs which were achieved by wet chemical method. Moreover, XPS spectra show that the MWCNTs were successfully functionalized with metal oxides nanoparticles. From BET analysis, surface area of metal oxide is enhanced with CNTs, which have one of the most attributed reasons for efficacy in MnO₂-MWCNTs and CuO-MWCNTs electrochemical behavior. The MnO₂ and CuO decorated

MWCNTs electrodes due to have higher pseudocapacitive properties and electrochemical stability showed more significant capacitive behavior. The specific capacitances of the CuO-MWCNTs and MnO₂-MWCNTs electrodes were 180.41 and 282.60 Fg⁻¹, respectively. Both CuO-MWCNTs and MnO₂-MWCNTs electrodes were the promising materials to be used as positive electrode in alkaline electrochemical supercapacitor. However, the capacitance properties of MnO₂-MWCNTs were better than CuO-MWCNTs.

References

1. B. E. Conway, *Electrochemical Capacitors: Scientific Fundamentals and Technological Applications*, Kluwer Academic/Plenum, Dordrecht, 1999.
2. L. Chuan, A. R. James and N. P. Branko, *J. Electrochem. Soc.* 12 (1998) 4097–4103.
3. B. E. Conway, V. Birss and J. Wojtowicz, *J. Power Sources* 66 (1997) 1–14.
4. C. Peng, S. Zhang, D. Jewell and G. Z. Chen, *Prog. Nat. Sci.* 18 (2008) 777–788.
5. E. Frackowiak and F. Béguin, *Carbon* 40 (2002) 1614–1617.
6. J. M. Miller, B. Dunn, T. D. Tra and R. W. Pekala, *J. Electrochem. Soc.* 144 (1997) 309–311.
7. Y. R. Nian and H. Teng, *J. Electrochem. Soc.* 149 (2002) 1008–1014.
8. Y. T. Kim and T. Mitani, *J. Power Sources* 158 (2006) 1517–1522.
9. K. H. An, K. K. Jeon, J. K. Heo, S. C. Lim, D. J. Bae and Y. H. Lee, *Electrochem. Soc.* 149 (2002) 1058–1062.
10. G. X. Wang, B. L. Zhang, Z. L. Yu and M. Z. Qu, *Solid State Ionics* 176 (2005) 1169–1174.
11. G. Arabale, D. Wagh, M. Kulkarni, I. S. Mulla, S. P. Vernekar, K. Vijayamohan and A. M. Rao, *Chem. Phys. Lett.* 376 (2003) 207–213.
12. S. B. Ma, K. W. Nam, W. S. Yoon, X. Q. Yang, K. Y. Ahn, K. H. Oh and K. B. Kim, *J. Power Sources* 178 (2008) 483–489.
13. H. Q. Wu, X. W. Wei, M. W. Shao, J. S. Gu and M. Z. Qu, *Chem. Phys. Lett.* 364 (2002) 152–156.
14. Y. Xie, L. Zhou, C. Huang, H. Huang and J. Lu, *Electrochim. Acta* 53 (2008) 3643–3649.
15. Y. Wang, X. Xu, Z. Tian, Y. Zong, H. Cheng and C. Lin, *Chem. Eur. J.* 12 (2006) 2542–2549.
16. M. Raja and S. H. Ryu, *J. Nanosci. Nanotechnol.* 9 (2009) 5940–5945.
17. M. Raja, A. M. Shanmugaraj and S. H. Ryu, *J. Nanosci. Nanotechnol.* 8 (2008) 4224–4226.
18. C. D. Wanger, W. M. Riggs, L. E. Davis, J. F. Moulder and G. E. Muilenberg, *Handbook of X-Ray Photoelectron Spectroscopy*, Perkin-Elmer: Eden Prairie, MN, 1978.

19. H. Wang, J. Z. Xu, J. J. Zhu and H. Y. Chen, *J. Crys. Growth*. 244 (2002) 88–94.
20. E. Frackowiak, K. Metenier, V. Bertagna and F. Beguin, *Appl. Phys. Lett.* 77 (2000) 2421–2423.
21. A. L. M. Reddy and S. Ramaprabhu, *J. Phys. Chem.* 111 (2007) 7727–7734.
22. V. Subramanian, H. W. Zhu, R. A. Vajitai, P. M. Ajayan and B. Q. Wei, *J. Phys. Chem. B* 109 (2005) 20207–20214.

Part 2

MULTIFUNCTIONAL HYBRID MATERIALS: FUNDAMENTALS AND FRONTIERS

Discotic Liquid Crystalline Dimers: Chemistry and Applications

Shilpa Setia¹, Sandeep Kumar² and Santanu Kumar Pal^{*1}

¹*Department of Chemical Sciences, Indian Institute of Science Education and Research (IISER) Mohali, SAS Nagar, Mohali, India*

²*Raman Research Institute, Sadashivanagar, Bangalore, India*

Abstract

Discotic liquid crystalline dimers have been attracting a great deal of interest in recent years both in theoretical and experimental studies not only for their ability to act as model compounds for semi-flexible main chain liquid crystal polymers but also due to their quite unusual properties as compared to conventional low-molar-mass mesogens. They are formed by linking two identical/different discotic mesogens via a flexible spacer or through a rigid spacer. These dimers show interesting behaviour depending on the length of the spacer and on the structure of the linking group. Due to their ability of self-organisation into different phases, such systems are quite useful in various organic electronics such as light-emitting diodes, field effect transistors, solar cells as well as in wide-view displays. Thus, they are immensely significant in both fundamental science and practical applications. Hitherto, more than 100 discotic dimers comprising 11 different discotic cores have been realised. Discotic cores that have been explored to create dimers are anthraquinone, benzene, cyclotetra-*per*-arylene, hexa-*peri*-hexabenzocoronene, phthalocyanine, porphyrin, pyranose sugars, pyrene, scylloinositol, and triphenylene. In this chapter, we cover the different dimeric liquid crystals formed of two discotic units tethered via a spacer.

Keywords: Liquid crystals, discotics, dimers, organic electronics, self-organisation

*Corresponding author: skpal@iisermohali.ac.in

7.1 Introduction

Since the discovery of liquid crystals in 1888 by F. Reinitzer [1], it was assumed that liquid crystal molecules are mainly composed of mesogenic core attached to which are one or more alkyl chains. However, during 1980s a new class of liquid crystals attracted particular attention acknowledged as the liquid crystal dimers. Liquid crystal dimers are formed by connecting two mesogenic cores through flexible/rigid spacers generally alkyl chains. Although this class of compounds has been discovered by Vorlander long back in 1927 [2], but these dimers didn't achieve considerable attention until their rediscovery by Griffin and Britt in 1980s [3]. Subsequently, several classes of dimeric liquid crystalline compounds have been prepared and studied extensively.

The initial interest in this class of compounds was caused by their similarity with semi-flexible main chain liquid crystal polymers. In order to understand polymeric molecules at the molecular level, dimeric systems can serve as the model compounds. Griffin and Britt [3] argued that the fundamental repeating unit for liquid crystalline polymeric materials consist of two mesogenic units connected through spacers, i.e. dimeric unit. This indeed proved to be correct and dimers do serve as model compounds for polymers.

Among the several categories of liquid crystalline dimers, discotic dimers have received considerable attention in recent years. A discotic dimer is composed of two identical/different discotic mesogens linked via a flexible spacer or through a rigid spacer. These dimers show interesting behaviour depending on the length of the spacer and on the structure of the linking group. Compared to large variety of liquid crystal dimers, discotic dimers are very less in number. This may be due to the difficulties involved in preparing the monofunctionalised discotic precursors. The various structural possibilities for discotic dimers are shown schematically in Figure 7.1.

Dimers in which two identical mesogenic discotic moieties tethered via a flexible or rigid spacer are the most widely synthesised and studied dimers (Figure 7.1(a)). It is generally difficult to link two different discotic mesogens and therefore, only a few examples of unsymmetrical dimers have been realised (Figure 7.1(b)). Figure 7.1(c) and (d) show the discotic mesogens laterally and terminally linked to a calamitic molecule, respectively. A number of dimers in which two discotic moieties are tethered by a metal atom are also known (Figure 7.1(e)). Cyclic dimers in which two discotic moieties are connected to each other via more than one spacer are shown in Figure 7.1(f).

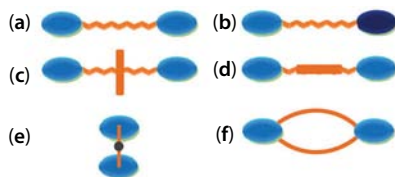


Figure 7.1 The various possibilities of molecular architectures for discotic liquid crystal dimers: (a) symmetric discotic dimer, (b) non-symmetric discotic dimers, (c) two discotic moieties laterally linked to a calamitic molecule, (d) two discotic moieties terminally linked to a calamitic molecule, (e) two discotic moieties tethered by a metal atom, and (f) cyclic dimers in which two discotic moieties are connected to each other via more than one spacer.

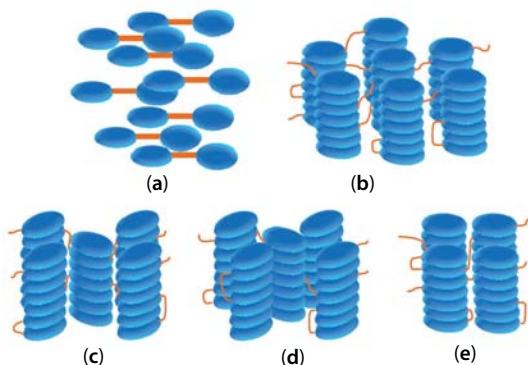


Figure 7.2 Schematic representation of most common mesophases formed by discotic dimers: (a) discotic nematic (N_D), (b) columnar hexagonal (Col_h), (c) columnar rectangular (Col_r), (d) columnar oblique (Col_{ob}), and (e) columnar tetragonal (Col_{tet}).

The spacer length has a profound effect on the arrangements of these dimers in mesophases. Depending on the length of the spacer, they show several assembling state (Figure 7.2) in LC phase. The least order mesophase is the discotic nematic phase (N_D) characterised by the presence of only the orientational order, but this phase is not so common. Majority of the discotic dimers form columnar mesophase in which disks stack on top of each other to generate columns, which then self-organise in various 2D lattices. Most common mesophases formed by discotic dimers are: (a) columnar hexagonal (Col_h), (b) columnar rectangular (Col_r), (c) columnar oblique (Col_{ob}), and (d) columnar tetragonal (Col_{tet}).

The various possible stacking arrangements for the discotic dimers in the columnar phase are shown in Figure 7.3. When the spacer length is greater than the peripheral chain length, then discotic dimers arrange themselves in inter-columnar manner with the two subunits of the dimer

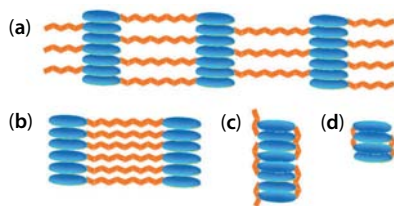


Figure 7.3 Possible stacking of discotic dimers into columnar structures at the mesophase. Discotic dimeric molecules arranged in inter-columnar manner (a) intercalated and (b) non-intercalated. Discotic dimeric molecules arranged in intra-columnar manner (c) intra-1,4 and (d) inter-1,3.

residing in neighbouring columns. Such an arrangement can further be of two types namely, (i) intercalated (Figure 7.3(a)) or (ii) non-intercalated (Figure 7.3(b)). But, when the spacer length is smaller than the peripheral chain length, then discotic dimers arrange themselves in intra-columnar manner with the two subunits of the dimer residing in same columns. Such an arrangement can further be of two types namely, (i) intra-1,4 (Figure 7.3(c)) or (ii) inter-1,3 (Figure 7.3(d)).

The thermotropic phase behaviour of discotic dimers is usually studied by using differential scanning calorimetry (DSC), polarised optical microscopy (POM) and wide-angle X-ray scattering (WAXS).

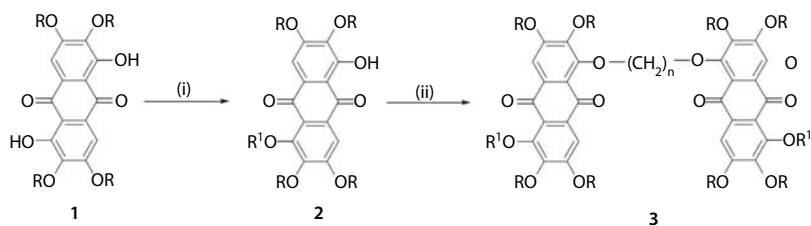
In this chapter, firstly the structure-property relationships of dimeric liquid crystals formed of two discotic units tethered via a spacer have been outlined. Discotic cores that have been explored to create dimers are anthraquinone, benzene, cyclotetraveratrylene, dibenzo[a,c]phenazine, hexa-*peri*-hexabenzocoronene, phthalocyanine, porphyrin, pyranose sugars, pyrene, scylloinositol, and triphenylene. Secondly, a general introduction of most important applications of discotic dimers is demonstrated.

7.2 Structure-Property Relationship of Discotic Dimers

7.2.1 Discotic Dimers Based on Anthraquinone Core

7.2.1.1 Dimers Connected through Flexible Spacer

Krishnan and Balagurusamy [4] synthesised a discotic dimer **3.1** derived from anthraquinone core. The starting material for the dimer 5-hydroxy-1-(4-nitrobenzyloxy)-2,3,6,7-tetrapentyloxy-9,10-anthraquinone **2** was prepared



Scheme 7.1 Synthesis of anthraquinone dimers connected through methylene spacers: (i) DEAD, PPh_3 , $\text{R}'\text{OH}$; (ii) K_2CO_3 , dibromoalkane, DMF, $(n\text{-C}_4\text{H}_9)_4\text{N}^+\text{I}^-$.

by treating 2,3,6,7-tetrapentyloxyanthraquinone **1** with 4-nitrobenzyl alcohol, diethyl azodicarboxylate (DEAD) and PPh_3 under Mitsunobu conditions. This was then reacted with half equivalent of 1,12-dibromododecane and excess of K_2CO_3 in DMF at 90°C for 20 h (Scheme 7.1). The main reason of attaching 4-nitrobenzyl group instead of alkyl group was the polar nature of this group. It was easier to purify this monomer as compared to 1-hydroxy-2,3,5,6,7-pentapentyloxy-9,10-anthraquinone monomer. In first heating, this dimer went from an unknown Col phase to Col_h phase at 147°C , which on further heating changed to isotropic at 180.4°C . During the cooling cycle, one transition corresponding to isotropic to Col appeared at 176.6°C . But, in the second heating scan, the first transition shifted to 114.7°C . The actual reason for this transition is not known. The complete homologues series of this dimer was prepared by Prasad *et al.* [5] by varying peripheral substituents as well as the length of linker. Generally, in case of dimers, the nature of mesophase is more sensitive to the change in spacer chain length rather than peripheral chain length. However, in this series, nature of mesophase didn't change on varying spacer chain length. When the spacer chain length was kept constant and peripheral chain length was varied, then mesophase varied from D_L to M_x phase. In addition to this, another two series containing benzyl and hexyl group in position 1 of anthraquinone have also been prepared. In both these series, peripheral alkyl chains were fixed, only the spacer length was varied. Here spacer chain length has a profound effect in showing the mesophase behaviour (Table 7.1).

A series of anthraquinone-imide-based dimers **6** have been reported by Chen *et al.* [6] (Scheme 7.2). These dimers were prepared by hydrosilylation of *N*-(hex-5-enyl)-6-(4'-((*S*)-2-methylbutoxy)phenyl)anthraquinone-2,3-dicarboxylic imide **5** and hydride-terminated siloxanes with different lengths. Although anthraquinone imide is not liquid crystalline by itself, all the dimers formed a SmA phase (Table 7.2). When a moderate pressure is applied on the powder of these dimers, the colour changed from

Table 7.1 Thermal behaviour (°C) of anthraquinone dimers connected through methylene spacers.

Str	R	R ¹	n	Mesophase behaviour	Ref.
3.1	C ₅ H ₁₁	4-nitrobenzyl	12	Col _x 147 Col _h 180.4 I	[4]
3.2	C ₄ H ₉	4-nitrobenzyl	12	Cr 124.9 D _L 186.1 I	[5]
3.3	C ₆ H ₁₃	4-nitrobenzyl	8	Cr 117.9 I	[5]
3.4	C ₆ H ₁₃	4-nitrobenzyl	10	Cr 73.1 D _L 140.2 I	[5]
3.5	C ₆ H ₁₃	4-nitrobenzyl	12	Cr 104 D _L 163.2 I	[5]
3.6	C ₈ H ₁₇	4-nitrobenzyl	12	Cr 92 D _L 119.2 I	[5]
3.7	C ₁₀ H ₂₁	4-nitrobenzyl	12	Cr 66.5 M _X 81.5 I	[5]
3.8	C ₁₂ H ₂₅	4-nitrobenzyl	12	Cr 39.7 M _X 67.8 I	[5]
3.9	C ₆ H ₁₃	benzyl	8	Cr 126.9 I	[5]
3.10	C ₆ H ₁₃	benzyl	10	Cr 120.3 I	[5]
3.11	C ₆ H ₁₃	benzyl	12	Cr 120.4 Col _h 138.6 I	[5]
3.12	C ₆ H ₁₃	C ₆ H ₁₃	8	Cr 99.5 I	[5]
3.13	C ₆ H ₁₃	C ₆ H ₁₃	10	Cr 97.7 I	[5]
3.14	C ₆ H ₁₃	C ₆ H ₁₃	12	Cr 92.9 Col _h 113.5 I	[5]

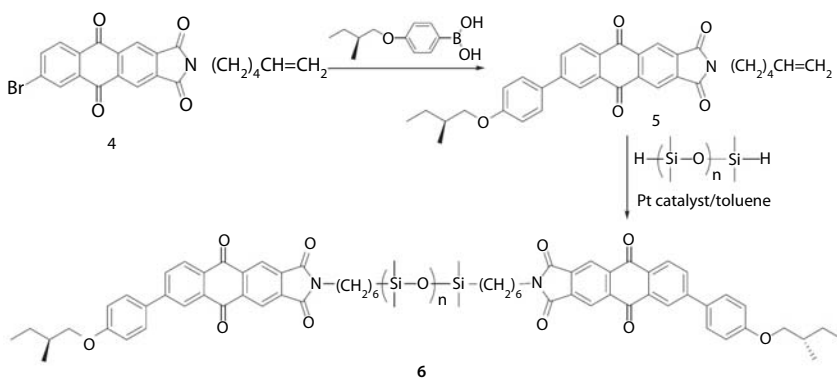
**Scheme 7.2** Synthesis of anthraquinone-imide based dimers.

Table 7.2 Thermal behaviour ($^{\circ}\text{C}$) of anthraquinone-imide based dimers.

Str	<i>n</i>	Mesophase behaviour	Ref.
6.1	1	Cr 261 SmA 278 I	[6]
6.2	2	Cr 252 SmA 274 I	[6]
6.3	3	Cr 256 SmA 273 I	[6]
6.4	7	Cr 220 SmA 239 I	[6]

light yellow to deep red. This process can be reversed by solvent. Upon one-electron reduction, the dimers are converted to radical anions and give intense NIR absorption at 844 nm. Such materials can find applications in fields such as nanostructured electronics/optics.

7.2.1.2 Dimers Connected through Metals

A number of β -diketonate metal complexes are known to exhibit mesophases like nematic, smectic, columnar and lamellar. 1-Hydroxy-2,3,5,6,7-pentakis(alkoxy)-9,10-anthraquinone **7** has the similar molecular architecture as of β -diketonate systems. Due to the similarity between monohydroxy-pentaalkoxy-anthraquinone and the β -diketonate systems, it is expected that metallomesogens of anthraquinone can also be realised like that of β -diketonate systems. To demonstrate this, Kumar and co-worker [7, 8] prepared a series of metal-bridged rufigallol dimers **8** by refluxing monohydroxy-pentaalkoxy-anthraquinone **7** with metal acetate in acetonitrile and pyridine (Scheme 7.3). Two homologues series of complexes, one with Cu and the other with Pd have been prepared. The thermal

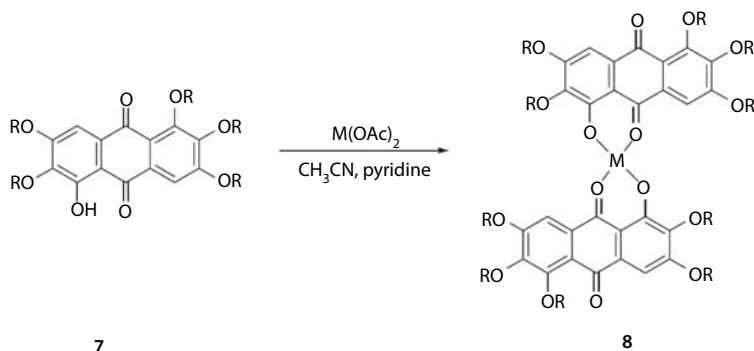
**Scheme 7.3** Synthesis of anthraquinone dimers connected through metals.

Table 7.3 Thermal behaviour (°C) of anthraquinone dimers connected through metals.

Str	R	M	Mesophase behaviour	Ref.
8.1	C ₄ H ₉	Cu	Cr 184 I	[7]
8.2	C ₅ H ₁₁	Cu	Cr 175 I	[7]
8.3	C ₆ H ₁₃	Cu	Cr 170 I	[7]
8.4	C ₈ H ₁₇	Cu	Cr 151.7 Col 156 Col 165.8 I	[7]
8.5	C ₁₂ H ₂₅	Cu	Cr 71.9 Col 121 Col 146.2 I	[7]
8.6	C ₄ H ₉	Pd	Dec	[7]
8.7	C ₆ H ₁₃	Pd	Dec	[7]
8.8	C ₇ H ₁₅	Pd	Dec	[7]
8.9	C ₈ H ₁₇	Pd	Dec	[7]
8.10	C ₉ H ₁₉	Pd	Dec	[7]
8.11	C ₁₀ H ₂₁	Pd	Dec	[7]
8.12	C ₁₂ H ₂₅	Pd	Dec	[7]

behaviour of these complexes is summarised in Table 7.3. Lower members of both the series were not liquid crystalline but columnar mesophase can be generated by doping with an electron acceptor trinitrofluorenone (TNF). The higher members of the series showed columnar phase, but the exact nature of phase was not revealed. Pd complexes were all found to decompose on heating. So thermal data of these complexes could not be reproduced and hence was not reported.

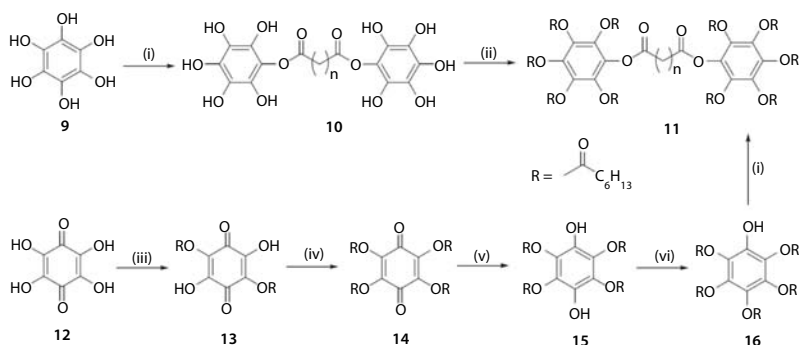
7.2.2 Discotic Dimers Based on Benzene Core

7.2.2.1 Benzene Rings Connected through Flexible Spacers

Lillya and Murthy [9] introduced the first discotic dimer based on benzene core. Two penta-*n*-heptanoyloxy benzene rings were connected via a methylene spacer to give dimer. An excess amount of hexahydroxybenzene **9** was treated with appropriate diacid chloride and the resulting mixture containing **10** was reacted with excess of heptanoyl chloride to afford **11**. An alternative route to prepare these dimers has also been explored by Zamir *et al.* [10]

Tetrahydroxy-1,4-benzoquinone **12** was heated with *n*-heptanoyl chloride to give 2,5-diheptanoyloxy-1,4-benzoquinone **13**. Tetraheptanoyloxy-1,4-benzoquinone **14** was obtained by heating **13** with *n*-heptanoyl chloride and a few grains of magnesium at 180°C. Reduction of the quinone with SnCl₂ in HCl furnished tetraheptanoyloxy-1,4-dihydroxybenzene **15**. The transesterification reaction of **15** with hexaheptanoyloxybenzene in the presence of dimethylaminopyridine (DMAP) provided pentaheptanoyloxyphenol **16**. The desired dimer **11** was achieved by reacting with an appropriate diacid chloride in CH₂Cl₂ and dry pyridine (Scheme 7.4).

All the dimers have the same peripheral group, while the spacer length was varied from 4 carbons to 18 carbons. The thermal behaviour of these dimers is summarised in Table 7.4. It can be seen from the table that on



Scheme 7.4 Synthetic routes to benzene-based discotic dimers connected through flexible spacers: (i) ClOC(CH₂)_nCOCl, pyridine, CH₂Cl₂; (ii) *n*-C₆H₁₃COCl; (iii) *n*-C₆H₁₃COCl, 90°C; (iv) *n*-C₆H₁₃COCl, Mg, 180°C; (v) SnCl₂, HCl; (vi) hexaheptanoyloxybenzene, DMAP.

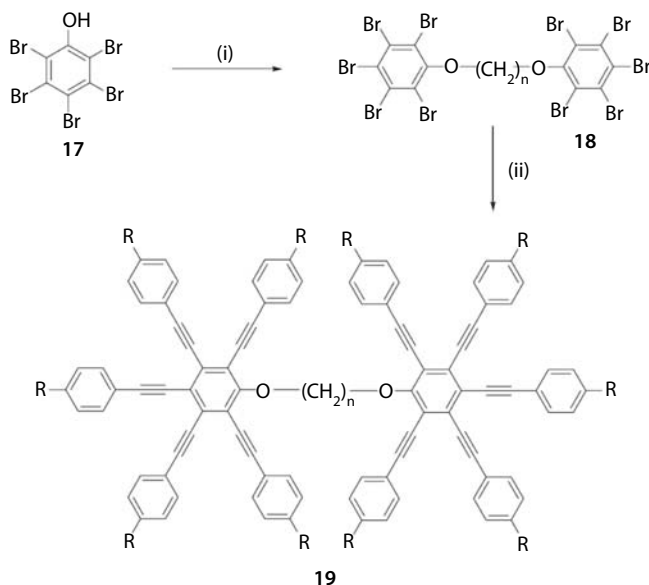
Table 7.4 Thermal behaviour (°C) of benzene-based discotic dimers connected through flexible spacers.

Str	<i>n</i>	Mesophase behaviour	Ref.
11.1	4	Cr 115.6 I	[10]
11.2	6	Cr 94 I	[10]
11.3	8	Cr 128 I	[9]
11.4	10	Cr 75 Col ₁ 96.8 I	[10]
11.5	12	Cr 77 Col ₁ 91.3 I	[10]
11.6	18	Cr 112 Col _h 120 I	[9]

increasing the spacer length, the tendency of symmetrical dimers to display liquid crystalline behaviour increases. Higher homologues of the series exhibited Col phase, while lowered members were non-mesomorphic. The thermal stability of these dimers was found to be greater than their monomeric counterparts. Thus, it can be concluded that if the spacer length is sufficiently long, discotic dimers can arrange themselves in columns, if the spacer length is about twice the length of peripheral chains or longer, the mesophases obtained are similar to that of the monomers.

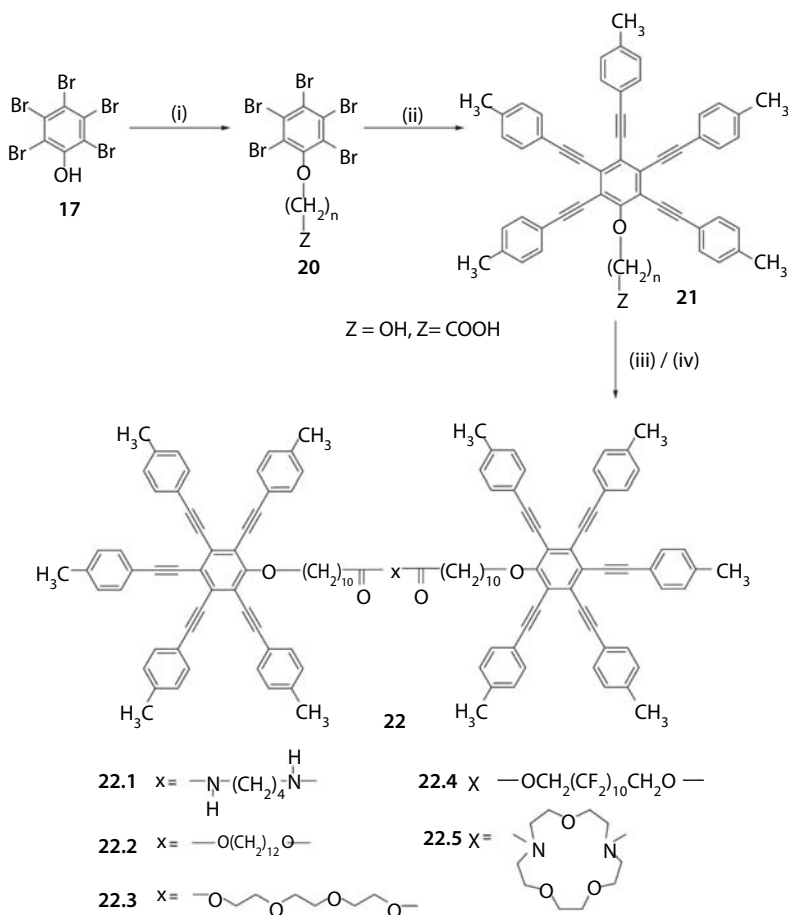
7.2.2.2 Alkynylbenzene-Based Discotic Dimers

Hexaalkynylbenzenes or multiynes are well-known discotic nematic liquid crystals. Connecting two bulkier pentaynes via a proper spacer may limit the free rotation of the monomesogenic units around the long axis of the dimeric molecule and therefore, can lead to N_b phase formation. This encouraged Praefcke and co-workers to design and synthesise a dimer based on pentyne units [11]. Subsequently, many other dimers have also been prepared based on pentyne units [12–17]. Pentabromophenol **17** was etherified with appropriate α,ω -dibromoalkane in the presence of sodium hydride in DMF to yield α,ω -bis(pentabromopentyloxy)alkane **18**. Tenfold palladium-catalysed alkylation of the twin ether **18** with suitable



Scheme 7.5 Synthesis of multiyne based twin ethers linked through methylene bridges: (i) $\text{Br}(\text{CH}_2)_n\text{Br}$, NaH; (ii) 4-alkylphenylacetylene, $\text{PdCl}_2(\text{PPh}_3)_2$, PPh_3 , CuI, NEt_3 .

4-alkyl-phenylacetylene furnished the desired pentyne ether dimers **19** in moderate yields (Scheme 7.5). Kouwer *et al.* used hydroxyl- or carboxyl-functionalised monomers to prepare a number of multiyne-based discotic dimers [16, 17]. These monomers were prepared from a straightforward reaction from **17** with the commercially available alcohol- or carboxylate-terminated spacers. These terminally functionalised monomers **21** were connected with each other via a variety of functional groups using classical coupling reactions, thus, esterification of **21** having $Z = \text{COOH}$ with α,ω -diols gave dimers **22.2–22.4**, while its reaction with diamino compounds yielded amides **22.1** and **22.5** (Scheme 7.6). Compounds **23** and **24** were



Scheme 7.6 Synthesis of multiyne-based discotic dimers having ester or amide groups in the spacer: (i) $\text{Br(CH}_2\text{)}_{10}\text{COOEt}$, K_2CO_3 , KI, DMF; (ii) $\text{HC}\equiv\text{CPhCH}_3$, $\text{PdCl}_2(\text{PPh}_3)_2$, PPh_3 , CuI, NEt₃, piperidine; (iii) aq KOH, EtOH; (iv) HOXOH or H_2NXNH_2 , DCC, DMAP, *p*-TSA, CH_2Cl_2 .

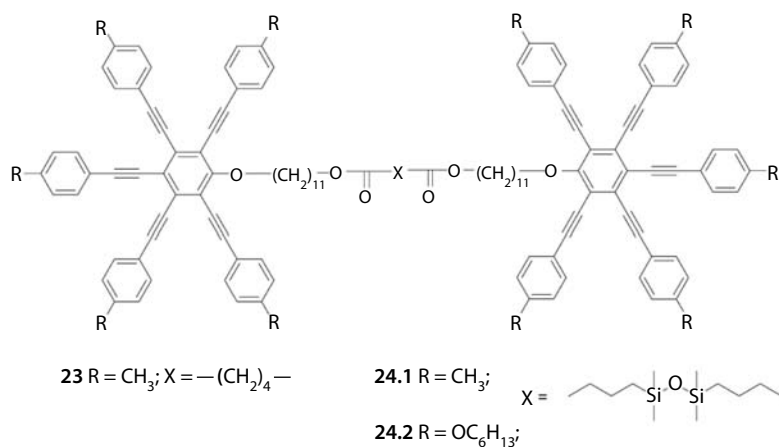
prepared from alcohol precursor via an esterification reaction with an appropriate diacid.

The thermal behaviour of all the pentyne dimers is presented in Table 7.5. All the dimers displayed a discotic nematic phase. As can be seen from the table, ether dyads with shorter spacers **19.1** and **19.2** showed very narrow or unstable mesophase. The mesophase range was comparatively broader for dimers **19.3–19.5** with longer spacers. The clearing temperatures of dimers show a significantly odd-even effect. For a steady spacer length (**19.5–19.7**), the length of a peripheral chain had a huge effect on crystalline-to-nematic point, clearing temperature, as well as the mesophase range. However, none of these dimers exhibited N_b phase.

Ester and amide linkages in the spacer led to increase in melting as well as clearing temperatures. Dimer **22.1** has the highest melting and clearing points may be due to the hydrogen bonding of amide linkage. The insertion of siloxane unit in the spacer led to decrease in the mesophase

Table 7.5 Thermal behaviour ($^{\circ}\text{C}$) of pentyne dimers.

Str	R	n	Mesophase behaviour	Ref.
19.1	C_5H_{11}	8	Cr 127 N_D 127.8 I	[12]
19.2	C_5H_{11}	9	Cr (112.5 N_D) 131 I	[12]
19.3	C_5H_{11}	10	Cr 129.1 N_D 153.5 I	[12]
19.4	C_5H_{11}	11	Cr 118.2 N_D 140.8 I	[12]
19.5	C_5H_{11}	12	Cr 121.4 N_D 156.2 I	[11]
19.6	C_6H_{13}	12	Cr 92 N_D 107 I	[14]
19.7	C_7H_{15}	12	Cr 76 N_D 85 I	[15]
22.1			Cr 202 N_D 230 I	[16]
22.2			Cr 159 N_D 180 I	[16]
22.3			Cr 167 N_D 197 I	[16]
22.4			Cr 166 N_D 196 I	[16]
22.5			Cr 158 N_D 172 I	[16]
23			Cr 169 N_D 209 I	[17]
24.1			Cr 142 I	[17]
24.2			Cr 38 N_D 55 I	[17]



Scheme 7.7 Multiyne-based dimers having ester or siloxane groups in the spacer.

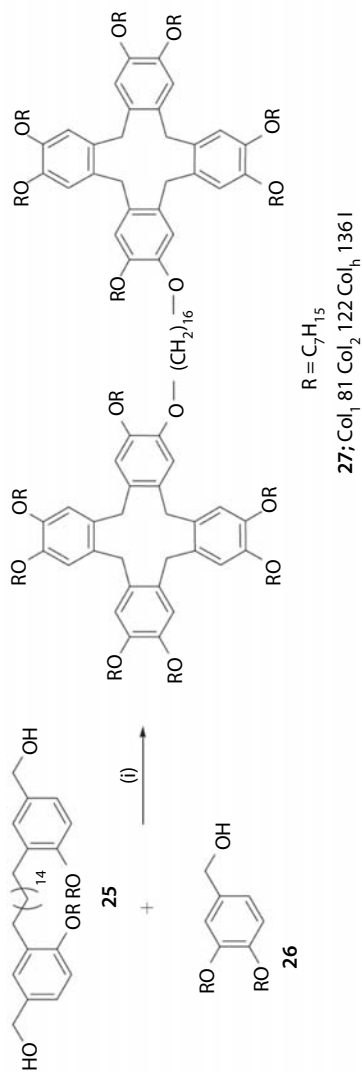
temperatures. Compound **24.1** (Scheme 7.7) with peripheral methyl group was not liquid crystalline, however, when this group was substituted with hexyloxy group as in compound **24.2**, then a low temperature nematic phase formed.

7.2.3 Discotic Dimers Based on Cyclotetrameratrylene Core

Percec and co-workers [20] have reported the synthesis of a cyclotetrameratrylene dimer **27** in which two cyclotetrameratrylene rings were joined through a hexadecane spacer. The condensation of alcohol **26** and dimeric alcohol **25** in the presence of a strong acid gave dimer and other branched oligomers of cyclotetrameratrylene mesogens (Scheme 7.8). The dimer exhibited liquid crystalline behaviour at room temperature. It showed three types of columnar mesophases. The high temperature mesophase was Col_h, while the nature of other two mesophases is unknown. The clearing temperature of this dimer is lower than the monomer.

7.2.4 Discotic Dimers Based on Dibenzo[a,c]phenazine Core

Discotic dimers based on dibenzo[a,c]phenazine core have been explored by Tzeng *et al.* [19] The intermediate **28** was prepared from the reaction of monoalkylated catechol with the appropriate dibromoalkane. A two step nitration of **28** gave the tetranitrated product which was then reduced to tetra-amine **29**. The target dimeric molecules were prepared by the condensation of tetra-amine **29** with 1,2-diketone derivatives **30** or **31**. The

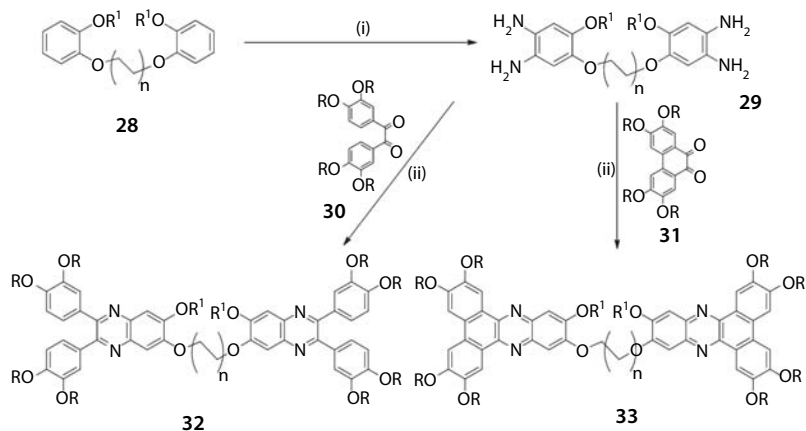


Scheme 7.8 Synthesis of cyclotetrameratrylene based discotic dimer: (i) CF_3COOH .

bisquinoxaline derivatives **32** were found to be non-mesogenic. The non-planarity of the unfused rings in derivatives **32** might preclude the mesophase formation. A rich polymorphism from Col_h to Col_r was observed for dimeric compounds **33.1–33.6**, irrespective of the peripheral chain length. On cooling, all of them form glasses to room temperature, which can last for a few hours to months. From the XRD studies, it was found that these mesogens adopt the folded conformation (mostly anti-parallel) in the liquid crystalline state. This has enabled liquid crystal formation for shorter spacers as well. Interestingly, these dimers also form organogels, indicating great ability to form a 3D network.

Ong and co-workers [20] designed a series of dimers **33.7–33.9** having a bulky isopropoxy group at the α -position to the linker. These compounds were prepared according to Scheme 7.9. Spacer length was made constant in these dimers. With increase in the peripheral chain length, mesophase changed from Col_h to D_L . The lamellar structure can be explained by the steric effect attributable to the isopropoxy group in proximity to the linker of the dimer, which prohibits intra-molecular and intercalated intermolecular packing. All the mesophases were readily frozen into a glassy state at room temperature (Table 7.6).

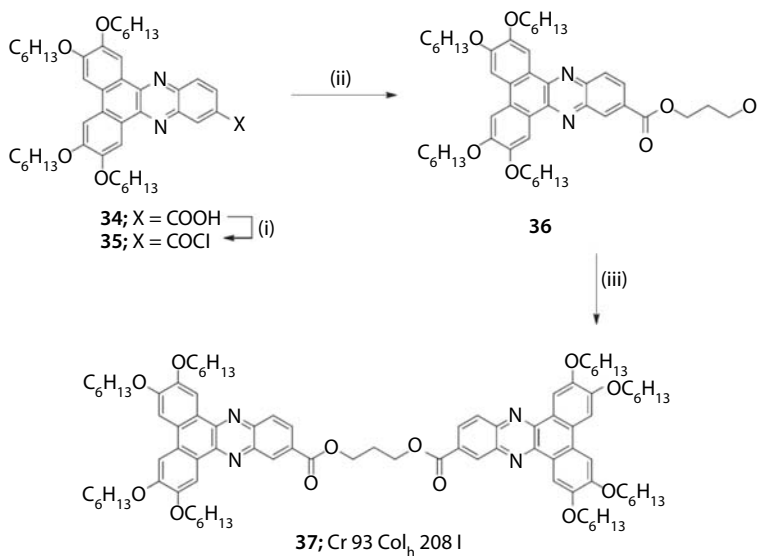
Bozek and Williams [21] prepared a dibenzophenazine based dimer **37** starting from carboxylic acid **34**, which was converted to corresponding acid chloride **35** on treatment with oxalyl chloride followed by addition of excess propane-1,3-diol to afford the monoester **36**. This monoester was then on treatment with acid chloride **35** gave dimer **37** (Scheme 7.10). This



Scheme 7.9 Synthesis of Dibenzo[a,c]phenazine dimers: (i) (a) HNO₃ and (b) H₂, Pd/C; (ii) 1 drop CH₃COOH, CH₂Cl₂, R.T.

Table 7.6 Thermal behaviour ($^{\circ}\text{C}$) of Dibenzo[a,c]phenazine dimers.

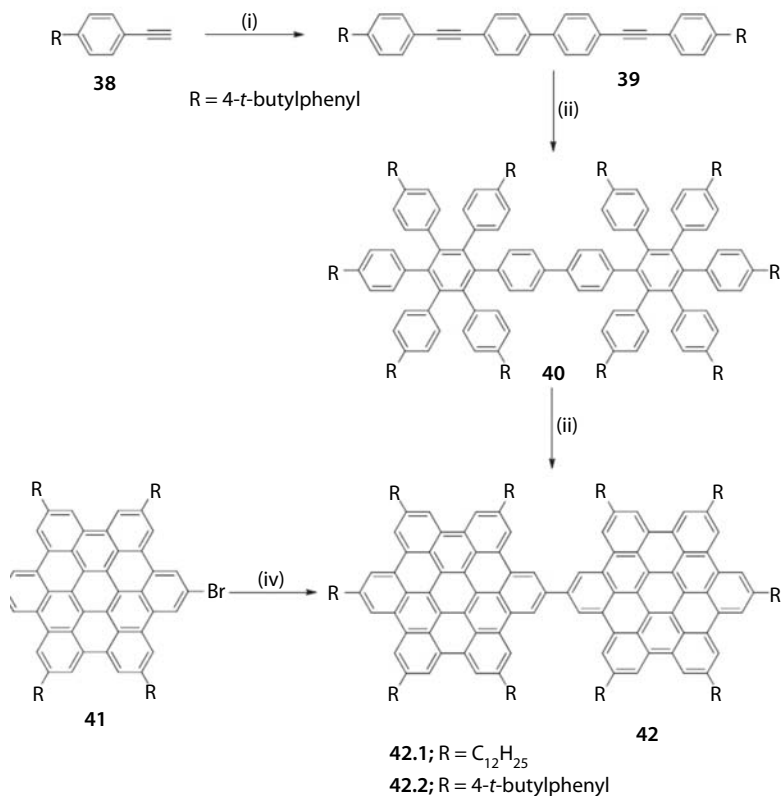
Str	R	R'	<i>n</i>	Mesophase behaviour	Ref.
32.1	C ₆ H ₁₃	C ₆ H ₁₃	3	Cr ₁ 15.5 Cr ₂ 74.2 I	[19]
32.2	C ₁₂ H ₂₅	C ₁₂ H ₂₅	3	Cr ₁ 26.7 Cr ₂ 82.0 I	[19]
33.1	C ₆ H ₁₃	C ₆ H ₁₃	3	Col _{ro} 53.7 Col _{ho1} 127.4 Col _{ho2} 158.2 I	[19]
33.2	C ₆ H ₁₃	C ₆ H ₁₃	5	Col _{ro} 52.5 Col _{ho} 180.5 I	[19]
33.3	C ₆ H ₁₃	C ₆ H ₁₃	6	Col _{ro} 47.5 Col _{ho} 173.5 I	[19]
33.4	C ₈ H ₁₇	C ₈ H ₁₇	3	Col _{ro} 54.6 Col _{ho} 134.2 I	[19]
33.5	C ₁₀ H ₂₁	C ₁₀ H ₂₁	3	G 49.1 Col _{ho} 87.0 I	[19]
33.6	C ₁₂ H ₂₅	C ₁₂ H ₂₅	3	I 75.8 Col _{ho} 20.8 G	[19]
33.7	C ₆ H ₁₃	CH(CH ₃) ₂	3	Col _{hg} 39.6 Col _h 181.2 I	[20]
33.8	C ₁₀ H ₂₁	CH(CH ₃) ₂	3	D _{Lg} 17.7 D _L 97.7 I	[20]
33.9	C ₁₂ H ₂₅	CH(CH ₃) ₂	3	D _{Lg} 38.6 D _L 101.0 X 105.0 I	[20]

**Scheme 7.10** Synthesis of dibenzophenazine dimer **37**: (i) (COCl)₂, DMF, DCM, RT, 3 h; (ii) 1,3-propanediol, pyridine, DCM, RT, 20 h; (iii) **35**, pyridine, DCM, RT, 20 h.

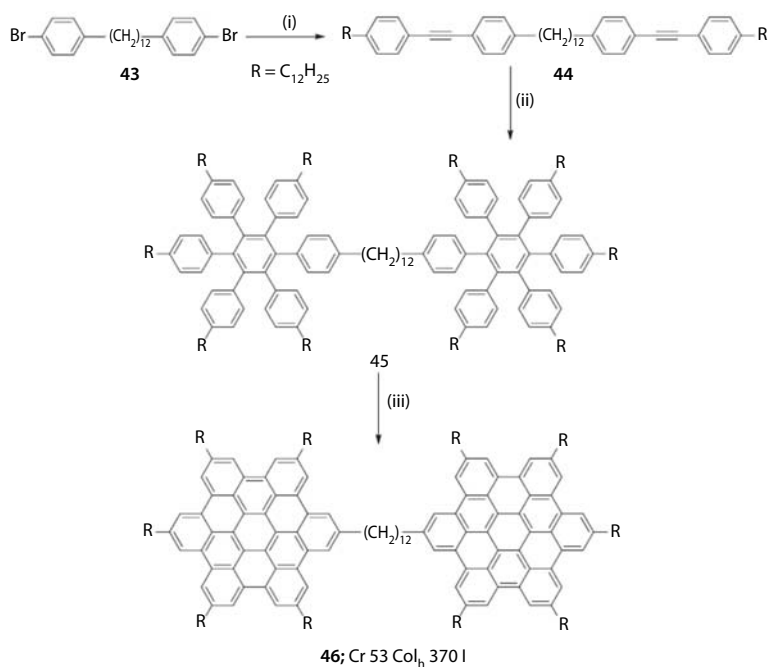
dimer possesses a broad mesophase, which supercools into a highly persistent glass. This compound also folds in the columnar phase and not in the solution.

7.2.5 Discotic Dimers Based on Hexa-*peri*-Hexabenzocoronene (HBC) Core

Mullen and co-workers [22] reported two varieties of symmetrical hexa-*peri*-hexabenzocoronene dimers **42** and **46** (Schemes 7.11 and 7.12). In the bis(hexa-*peri*-hexabenzocoronene) dimer **42**, the two rings were directly connected to each other, while in the dihexa-*peri*-hexabenzocoronenyldodecane **46**, long dodecyl chain was used to connect the two



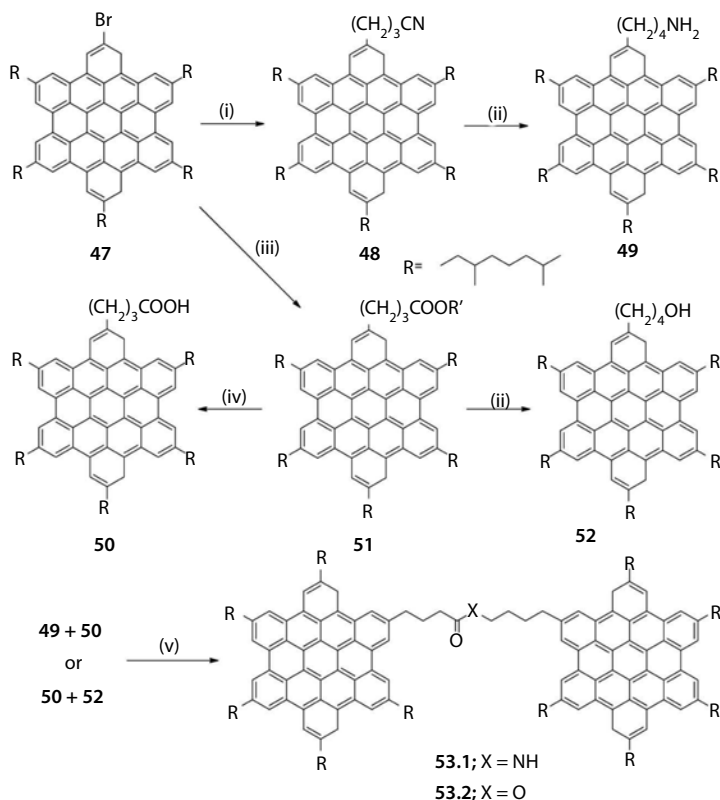
Scheme 7.11 Synthesis of bis(hexa-*peri*-hexabenzocoronene) dimer: (i) 4,4'-dibromo-biphenyl, $[\text{Pd}(\text{PPh}_3)_4]$, CuI, piperidine, 80°C ; (ii) tetra(4-*tert*-butylphenyl) cyclopentadiene, diphenyl ether, reflux; (iii) FeCl_3 , CH_2Cl_2 ; (iv) $[\text{Ni}(\text{COD})_2]$, 2,2'-bipyridyl, toluene, 60°C .



Scheme 7.12 Synthesis of dihexa-*peri*-hexabenzocoronenyldodecane dimer: (i) 4-*n*-dodecyloxyphenylacetylene, [Pd(PPh₃)₄], CuI, piperidine, 80°C; (ii) tetra(4-*tert*-butylphenyl)cyclopentadienone, diphenyl ether, reflux; (iii) FeCl₃, CH₂Cl₂.

rings. Two routes have been used to prepare bishexa-*peri*-hexabenzocoronene dimers **42** (Scheme 7.11). Nickel-catalysed reductive coupling of the bromo-substituted HBC **41** in the presence of 2,2'-bipyridyl and 1,5-cyclooctadiene (COD) afforded bis(hexa-*peri*-hexabenzocoronene) dimers. Alternatively, dimer **42** can be prepared from the oligophenylene precursor **39** via oxidative cyclodehydrogenation. The dihexa-*peri*-hexabenzocoronenyldodecane dimer **46** was obtained by making the use of cycloaddition and cyclodehydrogenation reactions. Compound **42.1** showed a solid to mesophase transition at 124°C on heating, but on further heating no clearing transition was noticed up to decomposition. The liquid crystalline nature was confirmed by X-ray diffraction. For compound **42.2**, authors didn't provide any information on mesophase behaviour. Compound **46** melted at 53°C to ordered hexagonal mesophase and went to isotropic phase at 370°C.

In order to understand the effect of hydrogen bonding on the supramolecular order of HBC dimers, Mullen and co-workers [23] prepared two dimers **53** connected through flexible spacer containing amide and ester



Scheme 7.13 Synthesis of HBC dimers: (i) $\text{BrZn}(\text{CH}_2)_3\text{CN}$, Pd catalyst; (ii) LiAlH_4 , THF; (iii) $\text{BrZn}(\text{CH}_2)_3\text{COOR}$, Pd catalyst; (iv) KOH , $\text{MeOH-H}_2\text{O}$; (v) EDC , CH_2Cl_2 .

groups. These dimers were prepared according to Scheme 7.13. Dimer **53.1** remained in the pseudo-crystalline phase over the temperature range of -100°C to 300°C . Compound **53.2** was found to be room temperature liquid crystalline exhibiting Col_{ho} phase. It didn't go to isotropic phase on heating up to 300°C . Solid state NMR indicated a very unstable pseudo-crystalline phase below 14°C . The formation of disordered 3D network due to the flexibility of the ester linkage was assumed to be the reason for the absence of any long-range pseudocrystalline phase for this dimer below 14°C . However, in case of dimer **53.1**, additional hydrogen bonding of amide linkage lead to the formation of very stable pseudocrystalline phase, and consequently the system failed to reach any mesophase before decomposition on heating.

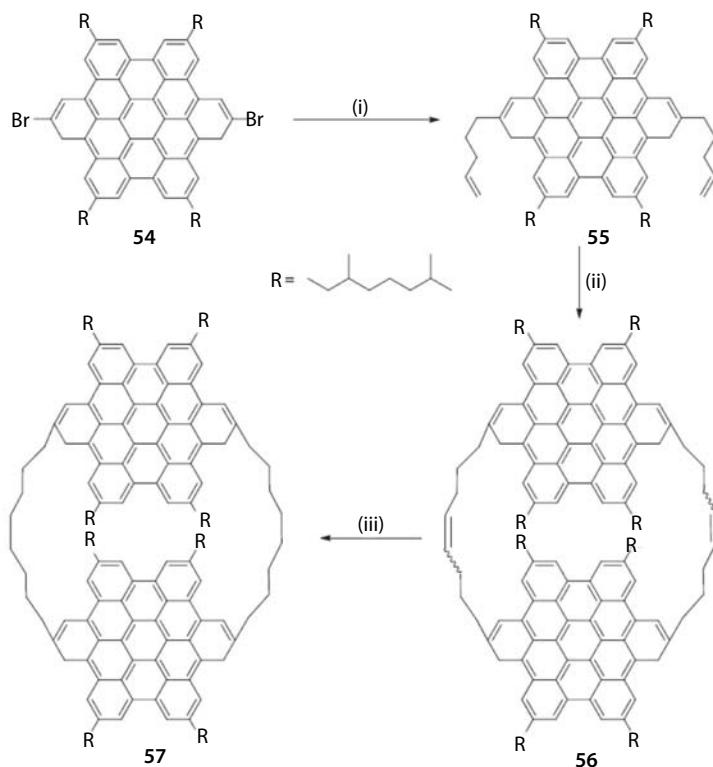
Watson *et al.* [24] prepared two cyclophane-like dimers **56** and **57** of HBC, in which two HBC rings were joined by an intramolecular ring-closing metathesis reaction of the diene derivative to yield an isomeric (cis

and trans) mixture of dimer **56**. The Pd catalysed hydrogenation of dimer **56** yielded dimer **57** (Scheme 7.14). Both the dimers were found to assemble in the 2D hexagonal columnar arrangement. Cyclophane **56** showed a reversible endothermic first order transition at 40°C on heating, while dimer **57** showed only a very weak second-order transition, most likely a glass transition at -10°C. The mesomorphism of both the dimers persisted up to 400°C on heating. Conversion of the double bond to the saturated single bond resulted in inhibition of bulk crystallisation tendency of HBC cores.

7.2.6 Discotic Dimers Based on Phthalocyanine Core

7.2.6.1 Phthalocyanine Double Deckers

Phthalocyanine double deckers, i.e. bis(2,3,9,10,16,17,23,24-octasubstituted-phthalocyaninato) metal complexes are the compounds in which a rare earth metal is sandwiched between two phthalocyanine moieties. The



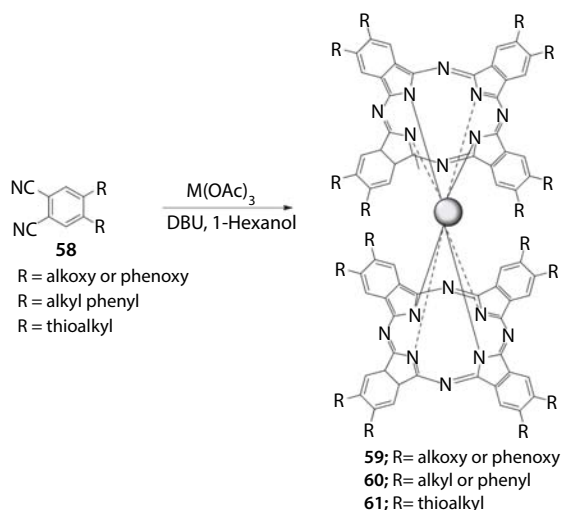
Scheme 7.14 Synthesis of cyclophane-like HBC dimer: (i) 4-phenylmagnesiumbromide, Pd catalyst, THF, 55°C; (ii) Ru_n , toluene; (iii) Pd/C, THF, H_2 .

two rings in these metal complexes are face-to-face linked, but they are at an angle of 45° with respect to each other. The valence state of this compound also shows a quite interesting feature. Out of the two rings, one ring is dianionic, while the other one is radical. As a consequence, one ring with radical is more distorted than the other ring. However, on heating, the free electron can delocalise on both the rings to make both rings structurally equivalent. As a result, charge carrier mobility increases generally on heating. These systems have gained much interest nowadays due to their very high charge carrier mobilities. Phthalocyanine double deckers have also been employed as resistive and voltammetric sensors.

First phthalocyanine double decker compound was reported by Piechocki *et al.* [25] Since then a number of compounds based on phthalocyanine have been prepared and studied for liquid crystalline behaviour.

Based on peripheral substitutions, these compounds can be divided into three categories: (i) compounds with peripheral alkoxy or phenoxy substituents **59.1–59.52**, (ii) compounds with peripheral thioalkoxy substituents **60.1–60.5** and (iii) compounds with peripheral alkyl or phenyl substituents **61.1–61.27**. All these phthalocyanine double deckers can be prepared according to Scheme 7.14.

Piechoki *et al.* [25] in 1985 reported the first phthalocyanine double decker compound with Lu (III) metal. Later on several complexes with metals like Eu, Tb, Lu, Ce, Gd, Sm, Dy, etc. have been synthesised and investigated for mesomorphic properties. The metal complexes with Lu (III) metal are still the most widely synthesised and studied complexes (Scheme 7.15).



Scheme 7.15 Synthesis of phthalocyanine double-decker compounds.

Table 7.7 summarises the mesomorphic behaviour of phthalocyanine complexes substituted with alkoxy or phenoxy groups. The lowest homologue of bis(octaalkoxyphthalocyaninato)lutetium(III) **59.5** was found to be non-liquid crystalline [25]. However, the oxidised form of this complex exhibits mesomorphism. All the other derivatives of this series **59.9**, **59.20**, **59.22**, **59.25** and **59.27** were found to have two kinds of mesophases, Col_r in the lower temperature range and Col_h in the higher temperature range. Crystal-to-mesophase temperature was found to increase with the length of the alkoxy chain, while the mesophase-to-isotropic temperature was found to decrease with increase in chain length. Longer chain derivatives **59.20**, **59.22**, **59.25** and **59.27** exhibited crystal-to-crystal transition also. Because of the high viscosity of the mesophase of compounds **59.22**, **59.25** and **59.27**, a rare superheated transition from a crystalline phase to a discotic phase was also observed.

Binnemans *et al.* [26] synthesised bis(octaalkoxyphthalocyaninato)erbium(III) complexes **59.1–59.4**, **59.7**, **59.8**, **59.10**, **59.21**, **59.23**, **59.24** and **59.26** with alkyl chain ranging from C4 to C18. These compounds exhibit a viscous mesophase over a broad temperature range. The melting and clearing points decrease with increase in the chain length. In order to see the effect of various other metal atoms, they also synthesised complexes containing same alkyl chain but different metals (**59.10–59.20**). It was found that variation of central metal atom has not much effect on the transition temperatures. As we go from lighter metal complex **59.11** to heavier metal complex **59.19** and **59.20**, a decrease in the mesomorphic range was observed. This might be due to the fact that here the metals are sandwiched between the two phthalocyanine rings, limiting as such possible additional interactions with neighbouring molecules. So, in these molecules the mesophase behaviour is governed only by the phthalocyanine rings.

Four poly(oxyethylene) substituted lutetium(III) double decker complexes **59.28–59.31** have been prepared by Toupance *et al.* [27] All these compounds were found to be soluble in a number of solvents including water. The stability domain of the mesophase for these complexes was found to be dependent on the chain length. For compounds **59.28** and **59.29**, only a single transition corresponding to crystal-to-isotropic was found and compound **59.31** was liquid at room temperature. Compound **59.30** displayed columnar tetragonal phase with a lattice constant of 26.7 Å.

Ohta and co-workers [28, 29] studied the mesomorphic behaviour of bis[2,3,9,10,16,17,23,24-octakis(3,4-dialkoxyphenoxy)-phthalocyaninato]

Table 7.7 Thermal behaviour (°C) of bis(2,3,9,10,16,17,23,24-octaalkoxyphthalocyaninato)lanthanum(III) complexes.

Str	R	M	Mesophase behaviour	Ref.
59.1	OC ₄ H ₉	Er	Cr 202 Col _h > 280 Dec	[26]
59.2	OC ₅ H ₁₁	Er	Cr 174 Col _h > 280 Dec	[26]
59.3	OC ₆ H ₁₃	Er	Cr 147 Col _h > 280 Dec	[26]
59.4	OC ₈ H ₁₇	Er	Cr 137 Col _h 263 I	[26]
59.5	OC ₈ H ₁₇	Lu	Cr 25 I	[25]
59.6	OC ₈ H ₁₇	Gd	Cr ₁ 15 Cr ₂ 61 Col _r 93 Col _h 141 I	[32]
59.7	OC ₉ H ₁₉	Er	Cr 93 Col _h 239 I	[26]
59.8	OC ₁₀ H ₂₁	Er	Cr 71 Col _h 180 I Cr 63 Col _{ho} 180 I	[26] [33]
59.9	OC ₁₀ H ₂₁	Lu	Cr 43 Col _{ro} 96 Col _h 215 I	[34]
59.10	OC ₁₂ H ₂₅	Er	Cr 68 Col _h 174 I Cr 54 Col _{ho} 174 I	[26] [33]
59.11	OC ₁₂ H ₂₅	Pr	Cr 74 Col _h 208 I	[26]
59.12	OC ₁₂ H ₂₅	Nd	Cr 66 Col _h 206 I Cr 57 Col _{ho} 167 I	[26] [33]
59.13	OC ₁₂ H ₂₅	Eu	Cr 65 Col _h 203 I Cr 60 Col _{ho} 173 I	[26] [33]
59.14	OC ₁₂ H ₂₅	Gd	Cr 68 Col _h 218 I	[26]
59.15	OC ₁₂ H ₂₅	Tb	Cr 72 Col _h 205 I	[26]
59.16	OC ₁₂ H ₂₅	Dy	Cr 83 Col _h 205 I	[26]
59.17	OC ₁₂ H ₂₅	Ho	Cr 85 Col _h 190 I	[26]
59.18	OC ₁₂ H ₂₅	Tm	Cr 68 Col _h 182 I	[26]
59.19	OC ₁₂ H ₂₅	Yb	Cr 84 Col _h 192 I	[26]

(Continued)

Table 7.7 (Cont.)

Str	R	M	Mesophase behaviour	Ref.
59.20	$\text{OC}_{12}\text{H}_{25}$	Lu	Cr 92 Col_h 188 I Cr 24 M 30 I Cr_1 18 Cr_2 61 Col_{ro} 90 Col_{ho} 196 I Cr 85 Col_{ho} 185 I Cr_1 41 Cr_2 85 Col_h 189 I	[26] [25] [34] [33] [35]
59.21	$\text{OC}_{14}\text{H}_{29}$	Er	Cr 58 Col_h 180 I	[26]
59.22	$\text{OC}_{14}\text{H}_{29}$	Lu	Cr_1 32 Cr_2 51 Col_{ro} 72 Col_{ho} 171 I	[34]
59.23	$\text{OC}_{15}\text{H}_{31}$	Er	Cr 44 Col_h 170 I	[26]
59.24	$\text{OC}_{16}\text{H}_{33}$	Er	Cr 43 Col_h 163 I	[26]
59.25	$\text{OC}_{16}\text{H}_{33}$	Lu	Cr_1 33 Cr_2 51 Col_{ro} 61 Col_{ho} 149 I	[34]
59.26	$\text{OC}_{18}\text{H}_{37}$	Er	Cr 65 Col_h 151 I Cr 61 Col_{ho} 154 I	[26] [33]
59.27	$\text{OC}_{18}\text{H}_{37}$	Lu	Cr 51 M 56 I Cr_1 41 Cr_2 54 Col_{ro} 64 Col_{ho} 131 I	[25] [34]
59.28	$\text{OCH}_2\text{CH}_2\text{OCH}_3$	Lu	Cr 246 I	[27]
59.29	$\text{O}(\text{CH}_2\text{CH}_2\text{O})_2\text{CH}_3$	Lu	Cr 138 I	[27]
59.30	$\text{O}(\text{CH}_2\text{CH}_2\text{O})_3\text{CH}_3$	Lu	Cr 53 Col_t 57.6 I	[27]
59.31	$\text{O}(\text{CH}_2\text{CH}_2\text{O})_4\text{CH}_3$	Lu	Liquid	[27]
59.32	$\text{OC}_6\text{H}_3[m,p-(\text{OC}_8\text{H}_{17})_2]$	Tb	Col_h 147 Col_r 262 I	[31]
59.33	$\text{OC}_6\text{H}_3[m,p-(\text{OC}_8\text{H}_{17})_2]$	Lu	Col_r 174 I	[29]
59.34	$\text{OC}_6\text{H}_3[m,p-(\text{OC}_8\text{H}_{17})_2]$	Eu	Col_{r1} 145 Col_{r2} 210 Col_{r3} 256 I	[30]
59.35	$\text{OC}_6\text{H}_3[m,p-(\text{OC}_9\text{H}_{19})_2]$	Tb	Col_h 149 Col_r 187 Cub 248 I	[31]
59.36	$\text{OC}_6\text{H}_3[m,p-(\text{OC}_9\text{H}_{19})_2]$	Lu	Col_r 152 Col_{tet} 168 I	[29]
59.37	$\text{OC}_6\text{H}_3[m,p-(\text{OC}_{10}\text{H}_{21})_2]$	Tb	Col_h 142 Cub 178 Cub 252 I	[31]

(Continued)

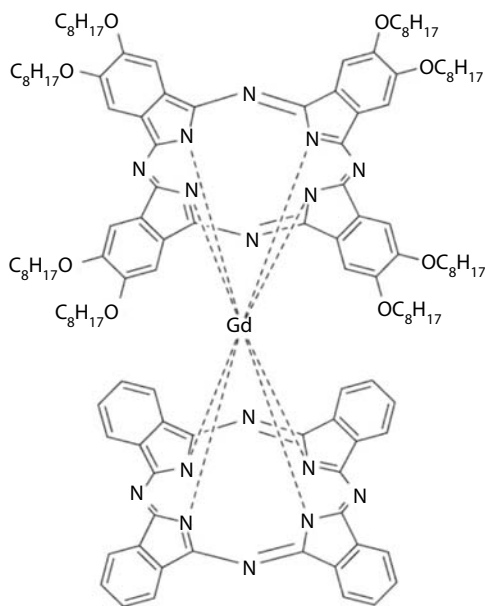
Table 7.7 (Cont.)

Str	R	M	Mesophase behaviour	Ref.
59.38	$\text{OC}_6\text{H}_3[m,p-(\text{OC}_{10}\text{H}_{21})_2]$	Eu	Col_h 144 Cub 178 Cub 247 I	[30]
59.39	$\text{OC}_6\text{H}_3[m,p-(\text{OC}_{11}\text{H}_{23})_2]$	Tb	Col_h 142 Cub 165 Cub 244 I	[31]
59.40	$\text{OC}_6\text{H}_3[m,p-(\text{OC}_{11}\text{H}_{23})_2]$	Lu	Col_r 72 Col_r 111 Col_{tet} 168 I	[29]
59.41	$\text{OC}_6\text{H}_3[m,p-(\text{OC}_{12}\text{H}_{25})_2]$	Lu	Cr 35 Col_h 139 Cub ₁ 164 Cub ₂ 216 Col_t 239 I	[28]
59.42	$\text{OC}_6\text{H}_3[m,p-(\text{OC}_{12}\text{H}_{25})_2]$	Tb	Col_h 142 Cub 165 Cub 245 I	[31]
59.43	$\text{OC}_6\text{H}_3[m,p-(\text{OC}_{12}\text{H}_{25})_2]$	Eu	Col_h 146 Cub 177 Cub 247 I	[30]
59.44	$\text{OC}_6\text{H}_3[m,p-(\text{OC}_{13}\text{H}_{27})_2]$	Lu	Cr 31 Col_h 122 Cub ₁ 143 Cub ₂ 166 Col_t 222 I	[28]
59.45	$\text{OC}_6\text{H}_3[m,p-(\text{OC}_{13}\text{H}_{27})_2]$	Tb	Cr 36 Col_h 140 Cub 169 Cub 232 I	[31]
59.46	$\text{OC}_6\text{H}_3[m,p-(\text{OC}_{14}\text{H}_{29})_2]$	Tb	Cr 38 Col_h 137 Cub 167 Cub 232 I	[31]
59.47	$\text{OC}_6\text{H}_3[m,p-(\text{OC}_{14}\text{H}_{29})_2]$	Lu	Cr 34 Col_{tet} 141 I	[29]
59.48	$\text{OC}_6\text{H}_3[m,p-(\text{OC}_{14}\text{H}_{29})_2]$	Eu	Cr 37 Col_h 136 Cub 165 Cub 228 I	[30]
59.49	$\text{OC}_6\text{H}_3[m,p-(\text{OC}_{15}\text{H}_{31})_2]$	Tb	Cr 46 Col_h 134 Cub 161 Cub 222 I	[30]
59.50	$\text{OC}_6\text{H}_3[m,p-(\text{OC}_{16}\text{H}_{33})_2]$	Tb	Cr 47 Col_h 133 Cub 165 Cub 217 I	[31]
59.51	$\text{OC}_6\text{H}_3[m,p-(\text{OC}_{16}\text{H}_{33})_2]$	Lu	Cr 52 Col_r 77 Col_{tet} 153 I	[29]
59.52	$\text{OC}_6\text{H}_3[m,p-(\text{OC}_{16}\text{H}_{33})_2]$	Eu	Cr 49 Col_h 133 Cub 158 Cub 216 I	[30]

lutetium(III) complexes **59.33**, **59.36**, **59.40**, **59.41**, **59.44**, **59.47** and **59.51**. These complexes exhibited three kinds of mesophases namely; Col_h , Cub and Col_{tet} . This is the first instance where a phthalocyanine derivative exhibited two Cub phases. In Col_{tet} phase, a monodomain spontaneous homeotropic alignment has been achieved. The low temperature Col_h phase gave a stacking distance of 10.1 Å. This large distance can be linked to steric hindrance of the eight peripheral phenoxy groups.

Similar phenoxy complexes with Eu(III) [30] **59.34**, **59.38**, **59.43**, **59.48** and **59.52** and Tb (III) [31] metals **59.32**, **59.35**, **59.37**, **59.39**, **59.42**, **59.45**, **59.46**, **59.49** and **59.50** have also been synthesised. Except for the lowest homologues with $n = 8$ and $n = 9$, all derivatives showed two Cub phases. Cub phase in the lower temperature range was found to have Pn3m symmetry and forms a bicontinuous structure with branched columns. The Cub phase in the higher temperature range had Pm3n symmetry and forms a discontinuous structure with short columns.

Two kinds of gadolinium containing octakis(octyloxy)phthalocyanine sandwich complexes **59.6** and **62** have been prepared by Zhang *et al.* [32] In complex **59.6**, gadolinium metal was sandwiched between two phthalocyanine rings and the other double decker complex **62** was between substituted and unsubstituted phthalocyanine rings. This compound exhibited rather simple phase transition as compared to the symmetrical complex. The clearing point and phase transition temperatures depend on the molecular structure of the sandwiched compounds.



62; Cr 72 Col_n 125 I

Table 7.7 also summarises the thermal behaviour of alkoxy complexes of various other rare earth metals, Pr (**59.11**), Nd (**59.12**), Eu (**59.13**), Tb (**59.15**), Dy (**59.16**), Ho (**59.17**), Tm (**59.18**) and Yb (**59.19**).

The thermal behaviour of octaalkyl and alkoxyphenyl substituted phthalocyanines lutetium complexes **60.1–60.5** is summarised in Table 7.8.

Table 7.8 Thermal behaviour (°C) of alkyl/phenyl substituted phthalocyanine lutetium(III) complexes.

Str	R	M	Mesophase behaviour	Ref.
60.1	C ₈ H ₁₇	Lu	Cr 79 Col _{hd} 82 I	[36]
60.2	C ₁₂ H ₂₅	Lu	Col _{ob} 32 I	[36]
60.3	C ₁₈ H ₃₇	Lu	Col _L 30 I	[36]
60.4	C ₆ H ₄ (<i>p</i> -OC ₁₈ H ₃₇)	Lu	Col _t 46.9 Col _{hd} 242 I	[37]
60.5	CH ₂ OC ₁₈ H ₃₇	Lu	Cr 51 Col _h 56 I	[37]

These derivatives displayed a variety of mesophases. The mesophase range of peripherally alkyl substituted complexes is very narrow. But for alkoxy-phenyl substituents, mesophase range is broader as compared to alkyl substituted ones. Compound **60.2** was the first phthalocyanine complex, in which a disordered oblique columnar phase was observed at room temperature. However, the mesophase range is too small and **60.2** went to isotropic phase at 32°C. But unusually this phase relaxes to columnar phase on leaving as such. Further heating lead to isotropisation at 44°C. Similar behaviour has also been observed for compound **60.3**. Compound **60.5** showed tetragonal columnar phase at room temperature. On heating, the stacking of molecules in the column becomes loose due to vigorous thermal mobility of alkyl chain. This resulted in transformation of lattice to hexagonal phase.

Table 7.9 presents the thermal data of thioalkyl substituted phthalocyanine double deckers of various rare earth metals, Eu (**61.5**, **61.9**, **61.13**, **61.17**, **61.21**), Tb (**61.6**, **61.10**, **61.14**, **61.18**, **61.22**, **61.25**), Lu (**61.1**, **61.7**, **61.11**, **61.15**, **61.19**, **61.23**, **61.26**), Ce (**61.8**, **61.12**, **61.16**, **61.20**, **61.24**, **61.27**), Gd (**61.2**), Dy (**61.3**) and Sm (**61.4**). Within the lanthanide series, the isotropisation temperature decreases as the chain length increases. As compared to alkoxy compounds, thioalkyl compounds exhibited lower clearing temperatures. For decylthio (**61.9–61.12**), dodecylthio (**61.13–61.16**) and tetradecylthio (**61.19**, **61.20**) substituted derivatives, an additional mesophase was also observed. It has been found that the lower temperature phase of compound **61.13** possess properties of both hexagonal and rectangular mesophases. The core-to-core distance was found to be 3.3 Å. On the basis of this distance and ratio of peaks, this phase has been assigned as pseudo-hexagonal. In this phase, the non-tilted disks were arranged in a hexagonal pattern, but overall have a rectangular arrangement. In x-ray diffraction, for smaller chain derivatives in

Table 7.9 Thermal behaviour (°C) of bis(2,3,9,10,16,17,23,24-octathioalkyl-phthalocyaninato)lanthanum(III) complexes.

Str	R	M	Mesophase behaviour	Ref.
61.1	SC ₆ H ₁₃	Lu	Cr 120 Col _h 242 I	[38]
61.2	SC ₆ H ₁₃	Gd	Cr 52 Col _h 258 I	[39]
61.3	SC ₆ H ₁₃	Dy	Cr 55 Col _h 250 I	[39]
61.4	SC ₆ H ₁₃	Sm	Cr 60 Col _h 240 I	[39]
61.5	SC ₈ H ₁₇	Eu	Cr 98 Col _h 252 I	[40]
61.6	SC ₈ H ₁₇	Tb	Cr 102 Col _h 242 I	[40]
61.7	SC ₈ H ₁₇	Lu	Cr ₁ 45 Cr ₂ 84 Col _h 219 I	[40]
61.8	SC ₈ H ₁₇	Ce	Cr 95 Col _{hd} 257 I	[41]
61.9	SC ₁₀ H ₂₁	Eu	Cr -1 Col 68 Col _h 209 I	[40]
61.10	SC ₁₀ H ₂₁	Tb	Cr 3 Col 56 Col _h 205 I	[40]
61.11	SC ₁₀ H ₂₁	Lu	Cr 6 Col 40 Col _h 192 I	[40]
61.12	SC ₁₀ H ₂₁	Ce	Cr 4 Col _{ho} 56 Col _{hd} 217 I	[41]
61.13	SC ₁₂ H ₂₅	Eu	Cr 22 Col 64 Col _h 181 I	[40]
61.14	SC ₁₂ H ₂₅	Tb	Cr 20 Col 53 Col _h 172 I	[40]
61.15	SC ₁₂ H ₂₅	Lu	Cr 27 Col 38 Col _h 167 I	[40]
61.16	SC ₁₂ H ₂₅	Ce	Cr -3 Col _{ho} 47 Col _{hd} 180 I	[41]
61.17	SC ₁₄ H ₂₉	Eu	Cr 13 Col _h 152 I	[40]
61.18	SC ₁₄ H ₂₉	Tb	Cr 22 Col 47 Col _h 144 I	[40]
61.19	SC ₁₄ H ₂₉	Lu	Cr 38 Col _h 145 I	[40]
61.20	SC ₁₄ H ₂₉	Ce	Cr 31 Col _{ho} 47 Col _{hd} 156 I	[41]
61.21	SC ₁₆ H ₃₃	Eu	Cr 50 Col _h 134 I	[40]
61.22	SC ₁₆ H ₃₃	Tb	Cr 46 Col _h 132 I	[40]
61.23	SC ₁₆ H ₃₃	Lu	Cr 46 Col _h 126 I	[40]
61.24	SC ₁₆ H ₃₃	Ce	Cr 49 Col _{hd} 139 I	[41]
61.25	SC ₁₈ H ₃₇	Tb	Cr 33 Col _h 116 I	[40]
61.26	SC ₁₈ H ₃₇	Lu	Cr ₁ 32 Cr ₂ 53 Col _h 110 I	[40]
61.27	SC ₁₈ H ₃₇	Ce	Cr 53 Col _{hd} 119 I	[40]

lower temperature range, two kinds of stacking distance of 7 and 3.5 Å has been observed corresponding to double-decker and single-decker phthalocyanines, respectively. Because of distortion in planarity caused by the radical nature, one of the phthalocyanine rings acquires a dome shape. At higher temperature, faster trampoline movement of the dome gives time-averaged, single-decker packing distance.

As compared to other lanthanide metal double-decker complexes, cerium based complexes **61.8**, **61.12**, **61.16**, **61.20**, **61.24** and **61.27** show different behaviour. Here both the rings are dianionic, hence cerium is in tetravalent oxidation state. The extent of distortion from planarity is the same for both phthalocyanine rings. As a consequence, cerium based sandwiched complexes show wider mesophase than other rare earth metal complexes. These compounds show a strong tendency towards homeotropic arrangement of their Col_h phase on a glass substrate, which persist at room temperature. Long chain homologues are in glassy state at room temperature, whereas shorter chain ones are liquid crystals.

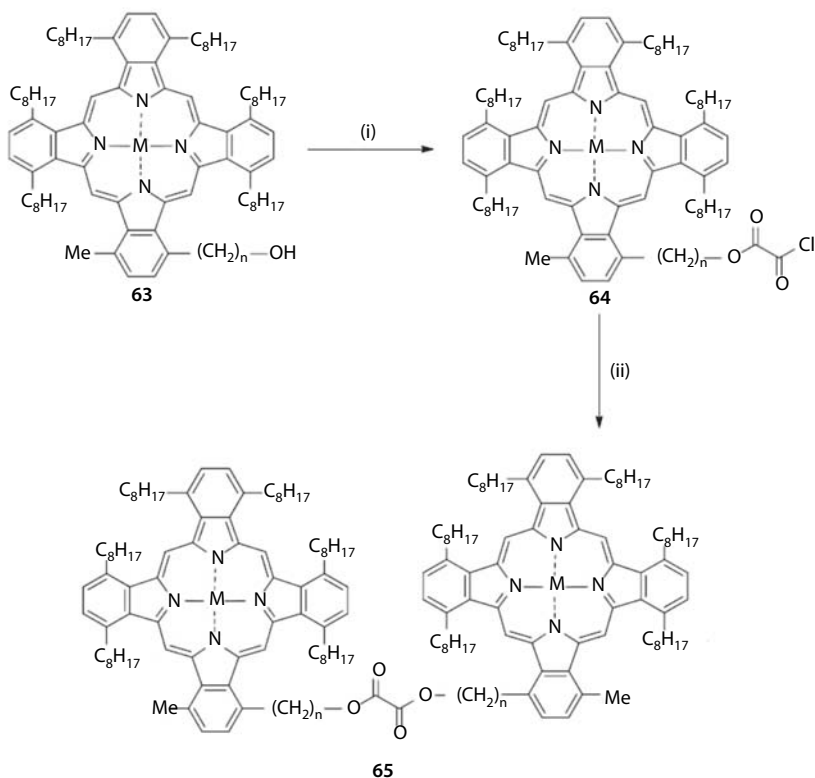
7.2.6.2 Phthalocyanine Complexes Connected through Flexible Spacers

Bryant *et al.* [43, 44] reported a number of dinuclear phthalocyanine complexes **65**, in which two phthalocyanine moieties were joined through a flexible spacer. The esterification of monohydroxyalkyl phthalocyanines **63** with excess of oxalyl chloride yields a phthalocyanine derivative **64** with a terminal carbonyl chloride group. This was followed by esterification with one equivalent of **63** to give the desired dimer **65** (Scheme 7.16). As can be seen from the Table 7.10, dimer with the smallest linking spacer **65.1** was not liquid crystalline. Higher homologues (**65.2–65.4**) exhibited two kinds of mesophases, i.e. Col_r and Col_h . On increasing the spacer length, a decrease in the Col_r to Col_h transition temperature can be observed. Compound **65.5** with longest spacer length exhibited only a single mesophase. Only a single compound **65.6** with Cu metal has been reported with chain length of C5. Compound **65.6** when compared to **65.3** compound was found to have higher melting temperature, clearing temperature as well as mesophase range.

7.2.7 Discotic Dimers Based on Porphyrin Core

7.2.7.1 Porphyrin Double Deckers

Ohta and co-workers [45] investigated mesomorphism in porphyrin double deckers linked through Ce metal **67.1–67.7**. These materials were synthesised by reacting metal free porphyrins **66** with cerium acetate as shown

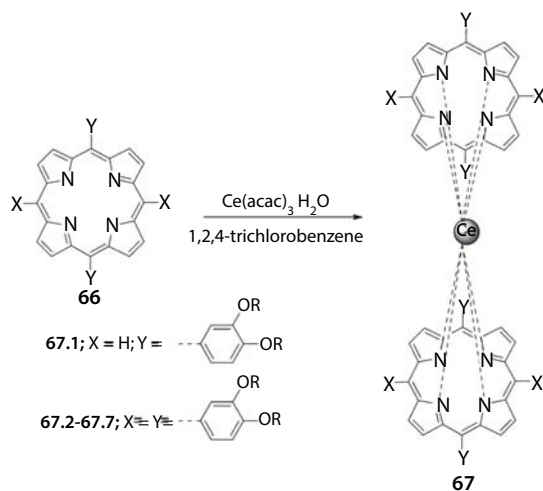


Scheme 7.16 Synthesis of dinuclear phthalocyanine complexes: (i) ClCOCOCl , DCM , K_2CO_3 ; (ii) 1,2-dichloroethane, K_2CO_3 .

Table 7.10 Thermal behaviour ($^{\circ}\text{C}$) of dinuclear phthalocyanine complexes.

Str	<i>n</i>	M	Mesophase behaviour	Ref.
65.1	3	2H	Cr 160 I	[43, 44]
65.2	4	2H	Col_r 144 Col_h 163 I	[43, 44]
65.3	5	2H	Col_r 135 Col_h 180 I	[43, 44]
65.4	6	2H	Col_r 123 Col_h 188 I	[43, 44]
65.5	8	2H	Col 175 I	[43, 44]
65.6	5	Cu	Col_r 161 Col_h 254 I	[43, 44]

in Scheme 7.17. The mesophase behaviour of these compounds is summarised in Table 7.11. It is clear from the table that number of alkyl chains in the dimers plays a significant role in exhibiting liquid crystalline behaviour. Compound **67.1** with eight alkoxy substitutions showed columnar lamellar phase, while compounds **67.2**, **67.3**, **67.6** and **67.7** with sixteen alkyl chains exhibited Col_r phase. Compound **67.1** was in crystalline state at room temperature and had the highest value of isotropic temperature among all other compounds of the series. Because of the high viscosity of the isotropic phase of **67.2**, **67.3**, **67.6** and **67.7**, it was not possible to



Scheme 7.17 Synthesis of porphyrin double deckers.

Table 7.11 Thermal behaviour ($^{\circ}\text{C}$) of porphyrin double deckers.

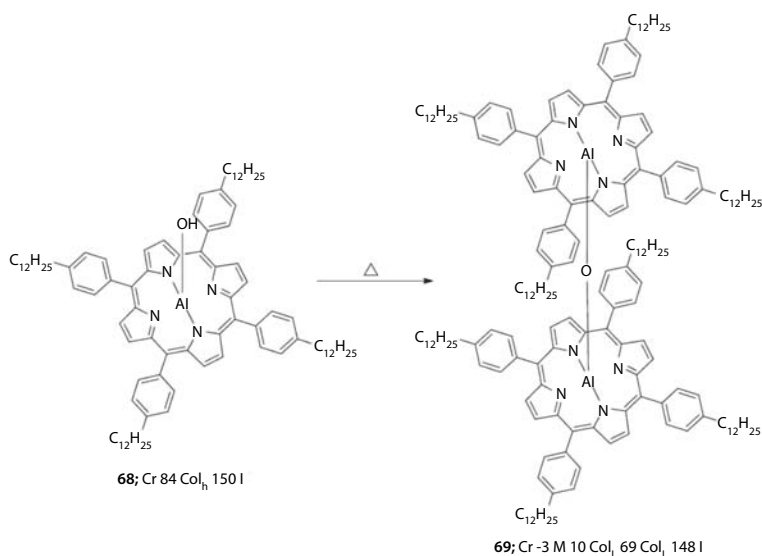
Str	R	Mesophase behaviour	Ref.
67.1	$\text{C}_{14}\text{H}_{29}$	Cr 93.3 Col_L 105.8 I	[45]
67.2	C_8H_{17}	Col_r 71 I	[45]
67.3	$\text{C}_{10}\text{H}_{21}$	Col_r 70.3 I	[45]
67.4	$\text{C}_{12}\text{H}_{25}$	Liquid	[45]
67.5	$\text{C}_{14}\text{H}_{29}$	Liquid	[45]
67.6	$\text{C}_{16}\text{H}_{33}$	Col_r 43.5 I	[45]
67.7	$\text{C}_{18}\text{H}_{37}$	Col_r 51.3 I	[45]

get back the Col_r phase while cooling. These compounds remained in the supercooled isotropic liquid state. The stacking distances corresponding to double decker (8.6 Å) and single decker (3.7 Å) were observed in x-ray for the lamellar phase of compound **67.1**.

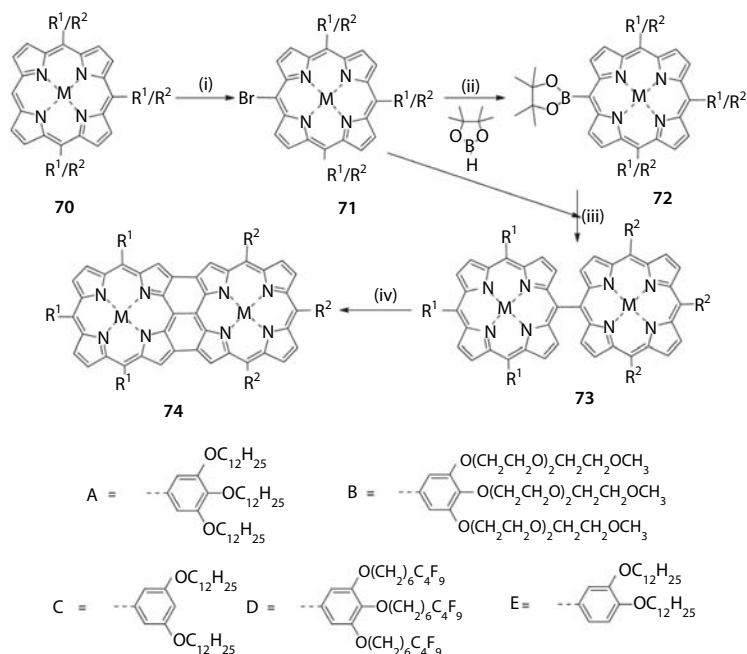
Shimizu *et al.* [46] reported the synthesis and mesomorphism of μ -oxo-dimer **69** formed by heating the hydroxoaluminium(III) complex of tetraphenylporphyrin **68** above its isotropic temperature (Scheme 7.18). This conversion has been proved by the absence of OH peaks in IR and NMR techniques. Monomeric compound **68** was crystalline at room temperature and exhibited a Col_h phase on heating to 84°C. On further heating, this compound changed to isotropic phase at 150°C. Dimeric compound **69** was liquid crystalline at room temperature. It exhibited two Col_L phases before going to isotropic state at 148°C.

7.2.7.2 Triply Fused Metalloporphyrin Dimers

Aida and co-workers [47] reported triply fused metalloporphyrin dimers **74** as the electroactive core by attaching to it differently substituted aromatic rings. These dimers were prepared according to Scheme 7.19. Bromo-substituted porphyrin **71** was reacted with 4,4,5,5-tetramethyl-1,3,2-dioxaborolane substituted derivative in the presence of $\text{Pd}(\text{PPh}_3)_4$ and Cs_2CO_3 to give singly fused product **73**, which was reacted with DDQ to give triply



Scheme 7.18 Synthesis of porphyrin μ -oxo-dimer.



Scheme 7.19 Synthesis of triply-fused metalloporphyrin dimers: (i) N-bromosuccinimide, pyridine, CHCl_3 ; (ii) $\text{PdCl}_2(\text{dppf})_2$, Et_3N , $\text{ClCH}_2\text{CH}_2\text{Cl}$; (iii) $\text{Pd}(\text{PPh}_3)_4$, Cs_2CO_3 , DMF ; (iv) DDQ , $\text{Sc}(\text{OTf})_3$, toluene.

fused product **74**. Zn substituted derivatives were prepared in this way. Zn substituted derivatives were then treated with HCl and then $\text{Cu}(\text{OAc})_2$ to give Cu metal substituted porphyrin dimers. The mesomorphic behaviour of these dimers is summarised in Table 7.12. As can be seen from the table, Cu complexes with dodecyloxy chains and triethylene glycol chains were non-mesomorphic. But compound **74.3** formed by a combination of these two chains showed Col phase. It was hypothesised by the authors that the amphiphilic molecular design of compound **74.3** leads to enhance π -stacking interactions due to a nanoscale phase separation between the hydrophobic and hydrophilic side chains. This compound was found to behave as n-type semiconductors in contrast to other porphyrin derivatives which mostly show hole transporting property. In order to see whether the electron transporting nature of this material is intrinsic to the core unit of the LC molecule or its particular design, they prepared two compounds **74.4** and **74.5** based on semi-fluorinated alkyl chains. These two compounds were found to show LC behaviour. Compound with mixed alkyl chains showed columnar rectangular phase, while columnar phase

Table 7.12 Thermal behaviour (°C) of triply-fused metalloporphyrin dimers.

Str	R ¹	R ²	M	Mesophase behaviour	Ref.
74.1	A	A	Cu	Non-mesomorphic	[47]
74.2	B	B	Cu	Non-mesomorphic	[45]
74.3	A	B	Cu	Cr -17 Col 99 I	[45]
74.4	A	D	Cu	G -22 Col _r 143 I	[45]
74.5	D	D	Cu	G -29 Col _{ortho} 188 I	[45]
74.6	A	A	Zn	Non-mesomorphic	[45]
74.7	C	C	Zn	Non-mesomorphic	[45]
74.8	E	E	Zn	G 15 Col _{r1} 128 Col _{r2} 200 I	[45]

with orthorhombic lattice was found for compound with semi-fluorinated chains only. So side chains employed hardly change the π -electronic properties, but only due to the change in the stacking geometry of the core, semiconducting properties changed. Number and position of the alkyl chains also affect the mesomorphic behaviour as is demonstrated by three types of porphyrin complexes of Zn metal.

7.2.8 Discotic Dimers Based on Pyranose Sugars

Cellobiose, a readymade dimer, can form liquid crystals if substituted with appropriate substituents. It is a disaccharide derived from the condensation of two glucose molecules. Though the molecule does not possess a disk shape, its derivatives have been reported as discotic liquid crystals. Vill and Thiem [48] prepared the perlauroyl cellobioside **75.1**, which gives a columnar mesophase. The acylation of dodecyl- β -D-cellobioside with an excess of acylating agent gave a mixture of hepta- (**75.2**) and hexa-(*p*-dodecyloxy)benzoate **76** that was separated by chromatography. Both the compounds (**75.2**, **76**) were found to show columnar phases similar to laurate **75.1**. A series of cellobiose octaalkanoates **77** were prepared by Watanabe and co-workers [49, 50]. The short chain compound **77.1** with $n = 6$ forms a rectangular columnar phase, while its homologue **77.2** with $n = 7$ exhibits a Col_h phase at higher temperature and Col_r phase at lower temperature (Table 7.13). Homologues **77.3–77.6** with $n = 8–13$ display

only Col_h phase. Similarly, esters derived from chitobiose **78** also exhibit an enantiotropic mesophase at temperatures ranging from 50°C to 200°C [49]. As expected, the amido groups in the chitobiose-derivatives stabilised the mesophase significantly. The exact nature of the columnar phase has not been revealed.

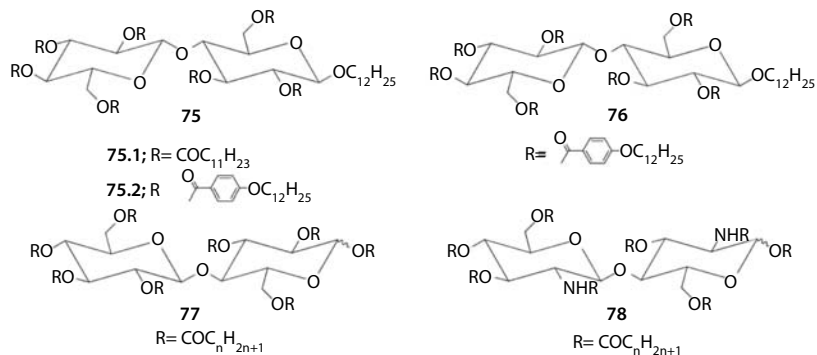


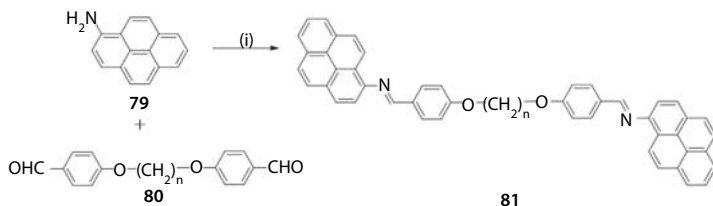
Table 7.13 Thermal behaviour ($^\circ\text{C}$) of discotic dimers based on pyranose sugars.

Str	n	Mesophase behaviour	Ref.
75.1		Cr 74 $\text{Col}_{92.7}$ I	[48]
75.2		Col_{120} I	[48]
76		Col_{145} I	[48]
77.1	6	Cr 4 Col_r 91 I	[50]
77.2	7	Cr 25 Col_r 62 Col_h 87 I	[50]
77.3	8	Cr 37 Col_h 86 I	[50]
77.4	9	Cr 43 Col_h 83 I Cr 66 Col_h 90 I	[50] [49]
77.5	11	Cr 49 Col_h 81 I	[50]
77.6	13	Cr 56 Col_h 73 I	[50]
78.1	9	Cr 65 Col_{207} I	[51]
78.2	13	Cr 70 Col_{196} I	[51]
78.3	17	Cr 73 Col_{185} I	[51]

7.2.9 Discotic Dimers Based on Pyrene Core

7.2.9.1 Pyrene Based Symmetrical Dimer

A homologues series of symmetric discotic liquid crystals **81.1–81.10** based on pyrene core has been synthesised by Attard and Imrie [52]. The α,ω -bis-(4-formylphenyl-4'-oxy)alkanes **80** were obtained by refluxing the appropriate α,ω -dibromoalkane, 4-hydroxybenzaldehyde, K_2CO_3 in ethanol. Symmetric pyrenimine benzyldiene dimers **81** were obtained by reacting each of the α,ω -bis-(4-formylphenyl-4'-oxy)alkanes **80** with 1-aminopyrene **79** in ethanol and 4-toluenesulfonic acid in catalytic amount (Scheme 7.20). The thermal transitions of the homologues series are listed in Table 7.14. With the exception of propyl and pentyl, all other



Scheme 7.20 Synthesis of pyrene based symmetrical dimer: (i) 4-toluenesulfonic acid, ethanol.

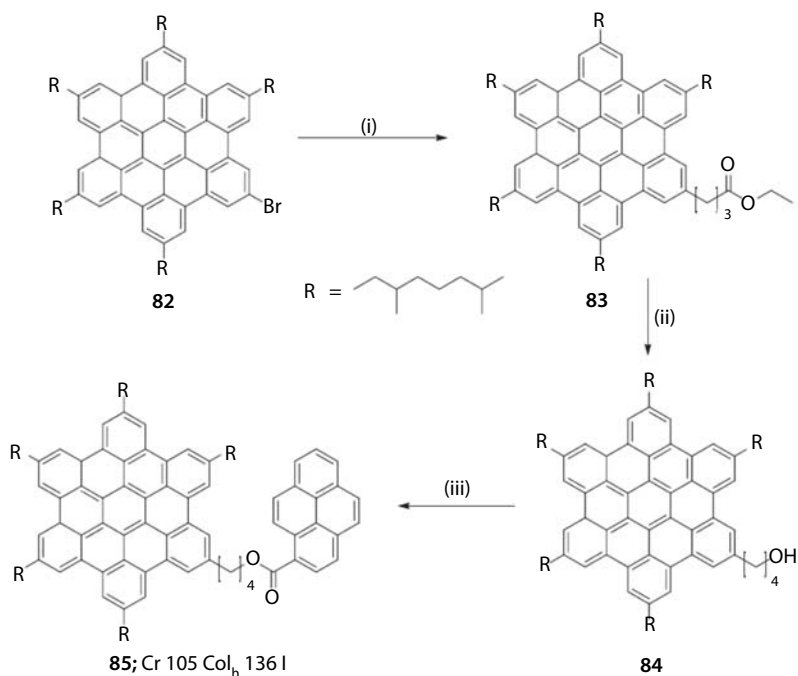
Table 7.14 Thermal behaviour ($^{\circ}C$) of dimers based on pyrene core.

Str	<i>n</i>	Mesophase behaviour	Ref.
81.1	3	G 70 Cr 190 I	[52]
81.2	4	G 66 Cr 187.9 N 213 I	[52]
81.3	5	G 64 Cr 155 I	[52]
81.4	6	G 66 Cr 95.4 SmA 171.7 N 204 I	[52]
81.5	7	G 51 Cr 110.7 N 194 I	[52]
81.6	8	G 54 Cr 101.1 SmA 157 N 184 I	[52]
81.7	9	G 44 Cr 107 I	[52]
81.8	10	G 44 Cr 76 SmA 147.2 N 167 I	[52]
81.9	11	G 41 Cr 120.8 N 130 I	[52]
81.10	12	G 35 Cr 132.9 N 152 I	[52]

dimers exhibited N phase. Compounds **81.4**, **81.6** and **81.8** with $n = 6, 8, 10$ also exhibited monotropic Sm phases. The clearing temperatures of the even homologues in the series initially fall rapidly as a function of increasing n . By contrast, the homologues with odd-membered alkyl chains show a rapid increase in the N-to-I transition temperature. All the members of the series also formed glassy phases above room temperature.

7.2.9.2 Pyrene Based Non-symmetrical Dimer

A discotic dimer **82** in which alkylated hexa-peri-hexabenzocoronene was covalently tethered to a pyrene unit has been prepared by Tchebotareva *et al.* [53] The synthesis of HBC-pyrene dyad **85** is outlined in Scheme 7.21. Negishi type coupling of 2-bromo-5,8,11,14,17-penta(3,7-dimethyloctanyl)hexa-peri-hexabenzocoronene **82** with commercially available 3-ethoxycarbonylpropyl-1-zincbromide provided ester-functionalised HBC **83**, which was reduced to the alcohol **84** with LiAlH_4 . Finally, N-(3-dimethylaminopropyl)-N-ethylcarbodiimide hydrochloride (EDC) promoted esterification of **84** with pyrene-1-carboxylic acid yielded the



Scheme 7.21 Synthesis of pyrene based symmetrical dimer: (i) $\text{BrZn}(\text{CH}_2)_3\text{COOEt}$, $\text{Cl}_2\text{Pd}[\text{dppf}] \cdot \text{CH}_2\text{Cl}_2$, THF; (ii) LAH, THF; (iii) pyrene-1-COOH, EDC, DMAP, CH_2Cl_2 .

desired target **85**. In DSC, this dimer exhibited two transitions, one corresponding to Cr-Col_h and the other for Col_h-I. The polycrystalline to mesophase transition increased by about 23°C relative to alkyl substituted HBC. The thermal behaviour suggests that the pyrene units are involved in the formation of the polycrystalline state, i.e. are not spectators randomly distributed within the liquid-like alkyl chain sheaths of the columns. This postulation was in very good accordance with the nanoscale phase segregation monitored in monolayers by STM.

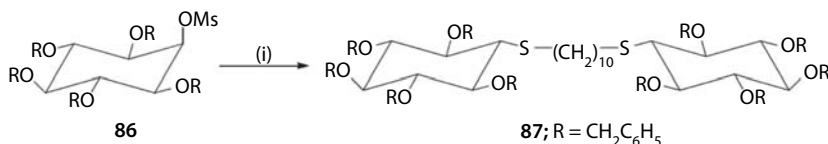
7.2.10 Discotic Dimers Based on Scylloinositol Dimer

Scylloinositol is a cyclohexanehexol stereoisomer and has the ability to form liquid crystals with appropriate peripheral substituents. As such the core is not disk-like, but some of its derivatives have been classified as DLCs. A dimer **87** *S,S'*-decamethylene-bis(penta-*O*-benzyl-monothioscylitol) was prepared from a reaction between 2-*O*-mesyl-1,3,4,5,6-penta-*O*-benzyl-myo-inositol **86** and disodium salt of decandithiol in the presence of *N,N'*-dimethylethylenurea (DMEU) at 100°C (Scheme 7.22). It was reported to exhibit a monotropic mesomorphism between 121°C and 149°C [54].

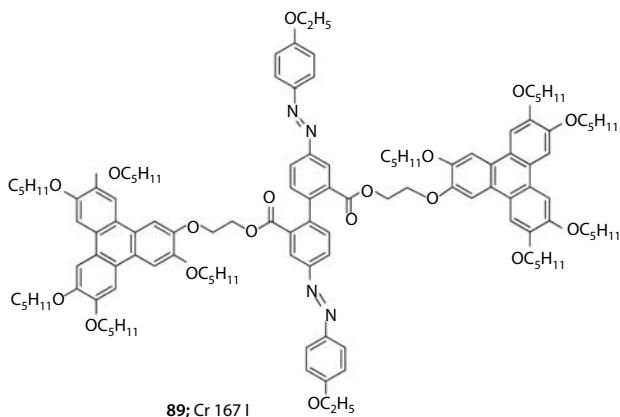
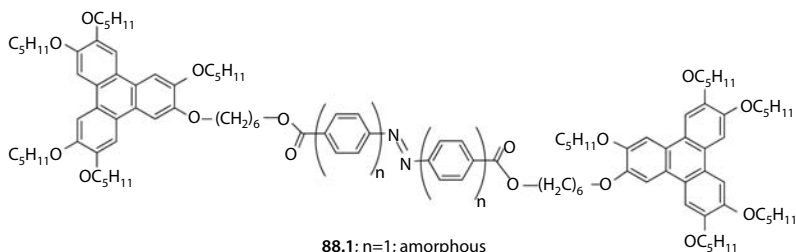
7.2.11 Discotic Dimers Based on Triphenylene Core

7.2.11.1 Triphenylene Based Symmetrical Dimers

The very first example of triphenylene-based dimers has been reported by Ringsdorf and co-workers [55]. They prepared three triphenylene dimers **88** and **89** linked through end on as well as lateral calamitic moieties. Compound **88.1** with $n = 1$ having azobenzene moiety as the linker between two triphenylene units was found to be amorphous, while compound **88.2** with $n = 2$ having azobiphenyl linker was mesogenic. The mesophase was found to be SmB phase. X-ray studies on this compound indicate a layer structure typical for smectic phase, but in which the molecular disks are regularly stacked as observed for Col mesophase. Compound **89**, a



Scheme 7.22 Synthesis of scylloinositol dimer: (i) NaS(CH₂)₁₀SNa, DMEU, 100°C.



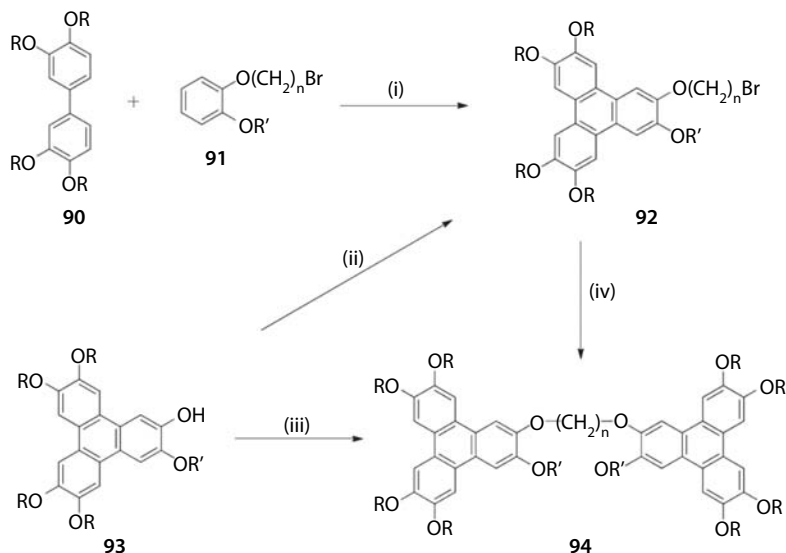
chemical equivalent of the “Wheel of Mainz”, was found to be spherulithic crystal clearing at 167°C.

Boden *et al.* [56] synthesised a series of triphenylene based symmetrical dimers **94** connected through flexible polymethylene chain. These symmetrical dimers have been synthesised in various ways. Starting from monohydroxypentaalkoxytriphenylene **93**, dimer **94** can be synthesised either in a single step by reacting with 0.5 equiv. of dibromoalkane, or in two steps, by reacting first with excess of dibromoalkane and then the resulting ω -bromosubstituted triphenylene **92** is reacted with monohydroxypentaalkoxytriphenylene **93** to give desired dimer. Second pathway is also useful in getting non-symmetrical triphenylenes. The mesomorphic behaviour of the symmetrical triphenylenes is summarised in Table 7.15. Dimers **94.4–94.6** with shorter linkers are not mesomorphic. Modelling studies suggested that only for those dimers for which $n > 7$ can form Col_h phase. Mesophase in all these dimers can be supercooled to relatively hard glassy state, in which columnar order is retained. The stability of this glassy state depends on the spacer length and on the symmetry of the molecules. Boden and co-workers also reported another symmetrical

Table 7.15 Thermal behaviour (°C) of triphenylene based symmetrical dimers connected through flexible polymethylene chain.

Str	R	R'	<i>n</i>	Mesophase behaviour	Ref.
94.1	C ₄ H ₉	C ₄ H ₉	2	Cr ₁ 62 Cr ₂ 150 I	[63]
94.2	C ₄ H ₉	C ₄ H ₉	3	Cr 154 I	[63]
94.3	C ₄ H ₉	C ₄ H ₉	4	Cr 113 I	[63]
94.4	C ₄ H ₉	C ₄ H ₉	5	Cr 80 Col _{tp} 120 I	[63]
94.5	C ₄ H ₉	C ₄ H ₉	6	Col _{hp} 81.8 Col _h 123.3 I	[63]
94.6	C ₄ H ₉	C ₄ H ₉	7	Col _{hp} 116.6 Col _h 130.7 I	[63]
94.7	C ₄ H ₉	C ₄ H ₉	8	Col _{hp} 151.3 I	[56]
94.8	C ₄ H ₉	C ₄ H ₉	9	Col _{hp} 154.2 I	[56]
94.9	C ₄ H ₉	C ₄ H ₉	10	Col _{hp} 144.8 Col _h 146.7 I	[58]
94.10	C ₄ H ₉	C ₄ H ₉	11	Col _{hp} 130.6 Col _h 140.8 I	[58]
94.11	C ₄ H ₉	C ₄ H ₉	12	Col _{hp} 103.3 Col _h 125.8 I	[58]
94.12	C ₅ H ₁₁	C ₅ H ₁₁	10	Cr 67 Col _h 135.6 I	[59]
94.13	C ₆ H ₁₃	C ₆ H ₁₃	3	Cr 81 I	[59]
94.14	C ₆ H ₁₃	C ₆ H ₁₃	5	Cr 98 I	[59]
94.15	C ₆ H ₁₃	C ₆ H ₁₃	7	Cr 69 I	[59]
94.16	C ₆ H ₁₃	C ₆ H ₁₃	8	Cr 58 Col _h (35 g) 91 I	[59]
94.17	C ₆ H ₁₃	C ₆ H ₁₃	9	Cr 72 Col _h (35 g) 92 I	[59]
94.18	C ₆ H ₁₃	C ₆ H ₁₃	10	Cr 50 Col _h (35 g) 104 I	[59]
94.19	C ₆ H ₁₃	C ₆ H ₁₃	12	Cr 68 Col _h (35 g) 107 I	[59]
94.20	C ₆ H ₁₃	C ₆ H ₁₃	16	Cr 41 Col _h (35 g) 84 I	[59]
94.21	C ₆ H ₁₃	CH ₃	10	Cr (98 Col _h 33 g) 84 I	[57]

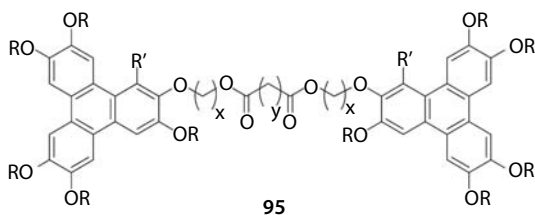
dimer **94.12** having eight long alkoxy chains and two methoxy substituents. The required monomer can be easily prepared via phenyl-biphenyl coupling as shown in Scheme 7.23. On heating, this compound showed a crystal-to-isotropic transition at 112°C, but on cooling exhibited Col_h phase at 98°C [56–62].



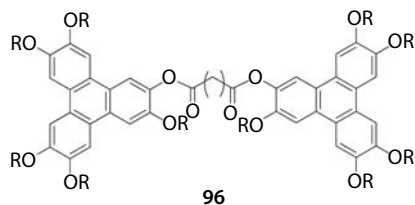
Scheme 7.23 Synthesis of triphenylene based symmetrical dimers connected through flexible polymethylene chain: (i) FeCl_3 , DCM; (ii) $\text{Br}(\text{CH}_2)_n\text{Br}$ (excess), K_2CO_3 ; (iii) $\text{Br}(\text{CH}_2)_n\text{Br}$ (0.5 equiv.), K_2CO_3 ; (iv) K_2CO_3 .

Molecular architecture and functionalisation are two important aspects in the molecular engineering of liquid crystalline materials. Some physical parameters such as supramolecular order of mesophase, stability of mesophase, processability and electronic properties of liquid crystalline materials need to be controlled for an efficient engineering of devices. Functionalisation of discotic systems can give materials with apt physical properties for device applications. Keeping this idea, Kumar and co-workers [64] prepared three triphenylene based dimers functionalised with NO_2 group (**95.1–95.3**). These were prepared from the precursor mononitro-mono-hydroxy-pentaalkoxytriphenylene which was alkylated with ω -hydroxybromoalkane. The resulting alcohol was coupled with various diacid chlorides to obtain the dimers. All the compounds were found to possess Col_h phase. As the spacer length increase, clearing temperature decreases. A similar dimer **95.4** but without NO_2 group has also been reported by Manikam *et al.* [65]. This compound was non-mesomorphic may be because of very short spacer length (Table 7.16).

Four symmetrical triphenylene dimers **96** in which two pentaalkoxytriphenylene units are connected via an ester linkage were reported by Kranig *et al.* [66] All the compounds were found to be liquid crystalline at room

Table 7.16 Thermal behaviour (°C) of functionalised triphenylene dimers.

Str	x	y	R	R'	Mesophase behaviour	Ref.
95.1	2	0	C ₄ H ₉	NO ₂	Cr (169.1 Col) 198.8 I	[64]
95.2	2	2	C ₄ H ₉	NO ₂	Col _h 163.0 I	[64]
95.3	2	4	C ₄ H ₉	NO ₂	Col _h 144.9 I	[64]
95.4	7	1	C ₅ H ₁₁	H	Cr 33.5 I	[65]

Table 7.17 Thermal behaviour (°C) of ester linked triphenylene dimers.

Str	y	R	Mesophase behaviour	Ref.
96.1	10	C ₅ H ₁₁	Col _h 180 I	[66]
96.2	12	C ₅ H ₁₁	Col _h 168 I	[66]
96.3	14	C ₅ H ₁₁	Col _h 147 I	[66]
96.4	14	C ₇ H ₁₄	Col _h 147 I	[66]

temperature. These dimers exhibit a much broader mesophase range compared with the dimers linked via ether bridges (Table 7.17).

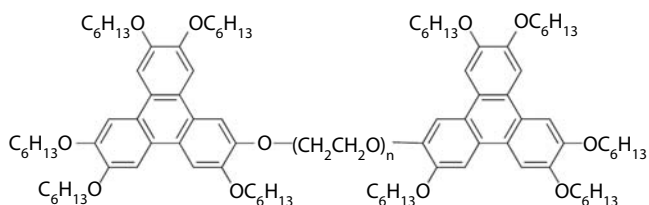
Mesomorphic dimeric molecules **97.1–97.5** consisting of discotic triphenylene rigid units and flexible ethylene oxide spacers have been prepared by Kato and co-workers [67]. The introduction of ethylene oxide chains into the triphenylene molecules lowers the melting and isotropisation

temperature of the molecules. Liquid crystallinity of these compounds is greatly dependent on the ethylene oxide spacers. The Lithium salt complexes of compound **97.2** (with $n = 4$) showed Col_h phase at lower concentration, while at higher concentrations mesophase was not found. These molecules can function as anisotropic materials for transport of ions and holes (Table 7.18).

During the preparation of main chain triphenylene polymers, Boden and co-workers [68] isolated a low-molar mass compound that was identified as a cyclic dimer having structure **98** or **99**. The similarity of the ^1H NMR spectrum of the dimer **98** with that of polymer supports structure **98** over **99**. The dimer shows a mesophase range of 130–140°C.

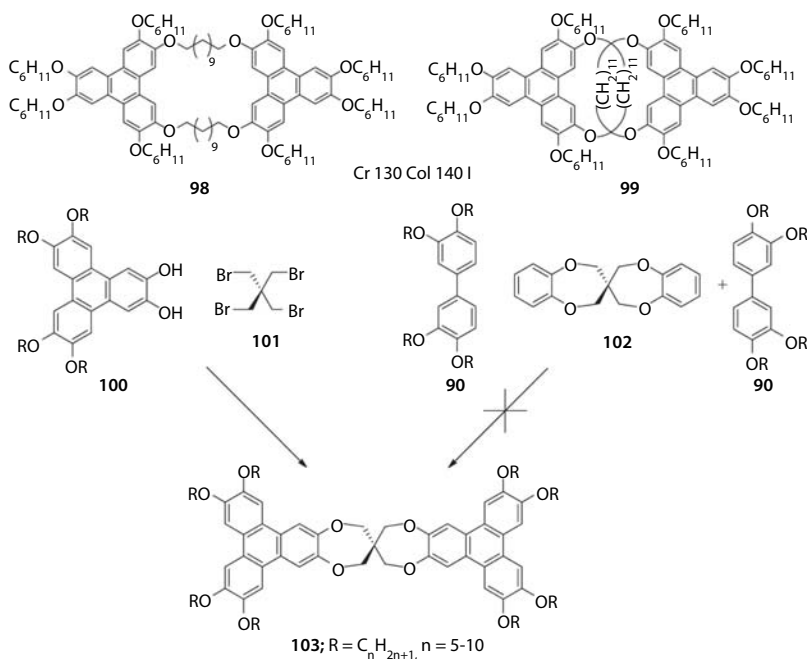
Schulte *et al.* [69] prepared six novel triphenylene-based spiro-twins **103** by condensing 1,2-dihydroxytriphenylenes **100** with a tetrabromide **101**. Although the phenyl-biphenyl coupling route to prepare a variety of symmetrical and unsymmetrical triphenylenes is well established, efforts to prepare these spiro-twins by this technique failed. The thermal behaviour of these compounds is summarised in Table 7.19. Whereas compounds **103.1** and **103.2** containing pentyloxy and hexyloxy chains, respectively,

Table 7.18 Thermal behaviour (°C) of triphenylene dimers with ethylene oxide spacers.



97

Str	R	n	Mesophase behaviour	Ref.
97.1	C_6H_{13}	3	Cr (54 Col_h)77 I	[67]
97.2	C_6H_{13}	4	Cr 50 Col_h 93 I	[67]
97.3	C_6H_{13}	5	Cr 50 Col_h 83 I	[67]
97.4	C_6H_{13}	6	Cr 43 I	[67]
97.5	C_6H_{13}	8	Cr 38 I	[67]



Scheme 7.24 Synthesis of triphenylene spiro-twins: (i) K₂CO₃, DMF, 120°C; (ii) FeCl₃.

Table 7.19 Thermal behaviour (°C) of triphenylene spiro-twins.

Str	R	Mesophase behaviour	Ref.
103.1	C ₅ H ₁₁	Cr 222 I	[69]
103.2	C ₆ H ₁₃	Cr 155 I	[69]
103.3	C ₇ H ₁₅	Cr 70 Col 103 I	[69]
103.4	C ₈ H ₁₇	Cr 65 Col 109 I	[69]
103.5	C ₉ H ₁₉	Cr 60 Col 121 I	[69]
103.6	C ₁₀ H ₂₁	Cr 56 Col 106 I	[69]

showed only crystal-to-isotropic transition, the higher homologues displayed columnar phase.

Discotic twins linked with long flexible alkyl spacers are well-known to form a Col phase because the molecules have sufficient flexibility to stack in columns. Linking two discotic units with a short spacer may experience some steric hindrance due to overlapping aliphatic alkyl chains and a

weak distortion of the planarity of the core, which can lead to reduced π - π interactions. Thus the rigid molecules may stay in more or less a parallel position having orientational order and so can give rise to N_D phase. With this concept, Kumar *et al.* [70] prepared three types of triphenylene dimers **100.1–100.3** tethered directly via rigid alkynyl spacers. These dimers were prepared from monobromopentaalkoxytriphenylene which was then converted to monoacetylenepentaalkoxytriphenylene intermediate. The final products were then obtained using $\text{Cu}(\text{OAc})_2$, THF and pyridine. The effect of various other β -substituents and peripheral substituents for the same compound has been investigated by Takezoe *et al.* [71] While the lower homologues exhibited N phase **104.1–104.3**, higher homologues **104.4** and **104.5** were crystalline solids. Branched chains also have profound effect on the mesomorphic properties (Figure 7.4). The introduction of branched chains at all positions of the dimer made the compound **104.6** non-mesomorphic. But presence of branched chains only at the β -position (**104.9**, **104.10**) didn't affect the phase behaviour. When the spacer was changed to ethynyl (**105**), the lower homologues showed nematic phase (**105.1**, **105.2**) and higher ones (**105.3**, **105.4**) exhibited Col as well as N phase. Hence, the important factor on the mesomorphism of these twins is the relative length between the rigid spacer and the β -substituted chain. Also, the saturated analogues of acetylene bridged dimers **111.2** and **111.3** (Figure 7.5) prepared by Cammidge and Gopee [72] were found to be non-mesomorphic.

Compound **104.12** containing one alkylsulfanyl chain in place of one of the five alkoxy chains was obtained from triphenylene monomer containing four alkoxy groups, a thioalkyl and a monoacetylene group via a multi-step synthesis. This change led to destabilised N_D phase [73].

Another π -conjugated discotic dimers in which mercury atom is located at the centre of two triphenylene units has been reported by Kumar and Varshney [74]. The crystalline compound **106.1** transformed into a highly viscous but shearable fluid phase at about 150°C . On further heating, this compound decomposed at 210°C . In order to decrease the isotropic temperature, one of the chains in compound **106.2** was changed to branched chain. On heating, this compound showed Cr-Cr transition at 110°C and finally became cleared at 186°C . On cooling, this compound showed a monotropic N phase at 185°C . But this N phase was found to having strong tendency to crystallise, which began in the mesophase and was completed around 180°C (Table 7.20). Synthesis of other homologues compounds has not been reported yet.

Hong and co-workers [75] synthesised diacetylene bridged triphenylene dimers **107–109** by utilising copper salt catalysed Eglinton coupling reaction. These diacetylene bridges were attached to the triphenylene via

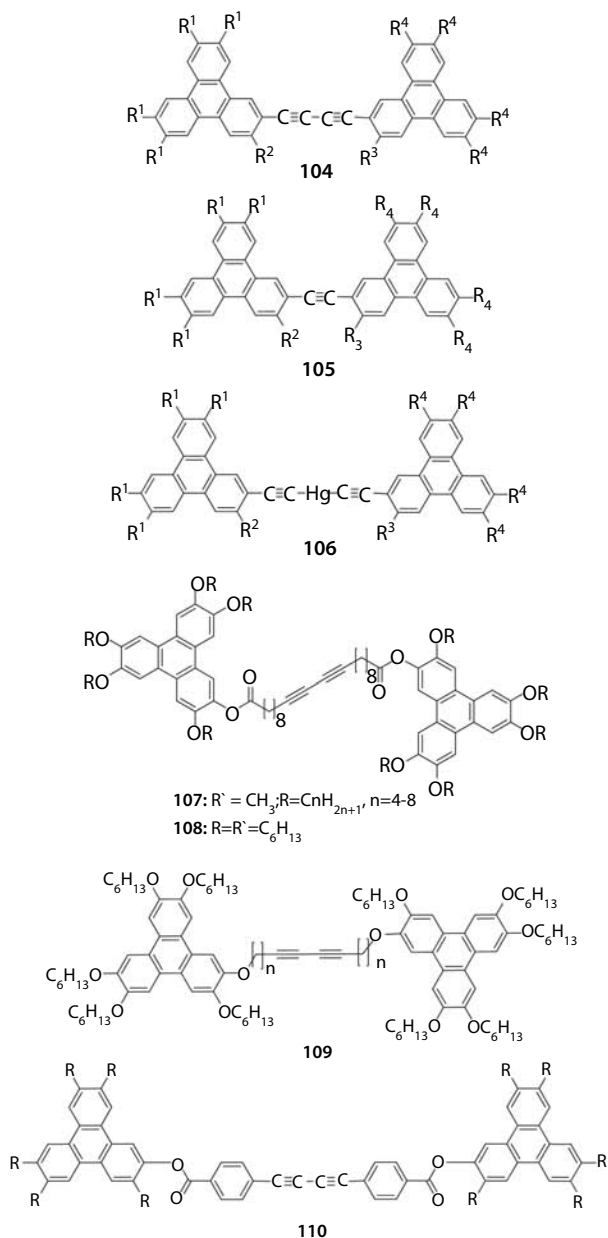
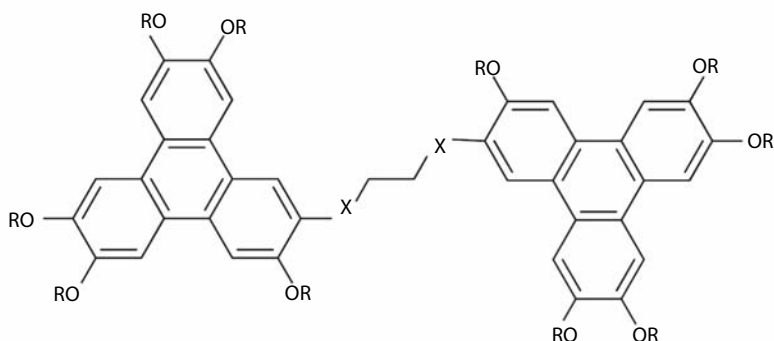


Figure 7.4 Chemical structure of alkyne bridged triphenylenes.



111.1, 111.2; X=CH₂

111.3; X=O

Figure 7.5 Saturated analogues of acetylene bridged dimers.

Table 7.20 Thermal behaviour (°C) of alkyne bridged triphenylenes.

Str	R	Mesophase behaviour	Ref.
104.1	$R^1 = R^2 = R^3 = R^4 = OC_4H_9$	Cr 188.6 N _D 243.5 I	[70]
104.2	$R^1 = R^2 = R^3 = R^4 = OC_5H_{11}$	Cr 161.0 N _D 215.9 I	[70]
104.3	$R^1 = R^2 = R^3 = R^4 = OC_6H_{13}$	Cr 135.3 N _D 172.8 I	[70]
104.4	$R^1 = R^2 = R^3 = R^4 = OC_7H_{15}$	Cr 125.4 I	[71]
104.5	$R^1 = R^2 = R^3 = R^4 = OC_8H_{17}$	Cr 112.4 I	[71]
104.6	$R^1 = R^2 = R^3 = R^4 = O(CH_2)_2C$ $H(CH_3)(CH_2)_3CH(CH_3)_2$	Liquid	[71]
104.7	$R^1 = R^4 = OC_5H_{11}$; $R^2 = R^3 = H$	Cr 189.3 I	[71]
104.8	$R^1 = R^4 = OC_5H_{11}$; $R^2 = R^3 = OCH_3$	Cr 185.7 N 202.9 I	[71]
104.9	$R^1 = R^4 = OC_5H_{11}$; $R^2 = R^3 = O(CH_2)_2CH(CH_3)$ $(CH_2)_3CH(CH_3)_2$	Cr 122.8 Col _f 135.6 N 149.1 I	[71]
104.10	$R^1 = R^4 = OC_5H_{11}$; $R^2 = R^3 = OCH_2CH(C_2H_5)$ $(CH_2)_3CH_3$	Cr 143.4 N 196.2 I	[71]

(Continued)

Table 7.20 (Cont.)

Str	R	Mesophase behaviour	Ref.
104.11	$R^1 = R^4 = OC_8H_{17};$ $R^2 = R^3 = OC_5H_{11}$	Cr 112.9 N 136.5 I	[71]
104.12	$R^1 = R^4 = OC_5H_{11};$ $R^2 = R^3 = SC_5H_{11}$	Cr 182.5 N _D 196.3 I	[73]
105.1	$R^1 = R^2 = R^3 = R^4 = OC_4H_9$	Cr 162.8 N 234.5 I	[71]
105.2	$R^1 = R^2 = R^3 = R^4 = OC_5H_{11}$	Cr 163.4 N 198.4 I	[71]
105.3	$R^1 = R^2 = R^3 = R^4 = OC_6H_{13}$	Cr 147.2 Col _I 161.6 N 163 I	[71]
105.4	$R^1 = R^2 = R^3 = R^4 = OC_7H_{15}$	Cr 136.5 Col _I 156.3 I	[71]
105.5	$R^1 = R^4 = OC_5H_{11};$ $R^2 = R^3 = OCH_3$	Cr 160 N 182.8 I	[71]
105.6	$R^1 = R^4 = OC_5H_{11};$ $R^2 = R^3 = O(CH_2)_2CH(CH_3)$ $(CH_2)_3CH(CH_3)_2$	Cr 113.5 Col _I 143.3 I	[71]
105.7	$R^1 = R^2 = OC_5H_{11};$ $R^3 = R^4 = OC_7H_{15}$	Cr ₁ 112 Cr ₂ 119.3 N 163.9 I	[71]
106.1	$R^1 = R^2 = R^3 = R^4 = OC_5H_{11}$	Cr 210 I	[74]
106.2	$R^1 = R^4 = OC_5H_{11};$ $R^2 = R^3 = OCH_2CH(C_2H_5)$ $(CH_2)_3CH_3$	Cr (185 N) 186 I	[74]
107.1	C_4H_9	G 20 I	[75]
107.2	C_5H_{11}	G -12 Col 57 I	[75]
107.3	C_6H_{13}	G -16 Col 63 I	[75]
107.4	C_7H_{15}	G -20 Col 72 I	[75]
107.5	C_8H_{17}	G -21 Col 77 I	[75]
108		G -25 Col 90 I	[75]
109.1	n = 1	Col 110 I	[75]
109.2	n = 3	Col ₁ 79 Col ₂ 116 I	[75]

(Continued)

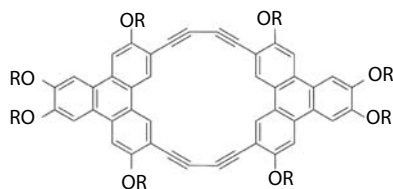
Table 7.20 (Cont.)

Str	R	Mesophase behaviour	Ref.
110.1	C ₄ H ₉	Col _h 263.4 I	[76]
110.2	C ₅ H ₁₁	Col _h 210.9 I	[76]
110.3	C ₆ H ₁₃	Col _h 208.1 I	[76]
110.4	C ₇ H ₁₅	Col _h 215.5 I	[76]
110.5	C ₈ H ₁₇	Col _h 222.3 I	[76]
110.6	C ₉ H ₁₉	Col _h 231.3 I	[76]
111.1	C ₅ H ₁₁	Cr 165 I	[71]
111.2	C ₆ H ₁₃	Cr 132 I	[72]
111.3	C ₆ H ₁₃	Cr 128 I	[72]

ether or ester linkage. The length of the peripheral chains of triphenylene influenced properties of liquid crystal dimers.

Zhao and co-workers [76] explored six triphenylene dimers **110.1**–**110.6** bridged through rigid alkyne spacers. These dimers showed good thermal stability and exhibited Col mesophase over a wide range. The clearing points of these dimers increase with the lengthening of peripheral alkyl chain.

Antiaromatic, planar discotic twins **112.1**–**112.2** (Figure 7.6) based on triphenylene have been prepared by Cammidge and co-workers [77] by treating acetylene based monomeric triphenylene with Pd and CuI. These twins were found to show N phase. X-ray structure of the dimer shows this to exist in the expected near-planar conformation and its packing is particularly intriguing, giving an arrangement where there is now electronic communication both along as well as across the stacks. Other higher cyclic oligomers prepared by authors were found to be non-mesomorphic.



112.1 R=C₆H₁₃, Cr 209 N > 2801

112.2 R=C₁₀H₂₁, Cr 110 N 1311

Figure 7.6 Antiaromatic triphenylene discotic twins.

Cambridge and co-workers [78] demonstrated a general strategy that presence of void region in the centre of the macrocycle can lead to N phase. They synthesised three types of discotic dimers **113**–**115** (Figure 7.7) in which triphenylene was combined with electron rich thiophenes and benzene. Triphenylene diacetylene was coupled with diiodobenzene or diiodothiophene to give diiodotriphenylene intermediate, which was coupled with triphenylene diacetylene to give the dimeric product. Such types of systems prohibit the possibility of formation of Col mesophase, because it would lead to free space through the centre of each stack. In addition, these structures can lead to additional enhancement of optoelectronic behaviour (Table 7.21).

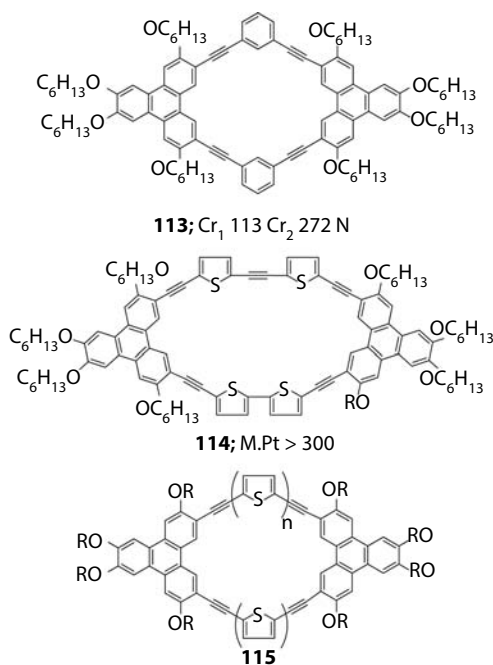
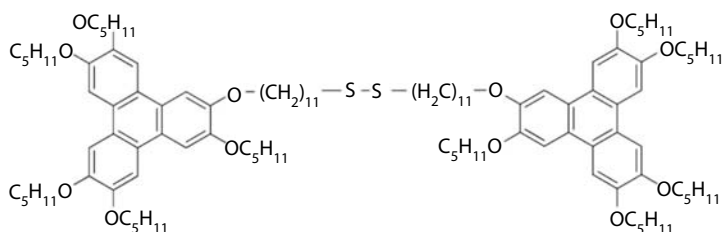
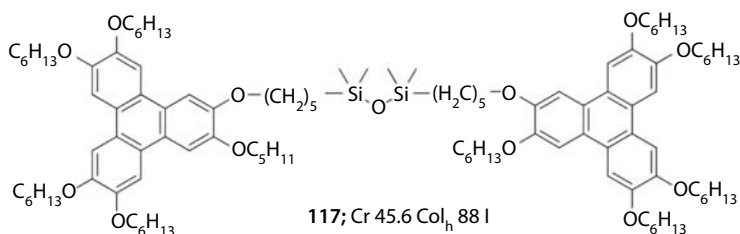


Figure 7.7 Triphenylene dimers with void region in the centre.

Table 7.21 Thermal behaviour (°C) of thiophene bridged triphenylene dimers (115.1–115.3).

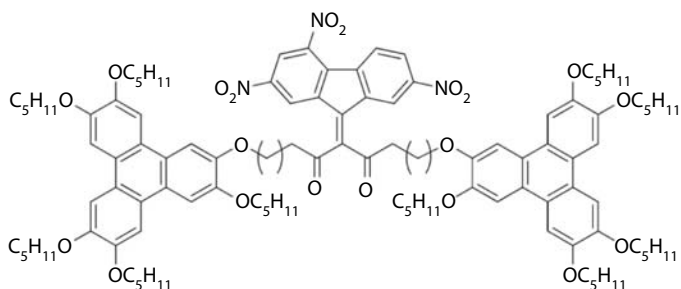
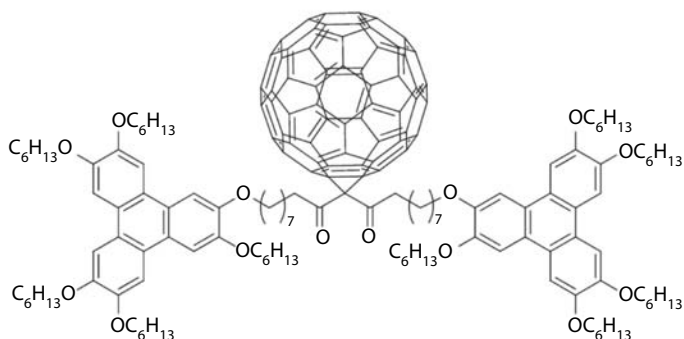
Str	R	<i>n</i>	Mesophase behaviour	Ref.
115.1	OC ₆ H ₁₃	1	Cr ₁ 69 Cr ₂ 291 N	[78]
115.2	OC ₆ H ₁₃	2	M.Pt. > 300	[78]
115.3	OC ₁₀ H ₂₁	2	Cr 210 N	[78]

**116**; Waxy Solid**117**; Cr 45.6 Col_h 88 I

Schönherr *et al.* [79] studied the self-assembled monolayers of different discoid molecules, one out of them was disulfide-bridged triphenylene dimer **116**. This dimer can be easily prepared by reaction of monohydroxypentapentyloxytriphenylene with bis-(11,11'-undecanol)disulfide using DEAD and PPh₃. The aromatic core of this dimer in the monolayer was found to be in edge-on orientation. AFM studies revealed the presence of lateral order in these monolayers which can extend over length scales exceeding 100 nm.

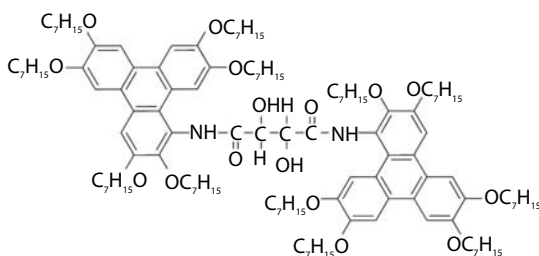
Zelcer *et al.* [80] prepared similar dimer **117** containing siloxane unit at the centre but with a shorter spacer. 2-Pentenyloxy-3,6,7,10,11-pentahexyloxytriphenylene was treated with tetramethyldisiloxane. This dimer exhibited Col_h phase.

Charge transfer interactions between electron-donor and electron-acceptor lead to increased core-core interactions and hence to alternating regular packing of the molecules in bulk LC phase. This interaction also promotes edge-on orientation of discotic molecules in thin films. In order to validate this point and to prevent different discotic moieties from phase separation, Tsukruk *et al.* [81] prepared covalently linked donor-acceptor twin **118** based on triphenylene and TNF. This dimer is a condensation product of diethyl ester of TNF and free alcohol derivative of triphenylene. It exhibits a Col phase. The Langmuir-Blodgett film formed by this dimer shows an edge-on orientation of the molecules, i.e. the columns lie parallel to a solid substrate.

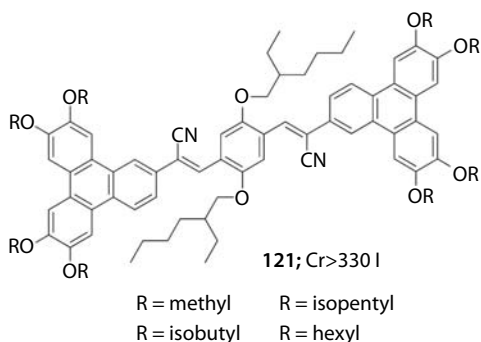
118; Cr 119 Col_h 176 I

119; Cr 581

Fullerene and its derivatives have received a great level of interest since it was discovered. The chemistry of this interesting compound is being explored throughout the world by many researchers. Incorporation of fullerene to the discotic moieties may lead to novel materials with interesting applications. To explore this possibility, Manickam *et al.* [65] synthesised C₆₀ Bingel cyclopropanation adducts **119** incorporating bis-triphenylene moieties. But this compound was found to be non-liquid crystalline.

120; Cr 13.2 Col_h, 25.5 Col_h, 44.0 I

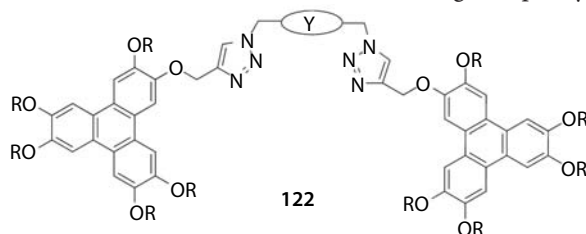
Akopova *et al.* [82] prepared triphenylene dimer **120** containing chiral substituents. Discotic dimer containing tartaric acid as the linker was found to show two types of mesophases. So introduction of chiral fragment favours the mesophase formation.



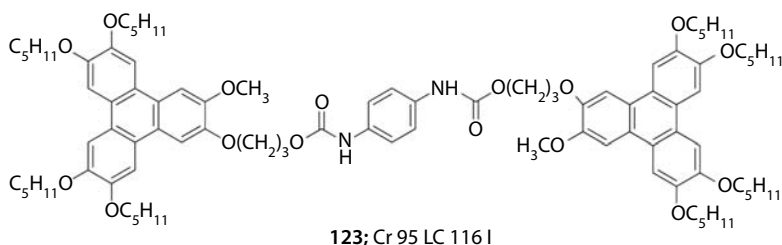
Hanack and co-workers [83] have designed and synthesised four novel conjugated-bridged triphenylene dimers **121** to be used as emissive layer in organic light emitting diodes. In these compounds, an electron-withdrawing cyano-substituted *p*-phenylenevinylene unit was linked to two triphenylene units. These dimers were prepared by double Knoevenagel reaction of mono-functionalised cyanomethyltriphenylene derivatives and a terephthalaldehyde derivative. All the dimers were non-mesomorphic and melted above 330°C. They exhibited orange to red photoluminescence and a strong bathochromic shift of more than 250 nm when compared with monomeric triphenylene.

Symmetrical triphenylene dimers **122.1–122.2** connected by a bis-triazole moiety have been synthesised by Thevenet and Neier [84] using a double Cu(I) catalysed azide-alkyne cycloaddition. Nature of the linker has profound effect on the mesophase. Incorporation of methylene linker promotes formation of Col_n mesophase, whereas phenyl linker suppresses the formation of mesophase (Table 7.22).

A triphenylene dimer **123** has been prepared by linking two mono-hydroxytriphenylene units via phenylene carbamate linkages, which was formed through a reaction between one 1,4-phenylene diisocyanate and two hydroxyl end groups on flexible substituents of triphenylene. The type of mesophase found in this dimer is not clear, but it has been found to exhibit high viscosity, and good film forming properties like polymers. This also showed sufficient charge-carrier mobility and good hole transporting properties [85].

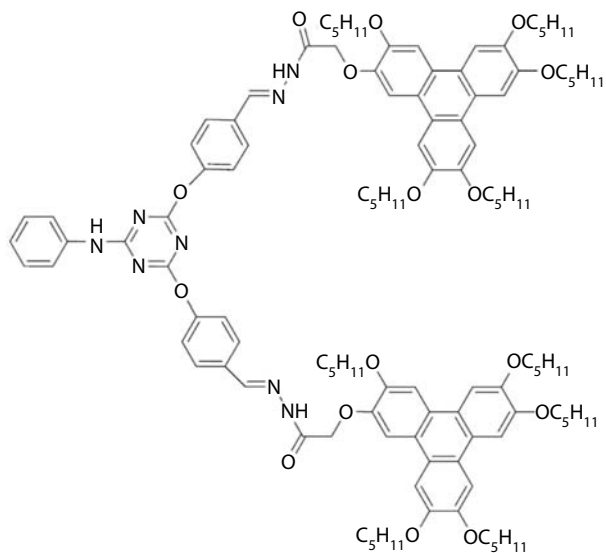
Table 7.22 Thermal behaviour (°C) of bis-triazole bridged triphenylene dimers.

Str	R	Y	Mesophase behaviour	Ref.
122.1	C ₆ H ₁₃	CH ₂	10 Col _h 153 I	[84]
122.2	C ₆ H ₁₃	C ₆ H ₄	Cr 154 I	[84]

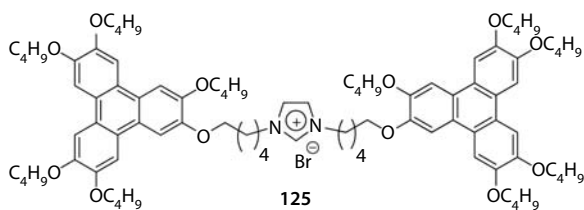


1,3,5-triazine-based triphenylene dimer **124** with large bridging polyaromatic core has been explored by Yang and co-workers [86]. Cyanuric chloride was treated with aniline at 0°C and then with 4-hydroxy benzaldehyde to give 1,3,5-triazine derivative. Triphenylene with hydrazide group was then reacted with 1,3,5-triazine derivative to give the dimer. This molecule possess Col_h phase over a wide temperature range. This study indicated that mesomorphic properties also depend on number of triphenylene units.

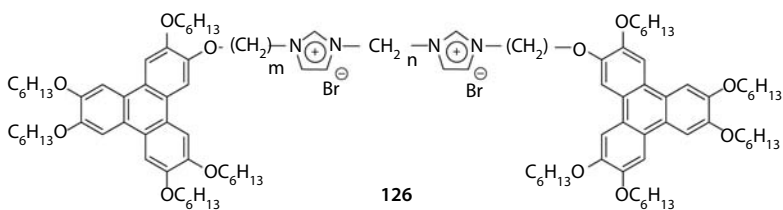
Pal and Kumar [87] synthesised triphenylene-imidazole based ionic dimer **125** in which they hybridised two triphenylene and one imidazole moiety to form dimer under microwave dielectric heating, since classical reaction didn't give the desired product. This dimer exhibited Col mesophase at 84°C on heating which finally cleared at 95°C. On cooling mesophase appeared at 92°C and no crystallisation observed up to room temperature. Interestingly, calamitic-discotic hybrid made by authors was found to be non-liquid crystalline.



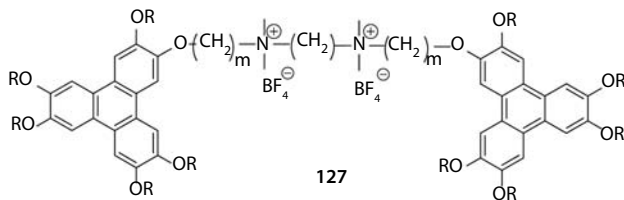
124; Cr 47.64 Col_n 104.87 I



125



126



127

Table 7.23 Thermal behaviour (°C) of ionic triphenylene dimers.

Str	R	<i>m</i>	<i>n</i>	Mesophase behaviour	Ref.
125				Cr 84 Col _r 95 I	[87]
126.1	C ₆ H ₁₃	6	4	Cr 48.3 Col _h 180.1 I	[88]
126.2	C ₆ H ₁₃	12	5	Cr 59.7 Col _h 120.6 I	[88]
126.3	C ₆ H ₁₃	8	8	Cr 58.7 Col _h 87.3 I	[88]
126.4	C ₆ H ₁₃	9	8	Cr 58.8 Col _h 86.3 I	[88]
127.1	C ₄ H ₉	8		Cr 84.2 Col _h 90.4 I	[89]
127.2	C ₄ H ₉	12		Cr 52.1 Col _h 99.1 I	[89]

A series of symmetrical Gemini dimers **126** based on imidazole and triphenylene moieties have been synthesised by Kumar *et al.* [88] using microwave dielectric heating. Dimer **126.1** with shorter spacer length displayed Col_h mesophase over a wide range of temperature. Transition temperatures of these compounds are given in the Table 7.23.

Two symmetrical Gemini dimers based on triphenylene and ammonia have been reported by Gupta *et al.* [89] These dimers **127** were prepared by reacting ω-brominated triphenylene with tetramethylene-1,2-diamine in toluene. These compounds exhibited enantiotropic behaviour with Col_h mesophase. Although degree of order present is less in these systems.

Two series of symmetrical triphenylene dimers **128–132** linked by phenyl spacer have been synthesised by Gupta *et al.* [90] Relative orientation of the two disk moieties have been changed in these dimers. None of the dimers exhibited liquid crystalline behaviour. These dimers when doped with TNF exhibited Col_h mesophase. As a consequence of charge transfer interaction with TNF, core-core interaction increased and so mixture showed LC properties (Table 7.24). Small conductivity values for these compounds demonstrated that π-π interaction is less efficient. Monolayer of Compound **132.3** was also studied at air-water interface. Effect of compression rate and temperature has been studied. It was found that the collapse of dimer monolayer is through the formation of nuclei of 3D crystallites [91].

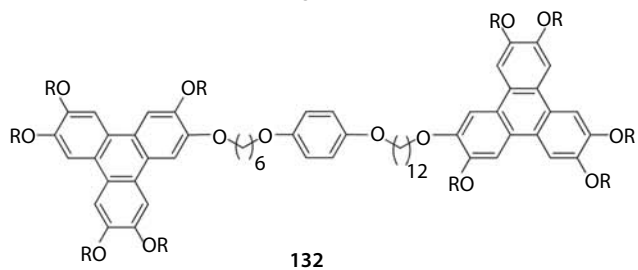
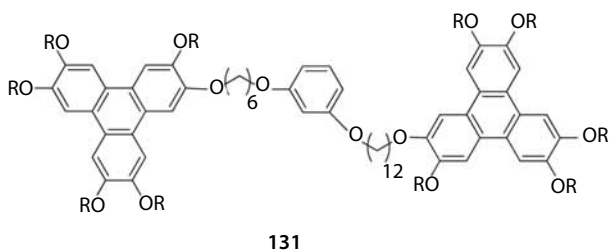
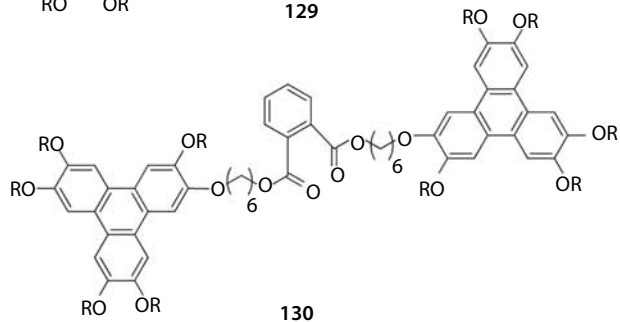
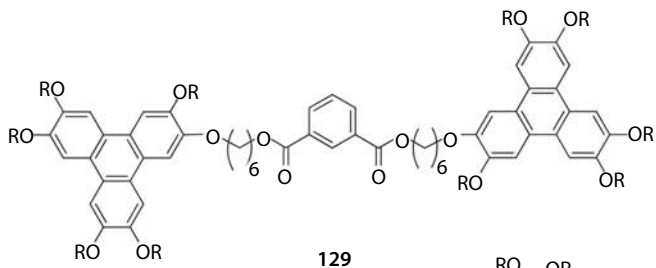
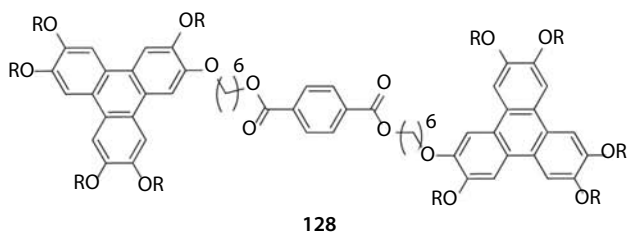
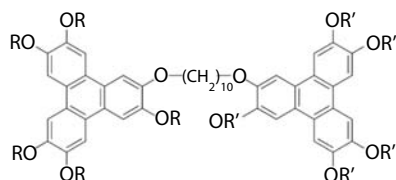


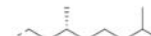
Table 7.24 Thermal behaviour (°C) of benzene bridged triphenylene dimers (128–132).

Str	Mixture	Mesophase behaviour	Ref.
128	–	Cr 72.5 I	[90]
129	–	Cr 50.8 I	[90]
130.1	–	Cr 61.6 I	[90]
130.2	130.1:TNF [1:1]	Cr 190 (Col _h 186) I	[90]
130.3	130.1:TNF [2:1]	Cr 170 (Col _h 167) I	[90]
130.4	130.1:TNF [4:1]	Cr 145 (Col _h 140) I	[90]
130.5	130.1:TNF [9:1]	Cr 78 (Col _h 68) I	[90]
131.1	–	Cr 39 I	[90]
131.2	131.1:TNF [1:2]	Cr 145 (Col _h 135) I	[90]
131.3	131.1:TNF [1:1]	Cr 135 (Col _h 126) I	[90]
131.4	131.1:TNF [2:1]	Cr 86 (Col _h 77) I	[90]
131.5	131.1:TNF [4:1]	Cr 40 I	[90]
132.1	–	Cr 36 I	[90]
132.2	132.1:TNF [1:1]	Cr 95 (Col _h 88) I	[90]
132.3	132.1:TNF [2:1]	Cr 85 (Col _h 75) I	[90]
132.4	132.1:TNF [4:1]	Liquid	[90]

7.2.11.2 Triphenylene Based Non-symmetrical Dimers

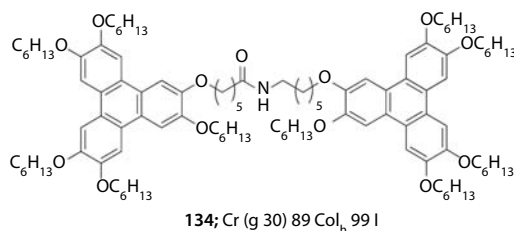


133.1 ; R = C₆H₁₃, R' = C₄H₉; Col_h (g30) 98 I

133.2 ; R = , R' = C₁₀H₂₁; Cr 34 Col_h 45 I

Unsymmetrical discotic twins can either retain the mesomorphic properties of the subunits either by columnar stacking of like subunits, or can

form supramolecular aggregates by columnar stacking of unlike subunits and thus might display novel mesomorphic properties. In this direction, a non-symmetrical dimer **133.1** in which penta-hexyloxytriphenylene unit was connected to pentabutyloxytriphenylene unit has been reported by Boden *et al.* [56] This dimer possess Col_h phase at room temperature and shows clearing transition at 98°C . Another dimer **133.2** reported by Hirst *et al.* [92] was formed by connecting chiral pentakis(3,7-dimethyloctyloxy)triphenylene with pentadecyloxytriphenylene via a decyl spacer. This showed a very narrow range of Col phase on heating, but on cooling the mesophase was stable up to 0°C . Both these dimers can be prepared via second route as shown in Scheme 7.23.

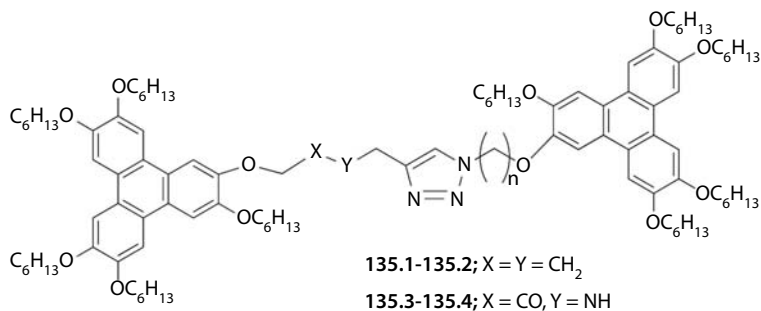


Boden *et al.* [56] synthesised an unsymmetrical dimer **134** based on triphenylene containing an amide linker. This compound was obtained by condensing an amine terminated triphenylene with acid chloride containing triphenylene. This dimer shows Col_h phase which transforms to glass on cooling. This glassy state is stable for months.

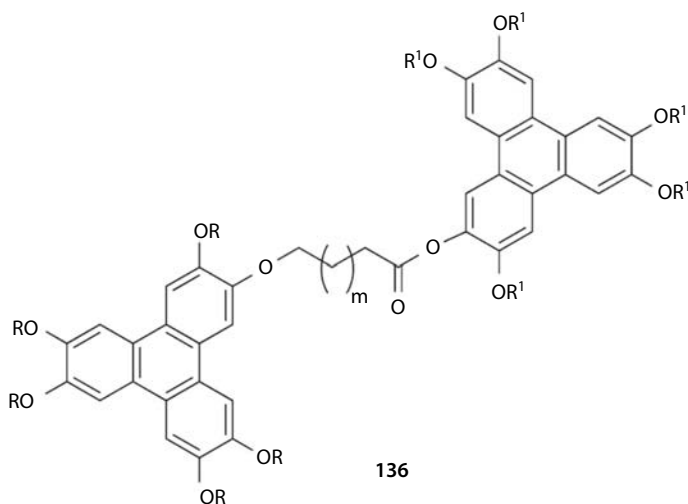
Zhao *et al.* [93] utilised click chemistry reaction between triphenylene azide and triphenylene alkyne in synthesising dimers **135.1–135.4**. Two different types of dimers based on different linkages have been prepared. All of these dimers show liquid crystalline behaviour. Further, the triazole moiety in the dimers can act as hydrogen bond acceptor and can also form ionic liquid crystals on reacting with alkyl halides (Table 7.25).

Non-symmetrical dimers **136** based on triphenylene possessing ester linkage on one side and ether linkage on the other side have been synthesised by Varshney *et al.* [94] These discotic dimers were obtained by connecting two monomeric units by means of a flexible spacer. The dimers have shown to exhibit Col_l mesophase (Table 7.26).

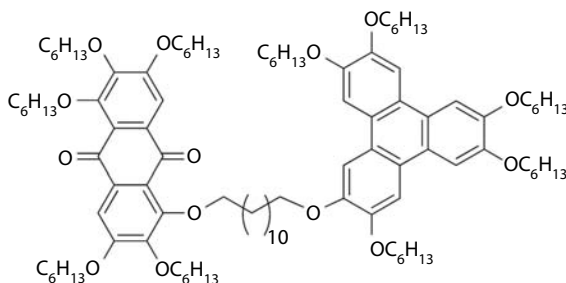
Kumar *et al.* [95] investigated the mesomorphic properties of a discotic dimer **137** bearing electron rich triphenylene connected to an electron deficient anthraquinone moiety via dodecyloxy spacer. This compound was synthesised by coupling ω -bromosubstituted triphenylene with monohydroxyanthraquinone. This was found to have a Col phase at room temperature.

Table 7.25 Thermal behaviour (°C) of triazole linked triphenylene dimers.

Str	R	Mesophase behaviour	Ref.
135.1	$n = 1$	Cr 48 Col ₁ 75 Col ₂ 88 I	[93]
135.2	$n = 3$	Cr 18 Col _h 95 I	[93]
135.3	$n = 3$	Cr 71 Col _h 97 I	[93]
135.4	$n = 6$	Cr 81 Col _h 104 I	[93]

Table 7.26 Thermal behaviour (°C) of unsymmetrical triphenylene dimers.

Str	<i>m</i>	R	R ¹	Mesophase behaviour	Ref.
136.1	5	C ₈ H ₁₇	C ₈ H ₁₇	Col _r 93.4 I	[94]
136.2	5	C ₈ H ₁₇	C ₄ H ₉	Cr 44.8 Col _r 123.1 I	[94]
136.3	9	C ₈ H ₁₇	C ₈ H ₁₇	Col _r 104.5 I	[94]



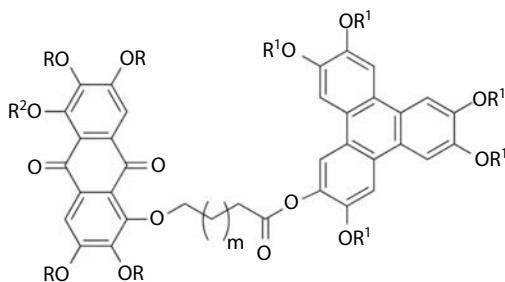
137; G 40 Col 96.91

Similar compounds **138** prepared from triphenylene and anthraquinone but possessing ester linkage on one side and ether linkage on the other side have been reported by Varshney *et al.* Peripheral alkoxy chains and length of the linker both affect the mesophase tremendously. When the peripheral chains were all alkoxy, then dimers exhibited Col_r phase (Table 7.27). But, if the peripheral group attached to anthraquinone was changed to hydroxyl and acetyloxy, mesophase behaviour changed and some of the compounds even showed N phase as well as both N and Col phase together. Acetyloxy group also has destabilising effect on liquid crystalline behaviour [94, 96].

7.3 Applications

7.3.1 Dopants for Liquid Crystal Display Mixtures

The performance of liquid crystal displays is strongly dependent on the liquid crystal mixtures used, and further improvements to such displays rely on the formulation of mixtures with enhanced properties. A number of different device configurations in commercial displays require mixtures with different display characteristics. For most of the display related applications, response speed is an important operational characteristic and any new mixtures must maintain the optimal electrical and operational

Table 7.27 Thermal behaviour (°C) of anthraquinone-triphenylene linked dimers.

138

Str	<i>m</i>	R	R ¹	R ²	Mesophase behaviour	Ref.
138.1	5	C ₈ H ₁₇	C ₈ H ₁₇	C ₈ H ₁₇	Cr 58.5 I	[94]
138.2	5	C ₈ H ₁₇	C ₄ H ₉	C ₈ H ₁₇	Col _r 88.65 I	[94]
138.3	9	C ₈ H ₁₇	C ₈ H ₁₇	C ₈ H ₁₇	Col _r 103.8 I	[94]
138.4	1	C ₄ H ₉	C ₄ H ₉	OH	Cr 121.9 I (I 118.7 N 102.4 Cr)	[96]
138.5	2	C ₅ H ₁₁	C ₅ H ₁₁	OH	SS 56 I	[96]
138.6	5	C ₈ H ₁₇	C ₈ H ₁₇	OH	N 43.8 I	[96]
138.7	5	C ₄ H ₉	C ₄ H ₉	OH	Col _h 165.5 I	[96]
138.8	9	C ₆ H ₁₃	C ₆ H ₁₃	OH	Col 117 I	[96]
138.9	9	C ₈ H ₁₇	C ₈ H ₁₇	OH	Col 80 I	[96]
138.10	5	C ₇ H ₁₅	C ₇ H ₁₅	OH	N 42.2 I	[96]
138.11	5	C ₈ H ₁₇	C ₈ H ₁₇	OH	SS 61 I	[96]
138.12	5	C ₈ H ₁₇	C ₈ H ₁₇	OAc	SS 66 I	[96]
138.13	9	C ₆ H ₁₃	C ₆ H ₁₃	OAc	Col 91 I	[96]
138.14	5	C ₇ H ₁₅	C ₇ H ₁₅	OAc	SS 62 I	[96]
138.15	5	C ₈ H ₁₇	C ₈ H ₁₇	OAc	Cr 106 (M _x 95) I	[96]

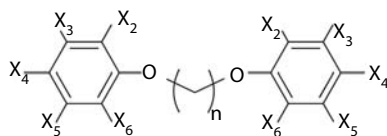


Figure 7.8 Benzene based LC dimer used as dopant to study the effect on relaxation time.

characteristics. The ability of the molecular shape of liquid crystal dimers to adapt to their mesophase environment provides a new concept to aid the design of mesogens for display mixtures. Keeping this in mind, Dunmur and co-workers [97] explored the possibilities of using dimers as dopants in display mixtures to reduce their rotational viscosity.

Commercially available nematic liquid crystal ZLI-4792 was used as the host material. This material is a mixture of fluoro-substituted two and three ring phenyl cyclohexanes. It exhibits a significant two phase region at the transition from N-to-I phase. This host material was then doped with small amounts (5% and 10% w/w) of the dimeric molecules to obtain different mixtures for this study. When compared on a shifted temperature scale, the order parameters of the spin probe in the mixtures are essentially unchanged. Most of the dopants reduce the relaxation time though to different extents. Longer chain flexible dimers, i.e. those with more methylene groups in the linking alkyl chain produce a smaller reduction of the rotational relaxation times than the shorter chain dimers. However, the chain length cannot be reduced too much, since the shorter dimers have high melting points and become insoluble in the nematic host. An optimum chain length seems to be 7 or 9 methylene groups, the odd parity dimers also appear to be slightly more effective at reducing the relaxation times than the even dimers.

The effects of different fluoro-phenyl substitution patterns of the dopants on the rotational relaxation times of the mixtures have also been investigated by them. Multiple symmetric fluorine substitution, as in 3,4,5 tri-fluoro-phenyl, perfluoro-phenyl or tri-fluoro-methyl-phenyl terminated dimers result in longer relaxation times and much reduced nematic-to-isotropic transition temperatures; both undesirable effects. However, flexible dimers having terminal phenyl groups with an unsymmetrical 2,3,4-fluorine substitution pattern produce mixtures with ZLI-4792 having reduced rotational relaxation times, with only relatively small reductions in nematic-to-isotropic transition temperatures.

This indicates that careful design of dimeric dopants can lead to significant improvements in the performance of display mixtures.

7.3.2 Organic Light-Emitting Diodes (OLEDs)

OLEDs allow the conversion of electrical energy into light energy. OLEDs generally consist of three sub-layers: a hole-transporting layer, an electron transporting layer and an emission layer. Low work-function electrode such as Al injects electrons into the LUMO of the electron-transporting material. A thin film of ITO deposited substrate, i.e. anode injects holes into the HOMO of the hole-transporting material. When voltage is applied to the electrodes, the charges start moving under the influence of electric field. Recombination of these charges takes place and therefore, electrical energy gets converted to light energy (Figure 7.9).

Efficient charge transport and light emission are the key features of OLEDs. Discotic liquid crystalline materials have caught attention for OLED applications, as excellent charge transport can be achieved in the columnar phase of discotic materials. He and co-workers [85] demonstrated the use of triphenylene based discotic dimer **123** as the hole transporting material in the OLEDs. In order to evaluate the hole injection property of discotic dimer **123** parallel devices have been prepared for comparison using HOMO values as a guide in the selection of hole injection materials. It has been reported that HOMO levels of hexa-alkoxytriphenylenes range between -5.3 and -5.4 eV, which is similar to the value from poly(N-vinylene carbazole) (PVK). Therefore, PVK was chosen for comparison.

Devices consisting of dimer **123** as well as PVK layers as hole transporting layer have been prepared. These were denoted as: device (a) ITO/**123** (60 nm)/AlQ₃ (30 nm)/Al and device (b) ITO/PVK (60 nm)/AlQ₃ (30 nm)/Al. The light emitting areas of both devices were 0.09 cm². The power efficiencies of the devices as a function of the bias voltages are shown in Figure 7.10. It was noticeable that the power efficiency of dimer device (a) was higher than that of the PVK device (b), which demonstrated an improvement in the external efficiency when triphenylene dimer **123** was used. Since the device was not fully optimised, then also

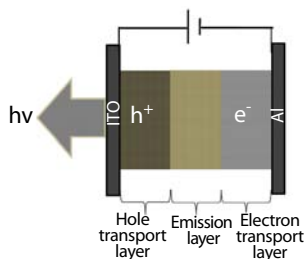


Figure 7.9 Schematic diagram of an OLED device.

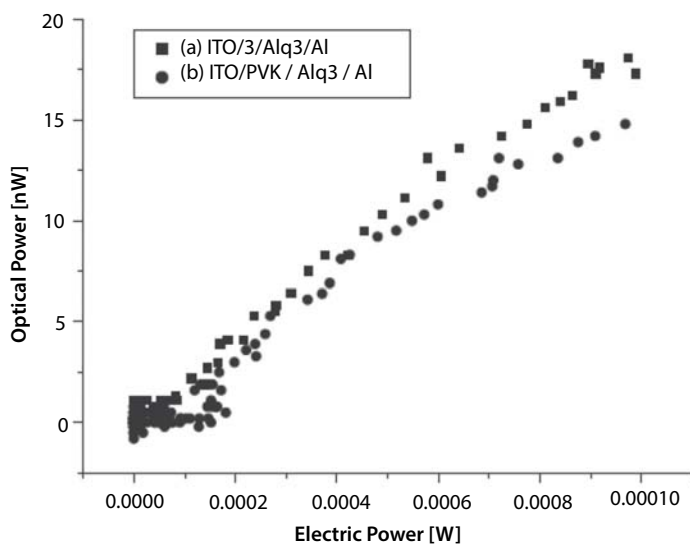


Figure 7.10 Plots of measured optical power as a function of input electronic power from device (a) ITO/123 (60 nm)/AlQ₃ (30 nm)/Al and device, (b) ITO/PVK (60 nm)/AlQ₃ (30 nm)/Al. Reproduced with permission from Ref. [85].

dimer **123** seems to combine sufficient charge-carrier mobility with good hole injection properties and so can be used as hole transporting material in OLEDs.

7.4 Conclusions and Outlook

In this chapter, in the first part, structure-property relationships of discotic dimers have been briefly outlined. The second part of this chapter deals with applications of discotic dimers in various fields. Discotic dimers play an important role as being the model compounds for polymeric liquid crystals. In recent decades, there has been increasing attention in developing the area of organic opto-electronic devices for reducing the demand of fossil fuels in the world. Among the diverse new materials for organic devices, dimers hold a particular promise due to the self-organisation and self-healing properties of discotic molecules in the phase. Since, the field of discotic dimers is quite young and the continuous efforts on finding better discotic dimers are expected to provide future smart materials and devices with improved properties and performance.

References

1. P. J. Collings and M. Hird. *Introduction to Liquid Crystals Chemistry and Physics*. In: G. W. Gray, J. W. Goodby, and A. Fukuda, Eds. Taylor and Francis Group, London and New York, 1997.
2. D. Vorlander. *Z. Phys. Chem.* Vol. 126, p. 449, 1927.
3. A. C. Griffin and T. R. Britt. *J. Am. Chem. Soc.* Vol. 103, p. 4957, 1981.
4. K. Krishnan and V. S. K. Balagurusamy. *Liq. Cryst.* Vol. 28, p. 321, 2001.
5. V. Prasad, A. Roy, N. G. Nagaveni, and K. Gayathri. *Liq. Cryst.* Vol. 38, p. 1301, 2011.
6. F. Chen, J. Zhang, and X. Wan. *Macromol. Chem. Phys.* Vol. 212, p. 1836, 2011.
7. J. J. Naidu and S. Kumar. *Mol. Cryst. Liq. Cryst.* Vol. 397, p. 17, 2003.
8. S. Kumar and J. J. Naidu. *Mol. Cryst. Liq. Cryst.* Vol. 378, p. 123, 2002.
9. C. P. Lillya and Y. L. N. Murthy. *Mol. Cryst. Liq. Cryst.* Vol. 2, p. 121, 1985.
10. S. Zamir, E. J. Wachtel, H. Zimmermann, S. Dai, N. Spielberg, R. Poupko, and Z. Luz. *Liq. Cryst.* Vol. 23, p. 689, 1997.
11. K. Praefcke, B. Kohne, D. Singer, D. Demus, G. Pelzl, and S. Diele. *Liq. Cryst.* Vol. 7, p. 589, 1990.
12. K. Praefcke, B. Kohne, B. Gündogan, D. Singer, D. Demus, S. Diele, G. Pelzl, and U. Bakowsky. *Mol. Cryst. Liq. Cryst.* Vol. 198, p. 393, 1991.
13. J. Contzen, G. Heppke, H. S. Kitzerow, D. Krüerke, and H. Schmid. *Appl. Phys. B* Vol. 63, p. 605, 1996.
14. C. J. Booth, D. Krüerke, and G. Heppke. *J. Mater. Chem.* Vol. 6, p. 927, 1996.
15. J. S. Patel, K. Praefcke, D. Singer, and M. Langner. *Appl. Phys. B* Vol. 60, p. 469, 1995.
16. P. Kouwer, G. Mehl, and S. Picken. *Mol. Cryst. Liq. Cryst.* Vol. 411, p. 387, 2004.
17. P. Kouwer, W. Jager, W. Mijs, S. Picken, K. Shepperson, and G. Mehl. *Mol. Cryst. Liq. Cryst.* Vol. 411, p. 377, 2004.
18. V. Percec, C. G. Cho, C. Pugh, and D. Tomazos. *Macromolecules* Vol. 25, p. 1164, 1992.
19. M.-C. Tzeng, S.-C. Liao, T.-H. Chang, S.-C. Yang, M.-W. Weng, H.-C. Yang, M. Y. Chiang, Z. Kai, J. Wu, and C. W. Ong. *J. Mater. Chem.* Vol. 21, p. 1704, 2011.
20. C. W. Ong, Y.-C. Chan, M.-C. Yeh, H.-Y. Lin, and H.-F. Hsu. *RSC Adv.* Vol. 3, p. 8657, 2013.
21. K. J. A. Bozek and V. E. Williams. *Soft Matter* Vol. 10, p. 5749, 2014.
22. S. Ito, P. T. Herwig, T. Böhme, J. P. Rabe, W. Rettig, and K. Müllen. *J. Am. Chem. Soc.* Vol. 122, p. 7698, 2000.
23. D. Wasserfallen, I. Fischbach, N. Chebotareva, M. Kastler, W. Pisula, F. Jäckel, M. D. Watson, I. Schnell, J. P. Rabe, H. W. Spiess, and K. Müllen. *Adv. Funct. Mater.* Vol. 15, p. 1585, 2005.
24. M. D. Watson, F. Jäckel, N. Severin, J. P. Rabe, and K. Müllen. *J. Am. Chem. Soc.* Vol. 126, p. 1402, 2004.

25. C. Piechocki, J. Simon, J.-J. André, D. Guillon, P. Petit, A. Skoulios, and P. Weber. *Chem. Phys. Lett.* Vol. 122, p. 124, 1985.
26. K. Binnemans, J. Sleven, S. De Feyter, F. C. De Schryver, B. Donnio, and D. Guillon. *Chem. Mater.* Vol. 15, p. 3930, 2003.
27. T. Toupance, P. Bassoul, L. Mineau, and J. Simon. *J. Phys. Chem.* Vol. 100, p. 11704, 1996.
28. K. Hatsusaka, M. Kimura, and K. Ohta. *Bull. Chem. Soc. Jpn.* Vol. 76, p. 781, 2003.
29. K. Hatsusaka, H. Mukai, and K. Ohta. *J. Porphyrin Phthalocyanines* Vol. 11, p. 846, 2007.
30. H. Mukai, M. Yokokawa, K. Hatsusaka, and K. Ohta. *J. Porphyrin Phthalocyanines* Vol. 13, p. 70, 2009.
31. H. Mukai, M. Yokokawa, M. Ichihara, K. Hatsusaka, and K. Ohta. *J. Porphyrin Phthalocyanines* Vol. 14, p. 188, 2010.
32. Y. Zhang, J. Jiang, X. Sun, and Q. Xue. *Aust. J. Chem.* Vol. 62, p. 455, 2009.
33. J. Sleven, C. Görrler-Walrand, and K. Binnemans. *Mat. Sci. Eng. C* Vol. 18, p. 229, 2001.
34. F. Maeda, K. Hatsusaka, K. Ohta, and M. Kimura. *J. Mater. Chem.* Vol. 13, p. 243, 2003.
35. Z. Belarbi, C. Sirlin, J. Simon, and J. J. Andre. *J. Phys. Chem.* Vol. 93, p. 8105, 1989.
36. T. Komatsu, K. Ohta, T. Fujimoto, and I. Yamamoto. *J. Mater. Chem.* Vol. 4, p. 533, 1994.
37. T. Komatsu, K. Ohta, T. Watanabe, H. Ikemoto, T. Fujimoto, and I. Yamamoto. *J. Mater. Chem.* Vol. 4, p. 537, 1994.
38. T. Basova, E. Kol'tsov, A. K. Hassan, A. Nabok, A. K. Ray, A. G. Gürek, and V. Ahsen. *J. Mater. Sci. Mater. El.* Vol. 15, p. 623, 2004.
39. A. G. Gürek, T. Basova, D. Luneau, C. Lebrun, E. Kol'tsov, A. K. Hassan, and V. Ahsen. *Inorg. Chem.* Vol. 45, p. 1667, 2006.
40. K. Ban, K. Nishizawa, K. Ohta, A. M. van de Craats, J. M. Warman, I. Yamamoto, and H. Shirai. *J. Mater. Chem.* Vol. 11, p. 321, 2001.
41. F. Nekelson, H. Monobe, and Y. Shimizu. *Mol. Cryst. Liq. Cryst.* Vol. 479, p. 205/[1243], 2007.
42. F. Nekelson, H. Monobe, and Y. Shimizu. *Chem. Commun.* p. 3874, 2006.
43. G. C. Bryant, M. J. Cook, S. O. Haslam, R. M. Richardson, T. G. Ryan, and A. J. Thorne. *J. Mater. Chem.* Vol. 4, p. 209, 1994.
44. G. C. Bryant, M. J. Cook, T. G. Ryan, and A. J. Thorne. *Tetrahedron* Vol. 52, p. 809, 1996.
45. T. Nakai, K. Ban, K. Ohta, and M. Kimura. *J. Mater. Chem.* Vol. 12, p. 844, 2002.
46. Y. Shimizu, J.-Y. Matsuno, K. Nakao, K. Ohta, M. Miya, and A. Nagata. *Mol. Cryst. Liq. Cryst. Sci. Tech. A* Vol. 260, p. 491, 1995.
47. T. Sakurai, K. Shi, H. Sato, K. Tashiro, A. Osuka, A. Saeki, S. Seki, S. Tagawa, S. Sasaki, H. Masunaga, K. Osaka, M. Takata, and T. Aida. *J. Am. Chem. Soc.* Vol. 130, p. 13812, 2008.

48. V. Vill and J. Thiem. *Liq. Cryst.* Vol. 9, p. 451, 1991.
49. T. Itoh, A. Takada, T. Fukuda, T. Miyamoto, Y. Yakoh, and J. Watanabe. *Liq. Cryst.* Vol. 9, p. 221, 1991.
50. A. Takada, T. Fukuda, T. Miyamoto, Y. Yakoh, and J. Watanabe. *Liq. Cryst.* Vol. 12, p. 337, 1992.
51. M. Sugiura, M. Minoda, J. Watanabe, T. Fukuda, and T. Miyamoto. *Bull. Chem. Soc. Jpn* Vol. 65, p. 1939, 1992.
52. G. S. Attard and C. T. Imrie. *Liq. Cryst.* Vol. 11, p. 785, 1992.
53. N. Tchegotareva, X. Yin, M. D. Watson, P. Samori, J. P. Rabe, and K. Müllen. *J. Am. Chem. Soc.* Vol. 125, p. 9734, 2003.
54. B. Kohne, P. Marquardat, K. Praefcke, P. Psaras, W. Stephan, and K. Turgay. *Chimia* Vol. 40, p. 360, 1986.
55. W. Kreuder, H. Ringsdorf, O. Herrmann-Schönherr, and J. H. Wendorff. *Angew. Chem. Int. Ed.* Vol. 26, p. 1249, 1987.
56. N. Boden, R. J. Bushby, A. N. Cammidge, A. El-Mansoury, P. S. Martin, and Z. Lu. *J. Mater. Chem.* Vol. 9, p. 1391, 1999.
57. N. Boden, R. J. Bushby, A. N. Cammidge, and P. S. Martin. *J. Mater. Chem.* Vol. 5, p. 1857, 1995.
58. A. Bacher, I. Bleyl, C. H. Erdelen, D. Haarer, W. Paulus, and H.-W. Schmidt. *Adv. Mater.* Vol. 9, p. 1031, 1997.
59. S. Zamir, R. Poupko, Z. Luz, B. Hueser, C. Boeffel, and H. Zimmermann. *J. Am. Chem. Soc.* Vol. 116, p. 1973, 1994.
60. D. Adam, P. Schuhmacher, J. Simmerer, L. Häußling, W. Paulus, K. Siemensmeyer, K.-H. Etzbach, H. Ringsdorf, and D. Haarer. *Adv. Mater.* Vol. 7, p. 276, 1995.
61. A. M. van de Craats, L. D. A. Siebbeles, I. Bleyl, D. Haarer, Y. A. Berlin, A. A. Zharikov, and J. M. Warman. *J. Phys. Chem. B* Vol. 102, p. 9625, 1998.
62. S. Kumar, P. Schuhmacher, P. Henderson, J. Rego, and H. Ringsdorf. *Mol. Cryst. Liq. Cryst. Sci. Tech. A* Vol. 288, p. 211, 1996.
63. Y. Wang, C. Zhang, H. Wu, and J. Pu. *J. Mater. Chem. C* Vol. 2, p. 1667, 2014.
64. S. Kumar, M. Manickam, and H. Schönherr. *Liq. Cryst.* Vol. 26, p. 1567, 1999.
65. M. Manickam, A. Smith, M. Belloni, E. J. Shelley, P. R. Ashton, N. Spencer, and J. A. Preece. *Liq. Cryst.* Vol. 29, p. 497, 2002.
66. W. Kranig, B. Hüser, H. W. Spiess, W. Kreuder, H. Ringsdorf, and H. Zimmermann. *Adv. Mater.* Vol. 2, p. 36, 1990.
67. M. Kimura, M. Moriyama, K. Kishimoto, M. Yoshio, and T. Kato. *Liq. Cryst.* Vol. 34, p. 107, 2007.
68. N. Boden, R. J. Bushby, and A. N. Cammidge. *J. Am. Chem. Soc.* Vol. 117, p. 924, 1995.
69. J. L. Schulte, S. Laschat, V. Vill, E. Nishikawa, H. Finkelmann, and M. Nimtz. *Eur. J. Org. Chem.* Vol. 1998, p. 2499, 1998.
70. H. K. Bisoyi and S. Kumar. *Chem. Soc. Rev.* Vol. 39, p. 264, 2010.
71. S. K. Varshney, H. Takezoe, V. Prasad, and D. S. S. Rao. *Mol. Cryst. Liq. Cryst.* Vol. 515, p. 16, 2009.

72. A. N. Cammidge and H. Gopee. *Liq. Cryst.* Vol. 36, p. 809, 2009.
73. S. Kumar and J. J. Naidu. *Liq. Cryst.* Vol. 29, p. 899, 2002.
74. S. Kumar and S. K. Varshney. *Liq. Cryst.* Vol. 28, p. 161, 2001.
75. H. Ji, K. Zhao, W. Yu, B. Wang, and P. Hu. *Sci. China Ser. B – Chem.* Vol. 52, p. 975, 2009.
76. K.-Q. Zhao, H. Zhou, W.-H. Yu, B.-Q. Wang, and P. Hu. *Acta Chim. Sin.* Vol. 69, p. 1895, 2011.
77. L. Zhang, H. Gopee, D. L. Hughes, and A. N. Cammidge. *Chem. Commun.* Vol. 46, p. 4255, 2010.
78. L. Zhang, D. L. Hughes, and A. N. Cammidge. *J. Org. Chem.* Vol. 77, p. 4288, 2012.
79. H. Schönherr, F. J. B. Kremer, S. Kumar, J. A. Rego, H. Wolf, H. Ringsdorf, M. Jaschke, H. J. Butt, and E. Bamberg. *J. Am. Chem. Soc.* Vol. 118, p. 13051, 1996.
80. A. Zelcer, B. Donnio, C. Bourgoigne, F. D. Cukiernik, and D. Guillon. *Chem. Mater.* Vol. 19, p. 1992, 2007.
81. V. V. Tsukruk, H. Bengs, and H. Ringsdorf. *Langmuir* Vol. 12, p. 754, 1996.
82. O. B. Akopova, M. G. Bulavkova, M. S. Gruzdev, and T. V. Frolova. *Russ. J. Gen. Chem.* Vol. 81, p. 714, 2011.
83. R. Freudenmann, B. Behnisch, and M. Hanack. *J. Mater. Chem.* Vol. 11, p. 1618, 2001.
84. D. Thevenet and R. Neier. *Synthesis* Vol. 2011, p. 3801, 2011.
85. H. Mao, Z. He, J. Wang, C. Zhang, P. Xie, and R. Zhang. *J. Lumin.* Vol. 122–123, p. 942, 2007.
86. F. Yang, J. Xie, H. Guo, B. Xu, and C. Li. *Liq. Cryst.* Vol. 39, p. 1368, 2012.
87. S. K. Pal and S. Kumar. *Tetrahedron Lett.* Vol. 47, p. 8993, 2006.
88. S. Kumar and S. K. Gupta. *Tetrahedron Lett.* Vol. 51, p. 5459, 2010.
89. S. K. Gupta and S. Kumar. *Liq. Cryst.* Vol. 39, p. 1443, 2012.
90. S. K. Gupta, V. A. Raghunathan, V. Lakshminarayanan, and S. Kumar. *J. Phys. Chem. B* Vol. 113, p. 12887, 2009.
91. B. Kumar, K. A. Suresh, S. K. Gupta, and S. Kumar. *J. Chem. Phys.* Vol. 133, p. 044701, 2010.
92. D. Hirst, S. Diele, S. Laschat, and M. Nimtz. *Helv. Chim. Acta* Vol. 84, p. 1190, 2001.
93. K. Q. Zhao, Y. F. Bai, P. Hu, B. Q. Wang, and Y. Shimizu. *Mol. Cryst. Liq. Cryst.* Vol. 509, p. 77/[819], 2009.
94. S. K. Varshney, H. Monobe, Y. Shimizu, H. Takezoe, and V. Prasad. *Liq. Cryst.* Vol. 37, p. 607, 2010.
95. S. Kumar, J. Naidu, and S. K. Varshney. *Mol. Cryst. Liq. Cryst.* Vol. 411, p. 355, 2004.
96. S. K. Varshney, H. Nagayama, V. Prasad, and H. Takezoe. *Mol. Cryst. Liq. Cryst.* Vol. 517, p. 97, 2010.
97. K. Araya, D. A. Dunmur, M. C. Grossel, G. R. Luckhurst, S. E. Marchant-Lane, and A. Sugimura. *J. Mater. Chem.* Vol. 16, p. 4675, 2006.

Supramolecular Nanoassembly and Its Potential

Alok Pandya^{*1}, Heena Goswami², Anand Lodha³ and Pinkesh Sutariya⁴

¹*Institute of life Sciences, School of Science and Technology,
Ahmedabad University, Ahmedabad, Gujarat, India*

²*Department of Science and technology, Gujarat National Law University,
Gandhinagar, Gujarat, India*

³*Department of Forensic Science, School of Sciences, Gujarat University,
Ahmedabad, Gujarat, India*

⁴*Department of Chemistry, School of Sciences, Gujarat University,
Ahmedabad, Gujarat, India*

Abstract

The principles and phenomena outlined within this chapter are based on the basic concepts of supramolecular nanochemistry. A blending of these phenomena can lead to intricate and complex designs that form the heart of the many facets of supramolecular nanoassembly, which have attracted significant attention due to implications in variety of areas such as sensing and catalysis. In sensing, detection of chemical and biological agents plays a crucial role in medicinal field, forensic, agricultural, and environmental and electronics. Thus, the challenges in development of novel detection systems have been concerned with getting better the recognition process as well as designing pioneering assemblies. Supramolecular nanoassemblies provide novel systems for the pursuit of new recognition and transduction processes, as well as increasing the signal-to-noise ratio through efficiency of the system components. This chapter provides recent research advances involving the use of supramolecule based nanoassemblies in the detection and diagnosis of analytes including metal ions, anions, large and small molecules.

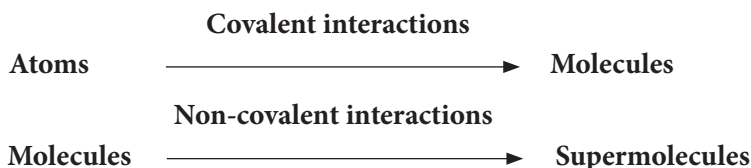
Keywords: Supramolecule, nanoparticles, calixarene, crown ether, self-assembly, detection

*Corresponding author: alokpandya20@gmail.com

8.1 Supramolecular Chemistry

Supramolecular chemistry dates back to the late 1960s, although early examples of supramolecular systems can be found at the beginning of modern-day chemistry, such as the invention of chlorine clathrate hydrate by Sir Humphrey Davy in 1810. Supramolecule chemistry has been described as “chemistry beyond the molecule”, whereas a “supermolecule” is held together by non-covalent interactions between two or more covalent molecules or ions. It has been described as “lego chemistry” in which each lego brick represents a molecular building block which is held together by intermolecular bond interactions of a reversible nature, to form a supramolecular aggregate. These intermolecular bonds interactions comprises in electrostatic interactions, hydrogen bonding, π - π interactions, dispersion interactions and hydrophobic or solvophobic effects [1].

Supramolecular Chemistry is defined as “The study of systems involving aggregates of molecules or ions held together by non-covalent interactions, such as electrostatic interactions, hydrogen bonding, dispersion interactions and solvophobic effects”.



Supramolecular chemistry is a multidisciplinary field which impinges on various other disciplines, such as the established areas of organic and inorganic chemistry by synthesizing the precursors for a supermolecule. Physical chemistry to understand the properties of supramolecular systems and computational modelling to understand complex supramolecular behaviour. A great deal of biological chemistry involves supramolecular concepts with addition a degree of technical knowledge is required in order to apply supramolecular systems to the real world, such as the development of nanotechnological devices.

Supramolecular chemistry can be divide into two broad categories; host-guest based chemistry (keeping in mind the lock-and-key principle and complementarity) and self-assembly. The dissimilarity between these two areas is a subject of size and shape. If one molecule is significantly larger than another and can enfold around it then it is termed the “host” and the smaller molecule is its “guest”, which becomes enveloped by the host (Figure 8.1). Definition of hosts-guests chemistry was given by Donald Cram and he said “The host component is defined as an organic molecule

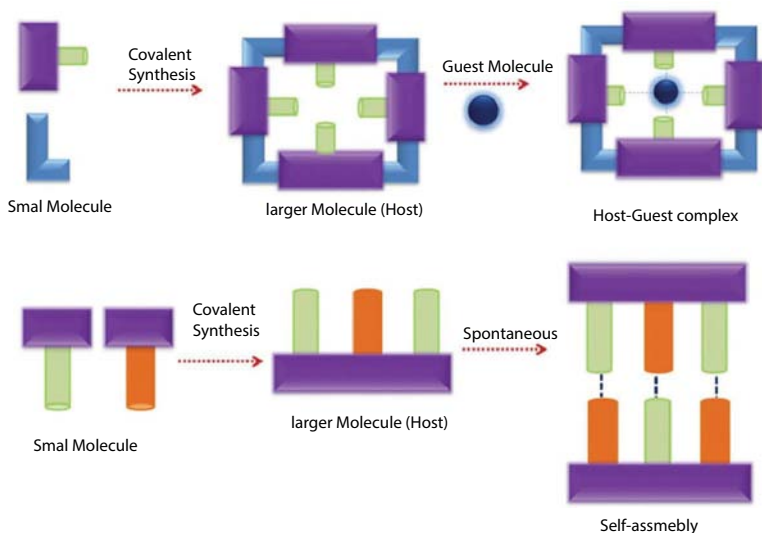


Figure 8.1 The development of a supramolecular system from molecular building blocks: (a) host-guest complexation and (b) self-assembly between complementary molecules.

or ion whose binding sites unite in the complex and the guest component is any molecule or ion whose binding sites diverge in the complex” [2]. A binding site is area of the correct size, geometry and chemical nature to interrelate with the other species.

Host-guest complexes include biological systems, such as enzymes and their substrates, with enzymes being the host and the substrates the guest. In terms of coordination chemistry, metal-ligand complexes can be thought of as host-guest species, where bulky (often macrocyclic) ligands or group act as hosts for metal cations. If the host possesses a permanent molecular cavity containing specific guest binding sites, then it will usually act as a host both in solution and in the solid state. The reasonable probability is that the solution and solid state structures will be similar to one another, whereas no significant difference in size and no species is acting as a host for another and the non-covalent joining of two or more species is termed self-assembly. Exactly, *self-assembly is equilibrium between two or more molecular components to produce an aggregate with a structure that is dependent only on the information contained within the chemical building blocks*. This process is usually spontaneous but may be influenced by solvation or templation effects.

Nature itself is full of supramolecular systems, for example, deoxyribonucleic acid (DNA) is made up from two strands which self-assemble via hydrogen bonds and aromatic stacking interactions to form the famous

double helical structure. The inspiration for many supramolecular species designed and developed by chemists has come from biological systems. The size and complexity of self-assembled capsids can readily be seen in the structure of TMV (Figure 8.2).

Supramolecular chemistry is known for high selectivity of binding site towards the guest molecule in host–guest interactions. To transpire host–guest interaction, the host molecule must acquire the appropriate binding sites for the guest molecule to bind. For example, if the host has many hydrogen bond donor functionalities such as primary ($-\text{NH}_2$) and secondary amines ($-\text{NH}-$) then the guest must ideally contain an equal number of hydrogen bond acceptor sites such as ($-\text{COOH}$, $-\text{OH}$), which are positioned in such a way that it is feasible for selective and multiple interactions between host and guest to take place. So, when host that displays a fondness for a particular guest, or family of guests, it is said to be a degree of selectivity towards these species. In terms of selectivity, the binding of one guest, or family of guests, significantly more strongly than others by a host molecule. Selectivity is measured in terms of the ratio between equilibrium constant.

Moreover, it will be exciting to look at the host–guest chemistry of anions, cations and neutral-guest species in solution. While it would be convenient to deal with these types of guest as separate topics, in reality there is a great deal of overlap, particularly with regard to solvation effects and the general design principles for creating selective hosts. Indeed, in the case of anion and cation binding, the two topics go hand-in-hand since the electrostatic charge on any ion must be balanced by a corresponding counter-ion. Thus a cation or anion host is always a host for an ion pair (either contact or solvent-separated) unless the host itself bears a formal net charge. However, there are a number of successful ion-pair binding hosts. Besides, ion-pairing can be used to great effect in phase transfer

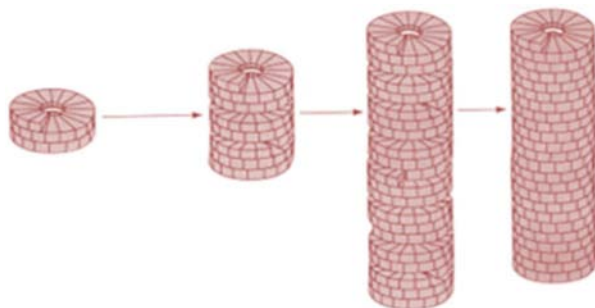


Figure 8.2 The size and complexity of self-assembled capsids of TMV.

catalysis. In general, the selective inclusion of guests by a nanomaterials based host molecule (supramolecular-nanoassembly) in solution is subject to an unprecedented level of design and control based on supramolecular principles which allows the preparation of modified systems for a wide range of applications, including sensing, food additives, drug delivery, imaging, biological modelling and in cosmetic therapy.

8.1.1 Supramolecular Interactions

Non-covalent interactions signify the energies that hold supramolecular species together. Non-covalent interactions are considerably weaker than covalent interactions, which can range between ca. 150 and 450 kJ mol⁻¹ for single bonds. Non-covalent bonds range from 2 kJ mol⁻¹ for dispersion interactions to 300 kJ mol⁻¹ for “ion-ion” interactions [3]. However, when these interactions are used in a co-operative manner a stable supramolecular complex can exist. The term “non-covalent” includes a wide range of attractions and repulsions which are summarised in Table 8.1 and will be described in more detail in the following subsections.

Ionic and dipolar interactions can be split into three categories: (i) *ion-ion interactions*, (ii) *ion-dipole interactions* and (iii) *dipole-dipole*

Table 8.1 Summary of supramolecular interactions.

Interaction	Strength (kJ mol ⁻¹)	Example
Ion-ion	200–300	Tetra butyl ammonium chloride
Ion-dipole	50–200	Sodium [15]crown-5
Dipole-dipole	5–50	Acetone
Hydrogen bonding	4–120	DNA, Spherand
Cation- π	5–80	K ⁺ In benzene
π - π	0–50	Benzene and graphite
van der Waals	< 5 but variable depending on surface are	Argon, packing in molecular crystals, Calixarene
Hydrophobic	Related to solvent-solvent interaction energy	Cyclodextrin inclusion compounds

interactions, which are based on the coulombic attraction between opposite charges (Figure 8.3). Electrostatic interactions play an important role in understanding the factors that influence high binding affinities, particularly in biological systems in which there is a large number of recognition processes that involve charge–charge interactions; indeed these are often the first interactions between a substrate and an enzyme [4].

The hydrogen bond is arguably the most important non-covalent interaction in the design of supramolecular architectures, because of its strength and high degree of directionality (Figure 8.3). It represents a special kind of dipole–dipole interaction between a proton donor (D) and a proton acceptor (A). There are a number of naturally occurring “building blocks” that are a rich source of hydrogen bond donors and acceptors (e.g. amino acids, carbohydrates and nucleobases) [5].

There are two main π -interactions that can be found in supramolecular systems, namely (i) *cation– π interactions* and (ii) *π – π interactions*. Van der Waals interactions are dispersion effects that comprise two components, namely the London interaction and the exchange–repulsion interaction (Figure 8.3). Van der Waals interactions arise from fluctuations of the electron distribution between species that are in close proximity to one another [6].

Hydrophobic effects arise from the exclusion of non-polar groups or molecules from aqueous solution. This situation is more energetically

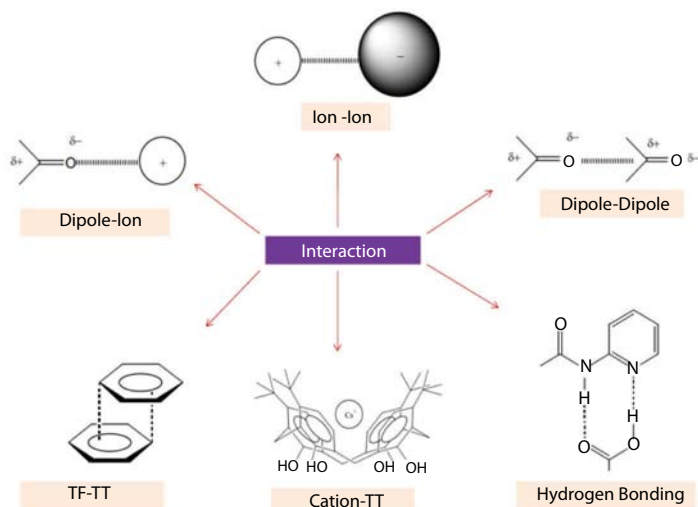


Figure 8.3 Types of supramolecular interactions.

favourable because water molecules interact with themselves or with other polar groups or molecules preferentially [7].

A union of these phenomena can lead to intricate and complex designs that form the heart of the many facets of supramolecular chemistry. In terms of “designer” host–guest chemistry, it is necessary to understand the nature of the target guest molecule. The host must be designed to be complementary to the guest in terms of size, shape and chemical properties (charge, hardness, acidity, suitable functionalities, etc.). Other factors must also be considered in the design process, such as the medium in which the binding must occur and any competing molecules which must be excluded from binding, therefore requiring a more selective host. Once all of the guest properties have been taken into consideration, the host may be designed in a specific manner, incorporating the basic phenomena outlined in this chapter, followed by a process of “trial and improvement” based on laboratory results. Moving away from the host–guest aspect of supramolecular chemistry, the underlying principles remain the same although the systems formed are often much more complex.

Supramolecular systems have a wide variety of uses, such as trapping molecules within solid state lattices, sensing and remediation of species from solution, understanding biological self-assembly and nanotechnological devices. Together, these topics form the focused concepts, which will be based on supramolecular chemistry with use of nanotechnology.

8.1.2 Types of Supramolecules

There are two major classes of host molecules: acyclic (podands) and cyclic (macrocycles, macrobicycles or macrotricycles) (Figure 8.4). Podand is an acyclic chain-like or branching host with a number of binding sites that are situated at intervals along the length of the molecule, or about a common spacer. Macrocyclic is a cyclic molecule usually with nine or more atoms in the ring and generally in supramolecular chemistry containing a number of binding sites that are arranged around the closed system. The synthesis of podand hosts is conceptually relatively straightforward and is generally achieved using conventional synthetic methods such as ether, sulphide or amide bond formation. However, the synthesis of macrocycles is a little more challenging and is accomplished by one or both of two general procedures, i.e. high-dilution synthesis and template synthesis. Further, we will focus on significant employ of macrocyclic molecules such as crown ether and calixarene on nanotechnological application.

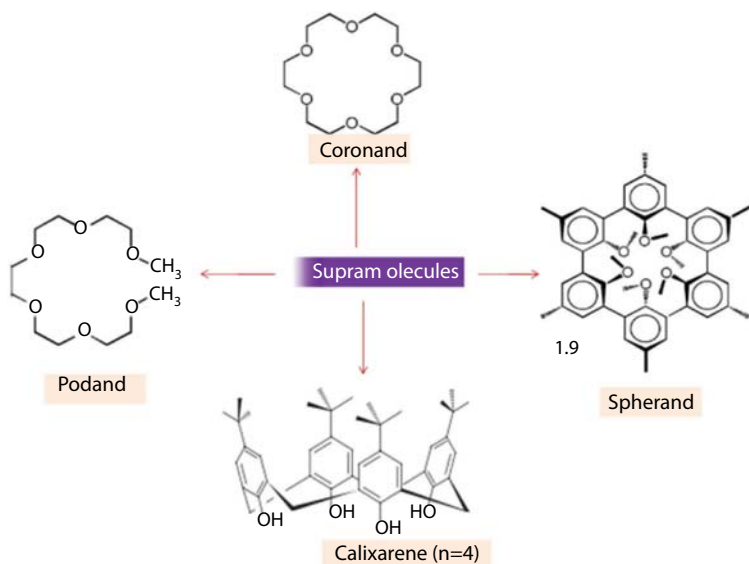


Figure 8.4 Different types of supramolecules.

8.1.2.1 Crown Ethers

The discovery of dibenzo[18]crown-6, by Charles J. Pedersen was a key step in the development of the discipline of supramolecular chemistry [9]. Dibenzo[18]crown-6 (which comprises an 18-membered ring with six oxygen donor atoms) was discovered serendipitously as a side-product during the attempted preparation of a bis(phenol) derivative. The formation of the crown ether was a fortuitous consequence of the presence of an alkali metal-containing base and hence the operation of the template effect. Pedersen *et al.* immediately began to investigate how various metal cations bound to the new macrocycle and a range of derivatives. Subsequent work has resulted in the preparation of a wide variety of analogues, including amine derivatives (azacrowns) and macrocycles with thioether binding sites (thiacrowns). Collectively, the family of crown ethers and related heteroatom donor macrocycles have been termed the corands. Shortly after the original crown ether work, Jean-Marie Lehn realised that donor atoms can be situated within a three-dimensional array to completely encapsulate the ion from the outside medium.

It was initially proposed that there is an optimal spatial fit between crown ethers and particular cations. It is true that [18] crown-6 is selective for K, whereas the larger [21] crown-7 has a higher affinity for Rb⁺ and Cs⁺ than K. However, modern understanding of these systems has

somewhat modified this simple “size fit” idea, particularly because of the flexibility of the crown ethers – their “size” is not a constant. Crown ethers have the significant property of sensing and binding to specific metal cations in complex mixtures. Subsequently, since their discovery, they have found numerous applications in science and industry and stimulated the field of molecular recognition and host-guest chemistry. This specificity of supramolecule offer new era for high sensitive detection system using nanochemistry, which will discuss further.

8.1.2.2 *Calixarenes*

The another important type of supramolecule are calixarenes, which are cyclic hosts synthesised by the condensation reaction between a *p*-substituted phenol and formaldehyde. The name comes from a Greek vase, called a calix crater, similar in shape to the bowl-like calix[4]arene. Using a number of different bases, varying thermal conditions and altering the ratio of reactants, it is possible to produce *p*-*t*-butylcalix[*n*]arenes (where *n* = 4–16), with the most common macrocycles being *n* = 4, 6 and 8. The tertiary butyl substituent blocks the para position of the phenol, hence preventing extensive cross-linking which would otherwise result in the formation of Bakelite-type phenol–formaldehyde polymers [10].

The calixarene framework is very versatile and many derivatives have been prepared by functionalising the groups on the “upper” and “lower” rims (the upper or wide rim is where the *t*-butyl substituents are located, while the hydroxyl groups are on the lower or narrow rim). By selectively changing the framework, chemists have been able to design hosts capable of binding cations, anions, neutral species or simultaneously combining different guests, such as toluene and Na [10]. The *p*-*t*-butylcalix[4]arene has been drawn in a “cone” conformation in which the hydroxy groups are pointing in the same direction. In solution, there is a high degree of rotation around the –CH groups connecting the phenol rings, giving four possible isomers of the calix[4]arenes (Figure 8.5).

Simultaneous receptors exist that can bind neutral and ionic guests. These types of receptors are large macrocycles, such as calixarenes, in which the ion is bound to the functional groups at the lower rim of the calixarene and the neutral (often solvent) molecule is encapsulated within the cavity of the bowl, e.g. tetramethoxy-*p*-*t*-butylcalix[4]arene. In the solid state, an Na ion is coordinated to the oxygen atoms of the lower rim of the calix[4]arene and the complex contains one molecule of toluene within the hydrophobic cavity [10].

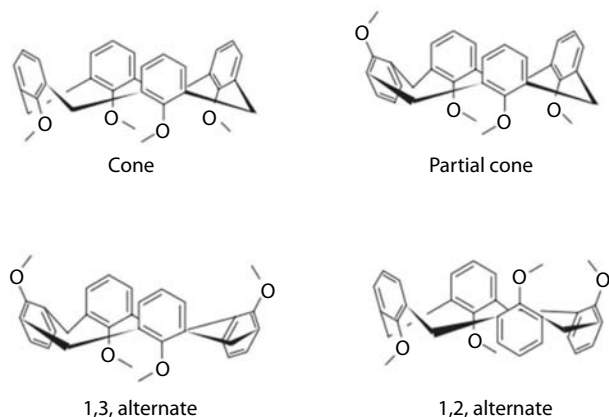


Figure 8.5 The four different conformers of calix[4]arenes.

Calixarenes are an important class of supramolecules studied widely due to their interesting properties, including the fact that they are valuable receptors besides, crown ethers, cyclodextrins, cryptands and cucurbiturils. Among several calix[*n*]arenes, calix[4]arene has been used as a popular building block due to its ability to exist in cone conformation and the ease of organic functionalization both at lower as well as upper rims [10]. Calix[4]arene derivatives are well-known for their high selectivity and binding efficiency towards ions and molecular species provided preorganized cores which are built onto the system, although these are flexible. Because of the importance in biology, environment and chemical processes, conjugates of calix[4]arene have been explored for their selective recognition of ions and molecules, and the extraction of various species [11–12]. Although there are a number of receptors including supramolecular ones in the literature, calix[4]arene-based conjugates received greater attention due to their versatility and the special features that they exhibit. All of this is further supported by the properties displayed by the calix[4]arene derivatives in the area of ion and molecular recognition, host guest chemistry, catalysis, enzyme mimics, interaction with biomolecules and ion extraction (Figure 8.6) [13–17]. All these properties gives the specificity as well as sensitivity towards guest molecule with assist of nanoassembly, which will be discuss later on.

8.2 Nanochemistry

Nanotechnology play very significant role in supramolecular based nanoassembly. Nanotechnology is the construction and use of functional

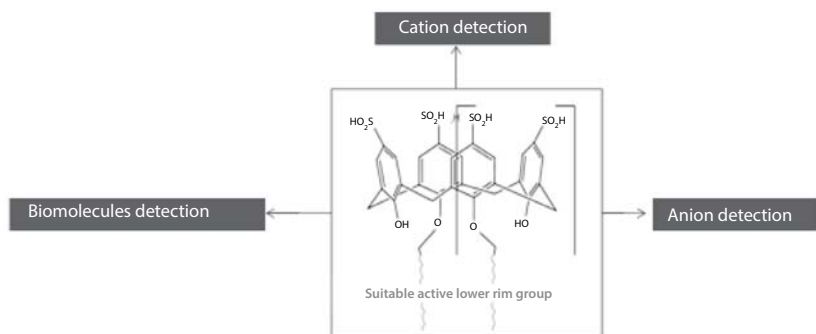


Figure 8.6 Calixarene with various applications with surface active lower rim group.

structures designed at molecular scale with at least one characteristic dimension measured in nanometres (10^{-9} m or 10\AA). Their size confers on them the ability to exhibit novel and improved physical, chemical and biological properties, phenomena and processes. When characteristic structural features are intermediate between isolated atoms and bulk materials in the range of about one to 100 nanometres the objects frequently display physical characteristics different from those evidenced by either atoms or bulk materials. Events at the nanometre scale are likely to constitute a completely new phenomenology. The properties of matter are not as predictable as those at larger scales. Changes in properties are due not only to the continuous modification of characteristics with diminishing size, but also to the occurrence of new phenomena such as quantum confinement, a typical example of which is that the colour of light emitted from semiconductor nanoparticles (NPs) depends on their sizes. Nanotechnology can provide us with unprecedented understanding of materials and devices that are useful in a variety of fields.

Back in December 1959, Nobel laureate Richard Feynman gave a visionary and now oft-quoted talk entitled “There’s Plenty of Room at the Bottom”. The occasion was an American Physical Society meeting at the California Institute of Technology. Although he didn’t intend it, Feynman’s 7,000 words were a defining moment in nanotechnology, long before anything “nano” appeared on the horizon. “What I want to talk about,” he said, “is the problem of manipulating and controlling things on a small scale.... What I have demonstrated is that there is room—that you can decrease the size of things in a practical way. I now want to show that there is plenty of room. I will not now discuss how we are going to do it, but only what is possible in principle.... We are not doing it simply because we haven’t yet gotten around to it.” The breadth of Feynman’s vision is staggering. In that lecture 54 years ago he anticipated

a spectrum of scientific and technical fields that are now well established, which includes electron-beam and ion-beam fabrication, molecular beam epitaxy, nano imprint lithography, projection electron microscopy, atom by-atom manipulation, quantum-effect electronics, spin electronics (also called spintronics) and microelectromechanical systems (MEMS). The lecture also projected what has been called the “magic” Feynman brought to everything he turned his singular intellect towards [18].

Feynman, however, did not use the term “nanotechnology” in his speech. It wasn’t until fifteen years later that Norio Taniguchi in 1974, a professor at Tokyo Science University, defined the word. “Nano-technology”, he wrote, “mainly consists of the processing of, separation, consolidation, and deformation of materials by one atom or by one molecule”. At the time that Taniguchi put forward this description, however, no one had actually seen an atom. Another seven years passed before that changed. In September 1981, two scientists at IBM’s Zürich Research Laboratory in Switzerland published a paper in *Applied Physics Letters*. In that breakthrough article, Heinrich Rohrer and Gerd Binnig described their invention of the first successful scanning tunnelling microscope (STM). Today nano-technology comprises numerous scientific disciplines, such as certain areas of cluster physics, surface physics and semiconductor physics, as well special fields of chemistry and material science. The term refers to the scale that is common to the all nano-disciplines, ranging from individual atoms with roughly 0.1 nanometres ($1 \text{ nm} = 1 \text{ millionth of a millimetre}$) to structures expanding to a size of 100 nm, which corresponds to a cluster of maximal 100,000 atoms [19].

Synthesis and self-assembly of molecular and nanoscale building blocks is the most promising route to create new macroscopic hybrid materials that contain unique functionalities. During the past decade, many molecular and nanoscale building blocks have been synthesized with different morphologies and compositions, including conjugated polymeric oligomers, inorganic nanocrystals, nanowires and nanotubes. Solvent and polymer template mediated assembly has been extensively investigated. Despite the continued advancements in various aspects, numerous challenges remain to be addressed at different stages on their way towards applications. This includes how to create functional nanoscale building blocks in a more systematic and controllable fashion, and how to engineer the interaction between the building blocks which would lead to unique self-assembly pathways [20]. This aims to stimulate interaction and build momentum among a diverse group of experts working on synthesis and directed assembly of molecular and nanoscale systems, with an ultimate goal to initiate new research directions in this field.

8.2.1 Why Nano

Nanotechnology is creating a wealth of new materials and manufacturing possibilities, which in turn will profoundly impact our economy, our environment and our society. Using nanotechnology, researchers and manufacturers can fabricate materials literally molecule-by-molecule. They can harness previously inaccessible properties of matter and “custom design” ultra-precise new structures, devices and systems with new, unique and often remarkable properties such as materials with vastly increased strength, vastly decreased weight, vastly greater electrical connectivity, or the ability to change shape or colour on demand. Nanotechnology is already enhancing everyday products such as sunscreens, golf clubs, clothing and cell phones. Within the next decade, it will have commonplace in drug therapies, water filters, fuel cells, power lines, computers, sensing, catalysis and a wide range of other applications.

By tuning the structure on the nanoscale, a useful sensing system should meet two requirements: satisfactory selective recognition sensing moiety for binding with target analytes and a measurable response process to signal the binding event. The ability of these two components is significantly related to the outcome of the detection process in terms of the response time, sensitivity, selectivity and stability of the system. Thus, the challenges in development of novel detection systems have been concerned with getting better the recognition process as well as designing pioneering assemblies. Nanoassemblies provide novel systems for the pursuit of new recognition and transduction processes, as well as increasing the signal-to-noise ratio through efficiency of the system components. So, combinely, supramolecular based nanochemistry will facilitate to provide significant detection system.

8.2.2 Chemical Approach of Nanomaterials

Traditionally, nanotechnological devices have been prepared by the breakdown of materials using techniques developed by solid state physicists. For example, a large block of silicon wafer can be reduced to smaller components by cutting, etching and slicing down to a desired size or shape. This is known as the top-down approach. Alternatively, the synthesis of nanostructures and nanomaterials through the utilisation of supramolecular and biomimetic materials is known as the bottom-up approach and forms the foundations of nanochemistry. Nanomaterials synthesised from the bottom-up method have novel physico-chemical proprieties that differ from the bulk material and can engender the emergence of novel characteristics. Both the top-down and bottom-up approaches to nanotechnology

have interfaces with biology and biomimetic chemistry, giving rise to the field of nanobiology.

Bottom-Up Approach: The synthesis of nanoscale structures and devices by chemically building up from the molecular level.

Top-Down Approach: The use of micro fabrication techniques that reduce bulk material into smaller components to form nanoscale features or objects.

8.2.2.1 *Colloidal Nanoparticles and Its Surface Modification*

NPs possess several distinctive physical and chemical attributes that make them promising synthetic scaffold for the creation of novel chemical and biological detection systems. Last few years, nanostructured materials, such as noble metal NPs, quantum dots and magnetic nano particles, have been employed in a broad spectrum of highly innovative approaches for assays of cations and anions detection, small molecules and protein and nucleic acid biomarkers [21]. In addition to the large surface-to-volume ratio that favours efficiency, NPs possess unique optical, electronic and magnetic properties depending on their core materials. Furthermore these properties of the nanomaterials depend on their size and shape, and vary with their surrounding chemical environment. Additionally, NPs can be formed with a wide range of small organic ligands and large bio-macromolecules by using various techniques of surface modification. Each of these capabilities has allowed researchers to design novel detection and diagnostic systems that offer significant advantages in terms of sensitivity, selectivity, reliability and practicality. This chapter provides recent research advances involving the use of nanoassemblies in the detection and diagnosis of analytes including metal ions, anions, amino acids, small molecules.

Colloidal NPs, e.g. inorganic nanocrystals, are very small, nano-scale objects dispersed in a solvent. Already synthesized of gold at the times of Faraday, they generated ever-increasing interest since with the development of high resolution transmission electron microscopy, the ability to synthesize those particles of desired size in a controlled fashion and finally the advent of a broad range of different material systems that have come up in the last few decades. Depending on the material they consist of, NPs can possess a number of different properties such as high electron density and strong optical absorption (e.g. metal particles), photoluminescence in form of fluorescent NPs [22]. NPs with those properties originating from the core material are then used as building blocks for larger, more complex structures, or for hybrid materials, e.g. in polymer blends. Besides this, so-called biological applications have gained in importance because they combine the unique properties of inorganic, synthetic NPs with complex biomolecules or biological systems such as cells or even organisms; the

most prominent application being labelling for microscopy. Naturally, surface modification starts with an existing surface and yields a new surface with possibly new properties, the area of surface modification taking place between the particle synthesis and final possible applications.

The ligand molecules bound to the NPs surface not only control the growth of the particles during synthesis, but also prevent aggregation of the NPs. The repulsive force between particles can in principle be due to electrostatic repulsion, steric exclusion or a hydration layer on the surface. Depending on the particle system, i.e. the core material, and the solvent in which the particles are dispersed, the choice of the right ligand might yield to stable particles. First the ligand molecules have to be bound to the particle surface by some attractive interaction, either chemisorption, electrostatic attraction or hydrophobic interaction, most commonly provided by a head group of the ligand molecule. Various chemical functional groups possess a certain affinity to inorganic surfaces, the most famous example being thiol to gold. Figure 8.7 displays some commonly used hydrophobic ligand molecules drawn to scale along with a particle of 5 nm diameter.

In aqueous solution, the ligand NPs interaction is basically the same but a number of different effects important for stability arise. Most commonly, hydrophilic NPs are stabilized by electrostatic repulsion by the equally charged ligand molecules on the particle surface. However, in presence of high salt concentration the electric field is shielded and the NPs can come close to each other until eventually attractive forces cause the particles to agglomerate, as e.g. induced dipole interaction, van-der-Waals force, or hydrogen bonds. Thiol groups are considered to show the highest affinity to noble metal surfaces, in particular to gold (~ 50 kcal/mol) [23].

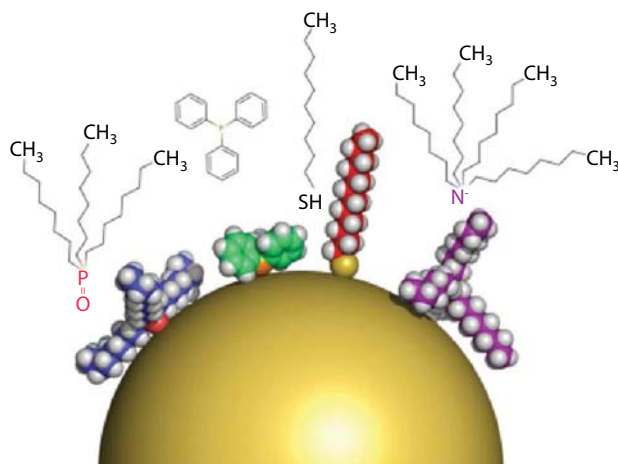


Figure 8.7 NPs of 5 nm core diameter with different hydrophobic ligand molecules.

While this binding is often termed “chemisorption”, sometimes also noted as covalent bond, the exact processes and the microscopic nature are still subject to research and discussion. Contrary to the case of self-assembled monolayers (SAMs) on a well-defined planar crystal face, the surface of a NPs consists not only of a number of different crystal facets but also to a large part of edges, terraces and vertices, resulting in binding sites with different affinities for the ligand molecules. This complicates the characterization of the ligand shell compared to “classical” SAMs, like the well-studied Au-thiol system [24]. Metal NPs, with diameters ranging roughly between 1 and 100 nanometres, are natural bridges between molecules and extended solids. They are complex many-electron systems, where reduced sizes and quantum confinement of electrons and phonons give birth to fascinating new effects, potentially tunable with particle size and shape. Metal NPs attract strong interest both because they open up a new field in fundamental science and because of their potential technological applications. They are convenient components for sub-wavelength optical devices, for nonlinear optics, for optical data storage, for surface-enhanced spectroscopy and catalysis, for biological labelling and sensing, and even for cancer therapy. So, functionalization via suitable linker to supramolecular assembly is important aspect of nanochemistry, which will be discuss further.

8.2.3 Gold and Silver Nanoparticles

Nowadays, metal NPs supported supramolecules have been focused in the direction of attaching with many ionophores and employed as a sensor. The introduction of recognition elements onto monolayer-protected cluster (MPC) surfaces has enabled the developed of nanoscale devices with potential applications as sensors, switches and new materials having tunable properties. A remarkable and promising path for analyte detection arises from the unique size and shape dependent optical, magnetic and electronic properties of nanomaterials. For instance, spherical gold NPs exhibit a variety of colours in solution from brown to violet as the core size increases from 1 to 100 nm. Spherical AuNPs usually exhibit an intense absorption peak from 510 to 560 nm, corresponding to the surface plasmon band of nanometer scale noble metal NPs [24]. This absorption arises from the collective oscillation of the valence electrons due to resonant excitation by the incident photons. Surface plasmon resonance (SPR) is absent in both small NPs ($d < 2$ nm) and bulk materials. It is strongly reliant on the particle size. Not only to the NPs size, the SPR is also sensitive to the surrounding environment such as ligand, solvent

and temperature. Most importantly, SPR is strongly dependent on the proximity to other NPs. Thus, clustering of AuNPs of appropriate sizes ($d > 3.5$ nm) evokes interparticle surface plasmon coupling, resulting in a significant red-to-blue bathochromic shifting (to ca. 680 nm) and broadening of the SPR band that can be readily observed by the naked eye at trace level concentrations.

The most common NPs are metallic gold NPs prepared by a process called “arrested nucleation and growth”. This occurs from the reduction of HAuCl_4 by sodium citrate or sodium borohydride [25]. Citrate is a very common reducing agent and has also been used to prepare other metal NPs, such as Ag from AgNO_3 , Pd from H_2PdCl_4 and Pt from $\text{H}_2\text{Pt}[\text{Cl}]_6$.

8.2.4 Self-Assembled Monolayer

Self-assembly can be used to form ordered two-dimensional monolayers by chemisorption of appropriately functionalised molecules onto substrate surfaces. Monolayers are typically formed by amphiphiles comprising long alkyl chains in conjunction with a polar head group, or long-chain molecules bearing a functional group at one end capable of surface binding. The resulting stable, ordered and dense layers have applications in anti-corrosion and wear protection, for example. Much of the early work on SAMs was carried out utilising thiols on gold surfaces, and these systems continue to be widely studied. The gold–thiolate interaction has approximately the strength of a hydrogen bond and hence the thiols have considerable surface mobility, contributing to the self-assembly process. However, there are many other systems that form SAMs, for example, siloxanes on hydroxylated surfaces and fatty acids on silver and alumina surfaces.

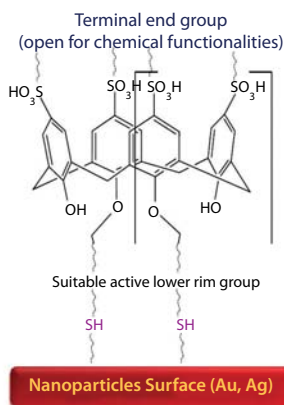
Thiol SAMs are the most common and extensively studied monolayers. They generally involve molecules appended with a thiol group at one end interacting with a gold surface. The films are relatively straightforward to synthesise. A well-polished gold substrate is immersed into a solution of thiol and the thiols rapidly attach randomly to the substrate. Over time, the thiols align themselves onto the surface forming a monolayer according to self-assembly principles. The advantage of this technique is that no double-layer formation is observed; therefore, high quality monolayers result if the substrate is allowed to sit in the solution for a few days. Another attractive property of thiol SAMs is the possibility of further derivatization of the monolayer once it has formed. Many functional groups can be appended at the end of the thiol, which leads to the use of thiol SAMs in molecular recognition, as bio-membrane mimics for modelling the interaction of

biomolecules at different surfaces, the study of enzymes on surfaces, pH sensing devices and the preparation of molecular wires. A similar technique is used to prepare thiol-coated NPs, e.g. as sensors

This chapter further focus on the introduction to nanochemistry from the view of the supramolecular chemist interested in synthesising and studying chemical aggregates on the nanoscale with great potential for the development of nanosensors which is called as “**supramolecular nanoassembly**”.

8.3 Supramolecular Nanoassembly

During the last few years, amphiphilic supramolecules such as crown ether, calix[n]arenes ($n = 4,6,8$) and especially water-soluble calixarenes have been the subject of growing interest in the chemical and biological domain [26–27]. The different studies concerning the specific interactions of calixarenes and crown based nanoassembly with molecules such as inorganic ions, peptides, polar or neutral organic molecules and biomolecules, including proteins and lipids have lead to the numerous applications of cation receptors, anion receptors, biomolecules receptors and pesticides receptor. Herein, further will be emphasized on recent advances on development of supra-nanoassembly and its sensing application.



Schematic of Supramolecules based nanoassembly for various applications

8.3.1 Cations Receptors

Cation complexes play an essential role in many biological systems; large quantities of sodium, potassium, magnesium and calcium ions, in particular,

are all critical to life. For example, a concentration gradient of K^+ and Na^+ across biological cell membranes is vital to nerve signal transduction. Menon *et al.* established [29] facile strategy, after series of experiments to prepare gold NPs (AuNP) crown ether assemblies by the generation of strongly binding dithiocarbamate (DTC) modified benzo-15-crown-5 for recognition of potassium ion which triggers particle aggregation via simple host-guest interactions and induces colorimetric, naked eye easy-to-measure colour changes (Figure 8.8). In which they have enhanced the stability of AuNP-DTC-CE assemblies by facile generation of a DTC ligand by reacting CS_2 with secondary amine modified crown ether. This strategy was not only increased the robustness of the AuNP-crown ether assembly but also it was inexpensive and less tedious as compared to the procedure reported by Chen and co-workers [29]. After the series of experiments they reported that there is no sign of aggregation between pH range 6-10 up to months and its stable at elevated temperature too after the storage of several months which indicates surface plasmon band wavelengths remained the same. Menon *et al.* reported that the crown capped gold NPs are very miscible with water and colloidal solutions appear red with absorption maxima at 522 nm, which shifts only slightly, within a few nanometres from that of the gold NPs at 528 nm. This novel approach of recognition physiological important potassium ion was further experimented over human blood serum sample with excellent visual detection limit of crown capped gold NPs.

Another example of supramolecule based nanoassembly is detection of iron. Iron metabolism is exquisitely regulated by all organisms from lower species to higher organisms. The various environmental factors which influence growth, such as the availability of nutrients like iron which enhances the physiological activities, profoundly affect gene expression in prokaryotes and are merely important in the metabolism of bacteria in their habitat. Various research groups have worked on FRET based sensors which are created in the form of a dyad or a triad in which the donor and the acceptor are covalently linked through a spacer with a certain length.

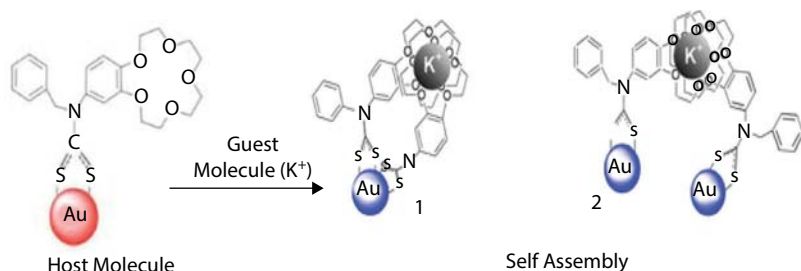


Figure 8.8 Schematic of Potassium recognition using AuNP-DTC-CE assemblies.

However, FRET-based sensors can also be created within colloidal NPs, such as capped quantum dots, dye doped silica and polymeric NPs, and these particle based FRET systems are to be used in biomedical and environmental applications, so it is essential that they are nontoxic and water-soluble to prevent aggregation, precipitation and should have a substantial photoluminescence quantum yield in water. To improve sensitivity and specificity, Menon *et al.* [30] demonstrate, a novel alternative strategy for constructing calix[4]arene modified silver NPs for detection of iron with excellent sensitivity at the nano level and selectivity over the other metals and biomolecules. So, new promising approach has been designed using a Ag NP based colorimetric sensing system (ANCSS) which forms a calix[4]arene-ethoxythiol functionalized Ag nanoprobe complex (CX-ET-AgNPs) for the detection of ferric ion in water (Figure 8.9).

Introduction of moieties containing O, N and S on the calixarene brings the selectivity towards transition metal ions. Appropriate functionalization can improve the solubility and can extend its range of applications in the ion and molecular recognition properties of the 1,3-disubstituted derivative of calix[4]arene. Thus, when it investigated spectrophotometrically, experimental observation indicated that the bathochromic shift is observed during interaction of the pSTEC₄-AgNPs with Fe³⁺ which is due to the existence of the calixarene manifold binding site complex with Fe³⁺. Plasmon absorption peak was red-shifted proportionally up to nanomolar level ferric ion, and good correlation was obtained between the wavelength shift and concentration pointing out the feasibility of the method for the quantitative measurement of ferric ion in human body fluid. The

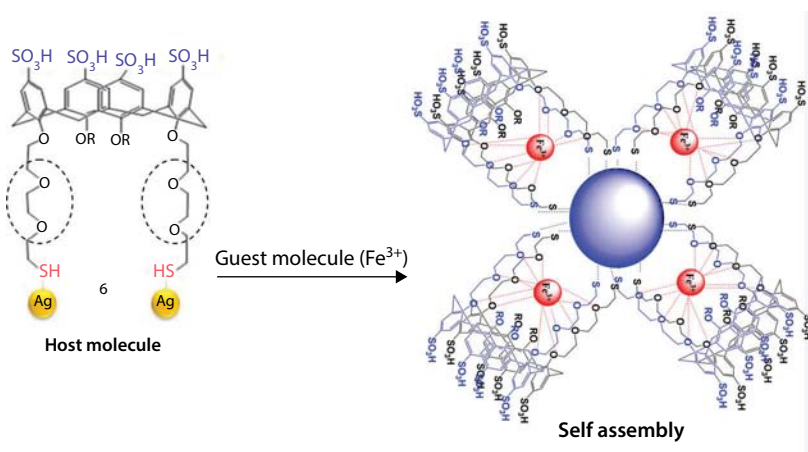


Figure 8.9 Schematics of the ferric ion sensing with pSTEC₄ modified AgNPs via nanoaggregation due to specific interaction between pSTEC₄-AgNPs and ferric ion.

developed pSTEC₄-AgNPs based human heme biosensor was proved to be simple, reliable and accurate. This method can also indirectly assist to medico-legal system for the routine investigation process.

8.3.2 Anion Receptors

Sulphide anion (S^{2-}) exists widely in industrial locations such as tanneries, food processing plants, petroleum refineries, and paper and pulp manufacturing plants, where it is either used as a reactant or is produced as a by-product of manufacturing or industrial processes. Sulphide is a highly undesirable contaminant in effluents because of its high toxicity to living organisms, its capacity to remove dissolved oxygen and its capability to produce hydrogen sulphide. The risk of S^{2-} toxicity is allied with exposure in a number of occupational settings. Continuous and high concentration contact of S^{2-} can cause various physiological and biochemical problems. Menon *et al.* [31] developed an advanced and proficient colorimetric sulphide sensor based on SAM protected gold nano cluster (MPC) of calixarene dithiocarbamate (CX-DTC) ligand assembly, which has been designed and synthesized by generation of strongly binding DTC (Figure 8.10). This molecular receptor competently and selectively recognizes sulphide ion via H-bonds. This sensor was based on DTC assembly of 25,27-bis(ethyleneaminecarbonylmethoxy)-26,28-dihydroxy-*p*-sulphanatocalix[4]arene (pSC₄A) and gold NPs.

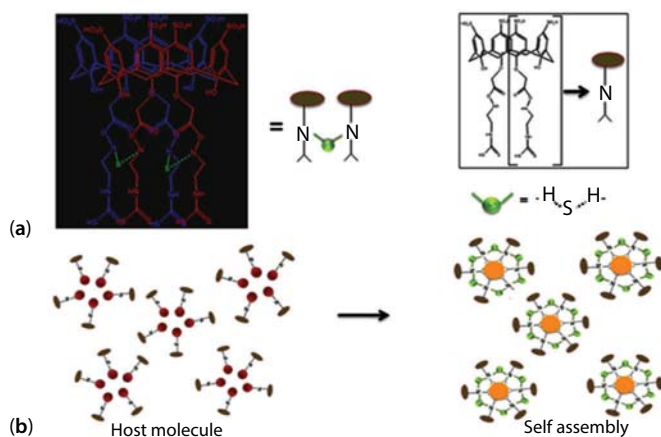


Figure 8.10 Schematics of the sulphide sensing with pSC₄A-DTC modified AuNP: (A) specific intramolecular hydrogen bonding between pSC₄A (-NH) and other pSC₄A (-NH), (B) sulphide induced aggregation of pSC₄A-DTC modified AuNP.

According to the proposed mechanism, the sulphide ion recognition triggers particle aggregation through ($-N-H...S$) hydrogen bonds and provides an easy to measure naked eye colorimetric colour change. However, no significant colour change was observed by the addition of sulphate, chloride, fluoride or bromide. This technique demonstrates a simple and relatively free from interference of closely associated ions method with successful application for the determination of sulphide from real samples of spiked water and leather waste water.

8.3.3 Biomolecule Receptor

The concept of supramolecular based nanosensors was further implemented for detection of biomolecule. It is well known that amino acids play a vital role in a variety of important cellular functions and have attracted attention because they are involved in numerous important functions in metabolism and cell regulations. Importantly, three amino acids (arginine, histidine and lysine) are essentially needed for infants and human body. Traditionally, amino acids are quantified by using derivatization procedures coupled with various chromatographic techniques, which requires specific organic molecules for their derivatization and extremely time consuming. Menon *et al.* [32] reported lys, arg and hist recognition by novel p-sulfonatocalix[4]arene-thiol functionalized gold NPs. This report mainly focused on the synthesis of very stable, chemically versatile water soluble novel 25,27-bis(12-thiol-1-oxydodecan)-26,28-dihydroxysulfonatocalix[4]-arene ligand, and its application as amino acids detection probe. In their experiment, it is investigated the molecular recognition ability of novel calix-capped gold NPs, 11 different aqueous solutions of amino acids in PBS buffer were added to calix capped gold NPs. Half an hour later, only the solutions containing lysine, arginine or histidine had changed colour from red to purple with changes in UV-vis spectrum at 524–550 nm region indicating broadening of the surface plasmon band due to aggregation, which indicated that the calix-capped gold NPs responded selectively to lys, arg and his but not for other amino acid. The proposed mechanism demonstrated by Menon *et al.* pSC4T possesses an electron-rich cyclic cavity that can attract the positively charged NH_3^+ of lys, arg and his. In the case of histidine, pSC₄T can bind the imidazole via host-guest interactions (Figure 8.11).

These interactions between one amino acid molecule and two calix-modified gold NPs tend to aggregate the assemblies more easily than the other amino acids tested in their experiments. The method was supported after the evaluation through the UV-vis, FT-IR and TEM. Further it has

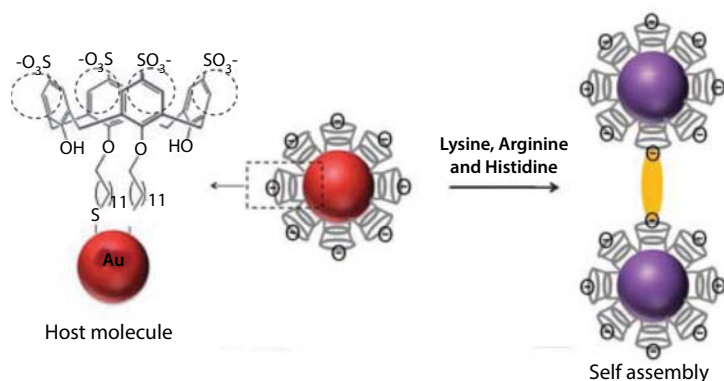


Figure 8.11 A schematic representation of the amino acid induced aggregation of calix-capped gold NPs.

been confirmed that in an aqueous environment, the calixarene retains its molecular recognition properties, which was utilized to bind the MPC selectively to amino acids. It has been established that MPCs can also act as readily detectable markers of specific recognition events demonstrating a high potential for simple, necked eye colour-based colorimetric diagnostic tests, for example, those required for many routine bio-analytical applications.

Another analogous conception was utilized for detection of sugar molecule which is essential biological molecules and simultaneously, it is crucial that blood sugar levels are kept as close to normal as possible and hence, there is a high demand for blood glucose monitoring. Significant efforts have been made in producing reliable glucose sensors for *in vitro* or *in vivo* applications, [33] which also play elemental roles in controlling an individual's birth, differentiation and immunity. Diabetes is a widespread ailment that occurs due to large deviation of insulin in body. More than 220 million of world's population were affected with diabetes in year 2011. Diabetes can damage heart, nerves, eyes, kidneys and blood vessels. Most of these methods are based on the immobilization of the enzyme glucose oxidase (GOx) on a solid substrate, which relies heavily on the properties of the supporting materials. They should provide a good environment for enzyme immobilization and should be able to maintain their biological activity. Menon *et al.* [34] developed a new, advanced, simple and non-enzymatic approach for the colorimetric detection of glucose, based on calix[4]arene/phenyl boronic acid (CX-PBA) functionalized gold NPs (AuNPs) (Figure 8.12). This molecular receptor proficiently and selectively recognizes glucose due to its ability to reversibly bind diol-containing compounds. The assembly

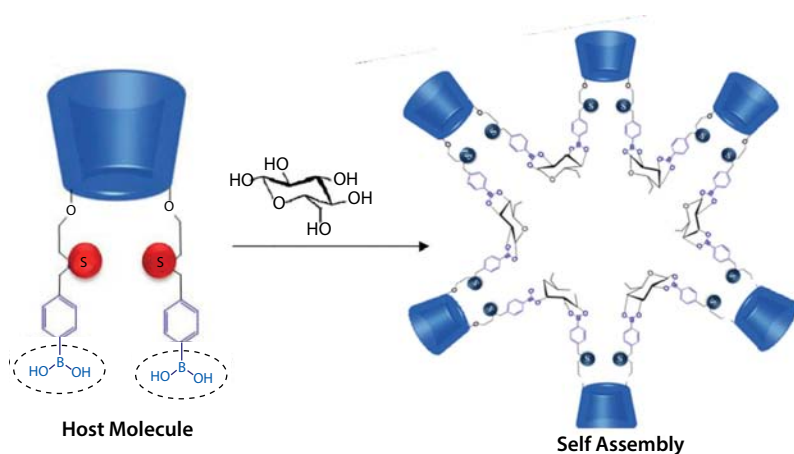


Figure 8.12 Schematics of the glucose sensing with pSC₄BA modified AuNPs via nanoaggregation due to specific interaction between pSC₄BA-AuNPs and glucose.

was characterized by transmission electron microscope (TEM), dynamic light scattering (DLS), UV-Vis, FT-IR, ESI-MS and ¹H NMR spectrometry, which demonstrated the higher binding affinity for glucose via boronic acid–diol interaction with excellent discrimination against other saccharides. The biosensor has been successfully applied to estimate the glucose in human blood serum samples and the results were compared with automatic analyzer. With the advantages of high sensitivity, selectivity and low sample volume, this method is potentially suitable for the on-site monitoring of glucose. The proposed approach seems to be significant for the rural population in third world countries.

8.3.4 Pesticide Detection

Organophosphorus (OP) pesticides are used widely for agriculture, vector control and domestic purposes. Despite the apparent benefits for these applications, acute OP pesticide poisoning is an increasing worldwide problem, particularly in rural areas. OP is among the most acutely toxic pesticides sold today, with most of these chemicals classified by the Environmental Protection Agency (EPA) as toxicity class I (highly toxic) or toxicity class II (moderately toxic). In order to explore sensing properties of nano-supramolecular assemblies.

Menon *et al.* [35] further extend the application of water-soluble calix[4]arene modified AgNPs assembly for the molecular sensing of organic molecule like insecticide. In this exploration, a new *p*-sulphonato

calix[4]resorcinarene (pSC_4R) compound were synthesized and modified with silver nano particle (pSC_4R -AgNPs) as a powerful sensing tool for colorimetric sensing of dimethoate with high sensitivity and selectivity at low concentrations. pSC_4R can bind the amino residues and two thiol linkage of dimethoate through host-guest interaction such as electrostatic forces between electron rich cavity of pSC_4R and electron deficient dimethoate (Figure 8.13). These interactions between dimethoate and two pSC_4R -modified AgNPs, results in pSC_4R -AgNPs tending to aggregate more easily than the other pesticides tested. Due to absence of any electron deficient group in other pesticide, do not show the aggregation. The different results for pSC_n -AgNPs are due to the different binding response of the pSC_n modifier to dimethoate. In comparison with pSC_4 , pSC_8 does not present a predefined host cavity due to the greater conformational flexibility, which means that pSC_4R -AgNPs cannot be induced into aggregation by dimethoate through host-guest interaction. The pSC_4R -AgNPs also act as readily detectable markers of specific recognition events demonstrating a high potential for simple, colour-based diagnostic tests, for dimethoate which is required for many routine environment applications

8.3.5 Other Nanomaterials Supported Supramolecules

Vitamin K_3 (VK_3) is a synthetic fat soluble vitamin which is used for blood coagulation and in the bone mineralization process. In recent years, it has drawn huge attention due to its remarkable anticancer properties. $2VK$ contains a naphthoquinone ring, and its basic structure is 2-methyl-1,4-naphthoquinone. These vitamins are named according to their side chains by

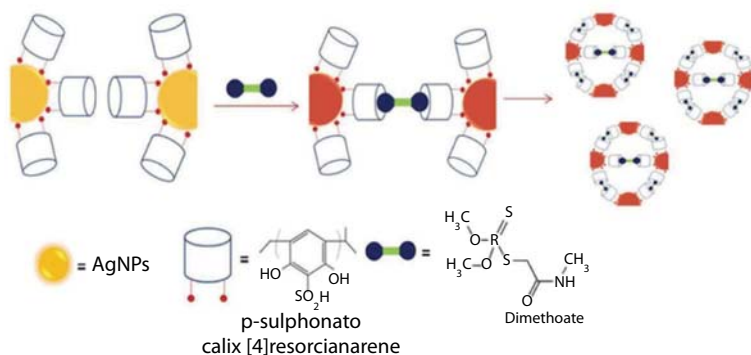


Figure 8.13 Schematic representation of the dimethoate inclusion complex with pSC_4R AgNPs.

forming new derivatives. VK_3 is obtained synthetically without a side chain and is named menadione. The physiological activity of VK is the strongest among the K group vitamins. It shows antitumor and anti-inflammatory activity because of the quinone group in its structure. In a series of in vitro and in vivo animal studies, VK_3 showed significant anti-neoplastic activities against both malignant cell lines and a variety of human tumour cells. Menon *et al.* [36] developed a highly sensitive and selective optical nanoprobe for menadione (VK_3) determination. That sensor was based on FL quenching by VK_3 through host-guest interaction with “cup type” calixarene coated ZnSQDs (Figure 8.14) It is known that a calix can provide accommodation to guest molecules in the cavity, when they are added in solution resulting in an inclusion complex. The reaction between pSC[4]A and ZnSQDs gave rise to a cup type cavity and led to the assembling of an inclusion complex with VK_3 . The remarkable blue shift (7 nm: 482/476 nm) in the FL spectra at a higher concentration of VK_3 also gives an indication that VK_3 was located in a more hydrophobic environment, which was supported by the inclusion of VK_3 within the aromatic cavity of pSC[4]A. In order to investigate the main driving force for the interaction between pSC[4]A-ZnSQDs and VK_3 , the effect of NaCl ionic strength on the inclusion process was examined where, the NaCl concentration is 0.5 mol L^{-1} , the FL intensity of pSC[4]A-ZnSQDs and VK does not undergo significant change, which demonstrated that the inclusion process was not affected by the ionic strength of NaCl. This means that electrostatic interaction is not the main driving force for the interaction between pSC[4]A-ZnSQDs and VK. Therefore, hydrophobic interaction was

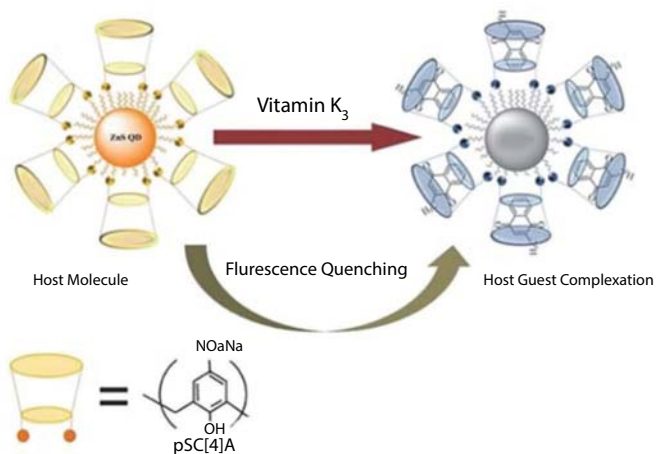


Figure 8.14 Schematic representation of a VK_3 inclusion complex with pSC [4] A-ZnSQDs.

considered to play the main role in the formation of the host–guest inclusion complex. It also have been demonstrated the stability in the effect of pH in the range of 2.0–12.0 in order to select the optimum conditions for the analysis. The study shows that the FL intensity of pSC[4]A-ZnS QDs was almost stable in the pH range 5.0–10.0. The application of this probe in real samples was investigated by the analysis of a VK_3 containing commercial preparation with the standard addition method. It was also confirm the selectivity and ensure that there was no interference by the accompanying compound, indicating the specificity of the probe. The simple, selective, sensitive and trace level detection approach of this method holds promise for application in future trends in biology.

Li and Qu synthesized [37] CdTe QDs nanocrystals in sol–gel-derived composite silica spheres coated with calix[4]arene and their applications as fluorescent probes for the detection pesticides. CdTe QDs nanocrystals in sol–gel-derived composite silica spheres were prepared from CdTe QDs via the Stober method [38]. TEM images and PCS measurements showed the average sizes of $SiO_2@CdTe$ NPs and $@SiO_2@CdTe$ NPs were approximately 70 and 100 nm, respectively. Fluorescence titrations (512 nm) of $SiO_2@CdTe$ NPs and functionalized $@SiO_2@CdTe$ NPs were conducted in water at pH = 8.0 with various pesticides (parathion-methyl, methomyl, optunal, fenamilthion and acetamprid) to evaluate their selectivity of complexation. Methomyl was shown to be the pesticide providing the most substantial increase in fluorescent intensity. This was attributed to the fact that the cavity of synthesized calix[4]arene was not sufficiently large to accommodate aromatic pesticides, as well as its preference for the linear methomyl. A detailed study conducted with methomyl indicated a complexation mechanism involving the filling of the calix cavity by methomyl with a conformational rigidification of the surface substituents suppressing the quenching pass to the medium by effective cone protection, giving rise to an increase in the fluorescent intensity, as illustrated in Figure 8.15.

A similar system was reported by Li *et al.*, [39] a simple, rapid ligand exchange route for the preparation of highly fluorescent, stable and water-soluble CdSe QDs was obtained using sulfanato-calix[4]arene rather than the original TOPO ligands. The ligands were found to exert a profound effect on the luminescence response of QDs to amino acids. The sulfanato-calix[4]arene coated CdSe QDs were sensitive to methionine. On the other hand, sulfanato-calix[4]arene derivative coated CdSe QDs turned out to be sensitive to phenylalanine. To demonstrate the detection capability of these new probes, sulfanato-calix[4]arene coated CdSe QDs were employed to detect methionine and phenylalanine in physiological buffer solution. Under optimal conditions, the relative fluorescence intensities of

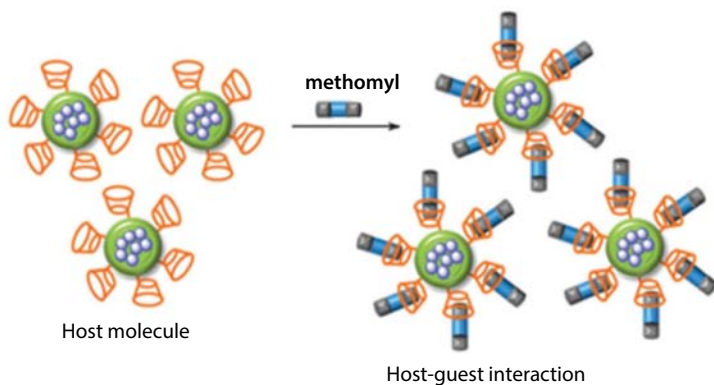


Figure 8.15 Schematic illustration of a possible structure of the functionalized @SiO₂@CdTe NPs-methomyl.

the sulfanato-calix[4]arene coated QDs increased in a linear fashion with increasing concentrations of amino acids. The enhancement of luminescence was proposed to be attributable to a complexation of amino acids in the cavity of sulfanato-calix[4]arene (Figure 8.16).

8.4 Conclusion and Future Prospects

The development of novel methods in chemical, biological and forensic fields that permit the real-time detection of different compounds with high accuracy, precision, reproducibility, low molecular detection limits and affordability is a profound challenge. This is probable, in particular, by virtue of the combination of the optical properties of nanostructured metals and the advanced chemical properties of self-assembled calixarenes. On the basis of the concepts and principles of supramolecular chemistry, particularly molecular recognition, self-assembly and nanomaterials, we have collected in this chapter, the nanoscaled construction and application of NPs based on supramolecule and different surfaces: gold, silver and quantum dots. Moreover, the host-guest interaction mechanism leading to the formation of a complex between functionalized NPs and different substrates has been highlighted. Several perspectives can be drawn in regard to the development of optical host-guest systems of supramolecule on the surfaces of NPs.

Chiral surface plasmon resonance has been previously described by the postsynthetic modification of gold particles with calixarene enantiomers, which may lead to the optical recognition of a chiral object. More

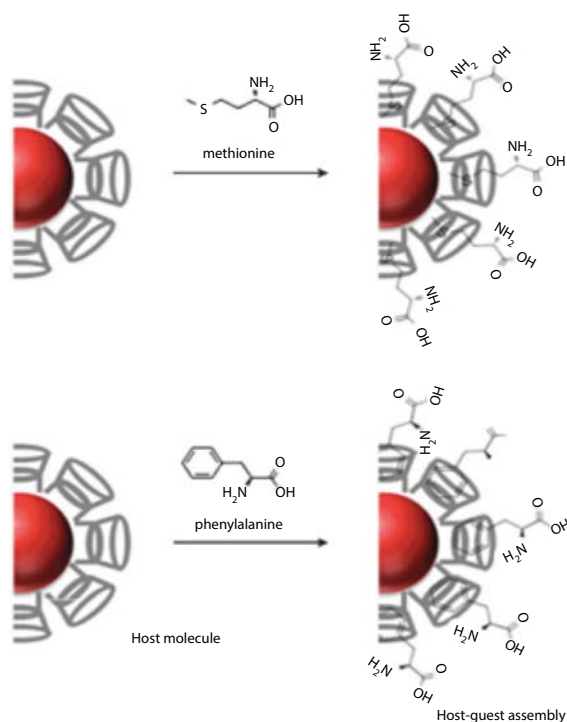


Figure 8.16 A schematic illustration of the possible mechanisms of methionine and phenylalanine enhancing the fluorescence of sulfonatocalix[4]arene coated CdSe QDs.

generally, plasmons in strongly coupled metallic nanostructures may be used to enlarge the panels of this type of optical system. New mineral solid surfaces have been reported which may be used as new supports, such as mesoporous non-oxide materials. In another field, hybrid materials could be prepared from polymers presenting channelled structures that may prove useful in the formation of organized molecular surfaces.

Innovations in the applications of supramolecular based nanoassembly in diagnostics are needed for the highly efficient detection of marker proteins. The potential applications of supramolecules derivatives displaying inhibition properties towards alkaline phosphatases from bovine intestine mucosa and shrimp and human placenta would indeed encourage supramolecules chemists to broaden their research areas. Moreover, the involvement of supramolecule based nanoassembly as synthetic ionophores in the challenging field of trans membrane ion transport has broadened their area of applications in biotechnology. Apart from their

binding ability to many organic and bioorganic molecules, the functionalized supramolecules also act as the antibacterial, antiviral and anticancer agents demonstrating their potential applications in the pharmaceutical industry. However, a more elaborated study on the modified supramolecular based nanoassembly derivatives is necessary for their real time monitoring of biomarkers and induction in the drug development and drug discovery.

References

1. D. H. Williams and M. S. Westwell, 'Aspects of weak interactions', *Chem. Soc. Rev.*, 1998, 27, 57–63.
2. D. J. Cram, 'Preorganization – from solvents to spherands', *Angew. Chem., Int. Ed. Engl.*, 1986, 25, 1039–1134.
3. G. A. Jeffery, *An Introduction to Hydrogen Bonding*, Oxford University Press, Oxford, UK, 1997.
4. E. V. Anslyn and D. A. Dougherty, *Modern Physical Organic Chemistry*, University Science Books, Sausalito, CA, USA, 2006, pp. 162–168.
5. C. Laurence and M. Berthelot, 'Observations on the strength of hydrogen bonding', *Persp. Drug Disc. Des.*, 2000, 18, 39–60.
6. C. A. Hunter and J. K. M. Sanders, 'The nature of π - π interactions', *J. Am. Chem. Soc.*, 1990, 112, 5525–5534.
7. N. T. Southall, K. A. Dill, and A. D. J. Haymet, 'A view of the hydrophobic effect', *J. Phys. Chem.*, 2002, 106, 521–533.
8. C. J. Pedersen, 'Cyclic polyethers and their complexes with metal salts', *J. Am. Chem. Soc.*, 1967, 89, 7017–7036.
9. C. D. Gutsche, *Calixarenes*, The Royal Society of Chemistry, Cambridge, UK, 1989; *Calixarenes Revisited*, The Royal Society of Chemistry, Cambridge, UK, 1997.
10. A. A. Dondoni Marra, *Chem. Rev.*, 2010, 110, 4949.
11. R. Joseph and C. P. Rao, *Chem. Rev.*, 2011, 111, 4658–4702.
12. J. S. Kim and D. T. Quang, *Chem. Rev.*, 2007, 107, 3780.
13. B. S. Creaven, D. F. Donlon, and J. McGinley, *Coord. Chem. Rev.*, 2009, 253, 893.
14. I. Leray and B. Valeur, *Eur. J. Inorg. Chem.* 2009, 3525.
15. P. D. Beer, *Acc. Chem. Res.*, 1998, 31, 71.
16. L. Baldini, A. Casnati, F. Sansone, and R. Ungaro, *Chem. Soc. Rev.*, 2007, 36, 254.
17. R. P. Feynman, *Eng. Sci.*, 1960, 23, 5, 22.
18. G. A. Ozin and A. Arsenault, *Nanochemistry: A Chemical Approach to Nanomaterials*, The Royal Society of Chemistry, Cambridge, 2005.
19. J. D. Halley and D. A. Winkler, *Complexity*, 2008, 14, 2.

20. G. A. Ozin and L. Cademartiri, *Small*, 2011, 7, 1, 49–54.
21. R. A. Sperling and W. J. Parak, *Phil. Trans. R. Soc. A*, 2010, 368, 1333–1383.
22. J. C. Love, L. A. Estroff, J. K. Kriebel, R. G. Nuzzo, and G. M. Whitesides, *Chem. Rev.*, 2005, 105, 4, 1103–1169.
23. K. Aslan and V. H. Pérez-Luna, *Langmuir*, 2002, 18, 16, 6059–6065.
24. M. Geissler and Y. Xia, *Adv. Mater.*, 2004, 16, 1249–1269.
25. B. V. Enustun and J. Turkevich, *J. Am. Chem. Soc.*, 1963, 85, 3317.
26. H. J. Kim, M. H. Lee, L. Mutihac, J. Vicens, and J. S. Kim, *Chem. Soc. Rev.*, 2012, 41, 1173–1190.
27. S. Balasaheb, N. T. Kim, *Chem. Soc. Rev.*, 2013, 42, 366–386.
28. G. Patel, A. Kumar, U. Pal, and S. Menon, *Chem. Commun.*, 2009, 1849–1851.
29. S. Y. Lin, C. H. Chen, M. C. Lin, and H. F. Hsu, *Anal. Chem.*, 2005, 77, 4821–4828.
30. A. Pandya, P. G. Sutariya, A. Lodha, and S. K. Menon, *Nanoscale*, 2012, 5, 2364–2371.
31. A. Pandya, K. V. Joshi, N. R. Modi, and S. K. Menon, *Sens. Actuators B*, 2012, 168, 54–61.
32. G. Patel and S. Menon, *Chem. Commun.*, 2009, 3563–4356.
33. C. F. Brewer, M. C. Miceli, and L. G. Baum, *Curr. Opin. Struct. Biol.*, 2002, 129, 616–623.
34. A. Pandya, P. G. Sutariya, and S. K. Menon, *Analyst*, 2013, 138, 2483–2490.
35. S. K. Menon, N. R. Modi, A. Pandya, and A. Lodha, *RSC Adv.*, 2013, 3, 10623–10627.
36. K. V. Joshi, B. K. Joshi, A. Pandya, P. G. Sutariya, and S. K. Menon, *Analyst*, 2012, 137, 4647.
37. H. Li and F. Qu, *Chem. Mater.*, 2007, 19, 4148–4154.
38. W. Stober, A. Fink, and E. Bohn, *J. Colloid Interface Sci.*, 1968, 26, 62–69.
39. X. Wang, J. Wu, F. Li, and H. Li, *Nanotechnology*, 2008, 19, 205501–205510.

Suggested Further Reading

1. A. D. Buckingham, A. C. Legon, and S. M. Roberts (Eds), *Principles of Molecular Recognition*, Kluwer Academic Publishers, Dordrecht, the Netherlands, 1993.
2. J. W. Steed, D. R. Turner, and K. J. Wallace, *Core Concepts in Supramolecular Chemistry and Nanochemistry*, John Wiley & Sons, Ltd, Chichester, UK, 2007.
3. P. J. Cragg, *Practical Supramolecular Chemistry*, John Wiley & Sons, Ltd, Chichester, UK, 2006.
4. J. M. Lehn, *Supramolecular Chemistry*, VCH, Weinheim, Germany, 1995.
5. J. M. Lehn, J. L. Atwood, J. E. D. Davies, D. D. Mac Nicol, and F. Vögtle (Eds), *Comprehensive Supramolecular Chemistry*, Pergamon, Oxford, UK, 1996.

6. G. A. Ozin and A. C. Arsenault, *Nanochemistry*, The Royal Society of Chemistry, Cambridge, UK, 2005.
7. H. J. Schneider and A. K. Yatsimirski, *Principles and Methods in Supramolecular Chemistry*, Wiley-VCH, Weinheim, Germany, 2000.
8. J. W. Steed and J. L. Atwood, *Supramolecular Chemistry*, John Wiley & Sons, Ltd, Chichester, UK, 2000.

Carbon-Based Hybrid Composites as Advanced Electrodes for Supercapacitors

S.T. Senthilkumar¹, K. Vijaya Sankar¹, J. S. Melo²,
A. Gedanken³, and R. Kalai Selvan^{*1}

¹*Solid State Ionics and Energy Devices Laboratory, Department of Physics,
Bharathiar University, Coimbatore, India*

²*Nuclear Agriculture and Biotechnology Division, Bhabha Atomic Research Centre,
Mumbai, India*

³*Center for Advanced Materials and Nanotechnology, Department of Chemistry,
Bar-Ilan University, Ramat-Gan, Israel*

Abstract

The energy demand is increasing day by day leading to the decrease in available non-renewable energy resources. To combat such a situation, a variety of energy storage and energy conversion devices are now being made available such as batteries, supercapacitors (SCs), conventional capacitors and fuel cells. Among these, the SCs are superior due to their remarkable properties of cyclic stability, safety, being environmental friendly, low cost, etc. However, the SC is deficient in the amount of energy it can store compared to batteries and fuel cell. So far, numerous type of carbon-based electrode materials have been used for preparing SC like activated carbons, carbon aerogels, graphene, carbon nanotubes and so on due to their high surface area, cycle life, high electrical conductivity and high power density. However, the carbon-based electrode materials are lacking in ability to store high energy density. In order to improve the energy density without losing their power density, the carbon-based electrode material has been modified to include composites with noble materials like metal oxides (MnO_2 , Co_3O_4 , NiO , etc.), metal hydroxides ($\text{Ni}(\text{OH})_2$, $\text{Co}(\text{OH})_2$, FeOOH , etc.) and conducting polymers (polyaniline (PANI), polypyrrole (PPy), polythiophene (PTh) and poly(3,4-ethylenedioxythiophene) (PEDOT), etc.). In this chapter, we present a detailed discussion on the advances made in the carbon-based electrodes for SC applications. Finally,

*Corresponding author: selvankram@gmail.com

we end the chapter with conclusion and prospects for future development of carbon-based electrode materials.

Keywords: Supercapacitor, hybrid electrodes, heteroatom doped carbon, redox additive

9.1 Introduction

9.1.1 Background

Today's competitive world is confronted with an energy crisis problem. The demand for energy is increasing day by day for domestic and industrial applications as the existing conventional energy resources fail to meet the requirements. It is very difficult to exploit the renewable sources like wind and solar throughout the year, and the non-renewable resources (e.g. fossil fuel) are not utilized to their fullest potential because of their own limitations. In addition, global warming is also a growing problem due to the emission of CO_2 and CO from the combustion of fossil fuels. Furthermore, over the past few years the cost of liquid fuel has been increasing which results in stress on the economy, especially in developing countries. This crisis-like scenario can be solved by developing an efficient electrical energy storage device that can facilitate efficient storage and usage of power. Subsequently, it will help to reduce the dependency on combustible and thermal sources like petroleum and, above all, will provide us with a perennial source of power.

Some of the aforementioned issues have been addressed partially by the developed energy storage devices especially Li-ion batteries (LIB), supercapacitors (SCs), hydrogen energy storage system, etc.. Among these, SCs and LIBs are the most promising systems. However, SCs are considered as an alternative energy storage devices to LIBs, since they possess an intermediate value of power density (P) and energy density (E), when compared with batteries or fuel cells and classical capacitors, *i.e.*, higher power density (kW kg^{-1}) than batteries or fuel cells and higher energy density (Wh kg^{-1}) than classical capacitors (Figure 9.1) [1, 2]. Other properties of SCs are compared with other energy sources and tabulated in Table 9.1 [3]. Due to its high power density, SCs are widely used in space and military applications. SCs are also used in mobile phones, digital cameras, digital communication devices, industrial equipments (cranes, elevators and forklifts), pulse laser technique, electric hybrid vehicles, uninterrupted power supply (UPS) and electric tools [4–6].

However, the SC encounters the problem of low energy density compared to batteries. It is well known that the energy density of SC depends

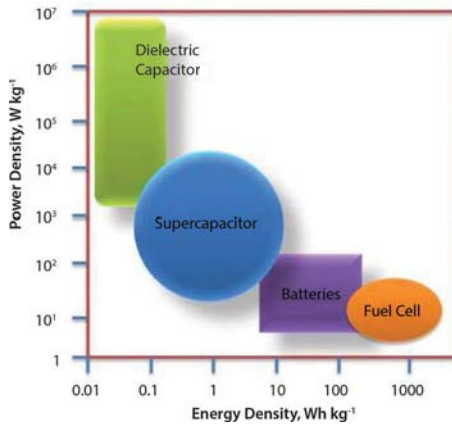


Figure 9.1 Ragone plot of energy storage devices [1].

Table 9.1 Comparison of electrochemical parameters of energy storage devices [3].

Parameters	Electrostatic Capacitor	Supercapacitor	Battery
Charge Time	10 ⁻⁶ –10 ⁻³ s	10–3 s	0.3–3 h
Discharge Time	10 ⁻⁶ –10 ⁻³ s	10–3 s	0.3–3 h
Energy Density (Wh kg ⁻¹)	<0.1	1–10	20–100
Power Density (W kg ⁻¹)	>10 000	1000–2000	50–200
Cycle Life	>500 000	>100 000	500–2000
Charge/Discharge Efficiency	~1.0	0.90–0.95	0.7–0.85

on the specific capacitance and potential window. The specific capacitance and energy density of the electrode depend on the type of electrode material used for SCs. Hence, the electrode materials play a main role in SCs. So far, numerous electrode materials [7–10] such as carbon materials (activated carbons (ACs), carbon aerogels (CAs), graphene, carbon nanotubes (CNTs), etc.), metal oxides (MOs) (MnO₂, Co₃O₄, NiO, etc.), metal hydroxides (Ni(OH)₂, Co(OH)₂, FeOOH, etc.) and conducting polymers (CPs) (polyaniline (PANI), polypyrrole (PPy), polythiophene (PTh), poly (3,4-ethylenedioxythiophene) (PEDOT), etc.) have been

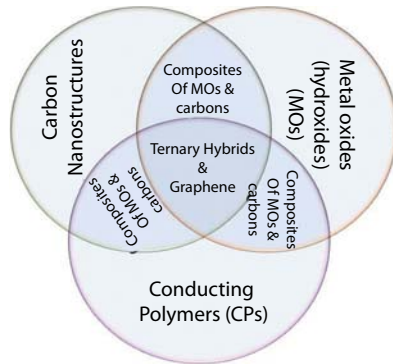


Figure 9.2 Type electrode materials used for SCs.

used in SCs (Figure 9.2). Unfortunately, these electrode materials are having some drawbacks like low energy performance of carbon materials and poor cyclic stability and rate capability of MOs, metal hydroxides and CPs [7, 10]. In this context, researchers and engineers are trying to find new electrode materials to solve these drawbacks.

9.2 Principle of Supercapacitor

9.2.1 Basics of Supercapacitor

SC is constructed of two electrodes that are immersed in an electrolyte and separated by a separator. The separator permits electrolytic ions to diffuse and also prevents the two electrodes from direct contact or short circuit, thereby avoiding any damage to the cell. When a voltage is applied across the electrodes, the electrolytic (positive and negative) ions are driven to accumulate at the surface of the electrode of opposite polarity (Figure 9.3). When the charged SC is connected with external load, the accumulated ions move back to the electrolyte and neutralize the system while it acts as a voltage source. Therefore, the stored capacitance on the electrodes is determined by the following equation [1, 2]:

$$C = \frac{\epsilon \cdot A}{d}, \quad (9.1)$$

where $\epsilon = \epsilon_0 \cdot \epsilon_r$, ϵ_0 is the permittivity of free space (8.854×10^{-12} F m⁻¹) and ϵ_r is the relative dielectric constant of the electrolyte as liquid or solid and depends on the ionic concentration of the electrolyte; A is the surface area of the electrodes (m²) and d is the thickness of the electric double layer (EDL) or Debye length (DL) (nm).

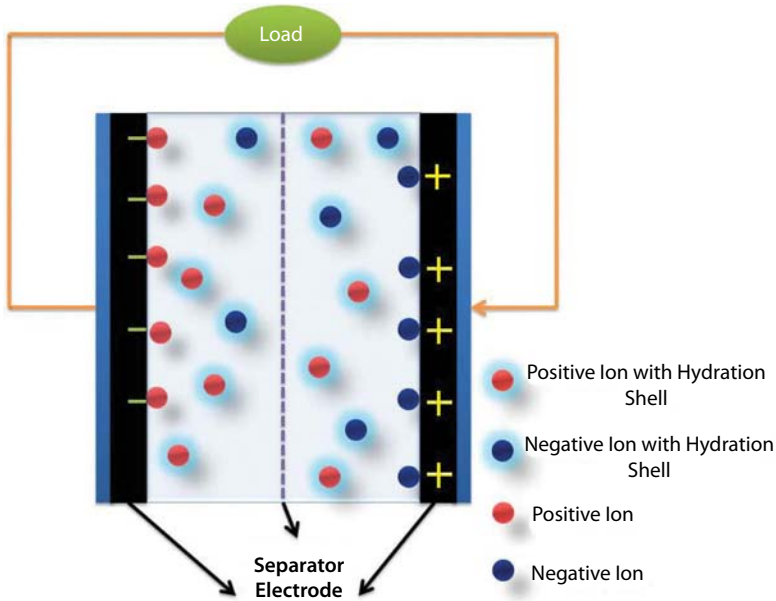


Figure 9.3 Schematic representation for the construction of SC.

However, an SC can be considered as two capacitors in series. So that the total cell capacitance can be written as

$$\frac{1}{C} = \frac{1}{C_1} + \frac{1}{C_2}, \tag{9.2}$$

where C_1 and C_2 are the capacitance for positive and negative electrodes, respectively. However, here the capacitance C_1 and C_2 should be equal to each other, i.e., $C_1 = C_2$. So that the capacitance becomes

$$C = \frac{C_1}{2}. \tag{9.3}$$

So, the capacitance of the SC cell is half of the capacitance of each individual electrode. On the other hand, the energy and power density of the SCs is dependent on the capacitance and operating voltage of the device according to the following relations:

$$E = \frac{1}{2}CV^2, \tag{9.4}$$

$$P_{\max} = \frac{V^2}{4R}, \quad (9.5)$$

where C , V and R represent the capacitance of SC (F), operating voltage (V) and equivalent series resistance (ESR) (Ω), respectively. Hence, it is noted that by increasing the SC voltage (V), both the energy and power can be significantly increased. However, SC voltage is often limited by the thermodynamic stability range of electrode, because the capacitance of SC is mainly based on the electrode material used. Moreover, the ESR can arise predominately from electrode material, binder, conductive agent, electrolyte solution and contact resistance between the current collector and the active materials, as well as the poor particle contact and closed pore structure reducing the ionic diffusion in the electrode material.

9.2.2 Charge Storage Mechanism of SC

In general, the charge is stored in the SC based on two mechanisms: (i) non-Faradic and (ii) Faradic or redox reaction. Based on this, SCs are mainly classified into two types.

9.2.2.1 Electric Double-Layer Capacitor (EDLC)

In EDLC, the charge is stored based on the separation of electronic and ionic charges at the electrode and electrolyte interfaces via electrostatic attraction. During charging and discharging process, there is no other transfer of electrons at the electrode/electrolyte interfaces. Also, there is no other chemical reaction between electrode and electrolyte solution, which leads to improved cyclic stability of the device. The charge storage in EDLC materials depends on the specific surface area, pore structures and type of pores. Even though it has high surface area which helps store the charge, it is limited because of the large number of micropores. In 1853, Helmholtz was the first person who proposed the EDL theory to describe the charge storage mechanism of EDLC electrode materials. He revealed that the EDLC material stores the charge like parallel-plate capacitor and described how two layers of opposite charge build up at the electrode/electrolyte interface via electrostatic interaction up to some atomic distance (Figure 9.4(a)). Unfortunately, this model does not consider adsorption of water molecules and counter ions. Therefore, in the early 1900s, it was further modified simultaneously by Gouy and Chapman who have proposed that the distribution of electrolyte ions in the electrolyte medium is due to the thermal motion, named as a diffusion layer (Figure 9.4(b)). But this

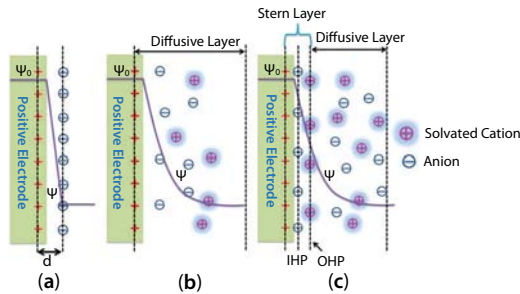


Figure 9.4 Models of the EDL at a positively charged surface: (a) the Helmholtz model, (b) the Gouy–Chapman model and (c) the Stern model, showing the IHP and OHP. The IHP refers to the distance of the closest approach of specifically adsorbed ions (generally anions) and OHP refers to that of the non-specifically adsorbed ions. The OHP is also the plane where the diffuse layer begins. d is the double-layer distance described by the Helmholtz model. Ψ_0 and Ψ are the potentials at the electrode surface and the electrode/electrolyte interface, respectively [2].

theory exhibited an overestimation of EDL capacitance. So, in 1924, Stern developed an alternate theory by combining the Helmholtz and Gouy–Chapman models, which explained the existence of two layers of ion distribution. First layer is called compact layer or Stern layer or Helmholtz layer. It is formed by adsorbed ions and non-specifically adsorbed counter ions on the electrode, and these two types of adsorbed ions are distinguished as inner Helmholtz plane (IHP) and outer Helmholtz plane (OHP) (Figure 9.4(c)). The second layer is called diffusion layer, which is the same as what the Gouy–Chapman model described. So, total capacitance (C_t) is built up by both the layers, i.e., compact layer (Helmholtz layer) and diffusion layer. The stored capacitance is termed as compact/Helmholtz double-layer capacitance (C_H) and diffusion layer capacitance (C_{diff}). So, the total capacitance can be expressed as follows [2, 4, 11]:

$$\frac{1}{C_t} = \frac{1}{C_H} + \frac{1}{C_{diff}}. \quad (9.6)$$

9.2.2.2 Pseudocapacitors

On the other hand, the pseudocapacitor stores the charge based on the fast surface redox reaction or Faradaic reaction or charge transfer reaction at the electrode surface, which leads to improved energy density of pseudocapacitor compared to EDL capacitor. Generally, the pseudocapacitance depends on the potential difference or cell voltage, which is indicated as follows:

$$C = \frac{\Delta q}{\Delta V}, \quad (9.7)$$

where Δq and ΔV indicate a stored charge and a change in potential, respectively [4, 10, 11]. In addition, the average capacitance of redox electrodes is denoted as

$$C = C_{\text{dl}} + C_{\text{p}}, \quad (9.8)$$

where C_{dl} is the EDL capacitance and C_{p} is the pseudocapacitance. However, pseudocapacitance is typically contributing 5–10% of the total capacitance and over 1 F m⁻² of specific capacitance can be achieved in pseudocapacitive electrodes [11].

Nonetheless, the theoretical capacitance of the redox electrode materials can be calculated as [7]

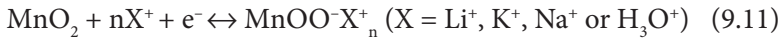
$$C = \frac{n.F}{M.V} \quad (9.9)$$

where n is the mean number of electrons transferred in the redox reaction, F is the Faraday constant, M is the molar mass of the MO and V is the operating voltage window. Also, the Faradaic or pseudocapacitance arises generally from

- i. Under-potential deposition
- ii. Surface redox reaction
- iii. Intercalation–de-intercalation reaction
- iv. Doping/dedoping process

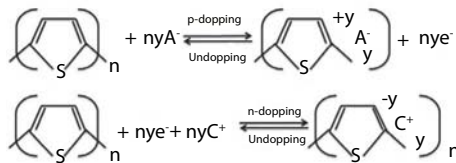
In under-potential deposition, the electroactive species in the electrolyte are adsorbed on the surface of the electrode and undergo redox reaction which transfers the electron. On the other hand, the surface redox reaction occurs when the electrolyte ions adsorb on the surface of the electrode and charge transfer occurs between electrode and electrolyte. Subsequently, the intercalation of electrolyte ions occurs into the electrode material and undergoes redox reaction without any phase change. In addition, the doping/dedoping process occurs in the CPs [5]. These processes depend on the surface area, while a relatively high surface area with micropores is desirable to efficiently distribute the ions to and from the electrodes.

For example, MnO₂ exhibits the pseudocapacitance via both electro-sorption (Eqn. 9.10) and intercalation/de-intercalation or insertion/de-insertion processes (Eqn. 9.11) [13–16]:



In addition, various MOs are employed as both positive and negative electrode materials for SCs, in which the MOs undergo redox reaction during electrochemical reaction. Furthermore, NiO [17], NiMoO₄ [18], Mn₃O₄ [19, 20], Co₃O₄ [21], Ni-Co double hydroxide [22], etc., have been identified as the suitable positive electrode materials. Subsequently, FeMoO₄ [23], Bi₂WO₆ [24, 25], Bi₂O₃ [26], etc., have been identified as negative electrodes. Recently, the researchers are interested on the mixed MOs including NiMn₂O₄ [27], ZnFe₂O₄ [28], and NiCo₂O₄ [29] due to the fact that their mixed metals have different oxidation states which lead to improved performance of the material. Overall, most of the identified electrode materials delivered high specific capacitance and energy density than carbon-based materials. However, the rate capability and cyclic stability were very less when compared with carbon-based materials, because the reversibility of the electrochemical reaction was less and the electrode resistance was high.

Subsequently, various CPs such as PANI, PPy, and PTh and its derivatives are employed as electrode material. Among these, PTh is involved in p-doping/dedoping and n-doping/dedoping process as shown in Scheme 9.1 [30].



Scheme 9.1

In Scheme 9.1, the p-doping occurs by releasing an electron (e^-) from the backbone of PTh and incorporation of an anion (A^-) from solution into the PTh to maintain the charge neutrality. Similarly, the n-doping takes place by the transport of electron (e^-) into the backbone of PTh while cation (C^+) enters from the solution to maintain the charge neutrality. The p- and n-dedoping processes occur in the reverse order of p- and n-doping processes. However, generally the p-doping/dedoping occurs at positive potential and n-doping/dedoping at negative potential.

9.2.2.3 Electrode Materials for Supercapacitors

There are different kinds of electrode materials that have been extensively employed in SCs (discussed earlier), and each of them exhibits its own and

different electrochemical performance. In addition, the charge storage performance of SC directly depends on the type of electrode material used. So, the best electrode material should possess the following characteristics [7]:

- High specific surface area: To improve the electrolyte accessibility or to accommodate more number of electrolyte ions
- Uniform pore size distribution: Significantly influences the specific capacitance and the rate capability of the electrode
- High electronic conductivity: Affects the rate capability and the power density of the electrode or device, and also reduces the equivalent serial resistance
- Better electrochemically active sites: For the contribution of pseudocapacitance
- High chemical and cyclic stability: For practical applications
- Low cost: To aid manufacturing

Recently, most of the commercial SCs are fabricated using carbon materials, i.e., ACs, CNTs and graphene which is also known as electric double-layer SC because of the following physical and chemical properties [2, 10, 31, 32]:

- Good electrical conductivity
- High surface area
- Good resistance to chemical corrosion
- High thermal stability
- Controlled pore size distribution
- Excellent cyclic stability
- No phase of electrode material
- Low cost

But, the drawback of current EDLC is their low energy density, i.e., 3–5 Wh kg⁻¹ when compared to electrochemical battery, 30–40 Wh kg⁻¹ for a lead acid battery and 10–250 Wh kg⁻¹ for a lithium-ion battery. Since we know that the performance of the SC is mainly dependent on electrode material, such carbon electrode materials cannot provide the requirement of high energy density for the SC devices.

To improve the energy performance, redox behaviour electrode materials such as MOs (MnO₂, Co₃O₄, NiO, etc.), metal hydroxides (Ni(OH)₂, Co(OH)₂, FeOOH, etc.) and CPs (PANI, PPy, PTh, PEDOT, etc.) have been examined in SC (since it is known as pseudocapacitor or redox SC)

as alternative electrode materials. The redox behaviour electrode materials exhibit one order higher specific capacitance as well as energy density for SC than the carbon electrodes. Unfortunately, these redox behaviour electrodes also have some drawbacks such as [7, 33–36]

- Low surface area
- Difficult to tailor pore size distribution
- Low electrical conductivity
- Low mechanical stability
- Slow ion transport
- Poor rate capability and cyclic stability
- High cost of raw materials
- Less flexibility

Hence, developing new materials with high capacitance as well as improved physical and chemical properties relative to existing electrode materials is the most important practice to defeat the above challenges. This can be resolved by binary or ternary hybrid composite electrode materials. The composite electrode materials are prepared in different configurations such as carbon/MOs (hydroxides), carbon/CPs and MOs/CPs. The composite electrode material has the following advantages [7]:

- The carbon materials exhibit significant physical support for MOs and CPs and provide the charge transport pathway. Moreover, MOs and CPs provide high specific capacitance and energy density.
- Carbon materials improve the rate capability and power density of the MOs and CPs even at a high discharge current because of their high electronic conductivity. Also, carbon benefits with good rate capability and cyclic stability.
- Possibly reduces the cost of the electrode material.

In this context, the carbon/MOs and carbon/CPs electrodes are widely investigated compared to MOs/CPs, because the carbon material increases the surface area, porosity and active site; reduces the diffusive path length; decreases the electron transfer path length; enhances the electrochemical accessibility of electrolyte ions; provides high electrical conductivity; and improves the flexibility and cyclic stability. So, let us see, various carbon nanostructured electrode materials and their hybrid composite electrode materials for advanced energy storage applications.

9.3 Activated Carbon and their Composites

AC is a non-graphitic (disordered) carbon, and it has the maximum amount of porous nature (Figure 9.5). Similarly, the inter-planar spacing (0.335 nm) of AC is smaller than the graphite (0.34–0.35 nm), and the AC is composed of a number of disordered graphene layers or basal layer, which is known as turbostratic carbon [37]. Currently, ACs are mainly used as electrode material in commercial SCs because of their high surface area, good electrochemical stability, electrical conductive properties and better porous nature [37–39]. Therefore, the conventional raw materials such as petroleum coke, tar pitches and coal cannot meet our demand for the large-scale production of ACs, because their availability is less and they are non-renewable in nature and also not cost-effective. Therefore, biomass is considered as the suitable precursor for the preparation of ACs because of its easy availability and renewability in nature, besides aiding in waste management and being cost-effective [40, 41]. In this regard, different kinds of bio-wastes have been identified so far and tested for SC applications, which is activated using different activating agents [42–60].

Among the reported bio-wastes, AC prepared from celtuce leaves [60] by KOH activation showed high surface area of $3404 \text{ m}^2 \text{ g}^{-1}$ and delivered a specific capacitance of 273 F g^{-1} at 0.5 A g^{-1} in 2 M KOH electrolyte. Similarly, KOH-activated AC derived from potato starch [58] delivered a specific capacitance of 335 F g^{-1} in 6 M KOH electrolyte, even though it possessed lower surface area of $2340 \text{ m}^2 \text{ g}^{-1}$ than celtuce leaves. On the other hand, NaOH-treated AC from apricot shell [48] showed a surface area of $2335 \text{ m}^2 \text{ g}^{-1}$ and provided a specific capacitance of 339 F g^{-1} in 6 M KOH electrolyte. Coffee beans-derived AC [58] treated with ZnCl_2 delivered a maximum specific capacitance of 368 F g^{-1} in $1 \text{ M H}_2\text{SO}_4$ electrolyte. However, among the identified bio-wastes, neem leaves-derived AC [59] showed a higher specific capacitance of 400 F g^{-1} in $1 \text{ M H}_2\text{SO}_4$, although it has a surface area of $1230 \text{ m}^2 \text{ g}^{-1}$. Interestingly, organic electrolytes also

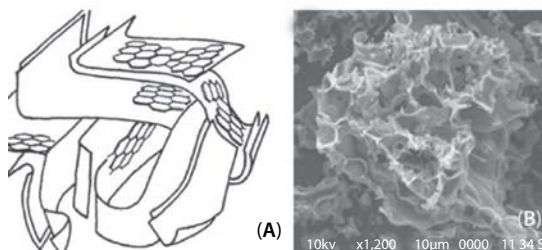


Figure 9.5 SEM image of AC [38].

provide a higher capacitance of 251 F g^{-1} in 1.2 M methyltriethylammonium tetrafluoroborate ($\text{MeEt}_3\text{NBF}_4$)/AN electrolyte for the AC prepared from wheat straw by KOH treatment [55]. In ionic liquid electrolytes, the coconut shell-derived AC treated with KOH exhibits a specific capacitance of 127 F g^{-1} in 1-ethyl-3-methylimidazolium tetrafluoroborate (EMImBF_4) [52].

AC has also been composited with TiO_2 , RuO_2 , Ni(OH)_2 , etc. [61–63]. For example, hydrous RuO_2 was synthesized by a sol–gel method on the surface of AC. It was established that the composite containing 30 wt.% Ru exhibited a specific capacitance of 333 F g^{-1} , but it was only 241 F g^{-1} for pure AC. On the other hand, AC and TiO_2 nanoparticle composites have been synthesized by a microwave method and achieved a specific capacitance of 92 F g^{-1} . However, there are no detailed and extensive studies for AC-based composite electrodes, wherein AC has been derived from biomass.

However, recently the performance of AC-based SCs was improved using the novel strategy of redox additive in electrolyte instead of using AC composite. Notably, Senthilkumar *et al.* [64] have prepared ACs from bio-wastes of *Eichhornia crassipes* and used KI as redox additive in H_2SO_4 . Interestingly, the specific capacitance and energy density of the SC were greatly improved from 472 to 912 F g^{-1} and 9.5 to 19.04 Wh kg^{-1} , respectively, by the addition of KI into H_2SO_4 . It was higher than KBr-added H_2SO_4 (572 F g^{-1} and 11.6 Wh kg^{-1}) and KI-added Na_2SO_4 (604 F g^{-1} and 12.3 Wh kg^{-1}) electrolytes. Similarly, VO_2 -added 1 M H_2SO_4 electrolyte enhances [65] nearly 43% of specific capacitance of 630.6 F g^{-1} compared with pristine in 1 M H_2SO_4 (440.6 F g^{-1}). Even the redox additive (Na_2MoO_4 -added PVA/ H_2SO_4) gel electrolyte was used in AC-based SC (Figure 9.6) and obtained 57% of improved specific capacitance and energy density from 412 F g^{-1} and 9.166 Wh kg^{-1} to 648 F g^{-1} and 14.4 Wh kg^{-1} , respectively [66]. Also, the hydroquinone-mediated PVA/ H_2SO_4 gel electrolyte [67] enhanced both specific capacitance and energy density from 425 F g^{-1} and 9 Wh kg^{-1} to 941 F g^{-1} and 20 Wh kg^{-1} , respectively.

9.4 Carbon Aerogels and Their Composite Materials

CAs are known as monolithic 3D porous network comprising of carbon nanoparticles [68]. CAs are also created in the form of irregular-shaped powder and thin-film composites [69]. Usually, CAs are derived from resorcinol-formaldehyde (RF), phenol-resorcinol-formaldehyde, phenolic-furfural, melamine-formaldehyde, polyurethanes and polyureas

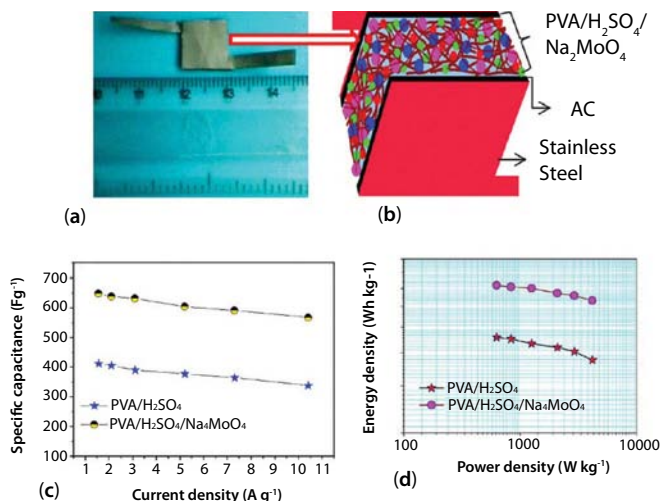


Figure 9.6 (a) Fabricated SC and (b) schematic diagram of polymer gel electrolyte used SC, (c) specific capacitance of SCs as a function of current density and (d) Ragone plots of PVA/H₂SO₄ and PVA/H₂SO₄/Na₂MoO₄ gel electrolyte used SCs. Reproduced with permission from Ref. [66]. Copyright 2014 American Chemical Society.

through sol-gel process followed by pyrolysis [70]. The CA is one of the striking electrode materials for EDLCs application and is used directly without any binders [71]. Furthermore, composites of CAs have also been applied for EDLCs electrode.

The surface area, particle size, pore volume and structure of the CA were evaluated based on (i) the molar ratio of resorcinol and catalyst (R/C), (ii) carbonization temperature or the synthesis conditions of sol-gel process [69, 71] and (iii) chemical activation. Zhu *et al.* [72] showed that when the ratio of R/C is increased (= 1, 2, 3 and 4) for the preparation of CAs, the surface area and pore volume also increased from 176 to 2760 m² g⁻¹ and 0.304 to 1.347 cm³ g⁻¹, respectively, whereas the pore diameter decreased from 4.4 to 2.5 nm. They found that the R/C (= 2) gave a higher capacitance of 294 F g⁻¹ at 1 mA cm⁻². In contrast, the particle size of CA and capacitance increased when increasing the R/C ratio, but the surface area (626 m² g⁻¹) and pore volume (1.2 cm³ g⁻¹) decreased [73]. However, spherical particles of less than 100 nm were obtained at an R/C ratio of 1500. These spherical particles (R/C = 1500) gave a higher capacitance value of ~183.6 F g⁻¹ in 6 M KOH solution with stable electrochemical performance. Li *et al.* [74] have reported a similar type of work, in which a sample with an R/C ratio of 1500 was synthesized, which exhibited an excellent specific capacitance of 110 F g⁻¹ in KOH electrolyte. Similarly, Lee *et al.* prepared

a CA with an R/C ratio of 500, which displayed the highest surface area ($706 \text{ m}^2 \text{ g}^{-1}$) with an average pore diameter of 10.9 nm, but the capacitance was 81 F g^{-1} . Furthermore, they also elucidated that shrinkage behaviour of CAs is based on gelation time and R/C ratio [70].

The activation with KOH is able to contribute to both the surface area and pore size of CAs, which establishes the specific capacitance. The larger pore size ($>40 \text{ nm}$) contributes to an increase in the capacitance of 245 F g^{-1} at 10 mV s^{-1} in 30% KOH electrolyte [75]. Recently, Katanyoota *et al.* [76] synthesized two types of benzoxazine precursors (BA-a and BA-teta) for CAs preparation. CA (BA-a) was derived from bisphenol-A and aniline, while CA (BA-teta) was derived from bisphenol-A and triethylenetetramine. The CA from BA-teta showed an effective specific capacitance of 55.78 F g^{-1} for corresponding surface area of $391 \text{ m}^2 \text{ g}^{-1}$. The capacitance of 187.2 F g^{-1} was obtained [77] from modified pitch-based CAs. The surface area and pore volume increased during the CO_2 activation at 900°C for 2 h. Further increase in the activation time (3 h) caused no change in the structure of the modified activated carbon aerogel (ACA). These samples ($900^\circ\text{C}/2 \text{ h}$) exhibited a specific capacitance of 146 F g^{-1} [78]. The surfactant, 0.25 wt.% of vtmos aqueous solution used for surface modification to enhance the hydrophobization of activated CAs, improved the wettability of the electrode [79]. This important step improved the EDL formation in a propylene carbonate (PC)-based electrolytic solution. Subsequently, they have modified the surface of ACAs via vtmos and sodium oleate surfactants (OAS). Here, the vtmos surface-modified ACA delivered a higher capacitance ($\sim 160 \text{ F g}^{-1}$) and energy density ($\sim 78 \text{ Wh kg}^{-1}$) with good charge/discharge stability due to the contribution of hydrophobic vtmos functional groups on ACA [80]. Kalpana *et al.* have reported [81] a ZnO-CA composite, where CA was used with a surface area of $2500 \text{ m}^2 \text{ g}^{-1}$. The capacitance of as-prepared 1:2 composite of ZnO-CA sample could reach 25 F g^{-1} (from CV) at 10 mV s^{-1} and 500 F g^{-1} (ZnO-CA, SC) at 100 mA cm^{-2} in 6 M KOH solution.

The SnO_2 -CA composite electrodes were prepared by two methods [82]: (i) directly SnO_2 was mixed in RF (resorcinol-formaldehyde) gel, and (ii) the ethanol-based SnCl_4 was impregnated into CAs. The combination of redox reaction (SnO_2) and EDLC (CA) behaviour delivered a good capacitance of 119.2 F g^{-1} from CV and 69.8 F g^{-1} from charge/discharge measurement. But when the impregnation time was increased, the surface area decreased. Similarly, Lee *et al.* have successfully elucidated the capacitance characterizations of metal-doped CA [83]. They have doped different concentrations of Co (1, 3, 5, 7, 10 and 15 wt.%) with CA. In particular, 7 wt.% of Co-doped CA exhibits a higher capacitance of 100 F g^{-1} than

the other compositions. Subsequently, various metals such as Cu, Fe, Mn and Zn (7 wt.%) were doped with CA and studied for their performance. Among these metals, Mn-doped CA reached a higher capacitance of 107 and 125 F g⁻¹ from CV and charge–discharge measurements, respectively. More recently, PPy and CA composite [84] synthesized using surfactants (sodium dodecyl sulphate, SDS) via chemical oxidation polymerization method showed abnormal redox peaks in CV curve and exhibited a capacitance of 433 F g⁻¹. This is higher than pristine CA (174 F g⁻¹) due to the additional contribution of redox reaction. Similarly, when coating the Mn₂O₃ on the spherical CA [85] by *in situ* method, this composite showed a higher capacitance of 368.01 F g⁻¹ with 90% capacitance retention after 5000 cycles.

The ACA and CNT composite as binderless electroactive material has also been explored [86]. The electrochemical behaviours of ACA and ACA-multi-walled CNT (MWCNT), where CNT is added at different wt.% (3–10), were studied in 5 M KOH. Notably, after the addition of CNT, the surface area is increased from 670 to 710 m² g⁻¹. The maximum capacitance was 218 F g⁻¹ for ACA/3 wt.% of MWCNTs with corresponding BET surface area of 710 m² g⁻¹ and charge/discharge characterization elucidating the excellent electrochemical stability. The conductive fillers (e.g., carbon black, MWCNT and vapour-grown carbon nanofiber in various mass fractions) also enhanced the capacitance performance while making the composite with CA [87]. By increasing the CNT content, the conductivity of CA-CNT composite was improved. Herein, the CA-CNT composite displayed a good capacitance (141.4 F g⁻¹ at 5 mV s⁻¹, 127.1 F g⁻¹) with the lowest percolation of CNT content. The observed capacitance value was even higher at higher scan rate, which is attributed to the conductive fillers like CNT. But, increase in the CNT can reduce the pore size distribution; hence, surface area also decreased, which hindered the ionic motion causing lower capacitance.

Recently, the synergistic effect of ordered mesopore carbon (OMC)/CA was reported by Wu *et al.* [88]. Here, the OMC-CA composite leads to a better capacitance than individual OMC and CA via combination of ordered mesopores structure (2D) of OMC and interconnected (3D) pores structure of CA. The OMC and CA samples showed a good rectangular-shaped CV curve, which means that the fast ions transport occurs at low scan rate. The mixed OMC-CA composite displayed a good rectangular CV curve with increasing scan rate compared to OMC and CA alone. Especially, the OMC-CA-30 (30% of CA content) revealed a good rectangular CV curve at a higher scan rate of 100 mV s⁻¹ and stabilized capacitance of 165, 158 and 156 F g⁻¹ for 10, 50 and 100 mV s⁻¹, respectively.

9.5 Carbon Nanotubes (CNTs) and their Composite Materials

In the past few decades, CNTs have been identified as possible material in electrochemical storage devices, especially in SC (EDLCs) electrodes, due to their flexibility [89], unique morphology, mechanical strength [90] and moderate surface area compared to ACs [91]. Also, their high mechanical resilience and open tubular network (1D mesopores) make them a good support active (electrode) material [4] for EDLCs. These open structures permit a rapid charge distribution over the surface area [92] and respond to low electrical resistivity. Furthermore, high porosity leads to quick ion accessibility [69], especially when single-walled CNTs (SWCNTs) are concerned as shown in Figure 9.7(a) and (b). In Figure 9.7(c), AC has an irregular pore structure and does not support better ion movement for quick charge storage.

Moreover, the capacitance value of CNTs is strongly based on the purity, morphology and electrolyte used [89]. In addition, it has low ESR and consequently increases the power of the devices [90]. In the past few years, SWCNTs and MWCNTs with their composites have been investigated as electrode material for SC in various electrolytes such as aqueous, non-aqueous and ionic liquids (ILS). Unfortunately, thus far the mechanism of CNTs in EDLCs electrode has remained unclear [93]. The electrochemical capacitor application of CNT has been reviewed in the literature [94]. In the subsequent section, some of the novel works on CNT and its composites for the SC applications have been discussed.

Shan *et al.* [92] produced vertically aligned MWCNTs, which was grown directly on commercially available metallic alloy (Inconel 600) substrate, and investigated the effect of CNT length. It has been reported that as the length of CNT increases, the specific capacitance also increases, which ranges from 10.75 to 21.51 F g⁻¹ with energy density from 2.3 to 5.4 Wh kg⁻¹ and a power density of 315 kW kg⁻¹. Similarly,

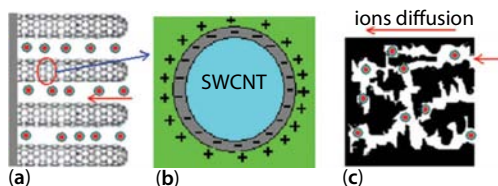


Figure 9.7 Comparison of charge storage mechanism in CNT (a–b) and AC (c).

Izadi-Najafabadi *et al.* [95] obtained a capacitance of 160 F g^{-1} for the well-defined SWCNTs synthesized through water-assisted chemical vapour deposition (CVD) at a working voltage of 4 V. Kim *et al.* [96] have synthesized vertically aligned CNTs of 6 nm in diameter on carbon paper (CP) using Al/Fe as catalyst. Also, they have studied its electrochemical behaviour. It was found that the SC displayed 200 F g^{-1} at 20 A g^{-1} with 20 Wh kg^{-1} in $1 \text{ M H}_2\text{SO}_4$, whereas it showed 100 Wh kg^{-1} in organic electrolyte ($1 \text{ M TEABF}_4\text{-PC}$). The tube-in-tube [89] CNTs exhibit an average capacitance of 203 F g^{-1} , which corresponds to its larger surface area, pore distribution and high conductivity.

The end caps of CNTs can be opened by many methods like heating it with oxygen, carbon dioxide, KOH, NaOH and treatment with acids. These methods can create some faults in CNTs, for example, in functional groups and holes. In this way, Yamada *et al.* [94] created holes on the side wall of metal-free SWCNTs by the combination of heat treatment in CO_2 and air. Furthermore, it was used as electrode and showed a maximum specific capacitance of 100 F g^{-1} because of the reduced carbonaceous component. A thin-film, flexible, lightweight and printable SC was fabricated using sprayed network of SWCNTs, which act as both electrode and current collector. Using this, high energy (6 Wh kg^{-1}) and power density of 23 and 70 kW kg^{-1} for both aqueous gel and organic electrolytes, respectively [97], can be achieved.

Generally, CNTs deliver relatively low energy density. In order to improve the energy density of EDLCs, many attempts were made using composites or additives. On these lines, Zhang *et al.* [98] have reported a novel type of CNT-ZnO composite electrode and gel electrolyte poly (vinyl alcohol)-phosphomolyhydric for SC. They deposited ZnO nanodots on CNT films by ultrasonic spray pyrolysis at different time intervals. These nanodots play an important role in improving the capacitance of CNT-ZnO nanocomposite electrode and obtained a higher specific capacitance of 323.9 F g^{-1} . The MoO_2 -SWCNT composite electrode prepared via electrochemically induced deposition method gave the highest specific capacitance of 597 F g^{-1} at 10 mV s^{-1} in $0.1 \text{ M H}_2\text{SO}_4$ solution with long-term cycle stability [99]. The MWCNT membrane coated with PPy was used directly as SC electrode without any binders and exhibited a remarkable specific capacitance as high as 427 F g^{-1} in $1 \text{ M Na}_2\text{SO}_4$ [100]. Liu *et al.* [101] examined the capacitance of the poly (3,4-ethylene dioxythiophene) nanotube (PEDOT)-based SC and found that it could be improved by incorporating nanotubular structure with a high power density of 25 kW kg^{-1} and energy density of 5.6 Wh kg^{-1} .

The RuO₂-CNT composite was synthesized based on the spontaneous reduction of Ru(VI) or Ru(VII) with CNT [102] and exhibited a good capacitance of 213 F g⁻¹ with over 20,000 stable charge/discharge cycles than Ru oxide and acid-functionalized MWCNT, despite the fact that the capacitance of Ru oxide is larger, *i.e.*, 803 F g⁻¹. Recently, oxidized CNT-CP composite electrodes have been prepared via oxidation treatment by Hsieh *et al.* [103]. The enhanced capacitance is attributed to carbonyl or quinone-type site and super hydrophilicity from oxidized CNT/CP surface. They found a capacitance value of 165 F g⁻¹ at 0.5 mA cm⁻² with less ESR. Recently, the capacitance values of CNT with PANI films on Pt electrode and PANI film were examined individually [104], and it was reported that PANI delivered lower capacitance (388 F g⁻¹) than CNT with PANI composite (516 F g⁻¹). The as-synthesized 3D CNT/graphene by CVD [105] also enhanced the specific capacitance to 385 F g⁻¹ in 6 M KOH at lower scan rate of 10 mV s⁻¹.

9.6 Two-Dimensional Graphene

In recent scenario, graphene is one of the modern materials in all fields of research like electronics, solar cells, energy storage and conversions, photo catalysis, sensors, and medical field. This is due to the unique properties of graphene like high charge carrier mobility (2,00,000 cm² V⁻¹ s⁻¹), being optically transparent, excellent flexibility, a high tensile strength (1 T pa), a good thermal conductivity (~5000 W m⁻¹ K⁻¹), an excellent theoretical specific surface area (2630 m² g⁻¹), which is higher than graphite (~10 m² g⁻¹), and a good theoretical specific capacitance of 550 F g⁻¹. Graphene was discovered by Novoselov and his group through the ground-breaking experiment of Scotch tape method. They received Nobel Prize in 2010 for the discovery of graphene. In general, graphene is two dimensional (2D) and has one-atom-thick sp²-hybridized carbon atoms with honeycomb-like structure [106–109]. In addition, graphene is the basic structure for the preparation of various carbon nanostructures such as 3D graphite, 1D CNTs, and 0D Bucky balls. In this sense, a variety of methods are explored to prepare graphene sheets such as CVD, eco-friendly chemical reduction (using NaOH, KOH, and L-ascorbic acid), liquid-phase exfoliation, sonochemical reduction, and thermal reduction [110–112]. Based on the aforementioned physical–chemical properties, graphene is the novel and outstanding electrode material for energy storage applications, especially in SCs.

9.6.1 Electrochemical Performance of Graphene

Generally, graphene stores the charge based on double-layer formation at the electrode/electrolyte interface. Also, the charge storage mechanism of graphene can be tuned by making composite with pseudocapacitive material or doping with heteroatom. Recently, Zhao *et al.* prepared thermally reduced graphene at different annealing temperatures like 200°C, 300°C, 400°C, 500°C, 700°C and 900°C. In this, the graphene oxide reduced at 200°C exhibits a higher specific capacitance of 260.5 F g⁻¹ at 0.4 A g⁻¹ than other samples. On the other hand, the specific capacitance of the electrode decreased with increasing annealing temperature. This is due to the removal of redox-active functional groups in the graphene when increasing the annealing temperature. It leads to a decrease in the overall specific capacitance of the electrode [113]. Similarly, the non-stacking reduced graphene oxide was prepared using thermal reduction. It provides the maximum specific capacitance of 236.8 F g⁻¹ at 1 A g⁻¹ in 6 M KOH electrolyte [114]. The thermally treated nitric acid graphene possesses a specific capacitance of 370 F g⁻¹ at 1 A g⁻¹ in 6 M NaOH electrolyte [115]. The electrochemically reduced graphene exhibits a specific capacitance of 223.6 F g⁻¹ at 5 mV s⁻¹ in 1 M H₂SO₄ electrolyte [116]. On the other hand, the hydrobromic acid-reduced graphene exhibits specific capacitance of 348 and 158 F g⁻¹ at 0.2 A g⁻¹ in 1 M aqueous H₂SO₄ and 1 M organic BMIPF₆ electrolytes, respectively [117]. Similarly, the vertically oriented graphene prepared using plasma-enhanced CVD also possesses specific capacitance of 129 and 112 F g⁻¹ at 20 mV s⁻¹ in 6 M KOH and 1 M TEABF₄/AN electrolytes, respectively [118]. It reveals that the graphene is electrochemically more active in acid electrolyte than organic electrolyte. This is due to the lower ionic size of aqueous electrolyte ions than organic ions. Mhamane *et al.* prepared graphene using tetraethylene glycol as reducing agent via green reduction. The graphene showed a specific capacitance of 97 F g⁻¹ at 0.1 A g⁻¹ in 1 M LiPF₆ in EC:DEC electrolyte [119]. From this, we realize that the electrochemical performance of graphene electrode depends on the method of synthesis, type of reducing agent, and type of electrolyte. The morphology of the graphene is also a deciding parameter for electrochemical performance. Recently, different nanostructured graphene were prepared like flat graphene sheets, heavily wrinkled sheets and crumbled graphene balls. In this, the crumbled graphene ball exhibits (150 F g⁻¹) a higher specific capacitance than the wrinkled (141 F g⁻¹) and flat (122 F g⁻¹) graphene sheets at 0.1 A g⁻¹ in 5 M KOH electrolyte. In addition, increasing mass loading in the electrode, the electrochemical

performance of the graphene gets diminished. This is due to the increase in electron transfer length and restacking of graphene layers [120]. The graphene nanoball prepared using CVD method exhibits a specific capacitance of 206 F g^{-1} at 5 mVs^{-1} . Subsequently, the electrode provides an excellent specific capacitance retention of 96% over 10,000 charge/discharge cycles at 20 A g^{-1} [121]. The graphene nanofiber prepared via CVD method possesses a specific capacitance of 193 F g^{-1} at 0.5 A g^{-1} in EMIBF₄ electrolyte [122]. Overall, graphene undergoes the restacking or reattachment problems during electrochemical process, which is a main limitation for commercialization. The restacking or reattachment of graphene sheet is due to the π - π interaction and strong van der Waals force of attraction that exists between the graphene layers. Recently, researchers are finding different ways to inhibit the restacking of graphene layers like (i) hybrid composites and (ii) doping of graphene with heteroatom. This is discussed in detail in the following.

9.6.2 Graphene Composites

9.6.2.1 Binary Composites

In general, the single-layer graphene undergoes reattachment while drying, which leads to reduced electrolyte accessibility. The reattachment can be avoided by introduction of spacer (carbon or MO or CPs) into the graphene sheets. It leads to an increase in the graphene surface area and electrolyte ion interaction with both sides of graphene. Based on this concept, the graphene/PANI composite was prepared using aniline and graphene oxide as starting precursors *via* electrochemical deposition method. The presence of PANI in the hybrid composite was confirmed by the presence of a couple of redox peaks in the CV curve. The calculated specific capacitance from GCDs curve was 640 F g^{-1} at 0.1 A g^{-1} in $1 \text{ M H}_2\text{SO}_4$ electrolyte. In addition, the electrode exhibits 90% of initial specific capacitance after 1000 cycles [123]. Similarly, the ethylene glycol-reduced graphene/PPy composite exhibits a specific capacitance of 420 F g^{-1} at 0.5 A g^{-1} . Also, it provides 93% initial specific capacitance after 200 cycles. The improved electrochemical performance is due to the good electrochemical utilization of PPy, enhanced charge carrier mobility, and prevention in swelling/shrinking by PPy chains during electrochemical cycling [124]. Subsequently, the graphene/PPy composite was prepared using electrochemical method with two different dopants, i.e., naphthalene disulfonate (NDS) (Ex-Gf/PPy-NDS) and 2-naphthalene sulfonate (NMS) (Ex-Gf/PPy-NMS). The Ex-Gf/PPy-NDS exhibits higher specific capacitance (351 F g^{-1}) than

Ex-GF/PPy-NMS (322 F g^{-1}), GF/PPy-NDS (240 F g^{-1}) and GF/PPy-NMS (148 F g^{-1}) in 3 M KCl at 1 A g^{-1} . The enhanced electrochemical performance of the composite is due to good electrical contact between PPy chain and graphene brought about through π - π interaction between graphene and PPy chains [125]. Yan *et al.* [126] and Wang *et al.* [127] have prepared graphene-PANI composites through *in situ* polymerization and obtained the maximum specific capacitance of 1046 F g^{-1} at 1 mV s^{-1} and 531 F g^{-1} at 200 mA g^{-1} . The platelet Co(OH)_2 was grown on high-surface-area graphene using hydrothermal method. The hybrid electrode exhibited a good specific capacitance of 572 F g^{-1} at 2 mVs^{-1} in 6 M KOH electrolyte. The enhanced specific capacitance is due to the synergistic effect and better electrochemical utilization of material [128].

Guan *et al.* prepared needle-like Co_3O_4 anchored to graphene using hydrothermal method. The hybrid composite possesses the maximum specific capacitance of 157.7 F g^{-1} at 0.1 A g^{-1} in 2 M KOH electrolyte. It maintains 70% initial specific capacitance up to 4000 cycles at 0.2 A g^{-1} . The improved specific capacitance and cycle life are due to the synergistic effect between the materials and multi-valence states of Co_3O_4 [129]. Dam *et al.* reported the sol-gel-synthesised NiO/graphene composite for pseudocapacitor applications. NiO loading was varied with respect to graphene. In this, NGNC79 possesses the maximum specific capacitance of 628 F g^{-1} at 1 A g^{-1} . It can be believed that the hybrid electrode has the highest electrochemically active surface area and stronger synergistic effect, which played a vital role in electron transfer. For comparison, NGNC79 was prepared by mixing, which yielded a specific capacitance of only 363.6 F g^{-1} . It is indicative of the specific capacitance of the electrode being strongly dependent on the method of preparation, mixing and drying, and composition content [130]. The layered (WS_2 /graphene) composite was synthesized using hydrothermal method. It provides a specific capacitance of 350 F g^{-1} at 2 mV s^{-1} in $1 \text{ M Na}_2\text{SO}_4$ electrolyte. Similarly, the hybrid electrode exhibits an energy density of 49 Wh kg^{-1} . The improved electrochemical performance is due to higher electrical conductivity and uniform decoration of WS_2 on graphene, which leads to enhanced effective utilization of electrolyte ions by the electrode [131]. The CoNi_2S_4 /graphene composite was prepared in different weight percentage loading of graphene (1%, 5%, 3%, 10% and 30%). In this, the CoNi_2S_4 /graphene (5 wt.%) provides an excellent specific capacitance of 2009.1 F g^{-1} at 1 A g^{-1} . The enhanced excellent electrochemical performance is due to the prevention of aggregation of graphene sheets and better interconnection between the materials [132]. On the other hand, when different nanostructured MnO_2 -decorated graphene composite such as graphene/ MnO_2 (flower-like nanospheres)

and graphene/MnO₂ (nanowires) were used, the flower-like nanosphere MnO₂-decorated graphene (405 F g⁻¹ at 1 A g⁻¹) exhibited a higher specific capacitance than nanowire MnO₂-decorated graphene (318 F g⁻¹ at 1 A g⁻¹) in 1 M Na₂SO₄ electrolyte [133]. Xu *et al.* prepared the Ni_{1-x}Co_xAl-LDH/graphene electrode that possesses the specific capacitance of 1902 F g⁻¹ at 1 A g⁻¹ [134].

Also, other carbon nanostructured materials were composited with graphene to inhibit the restacking of graphene sheets and to enhance the electrochemical performance of graphene. While using CNTs composited with graphene, the CNTs act as both spacer and conductive network between graphene sheets. In this sense, the CNT/graphene composite was prepared using one-pot pyrolysis method. The urea precursor concentration (3, 6, 15 and 30 g) was varied to tune the length of CNT. The hybrid composite had a specific surface area of 903 m² g⁻¹. The CNT/graphene added with 6 g of urea exhibits a higher specific capacitance of 413 F g⁻¹ at 5 mVs⁻¹ in 6 M KOH electrolyte. The improved electrochemical performance is due to the EDL capacitive and pseudocapacitive contribution from CNT and graphene and Co species [135]. Similarly, the SWCNT/graphene composite exhibits a specific capacitance of 244 F g⁻¹, which is higher than MWCNT/graphene (91 F g⁻¹). The improved specific capacitance of SWCNT/graphene is due to the 3D architecture of composite and high electrical conductivity [136]. The porous graphene/AC composite exhibits a high surface area of 2106 m² g⁻¹, which is due to the presence of huge amount of mesopores in the composite. Similarly, the hybrid electrode provides specific capacitance of 210 and 103 F g⁻¹ in 6 M KOH aqueous solution and 1 M Et₄NBF₄/PC organic electrolytes, respectively [137]. It also reveals that the electrochemical performance of graphene depends on the type of spacer material, composition of composites, type of electrolytes, mesopores, electrical conductivity, type of dopants used for CP, and morphology of the spacer material.

9.6.2.2 Ternary Hybrid Electrode

Furthermore, the rGO/CNTs/MnO₂ ternary composite was prepared, where CNT acts as a spacer that forms the 3D conductive network and prevents the agglomeration of graphene sheets. The hybrid electrode showed a better specific surface area of 140 m² g⁻¹ with a pore volume of 0.36 m³ g⁻¹. It also possessed the maximum specific capacitance of 319 F g⁻¹ at 0.5 A g⁻¹. Subsequently, the hybrid electrode exhibited a good cycling stability of 85.4% over 3000 cycles. The calculated energy density was found to be 44.3 Wh kg⁻¹ at a power density of 250 W kg⁻¹ [138]. The

rGO/TiO₂ NR/rGO composite shows the maximum specific capacitance of 114.5 F g⁻¹ at scan rate of 5 mVs⁻¹. The enhanced specific capacitance is due to the vertical alignment of TiO₂ NRs, the EDLC capacitance and good electrical conductivity of graphene, which improves the ion diffusion and electron transport [139]. Finally, it leads to improved electrochemical performance of the hybrid electrode. On the other hand, the graphene/PANI/CNT hybrid electrode exhibits higher specific capacitance (569 F g⁻¹ at 0.1 A g⁻¹) than the graphene/PPy/CNT (361 F g⁻¹ at 0.2 A g⁻¹) hybrid electrode. This is due to the high pseudocapacitive contribution from PANI rather than PPy [140, 141]. Figure 9.8 represents the formation mechanism of MnFe₂O₄/graphene/PANI. Sankar *et al.* reported that the effective role of graphene and PANI loading was optimized *via* electrochemical analysis. In this, when increasing the graphene loading beyond 20 wt.%, the specific capacitance retention dropped quickly with scan rate, which is due to the restacking of graphene sheets during electrochemical reaction. It leads to a decrease in the ionic diffusivity, increased electrode resistance and charge transfer resistance at the electrode/electrolyte interface. Subsequently, with an increase in the PANI loading into the MnFe₂O₄/graphene composite, the specific capacitance retention is decreased, which may be due to the covering of pores by PANI, increase in charge transfer resistance and low ionic conductivity of PANI in aqueous solution. Hence, the optimized graphene and PANI loading in MnFe₂O₄/graphene/PANI hybrid composite are 20 and 5 wt.% based on their electrochemical performance, respectively [142].

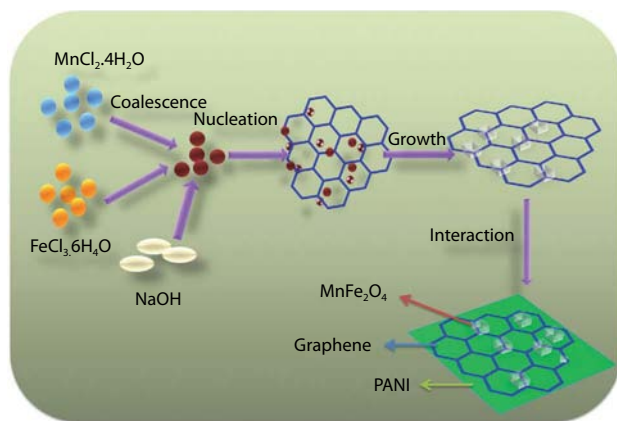
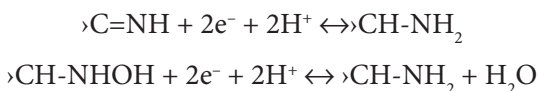


Figure 9.8 A plausible formation mechanism for the MnFe₂O₄ nanocube-decorated flexible graphene with wrapping of PANI [142].

The 3DG/CNTs/MnO₂ hybrid electrode exhibits good specific capacitance (343.1 F g⁻¹ at 2 mV s⁻¹) and excellent specific capacitance retention, which may be due to the enhancement in electrolyte ion diffusion and electronic conductivity [143]. The hydrothermal synthesis of CoFe₂O₄/graphene/PANI hybrid composite provides the maximum specific capacitance of 1133.3 F g⁻¹ at 1 mV s⁻¹ in 1 M KOH electrolyte. It is higher than CoFe₂O₄ (52.5 F g⁻¹), PANI (34.1 F g⁻¹) and graphene (218.7 F g⁻¹). The enhanced specific capacitance of ternary hybrid composite is due to the well-defined nanostructures, good electrical conductivity, controlled morphology, synergistic effect between the components and excellent pseudocapacitive contribution from PANI. Similarly, the π - π stacking, electrostatic interactions and hydrogen bonding between graphene and PANI are also beneficial for enhanced specific capacitance of hybrid electrodes [144]. Hence, we can believe that the preparation of hybrid electrode materials in the presence of graphene is also one of the keys to enhance the specific capacitance of the materials.

9.6.3 Doping of Graphene with Heteroatom

In the previous section, the complicated experimental procedures were carried out to improve the specific capacitance of the electrode. Recently, few groups have reported the improved electrochemical performance of graphene by doping with heteroatom. The doping of heteroatom leads to improved wettability and pseudocapacitance of the material. Also, the doping source acts as a spacer to inhibit the reattachment of graphene sheets. The N-doped graphene is prepared using thermal treatment, where dicyandiamide acts as a spacer that prevents aggregation of graphene sheets and also as a nitrogen (N) source. It possesses the maximum specific capacitance of 244.6 F g⁻¹ at 0.1 A g⁻¹ in 6 M KOH electrolyte [145]. On the other hand, Lee *et al.* prepared the N-doped few-layered graphene using microwave irradiation, where sodium amide was used as N source for doping the graphene. The N-doped graphene exhibits excellent electrical conductivity of 305 S cm⁻¹, which is due to the increase in sp² carbon network and decrease in O content. Subsequently, the N-doped graphene possesses the maximum specific capacitance of 200 and 130 F g⁻¹ in 1 M H₂SO₄ and 6 M KOH electrolytes at 0.5 A g⁻¹, respectively. The existence of high specific capacitance in acidic electrolyte is due to the pseudocapacitive contribution from pyridinic and pyrrolic N-doped graphene [146]. The possible reaction can be expressed as



Similarly, the heteroatom-codoped graphene is prepared and used for energy storage. It exhibits improved electrochemical performance due to the excellent wettability, higher pseudocapacitance and synergistic effect between codopents. The N/P-codoped thermally reduced graphene was prepared, where $(\text{NH}_4)_3\text{PO}_4$ was used as both N and P source and C/O ratio was decreased to 5.9. It provided a specific capacitance of 165 F g^{-1} . The improved electrochemical performance of N/P-codoped graphene is due to the pseudocapacitive contribution from both N and P heteroatom and prevention of graphene sheets restacking. Subsequently, the N/P-codoped electrode (91%) exhibits excellent specific capacitance retention than mono-N-doped (84%) and mono-P-doped (86%) graphene [147].

On the other hand, the N/B-codoped graphene exhibits good dispersability in alkaline and acidic solution implying the excellent diffusivity of electrolyte ions into the material. This is due to the presence of oxygen, N and B species in the graphene. In addition, the doped graphene exhibits 4–10 times greater specific capacitance than undoped graphene. This is due to the improved wettability and pseudocapacitive contribution from edge-doped N/B-graphene [148]. From this, we can believe that the edge fictionalization leads to improved electrical conductivity, increase in C/O ratio, wettability, electrochemical performance and reduced restacking of graphene and diffusive resistance of ions into the electrode.

Overall, the improved wettability and ionic diffusivity, prevention of restacking, increased electrical conductivity, improved electrochemical performance and reduction in charge transfer resistance can be achieved for graphene through composite with pseudocapacitive and EDL capacitive materials with suitable composition, type of electrolyte used, doping of graphene with heteroatom, and so on.

9.7 Conclusion and Outlook

Various carbon nanostructured electrode materials have been employed for SC applications. However, the carbon materials had their own drawbacks such as low energy density and restacking, which limits the commercialization and rate capability. Hence, carbon-based hybrid composites were used to fabricate SCs like carbon/MO, carbon/CPs, MO/CP and carbon/MO/CP in various compositions. It greatly improved the electrodes wettability, energy density, cycle life and reduced the charge transfer resistance. The experimental procedure for preparing hybrid material is a complicated and also time-consuming process.

Subsequently, the electrochemical performance of carbon-based electrode materials was enhanced via doping with heteroatom like N and P. The

carbon and heteroatom stored the charge based on ionic adsorption/desorption and Faradaic reaction, which leads to improved total specific capacitance and energy density.

Recently, researchers have been focussing on redox-active electrolyte to improve the electrochemical performance of AC. During charging, the redox additive species are adsorbed on the surface of the electrode and undergo redox reaction. However, only a limited number of reports are available on it for identification of new and suitable redox additive species to improve the energy storage capability of carbon-based materials in the future.

Acknowledgements

The authors are grateful to the Department of Atomic Energy—Board of Research in Nuclear Sciences (DAE-BRNS), Government of India (No. 2010/37P/46/BRNS/1443) and Department of Science and Technology (DST-SERB), Government of India (No. SR/FTP/PS-80/2009) for their financial support under the “Fast Track Young Scientist” scheme.

References

1. F. Beguin, E. Fręckowiak, *Supercapacitors Materials, Systems, and Applications*, KGaA, Boschstr. 12, 69469 Weinheim, Germany: Wiley-VCH Verlag GmbH & Co. (2013).
2. B. E. Conway, *Electrochemical Supercapacitors: Scientific Fundamentals and Technological Applications*, New York (USA): Kluwer Academic (1999).
3. <http://www.nuin.co.kr>.
4. L. L. Zhang and X. S. Zhao, *Chem. Soc. Rev.*, Vol. 38, 2520–2531, 2009.
5. G. Wang, L. Zhang, and J. Zhang, *Chem. Soc. Rev.*, Vol. 41, 797–828, 2012.
6. M. Conte, *Fuel Cells*, Vol. 10, 806–818, 2010.
7. M. Zhi, C. Xiang, J. Li, M. Li, and N. Wu, *Nanoscale*, Vol. 5, 72–88, 2013.
8. G. A. Snook, P. Kao, and A. S. Best, *J. Power Sources*, Vol. 196, 1–12, 2011.
9. M. E. Plonska-Brzezinska and L. Echegoyen, *J. Mater. Chem. A*, Vol. 1, 13703–13714, 2013.
10. S. Bose, T. Kuila, A. K. Mishra, R. Rajasekar, N. H. Kim, and J. H. Lee, *J. Mater. Chem.*, Vol. 22, 767–784, 2012.
11. X. Zhao, B. M. Sanchez, P. J. Dobson, and P. S. Grant, *Nanoscale*, Vol. 3, 839–855, 2011.
12. J. Zhang and X. S. Zhao, *ChemSusChem*, Vol. 5, 818–855, 2012.
13. F. Cheng, J. Zhao, W. Song, C. Li, H. Ma, J. Chen, and P. Shen, *Inorg. Chem.* Vol. 45, 2038–2044, 2006.
14. M. Toupin, T. Brousse, and D. Belanger, *Chem. Mater.*, Vol. 16, 3184–3190, 2004.

15. S. C. Pang, M. A. Anderson, and T. W. Chapman, *J. Electrochem.*, Vol. 147, 444–450, 2000.
16. S. L. Kuo and N. L. Wu, *J. Electrochem. Soc.*, Vol. 153, A1317–A1324, 2006.
17. F. Cao, G. X. Pan, X. H. Xia, P. S. Tang, and H. F. Chen, *J. Power Sources*, Vol. 264, 161–167, 2014.
18. B. Senthilkumar, K. Vijaya Sankar, R. Kalai Selvan, D. Meyrick, and M. Minakshi, *RSC Adv.*, Vol. 3, 352–357, 2013.
19. K. Vijaya Sankar, D. Kalpana, and R. Kalai Selvan, *J. Appl. Electrochem.*, Vol. 42, 463–470, 2012.
20. K. Vijaya Sankar, S. T. Senthilkumar, L. John Berchmans, C. Sanjeeviraja, and R. Kalai Selvan, *Appl. Surf. Sci.*, Vol. 254, 624–630, 2012.
21. Q. Guan, J. Cheng, B. Wang, W. Ni, G. Gu, X. Li, L. Huang, G. Yang, and F. Nie, *ACS Appl. Mater. Interfaces*, Vol. 6, 7626–7632, 2014.
22. Hao Chen , Linfeng Hu , Min Chen , Yan Yan , and Limin Wu, *Adv. Funct. Mater.*, Vol. 24, 934–942, 2014.
23. B. Senthilkumar and R. Kalai Selvan, *J. Colloid Interface Sci.*, Vol. 426, 280–286, 2014.
24. V. D. Nithya, R. Kalai Selvan, D. Kalpana, Leonid Vasylechko, and C. Sanjeeviraja, *Electrochim. Acta*, Vol. 109, 720–731, 2013.
25. V. D. Nithya, R. Kalai Selvan, Leonid Vasylechko, and C. Sanjeeviraja, *RSC Adv.*, Vol. 4, 4343–4352, 2014.
26. K. Gopalsamy, Z. Xu, B. Zheng, T. Huang, L. Kou, X. Zhao, and C. Gao, *Nanoscale*, Vol. 6, 8595–8600, 2014.
27. M. Zhang, S. Guo, L. Zheng, G. Zhang, Z. Hao, L. Kang, and Z. H. Liu, *Electrochim. Acta*, Vol. 87, 546–553, 2013.
28. A. Shanmugavani and R. Kalai Selvan, *RSC Adv.*, Vol. 4, 27022–27029, 2014.
29. Y. Lei, J. Li, Y. Wang, L. Gu, Y. Chang, H. Yuan, and D. Xiao, *ACS Appl. Mater. Interfaces*, Vol. 6, 1773–1780, 2014.
30. M. Mastragostino, C. Arbizzani, R. Paraventi, and A. Zanelli, *J. Electrochem. Soc.*, Vol. 147, 407–412, 2000.
31. R. Kotz and M. Carlen, *Electrochim. Acta*, Vol. 45, 2483–2498, 2000.
32. M. D. Levi, G. Salitra, N. Levy, and D. Aurbach, *Nat. Mater.*, Vol. 8, 872–875, 2009.
33. P. Sivaraman, S. K. Rath, V. R. Hande, A. P. Thakur, M. Patri, and A. B. Samui, *Synth. Metals*, Vol. 156, 1057–1064, 2006.
34. B. Muthulakshmi, D. Kalpana, S. Pitchumani, and N. G. Renganathan, *J. Power Sources*, Vol. 158, 1533–1537, 2006.
35. A. Laforgue, P. Simon, C. Sarrazin, and J. Fauvarque, *J. Power Sources*, Vol. 80, 142–148, 1999.
36. T. L. Kelly, K. Yano, and M. O. Wolf, *ACS Appl. Mater. Inter.*, Vol. 1, 2536–2543, 2009.
37. R. C. Bansal and M. Goyal, *Activated Carbon Absorption*, New York (USA): CRC Press Taylor and Francis (2005).

38. S. T. Senthilkumar, B. Senthilkumar, S. Balaji, C. Sanjeeviraja, and R. Kalai Selvan, *Mater. Res. Bull.*, Vol. 46, 413–419, 2011.
39. E. Frackowiak, and F. Beguin, *Carbon*, Vol. 39, 937–950, 2001.
40. L. Wei and G. Yushin, *Nano Energy*, Vol. 1, 552–565, 2012.
41. S. T. SenthilKumar, R. Kalai Selvan, and J. S. Melo, *AIP Proceed.*, Vol. 1538, 124–127, 2013.
42. S. T. Senthilkumar and R. Kalai Selvan, *Phys. Chem. Chem. Phys.*, Vol. 16, 15692–15698, 2014.
43. T. E. Rufford, D. Hulicova-Jurcakova, E. Fiset, Z. Zhu, and G. Q. Lu, *Electrochem. Comm.*, Vol. 11, 974–977, 2009.
44. V. Subramanina, C. Luo, A. M. Stephen, K. S. Nahm, S. Thomas, and B. Wei, *J. Phys. Chem. C*, Vol. 111, 7527–7531, 2007.
45. D. Kalpana, S. H. Cho, S. B. Lee, R. Misra, and N. G. Renganathan, *J. Power Sources*, Vol. 190, 587–591, 2009.
46. M. S. Balathanigaimani, W. G. Shim, M. J. Lee, C. Kim, J. W. Lee, and H. Moon, *Electrochem. Comm.*, Vol. 10, 868–871, 2008.
47. T. E. Rufford, D. H. Jurcakova, K. Khosla, Z. Zhu, and G. Q. Lu, *J. Power Sources*, Vol. 195, 912–918, 2010.
48. B. Xu, Y. F. Chen, G. Wei, G. P. Cao, H. Zhang, and Y. S. Yang, *Mater. Chem. Phys.*, Vol. 124, 504–509, 2010.
49. Y. P. Guo, J. R. Qi, Y. Q. Jiang, S. F. Yang, Z. C. Wang, and H. D. Xu, *Mater. Chem. Phys.*, Vol. 80, 704–709, 2003.
50. M. Olivares-Marin, J. A. Fernandez, M. J. Lazaro, C. Fernandez-Gonzalez, A. Macias-Garcia, V. Gomez-Serrano, F. Stoeckli, and T. A. Centeno, *Mater. Chem. Phys.*, Vol. 114, 323–327, 2009.
51. L. Wei, M. Sevilla, A. B. Fuertes, R. Mokaya, and G. Yushin, *Adv. Func. Mater.*, Vol. 22, 827–834, 2011.
52. J. Mi, X. R. Wang, R. J. Fan, W. H. Qu, and W. C. Li, *Energy Fuels*, Vol. 26, 5321–5329, 2012.
53. S. T. SenthilKumar, R. Kalai Selvan, M. Ulaganathan, and J. S. Melo, *Electrochim. Acta*, Vol. 115, 518–524, 2014.
54. M. Rajesh, K. V. Sankar, S. M. Chen, and R. K. Selvan, *RSC Adv.*, Vol. 4, 1225–1233, 2014.
55. Y. J. Kim, B. J. Lee, H. Suezaki, T. Chino, Y. Abe, T. Yanagiura, K. C. Park, and M. Endo, *Carbon*, Vol. 44, 1592–1595, 2006.
56. F. C. Wu, R. L. Tseng, C. C. Hu, and C. C. Wang, *J. Power Sources*, Vol. 138, 351–359, 2004.
57. L. Wei, M. Sevilla, A. B. Fuertes, R. Mokaya, and G. Yushin, *Adv. Energy Mater.*, Vol. 1, 356–361, 2011.
58. S. Zhao, C. Y. Wang, M. M. Chen, J. Wang, and Z. Q. Shi, *J. Phys. Chem. Solids*, Vol. 70, 1256–1260, 2009.
59. M. Biswal, A. Banerjee, M. Deo, and S. Ogale, *Energy Environ. Sci.*, Vol. 6, 1249–1259, 2013.

60. R. Wang, P. Wang, X. Yan, J. Lang, C. Peng, and Q. Xue, *ACS Appl. Mater. Interfaces*, Vol. 4, 5800–5806, 2012.
61. M. Selvakumar and D. Krishna Bhat, *Appl. Surf. Sci.*, Vol. 263, 236–241, 2012.
62. S. Y. Feng, W. Feng, B. L. Ying, and Y. Z. Hui, *New Carbon Mater.*, Vol. 22, 53–57, 2007.
63. J. H. Park, O. O. Park, K. H. Shin, C. S. Jin, and J. H. Kim, *Electrochem. Solid-State Lett.*, Vol. 5, H7–H10, 2002.
64. S. T. Senthilkumar, R. Kalai Selvan, Y. S. Lee, and J. S. Melo, *J. Mater. Chem. A*, Vol. 1, 1086–1095, 2013.
65. S. T. Senthilkumar, R. Kalai Selvan, N. Ponpandian, J. S. Melo, and Y. S. Lee, *J. Mater. Chem. A*, Vol. 1, 7913–7919, 2013.
66. S. T. Senthilkumar, R. Kalai Selvan, J. S. Melo, and C. Sanjeeviraja, *ACS Appl. Mater. Inter.*, Vol. 5, 10541–10550, 2013.
67. S. T. Senthilkumar, R. Kalai Selvan, N. Ponpandian, and J. S. Melo, *RSC Adv.*, Vol. 2, 8937–8940, 2012.
68. Y. Zhang, H. Feng, X. Wu, L. Wang, A. Zhang, T. Xia, H. Dong, X. Li, and L. Zhang, *Int. J. Hydrogen Energy*, Vol. 34, 4889–4899, 2009.
69. A. G. Pandolfo and A. F. Hollenkamp, *J. Power Sources*, Vol. 157, 11–27, 2006.
70. Y. J. Lee, J. C. Jung, and J. Yi, *Curr. Appl. Phys.*, Vol. 10, 682–686, 2010.
71. E. Frackowiak and F. Beguin, *Carbon*, Vol. 39, 937–950, 2001.
72. Y. Zhu, H. Hu, W. Li, and X. Zhang, *Carbon*, Vol. 45, 160–165, 2007.
73. J. Li, X. Wang, Y. Wang, and Q. Huang, *J. Non-Cry. Solids*, Vol. 354, 19–24, 2008.
74. J. Li, X. Wang, Y. Wang, and S. Gamboa, *J. Power Sources*, Vol. 158, 784–788, 2006.
75. X. Wang, Y. Wang, D. Wu, and R. Fu, *J. Power Sources*, Vol. 185, 589–594, 2008.
76. P. Katangoota, T. Chaisuwan, and A. Wongahaisuwat, *Mat. Sci. Eng. B*, Vol. 167, 36–42, 2010.
77. X. Zheng, O. Wu, and R. Fu, *Electrochim. Acta*, Vol. 53, 5711–5715, 2008.
78. Y. Zhu, H. Hu, W. C. Li, and X. Zhang, *J. Power Sources*, Vol. 162, 738–742, 2006.
79. B. Fang and L. Binder, *J. Power Sources*, Vol. 163, 616–622, 2006.
80. B. Fang and L. Binder, *Electrochim. Acta*, Vol. 52, 6916–6921, 2007.
81. D. Kalpana, K. S. Omkumar, S. Sureshkumar, and N. G. Ranganathan, *Electrochim. Acta*, Vol. 52, 1309–1315, 2006.
82. S. W. Hwang and S. H. Hyun, *J. Power Sources*, Vol. 172, 451–459, 2007.
83. Y. J. Lee, J. C. Jung, S. Park, and J. G. Seo, *Current Appl. Phys.*, Vol. 10, 947–951, 2010.
84. H. An, Y. Wang, X. Wang, L. Zhang, and X. Wang, *J. Power Sources*, Vol. 195, 6964–6969, 2010.
85. X. Wang, Li. Lu, X. Wang, L. Yi, C. Hu, and X. Zhang, *Mater. Sci. Eng. B*, Vol. 176, 1232–1238, 2011.
86. T. Bordjiba, M. Mohamadi, and L. H. Dao, *J. Power Sources*, Vol. 172, 991–998, 2007.

87. C. Lv, D. Wu, R. Fu, Z. Zhang, and Z. Su, *J. Non-Cry. Solids*, Vol. 354, 4567–4571, 2008.
88. D. Wu, X. Chen, S. Lu, Y. Zhang, and F. Xu, *Micro. Meso. Mater.*, Vol. 131, 261–264, 2010.
89. H. Pan, C. K. Poh, Y. P. Feng, and J. Lin, *Chem. Mater.*, Vol. 19, 6120–6125, 2007.
90. E. Frackowiak, *Phys. Chem. Chem. Phys.*, Vol. 9, 1774–1785, 2007.
91. W. Lu, L. Qu, K. Henry, and L. Dai, *J. Power sources*, Vol. 189, 1270–1277, 2009.
92. R. Shah, X. Zhang, and S. Talapatra, *Nanotechnology*, Vol. 20, 395202–395207, 2009.
93. Y. Yamada, Q. Kimizaka, K. Machida, S. Suematsa, K. Tamamista, S. Saeki, Y. Yamada, N. Yoshigama, O. Tannuikie, J. Yamashita, F. Don, K. Hata, and H. Hatori, *Energy Fuels*, Vol. 24, 3373–3377, 2010.
94. H. Pan, J. Li, and Y. P. Feng, *Nanoscale Res. Lett.*, Vol. 5, 654–668, 2010.
95. A. I. Najafabadi, S. Yasuda, K. Kobashi, T. Yamada, D. N. Futaba, H. Hatori, M. Yumura, and K. Hata, *Adv. Mater.*, Vol. 22, E235–E241, 2010.
96. B. Kim, H. Chung, and W. Kim, *J. Phys. Chem. C*, Vol. 114, 15223–15227, 2010.
97. M. K. Mpgen, C. K. Chan, J. Ma, Y. Uni, and G. Gruner, *Nano Lett.*, Vol. 9, 1872–1876, 2009.
98. Y. Zhang, X. Sun, L. Pan, H. Li, Z. Sun, C. Sun, and B. K. Tay, *Solid State Ionics*, Vol. 180, 1525–1528, 2008.
99. F. Gao, L. Zhang, and S. Huang, *Mater. Lett.*, Vol. 64, 537–540, 2010.
100. Y. Fang, J. Liu, D. J. Yu, J. P. Wicksted, K. Kalkan, C. O. Topal, B. N. Flanders, J. Wu, and J. Li, *J. Power sources*, Vol. 195, 674–679, 2010.
101. R. Liu, S. I. Cho, and S. B. Lee, *Nanotechnology*, Vol. 19, 215710–215718, 2008.
102. X. Lu, T. A. Huber, M. C. Kopac, and P. G. Pickup, *Electrochim. Acta*, Vol. 54, 7141–7147, 2009.
103. C. T. Hsieh, W. Y. Chen, and Y. S. Cheng, *Electrochim. Acta*, Vol. 55, 5294–5300, 2010.
104. V. Branzoi, F. Branzoi, and L. Pilan, *Surf. Inter. Anal.*, Vol. 42, 1266–1270, 2010.
105. Z. Fan, J. Yan, L. Zhi, Q. Zhang, T. Wei, J. Feng, M. Zhang, W. Qian, and F. Wei, *Adv. Mater.*, Vol. 22, 3723–3728, 2010.
106. M. M. Hantel, T. Kaspar, R. Nesper, A. Wokaun, and R. Kotz, *Chem. Eur. J.*, Vol. 18, 9125–9136, 2012.
107. B. Y. Zhu, S. Murali, W. Cai, X. Li, J. W. Suk, J. R. Potts, and R. S. Ruoff, *Adv. Mater.*, Vol. 22, 3906–3924, 2010.
108. N. O. Weiss, H. Zhou, L. Liao, Y. Liu, S. Jiang, Y. Huang, and X. Duan, *Adv. Mater.*, Vol. 24, 5979–6004, 2012.
109. X. Huang, Z. Zeng, Z. Fan, J. Liu, and H. Zhang, *Adv. Mater.*, Vol. 24, 5782–5825, 2012.

110. A. A. Green and M. C. Hersam, *J. Phys. Chem. Lett.*, Vol. **1**, 544–549, 2010.
111. L. L. Zhang, R. Zhou, and X. S. Zhao, *J. Mater. Chem.*, Vol. **20**, 5983–5992, 2010.
112. T. Kuila, A. K. Mishra, P. Khanra, N. H. Kim, and J. H. Lee, *Nanoscale*, Vol. **5**, 52–71, 2013.
113. B. Zhao, P. Liu, Y. Jiang, D. Pan, H. Tao, J. Song, T. Fang, and W. Xu, *J. Power Sources*, Vol. **198**, 423–427, 2012.
114. Y. Yoon, K. Lee, C. Baik, H. Yoo, M. Min, Y. Park, S. M. Lee, and H. Lee, *Adv. Mater.*, Vol. **25**, 4437–4444, 2013.
115. N. Xiao, H. Tan, J. Zhu, L. Tan, X. Rui, X. Dong, and Q. Yan, *ACS Appl. Mater. Interfaces*, Vol. **5**, 9656–9662, 2013.
116. J. Yang and S. Gunasekaran, *Carbon*, Vol. **51**, 36–44, 2013.
117. Y. Chen, X. Zhang, D. Zhang, P. Yu, and Y. Ma, *Carbon*, Vol. **49**, 573–580, 2011.
118. Z. Bo, Z. Wen, H. Kim, G. Lu, K. Yu, and J. Chen, *Carbon*, Vol. **50**, 4379–4387, 2012.
119. D. Mhamane, A. Suryawanshi, A. Banerjee, V. Aravindan, S. Ogale, and M. Srinivasan, *AIP Adv.*, Vol. **3**, 042112–042121, 2013.
120. J. Luo, H. D. Jang, and J. Huang, *ACS Nano*, Vol. **7**, 1464–1471, 2013.
121. J. S. Lee, S. Kim, J. C. Yoon, and J. Jang, *ACS Nano*, Vol. **7**, 6047–6055, 2013.
122. C. Cui, W. Qian, Y. Yu, C. Kong, B. Yu, L. Xiang, and F. Wei, *J. Am. Chem. Soc.*, Vol. **136**, 2256–2259, 2014.
123. X. M. Feng, R. M. Li, Y. W. Ma, R. F. Chen, N. E. Shi, Q. L. Fan, and W. Huang, *Adv. Funct. Mater.*, Vol. **21**, 2989–2996, 2011.
124. Y. Liu, Y. Zhang, Guoheng Ma, Z. Wang, K. Liu, and H. Liu, *Electrochim. Acta*, Vol. **88**, 519–525, 2013.
125. Y. Song, J. L. Xu, and X. X. Liu, *J. Power Sources*, Vol. **249**, 48–58, 2014.
126. Y. Yan, T. Wei, B. Shao, Z. Fan, W. Qian, M. Zhang, and F. Wei, *Carbon*, Vol. **48**, 487–493, 2010.
127. H. Wang, Q. Hao, X. Yang, L. Lu, and X. Wang, *Electrochem. Comm.*, Vol. **11**, 1158–1161, 2009.
128. D. Ghosh, S. Giri, and C. K. Das, *ACS Sustainable Chem. Eng.*, Vol. **1**, 1135–1142, 2013.
129. Q. Guan, J. Cheng, B. Wang, W. Ni, G. Gu, Xiaodong, L. Huang, G. Yang, and F. Nie, *ACS Appl. Mater. Interfaces*, Vol. **6**(10), 7626–7632, 2014.
130. D. T. Dam, X. Wang, and J. M. Lee, *ACS Appl. Mater. Interfaces*, Vol. **6**(11), 8246–8256, 2014.
131. S. Ratha and C. S. Rout, *ACS Appl. Mater. Interfaces*, Vol. **5**, 11427–11433, 2013.
132. W. Du, Z. Wang, Z. Zhu, S. Hu, X. Zhu, Y. Shi, H. Pang, and X. Qian, *J. Mater. Chem. A*, Vol. **2**, 9613–9619, 2014.
133. X. Feng, N. Chen, Y. Zhang, Z. Yan, X. Liu, Y. Ma, Q. Shen, L. Wang, and W. Huang, *J. Mater. Chem. A*, Vol. **2**, 9178–9184, 2014.

134. J. Xu, S. Gai, F. He, N. Niu, P. Gao, Y. Chen, and P. Yang, *Dalton Trans.*, Vol. 43, 11667–11675, 2014.
135. Z. Yang, Y. Zhao, Q. Xiao, Y. Zhang, L. Jing, Y. Yan, and K. Sun, *ACS Appl. Mater. Interfaces*, Vol. 6(11), 8497–8504, 2014.
136. F. Zeng, Y. Kuang, N. Zhang, Z. Huang, Y. Pan, Z. Hou, H. Zhou, C. Yan, and O. G. Schmidt, *J. Power Sources*, Vol. 247, 396–401, 2014.
137. C. Zheng, X. Zhou, H. Cao, G. Wang, and Z. Liu, *J. Power Sources*, Vol. 258, 290–296, 2014.
138. H. Jiang, Y. Dai, Y. Hu, W. Chen, and C. Li, *ACS Sustainable Chem. Eng.*, Vol. 2(1), 70–74, 2013.
139. A. Ramadoss, G. S. Kim, and S. J. Kim, *CrysEngComm*, Vol. 15, 10222–10229, 2013.
140. X. Lu, H. Dou, S. Yang, L. Hao, L. Zhang, L. Shen, F. Zhang, and X. Zhang, *Electrochim. Acta*, Vol. 56, 9224–9232, 2011.
141. X. Lu, F. Zhang, H. Dou, C. Yuan, S. Yang, L. Hao, L. Shen, L. Zhang, and X. Zhang, *Electrochim. Acta*, Vol. 69, 160–166, 2012.
142. K. V. Sankar and R. K. Selvan, *RSC Adv.*, Vol. 4, 17555–17566, 2014.
143. W. Chen, Y. He, X. Li, J. Zhou, Z. Zhang, C. Zhao, C. Gong, S. Li, X. Pan, and E. Xie, *Nanoscale*, Vol. 5, 11733–11741, 2013.
144. P. Xiong, H. Huang, and X. Wang, *J. Power Sources*, Vol. 245, 937–946, 2014.
145. P. Wang, H. He, X. Xu, and Y. Jin, *ACS Appl. Mater. Interfaces*, Vol. 6, 1563–1568, 2014.
146. K. H. Lee, J. Oh, J. Gon Son, H. Kim, and S. Lee, *ACS Appl. Mater. Interfaces*, Vol. 6, 6361–6368, 2014.
147. C. Wang, Y. Zhou, L. Sun, Q. Zhao, X. Zhang, P. Wan, and J. Qiu, *J. Phys. Chem. C*, Vol. 117, 14912–14919, 2013.
148. K. Fujisawa, R. Cruz-Silva, K. Yang, Y. A. Kim, T. Hayashi, M. Endo, M. Terrones, and M. S. Dresselhaus, *J. Mater. Chem. A*, Vol. 2, 9532–9540, 2014.

Synthesis, Characterization, and Uses of Novel-Architecture Copolymers through Gamma Radiation Technique

H. Iván Meléndez-Ortiz¹ and Emilio Bucio^{*,2}

¹ *Department of Advanced Materials, Research Center in Applied Chemistry, Saltillo, Mexico.*

² *Department of Radiation Chemistry and Radiochemistry, Nuclear Science Institute, National Autonomous University of Mexico, Mexico City, Mexico*

Abstract

Radiation processing has many advantages over other conventional methods. When using gamma radiation for material processing, no catalysts or additives are needed to initiate the reaction. Grafting techniques normally include the pre-irradiation, as well as the mutual or the simultaneous method. The main advantage of this radiation-assisted method is relatively simple; surface grafting of polymers has attracted great interest in the past few decades, as it allows the tailoring of surface properties of various polymer materials, and thus specific functionalities useful for many applications can be effectively produced. When polymers are exposed to ionizing irradiation, trapped radicals and peroxides or hydroperoxides are formed, and they are capable of initiating grafting copolymerization reactions. Various graft-polymerization approaches have been developed, including direct graft polymerization of vinyl monomers already containing desirable functional groups, graft copolymerization of two (or more) different types of monomers onto a polymer backbone, and graft polymerization of a precursor monomer that can be subsequently modified. This chapter revises and focuses the recent advances in the synthesis and characterization of graft copolymers with new architecture prepared by means of gamma radiation. Also, it describes the potential use of these copolymers in the biomedical area.

Keywords: Gamma radiation, grafting methods, copolymers, polymer characterization, drug delivery

*Corresponding author: ebucio@nucleares.unam.mx

10.1 Introduction

Radiation grafting is a suitable technique for surface modification of polymeric materials since it allows introducing active functional groups on the polymer backbone [1–5]. This method is applicable for many substrates and monomers combinations and, unlike chemically initiated grafting; it does not require initiators [6]. There are several methods of radiation grafting: (i) the direct (or mutual) grafting method in which the polymeric material is irradiated in contact with a monomer, homopolymerization being a collateral effect; (ii) the pre-irradiation method, which involves the irradiation of the polymer matrix in the absence of air and then the grafting is initiated by macroradicals trapped in the irradiated polymer; radiation dose is usually larger than in the direct method and polymer degradation may occur; and (iii) the pre-irradiation oxidative grafting method that consists in the pre-irradiation of the polymer in the presence of air or oxygen, so that the macroradicals formed are converted to peroxides and/or hydroperoxides, and when the irradiated polymer is heated in the presence of monomer the peroxides decompose to give the macroradicals [1, 7, 8]. Radiation processing has many advantages over other conventional methods. When using radiation for material processing, no catalysts or additives are needed in order to initiate the reaction, the energy source being either γ -ray, UV or electrons [9]. The main advantage of these radiation-assisted methods is that they are relatively simple; surface grafting of polymers has attracted great interest in the past few decades, as it allows the tailoring of surface properties of various polymer materials, and thus specific functionalities useful for many applications can be effectively produced [10]. When polymers are exposed to ionizing irradiation, trapped radicals and peroxides or hydroperoxides are formed as a result; these are capable of initiating grafting copolymerization reactions [11]. Various graft-polymerization approaches have been developed, including direct graft polymerization of vinyl monomers already containing desirable functional groups, graft copolymerization of two (or more) different types of monomers onto a polymer backbone, and graft polymerization of a precursor monomer that can be subsequently modified [12].

As the radiation, such as γ -ray or UV photografting, provides a sterilization effect and no initiator is required for copolymerization, no environmental pollution and biological toxic substances are generated. The grafting of various vinyl monomers onto thermoplastic rubber, ultrahigh molecular weight polyethylene (PE) and nonwoven fabric of polypropylene (PP) by γ -ray irradiation or UV treatment method had been reported in some studies [13, 14].

In recent years there has been remarkable growth in the research and development of synthetic polymers for biomedical, microelectronics, and other advanced technological applications [15]. In this context radiation processing technology represents a useful tool for the modification of polymeric materials including grafting of monomers onto polymers [1, 16, 17]. Radiation grafting in specific allows the modification of the surface composition of polymeric biomaterials without changing their mechanical properties. Radiation-induced copolymerization and crosslinking of copolymers has been increasingly used for creation of novel biomaterials [18]. Gamma radiation has successfully been used for grafting of polymers onto polymeric materials; the technique enables surface and bulk functionalization with groups such as amide, amine, carboxylic acid, or epoxy [19].

Polymers are an important class of materials for pharmaceutical and biotechnological applications; surface-functionalized medical devices are attracting raising interest owing to the possibility of improving their dealing with the host environment, while keeping the bulk features responsible for their therapeutic performance [20]. Enhanced biocompatibility and prophylaxis against infections are the most pursued aims of altering the surface structure/composition [21].

10.2 Ionizing Radiation

10.2.1 Type of Radiation

Polymer surfaces are commonly modified by physical deposition of other compounds (e.g., surfactants, polymers) by direct chemical modification of the polymer surface (e.g., oxidation, hydrolysis, sulfonation) or by chemical bonding of a different polymer (graft copolymerization) or “polymer-like” composition (via plasma discharge) on the substrate polymer surface. The most commonly used energy sources for the last two techniques are ionizing radiations [22–25] and radio-frequency or microwave gas discharges, also called plasma or glow discharges [26–28]. Photochemical initiations using UV light sources may also be used but they are less common and will not be included in this review. Ionizing radiations are commercially available as cobalt-60 gamma ray sources or as electron accelerators. The former are low intensity sources but have high depth of penetration, while the latter are high intensity sources but have relatively low depth of penetration.

The type of radiation to be used in preparation of graft copolymers is a parameter that has to be considered upon using high-energy radiation to

initiate radicals for graft copolymerization. Two main radiation sources are commercially available: Co-60 as source of γ -rays and electron beam accelerator as a source of electrons. From a grafting point of view, γ -rays, which is electromagnetic radiation (photons), are more advantageous in terms of high penetration power compared to electrons, which are particulate radiation in nature [29]. Upon crossing the matter, the electrons lose energy continuously through a large number of small energy transfers unlike γ -rays that tend to lose a relatively large amount of their intensity by interaction with the matter. The fractions of photons that do not interact with the finite thickness of the matter are transmitted with their original energy and directions. Therefore, the dose rate can be easily controlled by using a suitable attenuator without influencing the photons energy. Lead is the most widely used attenuator for γ -radiation as it exhibits a lower thickness compared to other attenuators. γ -radiation is normally utilized for fundamental studies and grafting processes requiring a low dose rate with deep penetration and is of particular interest when graft copolymerization is carried out using simultaneous irradiation method. On the other hand, an electron beam is often used in surface modification of polymers. Nevertheless, bulk grafting can be achieved using high energy electrons and thinner films.

10.2.2 X-Ray and Gamma-Rays

X-ray and gamma-rays are electromagnetic waves of the same nature as visible or ultra-violet light but of a much shorter wavelength. X-rays are generated when fast electrons are suddenly stopped by striking a solid obstacle. They usually present a very broad spectrum of energies, the maximum energy being very close to the energy of the incident electrons. The "effective energy" is approximately equal to one-half of the peak energy. The "effective wavelength" of an X-ray beam is defined as the wavelength of the mono energetic radiation which has the same half-value layer (HVL) for copper as the actual X-ray beam. The HVL is the thickness of copper which reduces the intensity of the beam to one-half. Gamma-rays are identical in nature with X-rays but the former term is used for electromagnetic radiations emitted by the nuclei of natural or artificial radioactive isotopes. Gamma-rays from a particular nucleus are usually emitted at several discrete frequencies. However, a number of isotopes give a very simple spectrum of gamma-rays. Thus, cobalt-60 gives two sharp lines of equal intensity at 1.17 and 1.33 MeV (mega electron volts) respectively. The physical properties of X-rays and gamma-rays depend strongly upon their initial energy. "Soft" X-rays of less than 100 keV are highly absorbed by

thin layers of light elements, whereas very hard X-rays and gamma-rays are capable of traversing layers of heavy metals of considerable thickness [10].

10.2.3 Electron Beam

Beta-rays are emitted by a large number of natural or artificially produced radioactive isotopes, some beta-ray emitters with their half-lives and the corresponding radiation energies. Many of these isotopes are commonly used in radiation chemistry. A very promising beta-ray source seems to be the fission product strontium-90 which is produced in large quantities in nuclear power plants. Unfortunately, strontium is absorbed by the human body and is concentrated in bones. This effect, together with its long half-life, makes the use of this radioisotope particularly dangerous and will prevent its practical use on a large scale until suitable methods are developed for enclosing it safely without absorbing too much of the radiation. The use of artificially accelerated electron beams in radiation chemistry was first described by Coolidge in 1925. This type of radiation has only been developed on a large scale, however, in recent years, several machines are now commercially available which produce very intense electron beams with energies ranging from 0.5 to 20 MeV, or even higher. Their rapid development is largely due to medical and industrial demands for powerful radiation sources. The penetration of fast electrons is much smaller than that of electromagnetic radiation having the same quantum energy. Charged particles of any kind have a finite range in matter; thus 2 MeV electrons are entirely absorbed by 1 cm of water. In the 1–10 MeV range, the penetration of electrons is approximately linear with their energy, a number of electron accelerators are being built, based on various quite different principles [10].

10.2.4 Alpha Particles

This group of radiations includes natural alpha-rays (fast moving helium ions emitted by several radioactive isotopes) and beams of protons, deuterons, etc., artificially accelerated in a machine such as an electrostatic accelerator, and a cyclotron. Radiations of this type are entirely absorbed in relatively thin layers of material but the density of the absorbed energy is highly concentrated along the tracks of the ionizing particle. Radioisotopes emitting alpha-rays, such as radon dissolved in the medium to be irradiated, have been used as “internar” radiation sources to initiate chemical reactions. Radon emits alpha-particles of several discrete energies ranging from 5.5 to 7.8 MeV. This radiation is entirely absorbed by 6–8 cm of air or

40–60 microns of a material of density 1 g cm^{-3} . Polonium can be used as an external source for irradiating very thin plastic films or for treating the surface of a polymer. This isotope emits alpha-particles of 5.3 MeV with practically no other associated radiation. The radiation is entirely absorbed by a layer of water 35μ thick. Artificially accelerated heavy particles are capable of producing extremely high radiation doses in thin layers of material. When working at high power levels such particle beams will “burn,” i.e. carbonize, most polymers or other organic substances, or heat them rapidly to their combustion temperature [10].

10.2.5 Neutrons

Neutrons are liberated in many nuclear processes induced by gamma-rays and neutrons reaction or by accelerated heavy ions. The most powerful source of neutrons, however, is the nuclear reactor, where fast neutrons are emitted at each fission of a uranium nucleus. These neutrons are subsequently slowed down by the moderator. It follows that the mixed radiation of a reactor includes both fast and slow neutrons and in addition a large amount of gamma radiation arising from nuclei disturbed in various nuclear processes. The mixed radiation of a reactor was widely used in radiation chemistry, particularly in those cases when very high radiation doses were required. Unfortunately, this type of radiation is unsuitable for precise quantitative work since its composition is usually not known with enough accuracy and serious problems are encountered in its dosimetry. Radiation doses delivered by the mixed radiation of a reactor are usually expressed in terms of the total radiation associated with a given flux of slow neutrons. The latter is easily determined experimentally by irradiating together with the sample small foils of gold or cobalt and subsequently measuring the induced radioactivity. Several attempts have been made to calibrate the mixed reactor radiation with a chemical dosimeter having a known radiation yield for gamma-rays. Such calibrations have shown that the total radiation associated with a slow neutron flux of $1017 \text{ neutrons/cm}^2$ is equivalent to doses of gamma radiation of 50 to 500 kGy, depending on the chemical system involved and on the type of reactor used [10].

10.3 Gamma-Ray Measurements

10.3.1 Dosimetry

High-activity industrial-scale gamma irradiation facilities need careful characterization to establish plant parameters, such as efficiency, overdose

ratio, and capacity, since the knowledge of these main parameters with respect to product density, for example, is of basic importance both for manufacturers and users [30]. Reliable high-dose dosimetry systems are generally required to achieve international standards in determining the dose distribution patterns and the delivered absorbed dose over a wide range of industrial products and processes which make use of ionizing radiation [31]. One of the most used high-dose dosimetry systems, the polymer-based dosimetry system, has been employed in high gamma dose dosimetry for more than 60 years [32–35]. Fiber-optic technologies using ultra-small probes attached to optical fibers with the capability for remote radiation dose measurement are finding increasing interest in clinical applications. Several classes of optical fiber dosimeters, differing primarily in the nature of radiation-induced changes that occur in the optical fiber sensor, have been developed [36]. For engineering dosimetry, the basic concern is represented by γ -radiation in the energy range up to 3 MeV; which includes the energy of the majority of natural isotopes and of typical nuclear waste [37]. During the last decades, sugar was considered as a promising radiation-sensitive material and used as a radiation detector for high-level dosimetry by applying different analytical methods [38]. In the field of radiation processing, system design engineers have typically made use of analytical techniques, while facility operators have perhaps relied more on routine dosimetry for processes or quality control purposes [39]. Recent recommendations and new norms for operational dosimetry by different international commissions have led to changes in the methods used for individual dosimetry, implying the development of new types of dosimeters. It is in this context that we have begun a study of the response of imaging plates to fast γ -rays [40].

The Fricke dosimeter, also called the ferrous sulfate dosimeter, is one of the most useful chemical dosimeters. It depends on the oxidation of ferrous ions (Fe^{2+}) to ferric ions (Fe^{3+}) by ionizing radiation. The increase in concentration of the ferric ions is measured spectrophotometrically at the optical absorption maxima at 224 and 303 nm. The Fricke dosimeter is 96% water (by weight), hence, its attenuation of radiation closely resembles that of water. It is usable in the dose range of 5–400 Gy and at dose rates up to 10^6 Gy/s. As applied to the Fricke dosimeter [41], the diffusion kinetic model uses a rather extensive array of chemical reactions, reaction rates, diffusion constants, and a set of linear differential equations through which it proceeds from initially formed radicals to the final differential yield. It makes use of an imaginative model of the energy deposition about an ion's path, including such terms as spurs, blobs, short tracks, penumbra, and core, the latter being one of its more vulnerable aspects. Neither

measurements nor Monte Carlo calculations of the radial dose distribution offer any hint of the track core in energy deposition specified in the diffusion kinetic model.

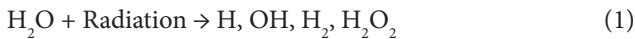
10.3.2 Fricke Dosimetry Method

The ferric ions concentration can be measured by a spectrophotometry technique comparing the wavelength at 585 nm (modified Fricke) band that corresponds to ferric ions concentration. The optical densities at 585 nm band before ($OD(D)$) and after ($OD(0)$) irradiation are measurements using a UV spectrophotometer. The absorbed dose is given by (Fricke, 1955):

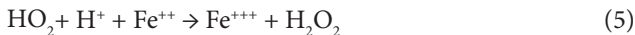
$$D = \frac{N_A \cdot e}{\rho \cdot l \cdot G(Fe^{3+})} \cdot \frac{OD(D) - OD(0)}{\epsilon_m} \quad (10.1)$$

where D is the absorbed dose, $G(Fe^{3+})$ is the chemical yield of Fe^{3+} (expressed in ions produced per 100 eV), ρ is the density in kg/L, N_A is Avogadro's number, e is the number of Joules per electron volt, l is the optical path length (width of the cuvette holding the solution), and ϵ_m is the molar extinction coefficient for Fe^{3+} . From equation (10.1), it is clear that the absorbed dose is proportional to the variation on the optical densities, considering that the other terms are constants.

When aerated ferrous sulfate solution is irradiated with X-ray, γ -rays, α particles, electrons, etc., first, water decomposes to give free radicals (H, OH) and molecular products (H_2 , H_2O_2):



Then the following series of reactions occur:



The last reaction does not occur in the high concentration of sulfuric acid, the each H atoms (radicals) lead, through formation of HO_2 , to the oxidation of three Fe^{++} ions; each OH radicals oxidizes one, and each H_2O_2 oxidizes two Fe^{++} ions. The ferric yield for this system is 15.6 [42, 43].

10.3.3 Units of Radioactivity and Radiation Absorption

The original unit for measuring the amount of radioactivity was the curie (Ci), first defined to correspond to one gram of radium-226 and more recently defined as: $1 \text{ curie} = 3.7 \times 10^{10}$ radioactive decays per second. In the International System of Units (SI), the curie has been replaced by the becquerel (Bq), where $1 \text{ becquerel} = 1 \text{ radioactive decay per second} = 2.703 \times 10^{-11} \text{ Ci}$. The magnitude of radiation exposures is specified in terms of the radiation dose. There are two important categories of dose: The absorbed dose, sometimes also known as the physical dose, defined by the amount of energy deposited in a unit mass in human tissue or other media. The original unit is the rad [100 erg/g]; it is now being widely replaced by the SI unit, the gray (Gy) [1 J/kg], where $1 \text{ gray} = 100 \text{ rad}$. Biological dose, sometimes also known as the dose equivalent, expressed in units of rem or, in the SI system, sievert (Sv). This dose reflects the fact that the biological damage caused by a particle depends not only on the total energy deposited but also on the rate of energy loss per unit distance traversed by the particle (or "linear energy transfer"). For example, alpha particles do much more damage per unit energy deposited than do electrons. This effect can be represented, in rough overall terms, by a quality factor, Q . Over a wide range of incident energies, Q is taken to be 1.0 for electrons (and for X-rays and gamma rays, both of which produce electrons) and 20 for alpha particles. For neutrons, the adopted quality factor varies from 5 to 20, depending on neutron energy. The biological impact is specified by the dose equivalent H , which is the product of the absorbed dose D and the quality factor Q : $H = Q D$ [44].

The unit for the dose equivalent is the rem if the absorbed dose is in rads and the Sv if the absorbed dose is in grays. Thus, $1 \text{ Sv} = 100 \text{ rem}$. As discussed below, 1 rem is roughly the average dose received in 3 years of exposure to natural radiation. 1 Sv is at the bottom of the range of doses that, if received over a short period of time, are likely to cause noticeable symptoms of radiation sickness. The dose equivalent is still not the whole story. If only part of the body is irradiated, the dose must be discounted with an appropriate weighting factor if it is to reflect overall risk. The discounted dose is termed the effective dose equivalent or just the effective dose, expressed in rems or sieverts [44].

10.4 Synthesis of Graft Polymers by Gamma-Rays

10.4.1 Radiation Grafting

The modification of polymers has received much attention recently. Among the methods of modification of polymers, grafting is one of the promising

methods. In principle, graft co-polymerization is an attractive method to impart a variety of functional groups to a polymer. Graft co-polymerization initiated by chemical treatment, photo-irradiation, high-energy radiation technique, etc. Considerable work has been done on techniques of graft co-polymerization of different monomers on polymeric backbones [45, 46]. Radiation-induced grafting has been found to possess potential to simplify the whole treatment process and reduces the cost of production. It is a convenient process due to its rapid and uniform formation of active sites for initiating the grafting reaction throughout the material [1]. The major advantages of radiation-induced grafting over the classical chemical polymerization are: the reaction is carried out in a wide range of temperature; the grafting is carried out in various states of monomers such as in bulk, solution, emulsion, and even at solid state; and the grafted material is free from residuals of initiator or catalyst [47–49]. This method is well known for its merits in modifying the surface properties of preexisting polymeric materials usually without changing their inherent properties. It is worth noting that radiation in high dose rate or high dose can cause degradation or crosslinking of some polymers. However, pre-irradiation-induced graft copolymerization can provide a method to combine two highly incompatible polymers [50].

Grafting using high-energy ionizing or non-ionizing radiations can be performed following different approaches: (i) direct method; (ii) pre-irradiation, and (iii) each of these methods has its advantages and disadvantages. This is useful when access to a radiation source is limited. The simultaneous method requires the use of the radiation source during the entire grafting process, however, graft yields are generally higher compared with the pre-irradiation methods due to less radical loss through decomposition reactions in the latter method [51]. By any methods, the rate and efficiency of the initiation is dependent upon the type of radiation, the radiation dose (total energy absorbed), the dose rate (rate at which energy is absorbed), and the radiation sensitivity of material involved [52–53].

10.4.2 Simultaneous or Mutual Method

This method is maybe the simplest (Figure 10.1). In this case, both polymer and monomers are introduced into a reactor and simultaneously irradiated. The polymer substrate is immersed in the monomer, which may be a liquid, vapor or solid diluted with a suitable solvent and may contain additives even, then exposed to ionizing radiation. As well as the formation of the grafted polymer, homopolymer will invariably also be formed as both the substrate and the monomer are exposed to radiation. This

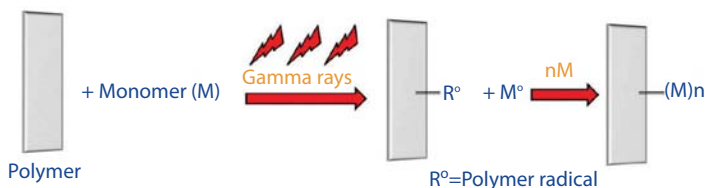


Figure 10.1 Radiation grafting applying a direct method.

technique should be carrying out only if the radiochemical yield of the polymer $G(R\cdot)P$ is higher than the monomer $G(R\cdot)M$ in order to avoid homopolymer formation, which is the main disadvantage [1, 11, 54], this can be reduced by addition of monomers in vapor phase or at low concentration in a suitable solvent, also polymerization inhibitors as Mohr's salt may be added [55–58].

10.4.3 Pre-irradiation Method

In this method, the polymer is pre-irradiated in vacuum or in inert gas (Figure 10.2). When radiation reaches the sample ionized and excited species are formed. These species form relatively stable free radicals which are the active sites, if monomers are introduced in liquid, vapor or as solution in a suitable solvent, the reaction of grafting polymerization usually at elevated temperatures start [59, 60]. The main advantage of this technique is that since the monomers is not exposed to radiation, the homopolymer formation is low, the disadvantages is that the radicals do not have long life time, requires inert atmosphere and grafting is usually low. Furthermore, if the polymer is scission type, small fragments are formed and then block polymers are formed instead of grafts. The grafting degree strongly depends of reaction conditions, such as pre-irradiation dose, monomer concentration, temperature, reaction time, material thickness, and solvent when it is used [1, 11].

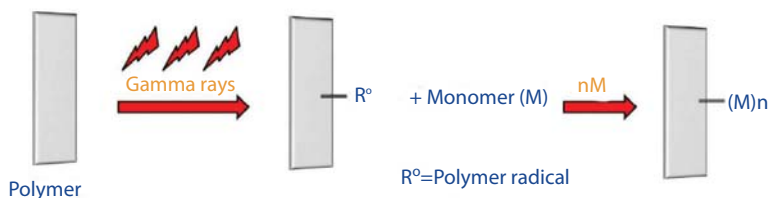


Figure 10.2 Radiation grafting applying a pre-irradiation method.

10.4.4 Pre-irradiation Oxidative Method

In this grafting, samples are irradiated in air or in oxygen (Figure 10.3). Free radicals in the polymer backbone react quickly with oxygen then form alkylperoxides and hydroperoxides. In a second step, the monomer or a solution containing it, is introduced and heated without oxygen. Both peroxides and hydroperoxides are homolytically broken and then they react with the monomer. In this case, the grafting degree depends on the conditions mentioned above. The main advantage of this technique is that samples pre-irradiated can be stored at low temperature [61]. The disadvantages are that require elevated temperatures, sometimes solvents, long reaction time, the hydroxyl radical can start homopolymerization and then the grafting is usually lower than simultaneous method [11, 62–64].

10.4.5 Parameter Influencing Grafted Copolymers Synthesis

10.4.5.1 Irradiation Dose and Dose Rate

The grafting yield for the polymers increases with the total radiation dose, as first demonstrated by Chapiro [11, 58] for PTFE and subsequently confirmed for other fluoropolymers by numerous other workers. At low doses, the grafting yields are approximately linear dependent on the dose, for grafting of DMA and NIPAAm onto PVDF. However, at higher doses, the slopes of the yield-dose plots can decrease, as demonstrated recently by Grondahl *et al.* [65] for grafting of styrene onto PFA. The most likely

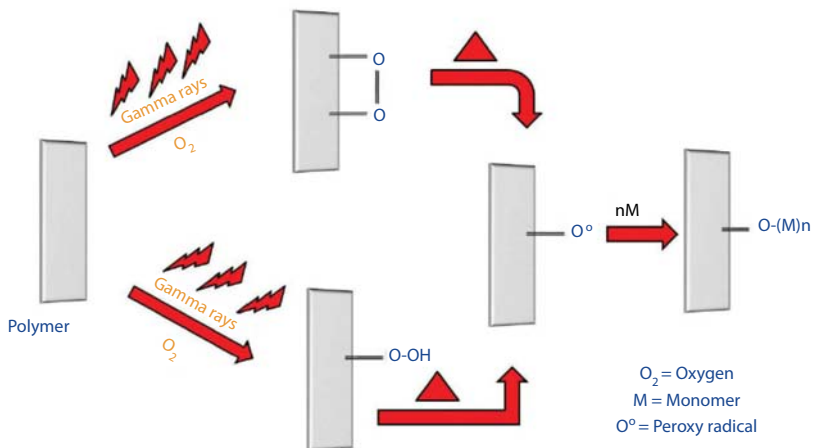


Figure 10.3 Radiation grafting applying a pre-irradiation oxidative method.

origins of the decreasing slopes at high radiation doses are (i) dose saturation in the formation of substrate radicals and (ii) an increase in the probability of radical termination reactions at higher doses/higher graft yields. In early studies of grafting of PTFE using bulk monomers [11, 58] is shown that the grafting yields were independent of the dose rate if this is low. However, at higher dose rates, the grafting percentage decreases with increasing dose rates. Iskander [66] has also found similar behavior for the grafting of DMA and NIPAAm onto PVDF membranes from aqueous solutions. Several possible reasons have been advanced for the decreasing grafting rate at high dose rates, including a higher rate of radiation-induced crystallization of the fluoropolymer substrate, increasing yields for the competing homopolymerization reaction and dose rate-dependent radical yields in the grafting process. The influence of exposure dose, on the grafting yield of (Sty/AAc) binary monomers onto LDPE films was investigated by Hegazy *et al.* [67]. It can be seen that the higher the exposure dose, the higher the grafting yield. From results, it can be assumed that the increase in exposure dose resulted in increasing the concentration of free radicals formed in the polymer substrate as well as in the (Sty/AAc) monomer.

10.4.5.2 *Effect of Solvent and Monomers*

Grafting conditions are playing a crucial role in the determination of not only the degree of grafting but also the structure built up inside the grafted polymer. Among grafting conditions, the solvent to be used for monomer dilution is of special interest as it is one of the essential elements towards a successful radiation-induced grafting process [68–70]. A solvent is basically used during grafting to bring about swelling of the base polymer and hence enhance the monomer accessibility to the grafting sites. The use of a poor-swelling solvent is most likely to lead to surface grafting due to the reduction in monomer diffusibility and, eventually, low degrees of grafting are obtained. However, the use of a good-swelling solvent results in bulk and homogeneous grafting. Increasing the swelling enhances the diffusion of monomer into the internal layers of the polymer substrate, and therefore the interactions between the internal active sites and the monomer molecules increase, leading to higher degrees of grafting [71]. The addition of solvent to a monomer/substrate combination can enhance the yield in the radiation-induced grafting and determine the specific nature of the graft copolymer [72]. The penetration of the grafting into the substrate is an important factor when preparing grafted surfaces for solid phase organic chemistry and is often dependent on the solvent used and the monomer concentration. It is common to observe a Trommsdorff phenomenon when

grafting styrene to polyolefins [73] and cellulose [74]. This phenomenon was first noticed when polymerizing bulk MMA using benzoyl peroxide in which the rate becomes explosively rapid at approximately 20–25% conversion [75]. This is explained by the restricted diffusion of the growing molecular chains, which hinders termination by combination with other growing chains, but does not appreciably disturb diffusion of the monomer. When the polymerization is carried out in a solvent, the explosive rate increase is not observed, however, when a non-solvent for poly(methyl methacrylate) (PMMA) is used the rate increase is even more rapid than the bulk polymerization and there is a higher degree of polymerization.

Maxima in the graft yield with variation in the monomer concentration have also been observed when grafting styrene to PTFE [76], FEP [77], and PFA [78]. In these cases, dichloromethane was used as a solvent and the greatest graft yields and grafting rates occurred at approximately 60% styrene concentration. Since dichloromethane is a good solvent for PS, the observed maxima cannot be due to a real Trommsdorff effect. Instead, the behavior has been attributed to an increase in the styrene diffusion and hence concentration in the grafting region, which reaches a maximum at approximately 60% styrene concentration. Above this concentration there was significant homopolymer formation, resulting in hindered monomer diffusion to the grafting sites and lower graft yield [78]. This explanation is a little spurious as it is unlikely that the diffusion of styrene would be hindered enough to prevent propagation unless a glassy state was reached. If the viscosity was high enough to prevent styrene diffusion, then termination would also be expected to be hindered due to the limited mobility of the growing chains.

However, the declining graft yields with increasing viscosity could be related to an increase in the cage recombination of radical species that initiate grafting. Cardona *et al.* [79] have compared the grafting of styrene to PFA for six solvents, dichloromethane, benzene, methanol, 1,2-dichlorobenzene, cyclohexane, and 1,1,1-trichloroethane. They found the yield of graft for the first three of these solvents was much higher than those of the latter three for all doses and dose rates investigated. They have correlated the efficiency of the grafting process with the solubility parameters for PS in the various solvents. The solvent and polymer chain transfer constants, as well as the polymer matrix viscosity, are also important factors. The nature of the monomer to be grafted onto a polymer substrate has an important effect on the efficiency and the uniformity of the grafting yield. Based on reactivity and sensitivity to radiation, monomers can be classified into two classes: reactive and non-reactive monomers. Reactive (radiation-sensitive) monomers such as acrylic acid (AAc) show high tendency to

homopolymerize during radiation-induced graft copolymerization process unlike that of non-active monomers such as styrene, which has less tendency for homopolymerization. For monomers to be grafted, it should have low viscosity and small dipole strength. The former enhances the amount and the rate of monomer diffusion into the base polymer, whereas the later reduces the tendency of the monomer to form free radicals.

10.4.5.3 Influence of the Polymer Substrate and Film Thickness

As grafting involves covalent attachment of a monomer to a pre-formed polymeric backbone, the nature of the backbone (viz. physical nature, chemical composition) plays an important role in the process. Radiation grafting can be used to modify either only the surface properties or also the bulk properties. For example, the bulk can be modified to impart ion-exchange or ion-transport properties. The resulting bulk-modified films are used [80] as membranes in electro dialysis, electrosynthesis, and pervaporation and as fuel cell membranes and battery separators. Monomer transport into the film is often the rate limiting step in radiation grafting. This is true even in the case of simultaneous radiation grafting of a monomer with some solubility in the polymer substrate, for example, styrene in PE. Even if the PE base film is pre-swollen in monomer, the grafting process is often diffusion limited. If the base polymer film does not swell in the grafting monomer solution and the pre-irradiation method is used, radiation grafting occurs by a grafting front mechanism [81]. Ranogajec and co-workers [82] have reported that grafting levels increased with film substrate thickness, although the effects were less pronounced at higher temperatures. In contrast, Matsuo and co-workers have reported [83] that the grafting levels of 200 μm or thicker films at constant grafting times were inversely proportional to the film thickness. However, the grafting levels decreased as the PP film thickness decreased further. Film orientation was not characterized in any of these investigations [84]. Basically, the base polymers have to meet certain requirements in order to produce efficient grafting with desirable and practical properties. They have to bear ability to easily generate stable free radicals upon exposure to ionizing radiation and high resistance towards radiolytic degradation. Preferably, the base polymers have to be hydrophobic materials with high thermal, chemical and mechanical stability.

10.4.5.4 Monomer Concentration

The concentration of the monomer to be grafted has a significant role to play during grafting copolymer preparation by the gamma-ray

copolymerization method. The content of the monomer in the bulk solution strongly affects its diffusivity to the grafting zone and consequently, the rate as well as the final degree of grafting varies. Grafting of monomers such as styrene onto polyolefin shows a Trammsdorff effect where restricted diffusion of graft-growing chains hinders termination by recombination with other chains without considerably distributing the diffusion [85]. Grafting of the styrene onto fluorinated polymers (PTFE, FEP, and PFA) does not exhibit Trammsdorff effect despite the presence of maxima in the degree of grafting with the variation of styrene concentration with a good solvent such as dichloromethane [86].

The concentration of DMAEMA also had an effect on grafting yield. At an irradiation dose of 50 kGy, then highest value of grafting percentage for LDPE-g-DMAEMA was 25% when immersed in a 60% (v/v) DMAEMA solution. Higher values of grafting were obtained for SR-g-DMAEMA, reaching 55% grafting in a 60% (v/v) DMAEMA solution. Furthermore, the pattern of SR-g-DMAEMA grafting as a function of monomer concentration sharply increased within the concentrations range studied. The higher grafting efficiency for SR than for LDPE is probably related to the ability of the pristine polymeric matrix to take up the solvent. LDPE and SR films were able to swell in toluene up to 13% and 134% (w/w), respectively, making penetration of dissolved DMAEMA in SR matrix easier than in LDPE. Therefore, DMAEMA can reach more sites to react with and to grow from in the SR [87].

10.4.5.5 Grafting Temperature

Temperature of the grafting medium is one of the most important parameters that have a strong effect on the grafting yield. Variation of the temperature permits control of the extent of grafting, graft deposition depth, and composition [88]. Contreras-García *et al.* [89] studied the dependence of DMAAm grafting on temperature, they found that sufficient grafting yield at 60°C with low homopolymerization. But at 70°C, the grafting process was complicated with essential formation of homopolymer. Therefore, 60°C was used in all grafting procedures as the optimal temperature. It is known that by the polymers irradiation in the presence of air, the peroxides and hydroperoxides are formed which decompose with temperature to give macroradicals for the grafting initiation but peroxides require a higher temperature (>80°C) for dissociation as compared with hydroperoxides [90]. Therefore, it is possible to suppose that only radicals formed by the thermal decomposition of the hydroperoxides at lower temperature serve as the active sites for graft polymerization. Nevertheless, in our

case the grafting efficiency was sufficiently high at 60°C, and this process practically was not complicated by the monomers homopolymerization. An increase of temperature increases the reactivity of the trapped radicals giving rise to the initial rate of grafting. After certain time of grafting and at high temperature, accumulation of the grafting monomer into the swollen grafted layers of the polymer matrix increases the viscosity and hinders the monomer diffusion resulting in insufficient monomer concentration to react with the active radicals. Unlikely, at low temperature, the trapped radicals have longer lifetime and lower reactivity. This slows down the termination in the growing chains and consequently higher grafting yield is obtained. It is noteworthy mentioning that the critical temperature at which grafting reaches the maximum level varies from one grafting system to another depending on other reaction parameters including method of grafting and inherent properties of the base polymer films such as glass transition temperature [91].

10.5 Different Architecture of Polymers

10.5.1 Stimuli-Responsive Networks Grafted onto Polypropylene for the Sustained Delivery of NSAIDs

Copolymers of N-isopropyl acrylamide (NIPAAm) and N-(3-amino-propyl) methacrylamide hydrochloride (APMA) were grafted on PP films by means of γ -ray pre-irradiation method (Figure 10.4), with the aim of developing medical devices able to load non-steroidal anti-inflammatory drugs (NSAIDs) and to control their release under physiological conditions. The NIPAAm/APMA molar ratio in the graft, estimated by FTIR-ATR and XPS analysis, resulted to be 4.76 and 1.23 for PP-g-(1NIPAAm-r-0.5APMA) and PP-g-(1NIPAAm-r-1APMA), respectively.

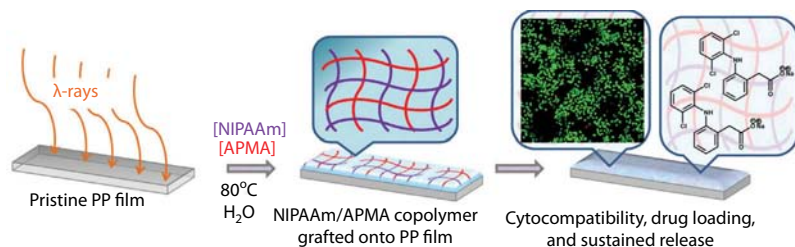


Figure 10.4 Preparation of PP-g-NIPAAm and PP-g-(NIPAAm-r-APMA) for hemocompatibility and protein adsorption.

Varying the reaction time, different degrees of grafting were achieved but keeping constant the monomers ratio. PP-g-(NIPAAm-r-APMA) films showed temperature-responsive swelling, smaller friction coefficient, hemolysis and thrombogenicity and higher cell compatibility, did not elicit secretion of cytokines, and up-took remarkable amounts of diclofenac and ibuprofen and sustained the delivery for several hours in pH 7.4 phosphate buffer. Coating with carboxymethyl dextran of the diclofenac-loaded PP-g-(NIPAAm-r-APMA) films caused minor discharge of the drug but did not altered drug release rate [92].

10.5.2 Radiation Grafting of Glycidyl Methacrylate onto Cotton Gauzes for Functionalization with Cyclodextrins and Elution of Antimicrobial Agents

Cotton gauzes were modified with cyclodextrins (CDs) in order to endow them with the ability to elute antimicrobial agents and to prevent infections. Gauzes were modified according to a two-steps approach: (i) pre-irradiation of the gauzes (Gamma beam) to graft glycidyl methacrylate (GMA), and (ii) covalent binding of CDs to the GMA-grafted gauzes (Figure 10.5). First the dependence of GMA grafting yield on the radiation dose (from 1 to 20 kGy) and the time of reaction was evaluated in detail. Anchorage of β -cyclodextrin (β -CD) and hydroxypropyl- β -cyclodextrin (HP- β -CD) was confirmed by FTIR, TGA, and 3-methylbenzoic acid sorption. Differently from pristine gauzes, CD-functionalized GMA-grafted gauzes were able to load an anionic antibiotic drug, specifically nalidixic acid, and to sustain the release for 6 h. Drug-loaded gauzes were tested in vitro against *E. coli* and the results prove the suitability of the functionalization approach to efficiently inhibit the growth of this microorganism [93].

10.5.3 Binary Graft Modification of Polypropylene for Anti-inflammatory Drug-Device Combo Products

Temperature- and pH-responsive copolymers were γ -ray grafted onto PP to endow its surface with the capability to load and to control the release of anti-inflammatory drugs (NSAIDs). First poly(N,N'-dimethylaminoethylmethacrylate) (PDMAEMA) or poly(4-vinylpyridine) (P4VP) were grafted onto PP films by means of a direct method and then the temperature-responsive poly(N-isopropylacrylamide) (PNIPAAm) was grafted applying a pre-irradiation method (Figure 10.6). The binary graft copolymers showed high hemocompatibility and certain capability to adsorb bovine serum albumin (BSA). (PP-g-DMAEMA)-g-NIPAAm

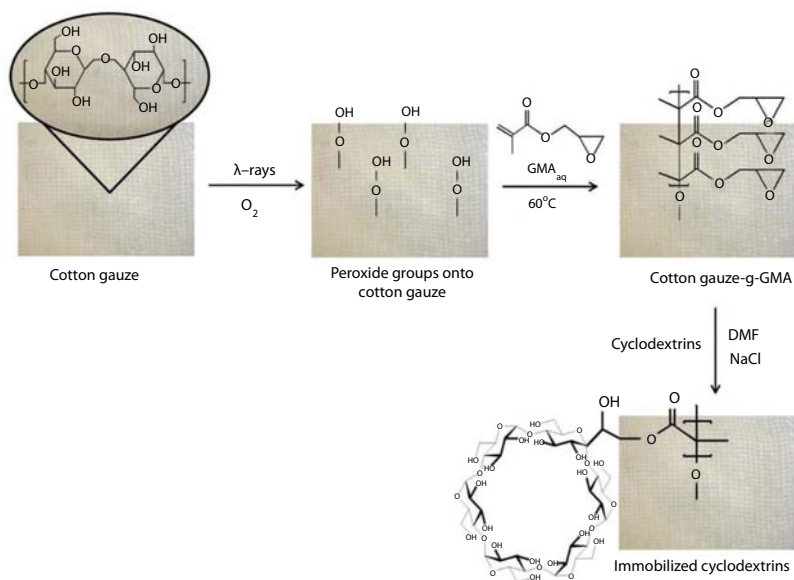


Figure 10.5 Functionalization of cotton gauzes with CDs: the gauzes were γ -ray pre-irradiated in the presence of air to form peroxide groups.

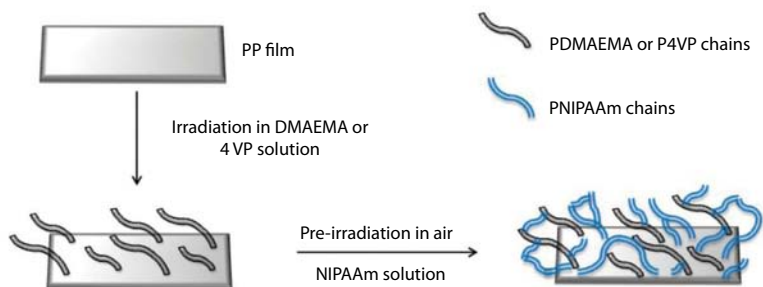


Figure 10.6 Preparation of the binary graft copolymers: in the first step, PP film immersed in DMAEMA or 4VP monomer solution was γ -ray irradiated to trigger the graft polymerization, secondly was γ -ray irradiated and then transferred to the NIPAAm.

showed higher affinity for ibuprofen and, particularly, diclofenac than (PP-g-4VP)-g-NIPAAm. Sustained release of these drugs was observed under physiological conditions. Further experiments of cytotoxicity and anti-inflammatory activity on RAW 264.7 macrophage cells were carried out with (PP-g-DMAEMA)-g-NIPAAm in order to evaluate its potential as NSAID-eluting material for combo products. First, concentration

dependences of the anti-inflammatory activity and the cytotoxicity of ibuprofen and diclofenac on RAW 264.7 cells were investigated in order to establish the ranges of drug concentration that the graft copolymers should provide. The optimal concentrations of diclofenac and ibuprofen at which they reduce inflammation while maintaining cell viability were determined to be 200 $\mu\text{g}/\text{mL}$ and above 400 $\mu\text{g}/\text{mL}$. Diclofenac-loaded (PP-g-DMAEMA)-g-NIPAAm fulfilled the in vitro requirements to avoid inflammatory response [94].

10.5.4 Temperature- and pH-Sensitive IPNs Grafted onto Polyurethane by Gamma Radiation for Antimicrobial Drug-Eluting Insertable Devices

Temperature- and pH-sensitive interpenetrating polymer networks (IPNs) and semi-interpenetrating polymer networks (s-IPNs) were γ -ray grafted onto polyurethane (Tecoflex[®]; TFX) to obtain vancomycin-eluting implantable medical devices with minimized risk of infections. N-isopropylacrylamide (NIPAAm) was grafted onto TFX catheters and films (Figure 10.7) via a pre-irradiation oxidative method or via a direct method. The PNIPAAm network facilitated AAc inclusion and subsequent polymerization/cross-linking, under specific reaction conditions. IPNs

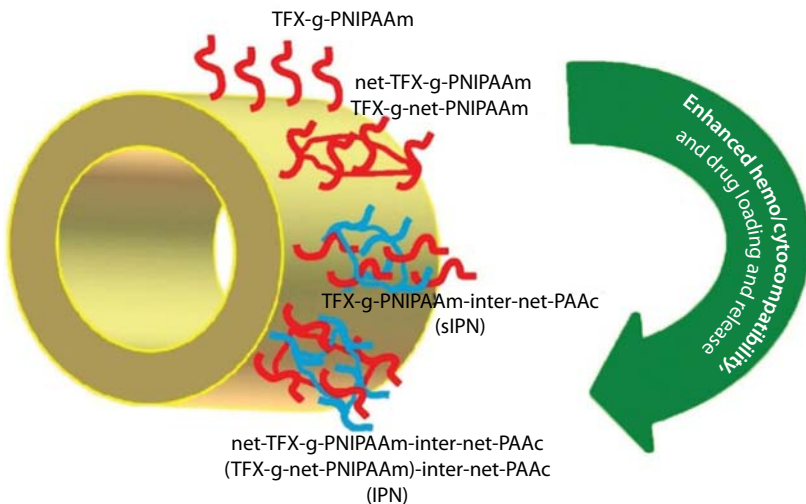


Figure 10.7 Polymerization and cross-linking of AAc interpenetrated within TFX-g-PNIPAAm, net-TFX-g-PNIPAAm and TFXc-g-net-PNIPAAm for Vancomycin loading and antimicrobial susceptibility testing.

and s-IPNs systems were characterized regarding the amount of grafted polymers, surface properties (FTIR-ATR, ESEM, EDX), thermal behavior (DSC and TGA), and their temperature and pH responsiveness. Loading and release of vancomycin for preventing *in vitro* growth of *Staphylococcus aureus* were also evaluated. Antimicrobial susceptibility tests and hemo- (hemolysis, protein adsorption, thrombogenicity) and cyto-compatibility (cell viability and production of cytokines and NO) assays indicated that the modification of TFX by γ -radiation may improve the performance of polyurethanes for biomedical applications [95].

10.5.5 Temperature-Responsiveness and Biocompatibility of DEGMA/OEGMA Radiation Grafted onto PP and LDPE Films

PP and low density polyethylene (LDPE) were modified by γ -ray grafting of di(ethylene glycol) methyl ether methacrylate (DEGMA) and oligo (ethylene glycol) methyl ether methacrylate (OEGMA300 or OEGMA475 with Mn 300 and 475 respectively) with different monomer concentration and mol ratio (Figure 10.8). The grafting percentage was evaluated as a function of the solvent, irradiation dose, reaction time, temperature, and monomers concentration. The grafted materials were more hydrophilic than the pristine polymers, as observed by contact angle and swelling in water. Temperature-responsive behavior was evaluated by DSC showing transitions between 34 and 48°C. *In vitro* hemocompatibility, protein adsorption, cytotoxicity and bacteria adhesion tests were also carried out. Overall, the DEGMA/OEGMA grafting provides hemo and cytocompatible materials that exhibit temperature-responsive hydrophilic features and decreased protein adsorption [96].

10.5.6 Acrylic Polymer-Grafted Polypropylene Sutures for Covalent Immobilization or Reversible Adsorption of Vancomycin

GMA and AAc were separately grafted onto PP monofilament sutures by means of pre-irradiation using a ^{60}Co γ -source, with the purpose of loading vancomycin via (i) covalent immobilization through the glycidyl groups of GMA and (ii) ionic interaction with AAc moieties (Figure 10.9). The effect of absorbed radiation dose, monomer concentration, temperature and reaction time on the grafting degree was evaluated in detail. GMA grafting ranged from 25% to 800% while the grafting yield of AAc onto

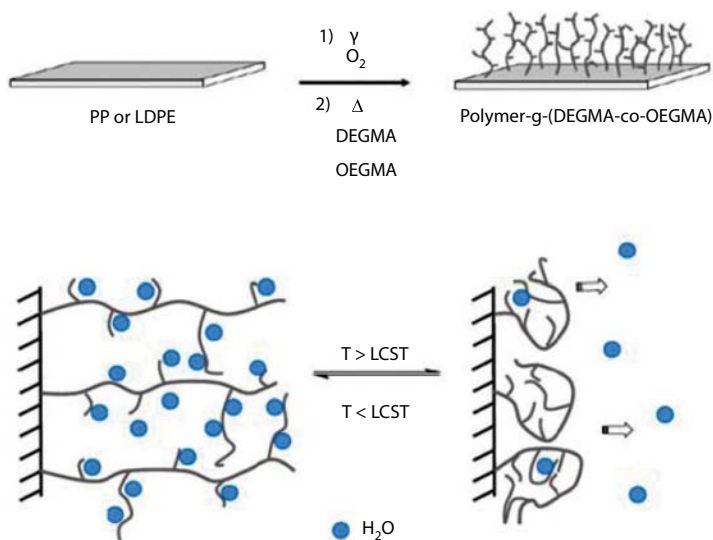


Figure 10.8 Simultaneous grafting of DEGMA/OEGMA copolymers from PP and LDPE and to elucidate the influence of the synthesis.

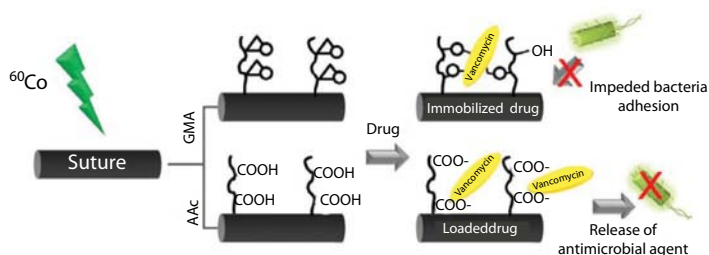


Figure 10.9 Effect of irradiation dose on the grafting yield of AAc and GMA onto PP sutures for vancomycin-immobilized AAc and GMA-functionalized sutures and bacteria adhesion.

PP could be tuned between 9% and 454%, at doses from 5 to 50 kGy and a dose rate 13.7 kGy/h. Grafting of GMA or AAc decreased the decomposition temperature and made the sutures swellable to a certain extent. GMA grafting led to a continuous, smooth and thick coating, which was suitable for immobilization of up to 1.9 μg vancomycin per gram. The immobilized vancomycin enabled a reduction in the *Staphylococcus aureus* CFU adhered to the suture surface. On the other hand, dried AAc-functionalized sutures exhibited a rough and cracked surface which was responsible for a minor increase in the coefficient of friction. PP-g-AAc sutures exhibited

pH-dependent swelling and remarkably high capability to host vancomycin (up to 109.9 mg/g), particularly those with an intermediate degree of grafting. Some AAc-functionalized sutures were shown able to inhibit bacterial growth after successive challenges with fresh lawns. Therefore, tuning the yield of grafting of GMA or AAc may enable the preparation of drug-suture combination products that retain or release, respectively, antimicrobial agents [97].

10.6 Polymer Characterization

There are several characterization techniques used for polymers, which vary according to the properties studied and the type of materials. Hence, this review focuses on characterization techniques used for graft copolymers.

10.6.1 Swelling Measurements

The equilibrium of swollen gels in distilled water is determined by swelling the dried grafted polymeric samples for different periods of time and weighing them on an analytical balance until a maximum and constant weight is obtained [98]. The degree of swelling of the films (%) is calculated according to the formula:

$$S (\%) = [(S_f - S_i)/S_i] \times 100 \quad (10.2)$$

Where S_f and S_i are the masses of the swollen and dried films, respectively.

10.6.2 Surface Plasmon Resonance Spectroscopy (SPR)

Is a surface-sensitive characterization based on the evanescent field of the surface plasmon. The latter is an electromagnetic wave traveling along the interface between a metal and a dielectric. Its electric field decays exponentially into both materials over a distance of a few hundred nanometers and the wave has a finite propagation length due to damping processes in the metal. The resulting data are a direct measure of the local average refractive index of the dielectric close to the surface, and with Fresnel calculations either the thickness or the refractive index of thin films at an interface can be determined. Furthermore, a time-dependent measurement mode enables the detection of changes in the local average dielectric constant due to the adsorption of molecules onto the surface or changes in film properties due to an external trigger [99].

10.6.3 Infrared (IR)

Infrared spectroscopy is generally used for the analytical techniques based on the interaction of electromagnetic radiation with matter and variation of particular physical quantity with frequency of radiation. In spectroscopy, the measurements of absorbance/transmittance of electromagnetic radiation, due to interaction with sample by molecules that are carried out in a gas or vapor state or dissolved molecules/ions or solid depending upon requirement. When IR radiation is incident on a sample, some of the IR radiation is absorbed by the sample and some of it is passed through (transmitted). The resulting spectrum represents the molecular absorption or transmission, creating a molecular fingerprint of the sample, IR is one of the most powerful analytical techniques, which indicates the possibility of chemical identifications. This technique has been shown to be useful for probing transitions, in addition changes in the infrared spectra provide information on the conformation and bonding state of the functional groups involved in the transition [100, 101].

10.6.4 Nuclear Magnetic Resonance Spectroscopy (NMR)

NMR is a physical phenomenon in which magnetic nuclei in a magnetic field absorb and re-emit electromagnetic radiation. This energy is at a specific resonance frequency which depends on the strength of the magnetic field and the magnetic properties of the isotope of the atoms. Is the use of the NMR phenomenon to study physical, chemical, and biological properties of matter. As a consequence, NMR spectroscopy finds applications in several areas of science. NMR spectroscopy is routinely used by chemists to study chemical structure using simple one-dimensional techniques. Two-dimensional techniques are used to determine the structure of more complicated molecules. These techniques are replacing X-ray crystallography for the determination of 3D structure. Time domain NMR spectroscopic techniques are used to probe molecular dynamics in solutions. Solid state NMR spectroscopy is used to determine the molecular structure of solids. Other scientists have developed NMR methods of measuring diffusion coefficients [102–103].

10.6.5 Thermal Transition

A true workhorse for polymer characterization is thermal analysis, particularly differential scanning calorimetry (DSC). Changes in the compositional and structural parameters of the material usually affect its melting

transitions or glass transitions and these in turn can be linked to many performance parameters. For semicrystalline polymers it is an important method to measure crystallinity. Thermogravimetric analysis (TGA) can also give an indication of polymer thermal stability and the effects of additives such as flame retardants. Other thermal analysis techniques are typically combinations of the basic techniques and include differential thermal analysis, thermomechanical analysis, dynamic mechanical thermal analysis, and dielectric thermal analysis [104–105].

10.6.6 Contact Angle

The contact angle is the angle, conventionally measured through the liquid, where a liquid/vapor interface meets a solid surface. It quantifies the wettability of a solid surface by a liquid via the Young equation. A given system of solid, liquid, and vapor at a given temperature and pressure has a unique equilibrium contact angle. However, in practice contact angle hysteresis is observed, ranging from the so-called advancing (maximal) contact angle to the receding (minimal) contact angle. The equilibrium contact is within those values, and can be calculated from them. The equilibrium contact angle reflects the relative strength of the liquid, solid, and vapor molecular interaction. This method consists of the measurement of advancing and receding contact angles by a dynamic method, or by the sessile drop method using the optical contact angle. The measurements of the contact angles for various samples are carried out at room temperature, 1 minute after water drops are deposited onto the surface of polymeric films, using direct microscopic measurement of the contact angles [106, 107].

10.6.7 Atomic Force Microscopy (AFM)

AFM is another popular and versatile surface characterization method. In AFM measurement, it is not necessary to coat insulating polymeric samples with metals. Noncoated insulating samples can be observed by scanning electron microscopy (SEM) if the electron acceleration voltage is very low; however, the lower acceleration voltage reduces resolution of SEM. In contrast to SEM, AFM can measure surface morphology even in solution. Although this is a great advantage of AFM over SEM, measurement of a soft surface is not so easy. Especially, extreme soft surfaces of highly swelled polymer nanocomposites is very difficult, since the AFM tip radius is generally very small (i.e. the tip is very sharp) and thus even with very small force applied to the tip can “sink” the tip into the surface of the polymer. Polymer morphology is a microscale property that is largely

dictated by the amorphous or crystalline portions of the polymer chains and their influence on each other. Microscopy techniques are especially useful in determining these microscale properties, as the domains created by the polymer morphology are large enough to be viewed using modern microscopy instruments [108–110].

Acknowledgments

This chapter was supported by DGAPA-UNAM Grant IN200714 and CONACYT-CNPq Project 174378. The authors thank to M.L. Escamilla and E. Palacios from ICN-UNAM for technical assistance.

References

1. C. Alvarez-Lorenzo, E. Bucio, G. Burillo, A. Concheiro. *Expert Opin. Drug Del.* Vol. 7, p. 173, 2010.
2. Y.S. Ramírez-Fuentes, E. Bucio, G. Burillo G. *Nucl. Instrum. Meth. B* Vol. 265, p. 183, 2007.
3. A. Contreras-García, G. Burillo, R. Aliev, E. Bucio. *Radiat. Phys. Chem.* Vol. 77, p. 936, 2008.
4. H.I. Meléndez-Ortiz, E. Bucio, G. Burillo. *Radiat. Phys. Chem.* Vol. 78, p. 1, 2009.
5. Z.S. Nurkeeva, A.S.A. Aal, A.I. Kupchishin, V.V. Khutoryanskiy, G.A. Mun, A.G. Beksyrgaeva. *Radiat. Phys. Chem.* Vol. 6, p. 793, 2003.
6. A. Vahdat, H. Bahramia, N. Ansaria, F. Ziaie. *Radiat. Phys. Chem.* Vol. 76, p. 787, 2007.
7. E. Bucio, A. Contreras-García, H.I. Meléndez-Ortiz, F.D. Muñoz-Muñoz, C. Alvarez-Lorenzo, A. Concheiro. *Smart polymers for biomedical applications and graft synthesis by gamma-rays. Smart Polymeric Materials for Biomedical Applications.* NOVA Science Publishers, Inc., New York, p. 277, 2010.
8. G. Burillo, E. Bucio. *Responsive copolymer films obtained by ionizing radiation Gamma radiation effects on polymeric materials and its applications.* Research Signpost. Kerala, India. p. 45, 2009.
9. G.R. Dennis, J.L. Garnett, Z. Elvis. *Radiat. Phys. Chem.* Vol. 67, p. 391, 2003.
10. Y.C. Nho, S.E. Park, H.I. Kim, T.S. Hwang. *Nucl. Instr. Meth. B* Vol. 236, p. 283, 2005.
11. A. Chapiro. *Radiation Chemistry of Polymeric System*, New York, Interscience Div. John Wiley and Sons, 1962.
12. S.W. Lee, Y. Bondar, D.H. Han. *React. Funct. Polym.* 68, p. 474, 2008.
13. J. M. Yang, H. T. Lin. *J. Membr. Sci.* Vol. 243, p. 1, 2004.
14. O. Palacios, R. Aliev, G. Burillo. *Polym. Bull.* Vol. 51, p. 191, 2003.

15. J.M. Rosiak, I. Janik, S. Kadlubowski, M. Kozicki, P. Kujawa, P. Stasica, P. Ulanski. *Nucl. Instr. Meth. Phys. Res.* Vol. 208, p. 325, 2003.
16. E. Bucio, G. Burillo. *Radiat. Phys. Chem.* Vol. 76, p. 1724, 2007.
17. H.P. Ferreira, D.F. Parra, A.B. Lugao. *Radiat. Phys. Chem.* Vol. 81, p. 1341, 2012.
18. G.M. Estrada-Villegas, E. Bucio. *J. Radioanal. Nucl. Chem.* Vol. 292, p. 1, 2012.
19. F. Muñoz-Muñoz, J.C. Ruiz, C. Alvarez-Lorenzo, A. Concheiro, E. Bucio. *Radiat. Phys. Chem.* Vol. 81, p. 531, 2012.
20. Y. Ikada. *Biomaterials* Vol. 15, p. 725, 1994.
21. U. Subramanyam, J.P. Kennedy. *J. Polym. Sci. Pol. Chem.* Vol. 47, p. 5272, 2009.
22. A.S. Hoffman. *Rad. Phys. Chem.* Vol. 9, p. 207, 1977.
23. A.S. Hoffman. *Rad. Chem.* Vol. 16, p. 12, 1981.
24. A.S. Hoffman. *Rad. Phys. Chem.* Vol. 18, p. 323, 1981.
25. A.S. Hoffman, D. Cohn, S.R. Hanson, L.A. Harker, T.A. Horbett, B.D. Ratner, L.O. Reynolds. *Rad. Phys. Chem.* Vol. 22, p. 267, 1983.
26. F. Truica-Marasescu, M.R. Wertheimer. *J. Appl. Polym. Sci.* Vol. 91, p. 3886, 2004.
27. F. Truica-Marasescu, S. Pham, M.R. Wertheimer. *Nucl. Instrum. Methods B* Vol. 265, p. 31, 2007.
28. F. Truica-Marasescu, M.R. Wertheimer. *Plasma Process. Polym.* Vol. 5, p. 44, 2008.
29. H. Luig, C. Keller, W. Wolf, J. Shani, H. Mizka, A. Zyball, A. Gerve, A.T. Balaban, A.M. Kellerer. *Weinheim: V. C. H. Publishers.* Vol. A22, p. 299, 1993.
30. A. Moussa, I. Othm, K. Alnaal. *Radiat. Phys. Chem.* Vol. 52, p. 585, 1989.
31. O.S.R. Liz, A.S. Medeiros, L.O. Faria. *Nucl. Instrum. Meth. B* Vol. 269, p. 2819, 2011.
32. L. Milman, V. Putyrsky, M. Naimark, V. Popov. *Radiat. Prot. Dosim.* Vol. 47, p. 271, 1993.
33. W.L. McLaughlin, B.A. Wei-Zhen, W.J. Chappas. *Radiat. Phys. Chem.* Vol. 31, p. 481, 1988.
34. M.K. Murphy. *Radiat. Prot. Dosim.* Vol. 136, p. 228, 2009.
35. A.M.S. Galante, O.L. Galante, L.L. Campos. *Nucl. Instrum. Meth. B* Vol. 619, p. 177 2010.
36. J.A. Tanyi, S.P. Krafft, T. Ushino, A. Huston, B.L. Justus. *Appl. Radiat. Isotope* Vol. 68, p. 364, 2010.
37. A.V. Rybka, L.N. Davydov, I.N. Shlyakhov, V.E. Kutny, I.M. Prokhoretz, D.V. Kutny, A.N. Orobinsky. *Nucl. Instrum. Meth.* Vol. 537, p. 147, 2004.
38. K. Marzougui, A.H. Hamzaoui, K. Farah, N.B. Nessib. *Radiat. Meas.* Vol. 43, p. 1254, 2008.
39. M. Sohrabpour, M. Hassanzadeh, M. Shahriari, M. Sharifzadeh. *Appl. Radiat. Isotopes* Vol. 57, p. 537, 2002.
40. A. Boukhair, C. Heilmann, A. Nourreddine, A. Pape, G. Portal. *Radiat. Meas.* Vol. 34, p. 513, 2001.

41. A. Chatterjee, J.L. Magee. *J. Phys. Chem.* Vol. 84, p. 3537, 1980.
42. C. Boudou, M.-C. Biston, S. Corde, J.-F. Adam, A. Joubert, A.-M. Charvet, C. Nemoz, C. Ferrero, F. Estève, H. Elleaume. *Nucl. Instrum. Meth. B* Vol. 548, p. 65, 2005.
43. L.N. de Oliveira, A. de Almeida, L.V.E. Caldas. *Radiat. Phys. Chem.* Vol. 98, p. 42, 2014.
44. P. Airey, T. Hinton, J. Twining. *Radioact. Environ.* Vol. 18, p. 1, 2012.
45. A. Bhattacharya, B.N. Misra. *Prog. Polym. Sci.* Vol. 29, p. 767, 2004.
46. B. Aydinli, T. Tinçer. *Radiat. Phys. Chem.* Vol. 60, 237, 2001.
47. J.H. Choi, C.H. Jung, D.K. Kim, R. Ganesan. *Nucl. Instrum. Meth. B* Vol. 266, p. 203, 2008.
48. L. Xu, J. Sun, L. Zhao. *Radiat. Phys. Chem.* Vol. 80, p. 1268, 2011.
49. R.P. Chaplin, N.J.W. Gamage, J.L. Garnett. *Radiat. Phys. Chem.* Vol. 46, p. 949, 1995.
50. Y.M. Wang, Y. Pan, Y.L. Wang, G.P. Wu, Y.J. Wang, L.N. Nikitin, X.B. Lu. *J. Supercrit. Fluids.* Vol. 44, p. 62, 2008.
51. I. Kamel, S. Machi, J. Silverman. *J. Polym. Sci. Pol. Chem.* Vol. 10, p. 1019, 1972.
52. D. Ratner, A.S. Hoffman. *J. Appl. Polym. Sci.* Vol. 18, p. 3183, 1974.
53. M.M. Nasef, E.A. Hegazy. *Prog. Polym. Sci.* Vol. 29, p. 499, 2004.
54. E. Bucio, R. Aliev, G. Burillo. *Polym. Bull.* Vol. 44, p. 571, 2002.
55. G. Moad, E. Rizzardo, S.H. Thang. *Aust. J. Chem.* Vol. 58, p. 379, 2005.
56. D.W. Jenkins, S.M. Hudson. *Chem. Rev.* Vol. 101, p. 3245, 2001.
57. J. Kunze, H.P. Fink. *Macromol. Symp.* Vol. 223, p. 175, 2005.
58. A. Chapiro. *Radiat. Phys. Chem.* Vol. 9, p. 55, 1977.
59. E. Bucio, R. Aliev, G. Burillo. *Radiat. Phys. Chem.* Vol. 52, p. 193, 1998.
60. A. Ramírez-Jiménez, C. Alvarez-Lorenzo, A. Concheiro, E. Bucio. *Radiat. Phys. Chem.* Vol. 99, p. 53, 2014.
61. O.H. Kwon, Y.C. Nho, K.D. Park, Y.H. Kim. *J. Appl. Polym. Sci.* Vol. 71, p. 631, 1999.
62. A. Bhattacharya, A. Das, A. De. *Ind. J. Chem. Tech.* Vol. 5, p. 135, 1998.
63. J. Li, K. Sato, S. Ichiduri, S. Asano, S. Ikeda, M. Lida, A. Oshima, Y. Tabata, M. Washio. *Eur. Polym. J.* Vol. 40, p. 775, 2004.
64. P. Marmey, M.C. Porte, C. Baquey. *Nucl. Instrum. Meth. B* Vol. 208, p. 429, 2003.
65. L. Grondahl, F. Cardona, K. Chiem, E. Wentrup-Byrne. *J. Appl. Polym. Sci.* Vol. 86, p. 2550, 2002.
66. G.M. Iskander, L.E. Baker, D.E. Wiley, T.P. Davis. *Polymer* Vol. 39, p. 4165, 1998.
67. E.S.A. Hegazy, H. Kamal, N. Maziad, A.M. Dessouki. *Nucl. Instru. Meth. B* Vol. 151, p. 386, 1999.
68. J.L. Garnett. *Am. Chem. Symp. Ser.* Vol. 48, p. 334, 1977.
69. B. Gupta, N. Anjum, A.P. Gupta. *J. Appl. Polym. Sci.* Vol. 77, p. 1401, 2000

70. Y. Kabanov, R. Aliev, L.P. Sidorova. *J. Polym. Sci. Polym. Chem.* Vol. 18, p. 791, 1980.
71. V. Stannet. *Radiat. Phys. Chem.* Vol. 35, p. 82, 1981.
72. M.M. Nasef. *Polym. Int.* Vol. 50, p. 338, 2001.
73. J.L. Garnett, N.T. Yen. *Polym. Let.* Vol. 12, p. 225, 1974.
74. S. Dilli, J.L. Garnett, E.C. Martin, D.H. Phuoc. *J. Polym. Sci. C* Vol. 37, p. 57, 1972.
75. Y.C. Nho, J. Chen, J.H. Jin. *Radiat. Phys. Chem.* Vol. 54, p. 317, 1999.
76. M.M. Nasef, H. Saidi, A.M. Dessouki, E.M. El-Nesr. *Polym. Int.* Vol. 49, p. 399, 2000.
77. M.M. Nasef, H. Saidi, H.M. Nor. *J. Appl. Polym. Sci.* Vol. 76, p. 220, 2000.
78. M.M. Nasef, H. Saidi, H.M. Nor, K.Z.M. Dahlan, K. Hashim. *J. Appl. Polym. Sci.* Vol. 73, p. 2095, 1999.
79. F. Cardona, G.A. George, D.J.T. Hill, F. Rasoul, J. Maeji. *Macromolecules* Vol. 35, p. 355, 2002.
80. H.P. Brack, G.G. Scherer. *Macromol. Symp.* Vol. 126, p. 25, 1997.
81. J. Chen, M. Asano, T. Yamaki, M. Yoshida. *J. Membr. Sci.* Vol. 269, p. 194, 2006.
82. F. Ranogajec, I. Dvornik, J. Dobo. *Eur. Polym. J.* Vol. 6, p. 1169, 1970.
83. H. Matsuo, K. Lino, M. Kondo. *J. Appl. Polym. Sci.* Vol. 7, p. 1833, 1963.
84. H.P. Brack, H.G. Bührer, L. Bonorand, G.G. Scherer. *J. Mater. Chem.* Vol. 10, p. 1975, 2000.
85. S.H. Choi, Y. C. Nho. *Radiat. Phys. Chem.* Vol. 58, p. 157, 2000.
86. N. Walsby, M. Paronen, J. Juhanoja, F. Sundholm. *J. Polym. Sci. A Chem.* Vol. 38, p. 1512, 2000.
87. A. Contreras-García, E. Bucio, G. Brackman, T. Coenye, A. Concheiro, C. Alvarez-Lorenzo. *Biofouling* Vol. 27, p. 123, 2011.
88. S. Hoffman. *Adv. Polym. Sci.* Vol. 57, p. 141, 1984.
89. A. Contreras-García, G. Burillo, R. Aliev, E. Bucio. *Radiat. Phys. Chem.* Vol. 77, p. 936, 2008.
90. R.J. Woods, A.K. Pikaev. *Applied Radiation Chemistry: Radiation Processing*. Wiley, New York, 1994.
91. L. Gubler, N. Prost, S.A. Gürsel, G.G. Scherer. *Solid State Ionics* Vol. 176, p. 2849, 2005.
92. A. Contreras-García, C. Alvarez-Lorenzo, C. Taboada, A. Concheiro, E. Bucio. *Acta Biomater.* Vol. 7, p. 996, 2011.
93. E. Hiriart-Ramírez, A. Contreras-García, M.J. Garcia-Fernandez, A. Concheiro, C. Alvarez-Lorenzo, E. Bucio. *Cellulose*. Vol. 19, p. 2165, 2012.
94. H.I. Meléndez-Ortiz, P. Díaz, C. Alvarez-Lorenzo, A. Concheiro, E. Bucio. *J. Pharm. Sci.-Us.* Vol. 103, p. 1269, 2014.
95. F. Muñoz-Muñoz, E. Bucio, B. Magariños, A. Concheiro, C. Alvarez-Lorenzo. *J. Appl. Polym. Sci.* Vol. 131, p. 39992, 2014
96. A. Ramírez-Jiménez, C. Alvarez-Lorenzo, A. Concheiro, E. Bucio. *Radiat. Phys. Chem.* Vol. 99, p. 53, 2014.

97. M. García-Vargas, C. Gonzalez-Chomón, B. Magariños, A. Concheiro, C. Alvarez-Lorenzo, E. Bucio. *Int. J. Pharm.* Vol. 461, p. 286, 2014.
98. J.G. Noh, Y.J. Sung, K.E. Geckeler, S.E. Kudaibergenov. *Polymer* Vol. 46, p. 2183, 2005.
99. M.E. Harmon, A. M. Thomas, K. Wolfgang, W.F. Curtis. *Macromolecules* Vol. 35, p. 5999, 2002.
100. A. Percot, X.X. Zhu, M. Lafleur. *J. Polym. Sci. Pol. Phys.* Vol. 38, p. 907, 2000.
101. Y. Katsumoto, T. Tanaka, H. Sato, Y. Ozaki. *J. Phys. Chem. A* Vol. 106, p. 3429, 2002.
102. E. Princi, S. Vicini, N. Proietti, D. Capitani. *Eur. Polym. J.* Vol. 41, p. 1196, 2005.
103. S. Blanquer, O. Guillaume, V. Letouzey, L. Lemaire, F. Franconi, C. Paniagua, J. Coudane, X. Garric. *Acta Biomater.* Vol. 8, p. 1339, 2012.
104. M. Heskins, J.E. Guillet. *J. Macromol. Sci. Chem.* Vol. 2, p. 1441, 1969.
105. A. Grinberg, Y. Grosberg, T. Tanaka. *Macromolecules* Vol. 33, p. 8685, 2000.
106. P. Letellier, A. Mayaffre, M. Turmine. *J. Colloid Interf. Sci.* Vol. 314, p. 604, 2007.
107. Y.G. Takei, T. Aoki, K. Sanui, N. Ogata, T. Sakurai, T. Okano. *Macromolecules* Vol. 27, p. 6163, 1994.
108. A.N.A. Ochoa, P. Pradáños, L. Palacio, C. Pagliero, J. Marchesi, A. Hernández. *J. Membr. Sci.* Vol. 187, p.227, 2001.
109. M. Gauthier, W.Y. Lin, S.J. Teertstra, C. Tzoganakis. *Polymer* Vol. 51, p. 3123, 2010.
110. C. Combellas, A. Fuchs, F. Kanoufi, D. Mazouzi, S. Nunig. *Polymer* Vol. 45, p. 4669, 2004.

Advanced Composite Adsorbents: Chitosan versus Graphene

George Z. Kyzas*

*Division of Chemical Technology, Department of Chemistry, Aristotle University
of Thessaloniki, Thessaloniki, Greece
Department of Petroleum and Natural Gas Technology, Technological Educational
Institute of Kavala, Kavala, Greece*

Abstract

Two of the most promising, trendy but challenging adsorbent materials of the recent literature are chitosan and graphene. Numerous papers have been published reporting the synthesis of derivatives of them, presenting different properties from their origins. Chitosan is a nitrogenous polysaccharide and can be characterized as a very promising and cheap material, which can be produced in large quantities (poly- β -(1 \rightarrow 4)-2-amino-2-deoxy-D-glucose). On the other hand, graphene and its oxide (graphene oxide) have been used as effective adsorbent toward environmental targets (pollutants). In this work, a direct comparison should be attempted regarding the major adsorption properties of chitosan- and graphene-based materials.

Keywords: Chitosan, graphene, adsorption, comparison

11.1 Introduction

Two of the most promising, trendy but challenging adsorbent materials of the recent literature is chitosan and graphene. Numerous papers have been published reporting the synthesis of derivatives of them presenting different properties from their origins.

On the one hand, chitosan is a nitrogenous polysaccharide and can be characterized as a very promising and cheap material, which can be

*Corresponding author: georgekyzas@gmail.com

produced in large quantities (poly- β -(1 \rightarrow 4)-2-amino-2-deoxy-D-glucose) (Figure 11.1) [1].

Owing to its biocompatibility, high biodegradability, non-toxicity and adsorption properties, chitosan has been proved (apart from pharmaceutical applications) as a promising environmental-friendly adsorbent material and has been extensively used for the removal of environmental pollutants from aqueous matrices [2–8]. However, to improve its adsorption capacity as well as its mechanical properties, the design and synthesis of novel chitosan adsorbents are still critical, challenging and of great interest. In this light, the number of papers in recent literature devoted to the application of chemically modified chitosan materials using cross-linking, grafting of functional groups or acetylation for removal of heavy metals (and/or trace-contaminants) from water matrices has grown rapidly [3, 9–11]. However, some features linked to the chitosan based materials are still open and further efforts should be made to develop more effective and low-cost adsorbents, which can achieve higher adsorption capacity for the removal of heavy metals from aqueous systems.

On the other hand, graphene and its oxide (graphene oxide (GO)) have been used as effective adsorbent toward environmental targets (pollutants) [12]. Graphite oxide, a precursor in the formation of graphene layers, has been studied as an adsorbent and its ability to remove cationic dyes has been demonstrated [13, 14]. From a structural point of view, graphite oxide is a highly-oxidized planar material containing 25–33% oxygen with good adsorption between layers. It is characterized to be a lamellar solid and can be easily prepared by chemical modification. Generally, graphite oxide can be synthesized by oxidation of graphite with strong oxidizing agents such as potassium chlorate, permanganate, bichromate and chlorine dioxides. The strong oxidation makes the graphite oxide to have multiple oxygen-containing functional groups (as for example carboxyl, hydroxyl, and epoxy) and could consequently be covalently attached to its layers. Moreover, the spatial distribution of functional groups on the carbon skeleton is also diverse. The epoxy and hydroxyl groups are near each other, and the carboxyl is possibly situated at the edges of graphite oxide. These oxygen functionalities make it extensively disperse in water, because the functionalities are hydrophilic, thus stabilizing it to be easily [15].

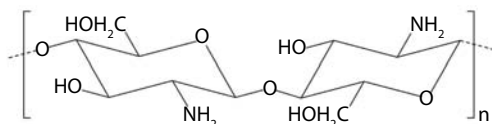


Figure 11.1 Chemical structure of chitosan.

In this work, a direct comparison should be attempted regarding the major properties of chitosan- and graphene-based materials. At first, some modification reactions will be reported which have the goal to improve the adsorptive ability of materials. Then, a detailed discussion will be developed including recent published results of them as adsorbents. A special mention will be done for the up-to-now results of my research group, which extensively employ with the aforementioned materials.

11.2 Chitosan-Based Materials

The origin of chitosan is chitin. Chitin is another promising material due to its abundance as natural biopolymer (totally is second among all biopolymers). It is derived from exoskeletons of crustaceans and perhaps from cell walls of fungi and insect [16]. Chitin (Figure 11.2) can be characterized as a linear heteropolymer of strong cationic nature (charge) with randomly distributed *N*-acetylglucosamine and glucosamine residues with β -1,4-linkage.

A crucial factor in chitin chemistry is its deacetylation, which can be even lower than 10%, while its molecular weight can be higher than 1–2.5 MDa (corresponding to polymerization degree of ca. 5,000–10,000). On the other hand, chitosan is produced by chitin after *N*-deacetylation in 40–50% of hot alkali medium (110–115°C) for few hours. Its deacetylation degree is between 40% and 98%, while the molecular weight ranges between 0.05 and 2 MDa [17, 18]. The adsorption properties of chitosan are strongly dependent on the chitin source. For example, as it was already referred in literature [19–22], chitosan has different capacities for a particular dye (Reactive red 222) on different types of chitosan after production from 3 fishery wastes (shrimp, crab and lobster shells). The adsorption capacities found were 293, 398, and 494 mg/g for chitosan (flakes) produced from for crab, lobster and shrimp chitin, respectively [19]. Moreover, the source of chitin affects both the crystallinity, purity and the polymer chains

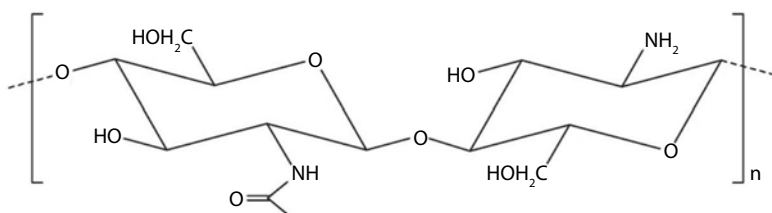


Figure 11.2 Chemical structure of chitin (origin of chitosan).

arrangement of chitosan [17]. When the chitin is originated from crustaceans, it is necessary to be graded of purity or/and color, because usually the residual protein and pigment can cause problems [17].

One basic characteristic of chitosan is the existence of 3 different types of functional groups; (i) amino-acetamido group, (ii), primary and (iii) secondary hydroxyl groups located at C-2, C-3, and C-6 positions, respectively. This is a basic advantage of chitosan which makes it easily modified. The amino contents are the main factors contributing to differences in their structures and physico-chemical properties, and its distribution is random, which make it easy to generate intra- and inter-molecular hydrogen bonds [23]. The deacetylation degree and polymerization degree are the most important factors suggesting the application of chitosan for various applications.

11.2.1 Synthesis and Various Modifications

The final chitosan-based material produced cannot be fixed each time. Any change of various parameters during synthesis can cause differences not only in the ultimate target (high adsorption capacity, but also in shape, nature, charge, and generally in the so-called “properties of adsorbent”. Figure 11.3 presents some different types of chitosan shape prepared by our research team. Chitosan powder is illustrated in Figure 11.3a, while after some changes in synthesis procedure, microspheres (beads) were finally produced (Figure 11.3b).

The preparation route for the production of the simplest chitosan adsorbent (in powder form) is very easy. Particular mass of chitosan is added to aqueous solution of acetic acid (usually 1–4% v/v). The solution resulted is

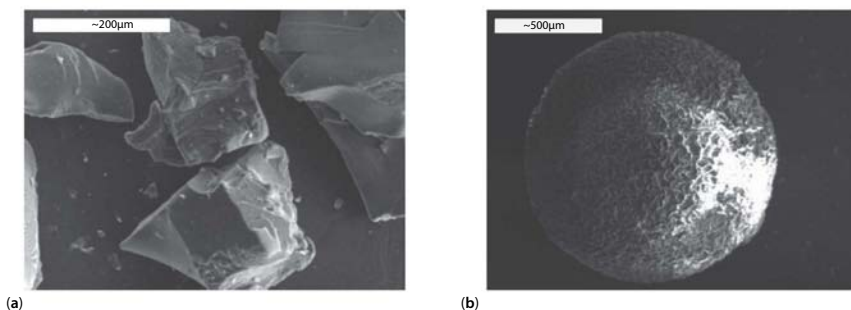


Figure 11.3 SEM micrographs of chitosan in (a) powder form and (b) spherical beads. Reprinted with permission; copyright American Chemical Society [24, 25].

gel-like (step 1). In order to take rigid particles, a quantity of cross-linker is then mixed with solution and after overnight stirring, the solution is filtered and the chitosan particle produced are then purified by extraction with water in a Soxhlet apparatus for 24 h (for removing any unreacted reagent). The main difference in the case of microspheres preparation is that the gel-like solution (from step 1) is added drop wise with pipette to the solution of cross-linker. In this way, the beads can be formed in spherical form.

However, the pure/raw chitosan cannot be easily applied in adsorption because it presents serious limitations. Its swelling degree is one of the most basic drawbacks of chitosan. For the case of aqueous adsorption experiments, under the term of swelling, the ability of bind water molecules is called not only in the external surface layers, but also in the inner of polymeric matrix. The discussion about the physical meaning of swelling is very interesting. The motion of the adsorbate species (ions, dye molecules, etc.) into the chitosan can be done through the liquid phase or from association site to other association site [26]. Different stages can be described in this way as (i) mass transfer from bulk liquid to the particle, (ii) localized adsorption-desorption on the association sites, and (iii) ion diffusion in the intraparticle liquid (i.e., pore diffusion) and ion diffusion among the association sites (i.e., surface diffusion) when the adsorbate species are ions [26].



Figure 11.4 Photos for the synthesis of cross-linked chitosan microspheres in different time periods (the photos were taken during the synthesis in our laboratory) (General & Inorganic Chemical Technology, Aristotle University of Thessaloniki, Greece).

The quantitative evaluation of swelling degree comes from the following experiment: particular mass of material was immersed in deionized water in order to be swollen for 24 h. The particles were left to be swollen, collected and measured at fixed time-intervals. When the last measurement is equal to the pre-last one, then the swelling phenomenon is completed. The swollen samples were weighted and the swelling degree (SD, %) was calculated by Eq. (11.1) (where M_t (g) is the mass of the swollen sample at time t , and M_0 (g) is the initial mass of the sample before swelling):

$$SD = \left(\frac{M_t - M_0}{M_0} \right) \cdot 100\% \quad (11.1)$$

Many works in literature were published revealing this drawback of chitosans. Specifically, when chitosan is in powder-form, it swells considerably and crumbles easily, and therefore plugging of the column is caused. In the case of non-modified completely pure chitosan, swelling degrees of 2000% have been reported [24, 27, 28]. In order to overcome this problem, a first class of modification reactions is cross-linking.

11.2.1.1 Cross-Linking

Many researchers have focused on the investigation of the suitable selection of cross-linking agent. The most common cross-linking agents reacted with chitosan are dialdehydes such as glyoxal, formaldehyde, and in particular glutaraldehyde [29,30]. Glutaraldehyde reacts with chitosan and it cross-links in inter- and intra-molecular fashion through the formation of covalent bonds mainly with the amino groups of the polymer. However, a specific drawback of glutaraldehyde is that it is considered to be toxic. Other cross-linkers of chitosan are epoxides such as epichlorohydrin [31–38], ethyleneglycol diglycidyl ether [39–42], isocyanates(hexamethylenediisocyanate) [43, 44] and other agents (tripolyphosphate sodium [33, 45–48], carboxylicacids, genipin, etc. [49, 50]). Covalent cross-linking, and therefore the cross-linking density, is affected by numerous parameters, but especially by the cross-linker's concentration. Figure 11.5 presents the structure and interactions of a triple cross-linked chitosan derivative using as agents glutaraldehyde, epichlorohydrin and tripolyphosphate.

Many cross-linking agents were applied in order to examine which is the best. However, controversial results have been presented. This may be due to the different nature of pollutant (cationic dye or anionic one; reactive dye or acid one; heavy metal cation or anion, etc.). Our previous study [26], which compared two cross-linked chitosan prepared after glutaraldehyde

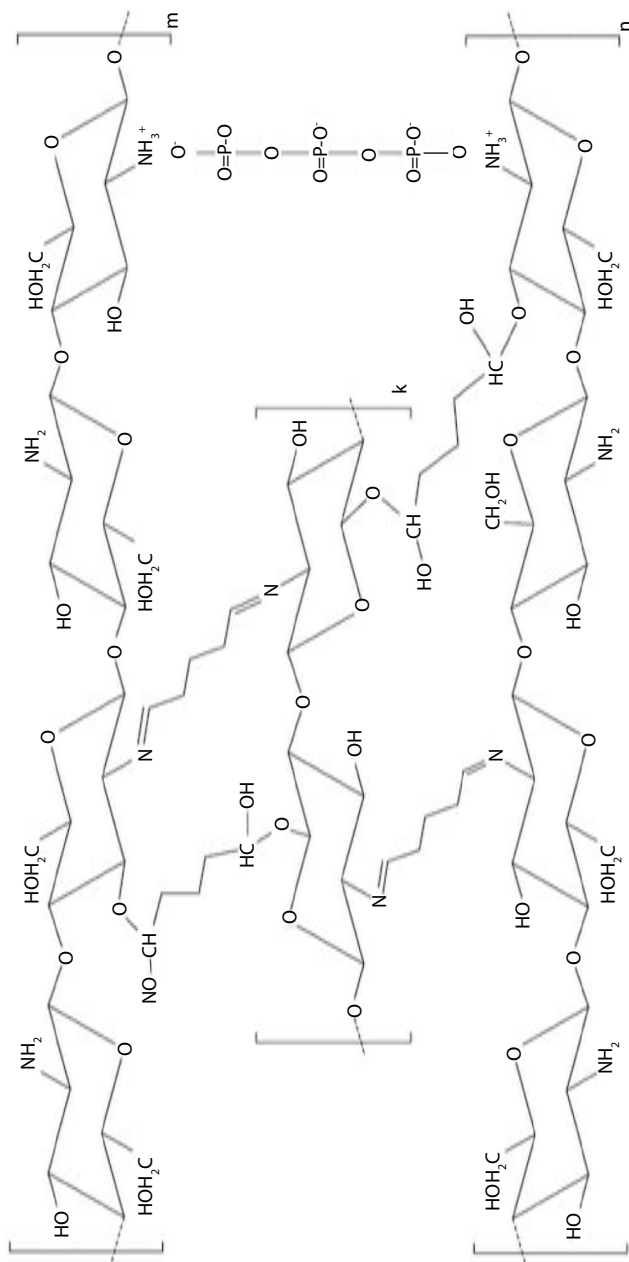


Figure 11.5 Structure and interactions of a triple cross-linked chitosan derivative using as agents glutaraldehyde, epichlorohydrin and tripolyphosphate.

(denoted as CS(G)) or epichlorohydrin (CS(E)) cross-linking, showed that the swelling degree was not the same; 58% for CS(G) and 65% for CS(E) (Figure 11.6). In the same study, some grafted derivatives were compared (grafting with poly(itaconic acid)) and showed differences of 12% and 11% respectively. The latter was probably due to the grafting of poly(itaconic acid). However, the swelling curve of non-grafted derivatives was impressively different compared to the grafted ones (denoted as CS-g-IA(G) and CS-g-IA(E)) (Figure 11.6).

Two stages were existed and swelling equilibrium was reached faster. This was readily explained, considering that without grafted groups the path of water molecules to approach and insert to the chitosan network was more “easy and open” [26]. As a result, the water molecules filled the chitosan network quickly. On the other side, after grafting of chitosan with carboxyl functional groups, its polymeric network became more complex, making the filling-path to water molecules more difficult [26].

A very important series of works was done by Chiou *et al.* [31–33, 51–53], who tested the adsorption capacity of chitosan beads cross-linked with different agents (glutaraldehyde, epichlorohydrin, and ethyleneglycol diglycidyl ether). The concluding remark was that the epichlorohydrin derivative presented a higher adsorption capacity than that of glutaraldehyde or ethyleneglycol diglycidyl ether. This remark can be also stated

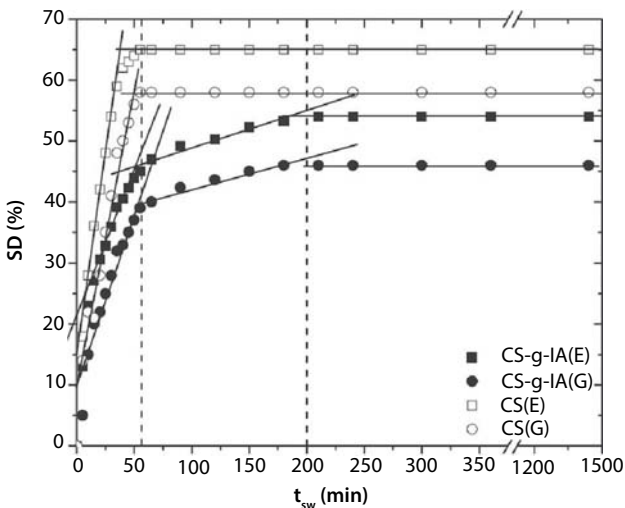


Figure 11.6 Effect of contact time on swelling percentage of CS-g-IA(G) and CS-g-IA(E). Reprinted with permission; copyright American Chemical Society [26].

because epichlorohydrin does not eliminate the cationic amine function of the polymer, which is the major adsorption site to attract the anionic dyes during adsorption [51, 53]. On the contrary, the cross-linking of chitosan with glutaraldehyde creates imine functions or reaction with ethyleneglycol diglycidyl ether decreases the availability of amine functions for the complexation of dyes and with a high cross-linking ratio the uptake capacity drastically decreases. A completely opposite conclusion was arisen by Kim and Cho [54]. They investigated the removal of Reactive black 5 using cross-linked chitosan beads and found that the adsorption capacity of non cross-linked beads was greater than that of cross-linked beads in the same experimental conditions.

11.2.1.2 Grafting

Numerous studies have been published in literature reporting the grafting of various functional groups onto chitosan backbone for the preparation of adsorbent materials. Crini *et al.* extensively describes in review articles the various grafted materials synthesized in 2000s [55–57]. The final quantitative adsorption evaluation is based on the calculation of the maximum theoretical adsorption capacity (Q_m), which mainly found from the fitting to the Langmuir (Eq. (11.2)) [58] and Freundlich (Eq. (11.3)) [59] equations:

$$Q_e = \frac{Q_m K_L C_e}{1 + K_L C_e} \quad (11.2)$$

$$Q_e = K_F C_e^{1/n} \quad (11.3)$$

where Q_e (mg/g) is the equilibrium drug concentration in the solid phase; Q_m (mg/g) is the maximum amount of adsorption; K_L (L/mg) is the Langmuir adsorption equilibrium constant; K_F ($\text{mg}^{1-1/n} \text{L}^{1/n}/\text{g}$) is the Freundlich constant representing the adsorption capacity; and n (dimensionless) is the constant depicting the adsorption intensity.

Although the Langmuir and Freundlich isotherms were firstly introduced about 90 years ago, they still remain the two most commonly used adsorption isotherm equations. Their success undoubtedly reflects their ability to fit a wide variety of sorption data quite well. The Langmuir model represents chemisorption on a set of well defined localized adsorption sites, having the same adsorption energies independent of surface coverage and no interaction between adsorbed molecules. Langmuir isotherm assumes monolayer coverage of adsorbate onto adsorbent. Freundlich isotherm

gives an expression encompassing the surface heterogeneity and the exponential distribution of active sites and their energies. This isotherm does not predict any saturation of the adsorbent surface; thus, infinite surface coverage is predicted, indicating physisorption on the surface.

In the last years, our research team was tested the synthesis of various grafted chitosan adsorbents either in beads or powder form for the removal of different type of pollutants (dyes, metals, ions, pharmaceutical compounds).

The grafting of anionic (poly(acrylic acid)) and non-ionic (polyacrylamide) compounds have been initially tested for the removal of either reactive (Remazol red 3BS, Remazol blue RN, Remazol yellow gelb 3RS) or cationic dyes (Basic blue 3G, Remacryl Red TGL, Basic yellow 37) [24, 25, 60]. As it was revealed, the optimum pH found was alkaline for the cationic dyes removal and acidic for the reactive ones. Beads presented lower adsorption capacities for the reactive dye ((Ch)b = 334, (Ch-g-Aa)b = 456, (Ch-g-Aam)b = 1058 mg/g) than the respective powders ((Ch)p = 417, (Ch-g-Aa)p = 527, (Ch-g-Aam)p = 1211 mg/g). The same was observed for basic dye ((Ch)b = 134, (Ch-g-Aa)b = 563, (Ch-g-Aam)b = 363 mg/g; (Ch)p = 333, (Ch-g-Aa)p = 595, (Ch-g-Aam)p = 528 mg/g).

Another study of our team was mainly focused on the interactions between other grafted chitosans and dyes (similarly reactive and cationic) [61]. Five derivatives of chitosan (Figure 11.8) (75–125 μm) were used for adsorption experiments: (i) non-grafted cross-linked chitosan (Ch), (ii) cross-linked and grafted with acrylamide chitosan (Ch-g-Aam), (iii) cross-linked and grafted with acrylic acid chitosan (Ch-g-Aa), (iv) cross-linked and grafted with N-vinylimidazole chitosan (Ch-g-VID), and (v) cross-linked and grafted with sulfonate groups chitosan (Ch-g-Sulf).

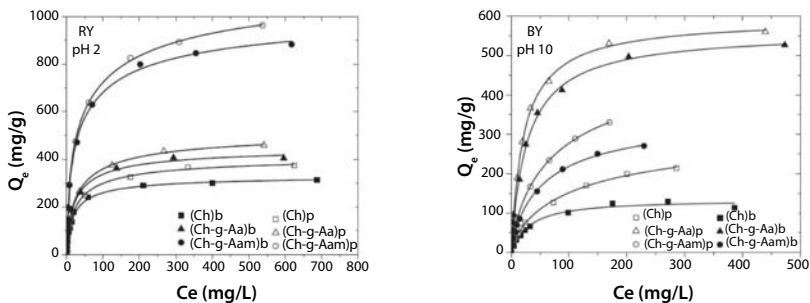


Figure 11.7 Isotherms for chitosan cross-linked derivatives grafted with poly(acrylic acid) or polyacrylamide (powders and beads) (removal of Remazol yellow gelb 3RS and Basic yellow 37). Reprinted with permission; copyright Elsevier [60].

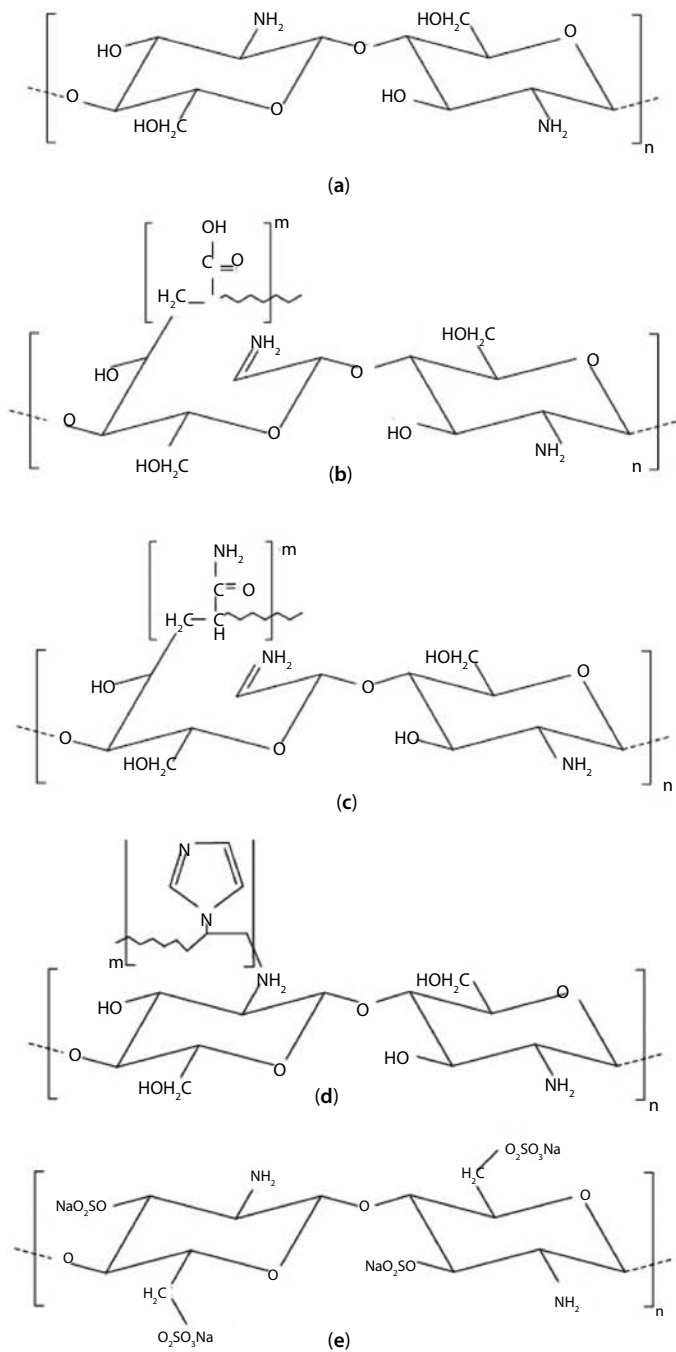


Figure 11.8 Structure of chitosan adsorbents used: (a) Ch, (b) Ch-g-Aa, (c) Ch-g-Aam, (d) Ch-g-VID, and (e) Ch-g-Sulf.

The calculated maximum adsorption capacities (Q_m) for Remazol blue RN removal were: Ch-g-VID, 1329 mg/g > Ch-g-Aam, 1160 mg/g > Ch-g-Aa, 552 mg/g > Ch, 398 mg/g > Ch-g-Sulf, 204 mg/g. The respective values for Basic blue 3G removal were: Ch-g-Sulf, 1022 mg/g > Ch-g-Aa, 595 mg/g > Ch-g-VID, 456 mg/g > Ch-g-Aam, 390 mg/g > Ch, 254 mg/g.

Moreover, we have synthesized another chitosan composite material which was grafted with imino groups [62]. Briefly, cross-linked chitosan beads suspended in water (total volume was 500 mL) were washed with 500 mL of isopropyl alcohol four times and then were finally suspended in isopropyl alcohol of 500 mL. 8.5 g of epichlorohydrin was added to the suspension. The amount of epichlorohydrin was 3 times equivalent moles per glucosamine residue of chitosan. The reaction was carried out at 50°C for 2 h. Thereafter, 100 mL of chitosan beads were well mixed in 100 mL of 30% poly(ethylene imine) aqueous solution at 80°C for 3 h. The final product was washed with water thoroughly. The adsorption experiments were run along with the previously prepared chitosan adsorbents (cross-linked material and amido derivative) for comparison in the same reactive dyes. The imino-adsorbent (Ch-g-PEI) showed the maximum adsorption capacity for all the dyes (RR, 1412 mg/L; RY, 1392 mg/L; RB, 1329 mg/L) following the order Ch-g-PEI > Ch-g-Aam > Ch.

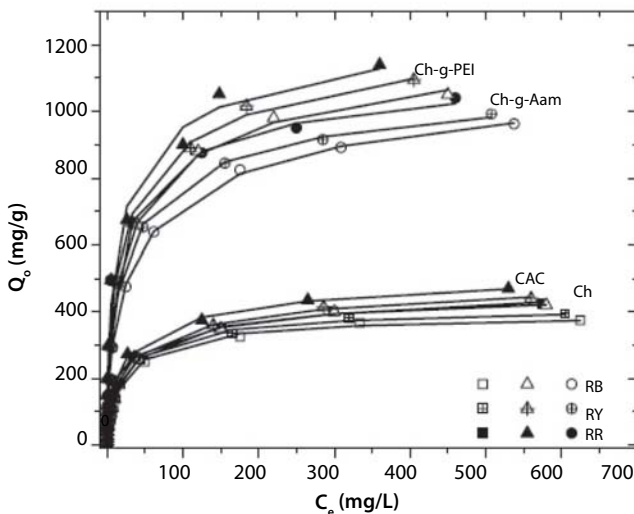


Figure 11.9 Isotherms for chitosan cross-linked derivatives grafted with polyethyleneimine (removal of reactive dyes). Reprinted with permission; copyright Elsevier [62].

Apart from the investigation of adsorption properties of various grafted chitosan on dyes, heavy metals and ions were also tested, synthesizing another grafted chitosan adsorbent. Cross-linked and grafted with *N*-(2-carboxybenzyl) groups (denoted as Ch-g-NCB), was evaluated as adsorbent to sufficiently remove both positively charged ions (Cu(II), Ni(II)) and negatively charged ones (Cr(VI), As(V)) from aqueous solutions [3]. The maximum adsorption capacities were 308 mg/g for copper and 381 mg/g for nickel ions, while 208 mg/g for As(V) and 175 mg/g for Cr(VI) (Figure 11.10).

However, before the above study, the already published grafted chitosan derivative with amido or carboxyl groups, were tested for Cu(II) and Cr(VI) uptake [2]. Equilibrium sorption experiments were carried out at different pH values and initial ion concentrations. The calculated maximum sorption capacity of the carboxyl-grafted sorbent for Cu(II) was found to be 318 mg/g at pH 6, while the respective capacity for Cr(VI) uptake onto the amido-grafted sorbent was found to be 935 mg/g at pH 4, which is considered to be of highest capacities in literature.

Another very toxic metal was studied by our team for removal. In particular, two chitosan derivatives were synthesized in order to compare their adsorption properties for Hg(II) removal from aqueous solutions [63]. The one (CS) is only cross-linked with glutaraldehyde, while the other (CSm), which is magnetic, is cross-linked with glutaraldehyde and functionalized with magnetic nanoparticles (Fe₃O₄). Similarly in this case, new interactions and adsorption mechanisms were proposed

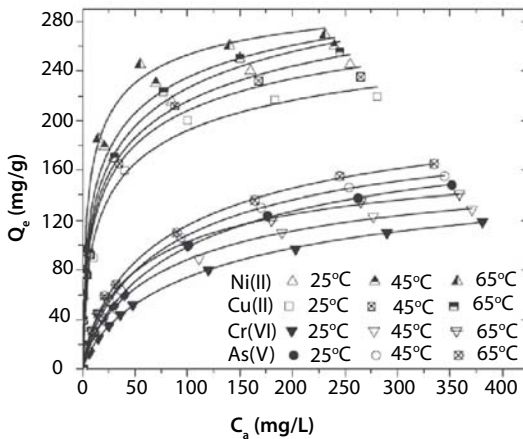


Figure 11.10 Effect temperature on equilibrium of adsorption of ions onto Ch-g-NCB (powder; pH = 5; 0–1000 mg/L ion concentration; 1 g/L adsorbent; T = 25°C, 45°C, 65°C; 140 rpm; 24 h contact). Reprinted with permission; copyright Elsevier [3].

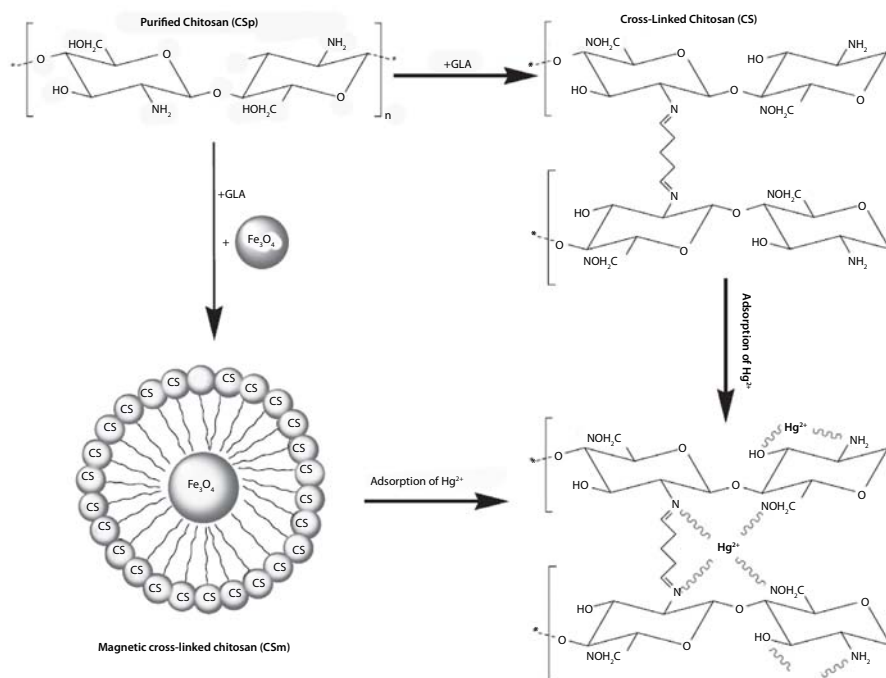


Figure 11.11 Preparation of CS and CSm and possible interaction with Hg(II). Reprinted with permission; copyright MDPI [63].

(Figure 11.11). The maximum adsorption capacity of CS and CSm at 25°C was 145 and 152 mg/g, respectively. An interesting finding was the increase of Q_m with the increase of temperature from 25°C to 65°C. In particular, CS augmented its Q_m from 145 mg/g at 25°C to 171 mg/g at 45°C (increase of 18%) and finally 175 mg/g at 65°C (increase of 2%). Similarly, the magnetic derivative (CSm) improved its Q_m from 152 mg/g at 25°C to 158 mg/g at 45°C (increase of 4%) and finally 184 mg/g at 65°C (increase of 16%). However, an interesting finding of the above is the different-type change of Q_m of two materials during the increase of temperature adsorption. Although, CS increased its Q_m 18% from 25°C to 45°C, a nearly zero change was observed from 45°C to 65°C (2%). In the case of CSm, the reverse fact was observed: CSm slightly increased its Q_m from 25°C to 45°C (4%), while a more intense increase was for the temperatures from 45°C to 65°C (16%). The difference of the temperature-behavior of materials could be explained due to their difference modification and the existence of magnetism on CSm. The latter can behave in different manner for various temperatures. In general, as

the majority of the chitosan-based materials [8], the Q_m augmentation with temperature increase is caused by the enhancement of the number of adsorption sites; the latter is due to the weakening and/or breaking of many structural bonds of network, existed near the edge of the active surface sites of materials. Another, possible explanation is the increase of diffusion (mainly surface diffusion [2]), which helps the penetration of mercury ions inside the structural network of materials.

Two other chitosan (CS) adsorbents were prepared in powder form, after modification with grafting of poly(itaconic acid) and cross-linking either with glutaraldehyde (CS-g-IA(G)) or epichlorohydrin (CS-g-IA(E)). New adsorption mechanisms were proposed (Figure 11.12).

Their adsorption properties were evaluated in batch experiments for Cd(II) or Pb(II) uptake [26]. The maximum adsorption capacity for Cd(II) uptake was 405 and 331 mg/g for CS-g-IA(G) and CS-g-IA(E), respectively, revealing the capacity enhancement after grafting (124 and 92 mg/g were the respective values before grafting, respectively).

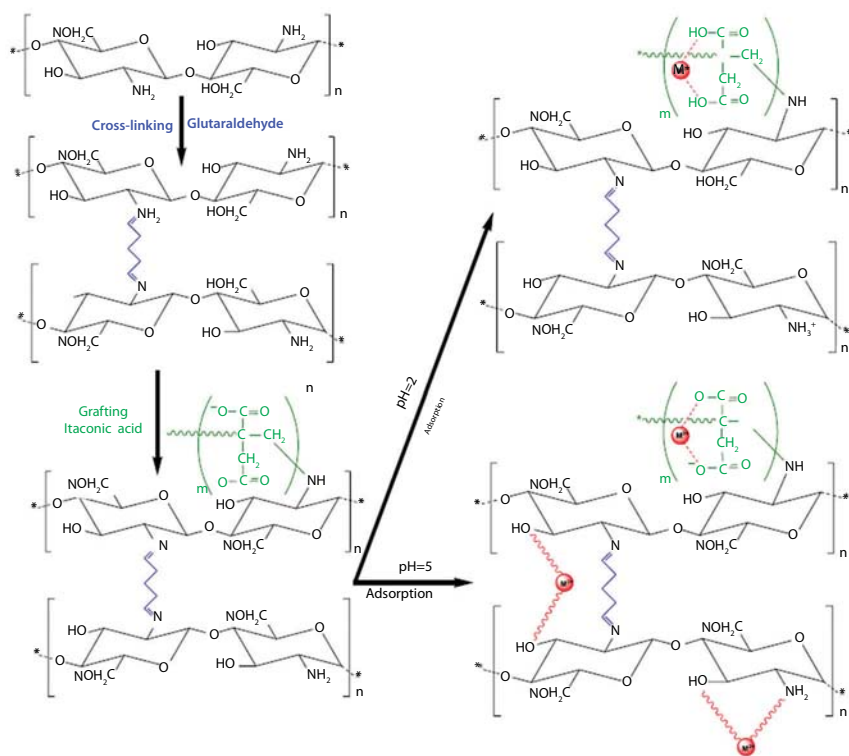


Figure 11.12 Cross-linked and grafted CS with IA and interactions between CS-g-IA(G) and metal ions. Reprinted with permission; copyright American Chemical Society [26].

11.3 Graphene-Based Materials

The “history” of graphene was old enough and initially posed by Boehm *et al.* in 1986, who attempted to describe and explain a single atomic sheet of graphite [64]. The decade of 2000 caused some surprise for the up-to-then theories. It was considered that two-dimensional crystals like graphene were thermodynamically unstable and presumed not to exist under ambient conditions [65]. However, Konstantin Novoselov succeeded in isolating and characterizing of a mechanically exfoliated graphene monolayer by Konstantin Novoselov [66]; Andre K. Geim and Konstantin S. Novoselov of the University of Manchester (UK) were honored with the 2010 Nobel Prize for their pioneering work with graphene. The term of IUPAC (International Union of Pure and Applied Chemistry) is clear for graphene: a single carbon layer of the graphite structure, describing its nature by analogy to a polycyclic aromatic hydrocarbon of quasi-infinite size [67]. In other word, graphene is considered to be a flat-like single layer of hybridized sp^2 carbon atoms, which are densely packed each other into an ordered 2D honeycomb network [68]. A unit hexagonal cell of graphene comprises two equivalent sub-lattices of carbon atoms, joined together by sigma (σ) bonds with a carbon–carbon bond length of 0.142 nm [69]. Each carbon atom in the lattice has a π -orbital that contributes to a delocalized network of electrons, making graphene sufficiently stable compared to other nanosystems [70]. The applicability of graphene is based on a advantageous network provided by this material: combination of high three-dimensional aspect ratio and large specific surface area, superior mechanical stiffness and flexibility, remarkable optical transmittance, exceptionally high electronic and thermal conductivities, impermeability to gases, as well as many other supreme properties. Due to all the above, Novoselov characterized it as miracle material [71].

GO is the result of the chemical exfoliation of graphite. It is considered to be a highly oxidative form of graphene, which has numerous and different-type oxygen functionalities. Many theories have been developed in past for the determination of the exact chemical structure of GO [72, 73]. This is mainly because of the complexity of the material (including sample-to-sample variability), and of course its amorphous, berthollide character, i.e., nonstoichiometric atomic composition [74]. Lerf–Klinowski model describes a theory according to which, the carbon plane in GO is decorated with hydroxyl and epoxy(1,2-ether) functional groups [75]. The consideration for the existence of some carbonyl groups is correct, most likely as carboxylic acids along the sheet edges but also as organic carbonyl defects

within the sheet [76, 77]. The synthesis of GO is based on three preparation methods: (i) Brodie's [78], (ii) Staudenmaier's [79], or Hummers' method [80]. The major part of all methods is the chemical exfoliation of graphite using oxidizing agent in the presence of mineral acid. Two methods (Brodie's and Staudenmaier's methods) apply a combination of KClO_4 with HNO_3 in order to oxidize graphite. The method of Hummers uses the addition of graphite to potassium permanganate and H_2SO_4 . The oxidation of graphite breaks up the π -conjugation of the stacked graphene sheets into nanoscale graphitic sp^2 domains surrounded by highly disordered oxidized domains (sp^3 C\C) as well as defects of carbon vacancies [81]. The GO sheets produced are consisted of phenol, hydroxyl and epoxy groups mainly at the basal plane and carboxylic acid groups at the edges [82], and can thus readily exfoliate to form a stable, light brown colored, single layer suspension in water [81].

11.3.1 Adsorption Applications

Many researchers have investigated the removal of different using GO adsorbent materials. The removal of Methylene blue was studied by Liu and co-workers presenting good results (153 mg/g). This value further increased (204 mg/g) from 25°C to 65°C [83]. The same pollutant was tested by Wu *et al.* [84], but the results were impressively higher (1520 mg/g) which was mainly due to π - π stacking interactions as inferred through fluorescence spectroscopy studies. Another cationic dye (Cationic red X-GRL) was studied for adsorption onto GO [85]; The Q_m found was 238 mg/g. Zhang *et al.* [86] presented $Q_m = 1939$ mg/g of GO for Methylene blue adsorption, while Li *et al.* [87] found that GO had 240.65 mg/g for the same dye (attributed to π - π electron donor-acceptor interactions and electrostatic attraction between positively charged dye ions and negatively charged adsorbent. Based on the above, it is obvious that changes are presented between Q_m of GO for Methylene blue adsorption. This may be due to the different experimental conditions employed during each study.

Hydrothermal treatment of GO with thiourea resulted in the formation of "graphene sponge" in other study [88]. The target of this study was to remove either anionic dyes (Methyl orange) or cationic ones (Methylene blue, Rhodamine B). The maximum adsorption capacities were 184, 73, and 12 mg/g for Methylene blue, Rhodamine B, and Methyl orange, respectively. The adsorption capacity for basic dye was much higher than for acid dye because of the ionic charges on the dyes and surface characteristics of graphene sponge [88].

The removal of various textile dyes (Methylene blue, Methyl violet, Rhodamine B and Orange G) using GO were investigated by Ramesha *et al.* [12]. GO showed a good binding affinity for cationic dyes following the order Methylene blue > Methyl violet > Rhodamine B. The latter was mainly attributed to the fact that Methylene blue and Methyl violet were positively charged while Rhodamine B included both positive and negative charge. On the other hand, GO did not present high capacity for Orange G, because this dye molecule had two sulfonic groups (negatively charged) resulting in electrostatic repulsion between the dye and the adsorbent, and hence no significant removal was observed.

In order to avoid repetitions, Tables 11.1 and 11.2 were obtained from the recent review article of Chowdhury and Balasubramanian [89], which summarizes interesting adsorption papers regarding GO and environmental pollutants.

Table 11.1 Reported results of batch adsorption studies on the removal of dyes from water by graphene-based materials. Reprinted with permission; copyright Elsevier [89].

Adsorbent	Dye	Capacity (mg/g)
Graphene	Methylene blue	153.85
Graphene	Cationic red X-GRL	217.39
Graphene	Methyl blue	1520
Graphene sponge	Methylene blue	184
Graphene sponge	Rhodamine B	72.5
Graphene sponge	Methyl orange	11.5
GO	Methylene blue	714
GO	Methylene blue	1939
GO	Methylene blue	17.3
GO	Methyl violet	2.47
GO	Rhodamine B	1.24
GO	Acridine orange	1428
GO	Methylene blue	240.65
In situ reduced GO	Acridine orange	3333
PES/GO	Methylene blue	62.5

(Continues)

Table 11.1 (Cont.)

Adsorbent	Dye	Capacity (mg/g)
RGO	Orange G	5.98
RGO-based hydrogel	Methylene blue	7.85
RGO-based hydrogel	Rhodamine B	29.44
Graphene/Fe ₃ O ₄	Fuchsine	89.4
Graphene/magnetite	Methylene blue	43.82
Magnetite@graphene	Congo red	33.66
Magnetite@graphene	Methylene blue	45.27
Graphene/Fe ₃ O ₄	Pararosaniline	198.23

Table 11.2 Reported results of batch adsorption studies on the removal of heavy metals from water by graphene-based materials. Reprinted with permission; copyright Elsevier [89].

Adsorbent	Metal	Adsorption Capacity (mg/g)
Graphene	Pb(II)	22.42
Graphene (heat treated at 773 K)	Pb(II)	35.21
Graphene (heat treated at 973 K)	Pb(II)	35.46
Graphene	Sb(III)	10.919
Graphene	Fe(II)	299
Graphene	Co(II)	370
CTAB modified graphene	Cr(VI)	22
Functionalized graphene (GNSPF6)	Pb(II)	406
Functionalized graphene (GNSPF6)	Cd(II)	74
Functionalized graphene (GNSC8P)	Pb(II)	75
Functionalized graphene (GNSC8P)	Cd(II)	30
GO	Pb(II)	367
GO	U(VI)	299
GO	Zn(II)	30

(Continues)

Table 11.2 (Cont.)

Adsorbent	Metal	Adsorption Capacity (mg/g)
GO	Cd(II)	15
GO	Pb(II)	36
GO	Cu(II)	117
GO	Pb(II)	693
GO	Cu(II)	294
GO	Zn(II)	345
GO	Cd(II)	530
GO	Pb(II)	1119
GO	Zn(II)	246
GO aerogel	Cu(II)	18
EDTA modified GO	Pb(II)	535
FGO	Pb(II)	842
FGO	Cd(II)	106
FGO	Co(II)	68
Graphene/Fe	Cr(VI)	162
SiO ₂ /graphene	Pb(II)	113
Magnetite/GO	Co(II)	13
Fe ₃ O ₄ /GO	U(VI)	69

Moreover, our team has also synthesized modified GOs (magnetic) but in different preparation routes by co-precipitation (mGOp) and impregnation (mGOi) in order to effectively remove Reactive black 5 from aqueous solutions [90]. The synthesis of mGOp particles can be briefly described as: GO (0.3 g) was dispersed in 150 mL water by sonication for 30 min in order GO to be formed. Then, 0.825 g FeCl₃·6H₂O and 0.322 g of FeCl₂·4H₂O were dissolved in 25 mL of water and the solution was added drop wise to GO solution at room temperature under a nitrogen flow with vigorous stirring. After completing ion exchange, 28% ammonia solution was added drop wise to make the pH of solution 10 for synthesis of magnetite nanoparticles. The temperature of the solution rose to 80°C. After stirring for about 45 min, the black precipitate was centrifuged, washed with ethanol several

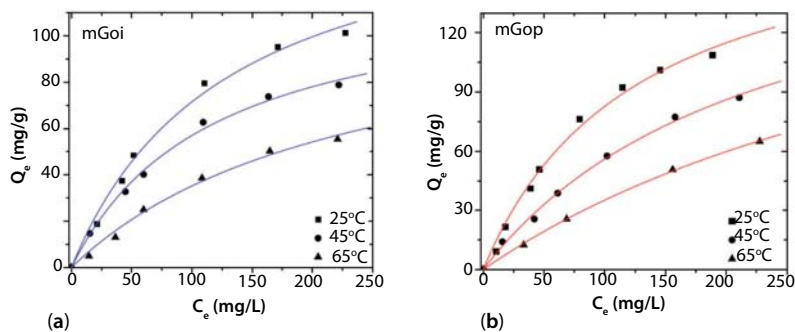


Figure 11.13 Isotherms of the adsorption of reactive black 5 onto (a) mGOi and (b) mGOp. Reprinted with permission; copyright MDPI [90].

times, and finally was freeze-dried. The synthesis of mGOi particles can be briefly described as: The graphite oxide dispersion (0.3 g GO in 300 mL distilled water) was sonicated for 30 min in order GO to be formed. An amount of Fe_3O_4 nanoparticles (0.3 g) was added to the dispersion. After 30 min of sonication, to obtain a homogenous suspension, the resulted nano-composites were collected by centrifuging and freeze-dried. The calculated maximum adsorption capacities (Q_m) for RB5 removal at 25°C (pH = 3) was 164, and 188 mg/g for mGOi, and mGOp, respectively (Figure 11.13).

11.4 Graphene/Chitosan Composite Adsorbents

In order to directly compare the adsorption properties of our prepared chitosan- or graphene-based materials, some composite materials were prepared and compared to their origin ones.

In our previous work [91], a novel composite material (GO-Ch) consisted of cross-linked chitosan (Ch) and graphite oxide (GO) was prepared for the removal of Reactive Black 5 dye. For the preparation of the novel GO-Ch composite [13, 14], chitosan solution (2% w/v) was prepared by dissolving 0.4 g of powder chitosan into 20 mL of acetic acid solution (2% v/v) under ultrasonic stirring for 2 h at room temperature. Also, 3 mL of GLA (50 wt% in water) were added to cross-linked chitosan. Then, 0.3 g of GO were added in the solution prepared and the mixed system was stirred continuously for 90 min in a water bath at 50°C. The pH of the reaction system was adjusted to 9–10 with micro-additions of NaOH (0.1 mol/L) and kept in the water bath for further 60 min at

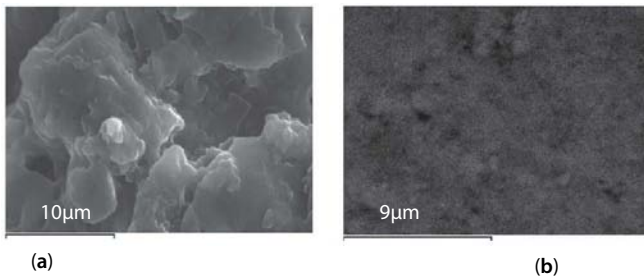
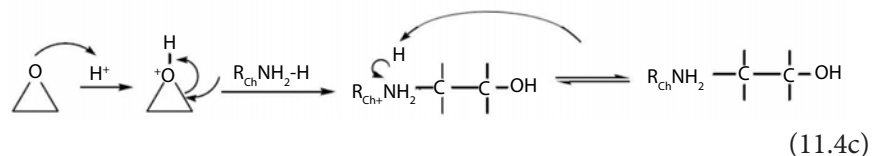
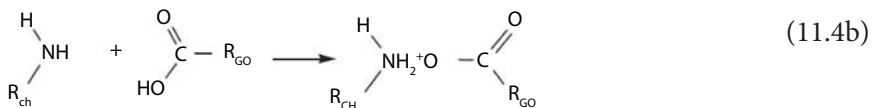
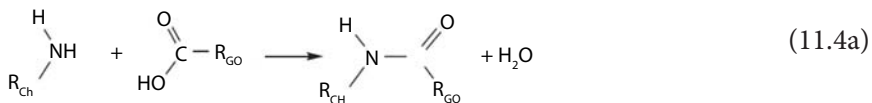


Figure 11.14 SEM image of (a) GO and (b) GO-Ch composite. Reprinted with permission; copyright Elsevier [91].

80°C. Black products were washed with ethanol and distilled water in turn until the pH was reached about 7 and dried in a vacuum oven at 50°C. The final product was the composite of graphite oxide/cross-linked chitosan (GO-Ch). All prepared products (GO, Ch, and GO-Ch) were ground to fine powders, with size after sieving 75–125 μm. As it can be seen from Figure 11.14, GO presents the common sheet-like structure (Figure 11.14a), while after functionalization with chitosan, a rougher surface is presented (Figure 11.14b), revealing that Ch had been assembled on the surface of GO layers with a high density [13,91].

In the same study [91], the functionalization of chitosan with graphite oxide has been explained using some reactions of theory. In particular, the amino groups of Ch react with oxygen-containing functional groups of GO with 3 possible ways: (i) after hydrogen-bonding interactions between the amino groups and the oxygen-containing functional groups of GO ($G-OH \cdots H_2N-R$) (Eq. (11.4a)), (ii) after protonation of the amine by the weakly acidic sites of the GO layers ($-COO^-H_3N-R$) with amides and amine carboxylate salts as reactions products (Eq. (11.4b)), and (iii) after nucleophilic substitution reactions on the epoxy groups of GO (Eq. (11.4c)) [92]:



where R_{Ch} is the residual part of Ch (especially its amino groups) and R_{GO} is the respective part of GO (especially its carboxyl groups).

The capacities found after fitting demonstrated that the functionalization of chitosan enhanced the Q_m (205, 224, and 277 mg/g (pH = 2) for GO, Ch, and GO-Ch) (Figure 11.15).

Another study of our team [93] reveals the use of magnetic chitosan (Chm) instead of pure (Ch) in the functionalization and synthesis of graphite oxide/chitosan composite. The procedure for synthesis was to initially prepare the magnetic nanoparticles. Briefly, 3.5 g of $FeCl_2 \cdot 4H_2O$, 9.5 g of $FeCl_3 \cdot 6H_2O$ and 400 mL of double distilled water were stirred in a water bath at $60^\circ C$ under N_2 for 1 h. Ammonia solution was added drop wise, purged with nitrogen until pH = 10. The precipitate thus obtained was decanted in a dialysis tubing cellulose membrane (Sigma Co.) and the latter was placed in a bath filled with distilled water. The chloride ions present in the initial suspension were slowly removed by osmosis through the membrane. The existence of Cl^- ions in the water bath was tested with an $AgNO_3$ (0.1 M) solution. The water of the bath was replaced several times, until no more chloride ions were detectable in it. The resulting cake on the membrane surface after decanting was freeze-dried in a bench freeze drier (Christ Alpha 1–4). Then, for synthesis of magnetic chitosan (Chm), 2 g of pure chitosan (Ch_{HMW}) was dissolved in 400 mL of acetic solution (2% v/v). 0.75 g of magnetic particles were added in the chitosan solution and

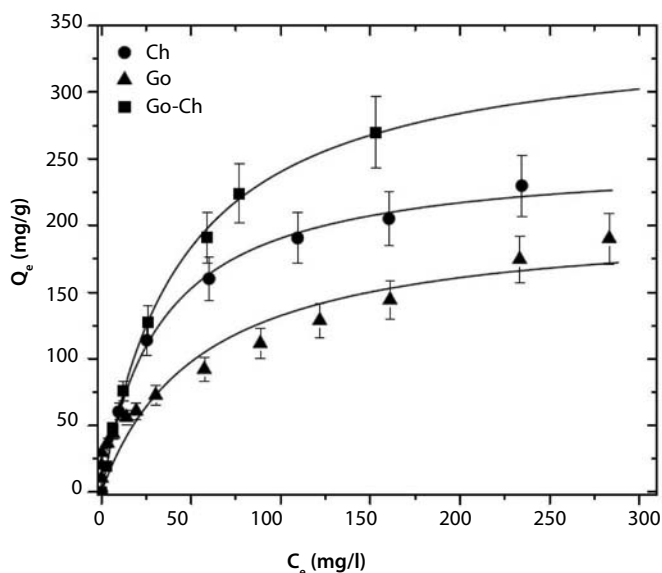


Figure 11.15 Effect of initial dye concentration on adsorption of RB5 onto Ch, GO, and GO-Ch. Reprinted with permission; copyright Elsevier [91].

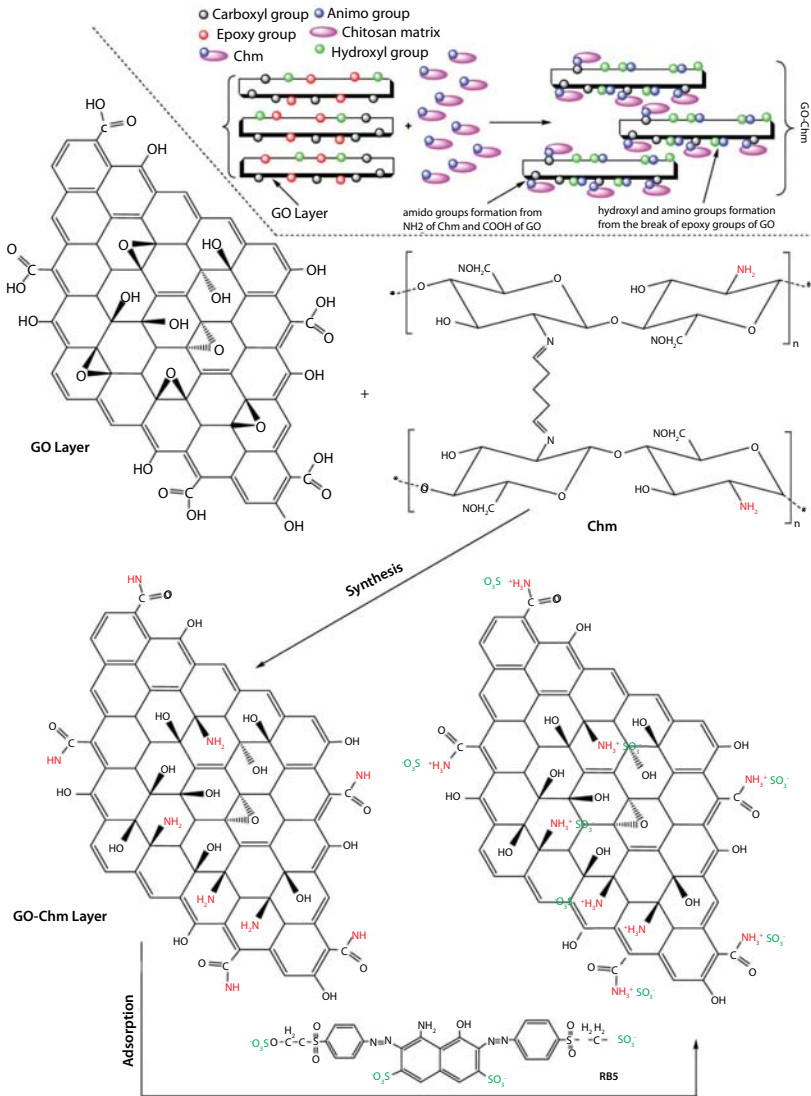


Figure 11.16 Proposed mechanism of synthesis of GO-Chm after functionalization of Chm onto GO. Proposed interactions of the RB5 adsorption onto the prepared GO-Chm. Reprinted with permission; copyright American Chemical Society [93].

the mixture solution was sonicated for 30 min. Then, GLA (cross-linker) was added to mixture solution in order to cross-link chitosan. The latter was carried out, because chitosan presents high swelling degree in aqueous solutions. In order to overcome this problem and given the use of chitosan-based nanocomposite (in this study) as adsorbent, chitosan has

to be cross-linked [24,28]. So, 15 mL of GLA (50 wt% in water) was added into reaction flask to mix with the solution and was vigorously stirred at 60°C for 2 h. The precipitate was washed with ethanol and distilled water in turn and was dried in a vacuum oven at 50°C. The obtained product was magnetic chitosan (Chm). And then, the functionalization with GO as described in the previous work [91].

After adsorption evaluation, it was found that for GO, the Q_m was 221 mg/g (pH3) and 391 mg/g for GO-Chm. So, the functionalization of GO with Chm impressively improved the Q_{max} (GO-Chm) at ~75%. Schematically, we have proposed the suitable interactions found after characterization techniques (Figure 11.16).

To cover more areas of environmental pollutants, our team synthesized a novel graphite oxide/poly(acrylic acid) grafted chitosan nanocomposite (GO/CSA) for use as biosorbent for the removal of pharmaceutical compound (dorzolamide) from biomedical synthetic wastewaters [94]. The results showed the superiority of composite material (GO/CSA, $Q_m = 334$ mg/g) than GO ($Q_m = 175$ mg/g) and CSA ($Q_m = 229$ mg/g) (Figure 11.17).

However, the quantitative sum of Q_m for GO and CSA did not equal to that of GO/CSA, which revealed that the adsorption was not a simple sum of interactions characteristic for the parent materials, but a complex combination of forces, bonds formation, electrostatic and repulsive interactions [94]. Some considerations about interactions are presented in Figure 11.18.

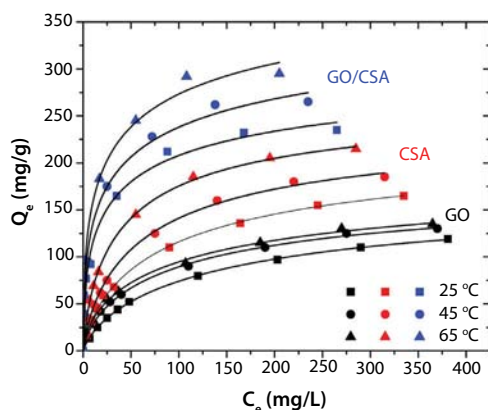


Figure 11.17 Effect of initial dye concentration on adsorption of RB5 onto Ch, GO, and GO-Ch. Reprinted with permission; copyright Elsevier [91].

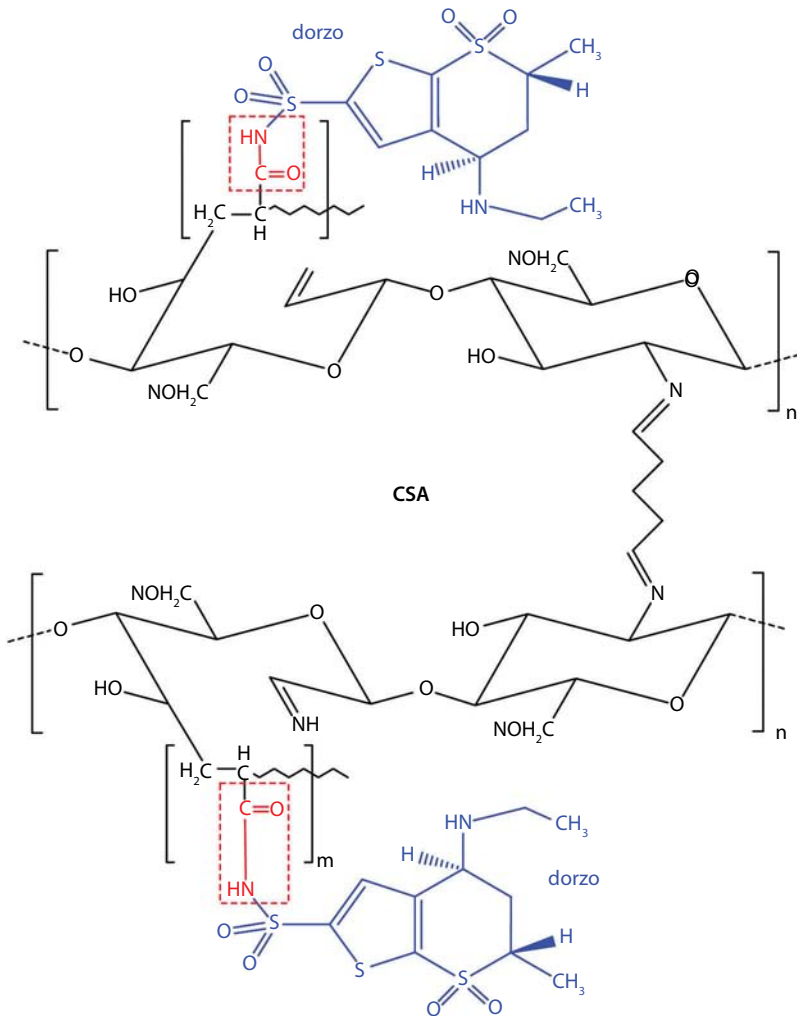


Figure 11.18 Interactions between CSA and dorzo. Reprinted with permission; copyright Elsevier [94].

11.5 Conclusions

Both chitosan- and graphene- present numerous advantages but also serious limitations/drawbacks. Chitosan is a polymer which can be easily modified and accept various functional groups with grafting reactions, while graphene transforms to its most known form as GO is. It is fact that a direct comparison regarding the adsorption properties of any material

cannot be done if some parameters change. The model pollutants and the conditions of adsorption experiments must be the same. Therefore, the only way to directly compare these two different materials is to make simultaneous experiments both with chitosan- and graphene- materials. Moreover, a very promising trend of nowadays is to effectively combine/functionalize both chitosan and GO in order to “gain” the advantages and “hinder” the drawbacks of each materials. Examples were given in this work mainly from the research field of our laboratory, which showed the superiority of those advanced composite materials.

References

1. R.A.A. Muzzarelli, *Natural chelating polymers: Alginic acid, chitin, and chitosan*, Oxford, Pergamon Press, 1973.
2. G.Z. Kyzas, M. Kostoglou, and N.K. Lazaridis, *Chem. Eng. J.*, Vol. 152, p. 440, 2009.
3. G.Z. Kyzas, M. Kostoglou, N.K. Lazaridis, and D.N. Bikiaris, *J. Hazard. Mater.*, Vol. 244–245, p. 29, 2013.
4. X. Liu, Q. Hu, Z. Fang, X. Zhang, and B. Zhang, *Langmuir*, Vol. 25, p. 3, 2009.
5. J. Guzmán, I. Saucedo, R. Navarro, J. Revilla, and E. Guibal, *Langmuir*, Vol. 18, p. 1567, 2002.
6. E. Guibal, M. Jansson-Charrier, I. Saucedo, and P. Le Cloirec, *Langmuir*, Vol. 11, p. 591, 1995.
7. W.S. Wan Ngah, L.C. Teong, and M.A.K.M. Hanafiah, *Carbohydr. Polym.*, Vol. 83, p. 1446, 2011.
8. E. Guibal, *Sep. Purif. Technol.*, Vol. 38, p. 43, 2004.
9. A.J. Varma, S.V. Deshpande, and J.F. Kennedy, *Carbohydr. Polym.*, Vol. 55, p. 77, 2004.
10. A.A.A. Emará, M.A. Tawab, M.A. El-Ghamry, and M.Z. Elsabee, *Carbohydr. Polym.*, Vol. 83, p. 192, 2011.
11. N.G. Kandile, and A.S. Nasr, *Carbohydr. Polym.*, Vol. 78, p. 753, 2009.
12. G.K. Ramesha, A. Vijaya Kumara, H.B. Muralidhara, and S. Sampath, *J. Colloid Interface Sci.*, Vol. 361, p. 270, 2011.
13. L. Fan, C. Luo, X. Li, F. Lu, H. Qiu, and M. Sun, *J. Hazard. Mater.*, Vol. 215–216, p. 272, 2012.
14. L. Fan, C. Luo, M. Sun, X. Li, F. Lu, and H. Qiu, *Bioresour. Technol.*, Vol. 114, p. 703, 2012.
15. Y.L. Wang, P. Gao, L.H. Huang, X.J. Wu, and Y.L. Liu, *Chin. J. Inorg. Chem.*, Vol. 28, p. 391, 2012.
16. M.G. Peter, in: A. Steinbuchel, R.H. Marchessault (Eds.) *Biopolymers for medical and pharmaceutical applications*, Wiley-VCH, Weinheim, Germany, 2005, pp. 419–512.

17. M. Rinaudo, *Prog. Polym. Sci. (Oxford)*, Vol. 31, p. 603, 2006.
18. M. Rinaudo, *Polym. Int.*, Vol. 57, p. 397, 2008.
19. F.C. Wu, R.L. Tseng, and R.S. Juang, *J. Hazard. Mater.*, Vol. 73, p. 63, 2000.
20. F.C. Wu, R.L. Tseng, and R.S. Juang, *Water Res.*, Vol. 35, p. 613, 2001.
21. F.C. Wu, R.L. Tseng, and R.S. Juang, *J. Hazard. Mater.*, Vol. 81, p. 167, 2001.
22. F.C. Wu, R.L. Tseng, and R.S. Juang, *Environ. Technol.*, Vol. 22, p. 205, 2001.
23. J. Zhang, W. Xia, P. Liu, Q. Cheng, T. Tahi, W. Gu, and B. Li, *Marine Drugs*, Vol. 8, p. 1962, 2010.
24. G.Z. Kyzas, D.N. Bikiaris, and N.K. Lazaridis, *Langmuir*, Vol. 24, p. 4791, 2008.
25. N.K. Lazaridis, G.Z. Kyzas, A.A. Vassiliou, and D.N. Bikiaris, *Langmuir*, Vol. 23, p. 7634, 2007.
26. G.Z. Kyzas, P.I. Siafaka, D.A. Lambropoulou, N.K. Lazaridis, and D.N. Bikiaris, *Langmuir*, Vol. 40, p. 120, 2013.
27. F.M. Goycoolea, W.M. Argüelles-Monal, J. Lizardi, C. Peniche, A. Heras, G. Galed, and E.I. Díaz, *Polym. Bull. (Berlin)*, Vol. 58, p. 225, 2007.
28. G.Z. Kyzas, N.K. Lazaridis, and M. Kostoglou, *Chem. Eng. Sci.*, Vol. 81, p. 220, 2012.
29. J. Berger, M. Reist, J.M. Mayer, O. Felt, and R. Gurny, *Eur. J. Pharm. Biopharm.*, Vol. 57, p. 35, 2004.
30. J. Berger, M. Reist, J.M. Mayer, O. Felt, N.A. Peppas, and R. Gurny, *Eur. J. Pharm. Biopharm.*, Vol. 57, p. 19, 2004.
31. M.S. Chiou, W.S. Kuo, and H.Y. Li, *J. Environ. Sci. Health – A Toxic/Hazard. Subst. Environ. Eng.*, Vol. 38, p. 2621, 2003.
32. M.S. Chiou and H.Y. Li, *J. Hazard. Mater.*, Vol. 93, p. 233, 2002.
33. M.S. Chiou and H.Y. Li, *Chemosphere*, Vol. 50, p. 1095, 2003.
34. P.T.B. Hanh, N.T. An, T.T.Y. Nhi, T.T.T. Thuy, D.A. Vu, N.T. Thanh, T.D. Thanh, and D.T. Thien, *J. Chem.*, Vol. 45, p. 318, 2007.
35. T.T. Kyaw, K.S. Wint, and K.M. Naing, *Int. Conf. Biomed. Eng. Technol. IPCBEE*, Vol. 11, p., 2011 .
36. C.G. Li, F. Wang, W.G. Peng, and Y.H. He, *Appl. Mech. Mater.*, Vol. 423–426, p. 584, 2013.
37. X. Li, M. Min, N. Du, Y. Gu, T. Hode, M. Naylor, D. Chen, R.E. Nordquist, and W.R. Chen, *Clin. Dev. Immunol.*, Vol. 2013, p. 1, 2013.
38. S. Stranges, M. Alagia, P. Decleva, M. Stener, G. Fronzoni, D. Toffoli, M. Speranza, D. Catone, S. Turchini, T. Prospero, N. Zema, G. Contini, and Y. Keheyang, *Phys. Chem. Chem. Phys.*, Vol. 13, p. 12517, 2011.
39. A.R. Cestari, E.F.S. Vieira, A.G.P. Dos Santos, J.A. Mota, and V.P. De Almeida, *J. Colloid Interface Sci.*, Vol. 280, p. 380, 2004.
40. T. Feng, F. Zhang, J. Wang, and Z. Huang, *Bioinf. Biomed. Eng. (ICBBE)*, Vol., p. 1, 2011 .
41. A. Kamari, W.S.W. Ngah, M.Y. Chong, and M.L. Cheah, *Desalination*, Vol. 249, p. 1180, 2009.
42. W.A. Morais, A.L.P. de Almeida, M.R. Pereira, and J.L.C. Fonseca, *Carbohydr. Res.*, Vol. 343, p. 2489, 2008.

43. K. Azlan, W.N. Wan Saime, and L. Lai Ken, *J. Environ. Sci.*, Vol. 21, p. 296, 2009.
44. M. Nagura, H. Yokota, M. Ikeura, Y. Gotoh, and Y. Ohkoshi, *Polym. J. (Tokyo, Jpn.)*, Vol. 34, p. 761, 2002.
45. R.D. Bhumkar and V.B. Pokharkar, *AAPS PharmSciTech*, Vol. 7, p., 2006 .
46. Z.G. Hu, J. Zhang, W.L. Chan, and Y.S. Szeto, *Polymer*, Vol. 47, p. 5838, 2006.
47. C. Liu, R. Bai, and L. Nan, *Proceed. Annu. Meeting*, Vol. p., 2004 .
48. X.Z. Shu and K.J. Zhu, *Int. J. Pharm.*, Vol. 201, p. 51, 2000.
49. H.M. Fahmy, Z.E. Mohamed, M.H. Abo-Shosha, and N.A. Ibrahim, *Polym. Plast. Technol. Eng.*, Vol. 43, p. 445, 2004.
50. Y. Shimizu, A. Taga, and H. Yamaoka, *Adsorpt. Sci. Technol.*, Vol. 21, p. 439, 2003.
51. M.S. Chiou and G.S. Chuang, *Chemosphere*, Vol. 62, p. 731, 2006.
52. M.S. Chiou, P.Y. Ho, and H.Y. Li, *J. Chin. Inst. Chem. Eng.*, Vol. 34, p. 625, 2003.
53. M.S. Chiou, P.Y. Ho, and H.Y. Li, *Dyes Pigm.*, Vol. 60, p. 69, 2004.
54. T.Y. Kim and S.Y. Cho, *Korean J. Chem. Eng.*, Vol. 22, p. 691, 2005.
55. G. Crini, *Prog. Polym. Sci. (Oxford)*, Vol. 30, p. 38, 2005.
56. G. Crini, *Bioresour. Technol.*, Vol. 97, p. 1061, 2006.
57. G. Crini and P.-M. Badot, *Prog. Polym. Sci.*, Vol. 33, p. 399, 2008.
58. I. Langmuir, *J. Am. Chem. Soc.*, Vol. 40, p. 1361, 1918.
59. H. Freundlich, *Z. Phys. Chem. (Muenchen, Ger.)*, Vol. 57, p. 385, 1906.
60. G.Z. Kyzas and N.K. Lazaridis, *J. Colloid Interface Sci.*, Vol. 331, p. 32, 2009.
61. G.Z. Kyzas, M. Kostoglou, and N.K. Lazaridis, *Langmuir*, Vol. 26, p. 9617, 2010.
62. G.Z. Kyzas, M. Kostoglou, A.A. Vassiliou, and N.K. Lazaridis, *Chem. Eng. J.*, Vol. 168, p. 577, 2011.
63. G.Z. Kyzas and E.A. Deliyanni, *Molecules*, Vol. 18, p. 6193, 2013.
64. H.P. Boehm, R. Setton, and E. Stumpp, *Carbon*, Vol. 24, p. 241, 1986.
65. P. Nemes-Incze, Z. Osváth, K. Kamarás, and L.P. Biró, *Carbon*, Vol. 46, p. 1435, 2008.
66. K.S. Novoselov, A.K. Geim, S.V. Morozov, D. Jiang, Y. Zhang, S.V. Dubonos, I.V. Grigorieva, and A.A. Firsov, *Science*, Vol. 306, p. 666, 2004.
67. Iupac, *Recommended Terminology for the Description of Carbon as a Solid (IUPAC Recommendations 1995)*, Vol. 67, p. 491, 1995.
68. A.L. Ivanovskii, *Russ. Chem. Rev.*, Vol. 81, p. 571, 2012.
69. P. Avouris and C. Dimitrakopoulos, *Mater. Today*, Vol. 15, p. 86, 2012.
70. Y. Zhu, S. Murali, W. Cai, X. Li, J.W. Suk, J.R. Potts, and R.S. Ruoff, *Adv. Mater. (Weinheim, Ger.)*, Vol. 22, p. 3906, 2010.
71. K.S. Novoselov, V.I. Fal'Ko, L. Colombo, P.R. Gellert, M.G. Schwab, and K. Kim, *Nature*, Vol. 490, p. 192, 2012.
72. O.C. Compton, S. Kim, C. Pierre, J.M. Torkelson, and S.T. Nguyen, *Adv. Mater. (Weinheim, Ger.)*, Vol. 22, p. 4759, 2010.
73. O.C. Compton and S.T. Nguyen, *Small*, Vol. 6, p. 711, 2010.
74. D.R. Dreyer, S. Park, C.W. Bielawski, and R.S. Ruoff, *Chem. Soc. Rev.*, Vol. 39, p. 228, 2010.

75. A. Lerf, H. He, M. Forster, and J. Klinowski, *J. Phys. Chem. B*, Vol. 102, p. 4477, 1998.
76. S. Pei and H.M. Cheng, *Carbon*, Vol. 50, p. 3210, 2012.
77. Z. Pei, L. Li, L. Sun, S. Zhang, X.Q. Shan, S. Yang, and B. Wen, *Carbon*, Vol. 51, p. 156, 2013.
78. B.C. Brodie, *Philos. Trans. R. Soc. London*, Vol. 149, p. 249, 1859.
79. L. Staudenmaier, *Ber. Dtsch. Chem. Ges.*, Vol. 31, p. 1481, 1898.
80. W.S. Hummers Jr and R.E. Offeman, *J. Am. Chem. Soc.*, Vol. 80, p. 1339, 1958.
81. D. Krishnan, F. Kim, J. Luo, R. Cruz-Silva, L.J. Cote, H.D. Jang, and J. Huang, *Nano Today*, Vol. 7, p. 137, 2012.
82. V. Singh, D. Joung, L. Zhai, S. Das, S.I. Khondaker, and S. Seal, *Prog. Mater. Sci.*, Vol. 56, p. 1178, 2011.
83. T. Liu, Y. Li, Q. Du, J. Sun, Y. Jiao, G. Yang, Z. Wang, Y. Xia, W. Zhang, K. Wang, H. Zhu, and D. Wu, *Colloids Surf. B*, Vol. 90, p. 197, 2012.
84. T. Wu, X. Cai, S. Tan, H. Li, J. Liu, and W. Yang, *Chem. Eng. J.*, Vol. 173, p. 144, 2011.
85. Y.H. Li, T. Liu, Q. Du, J. Sun, Y. Xia, Z. Wang, W. Zhang, K. Wang, H. Zhu, and D. Wuc, *Chem. Biochem. Eng. Q.*, Vol. 25, p. 483, 2011.
86. W. Zhang, C. Zhou, W. Zhou, A. Lei, Q. Zhang, Q. Wan, and B. Zou, *Bull. Environ. Contam. Toxicol.*, Vol. 87, p. 86, 2011.
87. Y. Li, Q. Du, T. Liu, X. Peng, J. Wang, J. Sun, Y. Wang, S. Wu, Z. Wang, Y. Xia, and L. Xia, *Chem. Eng. Res. Des.*, Vol. 91, p. 361, 2013.
88. J. Zhao, W. Ren, and H.M. Cheng, *J. Mater. Chem.*, Vol. 22, p. 20197, 2012.
89. S. Chowdhury and R. Balasubramanian, *Adv. Colloid Interface Sci.*, Vol. 204, p. 35, 2014.
90. G.Z. Kyzas, N.A. Travlou, O. Kalogirou, and E.A. Deliyanni, *Materials*, Vol. 6, p. 1360, 2013.
91. N.A. Travlou, G.Z. Kyzas, N.K. Lazaridis, and E.A. Deliyanni, *Chem. Eng. J.*, Vol. 217, p. 256, 2013.
92. A.B. Bourlinos, D. Gournis, D. Petridis, T. Szabó, A. Szeri, and I. Dékány, *Langmuir*, Vol. 19, p. 6050, 2003.
93. N.A. Travlou, G.Z. Kyzas, N.K. Lazaridis, and E.A. Deliyanni, *Langmuir*, Vol. 29, p. 1657, 2013.
94. G.Z. Kyzas, D.N. Bikiaris, M. Sereych, T.J. Bandoz, and E.A. Deliyanni, *Bioresour. Technol.*, Vol. 152, p. 399, 2014.

Antimicrobial Biopolymers

S. Sayed and M.A. Jardine*

Department of Chemistry, University of Cape Town, Cape Town, South Africa

Abstract

In recent times, biodegradable materials have generated considerable interest from all sectors due to the 'greener' nature of these materials. These materials are broken down to base elements by microorganisms present in the environment. When these materials possess antimicrobial or antifungal properties, they become even more valuable. When pathogenic bacteria act on these materials, they are affected by the antimicrobial or antifungal properties thereof. In some examples, biodegradable biopolymers with antibacterial or antifungal properties are grafted onto synthetic polymers, thereby opening up more functional polymer options. Currently, research has been focused on the production of biodegradable antibacterials or antifungals with emphasis on application in the packaging and food industries. There is also interest in these materials from a biomedical perspective as coatings for medical devices and as wound dressings. A common approach is to immobilize small molecule antimicrobials onto polymer supports through covalent or weaker modes of bonding. However, these types of materials are outside the scope of this review. Through this review, we aim to measure progress toward the ideal biodegradable material, which is easy to isolate or synthesize, has superior chemical and mechanical stability, is non-toxic, affordable and has inhibitory activity on a broad range of bacteria and fungi. There are a number of protocols for the evaluation of antimicrobial activity that will also be critically reviewed.

Keywords: Biomass, polymers, synthetic, natural, antimicrobial, antifungal, applications, metals

12.1 Introduction

Biodegradable materials are a sought after commodity in today's world, where the environmental impact caused by consumers are of grave concern.

*Corresponding author: anwar.jardine@uct.ac.za

It was reported that the global biomaterials market is estimated to reach \$88.4 billion by 2017 [1]. This rapid increase in the interest of biomaterials results from a shift toward more sustainable living, and a bio-based economy. A bio-based economy refers to the sustainable production and conversion of biomass into necessary items such as food, health, fibre and industrial products and energy. These production processes must provide products with lower contributions in terms of energy and minimal adverse environmental effects [2]. Ideally the products manufactured by these methods should not create additional waste. If the materials are biodegradable this is not a cause for concern.

Biodegradability makes materials more appealing to the modern consumer where it often influences the choice of a material fit for a purpose. There are many definitions of biodegradability, one such definition was proposed by Albertsson *et al.* [3]. The definition states that biodegradation can be defined as an event which takes place through the action of enzymes and/or chemical decomposition associated with living organisms (bacteria, fungi, etc.) and their secretion products. These organisms are not affected by the antimicrobial or antifungal activity of the material. In addition, it was noted that environmental factors which could alter the polymer before, during or instead of biodegradation need to also be accounted for. Examples of these factors include abiotic reactions such as photodegradation, oxidation and hydrolysis [3]. Biodegradable polymers can be divided into biosynthetic, semi-synthetic and chemosynthetic. Figure 12.1 shows a more general classification of biopolymers into biomass, microorganism,

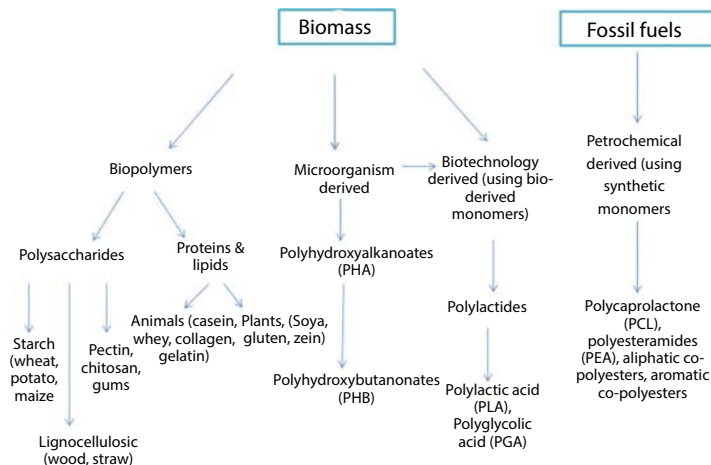


Figure 12.1 Division of biodegradable polymers according to the source from which they are derived.

biotechnology and petrochemical derived polymers. These materials are referred to as 'green' polymers when they are obtained from a renewable resource. Biopolymers are of particular interest as they may offer a solution for the development of economically viable technology and ecologically benign methods. By utilizing biopolymers, fossil fuels are being conserved; the polymers are biodegradable thereby reducing waste streams and possibly composting. This in turn leads to a decrease in CO₂ emissions and the development of a variety of applications for these polymers [4].

Since biodegradable polymers are so attractive, research on their processing and potential uses is of interest. Some biopolymers have been recommended as an alternative to plastic while others are studied for their biomedical uses which range from wound dressings to surgical implants. Biopolymers have also been applied in agriculture and investigated as controlled release supports for fertilizers or pesticides [5]. There have been a considerable number of applications which will be discussed in detail later.

Biodegradable polymers can be formulated in various physical forms. These include hydrogels which respond to external stimuli, porous scaffolds, membranes, adhesives, fibres, polymer composites, etc [6]. The different forms of these polymers can be obtained using a variety of methods. Natural polymers may also be modified to improve their inherent properties by the addition of an active functional group or the loading of an active component. However, the biodegradability and rates of degradation of these polymers are dependent on their source, chemical composition and the environment in which degradation takes place [3].

Biodegradation as mentioned previously takes place through the action of enzymes and/or chemical decomposition. It can be classified into different types, thermal, photo-oxidative, catalytic and mechanochemical biodegradation. Degradation refers to a change in the material properties (mechanical, optical or electrical characteristics) of a polymer which are evident as cracks, erosion and discolouration of the material and possibly phase separation. Francis *et al.* provides an excellent review of these degradation routes [7]. Factors which affect degradation of polymers include chemical composition, molecular weight, hydrophobic character, particle size, introduction of functionality, additives and environmental conditions [7].

There are many biodegradable polymers derived from renewable resources available on the market. These polymers are obtained from agricultural products or from biosynthesis. Common agriculture based polymers include cellulose and starch whereas those obtained from biosynthesis include polyhydroxyalkanoates (bacterial polyesters), pullulan, silk, chitin and polylactic acid. There are also biodegradable polymers

which are obtained from petroleum derived products such as polycaprolactone and polyvinyl alcohol [7]. Currently, the large scale manufacture of these polymers is limited due to high production costs therefore making cheaper, non-biodegradable materials more attractive. One example which highlights this point is that biodegradable plastics can potentially cost ten times more than conventional plastics. The challenge in the use of biodegradable polymers is not only related to economics, it also depends on whether the biodegradable materials can exhibit structural and functional stability during use and degrade when disposed of without adversely affecting the environment [4].

In an effort to overcome these problems, polymers have been combined to produce superior properties. Producing uniform polymers with desired properties is the ultimate goal. Scientists are continually seeking ways to effectively improve the large scale manufacture of these materials making it more cost effective. One such property is the antimicrobial activity of polymers which will be highlighted here. Selected biopolymers and synthetic polymers have been reviewed for their antimicrobial activities and the relevant applications thereof.

12.2 Biopolymers

Biopolymers or pure natural polymers are biologically derived materials which have been extensively studied with a particular emphasis on their use as biodegradable biomaterials. The majority of biopolymers break down through enzymatic degradation. Degradation times vary for different polymers where chemical modification of the polymer may alter its degradation rate. The properties which make a biopolymer attractive are, inherent bioactivity of the native polymer, transport of receptor-binding ligands to cells, response to proteolytic degradation triggered by cells and natural remodelling [8]. The two most common biopolymers under investigation which possess inherent antimicrobial/antifungal activity are ϵ -poly-L-lysine and chitosan.

12.2.1 ϵ -Poly-L-Lysine

ϵ -Poly-L-lysine (ϵ -PL) is derived from a natural amino acid, giving rise to a biodegradable ionic polymer. It is a homopolymer composed of approximately 25–30 residues of the amino acid L-lysine. Unlike normal peptide bonds, the bond in this polymer is from the α -carboxyl to the ϵ -amino group of L-lysine [9]. It was found to be water soluble, stable in acidic and

basic conditions, has low toxicity and able to tolerate high temperatures (up to 120°C) with no signs of thermal degradation. This polymer can be isolated from various strains of bacteria in particular *S. albulus* with differing chain lengths. Industrially, ϵ -PL is produced by fermentation of a mutated *S. albulus* [10]. However, production of ϵ -PL by this route has some problems which include enzymatic and pH-dependant degradation of ϵ -PL. Other organisms belonging to the genera *Streptomyces*, *Kitasatospora* and *Epichloe* sp. have also been found to produce ϵ -PL. Due to the production issues associated with ϵ -PL, research has been focused on finding alternative sources of this valuable polymer. Chheda *et al.* recently produced ϵ -PL by investigating the optimal medium composition utilizing *B. cereus* [11]. ϵ -PL was also recently isolated from *S. noursei* with a purity and yield greater than 90% [12]. In a recent study by Wibowo *et al.* ϵ -PL was isolated from a fermentation broth of *S. albus* using carboxymethyl cellulose-conjugated magnetic nanoparticles [13]. The concentration of ϵ -PL isolated from the bacteria is usually measured using an anionic dye, methyl orange which forms a water-insoluble complex with ϵ -PL. It has been reported that ϵ -PL possesses antimicrobial activity against a wide spectrum of microorganisms which includes fungi, Gram-positive and Gram-negative bacteria, yeast and certain moulds [10]. Yoshida *et al.* has reviewed the antimicrobial and antiphage activities of ϵ -PL [10]. The antimicrobial activity of this polymer can be attributed to the presence of the positively charged amine group when the pH of the solution is below its isoelectric point (pI \sim 9.0) [14]. This positive charge leads to a positive zeta potential which can be used to predict antimicrobial activity of the compounds prepared. It has been found to be active against a number of pathogenic bacteria, e.g. *C. albicans*, *E. coli*, and *S. aureus* [9]. Hiraki reported that the Minimum inhibitory concentration (MIC) of ϵ -PL against the majority of bacteria was 100 μ g/ml. The MIC against fungi and certain yeasts was found to be higher [15]. Due to its low toxicity and antibacterial properties, ϵ -PL was classified as a generally recognized as safe (GRAS) material, by the US Food and Drug Administration. It is currently widely used as a food additive since ϵ -PL degrades harmlessly to lysine in the human body [9, 16].

The antimicrobial mechanism of ϵ -PL has been extensively studied however, no conclusion as to its mechanism at the molecular level has been established [14]. ϵ -PL is adsorbed onto the cell surface due to an electrostatic attraction. As a result of this attraction ϵ -PL strips the outer membrane of the organism which in turn leads to an irregular cytoplasm distribution. The polymer enters the cytoplasm of the microbe and induces the generation of reactive oxygen species (ROS) and global response to DNA damage (SOS). The combination of these factors leads to cell death.

Li and colleagues also noted that damage of bacterial cells could have been the result of interference caused by ϵ -PL in the synthesis of bacterial cell proteins or the polymer may have promoted bacterial protein aggregation. In addition, the antimicrobial activity of ϵ -PL is also dependent on pH and polymer concentration [9, 10]. An in depth study by Ye *et al.* reports the effect of ϵ -PL on *E. coli* [14]. This study used propidium monoazide (PMA)-polymerase chain reaction (PCR), transmission electron microscopy (TEM) and atomic force microscopy (AFM) to study the effects of ϵ -PL on cell morphology and membrane integrity. In addition, the concentration of ROS in polymer treated *E. coli* was measured by a ROS probe. Real-time quantitative PCR was used to monitor the expression of genes related to oxidative stress, SOS response and virulence. The mechanism of action of the polymer was thought to be a combination of the factors discussed above [14].

As a result of the favourable properties of ϵ -PL, this polymer has been studied for a variety of applications. It has been noted that ϵ -PL has been utilized as food preservative, emulsifying agent, delivery agent, dietary supplement, biodegradable fibre, hydrogel, drug carrier, anticancer agent enhancer, biochip coating and many other uses [11, 12]. The review by Shukla *et al.* reports on the production, screening and detection of ϵ -PL, purification, characterization, conformation and the applications of the polymer in medicine [17].

The combination of ϵ -PL and other additives has been explored to improve the inherent properties of the polymer. This polymer has been used in conjunction with glycine, vinegar, ethanol and thiamine laurylsulfonate as a food preservative with some degree of success. When glycine was used in the presence of ϵ -PL, a synergistic effect was observed and the total amount of preservative required decreased [10]. However, due to the cationic charge present on the polymer, there are some challenges when it is applied in the food and beverage industries. The polymer tends to form insoluble precipitates (PEC, polyelectrolyte complex) with certain anionic constituents present in products. This in turn leads to a cloudy appearance of the product which is unappealing for consumption. Another possible disadvantage associated with ϵ -PL occurs when the polymer binds to anionic biopolymers present in the mouth which can result in a bitter taste sensation. In order to counter these disadvantages, the polymer can be bound to an anionic biopolymer which could potentially enhance the activity of the complex [18]. Chang *et al.* produced an electrostatic complex of ϵ -PL and gum arabic (GA) which was tested for any changes in the properties of the two polymers [18]. The different ratios of the polymers affected electrical charge, aggregation stability, solubility and antimicrobial

efficacy. Complexes were tested against two acid resistant spoilage yeasts: *Z. bailii* and *S. cerevisiae*. The study found that the antimicrobial activity was affected by the ratio of ϵ -PL to GA and depended on the organism tested. The lower the concentration of GA, the higher the positive charge and hence the antimicrobial activity observed [18]. Prior to this study, Chang *et al.* also investigated a complex of ϵ -PL and the anionic pectin where the effect of different degrees of esterification (DE) on antimicrobial activity was evaluated [19]. Similar results were obtained against the same model organisms [19].

Moschonas and colleagues studied the activity of caprylic acid, carvacrol, ϵ -PL and blends thereof against chosen strains of *Salmonella* [20]. Results indicated that inhibition of the pathogen was achieved using each polymer individually as well as a combination of the three [20]. Poly(ethylene terephthalate) (PET) nonwoven fabrics immobilized with both ϵ -PL and natanmycin (natural anti-fungal agent) were synthesized in a one-pot method. This was achieved using methacrylate nonwoven fabrics adhesives. The resulting nonwoven fabrics demonstrated antibacterial activity against *E. coli*, *S. aureus* and bacteriophage ϕ 2. These fabrics have a shelf life of more than two years and can be utilized for a variety of biomedical applications [21]. Yu *et al.* recently synthesized an emulsifier containing ϵ -PL modified with octenyl succinic anhydride which displayed antimicrobial activity. This modified polymer can potentially be applied as a surfactant, or emulsifier to be used in the delivery of nutraceuticals or drugs or as an antimicrobial itself [22]. Bacterial cellulose and ϵ -PL have been combined to produce coated nanofibre useful for hydroxyapatite deposition in bone tissue engineering and as a bacteriostatic sausage casing [23, 24]. Tikekar *et al.* conjugated curcumin to ϵ -PL *via* "click chemistry" in order to enhance the functionality of the biopolymer [25]. This study showed that the conjugate retains the properties of its constituents where the polymer exhibited antioxidant activity attributed to curcumin [25].

An interesting study of ϵ -PL covalently attached to multi-walled carbon nanotubes was recently conducted. The carbon nanotubes themselves possess antimicrobial properties, they inflict serious membrane damage when in contact with microbes. When combined with ϵ -PL the biocidal activity and anti-adhesive efficacy of this material was improved [26]. Lee and colleagues tested the antimicrobial efficacy of a medical adhesive consisting of ϵ -PL and an aldehyde derivative of dextran [27]. The adhesive was found to have low cytotoxicity and high adhesive strength together with good antimicrobial efficacy [27]. ϵ -PL was also conjugated to dextran utilizing a Maillard reaction performed in sub-critical water. The conjugate displayed an increase in emulsifying activity

at high temperatures. However, the antimicrobial activity reported corresponded to that observed for ϵ -PL below 110°C and decreased at higher temperatures [28]. The Maillard reaction was also used to combine the antimicrobial biopolymer chitosan and ϵ -PL to form edible films. Reaction conditions were optimized to produce films with advantageous properties including antimicrobial activity [29]. Both ϵ -PL and chitosan are reported to exhibit antimicrobial activities; therefore, this material has significant potential in the biomedical sector. Zhou *et al.* produced a hydrogel from ϵ -PL grafted to methacrylamide using photopolymerization [30]. These gels showed activity against *E. coli*, *P. aeruginosa*, *S. marcescens* and *S. aureus* as well as the fungi *C. albicans* and *F. solani* [30]. A thiolated chitosan- ϵ -PL hydrogel was developed by employing cross-linking *via* a Michael addition chemistry. This hydrogel has been applied as an adhesive and a haemostatic material [31]. A similar polyethylene glycol-maleimide modified ϵ -PL hydrogel was produced through Michael addition and cross-linked with thiolated chitosan. These polymers can be applied as biomaterials for tissue adhesion and sealing [32].

As evidenced from the considerable amount of research performed on ϵ -PL, there is significant interest in the utility of this polymer. Being biodegradable and having favourable properties such as antimicrobial activity thus places ϵ -PL on course for a wide variety of applications.

12.2.2 Chitin and Chitosan

Chitin is the second most abundant polymer obtained from nature after cellulose (10¹¹ tons produced annually). This polymer can be isolated from the exoskeletons of arthropods such as crustaceans, fungi (e.g. mushrooms), insects (e.g. silkworms, honeybees) and annelids [33]. Chitin is a cationic polysaccharide composed of long chains of *N*-acetylglucosamine bound through β (1 \rightarrow 4) glycosidic linkages. There are 3 forms of chitin, α , β and γ where they differ in terms of degree of hydration, unit cell size and the number of chitin chains per unit cell. In α -chitin, the crystalline structure is composed of antiparallel sheets with widespread hydrogen bonding while β -chitin consists of parallel sheets. The third form, γ -chitin is a combination of α and β -chitin with α -chitin being the most abundant in nature. The main function of chitin is as a supporting material in the organisms from which it is isolated.

Chitin is synthesized by the integral membrane proteins, chitin synthases which utilizes UDP-*N*-acetylglucosamine as the starting material. The different forms of chitin require different extraction methods, where α -chitin requires the harshest treatment due to the strong hydrogen bonds

present. Chitin is obtained from sea fishery waste *via* deproteinization (NaOH/KOH), demineralization (HCl) and decolourization. If the main aim is the isolation of protein or pigments, the order of the recovery steps is important. There are chemical and enzymatic methods for recovery of chitin where each method has their own merits. Chemical extraction is often harsh generating large quantities of waste and more often than not the isolated chitin has inconsistent physiological properties due to hydrolysis. Enzymatic methods can be quite time consuming, costly and in some cases residual protein still remains. Enzymes which have been used for the isolation of chitin includes: alcalase, chymotrypsin, papain and bromelain to name a few [33]. The extraction methods used need to be carefully considered on the basis of the application, the amount of energy required for the process, any adverse effects on the environment and any by-products produced. Development of these improved extraction processes are critical factors in the development of a bio-based product. This is especially important when assessing the potential of these products in fields such as biomedical application.

Chitin is such an appealing polymer as it possesses certain advantageous properties such as its nontoxic nature, biodegradability, biocompatibility and superior adsorption properties [34]. It also possesses limited antimicrobial properties and can chelate metals. A number of derivatives of chitin have been investigated where the modification confers favourable properties on the polymer. Chitin has been declared to be a GRAS material making its use very attractive. It has been investigated as a preservative for cosmetics and in the biomedical sector for the production of artificial skin, absorbable sutures, in wound care and as potential drug carrier. It has been used in agriculture to induce the defence mechanism in plants and as a fertilizer to promote crop growth [35, 36]. Industrially it is utilized in the food sector for a number of applications such as the production of edible films, or to thicken and stabilize foods [37].

Chitosan is the *N*-deacetylated derivative of chitin produced by removing *N*-acetyl groups until the polymer is soluble in dilute acid [34]. The polymer consists of randomly distributed β -(1-4)-linked *D*-glucosamine and *N*-acetyl-*D*-glucosamine units. Due to the free amine group, enhanced solubility and lower degree of crystallinity, chitosan possesses more desirable properties compared to chitin. In addition, chitosan may be further modified in order to improve its inherent properties. Due to these favourable properties, the utility of chitosan has been the focus for many scientists, all seeking to make full use of this promising biopolymer. The properties of chitosan depend on the degree of deacetylation (DDA) of the polymer. The variation in DDA leads to a difference in the molecular weight which

affects the properties of the polymer. Commercially there are four grades of chitosan available, agricultural, industrial, food & cosmetic and pharmaceutical grade where the DDA ranges from 65% to 95% [38]. Chitosan has been applied in water treatment, agriculture, biotechnology, food/health supplements, cosmetics, biomedical applications, textiles and in the paper industry [39]. It has antitumor, antimicrobial, anti-inflammatory, anti-diabetic and anti-hypercholesterolemic effects [38]. Chitosan also enhances absorption by opening tight junctions of cells allowing for the use of chitosan as a delivery agent.

As mentioned previously, chitosan is soluble in most dilute acids due to the presence of strong hydrogen bonds however; the solubility may be improved by functionalization of the polymer. The polymer can be functionalized at the three sites, the amine at C-2 or the hydroxyl groups at C-3 and 6 although the hydroxyl at C-3 is not favoured due to steric strain. Chemical modification of chitosan includes, alkylation, acylation, Schiff base formation, nitration, 'click chemistry', phosphorylation, sulfation, xanthation, hydroxyalkylation and graft co-polymerization [40]. Advantages of these modifications relate to the chemical, biological and functional activities of the modified compounds compared to native chitosan. These modifications have been reported to improve solubility, gelling properties, antimicrobial activity, film forming ability, chelating ability, etc [41]. As a result of these modifications, chitosan and its derivatives can be obtained in various forms including gels, films, nanoparticles, nanofibre, biocomposites, membranes, scaffolds, etc.

One of the properties which make chitosan such an interesting polymer is the biocompatibility of this polymer and its derivatives. Chitosan has been employed in the biomedical sector as a delivery agent (genes, drugs, peptides, proteins, biopharmaceuticals, vaccines, nucleic acids), in wound healing/tissue regeneration (scaffold for cell growth, resorbable sutures, to facilitate healing, haemostatic agent, delivery of growth factors), as an antimicrobial (wound dressings, surface coatings) and a variety of other uses (dietary supplement, slimming agent, bioimaging, hypocholesterolemic effect) [42].

The antimicrobial activity of chitosan is dependent on the cationic nature of the polymer, the DDA, concentration, the organism against which it is tested and the period of exposure. The mechanism of the antimicrobial action of the polymer is not fully understood. Chitosan is active against bacteria, fungi and yeast with enhanced activity reported for certain derivatives. Scientists speculate that the activity can be attributed to the polycationic nature of chitosan which is believed to disrupt metabolism in the cell by binding to the cell surface. When bound to the cell

surface, chitosan increases the permeability of the cell wall allowing the loss of intracellular contents leading to cell death. Another theory states that DNA transcription of RNA is prevented by the binding of chitosan to the DNA molecules. However, this theory depends on a low molecular weight (LMW) chitosan which can enter the cell [43]. The antimicrobial activity may be enhanced by the incorporation of active moieties onto the polymer backbone. The activity is noticeably enhanced when the modification of the polymer increases solubility, mucoadhesivity or the charge on the polymer all of which leads to greater interaction with microorganisms [43]. Modifications which have been shown to improve activity include thiolation and quaternization among others. Besides modification of the polymer, improved antimicrobial properties have been reported for chitosan micro- and nanoparticles [44]. This enhanced activity can be attributed to the properties of nanoparticles such as the small size/large surface area and the associated quantum size effects [45]. Chitosan based nanoparticles have a greater zeta potential and therefore can interact more efficiently with the negatively charged cell wall of certain microorganisms causing the inhibitory activity to be greater [44]. The loading of metal ions which possess antibacterial properties such as Ag^+ , Zn^{2+} , Mg^{2+} and Cu^{2+} onto the polymer is another way to improve the activity of the polymer [46]. Du *et al.* found that the zeta potential is directly proportional to the antimicrobial activity observed for chitosan tripolyphosphate nanoparticles which had been loaded with the metal ions Ag^+ , Cu^{2+} , Zn^{2+} , Mn^{2+} , or Fe^{2+} [47].

The insolubility of chitosan is a limiting agent to its application as an antimicrobial agent; therefore, strategies to improve solubility are important. Among the different routes proposed to increase solubility is the incorporation of polar moieties, hydrophilic groups, bulky groups, etc [48]. Another method involves the depolymerization of chitosan to produce chitosan oligomers which can be prepared by chemical (acid hydrolysis), enzymatic (e.g. lysozyme, chitin deacetylase) or physical methods (electromagnetic radiation, sonication). Some noteworthy derivatives which have improved properties including solubility are quaternized, alkyl, highly cationic, *N*-acylchitosans, *N*-carboxyalkyl/(aryl), *O*-carboxyalkyl, *N*-carboxyacyl-chitosan, thiolated, sugar derivatives, metal ion chelates and semisynthetic derivatives of chitosan. Examples of these modifications include thiolation which improves the inherent mucoadhesive properties of the polymer. Quaternization improves the solubility and the cationic charge of the polymer which leads to improved mucoadhesion to the negatively charged mucin [42]. Other modifications confer properties which will be discussed using examples.

One of the better known derivatives of chitosan which has been extensively investigated is *N,N,N*-trimethyl chitosan chloride (TMC). This polymer can be produced by the reaction of chitosan and methyl iodide where the degree of quaternization affects the properties of the polymer. The mucoadhesion of this polymer is superior to chitosan due to the greater cationic charge of TMC. This polymer has therefore been used as an absorption enhancer in the delivery of drugs such as mannitol and busserlin to name a few. TMC also displays improved antimicrobial (antibacterial and antifungal) activity compared to chitosan. TMC has been formulated as microparticles, nanoparticles, nanocomplexes and films either alone or in combination with other agents to improve its utility [49]. TMC displayed an inhibitory activity 4 times that of chitosan when tested against *S. aureus*. This activity can be attributed to the greater positive charge of the polymer. This polymer has so far been applied as a permeation enhancer for drug transport, in vaccine & gene delivery and to treat oral mucositis due to chemo-radiotherapy [34].

Another polymer which has gained interest lately is 6-deoxy-6-amino chitosan (6D6AC). This polymer was first synthesized by Satoh *et al.* via azido and halo intermediates. The polymer is soluble at neutral and physiological conditions and was first studied as a gene carrier where it was found to have low cytotoxicity and good transfection efficiency [50]. Sadeghi *et al.* synthesized the trimethylated and triethylated derivatives of 6D6AC and tested the antibacterial efficacy of these polymers. These polymers showed enhanced activity compared to chitosan and their parent polymers against *S. aureus* [51]. An improved synthetic method was reported by Jardine *et al.* which avoided the use of halogenated intermediates in its synthesis [52]. Yang *et al.* prepared 6D6AC of varying molecular weights and tested the antimicrobial activity of these polymers against *S. aureus*, *E. coli*, *P. aeruginosa* and *A. niger*. The MICs observed showed that the 6D6AC derivative displayed a wide spectrum of activity superior to chitosan [53].

Carboxymethyl chitosan (CMC) is a particularly well utilized derivative of chitosan. There are three different forms of this polymer, *N*-carboxymethyl chitosan (NCCMC), *O*-carboxymethylchitosan (OCCMC) and *N,O*-carboxymethyl chitosan (NOCMC). These derivatives can be prepared by reductive alkylation or direct alkylation. CMC as noted by Junginer *et al.* has been applied extensively in the biomedical field where it has been utilized as a moisture retention agent, bactericide, in wound dressings, as part of blood coagulants, in tissue engineering (artificial bone & skin), in vaccine delivery and as a drug delivery system [54]. The polymer possesses a zwitterionic character and has a number of interesting

properties such as high viscosity, large hydrodynamic volume and it can also form films, fibres and hydrogels [55]. The antibacterial activity of OCMC is greater and NOCMC lower than that of chitosan, this can be attributed to the number of NH_3^+ groups present on the polymers [56]. Farag *et al.* synthesized a nanogel combining CMC and poly-(vinyl alcohol) (PVA) and tested these gels against selected bacteria and fungi. Results indicated that the CMC/PVA nanogel had good activity against *E. coli*, *S. aureus*, *A. flavus* and *C. albicans* [55]. A quaternized CMC was synthesized by reacting CMC with 2,3-epoxypropyl trimethylammonium chloride. This polymer was tested together with its parent polymers CMC and quaternary chitosan against *E. coli* and *S. aureus*. Tests showed that the quaternized CMC displayed a higher antibacterial activity compared to the parent polymers where the activity was attributed to the degree of quaternization and the molecular weight of the polymer [57].

Thiolated derivatives of chitosan which have been synthesized thus far include: chitosan-cysteine (chitosan-NAC), chitosan-thioglycolic acid (chitosan-TGA), chitosan-4-thiobutylamidine (chitosan-TBA), *N*-(2-hydroxy-3-mercaptopropyl)-chitosan, *N*-(2-hydroxy-3 methylaminopropyl) chitosan, mercaptoacetate chitosan and the polymer (2S)-2-mercaptosuccinyl chitosan. These polymers have improved solubility, mucoadhesiveness, gelling and permeation properties compared to chitosan. The increase in mucoadhesivity of the polymers can be attributed to the covalent bonding of the immobilized thiol groups to cysteine rich subdomains of glycoproteins. This leads to an increase in the tensile strength of the thiolated chitosan while the gelling properties are as a result of disulfide bond formation. Fernandes *et al.* synthesized chitosan-NAC and chitosan-TBA to determine the antibacterial activity of these polymers when synthesized using different methods [58]. Results indicated that chitosan-NAC synthesized using a carbodiimide coupling methodology gave results similar to that observed for chitosan. However, the chitosan-TBA synthesized in direct coupling exhibited a superior inhibitory activity against both *E. coli* and *S. aureus*. This activity was attributed to the formation of a greater positive charge as a result of the amidine moiety present [58]. The same author later showed that sonochemically produced cationic nanocapsules of chitosan-TBA was capable of disrupting bacterial membranes and inducing bactericidal activity in *E. coli*. The chitosan-TBA nanocapsules were found to be more efficient compared to the polymer itself due to the electrostatic interaction of the polymer with the membrane which led to membrane surface defects [59]. Geisberger *et al.* compared the activities of TMC, CMC, LMW chitosan-TGA and medium molecular weight (MMW) chitosan-TGA against *S. sobrinus* (Gram-positive

bacteria), *N. subflava* (Gram-negative bacteria) and *C. albicans* (fungi). The study found that LMW chitosan-TGA possessed superior inhibitory activity compared to the other derivatives tested [60].

There are some natural polymers whose antimicrobial activity is short lived and therefore not as noticeable as ϵ -PL or chitosan. A study published by Wright *et al.* pointed out that common house spider silk possessed short lived activity when tested against *B. subtilis* [61]. Although natural polymers are highly attractive due to their renewable nature, there are disadvantages associated with them. In the case of ϵ -PL problems are encountered in the production of the polymer from bacterial sources. With chitosan, isolation of the polymer produces unwanted waste and the material obtained is not uniform in nature leading to a difference in properties observed. Solubility is also a limiting factor in the application of this polymer [62]. Therefore, researchers have begun to investigate synthetic biodegradable polymers with tuneable properties and efficient high yielding synthetic methods.

Table 12.1 shows the structures of ϵ -poly-L-lysine and chitosan together with their associated antimicrobial activities.

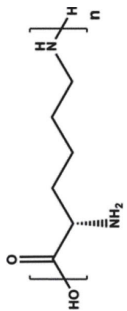
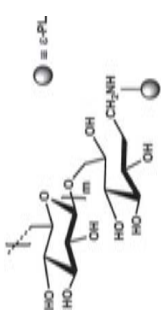
12.3 Synthetic Biodegradable Polymers

Synthetic biodegradable polymers which possess properties such as antimicrobial activity have come under the spotlight recently. Due to the development of microbial resistance, new materials with enhanced properties are being sought. These polymers can be made from renewable or synthetic monomers. Microbial contamination and resistance is a major problem which affects all areas including the healthcare sector, consumer products and day to day living. The development of materials which stop proliferation and kill these organisms is a challenge as more often than not these materials have unwanted draw backs. These include toxicity, short half-life, administration problems and the behaviour of the material in a complex system. A short overview of selected synthetic biodegradable materials possessing antimicrobial activity is given here.

12.3.1 Quaternary Polymers

The most popular synthetic antimicrobial polymers are based on those which possess a polycation such as quaternary ammonium or phosphonium, tertiary sulfonium and guanidinium groups [64]. These polymers are positively charged and bactericidal. The mode of action involves

Table 12.1 Biopolymers, their structures and associated antimicrobial activity with selected MIC values in brackets (µg/mL).

Polymer	Structure	Gram-positive	Gram-negative	Yeast	Fungi
ε-Poly-L-lysine (9, 10)		<i>B. coagulans</i> (10), <i>B. subtilis</i> (<3), <i>B. cereus</i> , <i>C. acetobutylicum</i> (32), <i>L. mesenteroides</i> (50), <i>L. brevis</i> (10), <i>L. plantarum</i> (5), <i>M. luteus</i> (16), <i>S. aureus</i> (12.5), <i>S. lactis</i> (100), <i>L. monocytogenes</i> (15)	<i>R. planticola</i> (8), <i>C. jejuni</i> (100), <i>E. coli</i> (12.5), <i>P. aeruginosa</i> (<100), <i>S. typhimurium</i> (16), <i>V. parahaemolyticus</i> , <i>V. cholera</i> , <i>S. marcescens</i> (<100)	<i>C. acutus</i> (6), <i>P. rhodozyma</i> (12), <i>P. anomala</i> (150), <i>P. membranacea</i> (<3), <i>R. lactase</i> (25), <i>S. roseus</i> (<3), <i>S. cerevisiae</i> (50), <i>Z. rouxii</i> (150)	<i>A. niger</i> (250), <i>T. mentagrophytes</i> (60), <i>C. albicans</i> (<100), <i>F. solani</i> (109)
ε-PL + Dextran (28)		<i>S. aureus</i> (100), <i>B. subtilis</i> (100)	<i>E. coli</i> (100), <i>S. typhimurium</i> (50)	<i>S. cerevisiae</i> (100)	<i>A. niger</i> (400)

(Continued)

Table 12.1 (Cont.)

Polymer	Structure	Gram-positive	Gram-negative	Yeast	Fungi
Chitosan (42, 43, 63)		<i>S. aureus</i> (20), <i>S. simulans</i> , <i>L. monocytogenes</i> , <i>B. megaterium</i> , <i>L. plantarum</i> , <i>L. bulgaricus</i> , <i>B. cereus</i> (1000), <i>C. mitchiganense</i> (10)	<i>E. coli</i> (20), <i>P. aeruginosa</i> (500), <i>S. typhimurium</i> (>1000), <i>P. fluorescens</i> (500), <i>V. parahaemolyticus</i> , <i>A. tumefaciens</i> (100), <i>E. carotovora</i> subsp. (200), <i>K. pneumonia</i> (700), <i>V. cholera</i> (100), <i>S. dysenteriae</i> (100), <i>P. agglomerans</i> , <i>P. melaninogenica</i> (100), <i>B. fragilis</i> (60)	<i>S. cerevisiae</i> (400), <i>Z. bailii</i> (100), <i>S. exiguous</i> (100), <i>S. pombe</i> (100), <i>S. ludwigii</i> (100)	<i>R. cercosporioides</i> , <i>A. niger</i> , <i>A. parasiticus</i> , <i>A. alternata</i> , <i>B. cinerea</i> , <i>C. gloeosporioides</i> , <i>R. stolonifer</i> , <i>S. sclerotiorum</i> , <i>R. Solana</i> , <i>F. oxysporum</i> , <i>F. solani</i> , <i>D. sorokiniana</i> , <i>M. nivalis</i> (10), <i>P. oryzae</i> (5000), <i>R. solani</i> (1000), <i>T. equinum</i> (2500)
CMC (43)		<i>S. aureus</i>	<i>E. coli</i>		<i>F. solani</i> , <i>C. lindemuthianum</i> , <i>A. flavus</i> , <i>A. parasiticus</i> , <i>S. parasitica</i>

adsorbing to and disrupting the cell wall, interference with the cell membrane, loss of cell contents accompanied by degradation of protein and nucleic acids and eventually lysis of the cell wall [65]. Kenawy *et al.* recently provided a detailed review of the synthesis, antimicrobial activity and applications of polymers with ammonium and phosphonium groups [66]. Recently an in depth review of polymers with antimicrobial activity was published. This review also include polymers with quaternary ammonium end groups, the oxazolines and polymers with quaternary nitrogen atoms within the main chain called ionenes. These polymers are quite useful due to their low toxicity, functional versatility and antimicrobial activity [67]. Synthetic and natural polymers have been quaternized and applied in various sectors such as water treatment, dental composites, cosmetics, food packaging, textiles and the biomedical sector (anticoagulant and cholesterol lowering agents). Highlighted here are a few of the most recently reported quaternized polymers which have exhibited superior antimicrobial activity.

Chin *et al.* synthesized a series of biodegradable quaternized polycarbonates with various active moieties including alkyl, aromatic and imidazolium groups [68]. The study showed that the *N,N*-dimethylbutylammonium functionalized polymer with a degree of polymerization of 20 yielded the best antimicrobial activity against clinically isolated drug-resistant Gram-positive and Gram-negative bacteria as well as fungi. This polymer was also shown to be active against *P. aeruginosa* [68]. In a later study, antimicrobial polycarbonates obtained using nitrogen containing heterocycles as the quaternizing agents were synthesized. These polymers were shown to be active against *S. aureus*, *E. coli*, *P. aeruginosa* and *C. albicans*. The authors postulate that the development of resistance is unlikely as these polymers act *via* a membrane-lytic mechanism [69]. A quaternized polymer based on an amine terminated polyacrylonitrile was recently synthesized using glycidyl trimethyl ammonium chloride. This polymer demonstrated antimicrobial activity against *E. coli*, *C. albicans*, *A. niger*, *A. flavus*, *P. aeruginosa*, *S. typhi*, *S. aureus* and *C. neoformans* [70]. Gozzelino *et al.* synthesized reactive quaternary ammonium monomers which were co-polymerized with diacrylic monomers using UV irradiation [71]. These polymers were active against *E. coli* and *S. aureus* with activity increasing with an increase in monomer content and length of the alkyl chain [71]. Other quaternary ammonium compounds commonly studied includes poly (diallyldimethylammonium chloride), quaternized poly(vinylpyridine) and a number of others covered in more detail in a review by Carmona-Ribeiro *et al.* [65].

Natural rubber was modified using a quaternary phosphonium salt and the antimicrobial activity was proven against *E. coli* and *S. aureus* [72]. An alkyne poly(butylene adipate) was coupled to a quaternary phosphonium group using Cu catalyzed 'click' chemistry approach. This polymer was studied for its use as antimicrobial packaging material and was shown to inhibit the growth of *E. coli* [73]. A quaternary *N*-phosphonium derivative based on the natural polymer chitosan has recently been synthesized. Derivatives with different degrees of substitution displayed varied activity with the highest activity displayed by the derivative with a 3% substitution. This derivative displayed better activity compared to chitosan, quaternary ammonium chitosan derivatives and (5-carboxypentyl)triphenylphosphonium bromide against *E. coli* and two strains of drug-resistant *S. aureus*. [74]

Kanazawa *et al.* was one of the first groups to study the antimicrobial activity of polymeric quaternary sulfonium salts. The derivatives were found to be active against *E. coli* and *S. aureus*, however; utility of these polymers was limited due to their thermal instability [75]. The guanidinium derivatives have been extensively studied as a result of their favourable properties such as water solubility, biocidal activity, broad antimicrobial efficacy and non-toxic nature. Poly(hexamethylene biguanidinium hydrochloride) was the first polymer to be successfully marketed as a disinfectant. Oligomers of guanidine have also been investigated for their antimicrobial efficacy; it was found that a molecular mass of 800 Da was required for activity [64, 67].

12.3.2 Polyethylenimine

Polyethylenimine (PEI) is a synthetic cationic polymer which displays a broad spectrum of antimicrobial activity. This polymer is obtained by the ring opening polymerization of the heterocycle aziridine. It is commonly used as a transfection agent in gene therapy as an alternative to viral vectors [65]. PEI can be either branched or linear possessing different molecular weights. This polymer can easily penetrate the cell walls of organisms however, no inhibitory effect on Gram-negative bacteria has been observed. Activity against *S. mutans* was observed for PEI nanoparticles incorporated in dental cements. Quaternized ammonium PEI nanoparticles has been shown to be active against *S. aureus*, *S. epidermidis*, *E. faecalis*, *P. aeruginosa* and *E. coli*. A PEI/carrageenan (κ , ι and λ) multilayer was recently synthesized and investigated for inhibitory activity against pathogenic bacteria, *E. cloacae*, *S. aureus* and *E. faecalis*. The study found

that PEI/iota carrageenan effectively inhibits *S. aureus* and *E. faecalis*, PEI/lambda carrageenan is most active against *E. cloaceae* and PEI/kappa carrageenan inhibits *E. faecalis*. Carrageenan was utilized as it is from a renewable resource (sea weed), biocompatible, non-toxic, is cheap and has gel forming properties. In addition, oligosaccharides of carrageenan display inhibitory activity against *E. coli*, *S. aureus*, *S. cerevisiae* and *Mucor* sp. In this study, the PEI and carrageenan worked synergistically in their inhibition of the bacteria [76]. PEI branched and linear polymers with varying molecular weights were investigated to determine whether their architectures and molar mass affected the antimicrobial efficacy of the polymers. These polymers were found to be active against *E. coli* and *S. aureus* with the linear polymers displaying greater activity while molar mass did not significantly affect activity [77].

12.3.3 Antimicrobial Peptide Mimics

Synthetic polymers which mimic the activity of antimicrobial peptides (AMPs) have come under the spotlight recently. AMPs have been discovered to be biocidal against organisms such as viruses, bacteria (Gram-positive and Gram-negative), fungi, parasites and showed anti-cancer properties [65]. These AMPs have also displayed activity against bacterial strains which are resistant to commonly used antimicrobials. AMPs are produced by most living entities (viruses, fungi, bacteria, plants and animals) to defend against invading organisms [78]. The peptides typically consist of amphiphilic and cationic moieties with different amino acid residues ranging from 12 to 50 units [79]. Peptides are classified according to their secondary structure which includes geometries such as the α -helix, β -sheet, loop and extended structure. The antimicrobial activity of these peptides can be attributed to a contact active mechanism. The cationic peptides binds to the microorganisms disrupting the cell wall and normal functioning of the cell, resulting in cell death [80]. These peptides are capable of distinguishing bacterial cells from host cells making them desirable antimicrobials. In addition the development of resistance is low since the bacterial membrane is the target of these peptides. However, despite their promising activity, AMPs have some disadvantages such as high production costs, chemical, proteolytic and physical instability, toxicity and achieving sufficient levels in blood/plasma to display activity [81].

In order to overcome these difficulties, synthetic polymers which mimic the activity of these AMPs have been studied. It is important that these mimics are synthesized in a simple environmentally friendly, cost effective

manner which also allows the peptides to be chemically manipulated to improve their physical properties. Some of the more recent work on these AMPs is highlighted below. A number of reviews have showcased the importance of AMPs. Arora *et al.* mentioned that these peptides are quite useful in antimicrobial studies due to their unique biochemical properties [82]. Alves and Sobczak *et al.* reviewed the immobilization of these peptides to polymers and the potential applications thereof [78, 83]. Wang *et al.* provided an in depth review on AMP mimics, phenylene ethynylene based conjugated polyelectrolyte polymers (CPEs) and oligomers (oligo-phenylene ethynylenes (OPEs)) [81]. These polymers and oligomers possess a broad spectrum of antimicrobial activity where their main target is thought to be the cell wall of the bacteria. This review focused on the membrane disruption mechanism of these polymers and the effect of molecular composition, size and side chain functionality on their antibacterial activity [81].

Rapsch and colleagues attached a number of synthetic and natural AMPs to a solid surface using different immobilization strategies [84]. Inhibitory activity was found to be dependent on the peptide used as well as the immobilization strategy [84]. Takahashi *et al.* designed a number of methacrylate co-polymers based on natural AMPs. These polymers were found to be effective against a broad spectrum of bacteria including drug-resistant *S. aureus*. In addition, these polymers did not induce resistance in *E. coli* after repeated exposure of the microbe to the polymer. These polymers can be tailored for specific uses opening up a host of new applications for these materials [80]. A series of guanidine/amine polymethacrylate co-polymers were recently synthesized containing AMPs as side chains. These polymers were synthesized *via* the RAFT (reversible addition–fragmentation chain transfer) method which allowed for control of composition, molecular weight, end groups and polydispersity index. Polymers were tested against *E. coli*, *S. aureus*, *S. epidermis* and *C. albicans* for inhibitory activity. The guanidine polymers were found to be more active compared to the amine derivatives tested [79].

Al-Ahmad *et al.* synthesized a series of poly(oxonorborene)-based synthetic mimics of AMPs [85]. Their antimicrobial activity was tested against *E. coli*, *P. aeruginosa*, *K. pneumonia*, *S. aureus*, methicillin-resistant *S. aureus* (MRSA) and *E. faecalis*. Results showed that the polymers were active against the microbes tested and were ‘doubly selective’ where the bacteria are selective for bacterial over mammalian cells and Gram-positive over Gram-negative bacteria [85]. The relationship between side chain amphiphilicity and antibacterial activity was investigated by varying the alkyl side chain of quaternized AMP mimics. The study found a

cost effective way to produce mimics which were stable in human plasma and active against a broad spectrum of bacteria. These polymers were also active against MRSA vancomycin resistant *E. faecium* and found to be non-hemolytic [86]. Lee *et al.* conducted a study on the antibacterial activity of nylon-3-based AMP mimics [87]. The data obtained suggests that the polymers operate *via* two interdependent bactericidal mechanisms. The polymers disrupt the cell membrane and bind to intracellular components such as DNA where the activity is reported to be concentration dependent [87]. Chattopadhyay and colleagues synthesized multifunctional poly(vinyl amine) containing azetidinium groups (four membered ring with a quaternary nitrogen) in a one pot approach [88]. These polymers mimic the structural properties of AMPs where their antimicrobial activity could be adjusted by varying the ratio and type of hydrophobic and hydrophilic groups present. These polymers were tested for their antimicrobial efficacy, cell selectivity (Gram-positive, Gram-negative and mammalian cells) and applicability as a surface coating. Results obtained were favourable indicating that these polymers displayed superior activity and selectivity. Therefore, these materials can potentially be used as surface coatings to reduce bacterial infections [88]. Figure 12.2 shows the structure of polyethyleneimine and examples of an AMP mimic and a quaternized polymer discussed above.

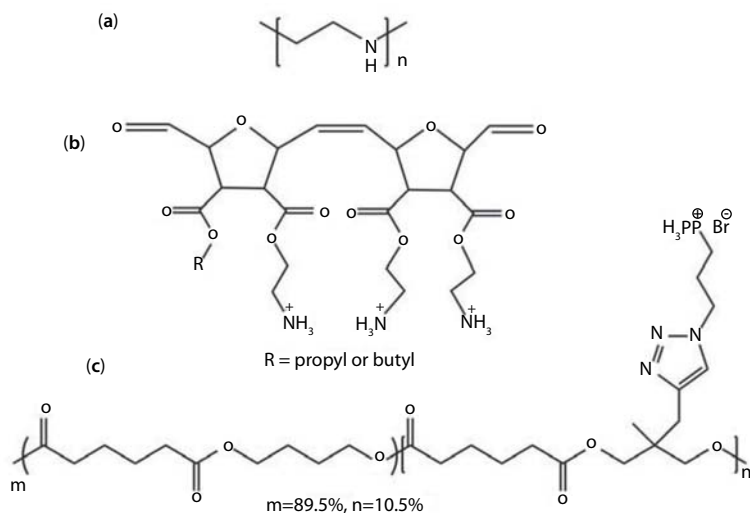


Figure 12.2 (a) PEI, (b) poly(oxonorborene)-based AMP and (c) quaternized alkyne functionalized poly(butylene adipate) [85, 73].

Natural and synthetic polymers have been shown to exhibit antimicrobial properties where some moieties are more active than others. To obtain even greater activities and expand the potential application of these polymers, loading polymers with a metal which possesses antimicrobial activity is a popular approach. Polymers whose activity has been enhanced by metal loading have been reviewed elsewhere and only some recent works in this area will be discussed with relevance to antimicrobial/antifungal polymers.

12.4 Metal Loading

Due to the rapid and wide spread development of antimicrobial resistance, new antimicrobial materials are constantly sought. Among the many materials investigated, metals have proven antimicrobial activities and have been used as such for centuries. Metals which have been used as antimicrobials include silver, copper, zinc, tin, lead, titanium, cadmium, chromium, cobalt, nickel, magnesium, molybdenum and zirconium [89]. The use of metals in biomedical applications is an appealing concept; however, their associated toxicity must be taken into account during application. Metals accumulate in the cells of the microbes where dissolved metal ions are assimilated into proteins rendering them non-operational or defective. Metal salts on the other hand form active radicals which affect the integrity of the cell wall leading to cell death. Metals studied thus far have varied in their antimicrobial activity where it has been noted that activity of a metal is bacteria specific. This activity is also dependent on the nature of the bacteria since differences in bacterial cell walls (Gram-positive and Gram-negative) can influence the activity of the metals. Gram-positive bacteria possess a thick cell wall which hinders the penetration of metal ions while Gram-negative bacteria possess only thin walls making them more susceptible [90].

The nanoscale benefits of materials have been intensively investigated in an effort to overcome drug resistance, toxicity and production costs in addition to improving properties of materials. Nanoscale metal particles are particularly appealing especially those which possess antimicrobial activity. Upon approaching the nanoscale a change in the properties of most materials is observed and the most favourable includes the increase in surface area. This change can possibly alter the reported antimicrobial activity of metals since activity is related to surface area [91]. Metallic nanoparticles have been noted to have greater antimicrobial activity, lower toxicity, are more stable and in some cases offer a long lasting action. These nanoparticles can be produced *via* a variety of methods including physical, chemical

or biological with greener synthetic methods being the ultimate goal [92]. Here follows a review of metal particles which have been well studied in recent literature.

12.4.1 Silver

One of the most studied nanoscale metals is silver (Ag). Ag has been widely used for medicinal purposes and has a broad spectrum of activity against many disease causing organisms. The exact mechanism of action is unknown; however, scientists have proposed some theories. Ag nanoparticles adhere to bacterial cells and disrupt the cell wall where another theory suggests the formation of free radicals all which lead to cell death. The generation of ROS, the destruction of cell DNA, interference in DNA replication and inhibition of bacterial signal transduction have also been proposed as a potential mechanism of action [93]. Ag nanoparticles have been used in combination with a variety of polymers to confer antimicrobial activity or boost the polymers inherent antimicrobial activity.

The review by Moritz *et al.* highlights the latest in the synthesis, immobilization and applications of antibacterial nanoparticles [94]. It includes a section on Ag nanoparticles and the matrices used for its immobilization such as cellulose, chitosan, parylene-coated glass, etc [94]. Fortunati *et al.* recently synthesized a poly(DL-lactide-co-glycolide) (PLGA) polymer which had been treated with oxygen plasma and Ag nanoparticles. The films thus produced, reduced bacterial adhesion and growth compared to the polymer alone [95]. Sileika *et al.* synthesized a multicomponent antimicrobial coating consisting of polydopamine, Ag nanoparticles and polyethylene glycol bound to a polycarbonate substrate [96]. The coating demonstrated antifouling and antimicrobial activity against *E. coli*, *P. aeruginosa* and *S. epidermidis* [96]. Electrospinning was recently utilized to form nanofibers of nylon-6 with Ag nanoparticles. These antimicrobial fibres can potentially be used as wound dressings or water membranes [97]. A later study applied a composite of nylon-6 and 2-substituted *N*-alkylimidazoles nanofibres incorporated with Ag nanoparticles [98]. Gao *et al.* published an in depth review of electrospun antibacterial nanofibres which included some polymers and the incorporation of Ag nanoparticles. Ag loaded polymers can be spun in one step producing fibres with a uniform dispersion of nanoparticles [99]. A wound dressing consisting of chitosan, Ag nanoparticles and polyvinyl alcohol was synthesized *via* a green method. These nanofiber mats were found to be effective against *E. coli* and are a promising alternative to normal dressings [100].

Ho and colleagues investigated the efficacy of Ag nanoparticles and modified polylysine as coating for surgical sutures [101]. The study found that the coatings contained highly stabilized nanoparticles which were effective against *S. aureus* and retained their activity after repeated washing [101]. Ag nanoparticles were synthesized in a one-step hydrothermal method using PEI as the reducing and stabilizing agent. The size of the particle produced could be manipulated by varying the temperature and mode of growth. The antibacterial efficacy of these particles was superior to that of the controls used (penicillin, chloramphenicol and erythromycin) [102]. Stevanović *et al.* produced a polymer consisting of poly(lactide-co-glycolide) encapsulating ascorbic acid and poly(L-glutamic acid)-capped Ag nanoparticles [103]. Antimicrobial testing against a panel of disease causing organisms (*C. albicans*, two strains of *S. aureus*, *E. faecalis*, *E. coli*, *K. pneumonia* and *P. aeruginosa*) showed that these particles displayed enhanced and prolonged activity [103].

12.4.2 Magnesium

Magnesium (Mg) metal has drawn significant attention in recent times. It is cheap, abundant and the cation Mg^{2+} is essential in mammals as it is vital to many biological processes. Nanoparticles are generally obtained as $Mg(OH)_2$ where these particles have been proven to exhibit antimicrobial activity. Two possible mechanisms for this activity was proposed by Dong *et al.* who theorize that cell death can be attributed to infiltration of the nanoparticles into the cell resulting in membrane disruption and death [104]. Another theory involves the adsorption of a thin water layer possessing a high enough pH with respect to the nanoparticle surface which when in contact with bacterial cells damages the cell membrane. This study also proved that $Mg(OH)_2$ nanoparticles are effective against *E. coli* and *B. phytofirmans* and can be incorporated into wood pulp in the manufacture of paper sheets [104]. Pan *et al.* noted that different synthetic methods produced Mg nanoparticles with varying properties. Accordingly, the antimicrobial activity differs according to the synthetic method used [105]. A poly(vinylidene fluoride)/PEG membrane loaded with $Mg(OH)_2$ nanoparticles for use as an antifouling agent has been prepared and evaluated. The produced films were effective in preventing the growth of *E. coli* [106]. Zhao *et al.* synthesized a nanocomposite film of cellulose nanofibrils, $Mg(OH)_2$ nanoplatelets and regenerated cellulose [107]. These films were robust, flame-retardant and displayed inhibitory activity against *E. coli* making them appealing for a variety of applications [107].

12.4.3 Zinc

Zinc (Zn) especially ZnO nanoparticles are of great interest due to their stability and reported antibacterial properties. ZnO nanoparticles are active against microbes at a neutral pH without the need for light where the mechanism is thought to be due to the generation of ROS and subsequent cell damage. These nanoparticles can be used in conjunction with polymers to extend their applications. A recent study reported the synthesis of ZnO-alginate nanocomposites which demonstrated strong activity against *E. coli* and *S. aureus* [108]. The manufacture of packaging films containing ZnO nanoparticles is a particular area of interest. Recently a polypropylene ZnO film and a starch coated polyethylene ZnO film were synthesized and evaluated for their antibacterial activity [109, 110]. Nafchi *et al.* produced two bionanocomposite antibacterial films containing ZnO nanorods, a sago starch and a bovine gelatin film [111]. In other studies, films of agar, carrageenan, carboxymethylcellulose and UV cured chitin containing ZnO nanoparticles and nanowires were prepared and tested for antibacterial properties [112, 113]. Combining a number of elements, a scaffold containing chitosan/nano-hydroxyapatite/nano-copper-zinc was synthesized and applied for bone tissue engineering. This scaffold displayed improved properties and the antibacterial activity was determined against *E. coli* and *S. aureus* [114]. The same group later synthesized a temperature sensitive ZnO chitosan/ β -glycerophosphate hydrogel for use as a scaffold [115]. ZnO nanoparticles as antibacterial coatings on fabrics such as cotton has also been studied [116].

12.4.4 Titanium

Titanium (Ti), in particular TiO₂ nanoparticles, is also utilized for a wide variety of applications. Polymer immobilized TiO₂ nanoparticles are commonly synthesized as self-cleaning or packaging films. The antimicrobial activity of this polymer is due to the generation of ROS when the nanoparticles are exposed to UV irradiation [94]. Pant *et al.* electrospun a nylon-6 nanofibre mat coated with TiO₂ nanoparticles and in an extension of this study further functionalized the mat with Ag nanoparticles to improve the antibacterial properties [117, 118]. Rahimpour and colleagues functionalized a poly(vinylidene fluoride)/sulfonated polyethersulfone blend membrane with TiO₂ nanoparticles. The antimicrobial activity was demonstrated against *E. coli* with UV activation of the membranes required for inhibitory activity [119]. In an extension of this work, Mollahosseini *et al.* produced a polysulfone based TiO₂ nanoparticles coated filtration

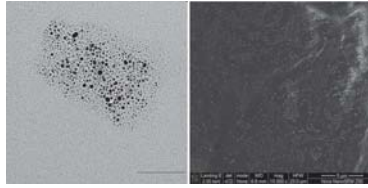


Figure 12.3 Chitosan stabilized Ag NPs using TEM (left) and SEM (right) [42].

membrane which also displayed antimicrobial activity [120]. A hybrid composite material consisting of microfibril cellulose bundles coated with Ti, chitosan and Ag nanoparticles was recently synthesized by a layer by layer method. The material displayed excellent antimicrobial activity when tested against *E. coli* and *S. aureus* [121].

Figure 12.3 shows chitosan stabilized Ag nanoparticles using two different imaging techniques, TEM and scanning electron microscopy (SEM). Other metals which are also utilized in conjunction with polymers and applied as antimicrobials include copper, tin, lead, cadmium, chromium, cobalt, nickel, molybdenum and zirconium. The metals reviewed here are those that have received increasing attention in recent literature. Reviews by Moritz, Swain and Rhim *et al.* give greater detail on these metals and their antimicrobial activity [94, 122, 123].

12.5 Assessment of Antimicrobial/Antifungal Testing Methods

One of the biggest threats to the health of individuals is the development of antimicrobial resistance. The World Health Organization (WHO) recognises the emergence of resistance as a serious global problem. It has been reported that resistance has developed to the majority of antimicrobial agents in use, thus placing an enormous burden on health systems. Hence making the treatment of pathogenic organisms challenging. In order to address this challenge, new antimicrobials are being developed however, methods for testing the efficacy of these antimicrobials needs more rigorous scrutiny.

MICs or minimum bactericidal concentrations (MBCs) are determined from these tests. The test methods utilized vary and numerous elements affect the results of susceptibility experiments; therefore, standard methods are required [124]. These standard methods must be reproducible by the researcher as well as other laboratories in order for

comparisons to be made. Testing strategies chosen also depend on the suitability of the method for the material being tested. The antimicrobial susceptibility testing (AST) methods currently used include diffusion (disk and Epsilometer test), dilution (broth or agar) and non-growth based methods. Antifungal testing is not as well studied as antimicrobial; however, many methods developed for AST can be employed for antifungal tests. The Clinical and Laboratory Standards Institute (CLSI) provides the standard for testing methods which can be used for antibacterial and antifungal testing [125, 126]. An overview of commonly used methods will be given here.

12.5.1 Diffusion

12.5.1.1 Agar Well Diffusion

Agar plates are prepared and inoculated by spreading the chosen bacteria across the plate. A sterile cork-borer is used to punch wells between 6 and 8 mm which are at least 30 mm apart. Either a fixed concentration or varying concentrations of the antimicrobial agent is added to the well. Incubation is typically at 37°C for 24 hours for bacteria or 48 hours for fungi. Thereafter, zones of inhibition (ZOIs) are measured. A disadvantage associated with this method is that certain materials do not diffuse effectively into the agar, thus giving a less accurate result [126].

12.5.1.2 Agar Disk Diffusion

Similar to the agar well diffusion, it requires paper disks (usually 6 mm in size) saturated with the antimicrobial agent or tablets of the agent applied to a pre-inoculated agar plate. After incubation ZOI are measured and analyzed using criteria from the CLSI. A drawback associated with this method, is that only a pure substance may be tested since a mixture of materials would more often than not have constituents with different diffusion rates [126]. In addition the manual measurement of ZOI makes it impractical for testing large volumes of samples. This method may also be applied in antifungal measurements [127].

12.5.1.3 Bioautography

There are three types, direct, contact and immersion bioautography. In direct bioautography, a known amount of the antimicrobial agent is applied to a silica thin layer chromatography (TLC) plate and developed with a suitable solvent. The plate is sprayed with the chosen bacteria and

incubated at 25°C for 48 hours in a humid area. Thereafter, microbial indicators typically tetrazolium salts are applied and the plates incubated at 37°C for 3–4 hours. Antimicrobial activity is observed as ZOI which are then measured. Contact bioautography involves bringing the TLC plate into contact with a pre-inoculated agar medium and immersion bioautography involves coating the TLC plate in agar and inoculating. This technique shows whether inhibition has occurred, however, there is no way to determine the concentration of the antimicrobial agent which diffused into the agar medium [128]. This technique may not be amenable to the testing of the efficacy of certain polymers. Certain materials cannot be successfully applied to TLC plates and hardly any literature reporting the use of bioautography and polymers has been found.

12.5.1.4 *Epsilon*meter Test (E-Test)

This test involves the use of a plastic test strip which has been loaded with a concentration gradient of the agent (antimicrobial or antifungal) to be tested. The strip is placed on a pre-inoculated agar plate and incubated for 24 hours. The MIC is determined by looking at the elliptical ZOI formed and the point at which this ellipse meets the strip is taken as the MIC. Advantages include reduced costs, ease of use and MICs generally correspond with those determined using broth or agar methods. A shortcoming associated with this test includes a systematic bias toward higher or lower MICs when certain samples have been tested [125]. These diffusion tests do not distinguish between bacteriostatic and bactericidal activity of the tested compound [126]. In addition, there are materials such as polymers which when applied to the strip will not diffuse into the agar medium thereby providing an inaccurate result.

12.5.2 Dilution

12.5.2.1 *Agar Dilution*

In the agar dilution method, different concentrations of the filter sterilized antimicrobial agent is applied to molten agar and the mixture is allowed to cool. Once the plate is set, it may be inoculated with a fixed amount of the chosen microorganisms. The MIC is defined as the lowest concentration of the agent at which no growth occurs. This method is the standard reference as indicated by the CLSI for testing of aerobic and anaerobic bacteria. This method is favoured as an accurate MIC can thus be obtained. More than one microorganism can be tested per plate, there is no limit to concentrations tested and this technique can be automated to a certain degree.

A disadvantage of this method is that it is time consuming and labour intensive which limits its application [129, 130]. Agar dilution has been applied in antifungal testing with acceptable results [127]. Incorporation of polymers into molten agar has produced good correlation of results with other testing methods applied.

12.5.2.2 *Broth Micro/Macrodilution*

The antimicrobial agent is serially diluted to desired concentrations and incubated with a known quantity of the chosen microorganism. Macrodilution involves the performance of this test in test tubes whereas the microdilution can be performed in 96 well plates. Turbidity of the wells are measured and used as an indicator for activity of the agent where the first clear well is taken as the MIC. Additionally, an indicator may be added which changes colour depending on whether growth has occurred. This method also allows for the determination of the MBC of the agent by culturing the samples (agar or broth) which showed no growth in the MIC test. This test method suffers from intensive sample preparation and possible contamination of solutions during preparation [125, 126]. In addition, while the concentration of the agent decreases, the amount of microorganisms applied does not. Hence, this could result in false negatives as suggested by Smith *et al.* [131] Broth dilution can be applied in antifungal studies; however, it is currently limited to *Candida* species. There are commercially available testing products available for these antifungal assays [127]. This testing method is acceptable for the study of the inhibitory activity of polymers.

12.5.3 **Metabolic Based Assays**

There are also some testing methods which are not based on growth patterns, one such example is flow cytometry. In flow cytometry, bacteria/fungi are suspended in a medium and lasers measure physical and chemical characteristics of the cells such as changes in membrane potential, metabolic activity and dye uptake in response to the presence of the chosen agent. An advantage of this technique is that it is not dependent on organism growth and can measure cidal and static activities depending on the dye used. However, this technique requires expensive equipment. Other non-growth methods which have been proposed include the ergosterol assay or the rapid susceptibility assay which monitors glucose uptake [127]. Butts *et al.* developed an alternative to growth based assays where a high throughput method was used to detect the release of the enzyme

adenylate kinase which indicates cell lysis [132]. The enzyme reacts and luciferase generated luminescence is observed [132].

The utility of fluorescent probes for the determination of growth or cell death is another common technique used. Rex *et al.* points out that fluorescent dyes have been used to study damage to yeasts and moulds by the agent being tested, and to determine MICs and minimal fungicidal concentrations for moulds [133]. Some commercially available test panels include a fluorescent dye allowing for growth determination by fluorescence measurements after incubation with the agent being tested [125]. A study conducted to compare selected methods for antimicrobial and membrane-permeabilizing activity utilized probes to show permeability of membranes and therefore activity of the peptides [134]. Cloete *et al.* used the fluorescent dyes Hoechst 33342 and propidium iodide to study the antimicrobial and antifungal activity of a maleimide modified poly(styrene-co-maleic anhydride) which had been incorporated into a latex film [135]. In an alternate strategy, luminescent bacteria (inherent or modified) can be utilized in testing avoiding the use of dyes. One such strategy is the TLC-bioluminescence method [128]. Another method includes the incorporation of fluoroquinolone-based materials which allows for detection of fluorescence [136].

Methods used to determine MBC include contact-kill-tests especially important for polymers, minimal lethal concentration determinations and the serum bactericidal test (SBT). These are not covered here; however, more detail can be found in the review published by Pfaller *et al.* [137]. A graphical representation of selected techniques is shown in Figure 12.4.

Since there are advantages and disadvantages associated with each antimicrobial/antifungal testing method, it is important to select the method which will give you the most information relevant to your study. When dealing with polymers this is an especially challenging area since there are such diverse polymers with different properties which need to be accounted for. The method chosen should not affect the activity of the material in any way; therefore, proper experimental design is essential. Very few articles deal with discrepancies in testing methods used; therefore, it is the aim of this review to highlight such discrepancies. Selected polymer based antimicrobial/antifungal studies will be discussed with specific focus on testing methods employed.

12.5.4 Discrepancies in Testing Methods

Since alternative therapies have been sought to combat resistance development, it is a challenge to determine the correct method of assessment for

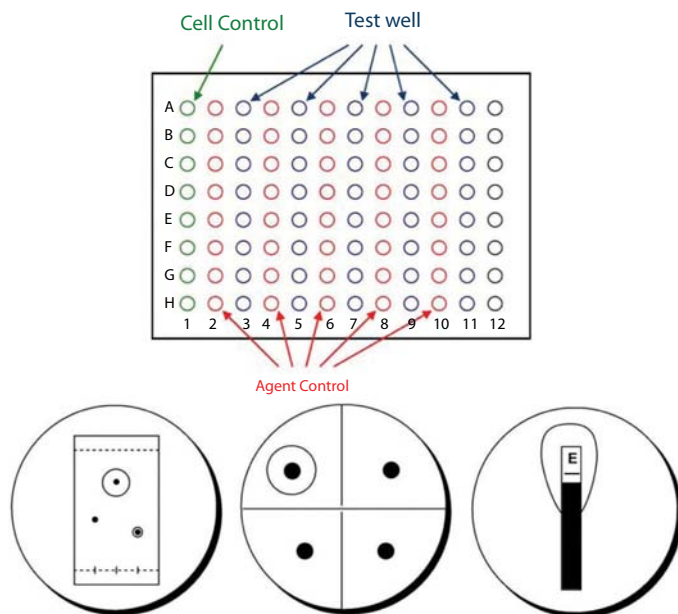


Figure 12.4 Broth micro/macrodilution (top), bottom: bioautography (left), disk diffusion (centre), E-test (right).

these new therapies. In the absence of standard methods for new materials it is important to assess which method of testing is most appropriate where reproducible results can be consistently obtained. A study conducted by Sánchez-Gómez *et al.* focused on this issue with a specific focus on testing the activity of cationic AMPs, in particular lactoferricin derived peptides [134]. This study determined the bacteriostatic, bactericidal and increase in cellular permeability of selected synthetic peptides. Methods used include the broth microdilution assay, an automated turbidimetry-based assay, an assay using media of different ionic strength and one where the type of plastic ware used was compared. This method also utilized different strains of bacteria to demonstrate variability in results. The study showed that certain changes to the testing methods employed have a significant effect on activity observed [134]. Narin *et al.* investigated the antibacterial activity of cobalt containing zeolite/poly(vinyl alcohol) hydrogel films [138]. It was found that the disk diffusion methods could not be used in this study as no inhibition was observed possibly due to incomplete contact of the disks with the agar or slow diffusion of the ions into the agar. Therefore, the films were tested using a modified broth method where films

were fixed in the wells using a stainless steel coil. Results indicated that the pure films did not display any activity while the films which contained a higher Co-zeolite content displayed significant inhibition [138].

The study performed by Lehtopolku *et al.* highlighted this discrepancy in testing methods used [139]. This study pointed out that the disk diffusion method was used incorrectly in the assessment of the susceptibility of *Campylobacter* species by comparing results obtained for both disk diffusion and agar dilution methods [139]. A study conducted on behalf of the European Surveillance of Sexually Transmitted Infections (ESSTI) network pointed out that laboratories in Western Europe use various methods for the diagnosis and AST of *N. gonorrhoeae*. This led to varying results which could not be compared making the development of standardized methods a necessity [140].

Most studies only utilize one method to determine antimicrobial activity; however, it is good practice to determine activity using more than one method. Thomas *et al.* determined the antimicrobial activity of chitosan and Ag nanoparticle loaded chitosan films qualitatively and quantitatively [141]. Methods utilized include zone inhibition measurements from disk diffusion, spread plate, viable cell count or killing kinetics [141]. This is especially important when materials consist of more than one component. Another example which demonstrated this principle is in the study of the multilayer of carrageenan/PEI. This material was formed using the layer-by-layer assembly absorption technique. Inhibitory activity was assessed using the broth dilution method, a combined paper strip method to determine synergistic effects and a ZOI test against three different bacterial species [142]. Wang *et al.* reported on the activity of compounds and polymers obtained from natural resin acids against six Gram-positive and seven Gram-negative bacterial species [143]. This study used the broth dilution and disk diffusion methods to determine activity. However, MICs obtained for the disk diffusion method was much lower than those recorded for the broth microdilution methods. Due to this discrepancy in testing methods used, only the disk diffusion method was used in the completion of the study [143].

It is also important to note if any procedures followed during the antimicrobial testing will have an influence on the results obtained. An example of this can include exposure to UV light to sterilize materials before testing. Nadarajah developed antimicrobial edible films of chitosan and noted that films should not be exposed to UV light for long periods due to previous studies proving that it could affect the physicochemical properties of the polymer [144]. In the study by Tran *et al.* composite films of cellulose and chitosan were synthesized and tested for their antimicrobial activity

[145]. However, prior to testing, the films were sterilized by exposing them to UV light for 2 hours. This study did not account for the effect of the UV light on the materials such as photodegradation which may affect the results obtained [145]. Another study compared the difference in the bactericidal action of poly(phenylene ethynylene) (PPE)-based cationic conjugated polyelectrolytes (CPEs) and OPEs in the presence and absence of light. The study found that activity is enhanced when these polymers are tested under UV light and that the mechanism of action differs against Gram-positive and Gram-negative bacteria [146].

Chitosan has reported antimicrobial and antifungal activity; however, a review of the literature shows a range of MIC values. These inconsistencies can be attributed to the type of chitosan used since factors such as molecular weight, DDA, pH and organisms tested all affect the observed activity. However, these differences can also be due to different testing methods and conditions used. Therefore, the results obtained using these diverse methods cannot be compared. Jiang studied the antimicrobial activity of chitosan using the disk diffusion, agar dilution and broth microdilution methods against a library of Gram-positive and Gram-negative bacteria [147]. According to this study, activity varied with the test method used, molecular weight and species tested [147]. Khaira *et al.* isolated and subsequently quaternized a biopolymer from the bacteria *K. terrigena* [148]. This polymer was investigated for its antibacterial activity using an agar disk diffusion assay, broth microdilution and the thin agar layer method (to determine the number of injured cells). Results indicated that the quaternized polymer displayed better properties compared to the native biopolymer. However, in the agar disk diffusion assay, a paper disk was impregnated with the biopolymers and applied to plates containing bacterial cultures (*L. monocytogenes* and *E. coli*) to determine if any activity occurred. This method is questionable since modification of the polymer may have altered diffusion rates compared to the native polymer possibly leading to wider diffusion and therefore higher activity was observed [148].

12.6 Conclusion

This aim of this review was to give an overview of selected bio-derived polymers which possess antimicrobial or antifungal activity. A short background necessary to understand the origin and application of these polymers has been provided with a focus on the antimicrobial applications. Clearly, two research niche areas emerged in the form of low value material for high volume markets as well as high value, technologically advanced,

low volume markets. In the biomedical, textile and water purification market, metal loading of biopolymers in the form of nanoparticles have demonstrated widespread utility and have been briefly reviewed. A better understanding of the antimicrobial mechanism of activity is limited due to the lack of standardization in testing and variability of inhibition data. Antimicrobial testing methods currently employed in the testing of materials have been reviewed. Some shortcomings of the general methods of antimicrobial testing have been noted. Testing methods amenable to high throughput can be considered as a screening tool that would improve standardization and speed of analysis simultaneously. The development of standard reference materials for antimicrobial testing is required. Only materials that demonstrate appreciable MICs could then be plated to generate CFUs as a more accurate measure of activity. The antiviral activity of the same polymers also has not yet been explored.

The area of great economic interest is low value and high volume biopolymer applications of functional packaging or coatings that can minimize food spoilage and hence waste. A high volume application that is expected to make a greater impact in time is the treatment of crops with antifungal biopolymers, thus improving food security while having a minimal environmental impact. Patent literature is packed with technology solutions that require major translational efforts to bring greener product options to market. However, a review of the patent literature in this regard is necessary. The chemical transformation and evaluation of native polymers into functional materials is driven by enabling technologies such as chemistry and nanotechnology. Chemical technologies will determine if biomass needs to be broken down all the way to monomers and then rebuilt or modified as a native polymer for specific applications. Either way, biopolymer research as a greener material is in its infancy and will continuously be driven by the consumer demand for high value functional materials in many different market segments.

References

1. Markets and markets, Biomaterials, <http://www.marketsandmarkets.com/>, 2013.
2. European Technology Platform, The European Bioeconomy in 2030, <http://www.plantetp.org>, 2011.
3. S. Karlsson and A. Albertsson, "Chemistry and Biochemistry of Polymer Degradation" in G. Griffin, ed., *Chemistry and Technology of Biodegradable Polymers*, Blackie Academic and Professional, pp. 7–17, 1994.
4. A. Mohanty, M. Misra and G. Hinrichsen, *Macromol. Mater. Eng.*, Vol. 276/277, pp. 1–24, 2000.

5. W. Amass, A. Amass and B. Tighe, *Polymer International.*, Vol. 47, pp. 89–144, 1998.
6. C. Pillai and G. Luckachan, *J. Polym. Environ.*, Vol. 19, pp. 637–676, 2011.
7. V. Francis, V. PhD thesis, Cochin University of Science and Technology, 2012.
8. C. Laurencin and L. Nair, *Prog. Polym. Sci.*, Vol. 32, pp. 762–798, 2007.
9. Y. Li, Q. Han, J. Feng, W. Tian and H. Mo, *Food Control*, Vol. 43, pp. 22–27, 2014.
10. T. Nagasawa and T. Yoshida, *Appl. Microbiol. Biotech.*, Vol. 62, pp. 21–26, 2003.
11. M. Vernekar and A. Chheda, *Food Biosci.*, Vol. 7, pp. 56–63, 2014.
12. S. Bankar, S. Chaudhary and R. Singhal, *J. Sci. Ind. Res.*, Vol. 73, pp. 33–40, 2014.
13. N. Wibowo, P. Yang and C. Lee, *Sep. Sci. Technol.*, Vol. 48, pp. 1086–1092, 2013.
14. R. Ye, H. i Xu, C. Wan, S. Peng, L. Wang, H. Xu, Z. Aguilar, Y. Xiong, Z. Zeng and H. Wei, *Biochem. Biophys. Res. Commun.*, Vol. 439, pp. 148–153, 2013.
15. J. Hiraki, *Fine Chem.*, Vol. 29, pp. 18–25, 2000.
16. M. Corrales, A. Fernandez and H. Jung, “Antimicrobial Packaging Systems” in J. Han ed. *Innovations in Food Packaging*, Academic Press, pp 133–170, 2014.
17. S. Shukla, A. Singh, A. Pandey and A. Mishra, *Biochem. Eng. J.*, Vol. 65, pp. 70–81, 2012.
18. Y. Chang, L. McLandsborough and D. McClements, *Food Hydrocolloids*, Vol. 35, pp. 137–143, 2014.
19. Y. Chang, L. McLandsborough and D. McClements, *J. Agric. Food Chem.*, Vol. 60, pp. 1837–1844, 2012.
20. G. Moschonas, I. Geonaras, J. Stopforth, D. Wach, D. Woerner, K. Belk, G. Smith and J. Sofos, *J. Food Sci.*, Vol. 77, pp. M405–M411, 2012.
21. S. Lin, Z. Wang, J. Qi, J. Wu, T. Tian, L. Hou, L. Hao and J. Yang, *Biomed. Mat.*, Vol. 6, pp. 1–7, 2011.
22. H. Yu, Y. Huang and Q. Huang, *J. Agric. Food Chem.*, Vol. 58, pp. 1290–1295, 2010.
23. C. Gao, Y. Wan, X. Lei, J. Qu, T. Yan and K. Dai, *Cellulose*, Vol. 18, pp. 1555–1561, 2011.
24. H. Zhu, S. Jia, H. Yang, W. Tang, Y. Jia and Z. Tan, *Food Sci. Biotechnol.*, Vol. 19, pp. 1479–1484, 2010.
25. R. Tikekar, M. Hernandez, D. Land and N. Nitin, *Food Res. Int.*, Vol. 54, pp. 44–47, 2013.
26. X. Qi and J. Zhou, *Lett. Appl. Microbiol.*, Vol. 52, pp. 76–83, 2010.
27. J. Lee, H. Kim, M. Lee, H. Taguchi, S. Hyon and J. Park, *J. Microbiol. Biotechnol.*, Vol. 21, pp. 1199–1202, 2011.
28. C. Li, F. Liu, Y. Gong, Y. Wang, H. Xu, F. Yuan and Y. Gao, *LWT – Food Sci. Technol.*, Vol. 57, pp. 612–617, 2014.
29. Y. Wang, F. Liu, F. Yuan and Y. Gao, *J. Sci. Food Agric.*, Vol. 94, pp. 2986–2991, 2014, doi: 10.1002/jsfa.6644.

30. C. Zhou, P. Li, X. Qi, A. Sharif, Y. Poon, Y. Cao, M. Chang, S. Leong and M. Chan-Park, *Biomaterials*, Vol. 32, pp. 2704–2712, 2011.
31. W. Nie, X. Yuan, J. Zhao, Y. Zhou and H. Bao, *Carbohydr. Polym.*, Vol. 96, pp. 342–348, 2013.
32. Y. Zhou, W. Nie, J. Zhao and X. Yuan, *J. Mater. Sci.: Mater. Med.*, Vol. 24, pp. 2277–2286, 2013.
33. S. Kim, ed., *Chitin, Chitosan, Oligosaccharides and Their Derivatives: Biological Activities and Applications*, CRC Press, 2011.
34. S. Kim, ed., *Chitin and Chitosan Derivatives: Advances in Drug Discovery and Development*, CRC Press, 2014.
35. M. Kumar, *React. Funct. Polym.*, Vol. 46, pp. 1–27, 2000.
36. M. Kim and B. Park, *Int. J. Mol. Sci.*, Vol. 11, pp. 5152–5164, 2010.
37. F. Shahidi, J. Arachchi and Y. Jeon, *Trends Food Sci. Technol.*, Vol. 10, pp. 37–51, 1999.
38. N. Inamdar and V. Mourya, *React. Funct. Polym.*, Vol. 68, pp. 1013–1051, 2008.
39. P. Dutta, J. Dutta and V. Tripathi, *J. Sci. Indust. Res.*, Vol. 63, pp. 20–31, 2004.
40. M. Zohuriaan-Mehr, *Iran. Polym. J.*, Vol. 14, pp. 235–265, 2005.
41. B. Sarmiento and J. das Neves, eds, *Chitosan-Based Systems for Biopharmaceuticals – Delivery, Targeting and Polymer Therapeutics*, John Wiley & Sons, 2012.
42. S. Sayed and M. Jardine, “Chitosan as an Advanced Healthcare Material” in A. Tiwari and A. Nordin, eds., *Advanced Biomaterials and Biodevices*, Scrivener Publishing, pp. 147–183, 2014.
43. E. Rabea, M. Badawy, C. Stevens, G. Smaghe and W. Steurbaut, *Biomacromolecules*, Vol. 4, pp. 1457–1465, 2003.
44. W. Du, Y. Xu, Z. Xu and C. Fan, *Nanotechnology*, Vol. 19, pp. 1–5, 2008.
45. L. Huang, X. Cheng, C. Liu, K. Xing, J. Zhang, G. Sun, X. Li and X. Chen, *Front. Biol. China*, Vol. 4, pp. 321–327, 2009.
46. O. Cota-Arriola, M.O. Cortez-Rocha, A. Burgos-Hernandez, J.M. Ezquerra-Brauer and M. Plascencia-Jatomea, *J. Sci. Food Agric.*, Vol. 93, pp. 1525–1536, 2013.
47. W. Du, S. Niu, Y. Xu, Z. Xu and C. Fan, *Carbohydr. Polym.*, Vol. 75, pp. 385–389, 2009.
48. C. Pillai, W. Paul and C. Sharma, *Prog. Polym. Sci.*, Vol. 34, pp. 641–678, 2009.
49. N. Inamdar and V. Mourya, *J. Mater. Sci.: Mater. Med.*, Vol. 20, pp. 1057–1079, 2009.
50. T. Satoh, H. Kano, M. Nakatani, N. Sakairi, S. Shinkai and T. Nagasaki, *Carbohydr. Res.* Vol. 341, pp. 2406–2413, 2006.
51. A. Sadeghi, M. Amini, M. Avadi, F. Siedi, M. Rafiee-Tehrani and H. Junginger, *J. Bioact. Compat. Polym.*, Vol. 23, pp. 262–275, 2008.
52. M. Jardine and G. Smith, Polymer Support, US patent 8,420,802 B2, April 16, 2013.
53. J. Yang, J. Cai, Y. Hu, D. Li and Y. Du, *Carbohydr. Polym.*, Vol. 87, pp. 202–209, 2012.

54. A. Sadeghi and H. Junginer, "Synthesis, Characterization, and Biomedical Applications of Chitosan and Its Derivatives" in S. Kim, ed. *Chitin and Chitosan Derivatives: Advances in Drug Discovery and Developments*, CRC Press, pp 15–68, 2014.
55. R. Mohamed and R. Farag, *Molecules*, Vol. 18, pp. 190–203, 2013.
56. V. Mourya, N. Inamdar and A. Tiwari, *Adv. Mater. Lett.*, Vol. 1, pp. 11–33, 2010.
57. L. Sun, Y. Du, L. Fan, X. Chen and J. Yang, *Polymer*, Vol. 47, pp. 1796–1804, 2006.
58. M. Fernandes, A. Francesko, J. Torrent-Burgués and T. Tzanov, *React. Funct. Polym.*, Vol. 73, pp. 1384–1390, 2013.
59. M. Fernandes, A. Francesko, J. Torrent-Burgués, F. Carrión-Fité, T. Heinze and T. Tzanov, *Biomacromolecules*, Vol. 15, pp. 1365–1374, 2014.
60. G. Geisberger, E. Gyenge, D. Hinger, A. Käch, C. Maake and G. Patzke, *Biomacromolecules*, Vol. 14, pp. 1010–1017, 2013.
61. S. Goodacre and S. Wright, *BMC Res. Notes*, Vol. 5, pp. 1–6, 2012.
62. G. Dräger, A. Krause, L. Möller and S. Dumitriu, "Carbohydrates" in A. Lendlein and A. Sisson, eds., *Handbook of Biodegradable Polymers, Synthesis, Characterization and Applications*, Wiley-VCH Verlag & Co. KGaA, 2011, 7.
63. M. Benhabiles, R. Salah, H. Lounici, N. Drouiche, M. Goosen and N. Mameri *Food Hydrocolloids*, Vol. 29, pp. 48–56, 2012.
64. J. Tiller and F. Siedenbiedel, *Polymers*, Vol. 4, pp. 46–71, 2012.
65. L. Carrasco and A. Carmona-Ribeiro, *Int. J. Mol. Sci.*, Vol. 14, pp. 9906–9946, 2013.
66. S. Kandil and E. Kenawy, "Synthesis, Antimicrobial Activity and Applications of Polymers with Ammonium and Phosphonium Groups" in A. Munoz-Bonilla, M. Cerrada and M. Fernandez-Garcia, eds., *Polymeric Materials with Antimicrobial Activity from Synthesis to Applications*, The Royal Society of Chemistry, 2014, 3.
67. M. Fernandez-Garcia and A. Muñoz-Bonilla, *Progr. Polym. Sci.*, Vol. 37, pp. 281–339, 2012.
68. W. Chin, C. Yang, V. Ng, Y. Huang, J. Cheng, Y. Tong, D. Coady, W. Fan, J. Hedrick and Y. Yang, *Macromolecules*, Vol. 46, pp. 8797–8807, 2013.
69. V. Ng, J. Tan, J. Leong, Z. Voo, J. Hedrick and Y. Yang, *Macromolecules*, Vol. 47, pp. 1285–1291, 2014.
70. M. El-Newehy, H. El-Hamshary, S. Al-Deyaba and A. Abdel-Megeed, *J. Macromol. Sci., A Pure Appl. Chem.*, Vol. 51, pp. 527–537, 2014.
71. G. Gozzelino, C. Lisanti and S. Beneveti, *Colloids Surf. A.*, Vol. 430, pp. 21–28, 2013.
72. C. Li, Y. Liu, Q. Zeng and N. Ao, *Mater. Lett.*, Vol. 93, pp. 145–148, 2013.
73. T. Anthierens, L. Billet, F. Devlieghere and F. Du Prez, *Innovative Food Sci. Emerging Technol.*, Vol. 15, pp. 81–85, 2012.
74. A. Guo, F. Wang, W. Lin, X. Xu, T. Tang, Y. Shen and S. Guo, *Int. J. Biol. Macromol.*, Vol. 67, pp. 163–171, 2014.

75. A. Kanazawa, T. Ikeda and T. Endo, *J. Polym. Sci., Part A: Polym. Chem.*, Vol. 31, pp. 2873–2876, 1993.
76. A. Briones, T. Sato and U. Bigol, *Adv. Chem. Eng. Sci.*, Vol. 4, pp. 233–241, 2014.
77. C. Wiegand, M. Bauer, U. Hipler and D. Fischer, *Int. J. Pharm.*, Vol. 456, pp. 165–174, 2013.
78. M. Pereira and D. Alves, *Biofouling*, Vol. 30, pp. 483–499, 2014.
79. K. Locock, T. Michl, J. Valentin, K. Vasilev, J. Hayball, Y. Qu, A. Traven, H. Griesser, L. Meagher and M. Haeussler, *Biomacromolecules*, Vol. 14, pp. 4021–4031, 2013.
80. H. Takahashi, E. Palermo, K. Yasuhara, G. Caputo and K. Kuroda, *Macromol. Biosci.*, Vol. 13, pp. 1285–1299, 2013.
81. Y. Wang, E. Chi, K. Schanze and D. Whitten, *Soft Matter*, Vol. 8, pp. 8547–8558, 2012.
82. S. Arora, V. Yadav, P. Kumar, R. Gupta and D. Kumar, *Int. J. Pharm. Sci. Rev. Res.*, Vol. 23, pp. 279–290, 2013.
83. M. Sobczak, C. Debek, E. Oledzka and R. Kozlowski, *Molecules*, Vol. 18, pp. 14122–14137, 2013.
84. K. Rapsch, F. Bier, M. Tadros and M. von Nickisch-Roseneck, *Bioconjugate Chem.*, Vol. 25, pp. 308–319, 2014.
85. A. Al-Ahmad, D. Laird, P. Zou, P. Tomakidi, T. Steinberg and K. Lienkamp, *PLoS ONE*, Vol. 8, p. e73812, 2013.
86. D. Uppu, P. Akkapeddi, G. Manjunath, V. Yarlagadda, J. Hoque and J. Haldar, *Chem. Commun.*, Vol. 49, pp. 9389–9391, 2013.
87. M. Lee, S. Chakraborty, N. Schimdt, R. Murgai, S. Gellman and G. Wong, *Biochim. Biophys. Acta*, Vol. 1838, pp. 2269–2279, 2014.
88. S. Chattopadhyay, E. Heine, H. Keul and M. Moller, *Macromol. Biosci.*, Vol. 14, pp. 1116–1124, 2014.
89. G. Narin, C. Albayrak and S. Ulku, *J. Sol-Gel. Sci. Technol.*, Vol. 69, pp. 214–230, 2014.
90. M. Yasuyuki, K. Kunihiro, S. Kurisser, N. Kanavillil, Y. Sato and Y. Kikuchi, *Biofouling*, Vol. 26, pp. 851–858, 2010.
91. M. Hajipour, K. Fromm, A. Ashkarran, D. de Aberasturi, I. de Larramendi, T. Rojo, V. Serpooshan, W. Parak and M. Mahmoudi, *Trends Biotechnol.*, Vol. 30, pp. 499–511, 2012.
92. N. Durán, P. Marcato, R. De Conti, O. Alves, F. Costa and M. Brocchi, *J. Braz. Chem. Soc.*, Vol. 21, pp. 949–959, 2010.
93. E. Poulouse and S. Prabhu, *Int. Nano Lett.*, Vol. 2, pp. 1–10, 2012.
94. M. Geszke-Moritz and M. Moritz, *Chem. Eng. J.*, Vol. 228, pp. 596–613, 2013.
95. E. Fortunati, S. Mattioli, L. Visai, M. Imbriani, J. Fierro, J. Kenny and I. Armentano, *Biomacromolecules*, Vol. 14, pp. 626–636, 2013.
96. T. Sileika, H. Kim, P. Maniak and P. Messersmith, *ACS Appl. Mater. Interfaces*, Vol. 3, pp. 4602–4610, 2011.
97. B. Pant, H. Pant, D. Pandeya, G. Panthi, K. Nam, S. Hong, C. Kim and H. Kim, *Colloids Surf. A*, Vol. 395, pp. 94–99, 2012.

98. P. Kleyi, C. Frost, Z. Tshentu and N. Torto, *J. Appl. Polym. Sci.*, Vol. 131, pp. 1–10, 2014.
99. Y. Gao, Y. Truong, Y. Zhu and I. Kyratzis, *J. Appl. Polym. Sci.*, Vol. 131, pp. 1–13, 2014.
100. A. Abdelgawada, S. Hudson and O. Rojas, *Carbohydr. Polym.*, Vol. 100, pp. 166–178, 2014.
101. C. Ho, E. Odermatt, I. Berndt and J. Tiller, *J. Biomater. Sci., Polym. Ed.*, Vol. 24, pp. 1589–1600, 2013.
102. Z. Liu, Y. Wang, Y. Zu, Y. Fu, N. Li, N. Guo, R. Liu and Y. Zhang, *Mater. Sci. Eng. C*, Vol. 42, pp. 31–37, 2014.
103. M. Stevanovic, I. Bracko, M. Milenkovic, N. Filipovic, J. Nunic, M. Filipic and D. Uskokovic, *Acta Biomater.*, Vol. 10, pp. 151–162, 2014.
104. C. Dong, J. Cairney, Q. Sun, O. Maddan, G. He and Y. Deng, *J. Nanopart. Res.*, Vol. 12, pp. 2101–2109, 2010.
105. X. Pan, Y. Wang, Z. Chen, D. Pan, Y. Cheng, Z. Liu, Z. Lin and X. Guan, *ACS Appl. Mater. Interfaces*, Vol. 5, pp. 1137–1142, 2013.
106. C. Dong, G. He, H. Li, R. Zhao, Y. Han and Y. Deng, *J. Membr. Sci.*, Vols. 387–388, pp. 40–47, 2012.
107. J. Zhao, X. Zhang, R. Tu, C. Lu, X. He and W. Zhang, *Cellulose*, Vol. 21, pp. 1859–1872, 2014.
108. L. Trandafilovic, D. Bozanic, S. Dimitrijevic-Brankovic, A. Luyt and V. Djokovic, *Carbohydr. Polym.*, Vol. 88, pp. 263–269, 2012.
109. R. Paisonsin, O. Pornsunthorntawe and R. Rujiravanit, *Appl. Surf. Sci.*, Vol. 273, pp. 824–835, 2013.
110. S. Bajpai and R. Tankhiwale, *Colloids Surf., B*, Vol. 90, pp. 16–20, 2012.
111. A. Nafchi, R. Nassiri, S. Sheibani, F. Ariffin and A. Karim, *Carbohydr. Polym.*, Vol. 96, pp. 233–239, 2013.
112. J. Rhim and P. Kanmani, *Carb. Polym.*, 2014, Vol. 106, pp. 190–199.
113. D. Omay and B. Kilic, *Mater. Sci. Semicond. Process.*, Vol. 20, pp. 35–40, 2014.
114. A. Tripathi, S. Saravanan, S. Pattnaik, A. Moorthi, N. Partridge and N. Selvamurugan, *Int. J. Biol. Macromol.*, Vol. 50, pp. 294–299, 2012.
115. R. Niranjana, C. Koushik, S. Saravanan, A. Moorthi, M. Vairamani and N. Selvamurugan, *Int. J. Biol. Macromol.*, Vol. 54, pp. 24–29, 2013.
116. I. Perelshtein, G. Applerot, N. Perkash, E. Wehrschetz-Sigl, A. Hasmann, G. Guebitz and A. Gedanken, *ACS Appl. Mater. Interfaces*, Vol. 1, pp. 361–366, 2009.
117. H. Pant, M. Bajgai, K. Nam, Y. Seo, D. Pandeya, S. Hong and H. Kim, *J. Hazard. Mater.*, Vol. 185, pp. 124–130, 2011.
118. H. Pant, D. Pandeya, K. Nam, W. Baek, S. Hong and H. Kim, *J. Hazard. Mater.*, Vol. 189, pp. 465–471, 2011.
119. A. Rahimpour, M. Jahanshahi, A. Mollahosseini and B. Rajaeian, *Desalination*, Vol. 285, pp. 31–38, 2012.

120. A. Rahimpour and A. Mollahosseini, *J. Ind. Eng. Chem.*, Vol. 20, pp. 1261–1268, 2014.
121. W. Xiao, J. Xu, X. Lu, Q. Hu and J. Huang, *J. Mater. Chem. B.*, Vol. 1, pp. 3477–3485, 2013.
122. P. Swain, S. Nayak, A. Sasmal, T. Behera, S. Barik, S. Swain, S. Mishra, A. Sen, J. Das and P. Jayasankar, *World J. Microbiol. Biotechnol.*, Vol. 30, pp. 2491–2502, 2014.
123. J. Rhim, H. Park and C. Ha, *Prog. Poly. Sci.*, Vol. 38, pp. 1629–1652, 2013.
124. D. White, “Laboratory Methodologies for Bacterial Antimicrobial Susceptibility Testing” in *World Organisation for Animal Health: Manual of Diagnostic Tests and Vaccines for Terrestrial Animals*, World Organisation for Animal Health (OIE), 2014.
125. M. Ferraro and J. Jorgensen, *Med. Microbiol.*, Vol. 49, pp. 1749–1755, 2009.
126. N. Ncube, S. Afolayan and A. Okoh, *Afr. J. Biotechnol.*, Vol. 7, pp. 1791–1806, 2008.
127. A. Wagner, “Antifungal Susceptibility Testing Methods: Non-CLSI Methods for Yeast and Moulds” in G. Hall, ed., *Interactions of Yeasts, Moulds, and Antifungal Agents*, Humana Press, 3, 2012, pp. 75–87.
128. E. Grzelak and I. Choma, *J. Chromatogr. A*, Vol. 1218, pp. 2684–2691, 2011.
129. I. Wiegand, K. Hilpert and R. Hancock, *Nat. Protoc.*, Vol. 3, pp. 163–175, 2008.
130. E. Goldstein, D. Citron and D. Hecht, “Antimicrobial Resistance of Anaerobic Bacteria” in I. Fong and K. Drlica, eds., *Antimicrobial Resistance and Implications for the 21st Century*, Springer, 2008, 6.
131. S. Smith, A. Beattie, M. Gillings, M. Holley, A. Stow, C. Turnbull, P. Wilson and D. Briscoe, *J. Microbiol. Methods*, Vol. 72, pp. 103–106, 2008.
132. D. Krysan and A. Butts, *PLOS Pathog.*, Vol. 8, p. e1002870, 2012.
133. J. Rex, M. Pfaller, T. Walsh, V. Chaturvedi, A. Espinel-Ingroff, M. Ghannoum, L. Gosey, F. Odds, M. Rinaldi, D. Sheehan and D. Warnock, *Clin. Microbiol. Rev.*, Vol. 14, pp. 643–658, 2001.
134. S. Sánchez-Gómez, M. Lamata, J. Leiva, S. Blondelle, R. Jerala, J. Andrä, K. Brandenburg, K. Lohner, I. Moriyón and G. Martínez-de-Tejada, *BMC Microbiol.*, Vol. 8, pp. 1–9, 2008.
135. W. Cloete, L. Verwey and B. Klumperman, *Eur. Polym. J.*, Vol. 49, pp. 1080–1088, 2013.
136. G. Cirillo, M. Mauro, U. Spizzirri, P. Cavalcanti, F. Puoci, C. Giraldi, O. Vittorio, N. Picci and F. Iemma, *J. Mater. Sci. Mater. Med.*, Vol. 25, pp. 67–77, 2014.
137. M. Pfaller, D. Sheehan and J. Rex, *Clin. Microbiol. Rev.*, Vol. 17, pp. 268–280, 2004.
138. G. Narin, C. Albayrak and S. Ulku, *J. Sol-Gel Sci. Technol.*, Vol. 69, pp. 214–230, 2014.
139. M. Lehtopolku, P. Kotilainen, P. Puukka, U. Nakari, A. Siitonen, E. Eerola, P. Huovinen and A. Hakanen, *J. Clin. Microbiol.*, Vol. 50, pp. 52–56, 2012.

140. C. Ison, I. Martin, C. Lowndes and K. Fenton, *J. Antimicrob. Chemother.*, Vol. 58, pp. 580–586, 2006.
141. V. Thomas, M. Yallapu, B. Sreedhar and S. Bajpai, *J. Biomater. Sci.*, Vol. 20, pp. 2129–2144, 2009.
142. A. Briones, T. Sato and U. Bigol, *Adv. Chem. Eng. Sci.*, Vol. 4, pp. 233–241, 2014.
143. J. Wang, Y. Chen, K. Yao, P. Wilbon, W. Zhang, L. Ren, J. Zhou, M. Nagarkatti, C. Wang, F. Chu, X. He, A. Decho and C. Tang, *Chem. Commun.*, Vol. 48, pp. 916–918, 2012.
144. K. Nadarajah, PhD Thesis, Louisiana State University and Agricultural and Mechanical College, 2005.
145. C. Tran, S. Duri and A. Harkins, *J. Biomed. Mater. Res. A*, Vol. 101A, pp. 2248–2257, 2013.
146. Y. Wang, S. Jett, J. Crum, K. Schanza, E. Chi and D. Whitten, *Langmuir*, Vol. 29, pp. 781–792, 2013.
147. L. Jiang, PhD Thesis, Louisiana State University and Agricultural and Mechanical College, 2011.
148. G. Khaira, A. Ganguli and M. Ghosh, *J. Appl. Microbiol.*, Vol. 116, pp. 511–518, 2013.

Organometal Halide Perovskites for Photovoltaic Applications

Sai Bai^{1,2}, Yizheng Jin^{*,3}, and Feng Gao^{*,1}

¹*Department of Physics, Biology, and Chemistry (IFM), Linköping University, Linköping, Sweden*

²*Solar and Photovoltaic Engineering Research Center (SPERC), King Abdullah University of Science and Technology (KAUST), 23955-6900 Thuwal, Saudi Arabia*

³*State Key Laboratory of Silicon Materials, Department of Chemistry, Zhejiang University, Hangzhou, People's Republic of China*

Abstract

This chapter discusses an emerging photovoltaic material, organometal halide perovskite, which delivers a power conversion efficiency of over 20%. We start with a brief introduction of this novel material and its applications in photovoltaic technology. We present a detailed explanation of the optoelectronic properties of organometal halide perovskites and different device architectures. We focus on the deposition methods as well as quality control of the perovskite films. Finally, we give a perspective concerning the challenges and opportunities for this promising material.

Keywords: Photovoltaic materials, organometal halide perovskite, photovoltaic technology

13.1 Introduction

Perovskites, which were discovered in 1839 and named after the Russian mineralogist Lew A. Perowski, refer to a large class of materials (ternary oxides, nitrides and halides) with the same type of crystal structure as calcium titanium oxide (CaTiO_3). Halide perovskites can be roughly divided into alkali-halide perovskites and organometal halide perovskites. The first alkali-halide perovskite with the chemical formula

*Corresponding authors: fenga@ifm.liu.se (FG); yizhengjin@zju.edu.cn (YJ)

of CsPbX_3 ($X = \text{Cl}, \text{Br}$ or I) was synthesized more than half a century ago. The photoconductivity observed from CsPbX_3 perovskites suggests that these colored materials can behave as semiconductors [1]. By replacing cesium with methylammonium (CH_3NH_3^+) cation, Weber first synthesized organometal halide perovskites in 1978 [2]. Unlike the popular oxide perovskites, halide perovskites received little attention until layered organometal halide perovskites were reported to exhibit a semiconductor-to-metal transition with increasing dimensionality. By increasing the number of inorganic layers in $(\text{C}_4\text{H}_9\text{NH}_3)_2(\text{CH}_3\text{NH}_3)_{n-1}\text{Sn}_n\text{I}_{3n+1}$ layered perovskites, these materials could transit from insulator to metal [3]. This property was considered to be important to achieve high-temperature superconductors based on organometal halide perovskites. The organometal halide perovskites with different dimensionality were firstly employed in optoelectronic devices by Mitzi and co-workers, who examined their applications for light-emitting diodes (LEDs) and thin film transistors (TFTs) [4, 5].

Although organometal halide perovskites have been studied for decades, their photovoltaic applications were not demonstrated until 2009 [6]. Since late 2012, the photovoltaic community has paid increasing attention to organometal halide perovskites [7, 8]. It has been demonstrated that the binding energy of the excitons produced by light absorption in methylammonium perovskites is comparable to the room temperature thermal energy of ~ 25 meV ($30\text{--}50$ meV for triiodide perovskite [9] and 55 meV for chlorine-containing perovskite [10]), meaning that most of the photo-induced excitons will dissociate very rapidly into free carriers at room temperature. Small effective mass of the electrons and holes in organometal halide perovskites results in high charge carrier mobilities (~ 10 $\text{cm}^2 \text{V}^{-1} \text{S}^{-1}$) [11]. As revealed independently by Snaith's group and Sum's group in 2013, solution processed methylammonium based perovskites also exhibit extremely long and balanced charge carrier diffusion lengths (~ 1000 nm for $\text{CH}_3\text{NH}_3\text{PbI}_{3-x}\text{Cl}_x$ and ~ 100 nm for $\text{CH}_3\text{NH}_3\text{PbI}_3$) [12, 13]. As a result of these unique properties and low processing cost, organometal halide perovskites are considered as a dream material for solution-processed photovoltaics.

In this chapter, we will start with a brief summary of the perovskites in photovoltaic applications, followed by an introduction to the optical, electrical characteristics of organometal perovskites. The development of device architectures as well as the deposition technologies for organometal halide perovskites are discussed in details. In the end, challenges facing the commercialization of perovskite solar cells and possible solutions are discussed.

13.2 Fundamentals of Organometal Halide Perovskite Solar Cells

13.2.1 Brief History of Perovskite Solar Cells

The progress of perovskite solar cell efficiencies in the past five years is illustrated in Figure 13.1. The organometal halide perovskite solar cells was first demonstrated by Miyasaka *et al.*, who pioneered the methylammonium perovskite $\text{CH}_3\text{NH}_3\text{PbX}_3$ ($X = \text{I}, \text{Br}$) dye sensitized solar cells (DSSCs) based on mesoporous titanium oxide (TiO_2) photoanodes [6]. The power conversion efficiencies (PCEs) were 3.81% for $\text{CH}_3\text{NH}_3\text{PbI}_3$ and 3.13% for $\text{CH}_3\text{NH}_3\text{PbBr}_3$ in a liquid electrolyte configuration. In 2011, utilizing 2–3 nm sized $\text{CH}_3\text{NH}_3\text{PbX}_3$ nanocrystals and optimized titania surface, Park *et al.* improved the PCE of $\text{CH}_3\text{NH}_3\text{PbI}_3$ based liquid DSSCs to 6.54% [14]. However, the perovskite absorbers dissolve or decompose very quickly (several minutes) due to the liquid electrolyte used in the cells and hence the device stabilities were poor in above two cases.

Grätzel and Park made a breakthrough in both device efficiency and device stability by replacing the problematic liquid electrolytes with a solid-state hole transporting material 2,2',7,7'-tetrakis-(N,N-dimethoxyphenyl-amine)-9,9'-spirobifluorene (spiro-MeOTAD) [8]. At the same time in mid-2012, Snaith *et al.* achieved a device efficiency up to 10.9% by using an insulating mesoporous aluminum oxide (Al_2O_3) instead of TiO_2 scaffold [7]. In their report, a mixed-halide $\text{CH}_3\text{NH}_3\text{PbI}_{3-x}\text{Cl}_x$ was used as the light harvesting absorber. This result also established that the perovskite materials could behave as n-type

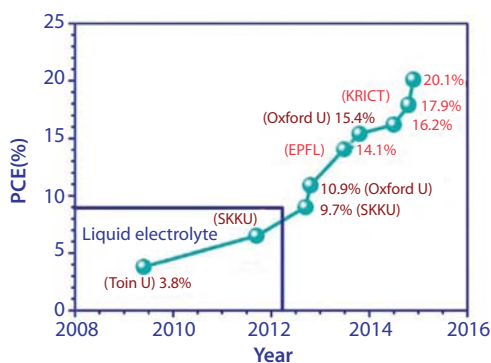


Figure 13.1 The reported and certified efficiencies (red values) of organometal halide perovskite solar cells since 2009.

semiconductors, transporting electrons. These two reports sparked an explosion of research activities on the materials and photovoltaic devices of perovskites. After that, several milestones in device performance are witnessed in the last two years. In May 2013, a two-step sequential deposition technology, which was originally developed by Mitzi and coworkers, was introduced by Grätzel's group to fabricate perovskite solar cells [15–17]. This deposition technology significantly improved film morphology of triiodide perovskites. A champion PCE of 15% with high reproducibility and a certified device efficiency of 14.1% were achieved. Further studies demonstrated that perovskites exhibit ambipolar behavior, meaning that these materials can transport both electrons and holes between the cell terminals [18]. This property makes it possible to reduce the thickness of scaffold and ultimately avoid the use of mesoporous structure without sacrificing efficiency. In the middle of 2013, Snaith and co-workers successfully achieved a well performing device with a PCE of 15.4% based on a simple planar structure by dual-source vapor deposition [19].

With the innovation in materials science, film deposition, interface engineering and device fabrication technologies, extremely rapid progress and remarkable synergistic achievements were made during the last two years with a certificated PCE reaching 20.1% in 2014 (Figure 13.1). Although it is still at an early stage for the commercialization of perovskite-based solar technology, an increasing number of start-ups are already starting to investigate its commercial potentials.

13.2.2 Crystal Structure and Optoelectronic Properties of Perovskites

Generally, the organometal halide perovskites can be described by the chemical formula AMX_3 , where A and M are organic and metal cations and X is a halogen anion that binds to both cations, as shown in Figure 13.2(a). The crystal structure and physical properties of organometal halide perovskites can be finely tuned by changing the tolerance factor t . The tolerance factor t is defined as the ratio of the bond length A-X to M-X ($t = (R_A + R_X) / \sqrt{2}(R_M + R_X)$), where R_A , R_M , and R_X are the ionic radii of A, M, and X. The relative ion size required for the stable cubic perovskite structure is stringent and slight distortion will produce distorted versions with lower-symmetry. A t value lies in the range 0.89–1.0 usually results in a cubic structure, while a lower t value gives less symmetric tetragonal or orthorhombic structures [20].

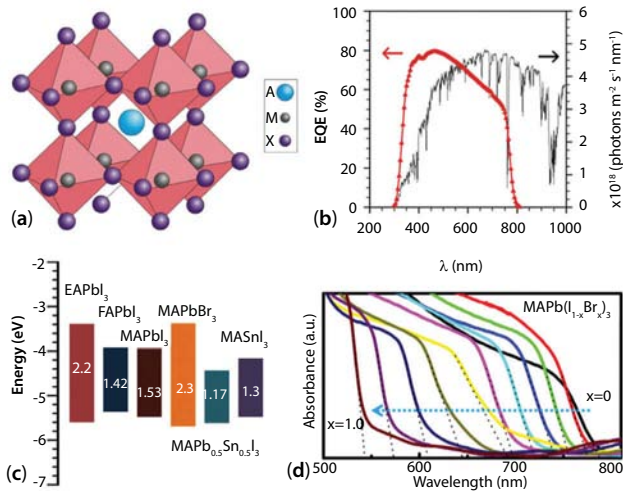


Figure 13.2 (a) The crystal structure of typical cubic organometal halide perovskite. Reprinted from Ref. [25]. (b) External quantum efficiency measured for a $CH_3NH_3PbI_3$ perovskite solar cell and AM 1.5 G solar cell spectra. Reprinted from Ref. [26]. (c) Schematic energy level diagram of EAPbI₃, FAPbI₃, MAPbI₃, MAPbBr₃, and MAPb_{1-x}Sn_xI₃, respectively. (d) UV-vis absorption spectra for different $TiO_2/CH_3NH_3Pb(I_{1-x}Br_x)_3$ films on the FTO glass. Reprinted from Ref. [38].

The commonly used photoactive methylammonium based perovskites $CH_3NH_3PbI_3$ and $CH_3NH_3PbI_{3-x}Cl_x$ have a similar small direct bandgap of 1.50–1.55 eV corresponding to an absorption onset of ~ 800 nm and making them excellent light absorbers over the whole visible solar spectrum (Figure 13.2(b)) [7, 21]. The absorption coefficient of $CH_3NH_3PbI_3$ perovskites was estimated to be $1.3 \times 10^5 \text{ cm}^{-1}$ at 550 nm, which was similar to those of conventional thin film photovoltaic materials [22]. Due to the reasonably high absorption coefficient of perovskite in the entire visible region, it is possible to form a sufficiently thin yet strongly absorbing film. However, for a single junction solar cell, considering the balance of the solar light absorption and the voltage of the cell device, the optimal bandgap of the light harvesting absorber is around 1.4 eV [23]. The bandgap around 1.55 eV of commonly used $CH_3NH_3PbI_3$ is not optimum for panchromatic absorption (Figure 13.2(b)). Moreover, due to the optical absorption overlapping between perovskite and silicon (1.12 eV) materials, the combination of perovskites solar cells with commercialized crystalline-silicon solar cells in a tandem architecture is restricted [24]. Therefore, bandgap engineering is required to adjust the absorption of perovskites to longer or shorter wavelengths without sacrificing the absorption coefficient.

As can be seen from Figure 13.2(c), the bandgap of organometal halide perovskites can be easily tuned by varying the combination of the cationic and anionic components in the structure. The electronic structures of organometal halide perovskites are dominated by the characteristics of the M-X bond based on first-principle studies: the valence-band maximum is characterized as an antibonding hybrid state of the M-*ms* (Pb: $m = 6$) and the X-*np* ($n = 3-5$) orbitals in the M-X chains. In $\text{CH}_3\text{NH}_3\text{PbI}_3$, it was estimated that the valence band maximum (VBM) consisted mainly of the s-antibonding states of Pb 6s and I 5p orbitals, and the conduction band minimum (CBM) was composed primarily of the s-antibonding states of Pb 6p and I 5s orbitals [27].

Although the organic cation does not play a major role in determining the band structure in perovskite structure with a particular metal and halide, the alteration of organic cation size will expand or contract the whole lattice, changing the M-X bond length or angle and thereby influencing the bandgap [28]. For example, several recent studies demonstrated that the replacement of methylammonium with a larger organic cation of formamidinium (FA) in $\text{CH}_3\text{NH}_3\text{PbI}_3$ would result in a decreased bandgap from 1.50–1.60 eV to 1.42–1.48 eV and push the absorption edge of perovskite towards the infrared region (Figure 13.2(c)) [29–31]. The decrease in the bandgap originates from the torsion of the lattices as a result of the varied distance between metal ions and halides. However, given a 3-dimensional perovskite structure, the allowed size range to broaden the bandgap is relatively small (1.6–2.6 Å) due to the strict tolerance factor as defined previously. If the size of organic cation is too large, lower dimensional layered or confined perovskite will be formed due to the instability of 3D crystal structure. If it is too small, the lattice would be too strained to form [32]. For example, a larger ethylammonium (EA) cation based wider bandgap perovskite has been explored previously in solar cells. Unfortunately, in this situation a 2H-type structure is formed because the size of the EA cation is too large to maintain the 3D perovskite structure. As a result, the isotropic charge transport and conductivity of the resulting perovskite dramatically decrease [33].

Another effective approach to tailor the bandgap of the perovskite is direct modification of the M-X bond. It has been reported that by stoichiometrically mixing the divalent metal iodides of Sn and Pb with MAI, perovskite of $\text{CH}_3\text{NH}_3\text{Sn}_{1-x}\text{Pb}_x\text{I}_3$ with a tunable bandgap between 1.17 and 1.55 eV can be easily synthesized [34, 35]. However, the Sn^{2+} cation is easily oxidized to Sn^{4+} and p-dope the perovskite, resulting in significant loss of device performance [36]. In addition to the cation replacement, halide anion substitution in the perovskite structure is also effective to tune the

bandgap. With increasing atomic size of the anions from chlorine (Cl) to bromine (Br) to iodine (I), the absorption spectra of halide perovskites shift to longer wavelength. The decrease in the bandgap stems from the increase in the covalent bonding of the halogen bonding with lead, as a result of the decrease in the electron-negativity of the halogen atom [37]. Although it is very difficult to tune the bandgap in the case of iodide-chloride mixed perovskites, the bandgap engineering of perovskite based on iodide-bromide or bromide-chloride mixture is very efficient [29, 38]. As shown in Figure 13.2(d), several recent studies have shown that the bandgap can be continuously tuned by incorporating Br into I-based perovskites [38]. As a result, perovskites with optical absorption covering almost the entire visible spectrum can be obtained by reasonably manipulating the ratio between two halides.

In addition, electrical properties, including charge separation and charge transport, are also critical to the performance of solar cells. Previous studies indicated that the photo-generated electron-hole pair in the $\text{CH}_3\text{NH}_3\text{PbI}_3$ perovskite is a Mott-Wannier exciton with a low banding energy of ~ 50 meV [27]. This means that the charge generation and separation can occur within the absorber and voltage drop due to the driving force needed to dissociate exciton can be avoided. The electron and hole transport properties can be measured in the perovskite layers by employing selective electron or hole quencher in a bilayer configuration, as shown in Figure 13.3(a) [12, 13]. Primary studies by Sum and coworkers based on femtosecond transient optical spectroscopy clearly revealed long and balanced electron-hole diffusion lengths of at least 100 nm in solution processed $\text{CH}_3\text{NH}_3\text{PbI}_3$ (Figure 13.3(b)) [13]. At the same time, Snaith and coworkers also performed optical quenching experiments and demonstrated that the mixed halide perovskite, $\text{CH}_3\text{NH}_3\text{PbI}_{3-x}\text{Cl}_x$, exhibits an extremely long diffusion lengths of >1 μm (Figure 13.3(c)) [12]. The diffusion lengths of perovskites are much longer than most other solution processed materials (e.g., ~ 10 nm for organic semiconductor and ~ 80 nm for quantum dots) [39, 40].

Charge carrier mobility of perovskites was elucidated by Herz *et al.* in collaboration with Snaith by using transient THz spectroscopy [11]. Their work shows that both monomolecular and bimolecular charge carrier recombination rates are abnormally low in methylammonium lead halides. The bimolecular recombination rates defy the Langevin limit by at least four orders of magnitude. And the diffusion lengths are only limited by monomolecular decay process under operating conditions. The lower bounds for the high-frequency charge mobility were determined to be 11.6 $\text{cm}^2 \text{V}^{-1} \text{s}^{-1}$ for $\text{CH}_3\text{NH}_3\text{PbI}_{3-x}\text{Cl}_x$ and 8 $\text{cm}^2 \text{V}^{-1} \text{s}^{-1}$ for $\text{CH}_3\text{NH}_3\text{PbI}_3$ perovskites [11].

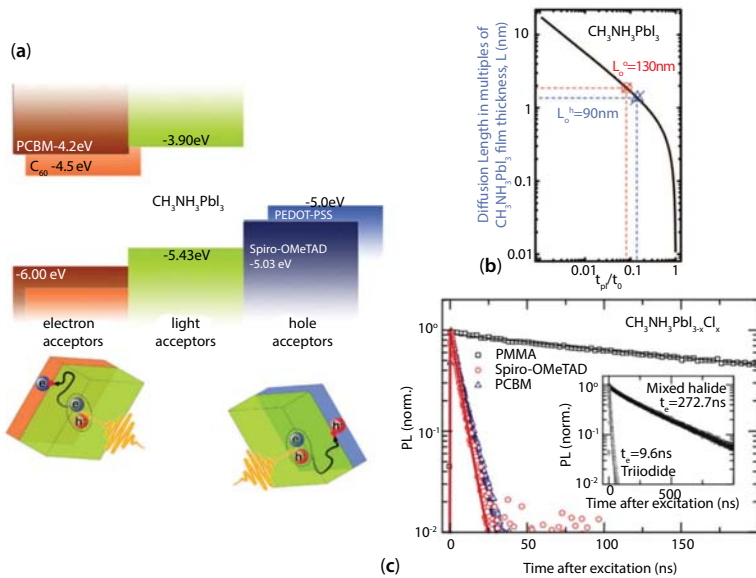


Figure 13.3 (a) Schematic illustration of the energy levels of the heterojunctions and depiction of the exciton generation, diffusion and quenching processes in the respective bilayers. Reprinted from Ref. [13]. (b) A plot of exciton diffusion length of $CH_3NH_3PbI_3$ layer versus PL lifetime quenching ratios. Reprinted from Ref. [13]. (c) Time-resolved PL measurements taken at the peak emission wavelength of the mixed halide perovskite with an electron and hole quencher. Reprinted from Ref. [12].

These values are remarkably high for solution-processed materials. The origins of extremely long electron-hole diffusion lengths stem from the high charge carrier mobility and low bimolecular recombination rates in the perovskites. Combined with weak non-radiative pathways under solar light intensities, it is therefore understandable why the perovskites have excellent photovoltaic performance [41].

13.2.3 Device Architecture Evolution of Solid-State Perovskite Solar Cells

Figure 13.4 shows the evolution of device architectures of solid-state perovskite solar cells. As shown in Figure 13.4(a), most studies in the area of solid-state perovskite solar cells are based on mesoporous titanium oxide (TiO_2) structure with a high-temperature derived compact TiO_2 layer as an electron transporting and hole blocking layer on the fluorine doped tin oxide (FTO) substrates. The anode interface is usually

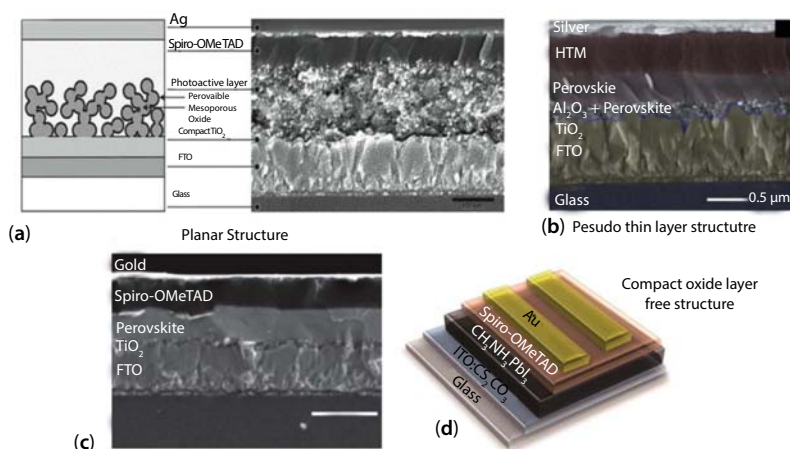


Figure 13.4 (a) Schematic representation of mesoporous structure perovskite solar cells, where the mesoporous oxide is either anatase TiO_2 or Al_2O_3 (left). Cross-sectional SEM image of a full device incorporating mesoporous Al_2O_3 (the scale bar is 500 nm) (right). Reprinted from Ref. [7]. (b–c) Cross-sectional SEM images of perovskite solar cells with pseudo-thin film and planar device structure, respectively. Reprinted from Refs. [44,47]. (d) Schematic illustration of the compact layer free perovskite solar cell. Reprinted from Ref. [50].

modified with solid-state hole transport materials (e.g., spiro-OMeTAD) with appropriate dopants [21, 42]. The TiO_2 mesoporous structure can be replaced by an insulating Al_2O_3 scaffold, revealing that the electron transport could occur through the perovskite film itself, as confirmed by photoinduced absorption spectroscopy measurements of $\text{Al}_2\text{O}_3/\text{CH}_3\text{NH}_3\text{PbI}_{3-x}\text{Cl}_x$ layers [7, 43, 44]. Compared to conventional DSSCs, this meso-superstructured solar cell (MSSC) with perovskite film as absorber exhibits significantly faster charge extraction rates. In addition to Al_2O_3 nanoparticles, there are also several reports of efficient perovskite solar cells utilizing insulating zirconium dioxide (ZrO_2) as the mesoporous scaffold [45, 46]. The employment of insulating Al_2O_3 or ZrO_2 circumvents energy losses at the electron acceptor/absorber interfaces and results in higher open-circuit voltages compared to devices based on TiO_2 mesoporous structure.

In addition to the electron transporting nature of the perovskite, Etgar *et al.* demonstrated that the perovskite could also function as hole transporting material in a device [18]. The perovskite film with a good coverage on the TiO_2 film could result in a thin capping layer and good back contact with the gold electrode, obviating the need for employing an additional hole transporting material. Recently, Han *et al.* reported an all-printable

triple layer perovskite solar cell by utilizing a simple TiO_2 /mesoscopic ZrO_2 /carbon electrode. This structure is hole transport layer free and gives a high certified performance of 12.8% [46]. Based on further understanding of the charge transport properties of perovskite films, Snaith and coworkers firstly fabricated an efficient “flat-junction” thin film solar cell via decreasing the thickness of Al_2O_3 nanoparticle film [44]. In this device configuration shown in Figure 13.4(b), the perovskite absorber performs the tasks of charge separation as well as ambipolar charge transport of both carrier species.

Further explorations into planar architectures have been performed to simplify the cell architecture as motivated by the success of the “pseudo-thin film” perovskite solar cells. This planar architecture avoided the use of any mesoporous structure and perovskite films could be directly deposited on a compact layer coated substrate. As shown in Figure 13.4(c), by carefully optimizing the atmosphere, annealing temperature and initial perovskite film thickness on compact TiO_2 coated substrates, Eperon *et al.* significantly improved the performance of planar heterojunction solar cells and achieved an efficiency of 11.4% using the $\text{CH}_3\text{NH}_3\text{PbI}_{3-x}\text{Cl}_x$ absorber [47]. A jump to a reported efficiency of 15.4% came from better-controlled film morphology via dual-source vacuum evaporation, as demonstrated by the Snaith group [19]. For this cell type, high temperature processed (500°C) compact TiO_2 layer is necessary to achieve highly efficient devices while lower temperature sintered TiO_2 always yields lower efficiency. To solve this problem, Snaith *et al.* developed a low temperature fabrication ($<150^\circ\text{C}$) approach of the TiO_2 compact layer using highly crystalline nanoparticles of anatase TiO_2 in alcoholic solvent combined with a small amount of titanium diisopropoxidebis(acetylacetonate) (TiAcAc). Dense TiO_2 layer obtained from this approach exhibited 100-fold higher conductivity than the high temperature derived TiO_2 and delivered a champion PCE of 15.9% for all-low-temperature processed perovskite devices [43]. Based on this, Yang’s group further increased the conductivity by doping yttrium into the low temperature processed TiO_2 nanoparticles and reduced the work function of ITO substrates with polyethyleneimineethoxylate (PEIE). As a result, they could enhance the electron extraction and transport properties in the planar structure perovskite solar cell. Combined with the optimized film reconstruction process under carefully controlled humidity in air, an average PCE of 16.6% was achieved [48].

In addition to the commonly used TiO_2 , a low-temperature processed ZnO electron transport layer was first employed in planar perovskite solar cells using electrodeposition technology by Kumar *et al.* PCEs of 5.54% and 2.18% on FTO and flexible ITO substrates were obtained respectively

[49]. A similar planar structure device utilizing spincoated ZnO nanocrystal interlayer as electron conductor avoided the high temperature sintering process and improved the PCE of ZnO based device to as high as 15.7%. Devices on flexible devices fabricated on this room-temperature processed ZnO interlayer also displayed PCEs exceeding 10% [48]. However, the device stability, especially the long-term operational stability and thermal stability, is still an issue for TiO_2 and ZnO based planar devices [22, 43]. For example, oxygen vacancy due to the light-induced desorption of surface absorbed oxygen may reduce the TiO_2 -based device stability, and ZnO-based electron conductor may accelerate the thermal decomposition of perovskite films even at a mild temperature of 80°C . Due to the low exciton binding energy in perovskite films, $\sim 98\%$ of the photogenerated excitons are capable to dissociate under normal operating temperatures, suggesting that a high surface area heterojunction formed by n-type electron conductor may not be strictly necessary to separate the excitons [10]. Very recently, compact layer free planar perovskite devices with similar (or slightly decreased) performance compared with devices based on compact n-type metal oxide interlayers were proposed (Figure 13.4(d)). By optimizing the film morphology of perovskites, planar devices based on cesium carbonate (Cs_2CO_3) modified or bare ITO substrates with efficiency of 15.1% and 13.5% were obtained [50, 51]. Devices stability under specific conditions based on this architecture was also improved. Compact-layer-free devices further simplify the device configuration and provide a promising and low-cost fabrication approach for planar perovskite devices.

Another emerging research area is referred to as “inverted” planar device structure, which involves the utilization of commonly used charge transport layers in organic photovoltaics for the implementation of perovskite-based devices. As shown in Figure 13.5(a), Chen and coworkers first developed a perovskite/fullerene planar-heterojunction device consisting of poly(3,4-ethylenedioxythiophene):poly(styrenesulfonic acid) (PEDOT:PSS) and fullerene derivatives of (6,6)-phenyl C_{61} -butyric acid methyl ester (PC_{61}BM) and indene- C_{60} bisadduct (ICBA) as the hole transport and electron transport layer respectively [52]. As can be seen from Figure 13.5(b), a donor-acceptor planar heterojunction was formed between the perovskite and the electron transport layer. They proposed that under light irradiation, the electrons and holes can be efficiently separated at the interfaces and collected by the electrodes, resulting in the photovoltaic effect. A thermally evaporated thin bathocuproine (BCP) film was used as exciton blocking layer in this device configuration. Through optimizing thickness of the electron transport layer and the processing conditions of perovskite films, a PCE of 3.9% has been delivered. Almost

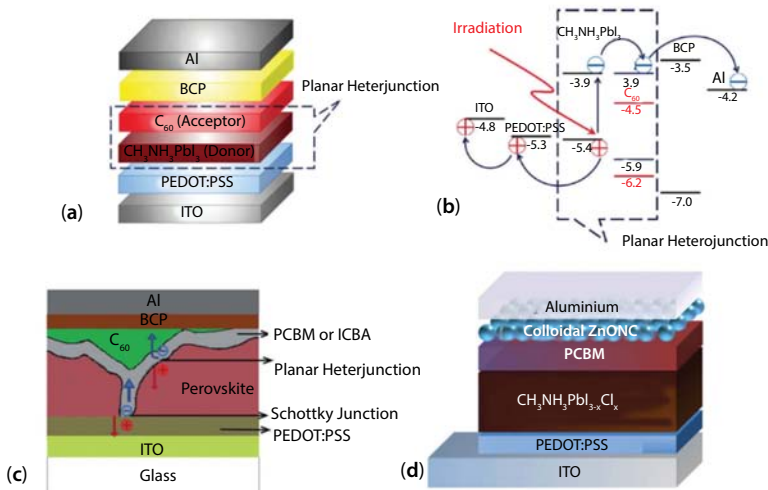


Figure 13.5 (a) Schematic device configuration and (b) energy levels of each layer used in the perovskite/fullerene planar heterojunction solar cells. Reprinted from Ref. [52]. Schematic device structure of perovskite/fullerene planar heterojunction with (c) a bilayer acceptor and (d) ZnO nanocrystal modified cathode interface. Reprinted from Refs. [53,55].

at the same time, Sun *et al.* succeeded in making a thicker perovskite film by introducing two-step sequential deposition into the planar device and increased the device performance to 7.41% [22]. It was also noticed by Wang *et al.* that the perovskite morphology on PEDOT:PSS is sensitive to the composition variation of precursors and a non-stoichiometry precursor with a molar ratio of 0.6–0.7 resulted in the best surface coverage and device performance [53]. As depicted in Figure 13.5(c), a double layer fullerene with a spun PCBM or ICBA followed by a thermal evaporated C_{60} was used as the electron transport layer. This device structure might include two types of perovskite/fullerene planar heterojunction and PEDOT:PSS/fullerene Schottky junction devices connected in parallel. The double fullerene layer of C_{60} or PCBM layer could effectively passivate the defects in perovskite films and lead to two orders of magnitude lower trap density in the whole defect spectral range, resulting a high PCE of 12.2% with a large fill factor of 0.8.

Snaith and coworkers further demonstrated the capability of materials used in organic photovoltaics, including nickel oxide (NiO_x) and vanadium oxide (V_2O_5) hole transport layers and poly[9,9-bis(30-(N,N-dimethylamino)propyl)-2,7-fluorene]-alt-2,7-(9,9-dioctylfluorene)] (PFN) electron transport layer in perovskite-based devices [54]. Although the most

efficient device with a PCE of 9.8% is still based on PEDOT:PSS and PCBM, PL quenching results in this work removed the barriers to adoption of the perovskite technology by the organic photovoltaic community. In their report, a low temperature (130°C) deposited TiO_x interlayer was added between the PCBM and the top electrode to further improve the cathode contact property and air stability.

However, due to the high temperature sensitivity of the diffusion lengths of perovskite films, any post-annealing process at temperature above 100°C on the perovskite films will result in decrease of the charge carrier diffusion lengths [55]. As shown in Figure 13.5(d), Bai *et al.* first introduced a room temperature deposited ZnO nanocrystal films to preserve the diffusion lengths and modify the cathode interface. They achieved planar devices with excellent air stability and high performance with a champion PCE of 15.9% [55]. From device stability and commercialization points of view, devices based on chemically stable inorganic semiconductors, especially p-type NiO_x hole transport interlayers, are more favorable compared to the commonly used organic materials. However, the device performance of NiO_x -based perovskites, in particular solution processed NiO_x , is still not satisfactory compared to the commonly used organic hole conductors [56–58]. The main reasons stem from the poor perovskite film morphology and poor surface coverage, leading to direct contact between the PCBM and metal oxides and generating a shunting path. The high series resistance caused by low conductivity of the NiO_x film is another reason for the loss of device performance. Very recently, high performance inverted planar perovskite devices based on solution processed copper doped NiO_x film exhibited an impressive PCE up to 15.4% and decent environmental stability [59]. This result demonstrates the potential of using inorganic interlayers, especially p-type metal oxide interlayers, to replace the problematic organic materials.

13.3 Deposition Methods and Crystal Engineering of Organometal Halide Perovskites

13.3.1 One-Step Precursor Deposition

Initial publications on perovskite solar cells were mostly based on direct spincoating of the mixed precursors of RAX (RA: methylamine, formamidine, X: I, Br) and PbX_2 (X: I, Br, Cl) with stoichiometry (1:1) or non-stoichiometry (3:1) mole ratio on the desired substrates, as depicted in Figure 13.6(a) [7, 21, 38]. Commonly used solvents are polar aprotic, such

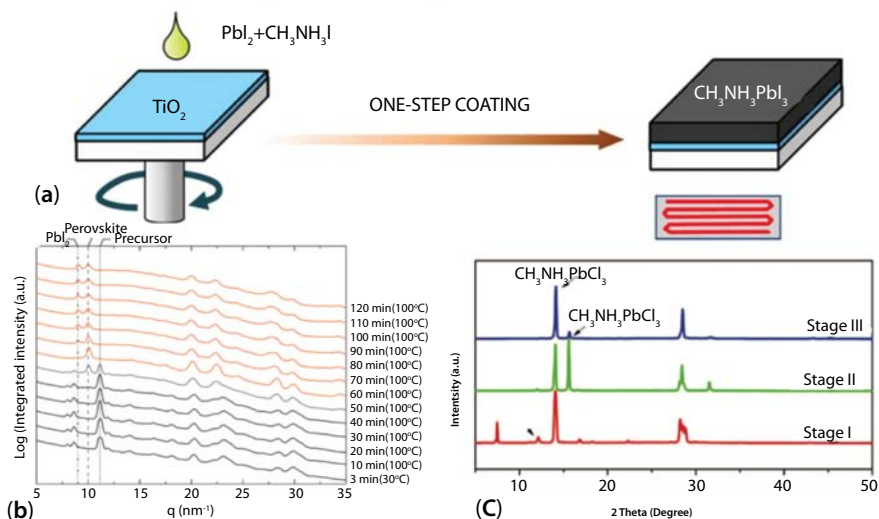


Figure 13.6 (a) One-step solution deposition procedures to deposit CH₃NH₃PbI₃ perovskite films. Reprinted from Ref. [62]. (b) Azimuthally integrated GIWAXS intensity plots of perovskite films with different annealing processes. Reprinted from Ref. [63]. (c) XRD patterns corresponding to perovskite film evolution with different annealing time under controlled relative humidity of 30 ± 5% (stage I: 20 min, stage II: 60 min, stage III: 85 min). Reprinted from Ref. [48].

as N, N-dimethylformamide (DMF), γ -butyrolactone (GBL), dimethylsulfoxide (DMSO), *etc.* Generally, simple drying and annealing processes are necessary to evaporate the residual solvents and complete crystallization of the perovskites. To obtain high quality perovskite films with better surface coverage, especially for planar structures, optimization of the precursor concentration and spincoating conditions are necessary. In the case of direct spincoating on mesoporous structure, excess solution on the top of the film may act as a reservoir during the spincoating process and the infiltration within the mesoporous structure depend critically on the concentration, solvent, and spincoating speed [42]. Due to different surface properties of the substrates, the processing parameters also need to be separately optimized for each kind of underlying layers [52, 56, 60, 61].

The annealing process of the one-step deposition technology is of crucial importance to the properties of crystalline perovskite films as well as the device performance. *In situ* time-resolved grazing incidence wide-angle X-ray scattering (GIWAXS) was employed to probe the structure evolution of CH₃NH₃PbI_{3-x}Cl_x perovskites during the thermal annealing process, as shown in Figure 13.6(b). Three distinct crystalline structures, including crystalline precursors, perovskites, and the degradation product

(PbI_2), were observed during thermal annealing. It was found that the evolution between three structures distinctly depends on the annealing conditions [62]. Optimal annealing temperature, annealing time, and the moisture in the environment dominated the perovskite film coverage, composition, and the performance of the final devices [63]. Studies by Dualeh *et al.* gave further detailed information on the influence of annealing temperature during the conversion process. They also pointed out that a minimum temperature of 80°C is needed to sufficiently form the crystalline perovskites but a higher temperature (above 120°C) will cause increased decomposition of perovskites to PbI_2 [64].

Due to the hygroscopic property of $\text{CH}_3\text{NH}_3\text{I}$ in the precursor, the moisture could result in accumulation of the water within grain boundaries, inducing grain boundary creep and merging adjacent grains during the perovskite crystallization. This effect not only increases the grain size and reduces pinhole formation but also enhances the charge carrier diffusion lengths with promoted perovskite grain growth [48, 65]. However, higher humidity in the environment will cause significant decomposition of perovskite films. As such, humidity conditions during the perovskite film growth need to be very carefully controlled. When the perovskite precursor was thermally annealed under a controlled relative humidity of $30 \pm 5\%$, as evidenced by X-ray diffraction (XRD) measurements, three distinct stages exhibiting different colors from light yellow to dark brown can be observed (Figure 13.6(c)). Devices based on the perovskite films obtained under the controlled humidity exhibit $\sim 20\%$ performance enhancement compared with the control devices [48].

Compared with the one-step precursor deposition, a better control on the crystalline perovskite formation and growth could be achieved through sequential deposition method. This technology was first used by Burschka *et al.* to fabricate mesoporous structure perovskite solar cells [16]. As shown in Figure 13.7(a), the PbI_2 films are first spincoated from DMF solution onto the substrates under appropriate conditions. After drying or mild annealing, the yellow colored substrates are dipped into a solution of $\text{CH}_3\text{NH}_3\text{I}$ in iso-propanol, and dark brown $\text{CH}_3\text{NH}_3\text{PbI}_3$ perovskite quickly forms in a few seconds and transform completely in several minutes (Figure 13.7(b)). With improved infiltration rate and film morphology, this technology achieved a highly crystalline film with complete coverage, and hence greatly increased the performance and reproducibility of mesoporous structured devices [16, 66]. However, unlike fast and complete conversion on mesoporous substrates, initial work by Mitzi and coworkers on sequential deposition technology demonstrated that 1–3 h conversion time was required for the planar structure [15]. A short dipping

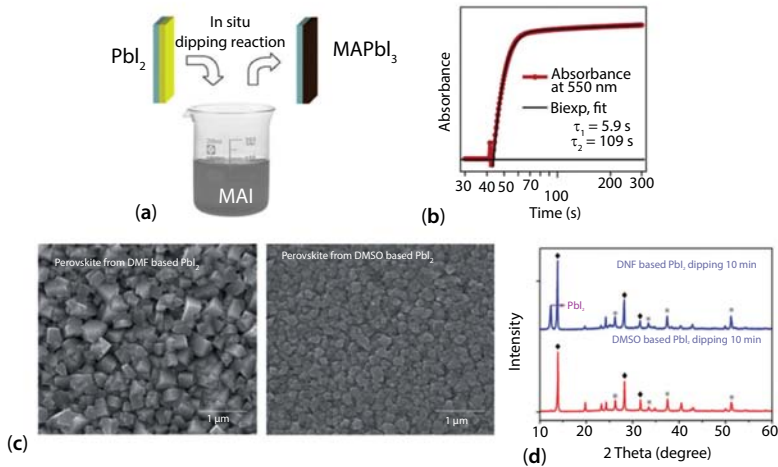


Figure 13.7 (a) Schematic representation of the sequential deposition procedure to prepare $\text{CH}_3\text{NH}_3\text{PbI}_3$ perovskite films. Reprinted from Ref. [66]. (b) Change in absorbance at 550 nm of a perovskite film during the film transformation. Reprinted from Ref. [16]. (c) SEM images and (d) XRD patterns of perovskite films obtained from DMF and DMMSO based PbI_2 films. Reprinted from Ref. [68].

time only converts part of PbI_2 and results in a perovskite- PbI_2 mixture with inconstant proportion from batch to batch, which is not favorable for the reproducibility of device based on planar structure. Limited by the finite reaction interface area in a relative thick film (several hundreds of nanometers) on the planar substrate, the prolonged two-step process often results in rough films that frequently peel off from the substrate [16, 67].

The difficulty to control the crystal growth process of the sequential deposition on planar substrates stems from the crystals with different sizes due to the easy crystallization nature of PbI_2 . The large crystals will decrease the accessibility of $\text{CH}_3\text{NH}_3\text{I}$ to the inner lead sites, resulting in incomplete conversions. Recently, Wu *et al.* significantly improved the reproducibility through replacing the commonly used solvent of DMF by DMSO [68]. Due to the improved coordination ability between Pb and the solvent molecules (1:1 for DMF and 1:2 for DMSO), the crystallization of PbI_2 can be efficiently inhibited, resulting in uniform amorphous PbI_2 films on the substrates. Compared with perovskite films obtained from DMF- PbI_2 films, the resulted perovskite films exhibit flat surface morphology and uniform size distribution of perovskite crystals when amorphous PbI_2 films were used (Figure 13.7(c)). Most importantly, there is no unreacted PbI_2 left after the reaction, as shown in Figure 13.7(d). It has been reported that the inclusion of chloride into the film benefits charge transport and

reduces recombination in the perovskite solar cells. With addition of PbI_2 , the solubility of PbCl_2 in DMF can be improved and after exposing the obtained film to $\text{CH}_3\text{NH}_3\text{I}$ solution, mixed perovskite $\text{CH}_3\text{NH}_3\text{PbI}_{3-x}\text{Cl}_x$ can be successfully obtained [69]. As demonstrated by a recent report, $\text{CH}_3\text{NH}_3\text{PbI}_{3-x}\text{Cl}_x$ can also be deposited by dipping the PbI_2 film into a mixture solution of $\text{CH}_3\text{NH}_3\text{Cl}$ and $\text{CH}_3\text{NH}_3\text{I}$ in isopropanol [70]. The PbI_2 can be fully converted to crystalline perovskite within 5 min, and the resulting films demonstrate complete coverage and extended charge diffusion lengths. Combined with increased absorption and reduced device series resistance, the photocurrent was significantly improved to over 22 mA cm^{-2} , enabling a PCE close to 15%.

13.3.2 Vapor Assisted Solution Process and Interdiffusion Method

Considering the limitations of one-step and sequential deposition on the controllability of film quality and the reproducibility of device performance for the planar structure, more novel film deposition methods have been developed in the preparation of high quality perovskite films and devices with planar architectures. In a recent report, Yang's group demonstrated a novel low temperature solution approach based on sequential deposition, known as the vapor assisted solution process [67]. In this method, PbI_2 films were solution deposited on compact TiO_2 coated FTO glasses, followed by thermal annealing in $\text{CH}_3\text{NH}_3\text{I}$ vapor at 150°C in N_2 atmosphere for 2 h to obtain the perovskite films, as depicted in Figure 13.8(a). This approach takes advantage of the kinetic reactivity of $\text{CH}_3\text{NH}_3\text{I}$ and thermodynamic stability of perovskite films during the in situ growth process. The perovskite films derived from this method exhibit well-defined grain structure with grain sizes up to micrometers, uniform surface morphology, full surface coverage, and complete transformation of PbI_2 films. Devices based on the high-quality perovskite films showed an impressive PCE of 12.1% in a planar configuration.

In addition to the vapor assisted solution process, a low-temperature solution processed method incorporating an interdiffusion process of PbI_2/MAI stacking layer films to fabricate planar perovskite device was developed by Huang's group [71, 72]. As shown in Figure 13.8(b), PbI_2 and MAI were first dissolved in DMF and iso-propanol solvents with varied concentrations. A supersaturated hot solution of PbI_2 was spincoated on a PEDOT:PSS covered ITO substrate, followed by the spincoating of MAI solution on top of the quickly dried pin-hole free PbI_2 film. Due to the low solubility of PbI_2 in iso-propanol, the second MAI spincoating step

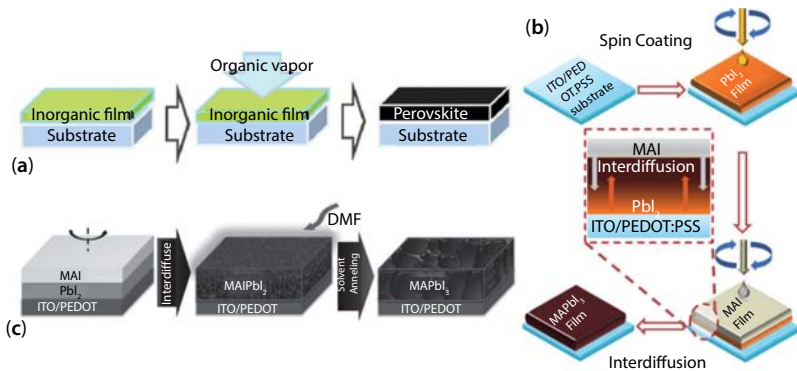


Figure 13.8 Schematic illustration of (a) the fabrication procedure of vapor assisted solution process and (b) interdiffusion process. Reprinted from Refs. [67,72]. (c) Schematic illustration of the solvent annealing method based on the interdiffusion approach. Reprinted from Ref. [73].

has little damage on the film underneath. The obtained bilayer film was then thermally annealed at a relatively low temperature of 100°C for ~2 h, which is critical to improve the device performance. Thermal annealing here will drive the interdiffusion of two precursors and ensure complete reaction between the compact PbI₂ film and MAI layer. In addition, the annealing process also induces the recrystallization and grain growth in the perovskite films. Unlike rough perovskite films originating from the randomly distributed crystal grains obtained from sequential deposition, perovskite films fabricated from the interdiffusion method exhibit a continuous and uniform surface morphology with a film thickness variation of less than 20 nm.

The thickness of perovskite films are ~300 nm for most of the best-performing devices. To absorb the sunlight completely, especially in the red to infrared range, a thicker perovskite film up to 1 μm is desirable. However, grain sizes of the solution-processed perovskite films are always around a couple of hundred nanometers due to the quick reaction of compositions in the precursor and the quick crystallization process of perovskite materials. Recently, Xiao *et al.* introduced a solvent annealing method into the interdiffusion process to further increase the crystallinity and grain size of CH₃NH₃PbI₃ films [73]. During the interdiffusion process, a small amount of solvents with large solubility to MAI and PbI₂, DMF and DMSO for example, were simultaneously introduced to provide a wet environment. As a result, the precursor ions and molecules could diffuse much longer distance than in the all solid-state thermal annealing process,

as depicted in Figure 13.8(c). Through optimizing the conditions of the solvent annealing process, average grain size of the perovskite films can be increased to 1 μm . After solvent annealing, the hole mobility of perovskite films increased from 30 to 45 $\text{cm}^2 \text{V}^{-1} \text{s}^{-1}$ and the extrinsic hole concentration decreased from 1.8×10^{14} to $6.2 \times 10^{13} \text{ cm}^{-3}$. In addition, the charge carrier diffusion length also improved to above 1 μm , as estimated from the transient photocurrent techniques. All the variations can be attributed to the larger grains with better crystallinity and decreased grain boundary density in the solvent annealed films. The champion device with inverted planar structure delivered an efficiency of 15.6% and the device with 1 μm thick perovskite film exhibited slightly dropped efficiency of 14.5%.

13.3.3 Vacuum Deposition

Most of the perovskite solar cells are fabricated based on solution deposition now. Apart from this, vacuum thermal evaporation has also been employed to produce perovskite films with high purity and homogeneous morphology. Followed the pioneering works of Salau [74] and Mitzi [75] on the vapor deposition of perovskite films under vacuum, Liu *et al.* modified the deposition conditions and developed a dual-source vapor deposition technique to prepare mixed halide perovskite films [19]. As shown in Figure 13.9(a), $\text{CH}_3\text{NH}_3\text{I}$ and PbCl_2 were co-evaporated from separate crucibles with an optimized molar ratio, followed by a mild annealing process to crystallize the as-deposited perovskites. Based on this dual source vapor deposited perovskite films, an efficient planar solar cell with an efficiency of 15.4% has been achieved. The vapor deposition could provide good control on the nominal stoichiometry of two reactants and is not limited by the solubility of materials used in the precursors. In addition, vapor deposition is efficient to prepare extremely uniform layered multi-stack thin films over large areas compared with the solution processes (Figure 13.9(b) and (c)). With the development of instrumentation and methodology, centimeter-scale ($5 \times 5 \text{ cm}^2$) films with superior uniformity, good crystallinity and high reproducibility were deposited [76]. It's also demonstrated that the vacuum deposited films exhibit significantly improved charge carrier mobility and increased charge carrier diffusion lengths ($\sim 3 \mu\text{m}$). Another example of dual source vapor deposition was demonstrated by Bolink and coworkers, who directly sublimated PbI_2 and $\text{CH}_3\text{NH}_3\text{I}$ under vacuum onto organic hole transport layer coated ITO substrates followed by a thin PCBM film on top as the electron transport layer [77]. In this way, an inverted planar perovskite solar cell with a high efficiency of 12% was achieved. Very recently, Lin *et al.* demonstrated in detail how the p-type

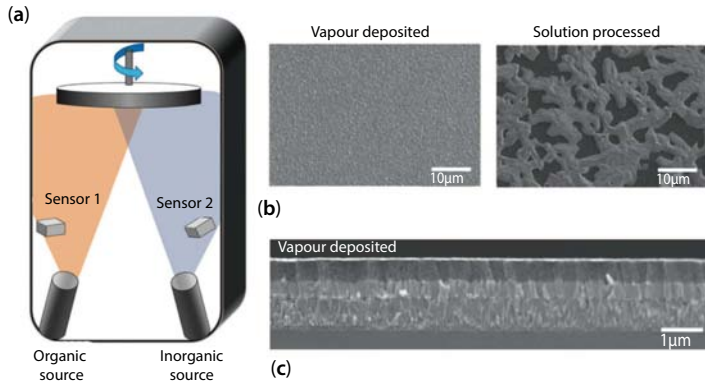


Figure 13.9 (a) Dual-source thermal evaporation system for perovskite film deposition, where the organic source and inorganic source is MAI and PbCl_2 , respectively. (b) SEM top views of a vapor-deposited and a nonoptimized one-step solution processed perovskite film. (c) Cross-sectional SEM image under high magnification of complete solar cell constructed from a vapor-deposited perovskite film. Reprinted from Ref. [19].

organic hole transport interlayers affect the composition, crystal structure of thermally evaporated perovskite films and hence the performance of planar devices [78]. An extremely low exciton-binding energy of ~ 2 meV for vacuum deposited perovskites has been estimated, confirming that the perovskite systems are predominantly non-excitonic. With optimized thickness of the perovskite film ~ 370 nm, a maximum PCE of 16.5% with an internal quantum efficiency (IQE) near 100% has been achieved.

Despite promising advantages of co-evaporation methods, random diffusion of $\text{CH}_3\text{NH}_3\text{I}$ inside the chamber will cause difficulty in monitoring and controlling the deposition rate using quartz microbalance sensors. To solve this problem, a novel method via a layer-by-layer sequential vacuum sublimation was developed by Chen *et al.* [79] In this procedure, a simple one material at a time deposition approach was used. Typically, PbCl_2 films were first thermally sublimed onto ITO substrates coated with PEDOT:PSS, and then the $\text{CH}_3\text{NH}_3\text{I}$ was vapor deposited onto the PbCl_2 layer with the substrate temperature kept at 75°C . The PbCl_2 will quickly react with the $\text{CH}_3\text{NH}_3\text{I}$ vapor and the perovskite thin films can be in situ formed. The temperature proves critical to extend the reaction penetration. The reaction penetration depth is ~ 25 nm at room temperature and more than 150 nm when the substrate temperature increases to 65 – 85°C . A post annealing process at 100°C in vacuum was applied for a very short period to fully crystallize the perovskite films and remove the residual $\text{CH}_3\text{NH}_3\text{I}$ on the surface. Uniform thin films with unusual large-scale homogeneous

crystalline structures were obtained, and inverted planar devices based on the sequential vacuum deposition perovskite films delivered a remarkable performance with a PCE as high as 15.4%.

13.3.4 Solution and Crystal Engineering

One of the most attractive features for perovskites is that high performance devices can be easily fabricated through cost-effective low-temperature solution processes. Although it is more difficult to control film quality compared with vacuum deposition, many promising techniques have been developed in the past few years. These techniques enable better control of morphology and uniformity of the solution processed perovskite thin films so that the film quality is comparable with those fabricated from thermal sublimation technologies.

The formation and crystal growth of perovskite films from the simple one-step deposition could be affected by many factors, including the annealing conditions, surface properties of the substrates, processing parameters, etc. At present, one of the main challenges in solution processed perovskite film is to control the crystallization and to understand its impact on the film quality. It has been demonstrated that various kinds of additives can significantly improve the controllability of the perovskite crystallization process. The effect of the additives during the film formation was first demonstrated by Eperon *et al.*, who introduced a small amount of hydroiodic acid (HI) to the stoichiometric FAI and PbI_2 (1:1) perovskite precursor solution to improve the perovskite film quality [29]. The addition of HI was helpful to solubilize the inorganic component and slow down the crystallization upon spincoating. As a result, a continuous, uniform and pinhole-free thin film comparable to vapor-deposited perovskite was obtained (Figure 13.10(a) and (b)). Apart from HI, inclusion of hydrobromic acid (HBr) or H_2O in a $\text{MAPbBr}_3/\text{DMF}$ precursor can also improve the surface coverage of perovskites on planar substrates through retarding the nucleation process during spincoating (Figure 13.10(c) and (d)) [80]. During the acceleration process of spincoating, excess solution on the substrate is spun off and the residual precursor solution is gradually dried by further evaporation of solvents, resulting in the crystallization of perovskites. The increased solvent solubility due to HBr addition is more favorable to reproducibly form dense thin perovskite films by using precursor solution with the same concentration. It was also reported that chloride additives such as MgCl_2 and ammonium chloride (NH_4Cl) can also improve the film morphology as a result of the prolonged crystallization process [70, 81, 82].

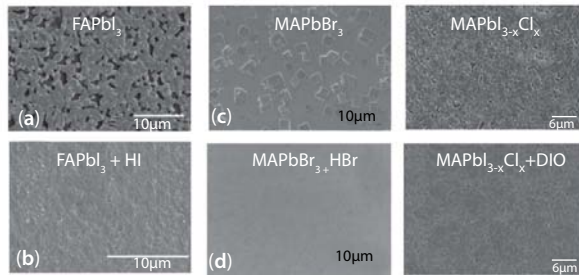


Figure 13.10 SEM images of FAPbI₃ perovskite films prepared (a) without and (b) with HI addition [29]; MAPbBr₃ films deposited (c) without using and (d) with using HBr [80]; MAPbI_{3-x}Cl_x films prepared without and with DIO additive [83].

Recently, Jen and coworkers demonstrated that crystallization rate of perovskite can also be efficiently controlled by incorporating a small amount (~ 1 wt%) of 1,8-diiodooctane (DIO) to the precursor (Figure 13.10(e) and (f)) [83]. It was proposed that the temporarily chelated bidentate halogenated additives with Pb²⁺ during the crystal growth encourage homogeneous nucleation. As soft Lewis bases, iodocarbons can coordinate with soft metal ions based on the hard-soft acid-base principle and improve the solubility of PbCl₂. The presence of DIO may also modify the interfacial energy, ultimately altering the reaction kinetics and making it more favorable for the crystal growth.

In addition to additives, solvent used to prepare the precursor solution also plays a major role in affecting the film quality. The commonly used solvents (GBL, DMF, DMSO) to prepare perovskite precursors always have an oxygen group to coordinate with Pb²⁺ [68]. When either DMF or GBL is used as the solvent, perovskite formation usually occurs immediately after evaporation of the solvent within a few minutes of annealing and results in perovskites with poor surface morphology [52]. Recently, Cheng *et al.* reported a fast deposition-crystallization procedure to obtain flat, uniform thin films using a one-step solution process [84]. After several seconds of spincoating of a DMF solution of CH₃NH₃PbI₃, a second solvent of chlorobenzene (CB) was quickly introduced on top of the wet film during the spincoating process to induce fast crystallization of the perovskite layer. The role of the CB solvent is to rapidly reduce the solubility of perovskites in the mixed solvent and thereby promote fast nucleation and growth of the crystals in the film. Based on the perovskite films fabricated from this fast crystallization approach, a maximum PCE of 16.2% and average efficiencies of $13.9 \pm 0.7\%$ were obtained in a planar heterojunction device structure. Through optimizing the solvent evaporation time with a mixture

of GBL and DMF (97:3, vol%) as the solvent, perovskite layers with an interconnected crystalline structure and appropriate film morphology on top of PEDO:PSS layer were also obtained by Kim *et al.* [85].

The recent work by Seok's group independently exploited a novel perovskite deposition technique, which combines the antisolvent fast crystallization concept with the advantages of mixed solvent [86]. As shown in Figure 13.11(a), a mixed solvent of GBL and DMSO (7:3 v/v) was used to dissolve $\text{CH}_3\text{NH}_3\text{Pb}(\text{I}_{1-x}\text{Br}_x)_3$ perovskite. Toluene, which does not dissolve the perovskite precursor film but is miscible with the perovskite precursor solvent, was dropped on top of the wet perovskite films during spin coating process. During spinning process, the composition of the film is quickly concentrated by the evaporation of GBL. The role of DMSO in the solvent is found to retard the rapid reaction between PbI_2 and MAI by forming DMSO- PbI_2 intermediate phase. The toluene helps to freeze the precursor constituents uniformly across the entire substrate surface and leads to rapid formation of the MAI- PbI_2 -DMSO phase via quick removal of the excess DMSO solvent. Finally, extremely uniform and dense perovskite films were obtained after a mild annealing process (Figure 13.11(b) and (c)). This novel deposition technology enables the fabrication of remarkably improved solar cells with a certified PCE of 16.2%. Based on this process, a module with 8.7% efficiency consisting of 10 serially connected perovskite cells with a total area of $10 \times 10 \text{ cm}^2$ were also demonstrated [87].

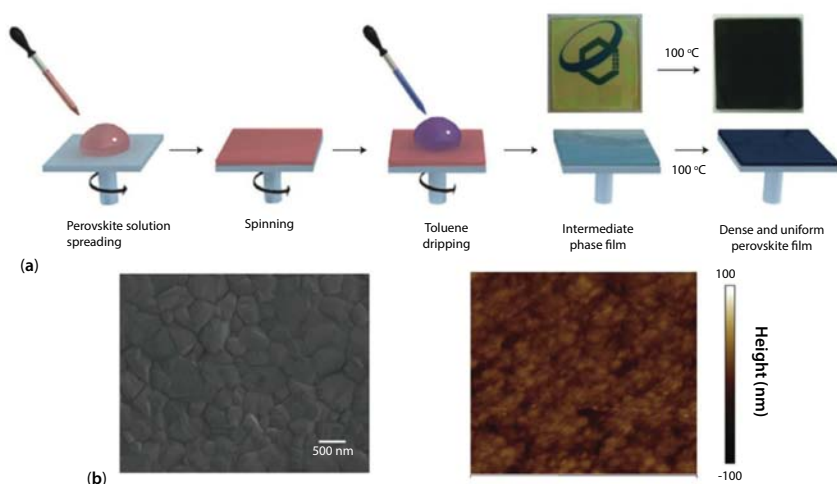


Figure 13.11 (a) Solvent engineering procedure for preparing the uniform and dense perovskite films. (b) SEM top view and the AFM topography of the upper perovskite film obtained from modified solvent engineering procedure. Reprinted from Ref. [86].

In the case of perovskite films prepared by the two-step spincoating deposition method, the crystal size of $\text{CH}_3\text{NH}_3\text{PbI}_3$ was found to be significantly affected by the concentration of $\text{CH}_3\text{NH}_3\text{I}$ in the second spincoating step [85]. When the concentration of the iso-propanol solution decreased from 0.063 to 0.038 M, the average perovskite crystal size increased from 90 to about 700 nm. It was also noted that due to the improved light harvesting efficiency, large crystals grown from low concentrations show higher J_{sc} than the small ones from high concentrations, and higher efficiency around 16.3% was obtained. In a recent report by Petrozza *et al.*, they found that the luminescence properties of sequential deposited perovskite films are significantly influenced by the crystal size [88]. By tuning the average crystallite dimension from tens of nanometers to a few micrometers, the optical bandgap is decreased and the photoluminescence lifetime is efficiently prolonged. This result is consistent with the increased V_{oc} , which correlates with the rate of charge carrier extraction and recombination rate.

The above results reveal the importance of solution chemistry in improving the device performance. Further understanding of the impact of various solution processing parameters on the device performance is expected to make perovskite solar cells more competitive in photovoltaic technology.

13.4 Commercialization Challenges and Possible Solutions

Although a high efficiency exceeding 20% has been realized in perovskite solar cells within a short time, fundamental questions in this emerging photovoltaic technology are still open and more efforts need to be made for the commercialization of perovskite solar cells in the future.

The long-term stability, including thermal and moisture stability, is a big issue for perovskite solar cells. Organometal halide perovskites are typically unstable in humid conditions and decomposition will happen under a high temperature or even at a relative low temperature if operated for a long time [38, 55, 62, 64]. One possible method to solve the moisture problem is the creation of a mixed halide perovskite of $\text{CH}_3\text{NH}_3\text{Pb}(\text{I}_{1-x}\text{Br}_x)_3$. The inclusion of bromide in $\text{CH}_3\text{NH}_3\text{PbI}_3$ is likely to enhance the stability of the CH_3NH_3^+ cation in the lattice. When the x value is above 0.2, the obtained mixed perovskite were much more stable under a humidity soaking test with 55% relative humidity [38]. Replacing the MA with a bigger cation of FA will enhance the thermal stability of perovskite without decomposition at 150°C in air, whereas the MA based perovskite discolors

after 30 minutes under the same condition [29, 30]. In a recent report, a two-dimensional layered hybrid perovskite of $(\text{PEA})_2(\text{MA})_2[\text{Pb}_3\text{I}_{10}]$ ($\text{PEA} = \text{C}_6\text{H}_5(\text{CH}_2)_2\text{NH}_3^+$, $\text{MA} = \text{CH}_3\text{NH}_3^+$) developed by Smith *et al.* exhibits more moisture resistant than the common used MA based perovskites and can be fabricated under ambient humidity levels [89].

In addition to the perovskite material itself, remarkable progresses have also been made on the electrodes. Snaith's group recently replaced the commonly used organic hole transport layer with poly(3-hexylthiophene) (P3HT) functionalized single-walled carbon nanotubes (SWCNT) embedded in an insulating poly(methylmethacrylate) (PMMA) matrix, as shown in Figure 13.12(a) [90]. The hydrophobic PMMA showed a significant waterproof property and retarded decomposition of the perovskite layer (Figure 13.12(b)). In addition, the perovskite solar cells demonstrated remarkable thermal stability without any significant efficiency loss after 96 h thermal stressing at 80°C in air. Han *et al.* reported a hole transport material free perovskite solar cells with a simple mesoscopic $\text{TiO}_2/\text{ZrO}_2/\text{C}$ structure as the scaffold. The thick carbon back electrode played an important role in resistance to moisture, and the solar cells exhibited excellent stability under operational conditions over 1000 h [46].

Another disadvantage of perovskite-based solar cells is the use of environmentally hazardous lead. The commonly used $\text{CH}_3\text{NH}_3\text{PbI}_3$ will convert to PbI_2 in contact with polar solvents such as water. PbI_2 is a moderately water-soluble carcinogen and banned to use in many countries. Lead free perovskites, where lead is replaced by a less toxic element, are necessary for the widespread applications of perovskite solar cells. The most viable replacements for lead in the perovskite materials are tin (Sn) and germanium (Ge). In the early 2014, Kanatzidis's group and Snaith's group

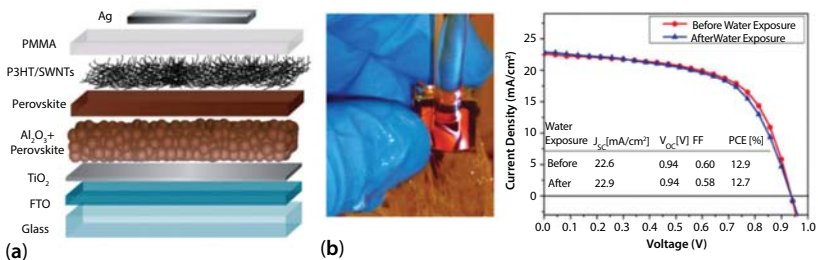


Figure 13.12 (a) Schematic illustration of a solar cell with a carbon nanotube/polymer composite as the hole-transporting layer. (b) A photograph of a complete perovskite solar cell under the water flow (left), and device performance of the solar cell before and after being placed under the running water for 60 s (right). Reprinted from Ref. [90].

independently reported lead-free and Sn-based perovskite solar cells, as shown in Figure 13.13(a) and (b) [91, 92]. However, the major problem with these perovskites is the chemical instability in the required oxidation state. As mentioned above, when the Sn^{2+} ion is oxidized, the resulting Sn^{4+} acts as p-type dopants within the material [36]. As a result, perovskites become metallic and the devices exhibit poor stability even without exposure to air. In addition, the diffusion length is limited to approximately 30 nm for Sn-based perovskites due to the recombination with self-doping carriers, making Sn-based perovskite not suitable for the planar structure [91]. Much more efforts are required to reduce the self-doping levels of the Sn-based perovskites and enable long-term stability of lead free perovskite solar cells.

While reported efficiencies based on perovskite solar cell have been sky-rocketing, the appearance of an anomalous hysteresis in the photocurrent-voltage curves leads to inaccurateness of the reported solar cell efficiencies, as shown in Figure 13.13(c) [86, 91, 93, 94]. The hysteresis

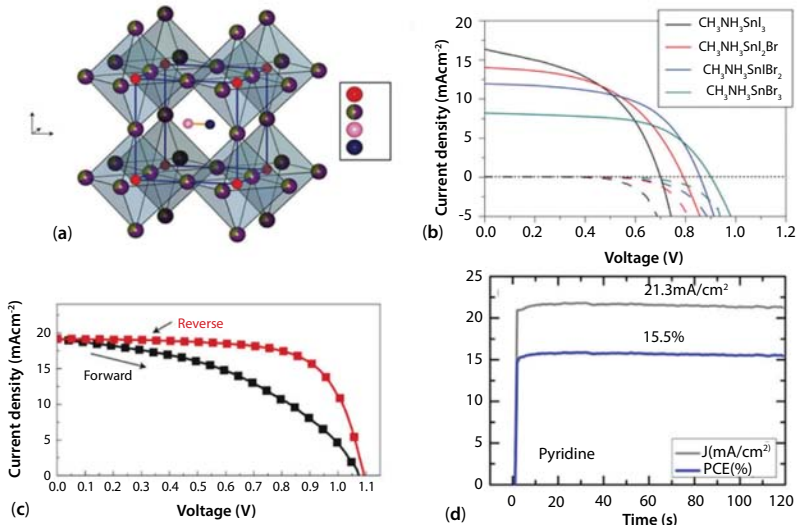


Figure 13.13 (a) Perovskite crystal structure of $\text{CH}_3\text{NH}_3\text{SnI}_{3-x}\text{Br}_x$ materials and (b) the corresponding photocurrent density-voltage characteristics for devices with these lead free perovskites. Reprinted from Ref. [92]. (c) Light J–V curves of a planar perovskite solar cell measured by forward (from short circuit to open circuit) and reverse (from open circuit to short circuit) scans with 10 mV voltage steps and 40 ms delay time. Reprinted from Ref. [86]. (d) Stabilized efficiency of pyridine passivated perovskite planar device measured by holding the device at its maximum power point for 120 s. Reprinted from Ref. [99].

phenomenon means that the measured device efficiency depends on the voltage scan direction and speed [91, 93]. In addition, as demonstrated by Seok *et al.*, the hysteretic effect is particularly severe for planar device configurations compared with devices with mesoscopic scaffolds [48]. However, a thicker mesoporous scaffold is not completely favorable to reduce this anomalous behavior. It has been reported that by reducing the voltage scan speed, it is possible to fully suppress the hysteresis behavior in a mesoporous perovskite device. The hysteresis phenomena in perovskite solar cells have been speculated to originate from ferroelectricity, trapping/de-trapping of charge carriers, or ion migration in perovskite materials [95–98]. Understanding and resolving the hysteresis is essential for future progress and further improvement of the device performance. Although the origin of this phenomenon is not clear, it has been shown that it is possible to achieve stabilized current and efficiency from the meso-structured solar cell. For a planar heterojunction device, the stabilized power output is typically half of that can be achieved via a fast scan [91]. In a recent report, Snaith *et al.* demonstrated that through treatment of the crystal surfaces with Lewis bases thiophene and pyridine, the under-coordinated Pb atoms within the perovskites can be efficiently passivated [99]. The obtained films exhibit significantly reduced nonradiative charge carrier recombination rate and the photoluminescence lifetime increases to 2 μs . Most interestingly, the hysteresis effect in planar devices based on these Lewis base passivated perovskite films is significantly reduced, as depicted in Figure 13.13(d). This result is consistent with the mechanism that the hysteresis is influenced by trap states in perovskites. Trap filling and surface passivation to decrease the number of the defect sites prove efficient to reduce or even eliminate the hysteresis phenomenon in perovskite solar cells [100, 101].

13.5 Summary and Conclusion

This chapter reviews the history of organometal halide perovskite, which is a promising photovoltaic material. We give an emphasis on the quick development during the past few years, covering materials optimization, device structures, and device physics analysis. In spite of some existing problems at this stage, e.g., toxic lead and poor device stability, we believe that a large multidisciplinary effort will be able to create a new and less expensive photovoltaic technology from this exciting research topic.

Acknowledgements

We acknowledge the financial support of the Swedish Research Council (VR), the Open Research Fund of State Key Lab of Silicon Materials (Zhejiang University), and the European Commission under a Marie Skłodowska-Curie action.

References

1. C. K. Moller, *Nature* 1958, 182, 1436–1436.
2. D. Weber, *Zeitschrift für Naturforschung B* 1978, 33, 1443–1445.
3. D. B. Mitzi, C. A. Feild, W. T. A. Harrison, A. M. Guloy, *Nature* 1994, 369, 467–469.
4. K. Chondroudis, D. B. Mitzi, *Chemistry of Materials* 1999, 11, 3028–3030.
5. C. R. Kagan, D. B. Mitzi, C. D. Dimitrakopoulos, *Science* 1999, 286, 945–947.
6. A. Kojima, K. Teshima, Y. Shirai, T. Miyasaka, *Journal of the American Chemical Society* 2009, 131, 6050–6051.
7. M. M. Lee, J. Teuscher, T. Miyasaka, T. N. Murakami, H. J. Snaith, *Science* 2012, 338, 643–647.
8. H.-S. Kim, C.-R. Lee, J.-H. Im, K.-B. Lee, T. Moehl, A. Marchioro, S.-J. Moon, R. Humphry-Baker, J.-H. Yum, J. E. Moser, M. Grätzel, N.-G. Park, *Scientific Report* 2012, 2, 591.
9. T. Ishihara, *Journal of Luminescence* 1994, 60–61, 269–274.
10. V. D’Innocenzo, G. Grancini, M. J. P. Alcocer, A. R. S. Kandada, S. D. Stranks, M. M. Lee, G. Lanzani, H. J. Snaith, A. Petrozza, *Nature Communication* 2014, 5, 3586.
11. C. Wehrenfennig, G. E. Eperon, M. B. Johnston, H. J. Snaith, L. M. Herz, *Advanced Materials* 2014, 26, 1584–1589.
12. S. D. Stranks, G. E. Eperon, G. Grancini, C. Menelaou, M. J. P. Alcocer, T. Leijtens, L. M. Herz, A. Petrozza, H. J. Snaith, *Science* 2013, 342, 341–344.
13. G. Xing, N. Mathews, S. Sun, S. S. Lim, Y. M. Lam, M. Grätzel, S. Mhaisalkar, T. C. Sum, *Science* 2013, 342, 344–347.
14. J.-H. Im, C.-R. Lee, J.-W. Lee, S.-W. Park, N.-G. Park, *Nanoscale* 2011, 3, 4088–4093.
15. K. Liang, D. B. Mitzi, M. T. Prikas, *Chemistry of Materials* 1998, 10, 403–411.
16. J. Burschka, N. Pellet, S.-J. Moon, R. Humphry-Baker, P. Gao, M. K. Nazeeruddin, M. Grätzel, *Nature* 2013, 499, 316–319.
17. D. B. Mitzi, *Chemistry of Materials* 2001, 13, 3283–3298.
18. L. Etgar, P. Gao, Z. Xue, Q. Peng, A. K. Chandiran, B. Liu, M. K. Nazeeruddin, M. Grätzel, *Journal of the American Chemical Society* 2012, 134, 17396–17399.
19. M. Liu, M. B. Johnston, H. J. Snaith, *Nature* 2013, 501, 395–398.
20. C. Li, X. Lu, W. Ding, L. Feng, Y. Gao, Z. Guo, *Acta Crystallographica Section B* 2008, 64, 702–707.

21. H.-S. Kim, C.-R. Lee, J.-H. Im, K.-B. Lee, T. Moehl, A. Marchioro, S.-J. Moon, R. Humphry-Baker, J.-H. Yum, J. E. Moser, M. Gratzel, N.-G. Park, *Scientific Reports* 2012, 2, 591.
22. S. Sun, T. Salim, N. Mathews, M. Duchamp, C. Boothroyd, G. Xing, T. C. Sum, Y. M. Lam, *Energy & Environmental Science* 2014, 7, 399–407.
23. W. Shockley, H. J. Queisser, *Journal of Applied Physics* 1961, 32, 510–519.
24. T. Soga, T. Kato, M. Yang, M. Umeno, T. Jimbo, *Journal of Applied Physics* 1995, 78, 4196–4199.
25. M. A. Green, A. Ho-Baillie, H. J. Snaith, *Nature Photonics* 2014, 8, 506–514.
26. P. P. Boix, K. Nonomura, N. Mathews, S. G. Mhaisalkar, *Materials Today* 2014, 17, 16–23.
27. K. Tanaka, T. Takahashi, T. Ban, T. Kondo, K. Uchida, N. Miura, *Solid State Communications* 2003, 127, 619–623.
28. I. Borriello, G. Cantele, D. Ninno, *Physical Review B* 2008, 77, 235214.
29. G. E. Eperon, S. D. Stranks, C. Menelaou, M. B. Johnston, L. M. Herz, H. J. Snaith, *Energy & Environmental Science* 2014, 7, 982–988.
30. J.-W. Lee, D.-J. Seol, A.-N. Cho, N.-G. Park, *Advanced Materials* 2014, 26, 4991–4998.
31. N. Pellet, P. Gao, G. Gregori, T.-Y. Yang, M. K. Nazeeruddin, J. Maier, M. Grätzel, *Angewandte Chemie International Edition* 2014, 53, 3151–3157.
32. D. B. Mitzi, in *Progress in Inorganic Chemistry*, John Wiley & Sons, Inc., 2007, 1–121.
33. J.-H. Im, J. Chung, S.-J. Kim, N.-G. Park, *Nanoscale Research Letters* 2012, 7, 353.
34. Y. Ogomi, A. Morita, S. Tsukamoto, T. Saitho, N. Fujikawa, Q. Shen, T. Toyoda, K. Yoshino, S. S. Pandey, T. Ma, S. Hayase, *The Journal of Physical Chemistry Letters* 2014, 5, 1004–1011.
35. F. Hao, C. C. Stoumpos, R. P. H. Chang, M. G. Kanatzidis, *Journal of the American Chemical Society* 2014, 136, 8094–8099.
36. Y. Takahashi, R. Obara, Z.-Z. Lin, Y. Takahashi, T. Naito, T. Inabe, S. Ishibashi, K. Terakura, *Dalton Transactions* 2011, 40, 5563–5568.
37. E. Mosconi, A. Amat, M. K. Nazeeruddin, M. Grätzel, F. De Angelis, *The Journal of Physical Chemistry C* 2013, 117, 13902–13913.
38. J. H. Noh, S. H. Im, J. H. Heo, T. N. Mandal, S. I. Seok, *Nano Letters* 2013, 13, 1764–1769.
39. O. V. Mikhnenko, H. Azimi, M. Scharber, M. Morana, P. W. M. Blom, M. A. Loi, *Energy & Environmental Science* 2012, 5, 6960–6965.
40. D. Zhitomirsky, O. Voznyy, S. Hoogland, E. H. Sargent, *ACS Nano* 2013, 7, 5282–5290.
41. C. Wehrenfennig, M. Liu, H. J. Snaith, M. B. Johnston, L. M. Herz, *Energy & Environmental Science* 2014, 7, 2269–2275.
42. J. H. Heo, S. H. Im, J. H. Noh, T. N. Mandal, C.-S. Lim, J. A. Chang, Y. H. Lee, H.-j. Kim, A. Sarkar, K. NazeeruddinMd, M. Gratzel, S. I. Seok, *Nature Photonics* 2013, 7, 486–491.

43. K. Wojciechowski, M. Saliba, T. Leijtens, A. Abate, H. Snaith, *Energy & Environmental Science* 2013, 7, 1142–1147.
44. J. M. Ball, M. M. Lee, A. Hey, H. J. Snaith, *Energy & Environmental Science* 2013, 6, 1739–1743.
45. D. Bi, S.-J. Moon, L. Haggman, G. Boschloo, L. Yang, E. M. J. Johansson, M. K. Nazeeruddin, M. Gratzel, A. Hagfeldt, *RSC Advances* 2013, 3, 18762–18766.
46. A. Mei, X. Li, L. Liu, Z. Ku, T. Liu, Y. Rong, M. Xu, M. Hu, J. Chen, Y. Yang, M. Grätzel, H. Han, *Science* 2014, 345, 295–298.
47. G. E. Eperon, V. M. Burlakov, P. Docampo, A. Goriely, H. J. Snaith, *Advanced Functional Materials* 2014, 24, 151–157.
48. H. Zhou, Q. Chen, G. Li, S. Luo, T.-b. Song, H.-S. Duan, Z. Hong, J. You, Y. Liu, Y. Yang, *Science* 2014, 345, 542–546.
49. M. H. Kumar, N. Yantara, S. Dharani, M. Graetzel, S. Mhaisalkar, P. P. Boix, N. Mathews, *Chemical Communications* 2013, 49, 11089–11091.
50. Q. Hu, J. Wu, C. Jiang, T. Liu, X. Que, R. Zhu, Q. Gong, *ACS Nano* 2014, 8, 10161–10167.
51. D. Liu, J. Yang, T. L. Kelly, *Journal of the American Chemical Society* 2014, 136, 17116–17122.
52. J.-Y. Jeng, Y.-F. Chiang, M.-H. Lee, S.-R. Peng, T.-F. Guo, P. Chen, T.-C. Wen, *Advanced Materials* 2013, 25, 3727–3732.
53. Q. Wang, Y. Shao, Q. Dong, Z. Xiao, Y. Yuan, J. Huang, *Energy & Environmental Science* 2014, 7, 2359–2365.
54. P. Docampo, J. M. Ball, M. Darwich, G. E. Eperon, H. J. Snaith, *Nature Communication* 2013, 4, DOI:10.1038/ncomms3761.
55. S. Bai, Z. Wu, X. Wu, Y. Jin, N. Zhao, Z. Chen, Q. Mei, X. Wang, Z. Ye, T. Song, R. Liu, S.-t. Lee, B. Sun, *Nano Research* 2014, 7, 1749–1758.
56. J.-Y. Jeng, K.-C. Chen, T.-Y. Chiang, P.-Y. Lin, T.-D. Tsai, Y.-C. Chang, T.-F. Guo, P. Chen, T.-C. Wen, Y.-J. Hsu, *Advanced Materials* 2014, 26, 4107–4113.
57. Z. Zhu, Y. Bai, T. Zhang, Z. Liu, X. Long, Z. Wei, Z. Wang, L. Zhang, J. Wang, F. Yan, S. Yang, *Angewandte Chemie International Edition* 2014, 53, 12571–12575.
58. L. Hu, J. Peng, W. Wang, Z. Xia, J. Yuan, J. Lu, X. Huang, W. Ma, H. Song, W. Chen, Y.-B. Cheng, J. Tang, *ACS Photonics* 2014, 1, 547–553.
59. J. H. Kim, P.-W. Liang, S. T. Williams, N. Cho, C.-C. Chueh, M. S. Glaz, D. S. Ginger, A. K. Y. Jen, *Advanced Materials* 2015, 27, 695–701.
60. B. Conings, L. Baeten, C. De Dobbelaere, J. D’Haen, J. Manca, H.-G. Boyen, *Advanced Materials* 2014, 26, 2041–2046.
61. J.-H. Im, H.-S. Kim, N.-G. Park, *APL Materials* 2014, 2, 081510.
62. K. W. Tan, D. T. Moore, M. Saliba, H. Sai, L. A. Estroff, T. Hanrath, H. J. Snaith, U. Wiesner, *ACS Nano* 2014, 8, 4730–4739.
63. M. Saliba, K. W. Tan, H. Sai, D. T. Moore, T. Scott, W. Zhang, L. A. Estroff, U. Wiesner, H. J. Snaith, *The Journal of Physical Chemistry C* 2014, 118, 17171–17177.

64. A. Dualeh, N. Tétreault, T. Moehl, P. Gao, M. K. Nazeeruddin, M. Grätzel, *Advanced Functional Materials* 2014, 24, 3250–3258.
65. J. You, Y. Yang, Z. Hong, T.-B. Song, L. Meng, Y. Liu, C. Jiang, H. Zhou, W.-H. Chang, G. Li, Y. Yang, *Applied Physics Letters* 2014, 105, 183902.
66. S. Pang, H. Hu, J. Zhang, S. Lv, Y. Yu, F. Wei, T. Qin, H. Xu, Z. Liu, G. Cui, *Chemistry of Materials* 2014, 26, 1485–1491.
67. Q. Chen, H. Zhou, Z. Hong, S. Luo, H.-S. Duan, H.-H. Wang, Y. Liu, G. Li, Y. Yang, *Journal of the American Chemical Society* 2013, 136, 622–625.
68. Y. Wu, A. Islam, X. Yang, C. Qin, J. Liu, K. Zhang, W. Peng, L. Han, *Energy & Environmental Science* 2014, 7, 2934–2938.
69. D. Wang, Z. Liu, Z. Zhou, H. Zhu, Y. Zhou, C. Huang, Z. Wang, H. Xu, Y. Jin, B. Fan, S. Pang, G. Cui, *Chemistry of Materials* 2014, 26, 7145–7150.
70. P. Docampo, F. C. Hanusch, S. D. Stranks, M. Döblinger, J. M. Feckl, M. Ehrensperger, N. K. Minar, M. B. Johnston, H. J. Snaith, T. Bein, *Advanced Energy Materials* 2014, 4, 1400355.
71. Z. Xiao, C. Bi, Y. Shao, Q. Dong, Q. Wang, Y. Yuan, C. Wang, Y. Gao, J. Huang, *Energy & Environmental Science* 2014, 7, 2619–2623.
72. C. Bi, Y. Shao, Y. Yuan, Z. Xiao, C. Wang, Y. Gao, J. Huang, *Journal of Materials Chemistry A* 2014, 2, 18508–18514.
73. Z. Xiao, Q. Dong, C. Bi, Y. Shao, Y. Yuan, J. Huang, *Advanced Materials* 2014, 26, 6503–6509.
74. A. M. Salau, *Solar Energy Materials* 1980, 2, 327–332.
75. D. B. Mitzi, M. T. Prikas, K. Chondroudis, *Chemistry of Materials* 1999, 11, 542–544.
76. L. K. Ono, S. Wang, Y. Kato, S. R. Raga, Y. Qi, *Energy & Environmental Science* 2014, 7, 3989–3993.
77. O. Malinkiewicz, A. Yella, Y. H. Lee, G. M. Espallargas, M. Graetzel, M. K. Nazeeruddin, H. J. Bolink, *Nature Photonics* 2014, 8, 128–132.
78. Q. Lin, A. Armin, R. C. R. Nagiri, P. L. Burn, P. Meredith, *Nature Photonics* 2015, 9, 106–112.
79. C.-W. Chen, H.-W. Kang, S.-Y. Hsiao, P.-F. Yang, K.-M. Chiang, H.-W. Lin, *Advanced Materials* 2014, 26, 6647–6652.
80. J. H. Heo, D. H. Song, S. H. Im, *Advanced Materials* 2014, 26, 8179–8183.
81. C. Zuo, L. Ding, *Nanoscale* 2014, 6, 9935–9938.
82. S. Colella, E. Mosconi, P. Fedeli, A. Listorti, F. Gazza, F. Orlandi, P. Ferro, T. Besagni, A. Rizzo, G. Calestani, G. Gigli, F. De Angelis, R. Mosca, *Chemistry of Materials* 2013, 25, 4613–4618.
83. P.-W. Liang, C.-Y. Liao, C.-C. Chueh, F. Zuo, S. T. Williams, X.-K. Xin, J. Lin, A. K. Y. Jen, *Advanced Materials* 2014, 26, 3748–3754.
84. M. Xiao, F. Huang, W. Huang, Y. Dkhissi, Y. Zhu, J. Etheridge, A. Gray-Weale, U. Bach, Y.-B. Cheng, L. Spiccia, *Angewandte Chemie International Edition* 2014, 126, 10056–10061.
85. H.-B. Kim, H. Choi, J. Jeong, S. Kim, B. Walker, S. Song, J. Y. Kim, *Nanoscale* 2014, 6, 6679–6683.

86. N. J. Jeon, J. H. Noh, Y. C. Kim, W. S. Yang, S. Ryu, S. I. Seok, *Nature Materials* 2014, 13, 897–903.
87. J. Seo, S. Park, Y. Chan Kim, N. J. Jeon, J. H. Noh, S. C. Yoon, S. I. Seok, *Energy & Environmental Science* 2014, 7, 2642–2646.
88. V. D’Innocenzo, A. R. Srimath Kandada, M. De Bastiani, M. Gandini, A. Petrozza, *Journal of the American Chemical Society* 2014, 136, 17730–17733.
89. I. C. Smith, E. T. Hoke, D. Solis-Ibarra, M. D. McGehee, H. I. Karunadasa, *Angewandte Chemie International Edition* 2014, 126, 11414–11417.
90. S. N. Habisreutinger, T. Leijtens, G. E. Eperon, S. D. Stranks, R. J. Nicholas, H. J. Snaith, *Nano Letters* 2014, 14, 5561–5568.
91. N. K. Noel, S. D. Stranks, A. Abate, C. Wehrenfennig, S. Guarnera, A.-A. Haghighirad, A. Sadhanala, G. E. Eperon, S. K. Pathak, M. B. Johnston, A. Petrozza, L. M. Herz, H. J. Snaith, *Energy & Environmental Science* 2014, 7, 3061–3068.
92. F. Hao, C. C. Stoumpos, D. H. Cao, R. P. H. Chang, M. G. Kanatzidis, *Nature Photonics* 2014, 8, 489–494.
93. E. L. Unger, E. T. Hoke, C. D. Bailie, W. H. Nguyen, A. R. Bowring, T. Heumüller, M. G. Christoforo, M. D. McGehee, *Energy & Environmental Science* 2014, 7, 3690–3698.
94. L. K. Ono, S. R. Raga, S. Wang, Y. Kato, Y. Qi, *Journal of Materials Chemistry A* 2015, DOI: 10.1039/C4TA04969A.
95. J. M. Frost, K. T. Butler, F. Brivio, C. H. Hendon, M. van Schilfegaarde, A. Walsh, *Nano Letters* 2014, 14, 2584–2590.
96. A. Dualeh, T. Moehl, N. Tétreault, J. Teuscher, P. Gao, M. K. Nazeeruddin, M. Grätzel, *ACS Nano* 2013, 8, 362–373.
97. C. C. Stoumpos, C. D. Malliakas, M. G. Kanatzidis, *Inorganic Chemistry* 2013, 52, 9019–9038.
98. I. Lyubomirsky, M. K. Rabinal, D. Cahen, *Journal of Applied Physics* 1997, 81, 6684–6691.
99. N. K. Noel, A. Abate, S. D. Stranks, E. S. Parrott, V. M. Burlakov, A. Goriely, H. J. Snaith, *ACS Nano* 2014, 8, 9815–9821.
100. F. Deschler, M. Price, S. Pathak, L. E. Klüntberg, D.-D. Jarausch, R. Higler, S. Hüttner, T. Leijtens, S. D. Stranks, H. J. Snaith, M. Atatüre, R. T. Phillips, R. H. Friend, *The Journal of Physical Chemistry Letters* 2014, 5, 1421–1426.
101. S. D. Stranks, V. M. Burlakov, T. Leijtens, J. M. Ball, A. Goriely, H. J. Snaith, *Physical Review Applied* 2014, 2, 034007.

Index

- 6-deoxy-6-amino chitosan, 504
- Acid treatment, 284
- Acrylic polymer-grafted polypropylene sutures, 453–455
- Activated carbon, 284
- Activated carbon (AC), 410–411
- Adsorption capacity, 465, 471, 474, 476
- Adsorption/ desorption, 289
- Air blast, 132–133
- Aliphatic alcohols, 21–30, 36–44
- Alpha particles, 437–438
- Amperometric plot, 8
- Anisotropic growth, 209
- Anode, 286
- Anomalous hysteresis of perovskite solar cells, 560, 561
- Antifungal, 493–494, 496, 504, 514, 518–522, 524–526
- Antimicrobial, 493–494, 496–526
- Antimicrobial peptides (AMP), 511–513, 523
- Antimicrobial susceptibility testing (AST), 518
 - agar dilution, 520, 523, 525
 - bactericide/bactericidal, 505, 509, 513, 518, 520, 522–524
 - bacteriostatic, 499, 520, 523
 - broth dilution, 518, 520–525
 - disk diffusion, 518–519, 522–525
 - epsilometer test, 518, 520, 522
 - gram-negative, 497, 506–507, 509–513, 524–525
 - gram-positive, 497, 506–507, 509, 511–513, 524–525
 - minimum bactericidal concentration (MBC), 518, 521–522
 - minimum inhibitory concentration (MIC), 497, 504, 507, 520–521, 524–525
 - thin layer chromatography (TLC), 519, 522
 - zone of inhibition (ZOI), 519, 520, 524
- Articular cartilage, 201–202
- Atomic force microscopy, 457–458
- Average particles sizes, 286
- Band alignment,
 - heterostructures, 223–224
 - type-II, 256
- Batteries, 283
- BET, 286, 289
- Binary composites, 419–421
- Binary graft modification, 450–452
- Biocompatibility, 201, 212–213
 - cell culture, 201
 - cytotoxicity, 201
 - statistical analysis, 201
- Biocompatibility of DEGMA/OEGMA radiation, 453
- Biocompatible/biocompatibility, 501–502, 511
- Biodegradable/biodegradation, 493–496, 498, 500–501, 506, 509

- Biomass, 494, 526
 Biomaterial, 494, 496, 500
 Biomedical, 493, 495, 499–503, 509, 514, 525
 Biopolymer, 493–496, 498, 500, 502, 507, 525
 BiVO_4 , 78, 86
 BN, 84, 111–112
 Carbon areogels, 284, 411–414
 Carbon coated Cu grid, 286
 Carbon electrode, 284
 Carbon fibres, 284
 Carbon nanotubes
 (CNTs), 284, 287, 289
 415–417
 Carboxymethyl chitosan
 (CMC), 504
 Cardiac grafts, 208–209
 Cardiomyocytes, 208–210, 218
 Cathode, 285
 $\text{Cd}_{10}\text{S}_{16}\text{C}_{32}\text{H}_{80}\text{N}_4\text{O}_{28}$, 81
 CdS, 81–82
 Cellulose, 286
 Centrifuging, 285
 CeO_2 , 69, 71–72, 75, 85, 86, 107, 108
 Chalcogenide, 128, 165, 166
 Chalcopyrite, 127, 128, 150–156, 176
 Chelating agents, 195
 citric acid (CA), 198–199
 organic acids, 198
 poly vinyl alcohol (PVA), 198–199
 Chemiresistor, 6–21
 Chemiresistors,
 conducting polymers
 nanostructures, 21–44
 semiconducting metaloxide
 nanostructures for, 6–21
 semiconducting nanocomposites,
 44–48
 ZnO nanotubes as, 17–21
 Chitin, 465, 500–501, 503, 517
 Chitosan, 463, 467, 494, 496, 500–506, 508, 510, 515–516, 518, 524–525
 Chondrocytes, 201–203
 Click chemistry, 499, 502, 510
 CMK-1, 80, 87–88, 90–91, 97, 99, 103–105, 113
 CMK-2, 80, 87, 90
 CMK-3, 80–81, 87–90, 97, 99–100, 102–113
 CMK-4, 87–90, 97, 99, 105
 CMK-8, 89–90, 111–112
 CMK-9, 89–90
 Co_3O_4 , 63, 69, 70–72, 74–75, 84–85
 Coating, 286
 Collagen, 198, 201–202, 204, 206, 208, 210–212, 215–217, 221
 Composite, 495, 502, 509, 515–517, 524
 Composite electrode material, 409, 411, 413, 416, 417
 Conducting polymers, 284
 Contact angle, 457
 Copper chloride, 285
 Copper oxide, 136, 172, 283, 284, 285, 290
 Counter electrode, 286
 Cr_2O_3 , 66, 69, 73, 84–85
 CrN, 84
 Cross-linking, 468
 $\text{Cs}_{2.5}\text{H}_{0.5}\text{PW}_{12}\text{O}_{40}$, 73
 CuCo_2O_4 , 72
 CuO, 68, 73, 104, 109, 284, 285, 287, 290–292
 CuO- MWCNTs, 283, 288, 291
 CVD, 65, 66, 88–90, 94–95, 100–101, 109
 Cyclic voltammetry (CV), 283, 285, 286, 289, 290
 Cyclovoltametry (CV) analysis, 14
 Deacetylation, 465
 Debye length (DL), 402
 Dental pulp stem cells
 (DPSC), 211–212
 Dermal wounds, 207

- Desorption, 467
- Differential scanning calorimetry (DSC), 202
- Diffusion, 467
- Discotic dimers, 297–300, 304–307, 309, 313, 316, 325, 330–332, 334, 341, 346, 355, 361
- Discotic liquid crystals (DLCs), 297, 330, 332, 334
- Dopant, 357, 359
- Dosimetry, 438–440
- Effect of solvents and monomers, 445–447
- Electric double-layer capacitor (EDLC), 404–405
 - drawback of, 408
- Electric doublelayer capacitors, 284
- Electric field, 132, 133
- Electro chemical workstation, 286
- Electrochemical, 283, 289, 292
- Electrochemical impedance spectroscopy (EIS), 26, 28, 39, 40, 41
- Electrode, 283, 290, 291, 292, 293
- Electrode materials, 284, 290
- Electrolyte, 285, 286
- Electron beam, 437
- Electrospinning,
 - collector, 199–201
 - spinneret, 199
 - syringe pump, 199–200
 - Taylor cone, 200
- Energy storage, 127, 129, 136, 167, 168, 171
- Energy storage devices, 283
- Environment pollutants, 36
- ϵ -Poly-L-lysine (ϵ -PL), 496–500, 506–507
- Escherichia coli (*E. Coli*), 210
- Ethanol, 286
- FDU-12, 64–66, 69–70, 72, 92
- Fe_2O_3 , 68–69, 76–77, 108
- Fe_3O_4 , 76
- Ferrihydrite, 69, 76–77
- Ferrites, 187
 - cubic ferrites, 187–188
 - hexagonal ferrites, 189
- Fibroblasts, 206–207, 212
- Flame spray pyrolysis, 4, 131, 169, 172
- Flexibility, 284
- Flexible, 127, 128, 131, 154, 156, 157, 164
- Fossil fuels, 284
- Fricke dosimetry method, 440
- Fulminant hepatic failure (FHF), 210
- Galvanostatic charge – discharge, 283, 285, 286, 291
- GaN, 83
- Generally Regarded as Safe (GRAS), 497, 501
- Gouy–Chapman model, 405
- Grafting, 471, 472
- Grafting temperature, 448–449
- Graphene, 463,
 - binary composites, 419–421
 - doping of, heteroatom, 423–424
 - electrochemical performance, 418–419
 - ternary hybrid electrode, 421–423
 - two-dimensional, 417–424
- Graphene (Gr) nanocomposite, 44–49
- Graphene oxide, 464
- Halide perovskites, 535
- Hard templating, 59, 60–61, 64, 65, 67–69, 71, 73, 80–81, 97, 100, 106–107, 112, 114–115
- HAuCl_4 , 67, 72
- Helmholtz layer, 405
- Hematite, 143, 144, 174
- Hepatocytes, 210
- Heteroatom, 423–424
- Heterojunctions,
 - anatase-rutile, 234
 - challenges, 234
 - core-shell, 231–232
 - indium tin oxide, 257–258
 - interface, 219, 257–258
 - multijunction, 258

- nanocomposites, 242
- plasmons, 238
- polymorphic, 236, 237
- silicon, 253
- Heterostructures,
 - challenges, 232–234
 - nanocomposites, 242, 245
 - silicon, 234–235, 253–254, 256–257, 262–263
 - TiO₂, 219
- Hexabenzocoronene, 297,
 - 300, 313, 314, 333
- High capacitance, 284
- High conductivity, 292
- Hollow mesoporous, 92, 94–95, 109
- Holothuroids, 22
- Human ligament fibroblasts (HLF), 212–213
- Hydrazine, 44–48
- Hydroxyapatite, 204–205, 212
- In₂O₃, 69, 74, 86
- INC-2, 65, 91, 102
- Indium oxide, 136, 137, 141, 172
- Infrared, 456
- Inner Helmholtz plane (IHP), 405
- Interdiffusion process of
 - perovskites, 551–553
- Interlayers in perovskite solar cells, 543–547
- Irradiation dose rate, 444–445
- Isotherms, 472
- Isotropic growth, 209
- ITO, 360, 361
- Keratinocytes, 206
- Kesterite, 150, 156, 158, 160, 168, 177
- KIT-6, 60, 65–66, 69–78, 81,
 - 83–86, 89–90, 104, 114
- KOH aqueous, 285, 291, 292
- Lead-free perovskite solar cells, 559–561
- LiCoO₂, 72
- Li-ion batteries (LIB), 400
- Limbic Stem Cell, 214
- Limit of detection (LOD), 16
- Linear dynamic range (LDR), 16
- Liquid crystal, 60
- Long-term stability of perovskite solar cells, 558, 559
- Low pressure spray pyrolysis, 129,
 - 135, 136, 137, 141, 170, 172
- Magnetism, 475
- Manganese oxide, 283, 284, 288,
 - 290
- Manganese chloride, 285
- Manganese hydroxide, 285
- Mass, 291
- MCF, MCCF, 89, 91–93
- MCM-41, 60, 64, 68–69, 80–83,
 - 86–87, 89, 100
- Mesenchymal stem cells (MSCs),
 - 202, 205, 210, 213
- Metal oxides, 283, 284, 289, 292
- Microstructure, 292
- Mn–Ce, 76
- MnCo₂O₄, 72, 74
- MnFe₂O₄, 76, 86
- MnO₂, 69, 71, 75–76, 86, 102,
 - 113, 284, 285, 287, 290,
291, 292, 401, 406,
408, 420, 421, 423
- MnO₂ – MWCNTs, 283, 288, 292
- Monomer concentration of
 - grafting, 447–448
- MoO₂, 75, 86
- Morphology, 292
- Multi walled carbon nanotubes,
 - 283, 284
- Multiyne, 306, 307, 309
- Murine myoblast cell line, 219
- MWCNTs, 283, 284, 285,
 - 287, 290, 292
- Myocardium, 210
- N,N,N-trimethyl chitosan chloride (TMC), 504
- Nanochannels, 65, 69
- Nanocrystalline, 127–130, 140,
 - 144, 150–168, 170, 176, 178
- Nanofibre, 499, 502, 515, 517

- Nanoparticle, 128–131, 134–142,
147, 151, 153, 168–174,
176, 177, 497, 502–504,
510, 514–518, 524–525
- Nanoparticles, 283, 286, 287,
288, 289, 292
- Nanopillar, 128, 142, 143, 174
- Nanoporous, 128, 130, 142, 143,
144, 146, 174, 181
- Nanorods, 64, 65, 69, 74, 75, 77,
80–81, 83, 89, 113
- Nanoscale, 514–515
- Nanostructure,
metal oxide, 6–21
- Nanowire, 69, 73–75, 77, 79, 80–83
- NCC-1, 89, 90
- NCS-1, 68, 105–106
- Neural stem cells, 220
- Neurite outgrowth, 220–221
- Neurites, 220
- Neutrons, 438
- NiAl_2O_4 , 75, 85–86
- Nickel mesh, 286
- NiCo_2O_4 , 72
- NiO , 63, 69–70, 74–75, 85, 97, 99
- Nuclear magnetic resonance
spectroscopy, 456
- One-step deposition of perovskites,
547–549, 555
- Organic light-emitting diode,
349, 360
- Organometal halide perovskites,
absorption, 539
bandgap engineering, 540, 541
charge carrier diffusion lengths,
536, 541
crystal structure, 538, 539
mobility, 541, 542
optoelectronic properties, 536,
539–542
- Osteoprogenitor cells, 205
- Outer Helmholtz plane (OHP), 405
- Pd, 98–99, 102
- Periosteum, 203
- Perovskite solar cells,
brief history, 537
device architecture evolution,
542, 543
inverted planar structure, 545–547
planar architectures, 544, 545
- Phenol chemical, 30–36
- Phenyl hydrazine, 6, 8, 10, 17
- Photocatalysis,
heterostructures, 261–262
 TiO_2 , 219–220
- Phthalocyanine, 297, 300, 316–318,
321–323, 325, 326
- Plasma treatment, 203
- p-Nitrophenylamine, 10–16
- polyaniline (PANI), 4, 21–36, 44–49
- Polyaniline nanosheets, 30–36
- Polyethyleneimine, 510–511,
513, 515, 524
- Polyindol, 4
- Polymer substrate and film
thickness, 447
- Polypyrrole (PPy) nanobelts, 36–44
- Polytetrafluoroethylene (PTFE), 286
- Polythiophene, 3, 4
- Porous morphology, ZnO , 10–16
- Porphyrin, 297, 300, 325, 327–330
- Pre-irradiation method, 443
- Pre-irradiation oxidative method, 444
- Pseudocapacitors, 284, 290,
293, 405–407
- Pt-Pd, 80
- Pt-Ru, 80, 102
- p-type semiconductors, 3, 4, 36
- Pyranose, 297, 300, 330, 331
- Pyrene, 297, 300, 332–334
- Quaternary polymers, 506
- Radiation grafting, 441–442
- Radiation grafting of glycidyl
methacrylate, 450
- Radiation grafting technique, 434–435
- Radioactivity and radiation
absorption, 441
- Raman analysis, 202

- Raman scattering spectrum, 8, 23, 25
Raman shift, 288
Raman spectroscopy, spectra,
286, 287
Reactive oxygen species, 497, 515–56
Redox additive, 411, 415
Redox reaction, 405–409
Re-epithelialization, 207
Regenerative medicine, 197
Repeat nanocasting, 104–105,
107, 115
Ruthenium oxide (RuO₂), 284
SBA-15, 60, 64–65, 67, 69–84,
86–91, 94–109, 113
SBA-16, 64–66, 69–70, 91
Scylloinositol, 297, 300, 334
Sea-cucumber-like hollow
 polyaniline spheres, 21–30
Selected area electron patterns
 (SAED), TiO₂, 6–7
SEM images, 466
Semiconducting nanocomposites,
44–48
Sensor, 127–129, 135–139, 143,
146, 150, 161–163, 165,
168, 172, 174–176, 178
Separator, 286
SiCN, 111–112
Silicon,
 heterojunction, 257–258
 heterostructures, 220, 253–254,
256–257, 261–262
 multijunction, 258–260
Simultaneous/mutual
 method, 442–443
Single walled carbon nanotubes
 (SWCNTs), 284
Single-crystal, 61, 73
SiOC, 111–112
Slurry, 286
SnO₂, 77–78, 102, 113
SNU-1, 89, 91
Sodium hydroxide, 285
Soft-templating, 60–61, 115
Solar cell, 137, 140, 143, 146, 147, 149,
151–153, 159–162, 164, 167,
168, 173, 174, 177, 178, 180
Solar energy,
 heterostructures, 219–220, 253
 nanocomposites, 241
Sol-Gel, 189
 applications, 194–195
 Sol-Gel processing, 189–194
Solid–liquid method, 63, 65
Solution and crystal engineering
 of perovskites,
 additives, 555, 556
 anti-solvent, 556–558
 solvents, 556, 557
Solvent evaporation, 63, 73, 112
Specific capacitance, 291, 292
Specific surface area, 284
Spinel, 72, 74–76, 85–86
Spinel ferrite nanoparticles, 199–200
Sequential deposition of perovskites,
549–551, 557, 558
Staphylococcus aureus (*S. Aureus*), 210
Stern layer, 405
Stimuli-responsive networks, 449–450
Supercapacitor (SCs),
 principle of, 402–409
Supercapacitors, 283, 284, 293
Supercapacitors (SCs),
 basics of, 402–404
 charge storage mechanism of,
404–409
 electric double-layer, 408
 electrode materials for, 407–409
Surface modification method,
65, 66, 76
Surface passivation of perovskites, 561
Surface plasmon resonance
 spectroscopy, 455
Swelling, 468
Swelling measurements, 455
Temperature- and pH-sensitive
 IPNs, 452–453
Ternary hybrid electrode, 421–423

- Thermal transition DSC and TGA, 456–457
- Thermogravimetric analysis (TGA), 202
- Thermotropic, 300, 334
- Thiolated chitosan, 500, 505
- TiN, 83
- Tin oxide, 138, 146, 161, 162, 168, 172, 174, 175, 176, 178
- TiO₂, 4, 5, 68, 71, 109, 110, 113, black TiO₂, 251
core-shell, 250–251
heterojunctions, 234–235, 238
heterostructure, 224, 231, 234
janus, 251
nanocomposites, 241–242, 245
nanotube arrays, 6–10
polymorphic, 236–237
quantum dot, 232
silicon, 219–220, 253–254
- Tissue engineering, 499–500, 504, 517
- Titanium Dioxide, 139, 140, 146, 162, 164, 173, 178
- Transmission electron microscopy (TEM), 283, 286, 287, 292
- Transition metal oxides, 284, 292
- Transmission electron microscopy, high resolution (HR) TEM, 6
- Triphenylene, 297, 300, 334–343, 345–350, 352, 354–358, 360
- Two-solvent, 63, 73
- Type of radiation, 435–436
- UF-MCN, 89, 91
- Ultra sonication, 285
- Ultrasonic generation, 134
- Vacuum deposition of perovskites, 553–555
- Vapor assisted solution process of perovskites, 551
- Volatile organic compounds (VOCs), 21, 36
- Wet chemical synthesis, 283, 284, 292
- WO₃, 69, 77
- Wound dressing/healing, 493, 495, 501, 504, 515
- X ray diffraction (XRD), 283, 286, 287
- X ray photoelectron spectroscopy (XPS), 283, 286, 292
- X-Ray and gamma-rays, 436–437
- X-ray diffraction (XRD), 206
full width at half maximum (FWHM), 207
- Y(NO₃)₃, 84
- YPO₄, 84, 114
- Zinc Oxide, 141, 147, 164, 168, 174, 176, 179
- ZLI-4792, 359
- ZnO,
morphological properties, 17–18
nanobelts (NBs), 11
nanorods, detection of ethanolamine chemical, 17–21
nanorods, detection of p-Nitrophenylamine, 10–16
nanostructures (NRs), 11–17
nanotubes (NTs), 17–21
nanowires (NWs), 11
- ZrO₂, 71, 78, 85, 109, 110, 113

Also of Interest

Check out these published volumes in the Advanced Materials Series

Advanced Theranostics Materials

Edited by Ashutosh Tiwari and Jeong-Woo Choi
Forthcoming 2015. ISBN: 978-1-118-99829-8

Advanced Functional Materials

Edited by Ashutosh Tiwari and Lokman Uzun
Published 2015. ISBN 978-1-118-99827-4

Advanced Catalytic Materials

Edited by Ashutosh Tiwari and Salam Titinchi
Published 2015. ISBN 978-1-118-99828-1

Graphene Materials

Fundamentals and Emerging Applications

Edited by Ashutosh Tiwari and Mikael Syväjärvi
Published 2015. ISBN 978-1-118-99837-3

DNA Engineered Noble Metal Nanoparticles

Fundamentals and State-of-the-art-of Nanobiotechnology

By Ignác Capek
Published 2015. ISBN 978-1-118-07214-1

Advanced Electrical and Electronics Materials

Process and Applications

By K.M. Gupta and Nishu Gupta
Published 2015. ISBN: 978-1-118-99835-9

Advanced Materials for Agriculture, Food and Environmental Safety

Edited by Ashutosh Tiwari and Mikael Syväjärvi
Published 2014. ISBN: 978-1-118-77343-7

Advanced Biomaterials and Biodevices

Edited by Ashutosh Tiwari and Anis N. Nordin

Published 2014. ISBN 978-1-118-77363-5

Biosensors Nanotechnology

Edited by Ashutosh Tiwari and Anthony P. F. Turner

Published 2014. ISBN 978-1-118-77351-2

Advanced Sensor and Detection Materials

Edited by Ashutosh Tiwari and Mustafa M. Demir

Published 2014. ISBN 978-1-118-77348-2

Advanced Healthcare Materials

Edited by Ashutosh Tiwari

Published 2014. ISBN 978-1-118-77359-8

Advanced Energy Materials

Edited by Ashutosh Tiwari and Sergiy Valyukh

Published 2014. ISBN 978-1-118-68629-4

Advanced Carbon Materials and Technology

Edited by Ashutosh Tiwari and S.K. Shukla

Published 2014. ISBN 978-1-118-68623-2

Responsive Materials and Methods

State-of-the-Art Stimuli-Responsive Materials and Their Applications

Edited by Ashutosh Tiwari and Hisatoshi Kobayashi

Published 2013. ISBN 978-1-118-68622-5

Other Scrivener books edited by Ashutosh Tiwari

Nanomaterials in Drug Delivery, Imaging, and Tissue Engineering

Edited by Ashutosh Tiwari and Atul Tiwari

Published 2013. ISBN 978-1-118-29032-3

Biomedical Materials and Diagnostic Devices

Edited by Ashutosh Tiwari, Murugan Ramalingam, Hisatoshi Kobayashi and Anthony P.F. Turner

Published 2012. ISBN 978-1-118-03014-1

**Intelligent Nanomaterials
Processes, Properties, and Applications**

Edited by Ashutosh Tiwari Ajay K. Mishra, Hisatoshi Kobayashi and
Anthony P.F. Turner

Published 2012. ISBN 978-0-470-93879-9

Integrated Biomaterials for Biomedical Technology

Edited by Murugan Ramalingam, Ashutosh Tiwari, Seeram Ramakrishna
and Hisatoshi Kobayashi

Published 2012. ISBN 978-1-118-42385-1

WILEY END USER LICENSE AGREEMENT

Go to www.wiley.com/go/eula to access Wiley's ebook EULA.